

Coronal and Prominence Plasmas



(NASA-CI-2442)
PLASMAS (NASA)

CORONAL AND PROMINENCE
435 P CSCL 633

N87-20871
1880
N87-20845
010118

G3/92 45233

Held at Goddard Space Flight Center

April 9-11, 1985

April 8-10, 1986

NASA

Cover Photograph courtesy of
Mdm. M. J. Martre

Observatoire de Paris
Section de Meudon
France

A large prominence as it remained stable on the solar limb. It was stable like this for over a day before it erupted.

NASA Conference Publication 2442

Coronal and Prominence Plasmas

*Edited by
A. I. Poland
NASA Goddard Space Flight Center
Greenbelt, Maryland*

Proceedings of Workshops
Held at Goddard Space Flight Center
April 9-11, 1985
April 8-10, 1986



National Aeronautics
and Space Administration

**Scientific and Technical
Information Branch**

1986

TABLE OF CONTENTS

<u>INTRODUCTION</u>	(A.I. Poland).....	1
<u>ATTENDEES</u>	3
<u>INVITED TALKS</u>		
	Some Crucial Corona and Prominence Observations (E. Tandberg-Hanssen).....	5
	Heating of the Stellar Corona (E.N. Parker).....	9
<u>PROMINENCES</u>		
I. Formation		
	Chapter Review: Formation and Support of Prominences (T.G. Forbes).....	21
	Contributed Papers	
	1. The Growth of Radiative Filamentation Modes in Sheared Magnetic Fields (G. Van Hoven).....	27
	2. Can Prominences Form in Current Sheets? (J.M. Malherbe and T.G. Forbes).....	33
	3. Condensation Modes in Magnetized Plasmas (C.H. An).....	41
	4. Filament Formation Due to Photospheric Shear (S.T. Wu and Y.C. Xiao).....	47
	5. Formation of Active Region and Quiescent Prominence Magnetic Field Configurations (C.H. An, J.J. Bao, and S.T. Wu).....	51
	6. Numerical Simulations of a Siphon Mechanism for Quiescent Prominence Formation (A.I. Poland, J.T. Mariska, and J.A. Klimchuk).....	57
	7. Alfven-Wave Dissipation- A Support Mechanism For Quiescent Prominences (E. Jensen).....	63
	8. Static Current-Sheet Models of Quiescent Prominences (F.Wu and B.C. Low).....	69
	9. Recent Observations of the Formation of Filaments (S.F. Martin).....	73
	10. On the Formation of Active Region Prominences (H α Filaments) (B. Rompolt and T. Bogdan).....	81
II. Diagnostics and Structure		
	Chapter Review: Diagnostis and Structure (J.C. Vial).....	89
	Contributed Papers	
	1. Temperatures of Quiescent Prominences Measured From Hydrogen Paschen and CaII IR Lines (E. Engvold and N. Brynildsen).....	97
	2. Dark Filaments Observed at 8.3mm and 3.1mm Wavelengths (E. Hiei, M. Ishigura, T. Kosugi, and K. Shibasaki).....	109
	3. VLA Observations of Solar Filaments at 6 and 20 cm Wavelengths (M. Kundu).....	117
	4. The Microwave Structure of Quiescent Solar Filaments at High Resolution (D. Gary).....	121

5. Interpretation of the Prominence Differential Emission Measure for Three Geometries (E. Schmahl and F. Orrall).....	127
6. The Prominence-Corona Interface and Its Relationship to the Chromosphere-Corona Transition (D. Rabin).....	135
7. Thermal Stability Analysis of the Fine Structure of Solar Prominences (P. Demoulin, J.M. Malherbe, B. Schmieder, and M. Raadu).....	143
8. The Density and Thickness of Quiescent Prominences (T. Hirayama).....	149
9. Partical Redistribution Effects in the Formation of Hydrogen Lines in Quiescent Prominences (P. Heinzel, P. Gouttebroze, and J.C. Vial).....	155
10. Non-LTE Hydrogen-Line Formation in Moving Prominences (P. Heinzel and B. Rompolt).....	163
11. Vertical Motions in Quiescent Prominences Observed in the He I $\lambda 10830\text{\AA}$ Line (O. Engvold and S. Keil).....	169
12. Constraints on Filament Models Deduced From Dynamical Analysis (G. Simon, B. Schmieder, P. Demoulin, J.M. Malherbe, and A.I. Poland)....	177
13. CIV Doppler Shifts Observed in Active Region Filaments (J. Klimchuk).....	183
14. Searching the UVSP Database, and a List of Experiments Showing Mass Motions (W. Thompson)..	191
15. On the Existence of Oscillations in Solar Filaments Observed in H α and CIV Lines (B. Schmieder, J.M. Malherbe, P. Mein, and E. Tandberg-Hanssen).....	197
16. Measurements of Magnetic Fields in Solar Prominences (E. Landi Degl'Innocenti).....	203
17. Magnetic Field Vector and Electron Density Diagnostics from Linear Polarization Measurements in 14 Solar Prominences (V. Bommier).....	209

III. Disappearance

Chapter Review: Filament Disappearances (W. Wagner).....	215
Contributed Papers:	
1. The Heating of Filaments as a Disappearance Process (Z. Mouradian and M.J. Martres).....	221
2. On The Thermal Durability of Solar Prominences, or How to Evaporate a Prominence ? (J.M. Malherbe and T.G. Forbes).....	225
3. Filament Eruption Connected to Photospheric Activity (G. Simon, L. Gesztelyi, B. Schmieder, and N. Mein).....	229
4. Magnetic Field Re-Arrangement After Prominence Eruption (R. Kopp and G. Poletto).....	235
5. A Dynamic Model of Filament Eruptions and Two Ribbon Flares (N.P. Kuin and P. Martens).....	241

Corona

I. Large Scale Structure

Chapter Review: Large Scale Structure of the Corona (M. Kundu).....	249
Contributed Papers:	
1. Large Scale Structure of the Sun's Radio Corona (M. Kundu).....	253
2. Synoptic Study of the Corona at Meter Wavelength (P. Lantos and C. Alissandrakis).....	257
3. The White Light Corona and Photospheric Magnetic Fields (M. McCabe).....	263
4. Quasistatic Evolution of Magnetostatic Coronal Structures (R. Wolfson).....	269
5. Three-Dimensional Magnetostatic Models of the Large-Scale Corona (T. Bogdan and B.C. Low).....	275

II. Diagnostics

Chapter Review: Coronal Diagnostics (K. Lang).....	279
1. Three Dimensional Structures of Solar Active Regions (M. Kundu).....	291
2. High-Spatial-Resolution Microwave and Related Observations as Diagnostics of Coronal Loops (G. Holman).....	297
3. Theoretical Models of Free-Free Microwave Emission From Solar Magnetic Loops (J. Brosius and G. Holman).....	303
4. Coronal Plasmas on the Sun and Nearby Stars (K. Lang).....	309
5. Measurement of Coronal Fields Using Spatially Resolved Microwave Spectroscopy (G. Hurford and D. Gary).....	319
6. Guided MHD Waves as a Coronal Diagnostic Tool (B. Roberts).....	325

III. Small Scale Structure

Chapter Review: Small-Scale Coronal Structure (D. Webb)....	329
Contributed Papers:	
1. Simultaneous Observations of Changes in Coronal Bright Point Emission at the 20cm Radio and He λ 10830 Wavelengths (S. Habbal and K. Harvey)....	343
2. VLA Observations of Coronal Bright Points at 6 and 20cm Wavelengths (M. Kundu).....	349
3. Compact, Variable, Moving Sources Observed on The Sun at 2cm Wavelength (K. Lang and R. Willson)...	353
4. The Association of Chromospheric and Coronal Phenomena With The Evolution of The Quiet Sun (K. Harvey, F. Tang, and V. Gaizauskas).....	359
5. Magnetogram and Soft X-ray Comparisons of XBP and ER (L. Golub, K. Harvey, and D. Webb)....	365
6. Small-Scale Eruptive Filaments on the Quiet Sun (L. Hermans and S. Martin).....	369

7. Observations of the Ca II K Line In Hel0830A Dark Points on August 3, 1985 (R. Holt, A. Park, J. Thompson, and D. Mullan).....	377
8. Magnetic Location of CIV Events in the Quiet Network (J. Porter, E. Reichmann, R. Moore, and K. Harvey).....	383
9. A Numerical Study of the Thermal Stability of Low-Lying Coronal Loops (J. Klimchuk, S. Antiochos, and J. Mariska).....	389
10. Small-Scale Structures and the Density Irregularity of the Inner Corona (F. Orrall and G. Rottman).....	395
11. Phlegethon Flow - A Proposed Origin for Spicules and Coronal Heating (K. Schatten and H. Mayr).....	401

IV. Non-Equilibrium/Coronal Heating

Chapter Review: Energy Conversion in the Coronal Plasma (P. Martens).....	407
1. Topological Constraints and the Existence of Force-Free Fields (S. Antiochos).....	419
2. The Topological Description of Coronal Magnetic Fields (M. Berger).....	425
3. A Coordinate Free Description of Magnetohydrostatic Equilibria (P. Martens).....	431
4. Cascade Model of Coronal Heating (A. van Ballegooijen).....	439
5. Heating of the Solar Corona by the Resonant Absorption of Alfven Waves (J. Davila).....	445
6. Magnetic Helicity as a Constraint on Coronal Dissipation (A. Choudhuri).....	451
7. The Stability of Coronal and Prominence Magnetic Fields (A. Hood).....	457
8. Resistive Ballooning Modes in Line-Tied Coronal Arcades (M. Velli).....	461
9. Effects of Flows on Viscous and Resistive Magnetohydrodynamic Stability (G. Einaudi).....	465
10. Large-Scale Electric Fields Resulting From Magnetic Reconnection in the Corona (R. Kopp and G. Poletto).....	469
11. Dynamic Evolution of Coronal Magnetic Fields (R. Steinolfson).....	475

Introduction

The Coronal and Prominence Plasmas (CPP) workshop series was inspired by the repair of the Solar Maximum Mission (SMM) satellite in April, 1984. Since the operation period was to be closer to solar minimum, with the accompanying decrease in solar activity, the instruments could be productively used to study the solar corona and prominences. Although this would not be a new area for research with the instruments, a concerted effort in this area had not been accomplished during the early part of the mission.

The first meeting in the series was held in Hilo Hawaii, March 20 to 22, 1984, just before the SMM repair. At this meeting we discussed the types of problems we felt could and should be addressed by the SMM and complementary ground based instruments. Although the number of people attending this meeting was small (15), several good ideas were sent by people who were unable to attend. In particular the Meudon group (headed by Brigitte Schmieder and Guy Simon) had run several prominence related experiments during the early SMM mission and had prepared a number of research programs for the repaired mission. We, of course, also had many good ideas for coronal observations from the Mauna Loa (HAO) group and for prominence observations from the Haleakala (University of Hawaii) group.

With the successful repair of SMM and the commencement of new coronal and prominence observations, I approached the SMM principle investigators and requested their support in running a series of SMM workshops on Coronal and Prominence Plasmas. With their support we (Dick Fisher, Einar Tandberg-Hanssen, and me) organized a workshop at Airlie House in Warrenton Virginia, April 9 to 11, 1985. The purpose of this workshop was to define research topics that could be addressed during the next year and arrange collaborations to encourage their completion. Several SMM observing programs directed at solving unanswered questions were developed at this meeting.

One of the more exciting developments at the Airlie meeting was the discussion of equilibrium versus non-equilibrium processes in the corona and prominences. This discussion was initiated by B.C. Low, Piet Martens, and Dan Spicer. It was decided to hold a special submeeting on this topic on October 25 to 26, 1985 at Goddard Space Flight Center. This meeting was quite stimulating and revolved primarily around the topic of Parker's non-equilibrium heating theory for the corona.

The final meeting was held at the Woods Inn in Berkeley Springs West Virginia, April 8 to 10, 1986. The purpose of this meeting was to present the results of our work discussed at the previous meetings. Two invited talks were given: one by Einar Tandberg-Hanssen whose work on prominences over the past several years has stimulated many of us in our studies of these still incomprehensible phenomena; the other by Eugene Parker whose work on coronal theory has inspired much of the current work in this field. The majority of the meeting was devoted to the presentation of results and the open discussion of the ideas presented in the papers that appear in this proceedings. It is clear from these papers that we have learned much about how prominences and the corona work, but we still do not know what the dominant physical processes are.

The presentations in this proceedings are purposely different than articles presented in journals. I requested that the presentations be short, contain recent results obtained in research, reference previous relevant work for the interested reader, and give some idea as to what the author thinks might be fruitful areas for future studies. In short, I would hope that one could learn from reading this proceedings, where we are now and what looks

promising for the future in the study of coronal and prominence plasmas.

The organization of the proceedings is the same as the meetings. We first divided into large groups on the Corona and Prominences, and then further subdivided into topic groups. This allowed for a very informal forum for discussion and provided good opportunities for collaborative research. Each subgroup chose a leader, who organized the group's activities and wrote the summary for his group that appears in this proceedings.

Since reviews exist elsewhere in these proceedings I will not summarize any of the scientific discussions here. However, I would like to point out a few of the ideas discussed at the meeting that are particularly stimulating. The first is the role of dynamic processes in the corona and prominences. Even prominences, that appear to be stable on the sun for extended periods of time, have significant velocities and show dynamic characteristics in their small scale structure. Our understanding of the phenomena is dependent on our understanding of the dynamics. The second is that there are several viable theories for coronal heating, but each is in need of more development. The non-equilibrium theories seem particularly exciting but need to be made more quantitative. Finally, as these proceedings show, we have significantly improved our ability to use radio observations for diagnostics. This is particularly true with respect to the magnetic field, which seems to mediate most physical processes in the corona.

I am deeply indebted to many people for their help and inspiration in organizing this series of workshops. My co-organizers, Richard Fisher and Einar Tandberg-Hanssen provided inspiration and direction. I cannot say enough about their contributions so I will say no more. Others who provided significantly to the organization of the workshops were: Grant Athay, Joe Davila, Ernie Hildner, Gordon Holman, John Mariska, Brigitte Schmieder, Guy Simon, and Jean Claude Vial. I would also like to thank the SMM project scientists, Bruce Woodgate and Joe Gurman, and the SMM PI's, Ed Chupp, Brian Dennis, Robert MacQueen, Keith Strong, and Einar Tandberg-Hanssen for approving the financial support for these workshops. The source of these funds was NASA Headquarters through the SMM project.

Arthur I. Poland

WORKSHOP-PARTICIPANTS

<u>NAME</u>	<u>INSTITUTION</u>	<u>NAME</u>	<u>INSTITUTION</u>
Chang-Hyuk An	NASA/MSFC	M. Martres	Meudon
Spiro Antiochos	Naval Res. Lab.	Marie McCabe	U. of Hawaii
R. Grant Athay	HAO/NCAR	M. Melozzi	U. of Maryland
Jin-Jun Bao	U. of Alabama	Don Mickey	U. of Hawaii
Mitchell Berger	HAO/NCAR	Zadig Mouradian	Meudon
Tom Bogdan	HAO/NCAR	Richard Munro	HAO/NCAR
Veronique Bommier	Meudon	Frank Orrall	Univ. of Hawaii
Jeffrey Brosius	NASA/GSFC	Gene Parker	Univ. of Chicago
Arnab Chuidhuri	HAO/NCAR	Art Poland	NASA/GSFC
Joe Davila	NASA/GSFC	Giannina Poletto	Arcetri, Italy
Giorgio Einaudi	Piza Italy	Jason Porter	NASA/MSFC
Gordon Emslie	U. of Alabama	Doug Rabin	Nat. Solar Obs.
Oddbjorn Engvold	U. of Oslo	Bernie Roberts	U. of Iowa
Richard Fisher	HAO/NCAR	Kristi Rock	HAO/NCAR
Terry Forbes	U. of New Hampshire	Bogdan Rompolt	Wroclaw, Poland
Vic Gaizauskas	Herzberg Institute	Bob Rosner	Center for Astro.
Charles Garcia	HAO/NCAR	Aaert Schadee	Utrecht
Dale Gary	Caltech	Ed Schmahl	U. of Maryland
Tom Gergely	U. Maryland	Brigitte Schmieder	Meudon
Shadia Habbal	Cent for Astro.	Paul Seagraves	HAO/NCAR
Petr Heinzl	Ondrejov, Czechoslo	Ken Shatten	NASA/GSFC
Eijiro Hiei	Mitaka, Japan	Guy Simon	Meudon
Ernie Hildner	HAO/NCAR	Dan Spicer	NASA/GSFC
Tadashi Hirayama	Mitaka, Japan	Rich Steinolfson	U. of Texas
Gordon Holman	NASA/GSFC	Keith Strong	Lockheed
Alan Hood	St. Andrews, Scotland	Einar Tandberg-Hanssen	NASA/GSFC
Gordon Hurford	Caltech	Bill Thompson	NASA/GSFC
Eberhart Jensen	U. of Oslo	Kanaris Tsinganos	U. of Crete, Greece
Stuart Jordan	NASA/GSFC	Aad VanBallegooijen	Center for Astro.
James Klimchuck	NRL	Gerry Van Hoven	U. of Cal
Roger Kopp	Los Alamos	Marco Velli	St. Andrews U.
Paul Kuin	NASA/GSFC	Jean-Claud Vial	LPSP, France
Mukul Kundu	U. of Md.	Bill Wagner	NOAA Boulder
Egidio Landi	Arcetri, Italy	Dave Webb	ASE & Emmanuel Col
Don Landman	U. of Hawaii	Rich Wolfson	Middlebury College
Ken Lang	Tufts Univ.	Fei Wu	HAO/NCAR
Pierre Lantos	Meudon	S.T. Wu	U. of Ala.
Boon Chye Low	HAO/NCAR	Ying-cai Xiao	U. of Ala.
Jean Marie Malherbe	Meudon	Eric Yasukawa	HAO/NCAR
John Mariska	NRL	Jack Zirker	Sac. Peak Obs.
Piet Martens	NASA/GS	Ellen Zwiebel	U. of Colorado
Sara Martin	Caltech.		

SOME CRUCIAL CORONA AND PROMINENCE OBSERVATIONS

E. A. TANDBERG-HANSEN
SPACE SCIENCE LABORATORY
MARSHALL SPACE FLIGHT CENTER, AL 35812

A number of theories and hypotheses are currently being developed to explain the often complex behavior of corona and prominence plasmas, and later today Parker will discuss some of the theoretical implications relevant to the topic of this workshop. In order to test the theories and hypotheses certain crucial observations are necessary, and I shall in this talk examine some of these observations and draw a few conclusions.

To set the stage let me remind you that already two thousand years ago Plutarch commented on an observation of crucial importance for coronal research when he wrote about solar eclipses: "There always appears around the circumference of the moon some light that does not permit total darkness." It took a long time before the proper theoretical explanation of that light was given. In a more lighthearted way Hirayama (1985) refers to crucial observations when he comments in his excellent review of Prominence Observations "Prominences are fascinating objects, abundant in variety, beautiful, and above all mysterious."

Prominence - corona mass balance

Since it is difficult to quantify "fascinating," "beautiful," and "mysterious," I shall start by looking at the material involved in the corona and prominence plasmas. The mass of the corona is, to an order of magnitude, given by

$$M_{\text{cor}} \approx n_p m_p A H, \quad (1)$$

where A is the area of the solar surface (photosphere), $H \approx 10^{10}$ cm the coronal scale height, and n_p and m_p are the number density and mass respectively of hydrogen atoms. Eq. (1) gives, with $n_p = 3 \times 10^8 \text{ cm}^{-3}$, the mass of the corona

$$M_{\text{cor}} \approx 4 \times 10^{17} \text{ g}.$$

A large quiescent prominence has a volume of roughly $V = 5 \times 10^8 \text{ cm} \times 5 \times 10^9 \text{ cm} \times 4 \times 10^{10} \text{ cm} = 10^{29} \text{ cm}^3$, and therefore a mass, taking $n_p \approx 3 \times 10^{11} \text{ cm}^{-3}$,

$$M_{\text{prom}} \approx n_p m_p V \approx 5 \times 10^{16} \text{ g}. \quad (2)$$

Consequently we find that half a dozen or so large prominences are as massive as the whole corona. From this one concludes that either a cycling of mass must continually be going on or the material must - more likely - come from lower, denser regions of the atmosphere. In either case we arrive at our first crucial observational consequence: the dynamic nature of the corona and prominence plasmas. Static models will no longer do. To understand the formation of prominences and their interplay with the corona a holistic approach is necessary. Figure 1 shows a sketch of the corona observed at the Nov. 12, 1966, eclipse (Saito and Tandberg-Hanssen, 1973), and two large quiescent prominences, seen as dark filaments on the disk, are situated under the helmet streamer at positions dictated by the coronal structure. To explore this situation further, we must look at solar magnetic fields.

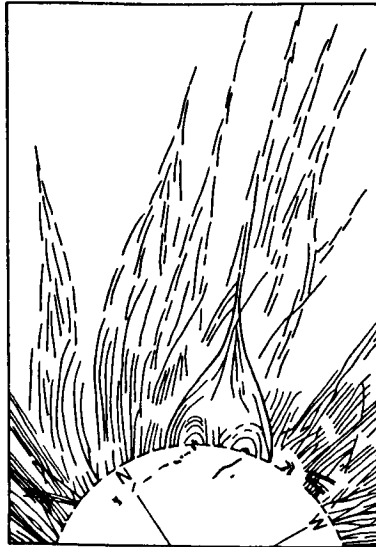


Figure 1

Corona and Prominence Classifications

We are so used to looking at the changing shape of the corona from solar maximum to solar minimum conditions that it is easy to forget the important message this change carries. The classification of coronal shapes, the observation of helmet streamers and the more recent information on coronal holes and the solar wind point all to the crucial importance of the magnetic field configuration. It is the magnetic field that completely determines the shape and behavior of the coronal plasma; we are in a low- β plasma, ($\beta \equiv 8\pi nkT/B^2$), and a theory that does not include this aspect cannot be complete.

On the other hand classification of prominences reveals a practical scheme as given in Table 1.

Table 1
Prominence Classification

Quiescent	occur in quiescent regions subset: eruptive	Associated with Corona
Active	Occur in active regions subset: sprays	Associated with Sunspots
Loops	Occur in active regions	Associated with corona and/or flares
Surges	Occur in active regions	Often associated with subflares

Examining pictures of some of these objects, like active, sunspot prominences or loops, we again cannot doubt the decisive influence of the magnetic field structure on these prominences

This structure also plays an important part in quiescent prominences, and measurements of prominence magnetic fields (e.g. Leroy et al 1984) are crucial in distinguishing between models of prominences (Malherbe et al 1983a), taking the dynamic nature of these objects into account (Malherbe et al 1983b).

Prominence formation and stability

Prominences can, theoretically, form either by ejection of matter from below or by condensation of matter from the corona. Surges and sprays from according to the former mechanism; coronal rain and postflare loops seem to owe their existence to the latter. In the case of quiescent prominences it is often assumed that they form by condensation of coronal matter, and even though this process may take place, we have seen above that it is difficult to account for the material needed for a big quiescent prominence by this mechanism. Rather, an ejection or a siphon-type mechanism probably supplies matter into a pre-existing magnetic structure capable of supporting the prominence Pikel'ner (1971). The very stable nature of many quiescent prominences is also due to the action of the magnetic field, i.e. to its loop-shaped structure. Observations leave little doubt that it also is the loop-shaped magnetic field that accounts for the shape and stability of phenomena like coronal arches, postflare loop prominences, sprays, and transition region loops. We therefore arrive at another crucial observational consequence: The ubiquity of the magnetic loop. Table 2 illustrates this phenomenon, and shows the importance of loop structures on nearly all observable lengthscales on the Sun.

Table 2

Loops - a basic structure in solar physics

- o Coronal arches - interconnect active regions
- o Coronal loops, hot ($> 10^6$ K), cool ($< 10^6$ K)
- o Flare loops - relationship to coronal loops?
- o Loop prominences = post-flare loops
- o Loop structures in quiescent prominences
- o Transition-region loops, high and low
- o Bright points (X-rays, UV) = small loops?

Eruptive Prominences-Coronal Mass Ejection

The last crucial observation I want to direct your attention to is the disappearance of prominences during flares and the correlated coronal response. It seems that only a holistic approach will suffice to let us properly explain this complicated flare manifestation. Borrowing from work by Moore et al (1986), we can ascertain that the prominence eruption and the accompanying coronal mass ejection both are caused by an underlying change in the magnetic field - a global instability of the field configuration in the region where the flare occurs - and are not caused by the energy release in the flare. Fig. 2 illustrates both the change in hard x-ray intensity, showing the impulsive phase of the flare, and the eruption of the H α prominence. We note that the eruption begins before the onset of the impulsive phase, probably caused by the same global instability in the magnetic field that also is responsible for the energy release that causes the flare.

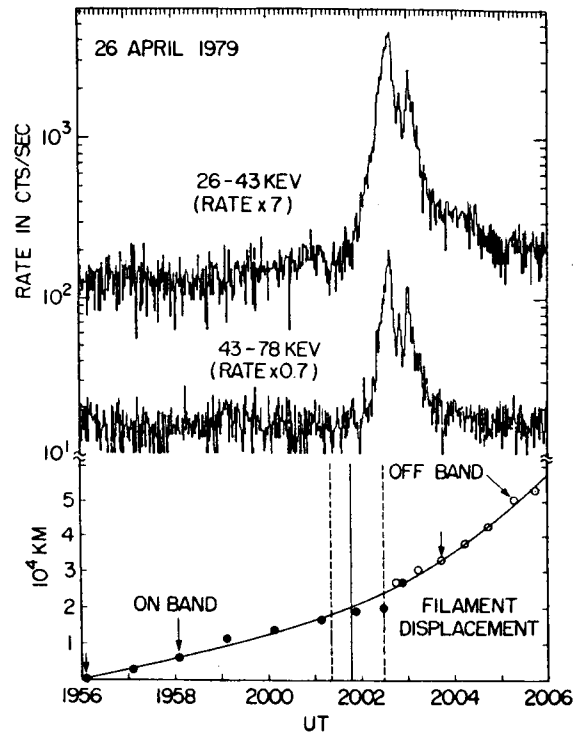


Figure 2

Other observations than the ones I have discussed may certainly be labeled crucial, and we are, for example interested in the diagnostic being discussed in Vial's and Lang's groups to furnish temperatures, densities, velocities etc. to properly model the observed prominences and coronal manifestations. However, the list of observations I have discussed and the preliminary conclusions drawn from them should form a basis from which we now can proceed to better explain the "fascinating" and "mysterious" objects that are among the topic of this workshop.

References

- Hirayama, T. 1985, *Solar Phys.* 100, 415.
 Leroy, J.L., Bommier, V., and Sahal-Brechot, S., 1984, *Astron. Astrophys.* 131, 33.
 Malherbe, J.M., Priest, E.R., Forbes, T.G., and Heyvaerts, J. 1983a *Astron. Astrophys.* 127, 153
 Malherbe J.M., Schmieder, B., Ribes, E., Mein, P., 1983b *Astron. Astrophys.* 119, 197.
 Moore, R.L., Kahler, S.W., Kane, S.R., and Zirin, H. 1986, *Bull. AAS* 18, No.2.
 Pikel'ner, S.B., 1971, *Solar Phys.* 17, 44
 Saito, K. and Tandberg-Hanssen, E. 1973, *Solar Phys.* 31, 105.

HEATING OF THE STELLAR CORONA

E.N. Parker
 Dept. of Physics
 Enrico Fermi Institute
 University of Chicago
 Chicago, Illinois 60637

INTRODUCTION

Coronal heating is the general cause of stellar X-ray emission, and it is also the cause of stellar mass loss in most stars. Hence a quantitative theory of coronal heating is an essential part of X-ray astronomy, and the development of a correct theory of coronal heating should be a primary concern of X-ray astronomers. The magnetohydrodynamical effects involved in coronal heating are not without interest in their own right, representing phenomena largely unknown in the terrestrial laboratory. Until these effects can be evaluated and assembled into a comprehensive theory of coronal heating for at least one star, the interpretation of the X-ray emissions of all stars is a phenomenological study at best, based on arbitrary organization and display of X-ray luminosity against bolometric luminosity, rotation rate, etc. The sun provides the one opportunity to pursue the exotic physical effects that combine to heat a stellar corona.

The hard work that has gone into studying the solar atmosphere and the solar photosphere over the past fifty years has finally, with the aid of modern technology, begun to get hold of the essential physical effects that cause the corona. A variety of theoretical effects have been proposed, many have been explored in some detail, and it is the purpose of this review to summarize the present state of development of the theory of coronal heating. The reader is also referred to other articles in these Proceedings which present quite recent results on additional effects not elaborated here.

To review the theoretical building blocks for coronal heating, the corona of the sun may be divided into two distinct states, representing qualitative differences in the magnetic field configuration. The active X-ray coronal regions are contained within strong closed (re-entrant) magnetic fields arching up from the surface of the sun (Vaiana, Krieger and Timothy, 1973). In contrast there are the coronal holes of low gas density to be found in regions of weak open field extending to infinity in the escaping solar wind (Altschuler, et al. 1972, Hundhausen, 1972; Krieger, Timothy and Roelof, 1973). There is, too, the so called 'quiet corona' to be found on the peripheries of the active regions and coronal holes. It is not entirely clear whether the quiet corona is best thought of as a weak form of active corona, or a nonexpanding coronal hole - probably the former.

The active corona and the coronal hole represent distinct coronal states that have little in common besides their high temperatures. The typical magnetic field strength in the active corona is of the order of 10^3 gauss, as opposed to 10 gauss in a coronal hole. The number density N in the active corona may be as high as 10^{10} atoms/cm³, as opposed to $N = 10^8$ atoms/cm³ in the coronal hole. It follows immediately that the active corona is the principal source of X-rays, while the coronal holes emit relatively little - so little that they appear as blank regions

in an X-ray photograph, from which they derive their name 'coronal hole.' The active X-ray corona has temperatures typically $2-3 \times 10^6$ K, with a sound speed of 250 km/sec, while a coronal hole has a temperature of $1.5-2 \times 10^6$ K and a sound speed of 200 km/sec (See Billings 1966; Kohl, et al. 1980, 1984; Withbroe et al. 1982a,b; Withbroe et al. 1985). The Alfvén speed V_A is about the same in both regions, of the order of 2000 km/sec, the lower field strength in the coronal hole compensated by the much lower gas density. The heat input is estimated (Withbroe and Noyes, 1977) to be $I = 10^7$ ergs/cm² sec to maintain the active corona, most of which is emitted as UV and X-rays. The heat input to coronal holes is of the order of $I = 10^6$ ergs/cm² sec, with most of it going into the expansion of the gas to produce the solar wind (Withbroe and Noyes, 1977). One of the more astonishing features of the active corona - beyond the fact that nature produces such a thing in the first place - is that the surface brightness of the active regions is approximately independent of the dimensions, from the small ephemeral active region with a characteristic scale $L = 10^4$ km to the large normal active region with a characteristic scale $L = 10^5$ km or more. Detailed studies of the active corona have shown that there is a close and detailed association between magnetic field strength B and heat input I (Rosner, Tucker and Vaiana, 1978; Golub et al. 1980). This immediately suggests the possibility that the active corona is heated by hydromagnetic waves, which propagate more copiously into the corona where the magnetic field is strongest. We examine this possibility first before considering the alternatives.

This is perhaps the appropriate place to note the extreme dynamical state of the solar corona. It is an atmosphere that would collapse in a matter of an hour if the heat supply were turned off. For instance, in the active corona the enthalpy density $\mathcal{E} = 5 NkT$ is about 14 ergs/cm³, with a characteristic pressure scale height $\Lambda = kT/\mu Mg = 10^{10}$ cm and a total thermal content, therefore, of the order of $\Lambda \mathcal{E} = 1.4 \times 10^{11}$ ergs/cm². The characteristic heating (and cooling) time $\tau = \Lambda \mathcal{E}/I$ is then 1.4×10^4 sec, or about four hours. The thermal capacity of the coronal hole is about a hundredth as great, so that the characteristic heating time is 1.4×10^3 sec, or 24 minutes! Hence the corona is sustained hour by hour by its heat source. The characteristic pass-through rate is enormous, with $\Lambda/\tau = 7$ km/sec in the active corona and 70 km/sec in the coronal hole.

WAVE HEATING IN THE ACTIVE CORONA

Consider how energy may be transported from the convective zone and deposited in the active corona by Alfvén waves, with all other modes dissipated in the chromosphere or refracted away from the vertical before reaching the corona (Leer, Holzer, and Fla, 1982; Hollweg, 1984). The interesting observational fact is that no Alfvén waves have been identified so far. The search for waves has produced only an upper limit on the rms fluid velocity $\langle v^2 \rangle^{1/2}$ in the line of sight based on the observed line widths and the expected thermal velocities. In the active corona the rms velocity in the line of sight is $\langle v^2 \rangle^{1/2} < 20$ km/sec (Beckers, 1976, 1978; Beckers and Schneeberger, 1977; Bruner, 1978, Cheng, Doschek and Feldman, 1979). At $r = 1.2 R_\odot$ in coronal holes the limit is apparently not much different (cf. Esser, et al, 1986). The maximum energy flux is $F = 2\rho \langle v^2 \rangle V_A$, achieved when all the waves are propagating in the same direction (presumably outward) along the magnetic field. The factor of two takes account of the two states of transverse polarization. With the numbers already quoted, then, the upper limit on F is 2.6×10^7 ergs/cm² sec. This is comfortably above the require

heat input of $I = 10^7$ ergs/cm² sec, until we come to the next question, viz. the dissipation of the waves.

Almost half of the upper limit F of the upward propagating waves must be dissipated to heat the active corona. But if half is dissipated, then half is not dissipated, and the surviving waves propagate around the magnetic field and down the other side where they contribute to the $\langle v^2 \rangle^{1/2}$ without contributing to the upward transport of energy. It is immediately obvious, then, that something over half of the wave energy must be dissipated in one pass around the arched magnetic field of the active corona. Roughly, the wave energy must decline by a factor of, say, four, so that the amplitude is down by half (Parker, 1983b, 1985a).

Oscillations at the surface of the sun are observed with periods of 100 sec, giving a wavelength of 2×10^5 km in the corona, where $V_A = 2 \times 10^3$ km/sec. The lengths of the lines of force above a normal active region are comparable to this wavelength, from which it follows that the wave must damp strongly in about one wavelength. Recalling that the same energy goes into an ephemeral active region with one tenth the dimensions, we are forced to postulate waves with periods of 10 sec, which damp equally effectively in one pass around the arched field of the ephemeral region. It is customary to make the best possible case for wave heating by assuming that $\langle v^2 \rangle^{1/2}$ is equal to the observational upper limit of about 20 km/sec. Note, then, that the requirement of damping Alfvén waves in approximately one wavelength cannot be accomplished by any conventional means. The waves are of small amplitude with $\Delta B/B = \langle v^2 \rangle^{1/2}/V_A = 10^{-2}$, so that nonlinear effects are negligible. Electron conduction velocities are of the order of a few km/sec at most, so that no anomalous resistivity is expected. Phase mixing has insufficient time to develop.

Hollweg (1984, 1986) has pointed out that the necessary conditions for dissipation are reminiscent of the breakup and dissipation of the eddies in classical hydrodynamic turbulence. Eddies with scale l and characteristic velocity v are broken up into smaller eddies in a time of the order of l/v . If we imagine then that the flux tubes (each attached to a separate fibril) oscillate independently where they are packed together in the corona, then there are velocity discontinuities between contiguous flux tubes. Such intense oscillating shears may be unstable, producing turbulence which cascades to smaller wavelengths and has the basic characteristics of classical turbulence. Hollweg refers to this theoretical possibility as the 'Kolmogoroff hypothesis' for the necessary dissipation to heat the active corona with waves. One needs, in addition to the 'Kolmogoroff hypothesis' a wave input spectrum at the photosphere extending with sufficient power to high frequencies (period of 10 sec or less). Very approximately, rms velocities of 0.4 km/sec are needed in each frequency interval. Indeed a very crude estimate can be made of the lower limit on the velocity amplitude in the photosphere necessary to produce a wave of given amplitude in the corona. The estimate is based on the fact that the amplitude of an Alfvén wave varies as $\rho^{-1/4}$ while propagating along a slowly varying magnetic field B in an infinitely conducting gas with slowly varying density ρ . If either ρ or B varies rapidly, there are reflections which reduce the transmitted waves. One could argue that resonances between reflection points might allow an accumulation of amplitude but that seems to be excluded in the present case by the necessary heavy damping. So it appears that $v \propto \rho^{-1/4}$ should give an upper limit to the wave amplitude in the corona for a given amplitude in the photosphere. The number density in the photosphere is of the order of 10^{17} atoms/cm³ and 10^{10} atoms/cm³ in the active corona,

so $\rho^{1/4}$ varies by about a factor of 50. Hence, an rms wave velocity of 20 km/sec in the corona requires an rms wave velocity of at least 0.4 km/sec in the photosphere in whatever frequency interval is appropriate for the scale (10^4 – 10^5 km) of the active region under consideration. And of course the inappropriate frequencies must not contribute much to the rms velocity in the active region or there cannot be enough energy transport within the overall observational upper limit of 20 km/sec. Hollweg estimates an rms photospheric velocity of about 1.2 km/sec over the entire range of frequencies would suffice. This translates into 60 km/sec in the corona unless one can think of a reason to exclude the frequencies inappropriate for heating the particular active region in mind.

TOPOLOGICAL DISSIPATION IN THE ACTIVE CORONA

There is a theoretical alternative to wave dissipation for heating the active corona, and that is the so called 'nonequilibrium' of a magnetic field in a highly conducting fluid when the footpoints of the field (at the boundary) are shuffled among each other in some random fashion, thereby randomly winding and wrapping the lines of force about each other in the corona above. It has come to be realized over the past two decades that the magnetostatic equilibrium of such fields involves internal tangential discontinuities, i.e. current sheets with the field direction changing by a finite amount across each discontinuity. The field is then in static equilibrium everywhere between the surfaces of discontinuity (Parker, 1972, 1979 pp. 359–391, 1981a,b, 1982, 1983a,b,c,d, 1985b, 1986; Yu, 1973; Tsinganos, 1982; Tsinganos, Distler and Rosner, 1984; Moffatt, 1985, 1986; Vainshtein and Parker, 1986 and references therein. Van Ballegooijen, 1985 maintains that discontinuities do not form).

There is a discontinuity in the direction of the field only in the limit of infinite electrical conductivity, of course. In any real situation, involving finite conductivity, finite ion cyclotron radius, etc. the 'discontinuity' has a finite thickness and the fluid within the finite thickness has no static equilibrium. The situation is the familiar neutral point nonequilibrium configuration in which the fluid is squeezed (by the pressure of the field on either side) away from the neutral point in the transverse component of the field (see discussion and sketches in Parker, 1979, pp. 392–439. See applications and references in Priest, 1981, 1982; Van Hoven, 1981; Parker, 1983d).

The point of interest for heating the active corona is that the neutral point nonequilibrium produces a current sheet that constantly grows thinner and more concentrated as the fluid squeezes out from between the opposite transverse fields on either side, so there is rapid dissipation no matter how small the electrical resistivity. As a matter of fact, the high electron conduction velocities within the current sheet may produce plasma turbulence and anomalous resistivity (cf. Drake, 1984 and references therein) and one expects the resistive tearing mode instabilities (cf. Steinolfson and Van Hoven, 1984; Horton, Tajima and Galvao, 1984 and references therein).

Suppose, then, that the turbulent convection beneath the photosphere causes the individual magnetic fibrils to wander at random among each other, taking steps of length λ at a velocity v . To keep the picture simple, suppose that λ is at least as large as the mean separation of independent fibrils. The magnetic flux tube extending up from each fibril becomes entwined among all the other tubes in complicated ways as the individual fibril wanders through the 'forest' composed of

all the others. The pathlength traversed by any one fibril after a time t is vt . Consider the simple situation where the lines of force are initially vertical and the far ends are fixed in a plane at a height L above the footpoints. It follows that the average line of force is deflected from the vertical by an angle θ , where $\tan \theta = vt/L$, after a time t . If the mean vertical field has an intensity B , the horizontal component is $B_{\perp} = B \tan \theta$. The inclined field trailing out behind the individual fibril pulls back on the fibril as the fibril wanders in and out among its neighbors. The mean force is $BB_{\perp}/4\pi$ dynes/cm², so that the rate at which the motion v does work on the field is (Parker, 1983b)

$$W = v BB_{\perp} / 4\pi$$

$$= (B^2/4\pi) v^2 t / L \text{ ergs/cm}^2 \text{ sec}$$

If we imagine that the random walk of the fibrils has a characteristic velocity v of 0.5 km/sec in an active region where $B = 10^2$ gauss, the energy requirement $W = 10^7$ ergs/cm² sec yields $B_{\perp} = 25$ gauss. That is to say, $B_{\perp} = B/4$ and $vt = L/4$. The lines of force are inclined on the average about 14° from the vertical. With $L = 10^5$ km for a normal active region a time $t = 5 \times 10^4$ sec (14 hours) is required to accumulate this degree of wrapping. The same state is reached in the ephemeral active region ($L = 10^4$ km) in about 1.4 hours. We suggest, that the neutral point reconnection, which is the principal (nonlinear) dissipation mechanism at the current sheets, becomes strong at this level of wrapping and destroys the current sheets as fast as they are created. Note that if the dissipation is less effective, the wrapping accumulates to higher levels and the energy input is greater.

HEATING CORONAL HOLES

The coronal hole, with its open magnetic field extending to 'infinity', presents quite a different problem from the active corona. There can be no significant wrapping and winding of the magnetic lines of force because the winding is propagated away to infinity at the Alfvén speed of 2000 km/sec. The only known mechanism for supplying the necessary 10^6 ergs/cm² sec (Withbroe and Noyes 1977) is Alfvén waves, with an rms velocity $\langle v^2 \rangle^{1/2}$ of about 35 km/sec in each direction transverse to the field $B = 10$ gauss. Using the simple relation that the wave amplitude varies as $\rho^{-1/4}$ during propagation from the photosphere into the corona, we find that $\rho^{-1/4}$ increases by a factor of 1.5×10^2 , so that $\langle v^2 \rangle^{1/2} = 35$ km/sec in the corona is associated with transverse motions of the order of 1/4 km/sec at the photospheric level.

The damping of Alfvén waves in a coronal hole is presumably a leisurely affair, occurring over distances of many solar radii. Waves with a period of 100 sec have wavelength $\lambda = 2 \times 10^5$ km, so that $10R_\odot$ (7×10^6 km) is equivalent to 35λ . Phase mixing increases the characteristic gradients in the wave to large values, and one may reasonably expect that a major portion of the wave energy is converted into heat (see discussion in Haeyverts and Priest, 1983; Nocera, Leroy, and Priest, 1984). Any wave motion that is not dissipated propagates out into the solar wind, where one sees Alfvén waves of large amplitude (Parker, 1965, 1966; Hundhausen, 1972; Terasawa et al. 1986; Hollweg, 1986 and references therein).

The acceleration of the solar wind in its relation to hydromagnetic wave transport of both energy and momentum has been treated by Leer, Holzer and Fla (1982). The

structure of the coronal hole has been studied with rocket observations of EUV (Orrall, Rottman, and Klimchuck, 1983 and references therein), and of La III out to about $4R_0$ (cf. Withbroe et al., 1982a,b, 1985; Esser et al., 1986) providing estimates of the kinetic temperature, the coronal expansion velocity and the residual $\langle v^2 \rangle^{1/2}$ that might be attributed to Alfvén waves (see also Hollweg, et al., 1982). On the basis of these works it appears that coronal holes are heated primarily by the dissipation of Alfvén waves introduced into the magnetic field by the granule motions at the photosphere. It is Alfvén waves, then, that supply the thermal energy that drives the solar wind and creates the heliosphere. The Alfvén waves that survive the dissipation to reach $r = 4R_0$ contribute their momentum to the solar wind, boosting the velocity of the high speed streams above that available from thermal expansion alone.

DISCUSSION

It is evident from the foregoing discussion that heating the active coronal regions presents a formidable theoretical problem. The observational upper limit of about 20 km/sec on the rms velocity in the active corona seriously constrains the theoretical options. Noting that $\langle v^2 \rangle^{1/2} = 15$ km/sec is required to carry in the necessary 10^7 ergs/cm² sec, there is little room left for reflected waves, etc. The damping must occur on the first pass around the coronal arch (see Hollweg, 1986). We are inclined to the view that the Alfvén waves are the primary source of energy input to the coronal hole, whereas in the active corona they contribute relatively little to the heating, with most of the heat input from the current sheets formed by the random walk of the footpoints of the field at the photosphere. The general occurrence of high speed micro-jets in the transition region shown by Deubner (these Proceedings) suggests neutral point reconnection at many small tangential discontinuities in the magnetic field throughout the active corona. But we do not feel that the issue is settled at this point in time. There are still too many unknown quantities. None of the theoretical ideas for heating either the active corona or the coronal holes is anything more than a sophisticated conjecture until additional theoretical possibilities have been explored and until observations establish the nature of the agitation of the field at the photosphere, and, hopefully, in the corona.

On the theoretical side, we should be aware that the coronal heating produced by spicules, and, indeed, the origin of the spicules has not been fully determined (see R. Kopp, these Proceedings). Hollweg's Kolmogoroff hypothesis needs careful consideration (see A. Van Ballegoijen, these Proceedings). The idea that there is strong wave resonance and intense dissipation in layers so thin as to escape observation (see Davila, these Proceedings) needs a careful evaluation, with particular attention to the strength of the waves within the resonant cavity compared to the waves presumed to drive the resonance by penetrating into the cavity from the outside. The question is, then, whether the scheme can be made to supply the 10^7 ergs/cm² sec without violating the observational upper limit of 20 km/sec.

A recent paper by Lee and Roberts (1986) explores the local transverse oscillations produced by the passage of Alfvén waves past a tangential discontinuity in the Alfvén speed V_A ($B \times \nabla V_A \neq 0$). Their calculations illustrate the possibilities for dissipation that may occur when Alfvén waves propagate along a field containing a number of tangential discontinuities in the field direction.

That is to say, the combination of waves plus discontinuities opens up the possibility of a wave contribution to heating the active corona that has not yet been properly assessed.

On the observational side, it is essential to determine the diameter, field strength, and internal structure of the individual magnetic fibrils at the photospheric level, and to determine the spacing and grouping of the individual fibrils, and their location in the granule and supergranule motions. Then, the individual and collective motions of the individual fibrils must be determined to show the form of the field distortions to be expected in the corona. In particular, the Fourier spectrum $F(\omega)$ and the random walk $F(0)$ of the individual fibrils in both active and quiet regions are essential input data, presently missing. We are all inclined to assume fibril motions of the order of 0.5 km/sec at our favorite frequency to evaluate the potential of various schemes for coronal heating. Sooner or later this 'not unreasonable' practice must be replaced by hard information from high resolution (0.1'') observations of the surface of the sun. An instrument comparable in performance to the late lamented SOT is an essential step in establishing the causes of the corona of the sun. And until that goal is achieved, stellar X-ray astronomy is mired in phenomenology, unable to advance to hard scientific interpretation.

This work was supported in part by the National Aeronautics and Space Administration under NASA Grant NGL-14-001-001.

REFERENCES

- Altschuler, M.D., Trotter, D.E., and Orrall, F.Q., 1972, Coronal Holes, Solar Phys., **26**, 354.
- Beckers, J.M., 1976, The Flux of Alfven Waves in Sunspots, Astrophys. J., **203**, 739.
- Beckers, J.M., 1978, Material Motions in Sunspot Umbrae, Astrophys. J., **213**, 900.
- Beckers, J.M. and Schneeberger, T.J., 1977, Alfven Waves in the Corona above Sunspots, Astrophys. J., **215**, 356.
- Billings, D.E., 1966, A Guide to the Solar Corona, Academic Press, New York.
- Bruner, E.C., 1978, Dynamics of the Solar Transition Zone, Astrophys. J., **226**, 1140.
- Cheng, C.C., Dorschek, G.A. and Feldman, U., 1979, The Dynamical Properties of the Solar Corona from Intensities and Line Widths of EUV Forbidden Lines of So VIII, Fe XI and Fe XII, Astrophys. J., **227**, 1037.
- Drake, J.F., 1984, Magnetic Reconnection and Anomalous Transport Processes, p. 61 in Magnetic Reconnection in Space and Laboratory Plasma, Geophysical Monograph No. 30, Washington, D.C., American Geophysical Union, ed. by E.W. Hones.
- Esser, R., Leer, E., Habal, S.R., and Withbroe, G.L., 1986, A two-fluid solar wind model with Alfven waves: Parameter study and application to observation, J. Geophys. Res., **91**, 2950.
- Golub, L., Maxson, C., Rosner, R., Serio, S. and Vaiana, G.S. 1980, Magnetic fields and coronal heating, Astrophys. J., **223**, 343.
- Hayvaerts, J. and Priest, E.R. 1983, Coronal heating and phase-mixed shear Alfven waves, Astron. Astrophys., **117**, 220.
- Hollweg, J.V. 1984, Resonances of coronal loops, Astrophys. J., **277**, 392.
- Hollweg, J.V. 1986, Transition region, corona, and solar wind in coronal holes, J. Geophys. Res., **91**, 4111.

- Hollweg, J.V., Bird, M.K., Volland, H., Edenhofer, P., Stelzried, C.T., and Seidel, B.L. 1982, Possible evidence of coronal Alfvén waves, J. Geophys. Res., **87**, 1.
- Horton, W., Tajima, T. and Galvao, R. 1984, Quasilinear evolution of tearing modes during magnetic reconnection, pp. 45-50 in Magnetic Reconnection in Space and Laboratory Plasmas, Geophysical Monograph No. 30, Washington, D.C., American Geophysical Union, ed. by E.W. Hones.
- Hundhausen, A.J. 1971, Coronal Expansion and Solar Wind, Berlin, Springer-Verlag, Chap. V.
- Kohl, J.L., Weiser, H., Withbroe, G.L., Noyes, R.W., Parkinson, W.H., Reeves, E.M., Munro, R.H. and MacQueen, R.M. 1980, Measurements of coronal kinetic temperatures from 1.5 to 3 solar radii, Astrophys. J. Letters, **241**, L117.
- Kohl, J.L., Weiser, H., Withbroe, G.L., Zapata, C.A. and Munro, R.H. 1984, Evidence for supersonic solar wind velocities at 2.1 RO, Bull. Am. Astron. Soc., **16**, 531.
- Krieger, A.S., Timothy, A.F. and Roelof, E.C. 1973, A coronal hole and its identification as the source of a high velocity solar wind stream, Solar Phys., **29**, 505.
- Lee, M.A. and Roberts, B. 1986, On the behavior of hydromagnetic surface waves, Astrophys. J. **301**, 430.
- Lee, E., Holzer, T.E. and Fla, T. 1982, Acceleration of the solar wind, Space Sci. Rev. **33**, 161.
- Moffatt, H.K. 1986a, Magnetostatic equilibria and analogous Euler flows of arbitrarily complex topology, J. Fluid Mech. **159**, 359.
- Moffatt, H.K. 1986b, Magnetostatic equilibria and analogous Euler flows of arbitrarily complex topology. Part 2. Stability considerations, J. Fluid Mech., in press.
- Nocera, L., Leroy, B. and Priest, E.R. 1984, Phase mixing of propagating Alfvén waves, Astron. Astrophys. **133**, 387.
- Orrall, F.Q., Rottman, G.J. and Klimchuk, J.A. 1983, Outflow from the Sun's polar corona, Astrophys. J. Letters **266**, L65.
- Parker, E.N. 1972, Topological dissipation and the small-scale fields in turbulent gases, Astrophys. J. **174**, 499.
- Parker, E.N. 1979, Cosmical Magnetic Fields, Oxford, Clarendon Press.
- Parker, E.N. 1981a, The dissipation of inhomogeneous magnetic fields and the problem of coronae. I. Dislocation and flattening of flux tubes, Astrophys. J. **244**, 631.
- Parker, E.N. 1981b, The dissipation of inhomogeneous fields and the problem of coronae. II The dynamics of dislocated flux tubes, Astrophys. J. **244**, 649.
- Parker, E.N. 1982, The rapid dissipation of magnetic fields in highly conducting fluids, Geophys. Astrophys. Fluid Dyn. **22**, 195.
- Parker, E.N. 1983a, Magnetic neutral sheets in evolving fields. I. General Theory, Astrophys. J. **264**, 635.
- Parker, E.N. 1983b, Magnetic neutral sheets in evolving fields. II. Formation of the solar corona, Astrophys. J. **264**, 642.
- Parker, E.N. 1983c, Absence of equilibrium among close-packed twisted flux tubes, Geophys. Astrophys. Fluid Dyn. **23**, 85.
- Parker, E.N. 1983d, The hydrodynamics of magnetic nonequilibrium, Geophys. Astrophys. Fluid Dyn. **24**, 79.
- Parker, E.N. 1985a, The magnetic structure of solar and stellar atmospheres, Proc. Workshop on Cool Stars, Santa Fe, N.M., Oct. 6-9, Ed. by M. Zeilik.

- Parker, E.N. 1985b, Equilibrium of magnetic fields with arbitrary interweaving of the lines of the force I. Discontinuities in the torsion, Geophys. Astrophys. Fluid Dyn. **34**, 243.
- Parker, E.N. 1986, Equilibrium of magnetic fields with arbitrary interweaving of the lines of force II. Discontinuities in the field, Geophys. Astrophys. Fluid Dyn. **35** (in press).
- Parker, E.N. 1965, Dynamical theory of the solar wind, Space Sci. Rev. **4**, 666.
- Parker, E.N. 1966, Dynamical properties of stellar coronas and stellar winds, V. stability and wave propagation, Astrophys. J. **143**, 32.
- Priest, E.R. 1981, Current sheets, Chap. 3 in Solar Flare Magnetohydrodynamics, New York, Gordon and Breach, ed. by E.R. Priest
- Priest, E.R. 1982, Solar Magnetohydrodynamics, Dordrecht, D. Reidel Publ. Co., pp. 345-381.
- Rosner, R., Tucker, W.H. and Vaiana, G.S. 1978, Dynamics of the quiescent solar corona, Astrophys. J. **220**, 643.
- Steinolfson, R.S. and Van Hoven, G. 1984, Fast spontaneous reconnection by the resistively coupled radiative instability, pp. 20-24, in Magnetic Reconnection in Space and Laboratory Plasmas, Geophysical Monograph No. 30, Washington, D.C., Am. Geophys. Union, ed. by E.W. Honer.
- Terasawa, T., Hoshino, M., Sakai, J.I. and Hada, T. 1986, Decay instability of the finite-amplitude circularly polarized Alfvén waves. A numerical simulation of stimulated Brillouin scattering, J. Geophys. Res. **91**, 4171.
- Tsinganos, K.C. 1982, Magnetohydrodynamic equilibrium IV. Nonequilibrium of non-symmetric hydrodynamic topologies, Astrophys. J. **259**, 832.
- Tsinganos, K.C., Distler, J. and Rosner, R. 1984, On the topological stability of magnetostatic equilibria, Astrophys. J. **278**, 409.
- Vaiana, G.S., Krieger, A.S. and Timothy, A.F. 1973, Identification and analysis of structures in the corona from X-ray photography, Solar Phys. **32**, 81.
- Vainshtein, S.I. and Parker, E.N. 1986, Magnetic nonequilibrium and current sheet formation, Astrophys. J. **304**, No. 2.
- Van Ballegoijen, A.A. 1985, Electric currents in the solar corona and the existence of magnetostatic equilibria, Astrophys. J. **298**, 421.
- Van Hoven, G. 1981, Simple loop flares: Magnetic instabilities, Chap. 4 in Solar Flare Magnetohydrodynamics, New York, Garden and Breach, ed. by E.R. Priest.
- Withbroe, G.L., Kohl, J.L., Weiser, H. and Munro, R.H. 1985, Coronal temperatures, heating, and energy flow in a polar region of the Sun at solar maximum, Astrophys. J. **297**, 324.
- Withbroe, G.L., Kohl, J.L., Weiser, H., Noci, G. and Munro, R.H. 1982a, Analysis of coronal H I Lyman alpha measurements from a rocket flight on 1979 April 13, Astrophys. J. **254**, 361.
- Withbroe, G.L., Kohl, J.L., Weiser, H. and Munro, R.H. 1982b, Probing the solar wind acceleration region using spectroscopic techniques, Space Sci. Rev. **33**, 17.
- Withbroe, G.L. and Noyes, R.W. 1977, Mass and energy flow in the solar chromosphere and corona, Annual Rev. Astron. Astrophys. **15**, 363.
- Yu, G. 1973, Hydrostatic equilibrium of hydromagnetic fields, Astrophys. J. **181**, 1003.

PROMINENCES

Prominence - February 22, 1974

PA(H)=128°

ORIGINAL PAGE IS
OF POOR QUALITY



Ca II K -0.15 Å

A



A-B (Velocity)

20 arc sec.



Ca II K +0.15 Å

B



A+B (Intensity)

Intensity and velocity of Prominences observed at Sac Peak Solar Observatory.

PRECEDING PAGE BLANK NOT FILMED

Photo Courtesy of

O. Engvold

Institute of Theoretical Physics University of Oslo, Blindern, Norway.

FORMATION AND SUPPORT OF PROMINENCES

T.G. Forbes

Space Science Center, Institute for the Study of Earth, Oceans,
and Space, University of New Hampshire, Durham, NH 03824

INTRODUCTION

This article is a short introduction to the concepts discussed by the group on the formation and support of prominences, and it is hoped that the reader will consult the individual contributions to obtain a more complete understanding. Only quiescent and long-lived active region prominences were considered, since transient prominence phenomena, such as sprays, surges, H α flare-loops, and coronal rain, are dynamically distinct from long-lived, prominences.

Stable prominences (which are often referred to as filaments when seen against the disk) can be subdivided into three categories, namely active region prominences, quiescent prominences and polar crown prominences. The third category is closely related to the second since a quiescent prominence will eventually evolve into a polar crown prominence if it lasts long enough. The distinction between the first and second categories is not sharp either since intermediates exist here as well (Martin, 1973).

SOME OBSERVATIONAL CONSTRAINTS

The mass contained in a typical quiescent prominence has been estimated to be $\gtrsim 5 \times 10^{16}$ gm - a value which is about 20% of the total mass of the corona (Tandberg-Hanssen, 1974). Although the density of the corona is often depleted in the vicinity of a quiescent prominence, the pre-existing mass of the depleted region (i.e. the coronal cavity) does not appear to be large enough to account for the mass of the prominence. Therefore, it has been inferred that for these prominences most of the mass is supplied by transport from the chromospheric level of the solar atmosphere.

The growth of a large prominence is thought to begin with the formation of a section on a time-scale of a few hours (see Figure 1a), and in the case of a quiescent prominence, several such sections may develop in a half a day or more. These sections are composed of fine-scale strands whose formation time is on the order of a few minutes, and whose behavior is chaotic.

Why sections exist is difficult to account for theoretically. One of the more physically attractive explanations that has been proposed is that they are due to the convection associated with the supergranulation cells. Plocieniak

and Rompolt (1972) found evidence that the "legs" of the sections tend to occur at the interstices of 3 or 4 cells where the circulation of the cells gathers the magnetic flux into a small region (cf. Figure 1b). In general it is very difficult to locate accurately the position of the section legs with respect to the supergranulation network, and so the correlation between the location of the legs and the network remains somewhat controversial. However, Plocieniak and Rompolt have suggested that some of this controversy may be due to the fact that

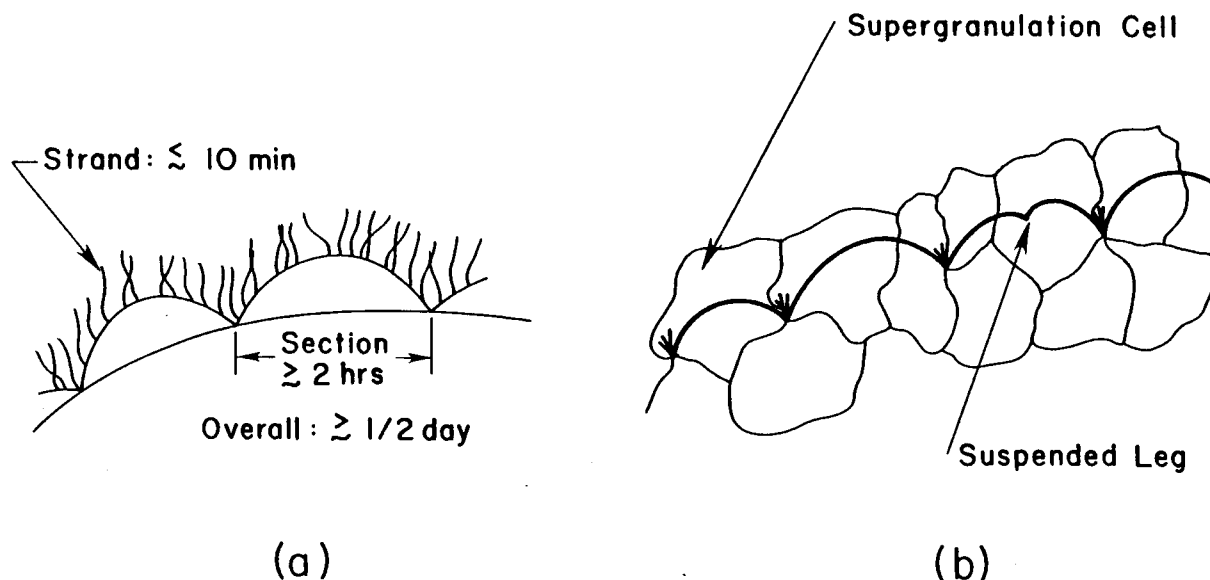


Figure 1. (a) Formation times of various prominence features. (b) Proposed location of prominence legs with respect to supergranulation cells.

sometimes legs occur at the center of a cell but do not extend all the way down into the chromosphere. They refer to these features as "suspended legs". In a separate study of the correlation between the photospheric magnetic field and the legs, Martin (1986) has found that the legs terminate at the chromosphere where underlying photospheric fields of opposite polarity move together and cancel. It has not yet been established whether these cancellation sites correspond to the interstices of the supergranulation cells, and so as yet there is no independent confirmation of the Plocieniak and Rompolt picture.

It is now fairly well accepted that shear in the chromospheric magnetic field is a prerequisite for prominence formation in active regions, and it seems likely that it may also be necessary for prominences in quiet regions (Martin 1973, 1986, Wu and Xiao 1986). About 10-30 minutes prior to the formation of a prominence, an alignment of fibrils is observed in the chromosphere. Such an alignment is referred to as a channel, and if it continues to exist after the disappearance of the prominence, the prominence will often reform in the same location (Martin 1973, 1986, Hagyard, 1986).

THEORETICAL MECHANISMS - MODELS

Our theoretical understanding of prominences is still in a relatively primitive state, and this is somewhat surprising when one considers that they have been observed for over 250 years. Perhaps, part of the explanation for this lies in the inherent difficulty of trying to create deductive models of plasmas. For example, in the MHD approximation, the number of degrees of freedom in a magnetized plasma is proportional to the cube of the magnetic Reynolds number, R_m (Parker, 1984). Typically, for a prominence in the corona $R_m \gtrsim 10^{12}$, and therefore, in the absence of any constraints, there are $\gtrsim 10^{36}$ possible states! This profusion of states underlies the basic difficulty that one has in trying to construct a quantitatively rigorous model upon the basis of a few observational constraints.

The theory of prominence formation involves several physical processes each of which alone are quite difficult to consider. The most important are thermal and gravitational stability, coronal wave-heating, anisotropic thermal conduction, radiation dynamics, and magnetic reconnection. The situation is complicated by the fact that all of these are highly nonlinear and interacting phenomena which must be considered within the context of a relatively unknown magnetic field geometry. To date theoretical efforts have been limited to exploring various aspects of one or more of the above processes within the context of highly idealized field geometries (such as a simple magnetic loop).

Possible mechanisms of prominence formation can roughly be divided into two categories, namely, condensation and injection. The first focuses on the formation of a cool dense plasma from a hot, ambient plasma, whereas the second is concerned with the transport of plasma from the chromosphere to the corona. Neither mechanism alone is likely to be sufficient, since the coronal plasma is not sufficient to supply the mass, and the direct injection of cold chromospheric plasma has never been observed.

Condensation Mechanisms

The classic study on condensation is the one by Field (1965), and much recent interest has focused on extending this work to include magnetic interaction aspects. Van Hoven (1986) has considered the thermal and condensation instabilities in the presence of an inhomogeneous, sheared magnetic field, and Malherbe and Forbes (1986) have numerically studied condensation in current sheets which are tearing unstable.

Injection Mechanisms

One can subdivide injection mechanisms into surge-like and evaporation-like models. In the first category material is launched ballistically from the chromosphere into the corona (cf. Figure 2b), whereas in the second a sustained heat release gives rise to a solar-wind-like evaporation (cf. Figure 2c).

For a surge-like injection one might reasonably assume an input injection velocity of 20 km/sec since this is a value characteristic of spicules.

However, with such a velocity one would only be able to ballistically lift material to a height of 4×10^3 km which is sufficient for some active region filaments but is too low for large quiescent prominences (An 1986, An et al. 1986). An interesting aspect of the surge-like models is that the input injection velocity must have a fairly precise value in order for material to be captured at the top of the loop. If the velocity is too small, or too large, then the injected material simply returns to the chromosphere. This might explain why prominences form on some loops but not on others.

An alternative to direct ballistic injection is a solar wind-like evaporation of chromospheric material (Poland et al., 1986). In this model an evaporative upflow of chromospheric material is produced by suppressing the coronal heating mechanism everywhere in the loop except at the foot points. This induces a condensation at the top of the loop, but the heating rate in the loop must be restored once the prominence has begun to form, otherwise realistic prominence densities can not be achieved in a reasonable time.

Support

Early models such as those of Kippenhahn and Schluter (1957) concentrated on the static support of the plasma by the magnetic field. Yet, H α films and

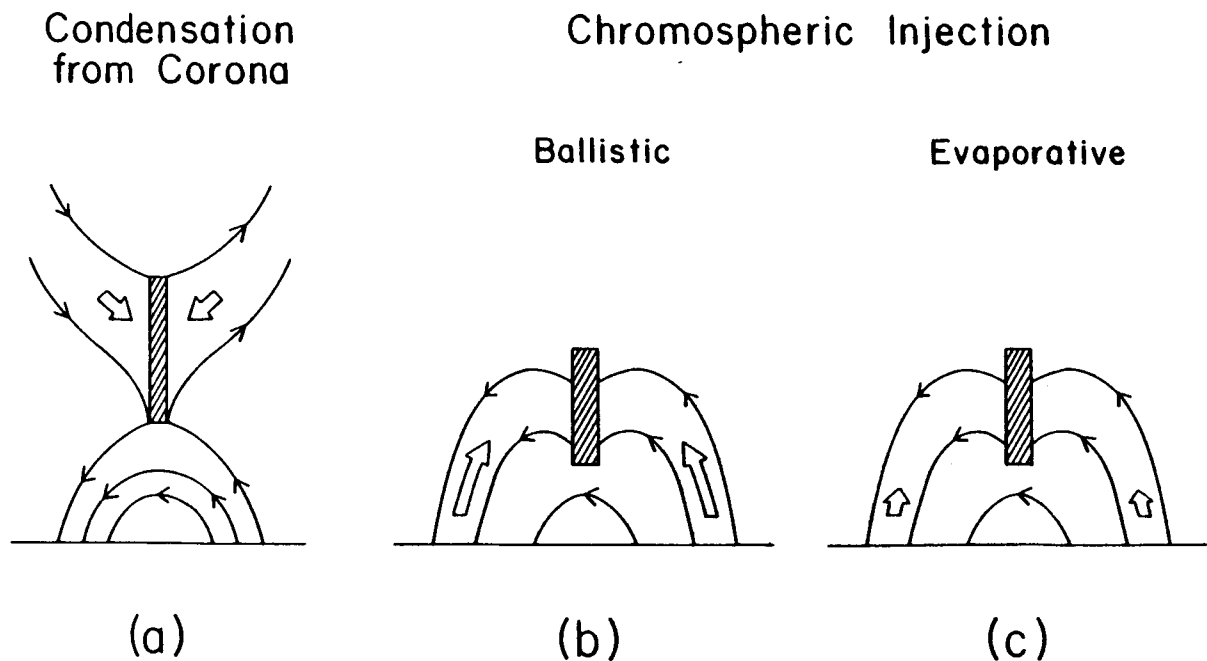


Figure 2. Schematic of three mechanisms involved in prominence formation: (a) condensation, (b) ballistic injection, and (c) evaporation.

direct measurements of Doppler shifts often indicate that even in quiescent prominences the plasma is not static, but is instead in continuous motion (Engvold et al, 1976; Schmieder et al., 1985). However, this motion is not simply due to free fall, and it is still necessary to invoke a force which opposes gravity. This has led to ideas for dynamic, non-static support. An early example of such a dynamic support mechanism is the one due to Kuperus and Raadu (1974) which incorporates reconnection (cf. Figure 2a). An alternate idea for dynamic support using Alfvén Waves has been proposed by Jensen (1986). The outward momentum flux of such waves is already thought to be important for the solar wind, and so he has suggested that it could also play a role in prominence support. This is an interesting idea, but it is not certain at the moment whether it can really account for the appearance of a quasi-steady-state structure like a prominence.

Interest in static support models continues since it is still possible that to first approximation one may be able to neglect flows and waves. Recent work for static support models has concentrated on trying to construct realistic three dimensional configurations (e.g. Wu and Low 1986, Wu and Xiao 1986).

SOME UNANSWERED QUESTIONS

Here are some questions concerning the problem of prominence formation and support, which, for the most part, have been around for 40 years or more. They are repeated here to emphasize that the prominence phenomenon is still very much an enigma.

1. Where does the prominence material originate - in the corona, the chromosphere, or both? If in the chromosphere, where exactly?
2. What is the three-dimensional magnetic field structure in and around the prominence before and after its appearance?
3. How is the prominence material supported against gravity? Is the support only partial or is it total as in a static situation?
4. To what extent does the physics of the coronal heating mechanism affect the appearance and dynamics of prominences?
5. What is the key photospheric factor that determines the location of a prominence? Is it the magnetic field, the velocity field, or both?
6. What physically distinguishes active region prominences from quiescent prominences? If it is simply the magnetic field strength, then exactly how does the variation in this quantity give rise to the quite different morphological properties of these two classes?

7. What is the role of sheared magnetic fields?

ACKNOWLEDGEMENT

This work was supported in part by NASA Grant NAGW-76 to the University of New Hampshire.

REFERENCES

- An, C.H. 1986 in this proceedings.
An, C.H., Bao, J.J. and Wu, S.T. 1986, in this proceedings.
Engvold, O., Malville, J.M., and Rustad, B.M. 1976, Solar Physics, 48, 137.
Field, G.B. 1965, Ap. J., 142, 531.
Forbes, T.G. and Malherbe, J.M. 1986 in Proceedings of the 1985 NSO/SMM Workshop on Low Temperature Phenomenon in Solar Flares, Sacramento Peak, in press.
Hagyard, M. 1986, Adv. Space Res., Proceedings of COSPAR XXVI, June 30-July 13, Toulouse, France, in press.
Jensen, E. 1986, in this volume.
Kippenhahn, R. and Schlüter, A. 1957, Z. Astrophys., 43, 36.
Kuperus, M. and Raadu, M.A. 1974, Astron. Astrophys., 31, 189.
Malherbe, J.M. and Forbes, T.G. 1986, in this proceedings.
Martin, S.F. 1973, Solar Phys., 31, 3.
Martin, S.F. 1986, in this proceedings.
Parker, E.N. 1984, in Magnetic Reconnection in Space and Laboratory Plasmas, ed. E.W. Hones, Jr., (Washington, D.C.: AGU), p. 32.
Plocieniak, S. and Rompolt, B. 1972, Solar Phys., 29, 399.
Poland, A.I., Mariska, J.T. and Klimchuk, J.A. 1986, in this proceedings.
Schmieder, B., Malherbe, J.M., Poland, A.I., and Simon, G. 1985, Astron. and Astrophys., 153, 64.
Tandberg-Hanssen, E. 1974, Solar Prominences, (Dordrecht: Reidel).
Van Hoven, G. 1986, in this proceedings.
Wu, F. and Low, B.C. 1986, in this proceedings.
Wu, S.T. and Xiao 1986, in this proceedings.

THE GROWTH OF RADIATIVE FILAMENTATION
MODES IN SHEARED MAGNETIC FIELDS

Gerard Van Hoven
Department of Physics
University of California
Irvine, CA 92717

ABSTRACT

Observations of prominences show them to require well-developed magnetic shear and to have complex small-scale structure. We show here that these features are reflected in the results of the theory of radiative condensation. We have studied, in particular, the influence of the nominally negligible contributions of perpendicular (to B) thermal conduction. We find a large number of unstable modes, with closely spaced growth rates. Their scale widths across B show a wide range of longitudinal and transverse sizes, ranging from much larger than to much smaller than the magnetic shear scale, the latter characterization applying particularly in the direction of shear variation.

INTRODUCTION

Coronal prominences owe their existence to a condensation process which occurs as a consequence of an instability in the thermal equilibrium of a diffuse medium (Parker, 1953; Field, 1965; Hildner, 1974). The condensation mechanism relies on optically thin radiation whose dependence on thermodynamic variables (e.g., density and temperature) is such that a cool, dense perturbation loses more energy through radiation than it gains through adiabatic and non-adiabatic heating processes and thermal conduction.

Prominences and filaments (as seen on the disk) in the solar atmosphere are often observed to form above a magnetic neutral (polarity-inversion) line in regions of increasing magnetic field shear as indicated by photospheric magnetograms (Martin, 1973; Leroy, 1978). Local heat conduction, which is strongly attenuated in directions perpendicular to the magnetic field, would dominate radiation and other forms of energy transport if no field were present, thereby suppressing the thermal instability. Thus, one can expect the equilibrium field structure to exert a strong influence over the formation of prominences.

These empirical and physical considerations have motivated previous computational studies of the dynamics of the thermal instability in a sheared magnetic field (Chiuderi and Van Hoven, 1979; Van Hoven and Mok, 1984; Van Hoven et al., 1984; Sparks and Van Hoven, 1985). One result of these theoretical studies is that a sheared background field is necessary for the existence of a true localized

condensation. Secondly, it is surprising that the width of the condensation in a direction perpendicular to the shear layer does not correspond to those points at which the magnetic field has tilted sufficiently that the radiation loss is roughly balanced by parallel thermal conduction, nor is it affected by realistic values of the perpendicular conductivity.

The present study is devoted to the delineation of some additional consequences of the presence of anisotropic thermal conduction in a sheared-field filament. One finds that new unstable excitations appear, with complicated transverse variations (multiple nodes), and that perpendicular conduction provides modes with shorter wavelengths and faster growth.

FORMULATION

To model a sheared, active-region, magnetic field, we use the planar force-free form $\mathbf{B}/B = F(y/a)\mathbf{e}_z + G(y/a)\mathbf{e}_x$ where $F(0) = 0$ and $F^2 + G^2 = 1$, which is consistent with uniform temperature (T) and density (ρ). [The example we use is $F(y/a) = \tanh y/a$.]

We describe the plasma dynamics by the compressible ideal MHD limit, and the energetics by the heat-transport equation (Chiuderi and Van Hoven, 1979)

$$\frac{dp}{dt} - \gamma p \nabla \cdot \mathbf{v} = (\gamma - 1) [H_0 - \rho^2 \Phi(T) + \nabla \cdot \mathbf{K} \cdot \nabla T] \quad (1)$$

which includes an unspecified (and unknown) constant heat input for thermal-equilibrium balance, optically thin radiation losses and anisotropic heat flow. If one considers $T(y, z, t) = T_0 + T_1(y) \exp(vt + ikz)$, one can linearize (1) as

$$\begin{aligned} \frac{\partial T_1}{\partial t} + (\gamma - 1) \frac{\partial \rho_1}{\partial t} = \Omega_\rho T_1 - \Omega_T \rho_1 \\ - [k^2 a^2 F^2 \Omega_{\parallel} + k^2 a^2 G^2 \Omega_{\perp} - \Omega_{\perp} (T_1''/T_1)] \end{aligned} \quad (2)$$

where T_1 and ρ_1 are fractional perturbations and $T_1' = a \partial T_1 / \partial y$. The heat-flow rates for the non-adiabatic terms on the right side of (2) include the radiation rate Ω at constant density and the generalized parallel-plus-perpendicular thermal conduction rate $\Omega_K \propto \kappa T_0 / a^2 p_0$ in the square bracket on the right.

When the two-dimensional dynamic equations are simplified, they reduce to the set of coupled equations (Van Hoven and Mok, 1984; Sparks and Van Hoven, 1985)

$$\begin{aligned} q'' - \alpha^2 F^2 (v^2 + \alpha^2) (v^2 + \alpha^2 F^2)^{-1} q - (\alpha^2 + \alpha_v^2) q = 0 \\ T_1 = [(\gamma - 1)v - \Omega_T] [v - \Omega_\rho + \Omega_K]^{-1} (\alpha_v^2 / v^2) q \end{aligned} \quad (3)$$

where $q = p_1 + \mathbf{B}_0 \cdot \mathbf{B}_1 / \mu_0$ is the total pressure perturbation. The normalized wave numbers are $\alpha \equiv \omega_0 / ka$ and

$$\alpha_v^2 \equiv v^4 (v - \Omega_p + \Omega_k)$$

$$\times [v^2 (v - \Omega_p + \Omega_k) + 1/2 \beta \gamma (v^2 + \alpha^2 F^2) (v - \Omega_p + \Omega_k / \gamma)]^{-1}$$

which depends implicitly on T_1''/T_1 (through Ω_k) when $\Omega_k \neq 0$ and provides the only energy-transport contribution to the q equation.

The solutions of equations (3), with boundary conditions requiring localization of the excitation near $y = 0$ and exponential decay as $y \rightarrow \pm \infty$, provide eigenfrequencies (growth rates) v which depend on ka , and eigenfunctions $T_1(y)$. Significant information about the allowable values of $v(ka)$, and about the structure of the eigenfunctions, can be obtained from the poles and zeros of α and from considering local solutions in a uniform field (Chiuderi and Van Hoven, 1979; Sparks and Van Hoven, 1985).

RESULTS

The simplest radiative-instability case to consider in a sheared field has $\Omega = 0$ so that radiation merely competes against adiabatic compression. The solutions of (3a) then provide a series of modes which have the essential characteristics of the solutions to more complete formulations. The modes exhibit increasing numbers of y -direction nodes, and growth rates approaching $\Omega = (\Omega_p + 1/2 \beta \gamma \Omega_p) / (1 + 1/2 \beta \gamma)$, the radiation rate for which perpendicular (to B) plasma motions occur at constant total pressure. In fact, these solutions have the typical property that the total-pressure perturbation q is much smaller than the thermal pressure p_1 , especially at shorter wavelengths (Sparks and Van Hoven, 1985).

The addition of the nominally dominant effects of parallel thermal conduction $\Omega_{||}$ does not change the situation very much. The principal modification is the introduction of a pole in α_v^2 , which prevents the existence of solutions at wavelengths shorter than the $s^2 = \infty$ curve of Fig. 1 (Chiuderi and Van Hoven, 1979).

It is necessary, finally, to add the effects of perpendicular thermal conduction Ω_{\perp} , which should not (a priori) be important, to be able to obtain a reasonably complete treatment of the structure and growth of these sheared-field radiative modes (Van Hoven and Mok, 1984; Van Hoven et al., 1986).

In order to see the important effects of Ω_{\perp} , I have shown a qualitative growth-rate curve in Fig. 1, which also displays the various instability rates identified by Field (1965). The behavior of the eigensolutions is different on the two sides of the curve $s^2 \equiv \alpha^2 + \alpha_v^2 (F=1, \Omega_{\perp}=0) \rightarrow \infty$ [or $\alpha = \alpha(v)$]. The growing modes on the lower left are variants of the original sheared-field modes found by Chiuderi and Van Hoven (1979). The addition of κ_{\perp} to the energy transport resolves the steep gradients of these solutions (Van Hoven and Mok, 1984) and allows them to have multiple radial nodes, within a width given by Eq. (18) of this earlier paper. It is somewhat unusual that the "fundamental" (no nodes) transverse-variation mode has the lowest growth rate. The practical consequence of this fact is unclear, however, since the growth-rate curves effectively lie on top of each other for typical solar coronal parameters.

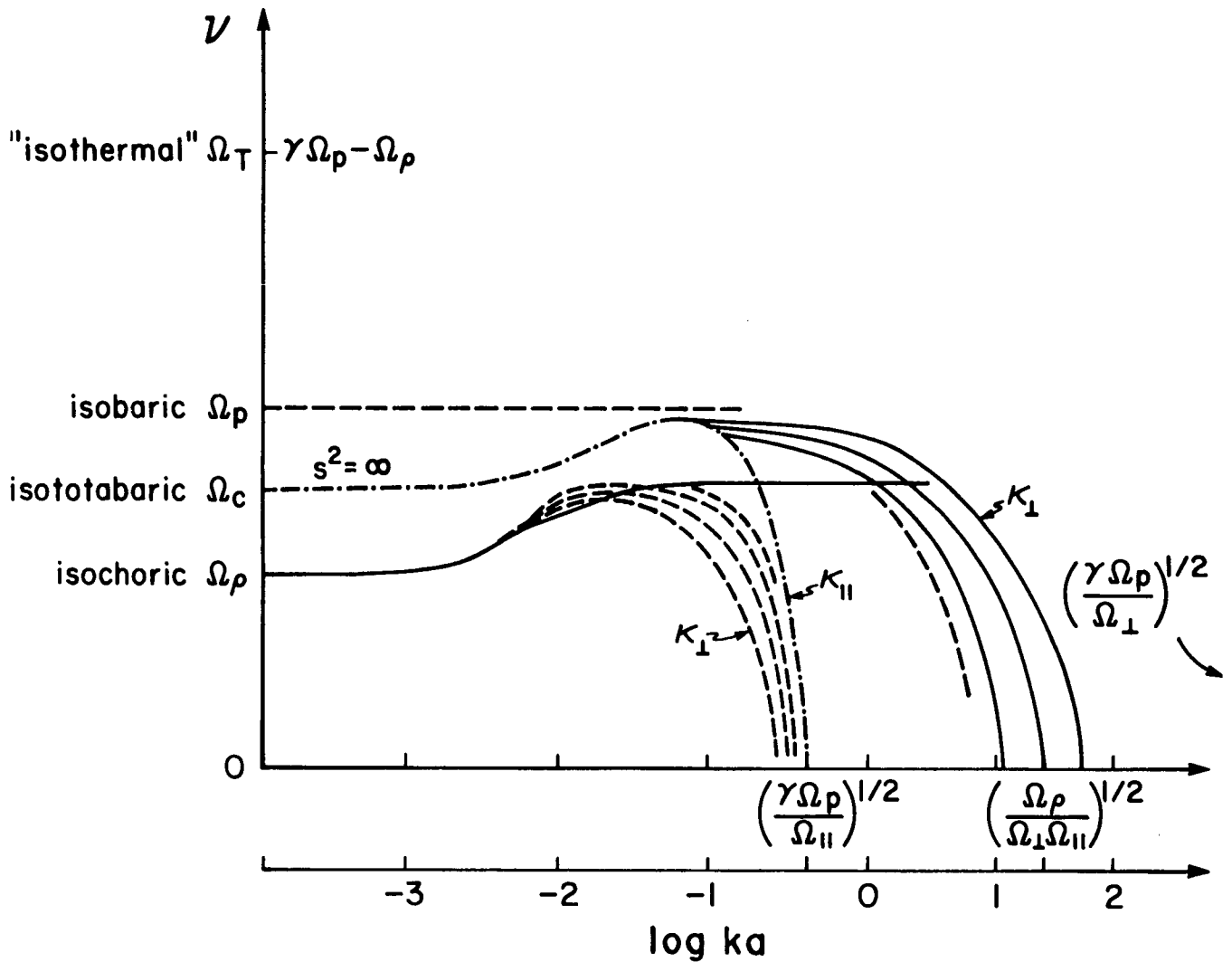


Figure 1. Radiative filamentation growth rates vs wavenumber.

The faster-growing, shorter-wavelength modes on the upper right in Fig. 1 only appear as a result of the presence of κ_{\perp} (Van Hoven, Sparks, and Tachi, 1986). [Small as this coefficient is ($\kappa_{\perp}/\kappa_{\parallel} \sim 10^{-10}$ in the corona), it resolves certain singularities which appear when $\kappa_{\parallel} \neq 0$.] For these modes, the fundamental is the fastest growing, although the inter-mode spacing near the peak is (again) negligible in practice. The transverse structure of these eigensolutions is unusual, for $\nu > \Omega_c$, in that the (negative) peak of the temperature perturbation is located away from the axis on each side (Van Hoven, Sparks, and Tachi, 1986). The inner and outer edges of the temperature peak(s) can be scaled from the equivalent of Fig. 1. One takes the α positions [$\alpha(\nu)$] of the $s^2 = \infty$ curve, at the relevant eigenvalue of $\nu(\alpha)$, divides it by $\alpha = ka$ and calculates $y/a = \tanh^{-1}(\alpha/\alpha_0)$. The resulting widths for reasonable parameters are $\sim 10^{-3}a$ (located at $\sim \pm 10^{-3}a$) for $\lambda/2 \sim 0.3a$, but one must remember that a number of modes grow at nearly the same rate. The outer edges of these modes, for which $\alpha_p^2 \approx \gamma(\Omega_p - \nu)/\Omega_{\parallel}$, exhibit the only direct dependence on the parallel conductivity.

DISCUSSION

The principal conclusion of our study of the linear eigensolutions of the radiative filament-condensation instability in a sheared magnetic field is that the theoretical results are nearly as complex as the observational results. The range of growth rates for the radiative instability is small, with $\Omega_p \sim 10^{-3} n_9 T_6^{-2} \lesssim \nu < \Omega_p = 1.8 \Omega_p$ for the usual estimate $\Phi(T) \propto T^{-1}$ (Hildner, 1974) at coronal temperatures $T \sim 10^6 T_6$ K and number densities $n \sim 10^9 n_9 \text{ cm}^{-3}$.

Not only is the range of growth rates narrow, but there are a large number of distinct eigenmodes within this range. There are two groups, one with wavelengths (the vertical width of the characteristic knife-blade form) greater than the magnetic shear scale, and the second with mainly shorter wavelengths. In most cases, there is an approximate balance between magnetic pressure increases and thermal pressure decreases.

These eigenmodes also exhibit a complex structure in the transverse direction, equivalent to the horizontal thickness of the knife-blade filament. The temperature (and density) profiles oscillate in this direction, with a number of nodes. The long wavelength modes are concentrated in the center of the shear layer, but the shorter modes often show a hollow profile with the coolest layers separated from the shear center. These latter excitations extend to the point where radiation is overtaken by parallel thermal conduction (which is relatively strong for short wavelengths).

We will not know which of these many excitations is (are) the dominant one(s) until we complete a series of nonlinear computations which are now in progress.

I wish to acknowledge the many contributions of Drs. L. Sparks and T. Tachi to this investigation. This work was supported, in part, by the National Science Foundation and by the National Aeronautics and Space Administration.

REFERENCES

- Chiuderi, C. and Van Hoven, G.: 1979, *Astrophys. J. Letts.* 232, L69.
Field, G. B.: 1965, *Astrophys. J.* 142, 531.
Hildner, E.: 1974, *Solar Phys.* 35, 123.
Leroy, J.-L.: 1978, *Astron. Astrophys.* 64, 247.
Martin, S. F.: 1973, *Solar Phys.* 31, 3.
Parker, E. N.: 1953, *Astrophys. J.* 117, 431.
Sparks, L. and Van Hoven, G.: 1985, *Solar Phys.* 97, 283.
Van Hoven, G. and Mok, Y.: 1984, *Astrophys. J.* 282, 267.
Van Hoven, G., Tachi, T., and Steinolfson, R. S.: 1984, *Astrophys. J.* 280, 391.
Van Hoven, G., Sparks, L., and Tachi, T.: 1986, *Astrophys. J.* 300, 249.

CAN PROMINENCES FORM IN CURRENT SHEETS ?

J. M. Malherbe

Observatoire de Paris - Section de Meudon
92195 - Meudon Principal Cedex, France

T. G. Forbes

Space Science Center, Institute for Study of Earths, Oceans
and Space, University of New Hampshire, Durham, N.H. 03824

ABSTRACT

Two-dimensional numerical simulations of the formation of cold condensations in a vertical current sheet have been performed using the radiative, resistive MHD equations with line-tied boundary conditions at one end of the sheet. Prominence-like condensations are observed to appear above and below an X-line produced by the onset of the tearing-mode instability. Cooling in the sheet is initiated by Ohmic decay, with the densest condensations occurring in the region downstream of a fast-mode shock. This shock, which is due to the line-tied boundary conditions, terminates one of the two supermagnetosonic reconnection jets that develop when the tearing is fully developed. This paper emphasizes the condensation properties of shock waves, which may trigger or considerably enhance the conditions for thermal condensations.

I. 2D NUMERICAL SIMULATION

The initial condition is a vertical current sheet in both mechanical and thermal equilibrium, and the half-width and the height of the sheet are 0.15 and 4.0 in units normalized to the horizontal size of the box. The sheet magnetic Reynolds number is 120; and the ratios of radiative, diffusive and tearing time scales to the Alfvénic one are 20, 120, and 11, respectively. A symmetry condition is used in the center of the sheet, free-floating boundary conditions are fixed at the top and the right edges of the box, and line-tying conditions are used at the base. The initial plasma β outside the current sheet is 0.1 (Forbes and Priest 1983, Malherbe et al. 1984, Forbes and Malherbe 1986a,b).

We now present an order of magnitude model to investigate the thermal effects of hydrodynamic shock waves and explain their condensing properties in the solar corona.

II. A SHOCK CONDENSATION MECHANISM FOR PROMINENCES

Consider a hot coronal equilibrium (subscript o quantities) described by:

$$0 = h\rho_o - \rho_o^2 Q(T_o), \quad (1)$$

where the wave heating term $h\rho_o$ balances the radiative loss term

ORIGINAL PAGE IS
OF POOR QUALITY

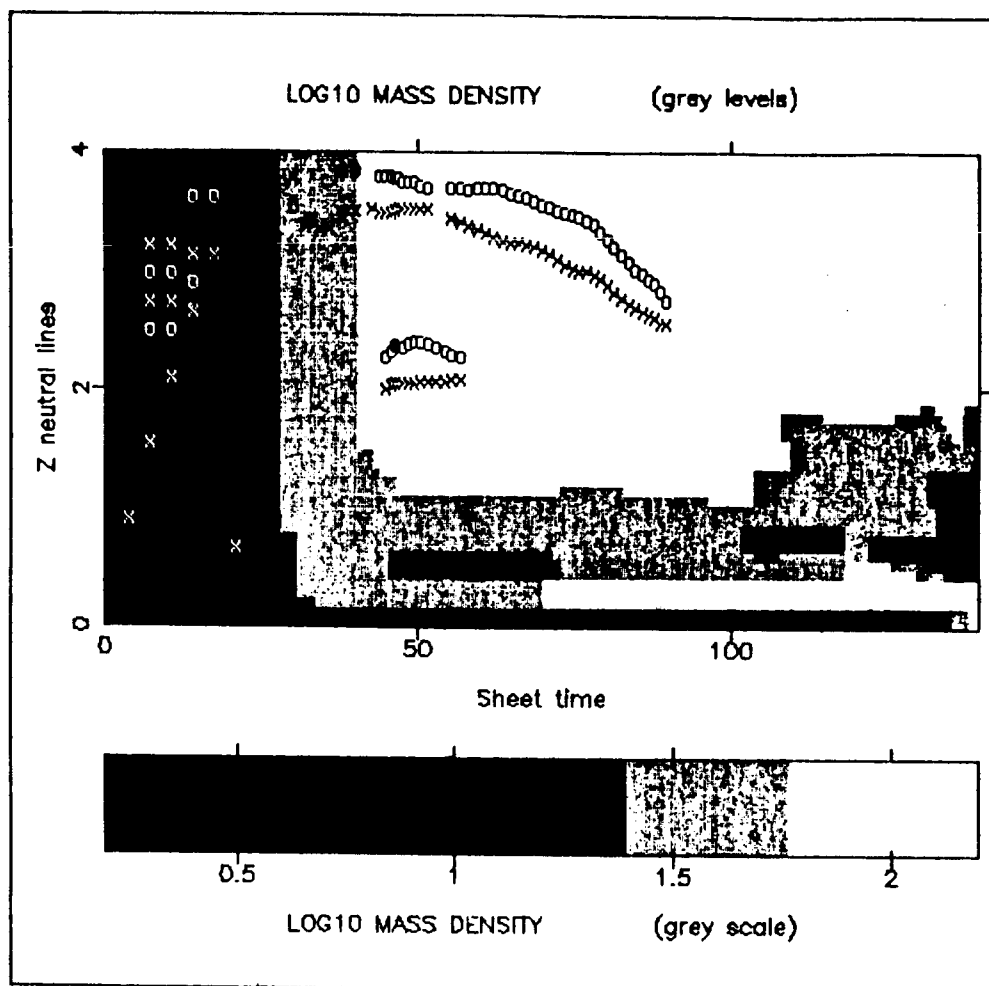


Figure 1. Time evolution of the mass density in the center of the sheet, together with locations of X and O magnetic lines. The time is in units normalized to the sheet Alfvénic time t_A . Two condensations separated by a more tenuous region appear.

$Q(T) = \chi T^\alpha$ given by Hildner (1974) as:

T(K)		χ (MKSA)	α
1.5×10^4 8×10^4 3×10^5	$T < 1.5 \times 10^4$	1.759×10^{-13}	7.4
	$T < 8 \times 10^4$	4.290×10^{10}	1.8
	$T < 3 \times 10^5$	2.860×10^{19}	0
	$T < 8 \times 10^5$	1.409×10^{33}	-2.5
	$T > 8 \times 10^5$	1.970×10^{24}	-1.0

ORIGINAL PAGE IS
OF POOR QUALITY

Now perturb this equilibrium at constant gas pressure, incorporating conduction

$$\rho C_p (\partial T / \partial t) = h_p - \rho^2 Q(T) + k_o T^{5/2} (T_c - T) / L^2, \quad (2)$$

$$\rho T = \text{constant}. \quad (3)$$

T_o is the hot initial temperature, k_o is a constant, and L is a typical thermal length-scale along a magnetic field line. Letting $u = (T - T_o) / T_o$, equations (1) to (3) reduce to

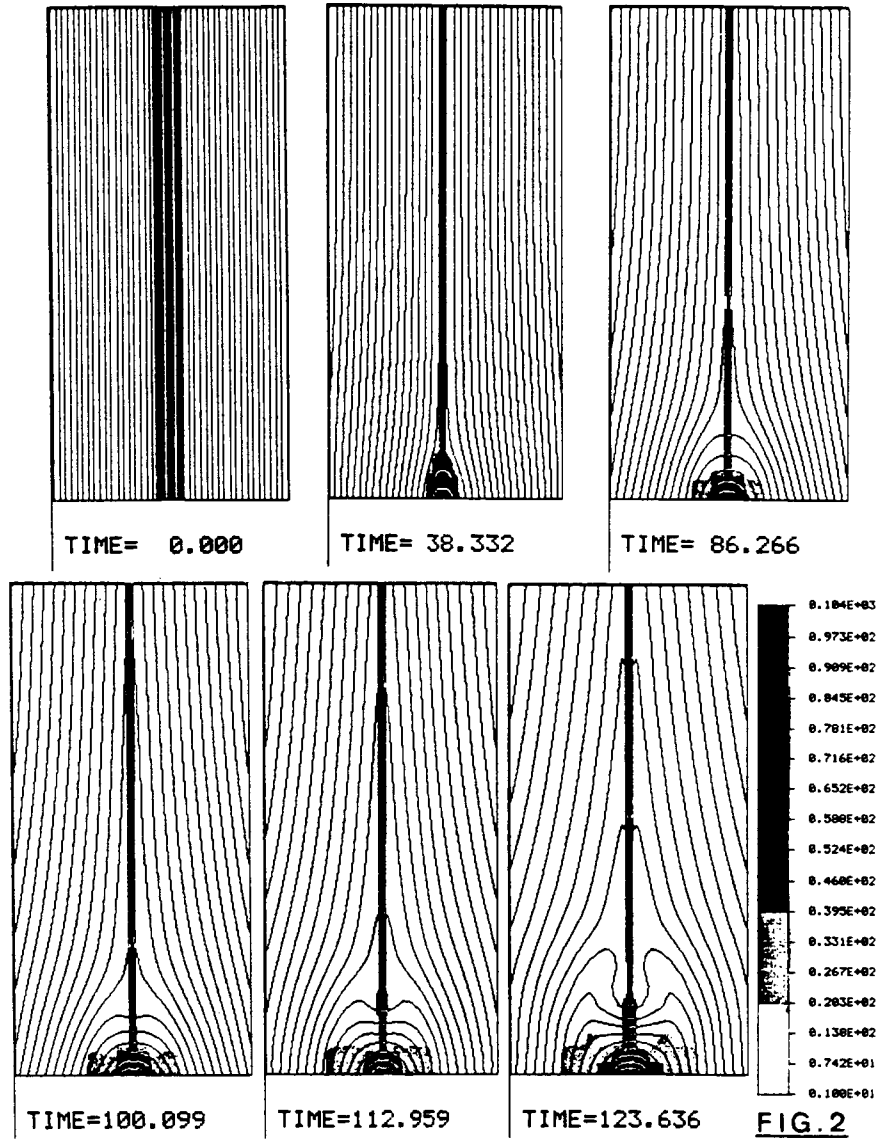


Figure 2. Magnetic field lines, together with the mass density (in grey levels) at different times. A strong condensation develops after $t = 100$ at the top of the closed reconnected region. The dip in field lines is not caused by gravity (which is not included in the code), but by the force of the supermagnetosonic jet issuing from the reconnection site above.

$$\partial u / \partial t = -u [\tau_c^{-1} - \tau_R^{-1} (1-\alpha)] = -u/\tau,$$

where $\tau_c = (\rho_o L^2 C_p) / (k_o T_o^{5/2})$ and $\tau_R = (T_o C_p) / [\rho_o Q(T_o)]$ are the conductive and radiative time-scales. The hot equilibrium is stable when

$$\tau^{-1} = \tau_c^{-1} - (1-\alpha) \tau_R^{-1}$$

With no conduction ($\tau_c = \infty$) this relation is always satisfied for $\alpha > 1$ or $T_o < 8 \times 10^4$ K. So a cold equilibrium is always stable and a hot one always unstable. With conduction, the equilibrium is stable when $\tau_R/\tau_c > 1-\alpha$ and this is always the case when $\alpha > 1$ (cold equilibrium). It may also be the case when $\alpha < 1$ (hot equilibrium), if the following inequality is satisfied:

$$L < L_c = [k_o T_o^{7/2}]^{1/2} [\rho_o^2 Q(T_o) (1-\alpha)]^{-1/2}.$$

If $L > L_c$, the hot equilibrium becomes unstable.

Suppose now that a fast-mode MHD shock occurs in the reconnection jet, and let us examine the quantities τ_R , τ_c , τ , and L , upstream (supersonic flow denoted by subscript u) and downstream (subsonic flow denoted by subscript d) of the shock. Because the magnetic field in the jet has almost been completely annihilated we can use the hydrodynamic jump relations. For a monatomic gas with $\gamma = 5/3$, these give

$$1 \leq \rho_d/\rho_u \leq 4.$$

Defining the compression factor across the shock as $\chi = \rho_d/\rho_u$, we have

$$V_u/V_d = \chi, \quad P_d/P_u = (4\chi-1)/(4-\chi), \quad T_u/T_d = \chi(4-\chi)/(4\chi-1).$$

From (4), we obtain

$$\begin{aligned} \tau_{Ru}/\tau_{Rd} &= \chi^{2-\alpha} [(4-\chi)/(4-1)]^{1-\alpha} \\ \tau_{cu}/\tau_{cd} &= \chi^{-7/2} [(4\chi-1)/(4-\chi)]^{5/2} \\ L_{cu}/L_{cd} &= \chi^{11/4-\alpha/2} [(4-\chi)/(4\chi-1)]^{7/4-\alpha/2}, \quad (\alpha < 1) \end{aligned}$$

At high temperatures ($T > 3 \times 10^5$ K, $\alpha < 0$) and in the absence of conduction, the shock decreases the radiative losses ($\tau_{Ru}/\tau_{Rd} < 1$). However, at lower temperatures ($T < 3 \times 10^5$ K, $\alpha \geq 0$), it increases the radiation losses, and the cooling time becomes faster.

When the temperature is high ($T > 3 \times 10^5$ K), the shock makes the triggering of a thermal instability more difficult in the presence of conduction (L_{cu}/L_{cd}). But, when $T \leq 2 \times 10^5$ K ($\alpha = 0.9$), it is possible to have a thermally stable upstream ($L < L_c$) and an unstable downstream ($L > L_c$). This is the case when $L_{cu}/L_{cd} > 1$ and when $L_{cd} < L < L_{cu}$. As one can see from Figure 3 this corresponds to a shock strength χ smaller than 2 when $\alpha = 0.9$. Hence, under certain conditions (e.g. transition zone like temperatures) the shock may trigger

a thermal condensation, when conduction is included in the set of equations. The shock always triggers a condensation in the absence of conduction if $\alpha < 1$. This result is similar to that deduced by Fisher (1986) from his numerical experiments.

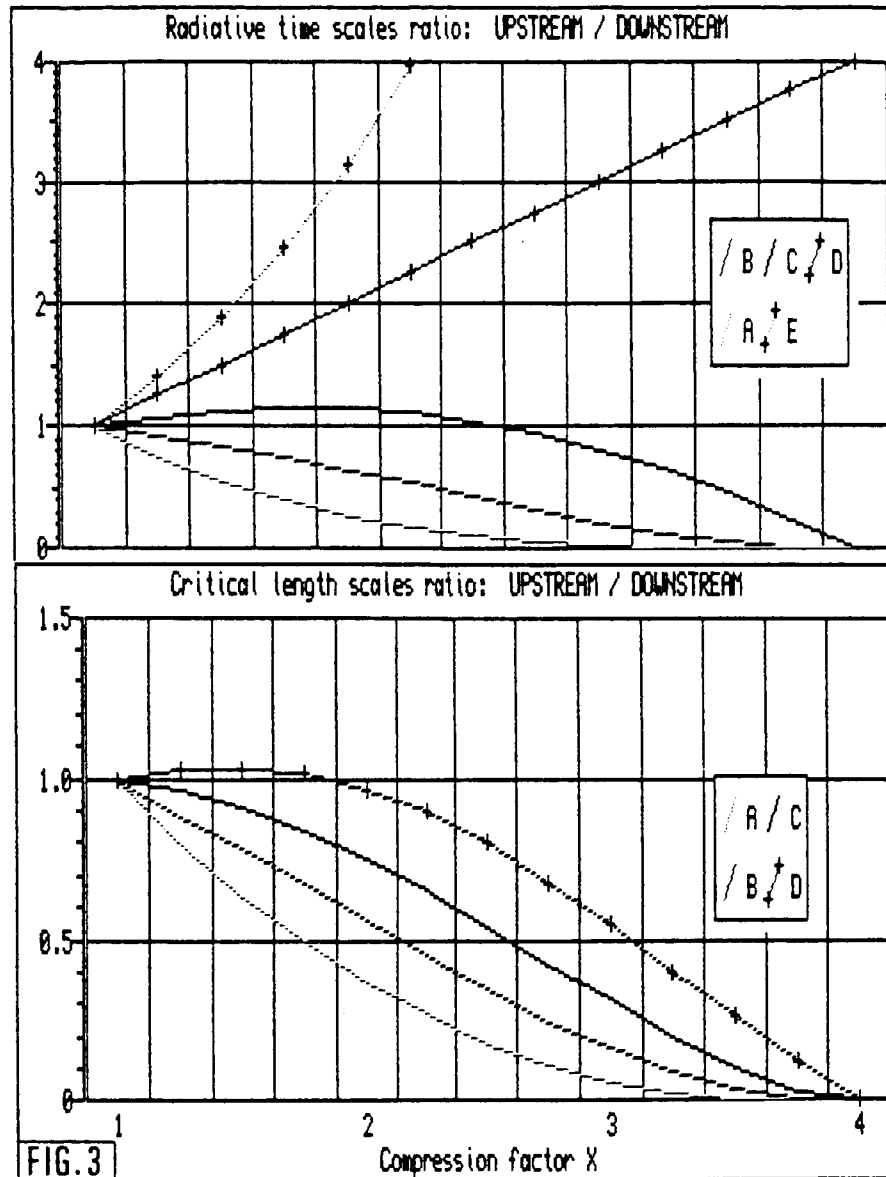


Figure 3, Top panel: The ratio τ_{Ru}/τ_{Rd} as a function of χ for different values of α (A: - 2.5, B: -1.0, C: 0.0, D: 1.0, E: 1.8), corresponding to different temperature ranges. Bottom panel: The ratio L_{Ru}/L_{Rd} as a function of χ for different α values (A: - 2.5, B: -1.0, C: 0.0, D: 0.9).

What is the effect of a shock at very low temperatures ($T < 8 \times 10^4$ K and $\alpha > 1$)? In this regime, a cold flow is always thermally stable and the ratio of cooling times τ_u/τ_d may be expressed as

$$\tau_u/\tau_d = (\tau_{Ru}/\tau_{Rd}) [(\tau_{Rd}/\tau_{cd}) - 1 + \alpha][(\tau_{Ru}/\tau_{cu}) - 1 + \alpha]^{-1}.$$

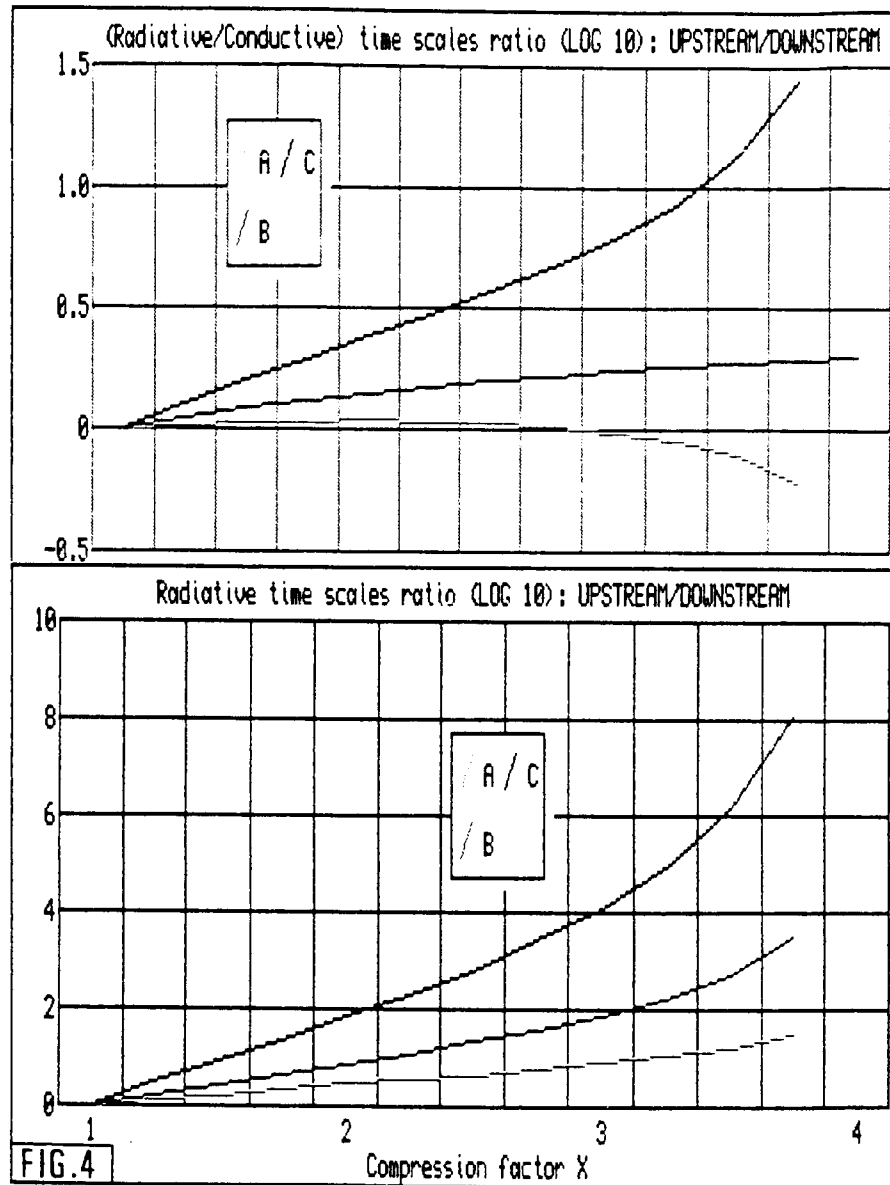


Figure 4. Top panel exhibits the quantity $\text{Log}_{10} [(\tau_{Ru}/\tau_{cu})/\tau_{Ru}/\tau_{cd}]$ as a function of X and α (A: 1.8, B: 3.5, C: 7.4). Lower panel represents the function $\text{Log}_{10} [\tau_{Ru}/\tau_{Rc}]$ for the same α values. The variations of the former quantity are almost negligible compared to the variations of the latter one, and consequently $\tau_u/\tau_d \approx \tau_{Ru}/\tau_{Rd}$. This ratio is much greater than 1, and shows that the presence of a shock at chromospheric like temperatures considerably enhances the radiative losses and the cooling time.

ACKNOWLEDGEMENTS

This work was supported by the Observatoire de Paris and by NASA Grant NAGW-76 and NSF Grant ATM-8507035 to the University of New Hampshire.

REFERENCES

- Fisher, G.H., 1986, in Radiation Hydrodynamics in Stars and Compact Objects, IAU Colloquium No. 89, in press.
- Forbes, T.G., Priest, E.R., 1983, Solar Phys., 84, 170.
- Forbes, T.G., Malherbe, J.M., 1986a, Ap. J. Letters, 302, L67.
- Forbes, T.G., Malherbe, J.M., 1986b, in The Lower Atmosphere of Solar Flares, ed. D.F. Neidig, (Sacramento Peak: National Solar Observatory), p 443.
- Hildner, E., 1974, Solar Phys., 35, 123.
- Malherbe, J.M., Forbes, T.G., and Priest, E.R. 1984, in the Hydromagnetics of the Sun, ESA SP-220, (Noordwijkerhout:ESA), p. 119.

CONDENSATION MODES IN MAGNETIZED PLASMAS

Chang-Hyuk An
NASA/Marshall Space Flight Center

ABSTRACT

I have studied condensation modes in magnetized cylindrical plasmas, concentrating on how magnetic field affects the stability. It is found that the effects of magnetic field (shear, twist, and strength) on the condensation modes are different depending on the wave vector. For modes whose wave vector is not perpendicular to magnetic field lines the plasma motion is mainly along the field lines; the effects of magnetic field on the modes are negligible except on the heat flow parallel to the field line. For a mode which is localized near a surface where the wave vector is perpendicular to the field line, the plasma moves perpendicular to the line carrying the field line into the condensed region; magnetic field affects the mode by building up magnetic pressure in the condensed region.

The stability of condensation modes strongly depends on how density and temperature vary with field twist. The stable nature of global quiescent prominence magnetic configurations implies that prominences form for low field twist for which ideal MHD modes are stable; plasma temperature should increase with field twist for stable prominence formation.

1. INTRODUCTION

Solar prominences are a very intriguing phenomenon. They are cool dense material imbedded in hot and tenuous coronal plasmas. After Field(1965) various authors(Nakagawa 1970; Hildner 1971; Heyvaerts 1974; Chiuderi and Van Hoven 1979) have studied condensation modes in a plane slab geometry to understand the prominence formation. I have studied the condensation modes(An 1984a, 1985) assuming that prominences are formed in a cylindrical magnetic geometry(Anzer and Tandberg-Hanssen 1970; Pneuman 1983). This magnetized cylindrical plasma is subject to ideal MHD as well as radiative(condensation) instabilities. For coronal conditions, the radiative time scale($\tau_r \sim 10^3$ sec.) is much longer than the MHD time scale($t_m \sim 1$ sec.), and condensation modes appear as a first order of $\epsilon = (t_m/\tau_r)^2 \sim 10^{-6}$ (An 1985). The possible coexistence of ideal MHD and condensation modes with very different time scales requires a careful analytic manipulation for the study of condensation modes. I developed a mathematical technique for the study(An 1985).

Questions about condensation modes in magnetized plasmas are how magnetic field (twist, shear, and strength) affects the modes and how the stability depends on different choice of temperature and density profiles. Here, magnetic shear arises from different field twist on each flux surface. Magnetic shear is an important stabilizing mechanism for ideal MHD instabilities and has been considered to be important for condensation modes(Chiuderi and Van Hoven 1979). I will show that magnetic structure (twist and shear) does not have important effects on condensation modes and will prove mathematically the insignificance of MHD effects on the modes for general magnetic field configurations. Since condensation modes are hydrodynamic in nature it is necessary to study the stability of an equilibrium with different temperature and density profiles for better

understanding the prominence formation and stability.

II. DERIVATION OF CONDENSATION MODE EQUATION

I assume that the plasma is governed by ideal MHD equation with radiation and heat conduction. The ambient heating rate is assumed constant in time and the optically thin radiative energy loss rate is used. Due to the two components of magnetic field (longitudinal B_z and poloidal B_θ), the field lines are twisted. Since MHD and radiative time scales are very different we make the governing equations dimensionless. Physical quantities, P , B , ρ , T are normalized with their standard values and time t is normalized by the radiative time scale t_r . Here radiative and MHD time scales are defined as $t_r = P_0/R$ and $t_m = \rho_0 a^2 / B_0^2$ respectively. The quantity ϵ is defined as $\epsilon = (t_m/t_r)^{1/2}$ which is much smaller than 1 for coronal plasmas. The quantities P_0 , ρ_0 , and B_0 are standard ambient coronal plasma pressure, density, and magnetic field and a is the radius of the cylinder cross section. H is the ambient heating and R is the radiative energy loss rate. β is defined as P_0/B_0^2 . I derive the linear stability equation by linearizing the governing equations and assuming that the perturbed quantities have the form $f(\vec{r}, t) = f(r) \exp[i(m\theta + kz) + \omega t]$. The second order differential equation for linear stability has the following form,

$$LX=0 \quad (1)$$

Here X is an eigenfunction and L is a second order differential operator and depends on ω , ϵ , and equilibrium quantities. The condensation mode equation can be derived, noting $\epsilon \ll 1$, by expanding L and X in power of ϵ and by taking zero and first order equations. The explicit expression of zero and first order equations are as follows.

$$\frac{d}{dr} \left[\frac{(k \cdot B_0)^2}{rK} \frac{dX_0}{dr} \right] - \left\{ \left[\frac{2mB_\theta(k \cdot B_0)}{r^3K} \right]' + \frac{1}{r} \left[(k \cdot B_0)^2 - 2B_\theta \left(\frac{B_\theta}{r} \right)' - \frac{4k^2 B_\theta^2}{r^2 K} \right] \right\} X_0 = 0. \quad (2)$$

$$L_0 X_1 + \left(\frac{X'_0 \rho_0}{rK} \right)' - \left[\frac{X_0 \rho_0 (\gamma - 1) dR/dr}{rK(\phi \rho_0 + \gamma P_0 \omega)} \right]' + X_0 \left\{ \frac{2kB_\theta(kB_\theta - mB_z/r)\rho_0[(\gamma - 1)/r]dR/dr}{rK(k \cdot B_0)^2(\phi \rho_0 + \gamma P_0 \omega)} - \frac{\rho_0(2kB_\theta)^2}{r^3 K(k \cdot B_0)^2} \right\} - \frac{\rho_0}{r} X_0 = 0. \quad (3)$$

Here $K = k^2 + m^2/r^2$ and $\phi = \frac{(\gamma - 1)T_0}{\rho_0} \left[\frac{3}{2} \left(\frac{\partial R}{\partial T} \right)_r + \frac{T_0^{5/2}}{B_0^2} \frac{t_r}{t_c} (k \cdot B_0)^2 \right]$
Prime(') denotes a derivative with r .

For the derivation of eq.(2) and (3) we assume that $\vec{k} \cdot \vec{B} \neq 0$ and $\phi \rho_0 + \gamma P_0 \omega = 0$ in the plasma. The condition $\vec{k} \cdot \vec{B} \neq 0$ means that the plasma should be stable to the ideal MHD mode. In order to study condensation modes, we have to solve equation (2) and (3) for a given boundary condition of X_0 and X_1 .

III. STABILITY

The effects of magnetic fields on condensation modes vary depending on whether $\vec{k} \cdot \vec{B}$ is zero or not in the plasma. Let us discuss how the magnetic field affects the mode of $\vec{k} \cdot \vec{B} = 0$. We cannot use Equ.(3) because it is derived assuming $\vec{k} \cdot \vec{B} \neq 0$ in the plasma. According to An(1984b,c) the eigenfunction of Equ(1) becomes localized near $r=r_s$ where $\vec{k} \cdot \vec{B} = 0$ as m and k go to infinity. In this limit the growth rate of the condensation mode is

$$\omega = -\left(\frac{\bar{Q}}{\bar{P}} + \frac{W}{Y\bar{P}}\right), \quad (4)$$

Here,

$$\begin{aligned} \bar{P} &= \rho_0(C_m^2 + C_s^2); \\ \bar{Q} &= \frac{(\gamma - 1)}{\gamma} C_s^2 \left[\left(\frac{C_m^2 \gamma}{C_s^2} + 1 \right) \left(\frac{\partial R}{\partial T} \right)_\rho - \frac{\rho}{T} \left(\frac{\partial R}{\partial \rho} \right)_T \right]; \\ W &= -\frac{2B_\theta^2}{r^2} (\gamma - 1) \beta \frac{dR}{dr} - \frac{C_m^2 C_s^2 (\gamma - 1)^2}{\gamma} \frac{4\rho_0 B_\theta^4}{\bar{P} r^3 B_0^2} \left(\frac{\partial R}{\partial T} \right)_s; \\ C_s^2 &= \beta \gamma P_0 / \rho_0, \quad C_m^2 = B_0^2 / \rho_0; \\ \left(\frac{\partial R}{\partial T} \right)_s &= \left(\frac{\partial R}{\partial T} \right)_\rho + \frac{\rho_0}{(\gamma - 1) T_0} \left(\frac{\partial R}{\partial \rho} \right)_T; \\ Y &= \frac{B_{0\theta}^2 B_{0z}^2 (q'/q)^2}{4r B_0^2} + \frac{2B_{0\theta}^2 \beta P_0}{r^2 B_0^2} + \frac{4B_{0\theta}^4 \beta_i P_0}{r^3 B_0^2 (B_0^2 + \beta_i P_0)}. \end{aligned}$$

The growth rate, Equ.(4), does not have a heat conduction term because the term appears with $\vec{k} \cdot \vec{B}$, which is zero at $r=r_s$. The local mode will stay unstable while other global modes are stabilized by heat conduction. Equ.(4) shows that magnetic field directly affects the stability. If $W < 0$, magnetic shear plays a stabilizing effect through Y which determines ideal MHD stability. As the magnetic field goes to infinity with plasma pressure fixed, ω becomes the isochoric mode growth rate; magnetic pressure does not allow plasma condensation.

For $\vec{k} \cdot \vec{B} \neq 0$, Equ.(3) can be used for condensation modes. I have studied the stability of two different equilibria with a longitudinal current density profile defined as $J_z(r) = J_0 (1 - r^2)^\alpha$. The magnitude of α determines magnetic shear; a higher value of α produces higher shear. Profile(A) has the density and temperature profiles defined as $\rho(r) = 1 + \delta_1(1 - r^2)$ and $T(r) = P(r) / \rho(r)$ respectively while profile (B) has $T(r) = 1 - \delta_2(1 - r^2)$ and $\rho(r) = P(r) / T(r)$. Since plasma pressure increases with field twist, $T(r)$ of (A) and $\rho(r)$ of (B) increase with the twist while $\rho(r)$ of (A) and $T(r)$ of (B) do not change. By solving Eqs (2) and (3) for different q we study the stability of condensation modes for profile (A) and (B). Here q_0 is $q(=2\pi B_z r / AB_\theta)$ at $r=0$ and A is an aspect ratio. q stands for the degree of field twist; higher q implies lower field twist.

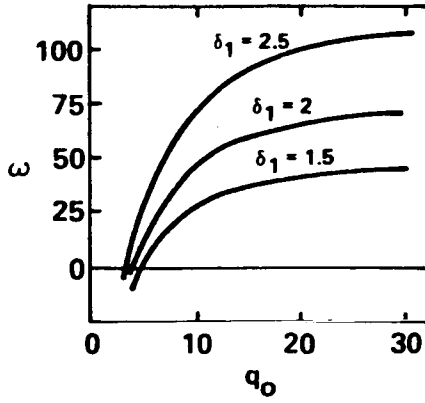


FIG. 1

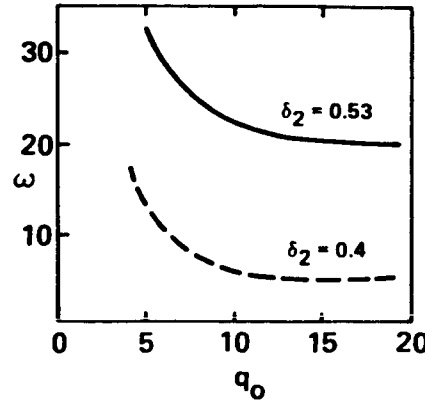


FIG. 2

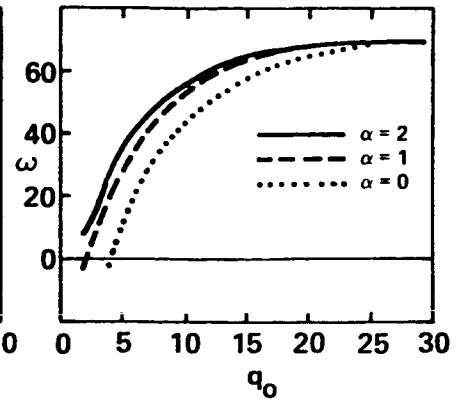


FIG. 3

Fig. 1 shows growth rate ω v.s. q_0 for profile(A). Note that the temperature increases but density is constant as twist increases (i.e. lower q_0 values). Higher field twist stabilizes the condensation mode due to the increase of temperature (higher heat conduction and lower radiation loss). Growth rate increases with δ_1 for given q_0 because density at $r=0$ increases as $1+\delta_1$ resulting in higher radiation rate. Fig.(2) shows the stability of profile(B). It shows that the mode becomes more unstable as twist increases because density of (B) increases with field twist. The growth rate of $\delta_2=0.53$ is higher than that of $\delta_2=0.4$ for a given q_0 because temperature at $r=0$ decreases with δ_2 as $1-\delta_2$ resulting in lower heat conduction and higher radiation. Fig.1 and 2 have poloidal and longitudinal mode number m and n equal to 1, aspect ratio $A=10$, and longitudinal magnetic field 10 Gauss. Because we use $\alpha=0$ the equilibrium does not have shear, in other words, every flux surface has same field twist. Fig. 3 shows the stability of equilibria with different α values. The result seems to show that magnetic shear affects the condensation mode. However, a careful study shows that the different stability is not due to magnetic shear but due to different pressure profiles caused by different choice of α .

It is found from the results that the effect of magnetic field on the global condensation modes with $\vec{k} \cdot \vec{B} \neq 0$ is negligible while the local mode with $\vec{k} \cdot \vec{B} = 0$ is affected by magnetic field. Why are the effects of the field on the two modes different? We find the answer by deriving a relation between parallel and perpendicular components of plasma displacements.

$$\left[i \frac{2kB_\theta B_0^2}{r^2} X + \frac{iB_0^2}{r} \left(\frac{mB_z}{r} - kB_\theta \right) X' - B_0^2 K(\xi \times B_0)_r \right] \frac{(k \cdot B_0)}{kB_\theta - mB_z/r} = \epsilon \rho_0 \omega^2 (\xi \cdot B_0).$$

If $\vec{k} \cdot \vec{B} \neq 0$ the perpendicular displacement is $\epsilon \ell_0 \omega^2$ times the parallel component. Since $\epsilon \sim 10^{-6}$, the equation implies that plasma moves mainly parallel to the field line when it condenses. For $\vec{k} \cdot \vec{B} = 0$ parallel motion is zero, in other words, plasma moves perpendicular to the field lines carrying the field lines into the condensed region; magnetic field affects the modes.

IV. CONCLUSION

The stability of condensation modes strongly depends on how density and temperature vary with field twist. If plasma temperature increases with twist but density does not (e.g. profile(A)), then condensation modes are unstable for low field twist-when ideal MHD modes are stable. This result implies that prominences form in a globally stable magnetic configuration, which may explain the stable nature of prominences. On the other hand, if plasma density increases with twist but temperature does not (e.g. profile(B)), condensation modes becomes more unstable. If plasmas obey profile (B), we may not observe stable quiescent prominences.

If the effect of magnetic field on condensation modes is insignificant, what is the role of the field on the prominence formation? We may say that the magnetic field has active and passive roles in the formation. The passive role is to insulate the prominence material from hot corona and to guide the plasma motion along the field lines when condensing. The active roles are to trap the outflowing plasmas (solar wind, spicules, and etc.) which then accumulate on the field lines, and to hold and support them against gravity. Depending on the strength and configuration, the magnetic field can trap the plasma effectively, enhancing the density sufficiently to initiate condensation, and can support the condensed plasmas to form a prominence(An, et.al 1986). Without the passive role, however, no prominence can form in a hot coronal plasma.

This research is supported by NAS/NRC and NASA Office of Solar and Heliospheric Physics and Office of Space Plasma Physics.

REFERENCES

- An, C.-H., 1984a, *Astrophys. J.*, 276, 755
_____, 1984b, *Astrophys. J.*, 276, 352
_____, 1984c, *Astrophys. J.*, 284, 422
_____, 1985, *Astrophys. J.*, 298, 409
An, C.-H., Suess, S.T., Tandberg-Hanssen, E., and
Steinolfson, R.S., 1986, *Solar Phys.*, (in press)
Anzer, U. and Tandberg-Hanssen, E., 1970, *Solar Phys.*, 11, 61
Chiuderi, C., and Van Hoven, G., 1979, *Astrophys. J. (Letters)*,
232,L69
Field, G.B., 1965, *Astrophys. J.* 142, 531
Heyvaerts, J., 1974, *Astron. Astrophys.* 37, 65
Hildner, E., 1971, Ph.D. thesis, Univ. of Colorado
Nakagawa, Y., 1970, *Solar Phys.*, 12, 419
Pneuman, G.W., 1983, *Solar Phys.* 88, 219

FILAMENT FORMATION DUE TO PHOTOSPHERIC SHEAR

S. T. Wu

Y. C. Xiao

The University of Alabama in Huntsville
Huntsville, Alabama 35899

INTRODUCTION

Recently, Wu *et al.* (1983, 1986) have developed a three-dimensional, time-dependent axisymmetric ideal magnetohydrodynamic (MHD) model which has been used to study lower solar atmospheric responses due to photospheric motion. They have shown that various observed solar features can be formed from these numerical simulation experiments. In this short note, we shall report some work currently in progress which has resulted from a specific numerical simulation experiment. These results may elucidate the possible physical mechanism of formation of filament.

NUMERICAL RESULTS

The initial state for this ideal MHD model is an isothermal ($T = 10^5$ K) in hydrostatic equilibrium ($n = 10^{10}$ cm $^{-3}$); and permeated by a dipole potential magnetic field that has a strength of 8 Gauss at the photospheric level (i.e., x-z plane) which gives a plasma beta being 0.14. With this initial equilibrium state, we introduce a spatially-distributed sine curve type of shear motion (i.e., in the x-z plane). The shear speed is zero at the neutral line and is a maximum (1.0 km s $^{-1}$) at the edge of the magnetic arcade. The evolution of the magnetic field configuration due to this prescribed shear motion is shown in Figure 1. The corresponding induced current distribution is shown in Figure 2a,b for several times at two specific heights ($y = 1,500, 2,500$ km) and distributed over a relatively small (8,000 km) scale in the horizontal direction (x-axis). Also, the induced current distribution as a function of altitude at a horizontal position of 2,500 km from the neutral line is shown in Figure 2c. The corresponding plasma properties (i.e. density and temperature) at a specific height and horizontal position are given in Figure 3. To summarize these results, we make the following observations;

- (a) Figure 1 shows that the field lines have orderly changes up to 2,000 s after introduction of the shear motion in the x-z plane. A drastic deformation of magnetic field topology occurs during the interval between 2,000 s and 2,500 s.

Physically, this result shows that some of the field lines collapsed to form a current sheet (Figure 1). The appearance of a high density region is coincident with the current sheet; it further shows that the outer edge of the magnetic field has locally been pushed open.

- (b) A further, specific, comment may be made about the current sheet. From Figure 2, we can identify the location at $t = 2,500$ s, of the maximum current density ($\sim 10^3$ Amp km $^{-2}$). Specifically, this peak is located at 3,500 km from the neutral line and within the height interval between 1,500 km and 2,500 km.

- (c) The density and temperature plots in this region (Figure 3) show that the density has been enhanced 30% ~ 40% and temperature has decreased ~20%. Based on these physical properties, we suggest that the shear motion induced a region which is characterized by a high current plasma density, high density and low temperature. This combination of physical parameters contains all the characteristics for a filament. Since the MHD model for this simulation incorporates ideal MHD theory, we may conclude that the filament could be formed by a plasma pinch effect. Details of this simulation will be given by Wu (1986).

ACKNOWLEDGEMENT

This work is supported by a NAGA Headquarters Grant NAGW-9, NASA/MSFC Grant NAG8-053, and NASA/MSFC Contract (NAS8-33526).

REFERENCES

- Wu, S. T., Y. Q. Hu, Y. Nakagawa and E. Tandberg-Hanssen, "Induced Mass and Wave Motions in the Lower Solar Atmosphere. I. Effects of Shear Motion of Flux Tubes", Ap. J. 266, 866-881, 1983.
- Wu, S. T., Y. Q. Hu, Y. Nakagawa and E. Tandberg-Hanssen, "Induced Mass and Wave Motions in the Lower Solar Atmosphere II. Effects of Converging and Diverging Photospheric Motions", Ap. J., 1986 (in press).
- Wu, S. T., "Magnetohydrodynamic (MHD) Modelling of Solar Active Phenomena Via Numerical Methods" Solar Physics, 1986 (submitted).

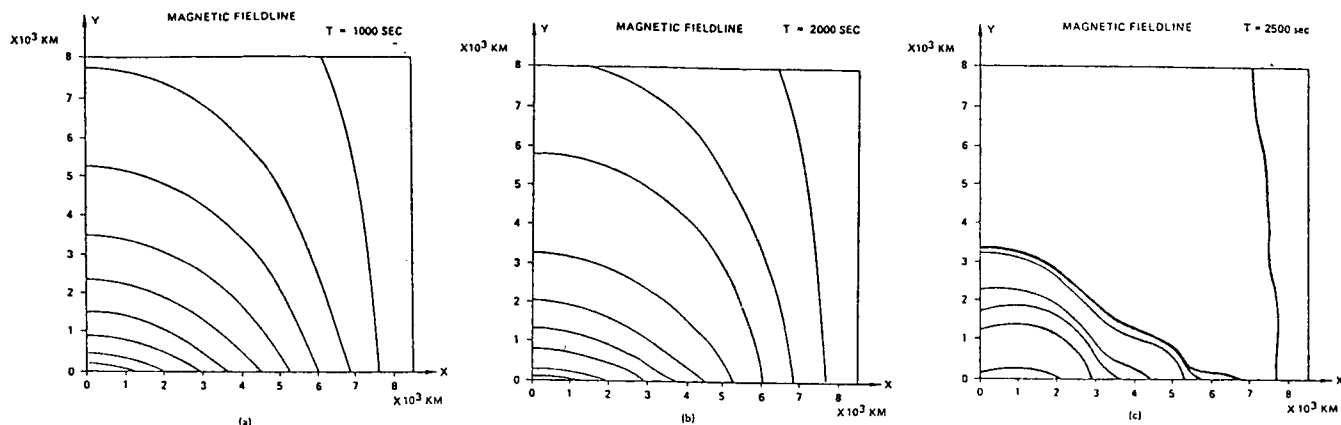


Figure 1. Computed evolution of magnetic field lines due to photospheric shear.

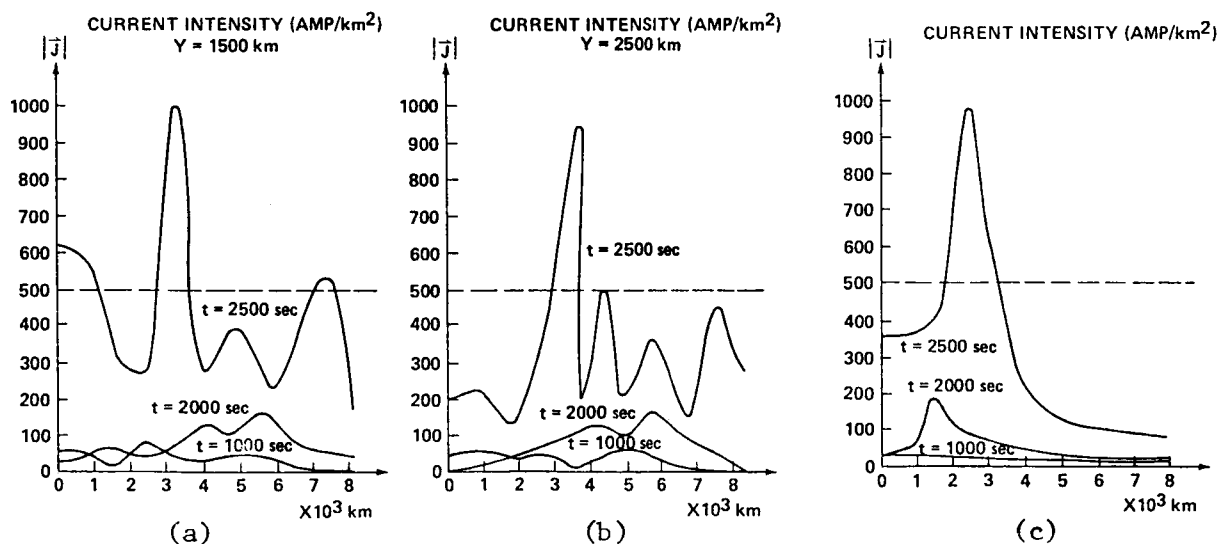


Figure 2. Computed induced current intensity vs horizontal axis at two specific heights (i.e., $y = 1,500 \text{ km}$ and $2,500 \text{ km}$; 2a, 2b) and vs height at a specific horizontal position ($x = 2,500 \text{ km}$) with several times (1,000 s, 2,000 s, and 2,500 s).

ORIGINAL PAGE IS
OF POOR QUALITY

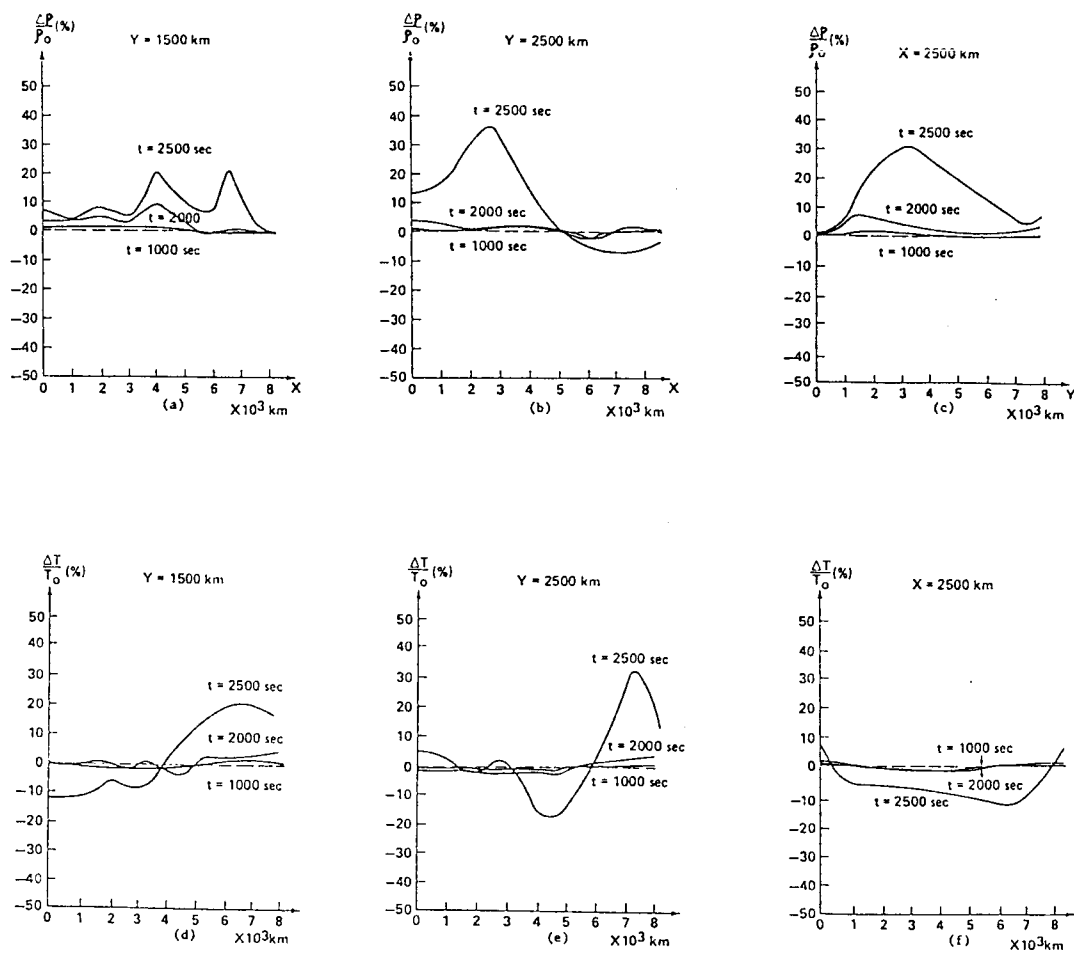


Figure 3. The plasma density (a,b,c) and temperature (e,f,g) distribution as a function of height and horizontal axis at several times (1,000 s, 2,000 s, and 2,500 s).

FORMATION OF ACTIVE REGION AND QUIESCENT PROMINENCE MAGNETIC FIELD CONFIGURATIONS.

C.-H. An
NASA/Marshall Space Flight Center

J. J. Bao and S. T. Wu
University of Alabama in Huntsville

ABSTRACT

To investigate the formation of prominences, we have studied chromospheric mass injection into an overlying coronal dipole magnetic field using a 2-D ideal magnetohydrodynamic(MHD) numerical model. We propose that active region prominences are formed by chromospheric plasmas injected directly into the overlying coronal magnetic field and that quiescent prominences are formed by plasmas evaporated at the interface between spicules and corona.

Hence, for the simulation of an active region prominence magnetic field we inject the mass from one side, but use a symmetric mass injection to form a quiescent prominence field configuration. We try to find optimum conditions for the formation of Kippenhahn-Schluter(K-S)type field configuration for stable support of the injected plasmas. We find that the formation of K-S type field configuration by mass injection requires a delicate balance between injection velocity, density, and overlying magnetic fields. This results may explain why a prominence does not form on every neutral line.

I. INTRODUCTION

A quiescent prominence(QP) forms along a neutral line in a quiet sun region. It is imbedded in the corona at the bottom of a global coronal streamer, which is sometimes surrounded by a dark region called a coronal cavity (Tandberg-Hanssen, 1974). Active region prominences(ARP) are transient in nature. Observations show that the early stage of the formation starts with the appearance, in H-alpha, of dark strips along a neutral line. The individual dark strip appears and disappears with time scale about 10-20 minutes. If the appearance rate is higher than the disappearance rate the dark and cool dense material keeps accumulating to form an ARP(Martin, 1973). It is observed that the appearance of a dark strip is a direct chromospheric mass injection into overlying magnetic fields.

Most of past model for the formation of prominences are divided into two categories; the first assumes that prominences are formed by the condensation of coronal plasmas in (sheared) magnetic fields (Kuperus and Tandberg-Hanssen 1967; Hildner 1971; Raadu and Kuperus 1973; Chiuderi and Van Hoven 1979; Mason and Bessey 1983; Pneuman 1983; An 1985). The second is that the initial magnetic field has a dip so that plasmas in the dip are cool and condensed, and plasmas at the foot points are sucked into the dip due to pressure imbalance (Pikel'ner 1971; Priest and Smith 1979; Ribes and Unno 1980; Poland and Mariska 1986). These two approaches explain some features of prominence formation but fail to provide satisfactory answers to the following important questions. Since the total mass of a well developed

prominence is about one fifth of the mass of total coronal plasmas it is hard to believe that prominence material is supplied by the condensation of coronal plasmas (Saito and Tandberg-Hanssen 1973). An important question for a prominence model to answer is then the source of prominence material. A succesful prominence model also has to answer the following questions; why does a prominence not form everywhere along a neutral line? If prominences are formed by the condensation of coronal plasmas, why does all the corona not cool to chromospheric plasmas? By what mechanism does the initial field have a dip so that plasma accumulates in it? How can we explain very transient nature of ARP but nearly steady state nature of QP? In order to answer these questions we propose that QP and ARP are formed by the plasmas supplied from chromosphere. A 2-D ideal MHD numerical model is used to simulate K-S type field configurations and to find optimum conditions for the formation.

II. MODEL

The numerical model used is based on ideal MHD. The basic MHD equations for the model are expressed in cartesian coordinate(x,y,z). These equations are the conservation laws, plus the induction equation to represent the coupling between the field and the plasma. All the equations are given by Wu, et.al(1983) and will not be reproduced here. The potential field which permeates the atmosphere can be represented by the following equations,

$$B_x = B_0 e^{-ky} \cos(kx),$$

$$B_y = -B_0 e^{-ky} \sin(kx),$$

$$B_z = 0.$$

The size of the computing domain is 8000km in height and 16000km in width. Mass is injected parallel to the field lines from the lower boundary. Mass injection is treated as a perturbation of density and velocity at the lower boundary and the characteristic method is applied to treat the initial and boundary value problem (Hu and Wu 1984). The dynamic response of magnetic field to the injected mass is studied for different injection velocities, densities, and magnetic field strength.

III. RESULTS

The study of mass injection from one side has been performed in order to understand the formation of ARP. In the following we will discuss under what conditions a K-S type field configuration forms. Since active region field strength is about a hundred gauss and temperature and density of chromospheric plasma are about 10^4 K and 10^{12} cm⁻³ respectively β is much less than 1. Therefore, we take results of $\beta = 0.1$, which is the smallest value of β we use, for the study of ARP. Fig.1(a, b, c) show how sensitively magnetic structure depends on injection velocity and density. Fig.1(a) shows field evolution for injection density ratio(the ratio of injection to ambient density) 1.2 and velocity 3.5km/s. Within a time scale comparable to the ARP life time (about 20 min.), the field line does not show any pit resulting in no stable accumulation of injected plasmas. If

injected velocity increases to 20km/s with the density ratio 1.2 (see Fig.1(b)) the magnetic field lines on the injection side(left side) move up higher than the right side. Due to gravity the field lines at and below the injection region fall down forming an asymmetric pit or a flat top on each field line. Injected plasma at the asymmetric pit may not accumulate on the field lines, while the plasmas at the flat top may accumulate but the stability is not certain. Note that the density ratio is unrealistically low but the velocity is realistic for chromospheric mass injection.

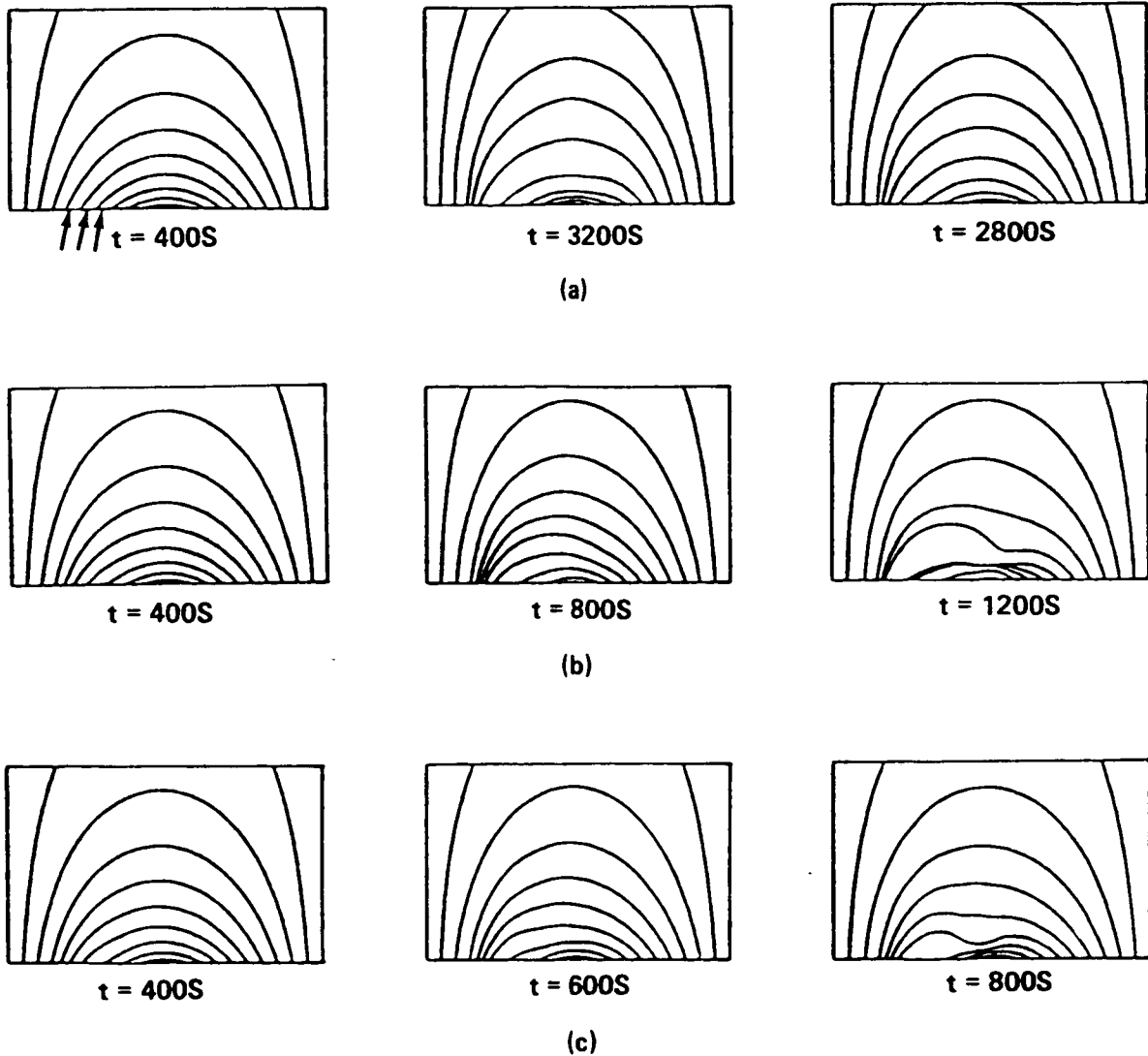


FIGURE 1; MAGNETIC FIELD EVOLUTION OF $\beta = 0.1$ DUE TO LEFT-SIDE INJECTION.
 (a) DENSITY RATIO 1.2 AND INJECTION VELOCITY 3.5km/s.
 (b) DENSITY RATIO 1.2 AND INJECTION VELOCITY 20km/s.
 (c) DENSITY RATIO 10 AND INJECTION VELOCITY 20km/s.

Fig.1(c) shows mass injection of $v=20\text{km/s}$ and density ratio 10, which is realistic for chromospheric mass injections like spicules. The figure shows a nearly symmetric pit on top of a field line at the injection region at a

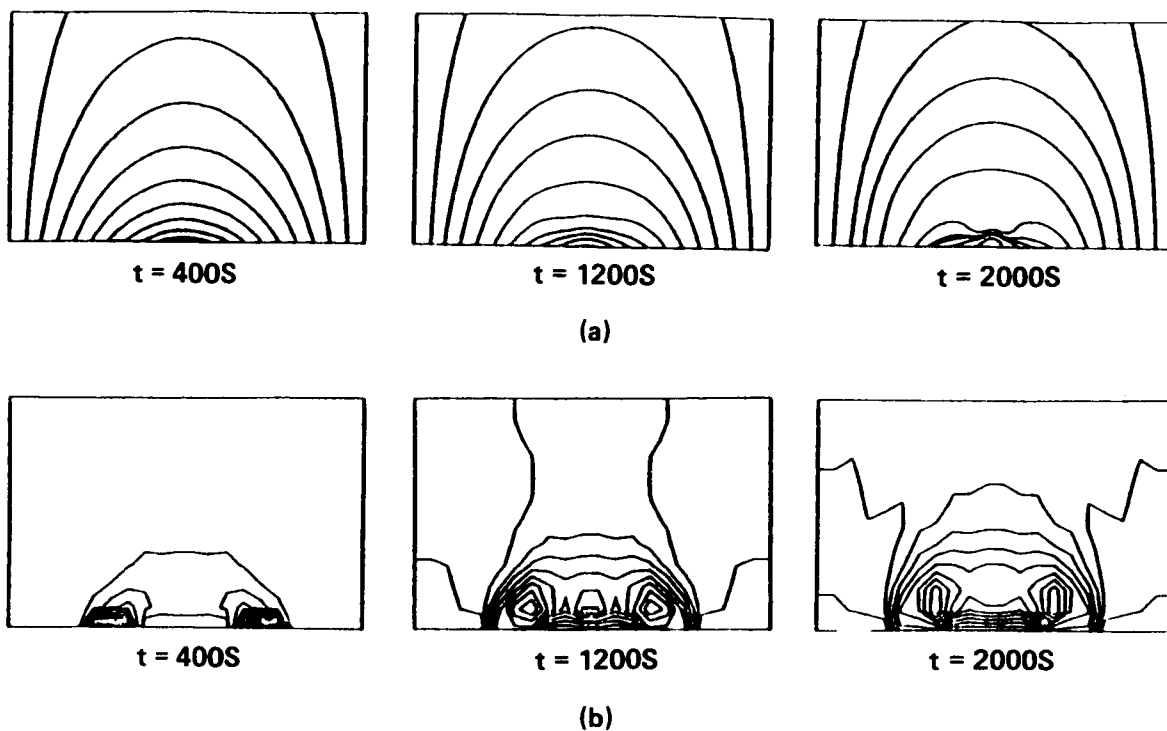


FIGURE 2. SYMMETRIC MASS INJECTION FOR $\beta = 2$, DENSITY RATIO 1.2, AND INJECTION VELOCITY 3.5m/s. (a) FIELD LINES, (b) DENSITY CONTOURS.

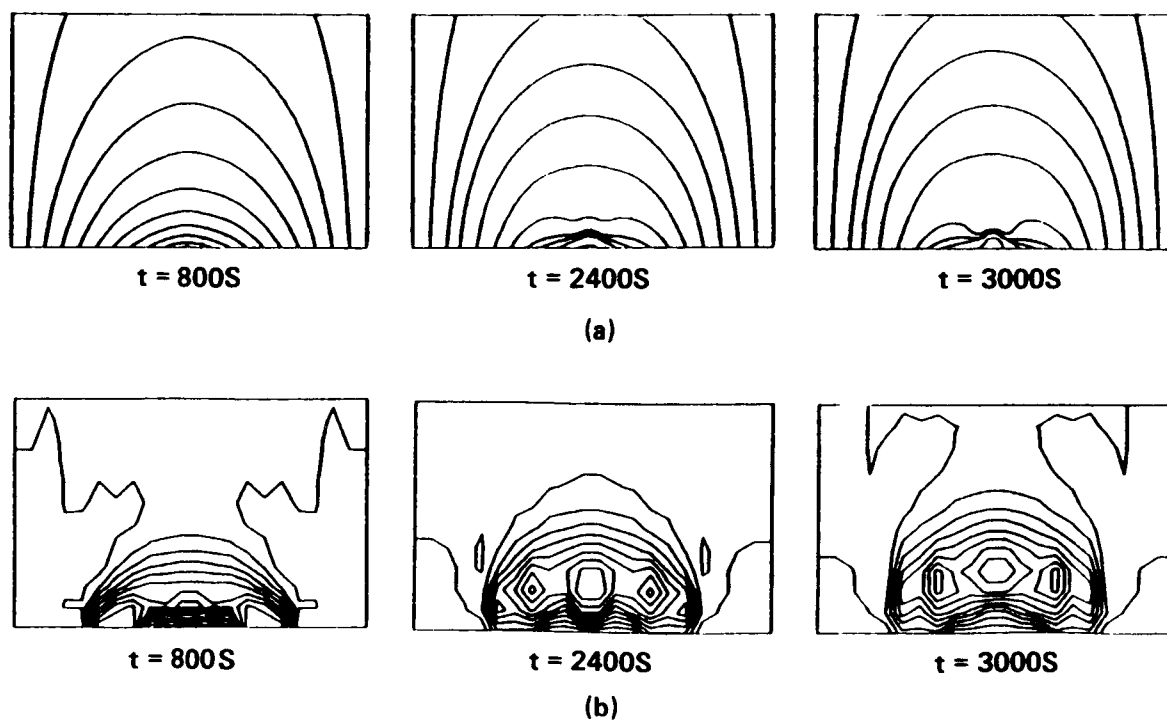


FIGURE 3. SAME AS FIG. 2 WITH $\beta = 0.5$

time comparable to the life time of an individual dark strip in an early stage of ARP formation. The injected plasmas might stably accumulate in the pit to form an ARP. The figure shows that the spicule-like mass injection is the most favorable condition for the formation of ARP. Since we have not considered sheared fields, which is an important characteristic of ARP (Tandberg-Hanssen 1974), we cannot claim that we simulate the formation. However, the results show that not only shear but also injection velocity, density, and magnetic strength should be right for the formation to precede. The reason why every neutral line does not have a prominence along it may be attributed to that only certain neutral lines have right mass injection and magnetic field for the formation.

The study of symmetric mass injection is aimed at understanding the formation of QP. Since the evaporated plasmas may have nearly the same density as ambient coronal plasmas, injection density is assumed to be 20% higher than ambient density. The injection velocity is assumed to be 3.5km/s but a realistic velocity for the evaporated plasma is not known. For the formation we need radiative cooling to have low temperature and high density plasmas which are not provided directly by evaporation. Since we do not include radiation and heat conduction in our numerical model we cannot simulate the formation at present time. However, we can understand the mechanism of forming a pit at the top of injection field lines. We believe that a necessary condition for the formation of a QP is the formation of a pit in a time scale shorter than condensation time scale of the injected plasmas. If the time scale of forming a pit is longer than the radiative cooling time scale, the injected plasma will condense and, due to gravity, flow down along field lines before a pit forms for a stable support. On the other hand, if the time scale of forming a pit is much shorter than the condensation time scale, the injected plasmas accumulate in the pit and condense to form a prominence. Fig. 2 and 3 show evolutions of magnetic field(a) and density(b) for $\beta = 2, 0.5$ respectively. The figures show that a pit starts to form at $t=1500s$ for $\beta = 2$ and at $t=2000s$ for $\beta = 0.5$. The field lines of $\beta = 2$ cannot support the injected plasmas in the pit but collapse in $t=3000s$. On the other hand, the field lines of $\beta = 0.5$ can support the plasmas against gravity up to $t=6000s$ at which the calculation terminates. In order for the field lines to support the injected plasmas, the magnetic field strength should be high-but too high a field strength cannot form a pit in radiative cooling time scale in which the injected plasmas accumulate. Therefore, a narrow range of field strengths may be required for the formation of a QP. Observations(Nikolsky, et.al 1984; Leroy 1977; Tandberg-Hanssen 1970; Kim, et.al 1982) show that there is an optimum magnetic strength for the formation, which may be explained by the above argument. The formation may also depend on the degree of symmetry of the injection. As an extreme example, one sided injection requires a delicate balance between injection velocity, density, and magnetic strength for the formation of a pit.

IV. CONCLUSIONS.

We have generated magnetic field configuration similar to the K-S model through symmetric and one side mass injection for quiescent and active region prominence formation respectively. Since we do not have radiation and heat conduction in our numerical model and use a computational domain that is smaller than the dimension of observed prominences, we do not intend

to make direct comparison of the results with observations. However, we obtain very important results for understanding the formation of K-S model field configurations. The study shows that the formation requires a delicate balance between injection density, velocity, and magnetic field strength, implying that a prominence should not be expected to form on every neutral line. The result also implies that there is an optimum field strength for the formation. The formation of an ARP by direct chromospheric mass injection and a QP by evaporated plasmas may explain the transient nature of ARP and nearly steady state nature of the global configuration of a QP respectively. We have discussed the ideal MHD aspect of prominence formation without considering plasma heating which may play a crucial role for the formation (Davis and Krieger 1982). Since the heating mechanism is not known, a quantitative study of its effect on the formation is out of scope of this study. The future study of mass injection with sheared field and with more realistic dimensions will provide the optimum condition for the formation of prominences along a neutral line. Including radiation, heat conduction, and heating will be major improvements over the present model for better understanding the process of prominence formation.

This research is supported by NAS/NRC, NASA Office of Solar and Heliospheric Physics and Office of Space Plasma Physics. It is also supported by a NASA grant NAGW-9 and MSFC grant NAG8-053.

REFERENCES.

- An, C.-H., 1985, *Astrophys. J.* 298, 409
 Chiuderi, C., and Van Hoven, G., 1979, *Astrophys. J. (Letter)*, 232, L69
 Davis, J.M., and Krieger, A.S., 1982, *Solar Phys.*, 81, 325
 Hildner, E., 1971, Ph.D. thesis, U. of Colorado.
 Hu, Y.Q., and Wu, S.T., 1984, *J. Compt. Phys.*, 55, 33
 Kim, I.S., Koutchmy, S., Nikolsky, G.M., and Stellmacher, G., 1982, *Astron. Astrophys.* 114, 347
 Kippenhahn, R., and Scholte, A., 1957, *Z. Astrophys.*, 43, 36
 Kuperus, M., and Tandberg-Hanssen, E., 1967, *Solar Phys.*, 2, 39
 Leroy, J.L., 1977, *Astron. Astrophys.*, 60, 79
 Mason, S.F., and Bessey, R.J., 1983, *Solar Phys.* 83, 121
 Martin, S., 1973, *Solar Phys.*, 31, 3
 Nikolsky, G.M., Kim, I.S., Koutchmy, S., and Stellmacher, G., 1984, *Astron. Astrophys.*, 140, 112
 Pikel'ner, S.B., 1971, *Solar Phys.*, 17, 44
 Pneuman, G.W., 1983, *Solar Phys.*, 88, 219
 Poland, A.I., and Mariska, J.T., 1986 (preprint)
 Priest, E.R., and Smith, E.A., 1979, *Solar Phys.*, 64, 267
 Raadu, M.A., and Kuperus, M., 1973, *Solar Phys.*, 28, 77
 Ribes, E., and Unno, W., 1980, *Astron. Astrophys.*, 91, 129
 Saito, K., and Tandberg-Hanssen, E., 1983, *Solar Phys.*, 31, 105
 Tandberg-Hanssen, 1970, *Solar Phys.*, 15, 359
 1974, *Solar Prominence*, D. Reidel, Dordrecht, Holland.
 Wu, S.T., Hu, Y.Q., Nakagawa, Y., and Tandberg-Hanssen, E., 1983, *Astrophys. J.*, 266, 866

NUMERICAL SIMULATIONS OF A SIPHON MECHANISM
FOR QUIESCENT PROMINENCE FORMATION

A. I. Poland

Laboratory for Astronomy and Solar Physics
Goddard Space Flight Center
Greenbelt, MD 20771, U. S. A.

and

J. T. Mariska and J. A. Klimchuk

E. O. Hulburt Center for Space Research
Naval Research Laboratory
Washington, DC 20375-5000, U. S. A.

INTRODUCTION

Quiescent prominences represent a significant challenge to our understanding of the flow of mass and energy in the outer layers of the solar atmosphere. A small number of quiescent prominences contain as much mass as the entire corona (Athay, 1976). The problem then is how to get that much material into the relatively small volume of a prominence and maintain it at a temperature of 10,000 K in close proximity to material at one million K. The thermal insulation to conduction provided by the magnetic field explains the disparate temperatures. The mass source problem is less well understood.

One method for supplying mass to the prominence is to siphon it from the chromosphere. The siphon mechanism begins with a magnetic loop that evolves into a configuration with a gravitational well, such as that described by Kippenhahn and Schluter (1957). This could be formed, for example, by a twist in the magnetic field as shown in Figure 1a. A gravitational well could also be formed by a condensation induced sag in the field. This could further enhance the condensation process and lead to a geometry such as that shown in Figure 1b. Once this well has formed, or as it is forming, the material in the well area of the loop must cool and condense to the point where radiative losses exceed any heat input. Additional material must also flow into the well from the underlying chromosphere to supply the mass required to form the prominence. A number of authors have discussed this general scenario (e.g., An, 1985; Engvold and Jensen, 1977; Pickel'ner, 1971; Ribes and Unno, 1980).

In this contribution we present one example from a series of numerical simulations that we have performed to study the formation of quiescent prominences.

MODEL CALCULATIONS

The numerical model we use describes convective, wave, and heat transfer phenomena in magnetically confined plasmas under conditions typical of those in the outer layers of the solar atmosphere. In a specified magnetic geometry, we solve the time-dependent equations for mass, momentum, and energy conservation, including conduction, radiation, gravity, and heating. Details of the numerical model and the solution techniques are discussed in Poland and Mariska (1986), Mariska et al. (1982), and Mariska and Boris (1983).

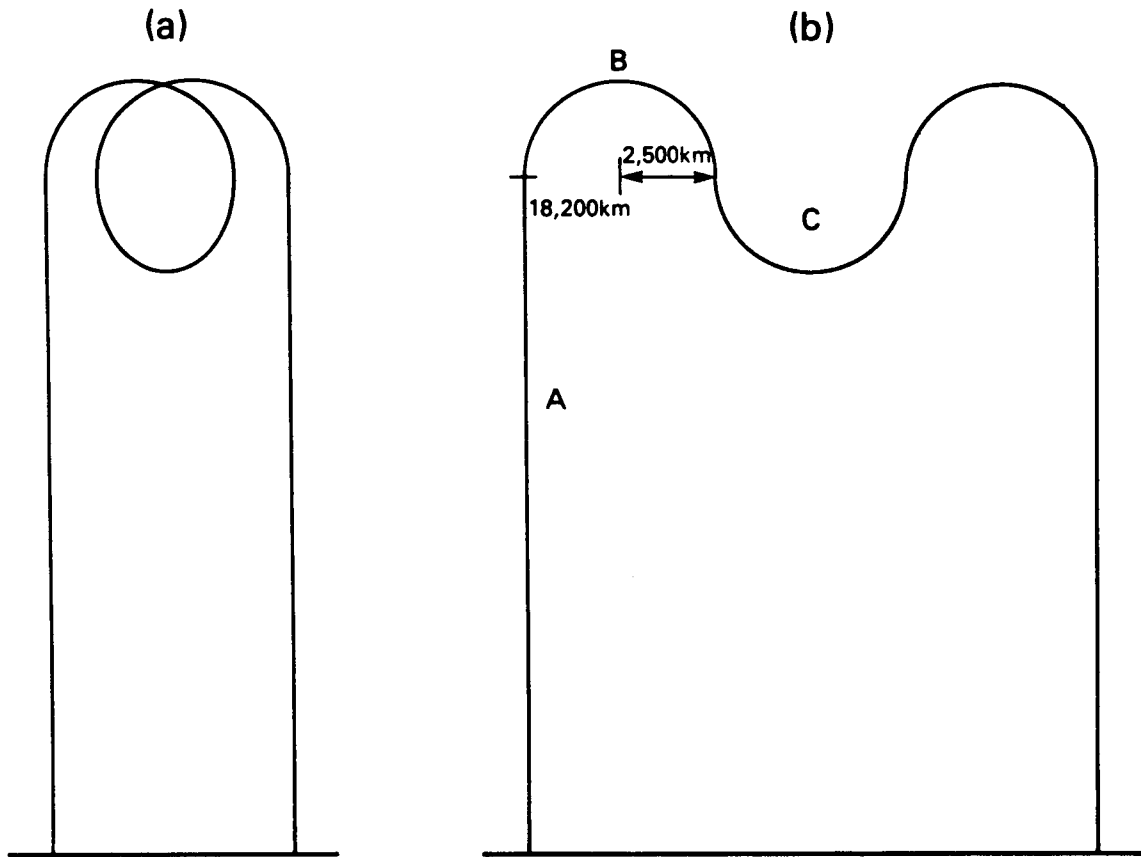


Figure 1

Figure 1b shows the geometry for the simulation. This is basically a very simple representation of a Kippenhahn-Schluter type geometry. Since the loop is symmetric about the top, we only compute half of it. The total length of the half-loop is 30,000 km, with 1100 km of that being chromospheric material at the base. Within this geometry we construct an initial static temperature-density distribution. This distribution is shown as the topmost of each pair of curves in Figure 2. The peak temperature is about 1.5 million K, and the pressure is about $2.5 \text{ dynes cm}^{-2}$.

From this initial model we attempt to form a prominence. It turns out that this is quite difficult without artificially injecting mass into the system. The model is stable against small perturbations. Our simulations to date suggest that the only way to form a prominence from this initial model is through a multistep process. The first step in the process is to reduce the heating to about 1% of the value required to maintain the initial loop. This produces a small cool region at the bottom of the gravitational well. Values of the heating larger than a few percent simply result in a slightly cooler coronal loop, but of essentially the same character as the initial model.

The result of this initial cooling is shown as the lower of each pair of curves in Figure 2. Here, along with the initial model, is the result of reducing the heating everywhere to 1% of the initial rate and letting the loop evolve for 4000 s, a little over one hour. The temperature structure now has a cool region in the well at the top, and the density in the loop legs has dropped dramatically. Note, however, that the density of the material in the well has not changed by much. It is still far below prominence densities.

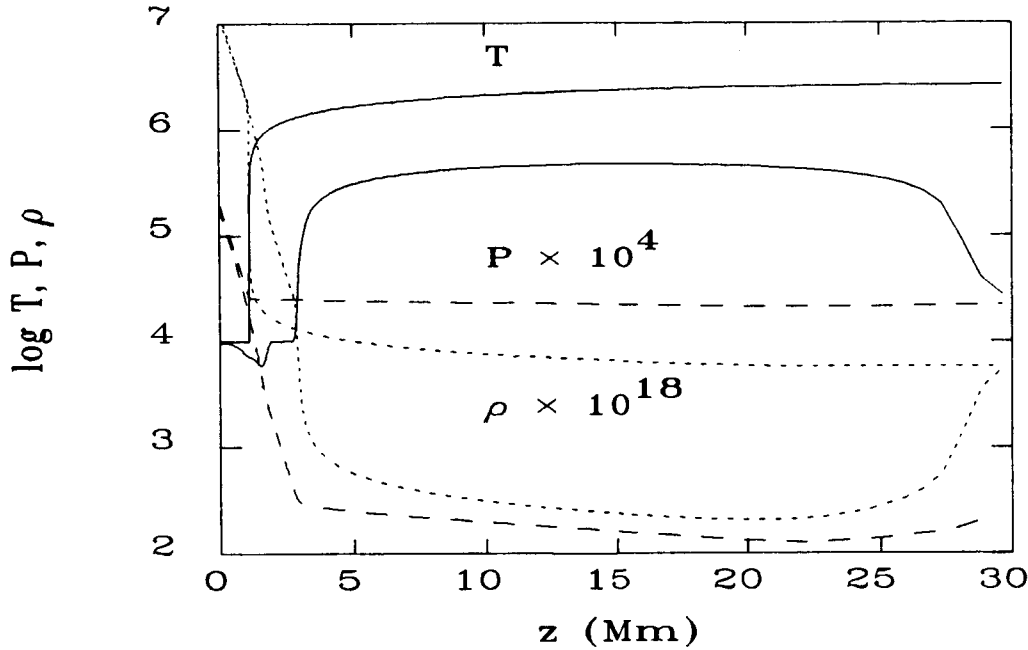


Figure 2

We have found that one way to go from this state to a high density prominence-like configuration is to drive mass upward into the well by heating only the loop legs. We do this in two phases. First, we heat only the legs at the same reduced heating rate that was used to produce the initial condensation. This slowly moves material from the chromosphere to the well. The flow velocity is only about 2 km s^{-1} , however. After about 21 hours at this rate, the electron density at the top has increased to about 10^{10} cm^{-3} , which is still somewhat low for most prominences (Hirayama, 1985; Bomnier *et al.*, 1986). It is high enough, however, that we can now increase the heating rate in the legs back toward the initial heating rate, say to 50%, and not destroy the condensation in the well. In just 5 more hours at this rate, the electron density in the well has reached 10^{11} cm^{-3} , which is typical of prominence conditions. Figure 3 shows the results of that reheating of the legs. The lower most of each pair of curves is the model at the end of the initial one hour cooling. The upper most of each pair of curves is the model after the reheating. The material in the well is clearly now more representative of prominence conditions.

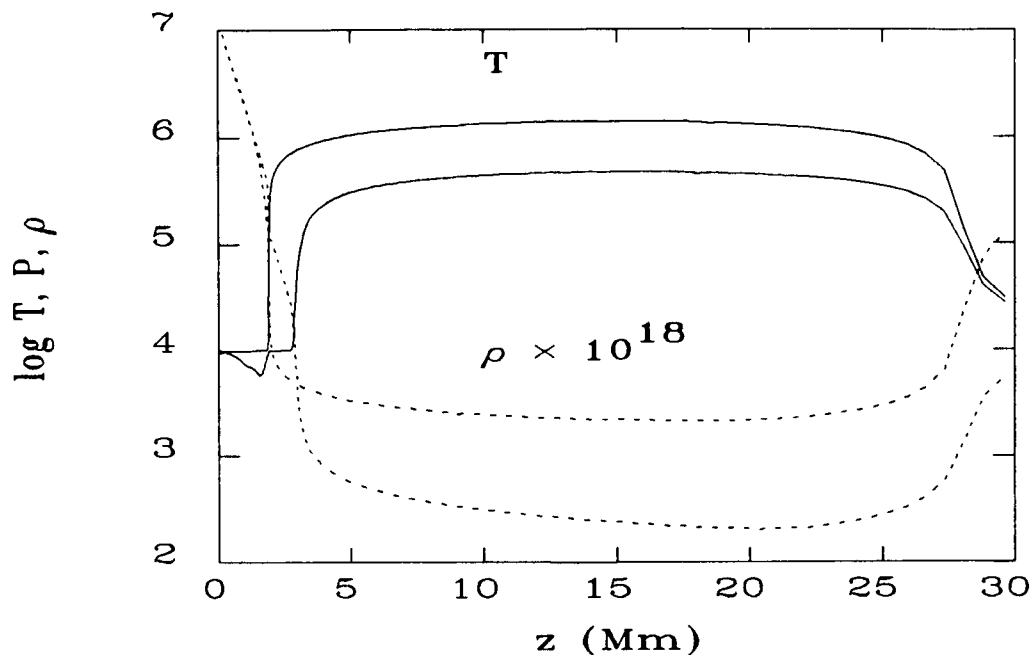


Figure 3

DISCUSSION

Our work indicates that forming a prominence from an active region loop is not as easy as some earlier studies would lead one to believe. It appears to require first a major disruption of the heating. This must then be followed by a gradual return of energy deposition, but only to the loop legs. One possible geometry in which this might occur is shown in Figure 1a. A loop with a twist in it might provide a natural way of forming a gravitational well at the top, while at the same time cutting off the heating to the region.

The necessity of the second phase, in which material is siphoned from the chromosphere through localized heating, is very significant. We have considered an alternate geometry of a low-lying loop with a very long and shallow gravitational well. Although there is ample material in the well initially to form a dense condensation at the bottom, we find that this does not occur. When the heating is first reduced, material is drawn up and out of the well, rather than settling to the bottom. This perhaps surprising result is apparently related to the extremely efficient cooling capacity of the lower transition region in the loop legs. There the radiation rates are at a maximum and cooling is most rapid. It would seem that a subhydrostatic pressure deficit is maintained which is able to suck material out of the well. We are presently exploring this scenario more closely.

A second significant discovery of our work is that once the prominence is formed it is very difficult to destroy. A large amount of heating is required to overcome radiative cooling in the condensed material. The exact amount needed depends, of course, on the prominence density. Once the heating rate does exceed the cooling rate, however, the prominence returns to a hot coronal loop configuration in only a few minutes.

While our calculations have shown that it is possible to produce a prominence by a siphon-like mechanism, they have not directly provided a basis for comparison with observations. We are currently developing more detailed calculations that will allow such a comparison. For example, we need a better resolved numerical grid in the vicinity of the transition to prominence temperatures and densities at the top of the loop. This would provide better estimates of observable velocities, emission measures, and UV line emissivities at this crucial interface. We are also examining the shocks that result from the condensation process to see how they might relate to the apparent motions observed in prominences. It is clear from time lapse photographs of prominences that they are dynamic phenomena. We hope to try to understand some of those observations in the context of our dynamic models.

Portions of this work were supported by the NASA Solar Terrestrial Theory Program and by the Office of Naval Research. JAK is an NRC-NRL Cooperative Research Associate.

REFERENCES

- An, C. -H. 1985, Ap. J., 298, 409.
- Athay, R. G. 1976, The Solar Chromosphere and Corona: Quiet Sun, (Dordrecht: D. Reidel), p. 91.
- Bommier, V., Leroy, J. L., and Sahal-Bréchet, S. 1986, Astr. Ap., 156, 90.
- Engvold, O., and Jensen, E. 1977, Solar Phys., 52, 37.
- Hirayama, J. 1985, Solar Phys., 100, 415.
- Kippenhahn, R., and Schluter, A. 1957, Z. Astrophys., 43, 36.
- Mariska, J. T., and Boris, J. P. 1983, Ap. J., 267, 409.
- Mariska, J. T., Boris, J. P., Oran, E. S., Young, T. R., Jr., and Doschek, G. A. 1982, Ap. J., 255, 783.
- Pickel'ner, S. B. 1971, Solar Phys., 14, 44.
- Poland, A. I., and Mariska, J. T. 1986, Solar Phys., in press.
- Ribes, E., and Unno, W. 1980, Astr. Ap., 91, 129.

ALFVEN-WAVE DISSIPATION -
A SUPPORT MECHANISM FOR QUIESCENT PROMINENCES

Eberhart Jensen
Institute of Theoretical Astrophysics
P.O. Box 1029, Blindern
N-0315 Oslo 3, Norway

High resolution filtergrams or spectrograms of the main body of quiescent prominences often show a very vivid dynamical picture that cannot be reconciled with static models. Even if large differences exist between individual prominences in this respect, at least parts of the prominence are usually found to be in a "choppy", turbulent state.

Evidence for systematic flows are found in local regions in the prominence and also in the transition zone in the surroundings. These two regions are probably decoupled magnetically.

Alfven waves are generally believed to be responsible for the heating in the upper chromosphere and corona (Hollweg 1986). Since evidence for the presence of Alfven-waves has also been found in the solar wind field, it is highly probable that such waves are generated in the convection zone of the sun and propagated outwards in the solar atmosphere wherever a proper magnetic field is present to carry the waves. The most basic magnetic formations in the solar atmosphere are simple loops. They occur all over the solar surface and cover a large range of magnetic field strengths. Loops with the strongest magnetic fields are found in active regions. It is to be expected that the Alfven-wave flux which is channelled into the loops from below, could show considerable variation both with heliocentric latitude, with time and locally between neighbouring loops.

Let us see what happens when a magnetic loop is exposed to the appropriate Alfven-wave flux required to heat the upper solar atmosphere. Usually a flux of about 5×10^5 c.g.s. is quoted. The wave-flux may be written:

$$F_A = \frac{1}{2} \rho (\Delta V)^2 V_A = \frac{1}{8\pi} (\Delta B)^2 V_A ,$$

where $V_A = B/\sqrt{4\pi\rho}$ is the Alfvén velocity.

For the fluctuations we get:

$$\Delta V = \text{const } \rho^{-1/4} F_A^{1/2} B^{-1/2}, \quad \Delta B = \text{const } \rho^{1/4} F_A^{1/2} B^{-1/2}.$$

The measured densities in quiescent prominences are of the order of $10^{-13} \text{ g cm}^{-3}$, about two orders of magnitude higher than in the surrounding corona. Measurements of magnetic fields in quiescent prominences, both from using the Zeeman-effect and the Hanle-effect, indicate values in the range from 5 to 12 gauss in the main body. The strongest fields observed are around 20 gauss. In the lower vertical structures, at the footpoints, the few observations available indicate fields of the order of 100 gauss.

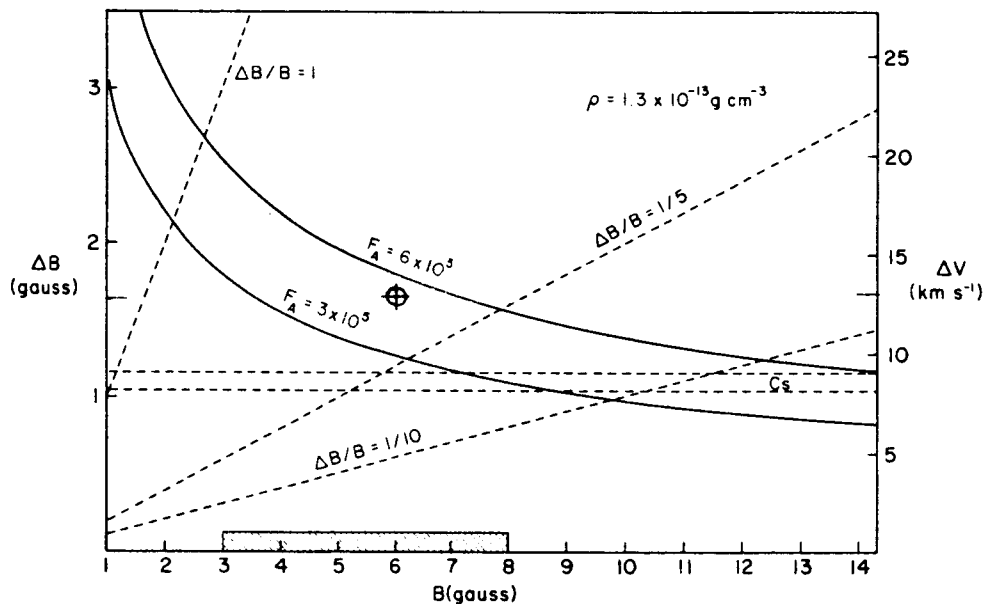


Fig. 1. The magnetic amplitude in the Alfvén wave, ΔB as a function of the carrier field, B , for two values of the flux density, F_A . We have assumed $\rho = 1.3 \times 10^{-13} \text{ g cm}^{-3}$. The velocity amplitude in the wave, ΔV , may be read on the vertical scale to the right. The two horizontal lines indicate the limits for the velocity of sound, C_s , corresponding to temperatures of 6500 and 9000 K. The hatched area indicates the main observed range in $B_{||}$.

These values of the field strengths together with the high observed densities, give Alfvén-velocities that are relatively low, of the order of 50-100 km/s in the main body of the prominence. A low Alfvén velocity will give large amplitudes for the waves creating a situation similar to a tsunami-wave hitting shallow water, though maybe not quite as dramatic.

This is illustrated in the Figure 1, which shows how the amplitudes ΔB and ΔV vary with the value of the magnetic carrier field B for two values of the wave flux. Choosing $B=6$ gauss, the amplitudes in the magnetic fluctuation becomes $B=1.5$ gauss, which corresponds to 25% of the carrier field. The corresponding velocity amplitude is $V=13$ km/s = 1.6 Cs, where Cs denotes the velocity of sound. Thus the waves can no longer be considered linear, and compressibility effects will be of importance.

Under these conditions a multitude of modes may be created. How fast the various modes decay is difficult to specify, but since compressibility is involved it is good reason to believe that they decay over a much shorter length than ordinary Alfvén-waves.

In the dissipation process the momentum lost by the waves is transferred to the matter, providing a stochastic support mechanism for the prominence.

Using expressions for the dissipation lengths given by Wentzel (1977), the dissipation length becomes of the order of 10^2 - 10^3 km.

The resulting force $K_A \sim \frac{1}{2} \rho (\Delta v)^2 / L = \frac{F_A}{L v_A}$ turns out to be of the right order of magnitude to counteract gravity (Jensen, 1983).

This would mean that the Kippenhahn-Schlüter and similar static models, which relies on smooth magnetic fields with a conveniently located dip at the top could be abandoned altogether.

As appears from the figure one would expect a magnetic loop with a field of the order observed in quiescent prominences to be badly "deformed" or broken up by non-linear effects when a wave-flux of the order required to heat the corona is carried.

For stronger fields, say 25 gauss, $\Delta B/B$ is 3.2%, and for a field of 50 gauss, the relative fluctuation is only 1.1%. A loop with magnetic field of this order will not be much affected by the waves and presumably retain its shape. The sharp lower boundaries of arches sometimes found to join adjacent footpoints may be such an example.

We mentioned that the measured field strength in the prominence "feet" seems to be of the order of 100 gauss. For the fields of this order the relative wave-amplitude would be less than half a percent in keeping with the parallel, ordered structure observed in these

features.

The damping of the waves in the prominence "feet" will be less than in the main body, as the damping length for Alfvén-waves is very sensitive to the field strength, being proportional to B to the fourth power. Thus waves ducted into the prominence from below will not suffer strong damping until the amplitude increases strongly in the main body of the prominence.

Both the generation and propagation of the wave-flux into the prominences will show local variations within one and the same prominence. A local increase in the wave-flux will lead to increased heating and at the same time to an enhancement of the supporting force. This would cause a high excitation spectral line in filaments to show different Doppler displacement from lines of low excitation (Engvold et al. 1986). As pointed out by Engvold observations indicate such an effect, when measurements in He 10830Å is compared to the K-line of Ca II. This also fits in with the extended work on filaments as observed in H_{α} by the French group at Meudon (Malherbe et al. 1981, Malherbe et al. 1983, Martre et al. 1981, Mein 1977, Schneider 1984).

Changes in the wave-flux with phase in the solar cycle could also explain the changes in magnetic fields observed in polar crown prominences (Leroy et al. 1983). With a lower wave-flux at minimum phase a lower magnetic field could be the carrier without being broken up by non-linear effects.

Similarly active region filaments have higher values of their magnetic fields because they are exposed to a stronger wave field. The weaker fields being "shaken" out of existence in or close to active regions.

In my opinion static models for quiescent prominences are unsatisfactory. It is high time that alternative models emphasizing the observed dynamical aspects are being investigated.

Let us sum up some of the observations that our dynamical, Alfvén-wave model may explain:

The geometry is described as a collection of simple loops, deformed by non-linear effects in the choppy part, where B is low. This is not contrary to the observation by Harvey that prominences show a systematic sign of its magnetic fields. The field is fluctuating and may be highly inhomogeneous, leaving some less perturbed flux tubes to show a systematic direction (Poland et al. 1983). In the arches that have a smooth outline also systematic flow-patterns are found. Here the magnetic field is probably higher.

The velocity-fields in the turbulent part of the prominence are

partly in the supersonic range, making mode-conversion and enhanced dissipation plausible.

The edge-effects observed in the velocity-field finds a natural explanation from the fact that $\Delta V \propto \rho^{-1/4} B^{-1/2}$ and thus should increase in the outer parts. Large ΔV leads to compressibility, and to enhanced dissipation and temperature, resulting in the observed intensity fluctuations.

The support-mechanism is a stochastic process. Matter may rise or fall according to local conditions that change with the time.

A local reshuffling will result rather than a net transfer of matter. Even in places with moderate dissipation, as in the feet of the prominences, matter may rise due to the suction effect created by compression and subsequent cooling in the upper parts of a tube of force.

Further observational tests:

Observations with high spatial resolution of the magnetic field everywhere in the prominences are needed. In particular in the feet knowledge is scanty. Here also velocities should be studied both in filaments away from the center of the disk and on the limb.

Magnetic fluctuations $\Delta B \propto \rho^{1/4} B^{-1/2}$ should be searched for. Simultaneous observations of ΔV and ΔB give an independent determination of the density ρ .

Evolution of microstructure elements, how the thermodynamical parameters change with time, should be investigated from high resolution data.

REFERENCES

- Engvold, O., Keil, S.L. 1986, these proceedings.
Hollweg, J.V. 1984, in Chromospheric Diagnostics and Modelling, ed. B. Lites.
Jensen, E. 1983, Solar Phys. 89, 275.
Leroy, I.L., Bommier, V., Sahal-Brechot, S. 1983, Solar Phys. 83, 135.
Malherbe, J.M., Schmieder, B., Mein, P. 1981, Astron. & Astrophys. 102, 124.
Malherbe, J.M., Schmieder, B., Ribes, B., Mein, P. 1983, Astron. & Astrophys. 119, 197.
Martres, M.J., Mein, P., Schmieder, B., Soru-Escot, I. 1981, Solar Phys. 69, 301.
Mein, P. 1977, Solar Phys. 54, 45.
Poland, A., Tandberg-Hanssen, E., 1983, Solar Phys. 84, 63.
Wentzel, D.G. 1977, Solar Phys. 52, 163.

STATIC CURRENT-SHEET MODELS OF QUIESCENT PROMINENCES

F. Wu¹

B. C. Low

High Altitude Observatory
National Center for Atmospheric Research²

INTRODUCTION

A particular class of theoretical models idealize the prominence to be a discrete flat electric-current sheet suspended vertically in a potential magnetic field. The weight of the prominence is supported by the Lorentz force in the current sheet. These models can be extended to have curved electric-current sheets and to vary three-dimensionally.

The equation for force balance is

$$\frac{1}{4\pi}(\nabla \times \mathbf{B}) \times \mathbf{B} - \nabla p - \rho g \hat{\mathbf{z}} = 0.$$

Using Cartesian coordinates we take, for simplicity, a uniform gravity with constant acceleration g in the the direction $-\hat{\mathbf{z}}$. If we are interested not in the detailed internal structure of the prominence, but in the global magnetic configuration around the prominence, we may take the prominence plasma to be cold. Let us consider how such equilibrium states can be constructed. To simplify the mathematical problem, suppose there is no electric current in the atmosphere except for the discrete currents in the cold prominence sheet. Let us take the plane $z = 0$ to be the base of the atmosphere and restrict our attention to the domain $z > 0$. The task we have is to solve for a magnetic field which is everywhere potential except on some free surface S , subject to suitable boundary conditions. The surface S is determined by requiring that it possesses a discrete electric current density such that the Lorentz force on it is everywhere vertically upward to balance the weight of the material $m(S)$. Since the magnetic field is potential in the external atmosphere, the latter is decoupled from the magnetic field and its plane parallel hydrostatic pressure and density can be prescribed quite separately. Instead of solving this difficult free boundary problem, classes of illustrative models can be constructed by solving for particular solutions to Ampere's equation for a discrete current density $\mathbf{J}(S)$ in a potential magnetic field such that the Lorentz force at the surface S is everywhere vertically upward. Then we can define the equilibrium mass distribution $m(S)$ having just the right weight to balance the Lorentz force.

TWO DIMENSIONAL MODELS

If the magnetic field has no x -component and is everywhere potential except on the sheet, the magnetic field can be represented in terms of an analytic function of the complex variable $w = y + iz$. Priest and Raadu (1975) have given an example for a plane vertical current sheet not threaded by magnetic lines of force. The electric current in the sheet is directed in the x direction. We can superpose an additional dipole source in the region $z < 0$ to this current sheet model. The additional magnetic field introduced at the current sheet is horizontal and the Lorentz force that results is everywhere upward (see Figure 1). Evaluating the Lorentz force on the current sheet, we get the mass distribution on the current sheet. By changing the strength of the additional dipole source we can get both the so-called Kuperus-Raadu model and the Kippenhahn-Schluter model (Kippenhahn and Schluter 1957, Kuperus and Raadu 1974).

¹Permanent address: Beijing Astronomical Observatory, Academia Sinica, China.

²The National Center for Atmospheric Research is sponsored by the National Science Foundation.

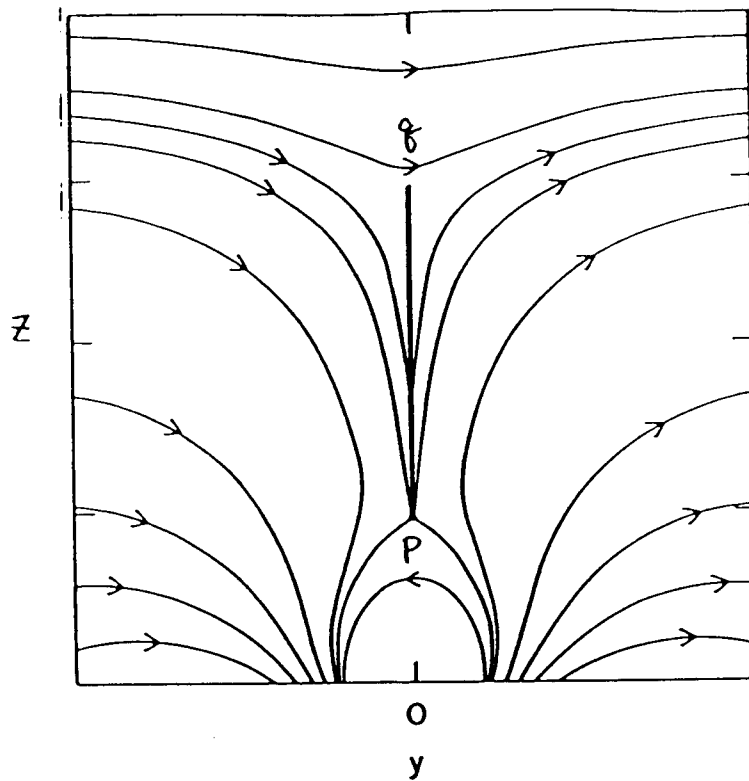


Figure 1. Field lines in the $y-z$ plane obtained by superposing an additional dipole source located in the $z < 0$ plane with the finite current sheet which runs along the y axis, extending from $z = p$ to $z = q$.

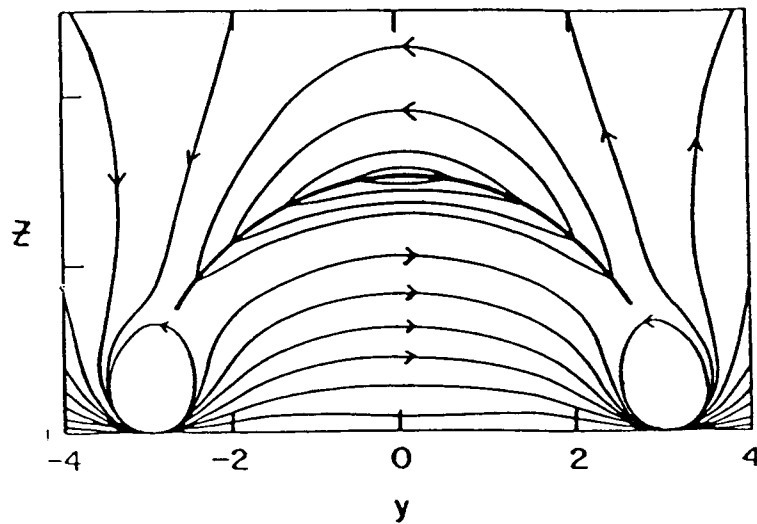


Figure 2. Field lines in the $y-z$ plane obtained by superposing a circular current sheet denoted by the thick arc with an additional potential field which is strictly horizontal everywhere on the current sheet.

A similar construction can be carried out if explicit solutions for the curved current sheets are given. Solutions for current sheets which are circular in shape have been obtained by Hu and Low (1982) and Hu (1984). To these solutions, the superposed potential field should be strictly horizontal on the circular sheet in order that the Lorentz force on the circular sheet is everywhere vertically upwards (see Figure 2). Then a certain amount of mass can be supported by the Lorentz force. Several examples can be found in the paper by Wu and Low (1986). It is interesting to note that the tension force at the current sheet is no longer vertical, and there is a discontinuity in the magnetic pressure at the current sheet. It is the combination of the pressure force, normal to the current sheet, and the oblique tension force that supports the weight. This is a novel feature not found in the case of a vertical current sheet.

THREE-DIMENSIONAL MODELS

As a step of further sophistication, the superposed potential field may be allowed to vary in three dimensions. We present two simple examples obtained by superposing the vertical plane current sheet solution given by Priest and Raadu (1975), with a periodic three dimensional potential field in one case, and with a non-periodic three dimensional potential field due to a finite number of dipole sources in the other (see Wu and Low 1986). The x variation in these models provides a natural length scale over which a total energy can be meaningfully defined. When a quiescent prominence is observed in H_α at the solar limb, it sometimes appears like a hedgerow with a repetitious structure. We may take the periodic solution to model such a structure. For the non-periodic solution, the distance in the x direction over which the dipole sources are distributed is a characteristic length of the prominence. Let us insert parametric values characteristic of prominences into these two sets of solutions to examine the energy content.

If we neglect the energy due to the plane parallel hydrostatic atmosphere outside the electric current sheet, the total energy consists of the magnetic energy and the gravitational potential energy of the suspended mass. Put the lower edge of the current sheet at a height of about 2×10^4 km and the top edge of the current sheet at about 5×10^4 km (see, e.g., Tandberg-Hanssen 1974). By choosing suitable constants in the periodic solution, the normal field at the base of corona is about 80 G. If we take each period in the x direction to be a single hedgerow component of a prominence, the length in that direction is about 6×10^4 km. With these parameters set and using a uniform gravitational acceleration of $g = 1.6 \times 10^4$ cm s⁻², the total mass in one period is of the order of 2×10^{14} gm. This total mass is equal to the total mass of a prominence which has the same length, a thickness of 5×10^3 km and an average density of 10^{10} protons cm⁻³, in agreement with observations (Tandberg-Hanssen 1974). The free magnetic energy is about 3×10^{28} erg, which is the same order of magnitude as the gravitational potential energy of 1.3×10^{28} erg. Using suitable parameters for the non-periodic case the normal field at the base of the corona is about 54 G. Let the prominence have a length of 2×10^5 km, the total mass in the current sheet is about 6.4×10^{14} gm. The gravitational potential energy is about 4×10^{28} erg. The free magnetic energy is about 9×10^{27} erg. In these above examples, the gravitational potential energy turns out to be larger than the magnetic free energy. It follows that if the prominence erupts, draining a fraction of the suspended mass to the base of the corona, the gravitational potential energy associated with the drained material may have an important role in driving the remaining mass outward from the Sun.

It will be interesting to pursue the following further development of the current sheet model. To support the weight of the current sheet, the electric current must be horizontal in order that the Lorentz force associated with it is vertical to balance the force of gravity. This implies that the electric current must either flow horizontally to infinity, such as in the models shown in Figure 1 and 2, or else close upon itself in horizontal loops. It will be interesting to generate classes of solutions corresponding to the latter possibility. A simple case would be a solution with current sheets in the form of surfaces of revolution about a vertical axis of symmetry. More general are the solutions with current sheets that are of complex geometries and closing upon themselves in a localized region of the atmosphere. In the realistic prominence, electric currents may actually flow along magnetic field lines to close themselves in the photosphere; see the three-dimensional solutions of Low (1984). Finally, we point out that the availability of explicit

equilibrium solutions opens up the opportunity of studying the linear hydromagnetic stability of magnetically suspended mass sheets. The stability of the solutions in Figure 1 and 2 will be taken up elsewhere (Wu 1986).

REFERENCES

- Hu, Y. Q., 1984, *Acta Astrophysica Sinica*, **4**, 14.
- Hu, Y. Q., and Low, B. C., 1982, *Solar Phys.*, **81**, 107.
- Kippenhahn, R., and Schluter, A., 1957, *Z. Astrophys.*, **43**, 36.
- Kuperus, M., and Raadu, M. A., 1974, *Astron. Astrophys.*, **31** 189.
- Low, B. C., 1984, *Ap. J.*, **277**, 415.
- Priest, E. R., and Raadu, M. A., 1975, *Solar Phys.*, **43**, 177.
- Tandberg-Hanssen, E., 1974, *Solar Prominences*, (Dordrecht: Reidel)
- Wu, F., 1986, (in preparation)
- Wu, F., and Low, B. C., 1986, *AP. J.*, (submitted)

RECENT OBSERVATIONS OF THE FORMATION OF FILAMENTS

Sara F. Martin
Solar Astronomy 264-33
Caltech
Pasadena, CA 91125

Abstract

Two examples of the formation of small filaments in $H\alpha$ are described and illustrated. In both cases, the formation is seen to be the spontaneous appearance of strands of absorbing mass that evolve from no previous structure. The initial development of the filaments appears to consist of the accumulation of these absorptive strands along approximately parallel paths in a channel between large-scale, opposite polarity magnetic fields on either side of the filaments. The strands exhibit continuous changes in shape and degree of absorption which can be due to successive condensations resulting in new strands, mass motions within the strands, and outflow of the mass from the strands. For at least several hours before the formation of both filaments, small-scale fragments of opposite polarity, line-of-sight magnetic flux adjacent to or immediately below the filaments, and at the ends of the filaments, were cancelling. This type of magnetic flux disappearance continued during the development of the filaments and is commonly observed in association with established filaments. Cancellation is interpreted as an important evolutionary change in the magnetic field that can lead to configurations suitable for the formation of filaments.

INTRODUCTION

A few examples of the formation of filaments taking place over intervals of one to several days can be found in Smith (1968) and in the review by Martin (1973). Two examples of new filaments forming on time scales of minutes are illustrated and discussed in this paper. These examples were found in time-lapse series of $H\alpha$ filtergrams recorded at the Big Bear Solar Observatory during the past two years. Videomagnetograms of the line-of-sight component of photospheric magnetic fields were continuously acquired at the time of formation of these filaments.

DESCRIPTION OF INDIVIDUAL EXAMPLES

5 August 1984 Filament Formation

The minute by minute evolution of a small active region in $H\alpha$ images and videomagnetograms was recorded for about 10 hours per day from 31 July until 8 August 1985. The formation of a new filament was observed on 5 August during the decaying phase of the region. Additional growth of the filament occurred during the night hours of the Big Bear Solar Observatory. The day to day evolution of this active region and the details of the decay of

its magnetic flux are is discussed and illustrated in Martin et al. (1985). In this paper, we present only the details of the formation of the new filament.

Images before, during, and after the formation phase are shown in Figure 1. This filament forms completely in the 14 minute interval between 2208 and 2222. At 2216:46, the developing filament appears to consist of 3 absorptive strands aligned end to end. After formation, the filament lengthens and shortens while increasing and decreasing in absorption but remains a distinct feature until the end of the observing day (0127, 6 Aug.). The formation of the filament in $H\alpha$ consists of the spontaneous appearance of roughly parallel, short strands of absorbing mass. The strands do not originate from any pre-existing structure but they are approximately aligned with the underlying chromospheric fibrils. The strands of absorption continuously change shape and lengthen or disappear in periods of a few minutes. The formation appears as a sporadic but gradually increasing accumulation of these linear absorptive strands until they constitute a completely-formed filament.

By the following day, the newly formed filament is part of a much longer filament that occupies nearly the entire length of the polarity inversion zone of the decaying active region (Fig. 12, Martin et al. 1985).

The development of the new filament relative to the surrounding line-of-sight component of the magnetic flux of the active region can be seen in videomagnetograms in the right side of Figure 1. All of the magnetic fragments correspond to concentrations of plage in $H\alpha$. In these magnetograms from the Big Bear Solar Observatory, negative fields are black and positive fields are white except within the contours of the stronger fragments of flux. Each successive inner contour where the color reverses from white to black or black to white, represents an increase in the field strength by about a factor of 2. The lowest contours in Figures 1 correspond to field strengths of approximately 50 Gauss. The weakest fields in these magnetograms are on the order of 10 Gauss.

Comparison of the magnetograms and $H\alpha$ images in Figure 1 shows that the new filament is bounded by fragments of mostly negative flux on the left and mostly positive flux on the right. To the left side of the filament is a small fragment of positive flux adjacent to the larger fragments of negative flux. The positive fragment is cancelling with the negative fragments at a rate of 10^{19} Maxwells per hour (cancelling feature PN25 in Martin et al. (1985)). Within 10 minutes after the formation of the new filament, this cancellation ceases because all of the positive fragment has disappeared. An obvious result of this cancellation is the shifting of the center of the polarity inversion zone to the right of its former site. It is unlikely that the filament could have formed any earlier at its precise location because it would have been surrounded by substantial positive flux rather than being between opposite polarity fields.

Cancellation sites also exist close to the upper end of the newly formed filament (P26, P27/N27 in Fig. 6, Martin et al. 1985). The magnetograms on the next observing day show that there was substantial loss of magnetic flux along the division between opposite polarities since the preceding day. Because the filament develops further during this stage of rapid loss of flux, we question whether the the cancellation of flux and the growth of filament are physically related, indirectly related, or whether they are simply coincident but unrelated phenomenon. Zwaan (1978) anticipated these observations of disappearing magnetic flux near the sites of filaments and suggested that the maintenance of filaments might be related to the disappearance of magnetic flux by means of magnetic reconnection.

5 AUG 1984

30,000 Km

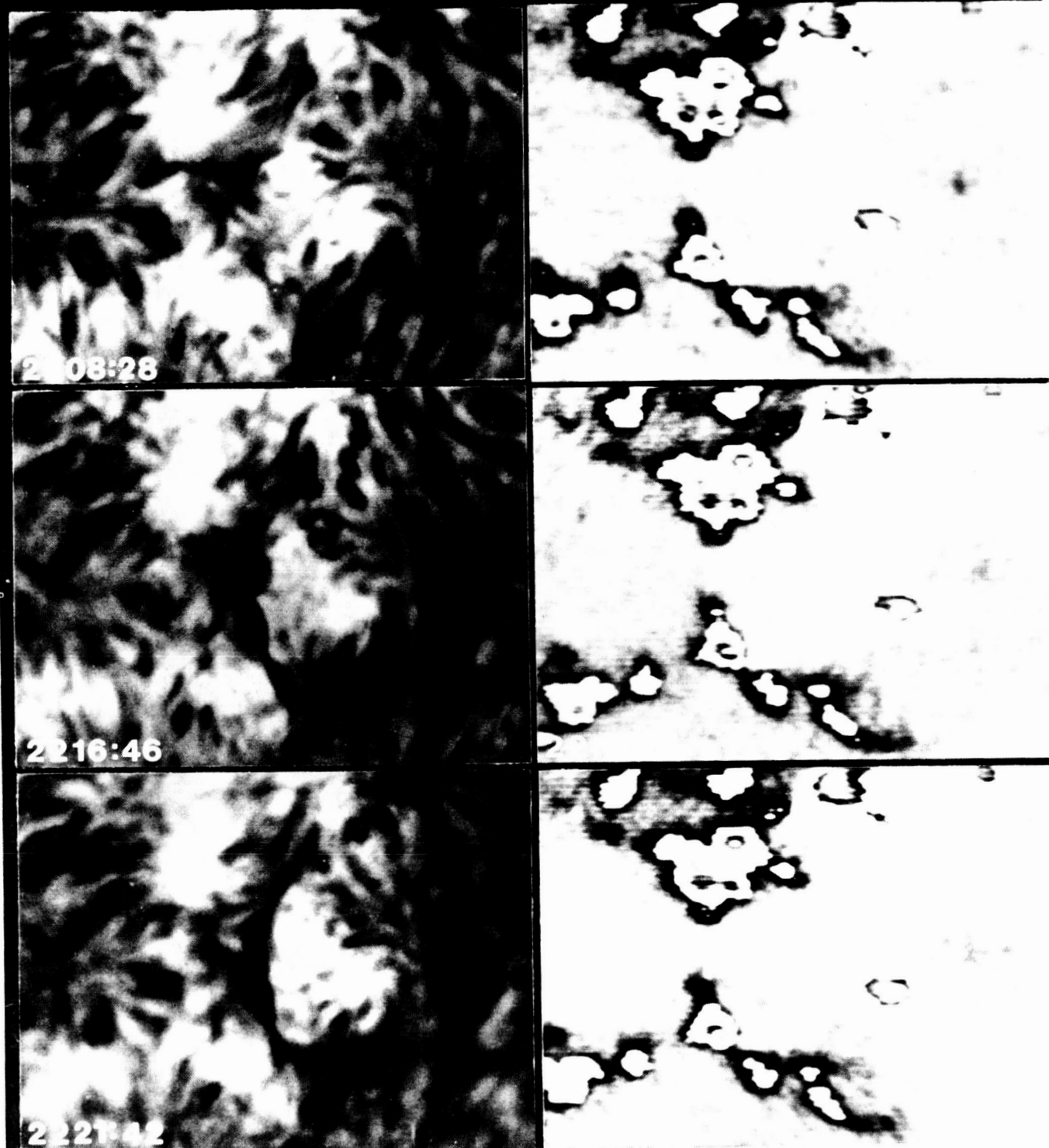


Fig. 1. The initial stages of the formation of a filament within a decaying active region are seen in $H\alpha$ images at the left. The formation consists of the spontaneous appearance of short strands of absorptive mass. The magnetograms show that the formation is coincident with the final few minutes of the cancellation of a positive (white) fragment of flux with the negative flux (black) to the left of the site of formation. Slower cancellation of fragments of flux at the upper end of the filament also occurs before and during the development of the filament. The polarity of individual clumps of magnetic flux containing contours are the same as around the periphery of the contoured areas.

ORIGINAL PAGE IS
OF POOR QUALITY

On this date, the formation of a small quiescent filament was observed on the quiet sun. A series of $H\alpha$ images depicting typical changes before, during and after its formation are shown in Figure 2. The formation of this quiescent filament takes place more slowly than the formation of the filament in the decaying active region. Otherwise, the formation is similar to the example above. Intermittent strands developed and faded from the beginning of the observing day at 1500 UT until 1710 UT. At 1710 the conspicuous strand, visible in the frame image at 1722 in Figure 2, formed. From that time until the end of the day, the filament was a continuously enduring structure. The filament occupies the same path as the earlier short-lived pre-formation strands. The strands are approximately parallel to the chromospheric fibrils assumed to be below the strands. From the beginning of the day, the chromospheric fibrils were already in the sheared configuration (Hagyard et al. 1984). The filament develops about midway between the adjacent opposite polarity fields and appears to divide rather than join the dominant large scale fields on opposite sides of the filament channel.

The series of images in Fig. 2 reveals how the structure within the filament is continuously changing during and after its formation. As in the other example, there is no evidence that the filament mass originates from any pre-existing chromospheric structure. Although we cannot discern exactly how the formation takes place, these observations are consistent with the well-known prominence observations at the limb which show prominence mass appearing to condense out of the corona. In this example strands of absorptive material spontaneously develop against the background of the chromosphere. They become darker and longer in periods of a few minutes to tens of minutes and then fade from view. Some of the strands are irregular in shape and hence may be composed of smaller unresolved strands.

Prior to the time that the absorptive strands become a completely developed filament (1722 in Fig. 2) earlier strands are seen to appear and disappear sporadically. The disappearance could be due to reheating of the strands. However, their changing shape and disappearance would also be consistent with the flow of mass from the corona to the chromosphere as is also often observed in time-lapse prominence films over the limb.

After the filament has formed, it continues to reveal continuous absorptive changes in the darkness of its resolvable internal structure and in its overall width and length. Again, this dynamic behavior would be consistent with the continuous process of condensation of mass from the corona and its subsequent flow into the chromosphere.

The magnetic flux around the newly formed filament is shown in the last frame in Figure 2. In the magnetogram there is a uniformly gray vertical streak that intersects a similar gray horizontal streak. These are artifacts where no magnetic field was recorded. In spite of this deficiency, the magnetograms do clearly show that opposite polarity fields exist on either side of the site where the filament formed. Additionally, the time-lapse sequence of magnetograms shows that cancellation of small fragments of flux occurs under the filament and near the upper end during and after its formation.

MAGNETIC FLUX CHANGES ASSOCIATED WITH FILAMENTS

We have recorded the line-of-sight magnetic fields under and adjacent to filaments on several occasions during the last year. Representative images from the time-lapse films taken

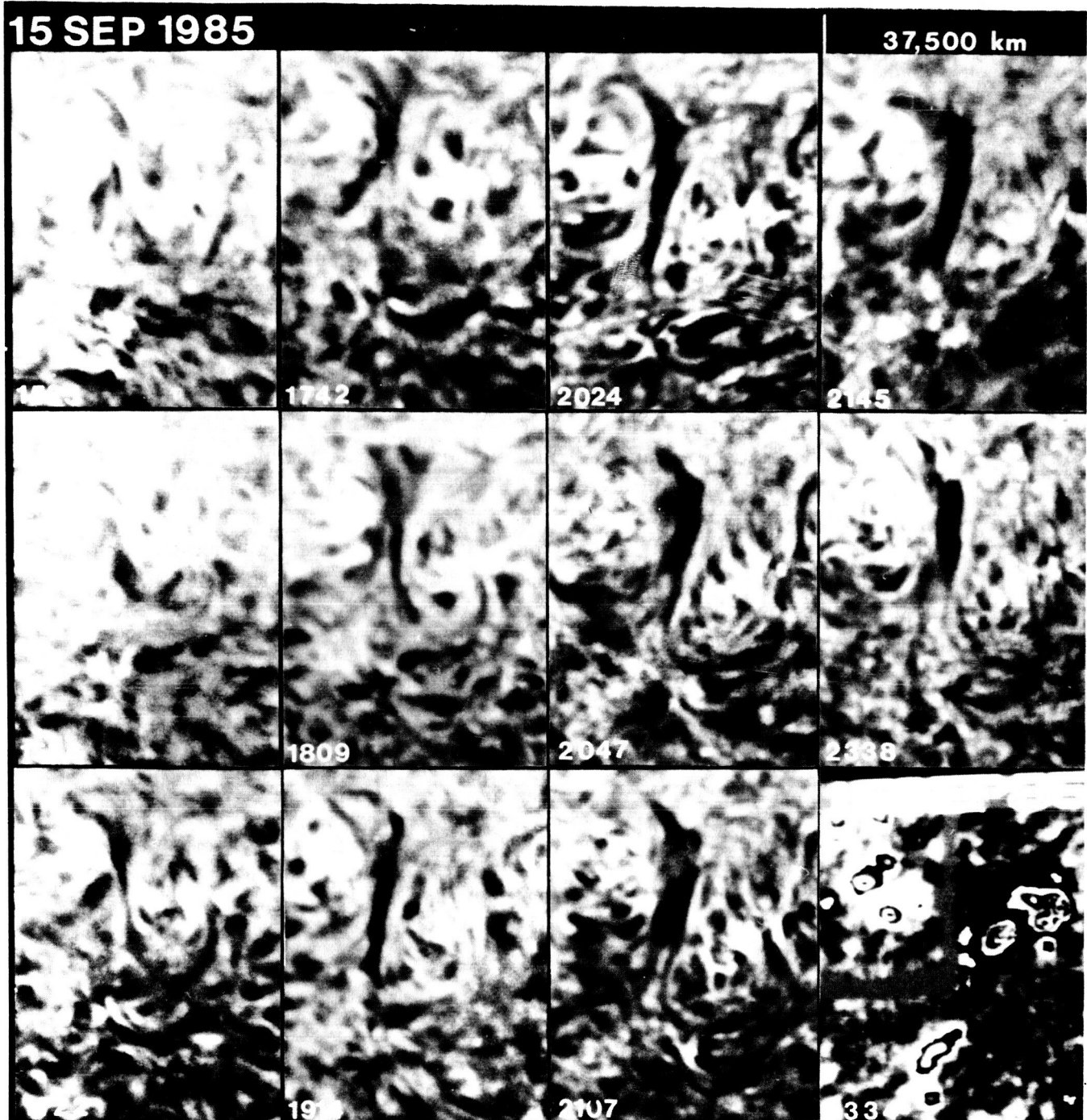


Fig. 2. The formation of this filament on the quiet sun takes at least 2 hours. After 1710, it is a continuously visible structure. Prior to this time, absorptive strands appear and disappear along the path where the filament will form. The continuous changes in the shape of the filament after its formation can be interpreted as the continued formation and disappearance of additional strands that appear to be merged in our line of sight. The magnetogram in the last frame shows that the filament is forming between line-of-sight magnetic flux of opposite polarity.

on 29 and 30 August 1985 are shown in Figure 3. The time-lapse magnetograms show that fragments of opposite polarity magnetic flux frequently move into juxtaposition and become small sites of cancelling magnetic flux. Filaments usually become very narrow where they cross cancelling fragments of magnetic flux. In other cases, such as at the left end of the filament in Figure 3, the end of the filament or a segment of the filament appears to terminate at the site of the cancelling fields rather than threading its way between the opposite polarity fragments. These circumstances suggest the possibility of a direct magnetic linkage between the sites of disappearing line-of-sight magnetic flux and the maintenance or growth of the predominantly horizontal field of filaments, an association already made in a general way by Zwaan (1978).

Very small-scale filaments illustrated and discussed by Hermans and Martin (1986, this volume) often have one end that terminates at the polarity division of small-scale cancelling features, similar to the two examples of newly formed filaments described herein. On the other end of size spectrum, large-scale filaments such as in Figure 3 appear to be just longer versions of the small filaments such as the one in Figure 2. All of these filaments, ranging from very small to large, are associated with sites of cancelling flux.

Cancellation is not unique to filament channels but it is the primary magnetic change that takes place under filaments or at the ends of filaments or the ends of filament segments. Cancellation can take place between any closely spaced magnetic flux fragments of opposite polarity (Martin 1984; Livi et al. 1985; Martin et al. 1985). Under filaments, such as in Figure 3, the cancellation of opposite polarity network is common, but the emergence of new flux under the filament may also create new sites of cancellation wherever the new flux is adjacent to opposite polarity network.

A test of the significance of the coincidence of cancellation to the formation or maintenance of filaments, could be made by observing filament channels with and without filaments. If the coincidence is physically significant, one would expect to find that filament channels without filaments would also have a deficiency of cancelling fragments relative to the number of cancelling fragments in filament channels occupied by a filament. Conversely, one would expect filaments to preferentially form or form earlier in zones where opposite polarity magnetic fields are converging such as between adjacent spreading active centers. Tang (1986) has recently shown that quiescent filaments on the quiet sun occur more often at polarity boundaries between active centers than within active centers.

DISCUSSION

The formation of the filaments illustrated in this paper does not occur by the migration of opposite polarity fields in opposite directions along the polarity inversion zone. Neither do they evolve from fibrils or field transition arches which one could imagine to gradually turn from connecting opposite polarities to dividing opposite polarities. The filament is a new structure. It divides or separates opposite polarities. Within the resolution of our images, even the ends of filaments appear to terminate closer to the division between opposite polarities rather than to the concentrations of magnetic flux on either side of the polarity division. This is a difficult distinction to make with the data because the magnetograms have lower spatial resolution than the $H\alpha$ filtergrams. The magnetograms consist of video frames integrated over many seconds to minutes while exposure for the $H\alpha$ filtergrams is a fraction of a second. Due

to image motion during the greater exposure time required for the magnetograms, the spatial resolution of the videomagnetograms is degraded relative to the $H\alpha$ images. Magnetograms having higher spatial resolution are needed to more precisely define the association of $H\alpha$ features with the small elements of magnetic flux.

Because there is insufficient mass in the corona around filaments to account for their mass (references in review by Forbes 1986), one looks to an alternative supply of mass from the chromosphere. However, during the formation of these filaments, the $H\alpha$ time-lapse images give no direct evidence of the transport of mass from the chromosphere into a filament. The

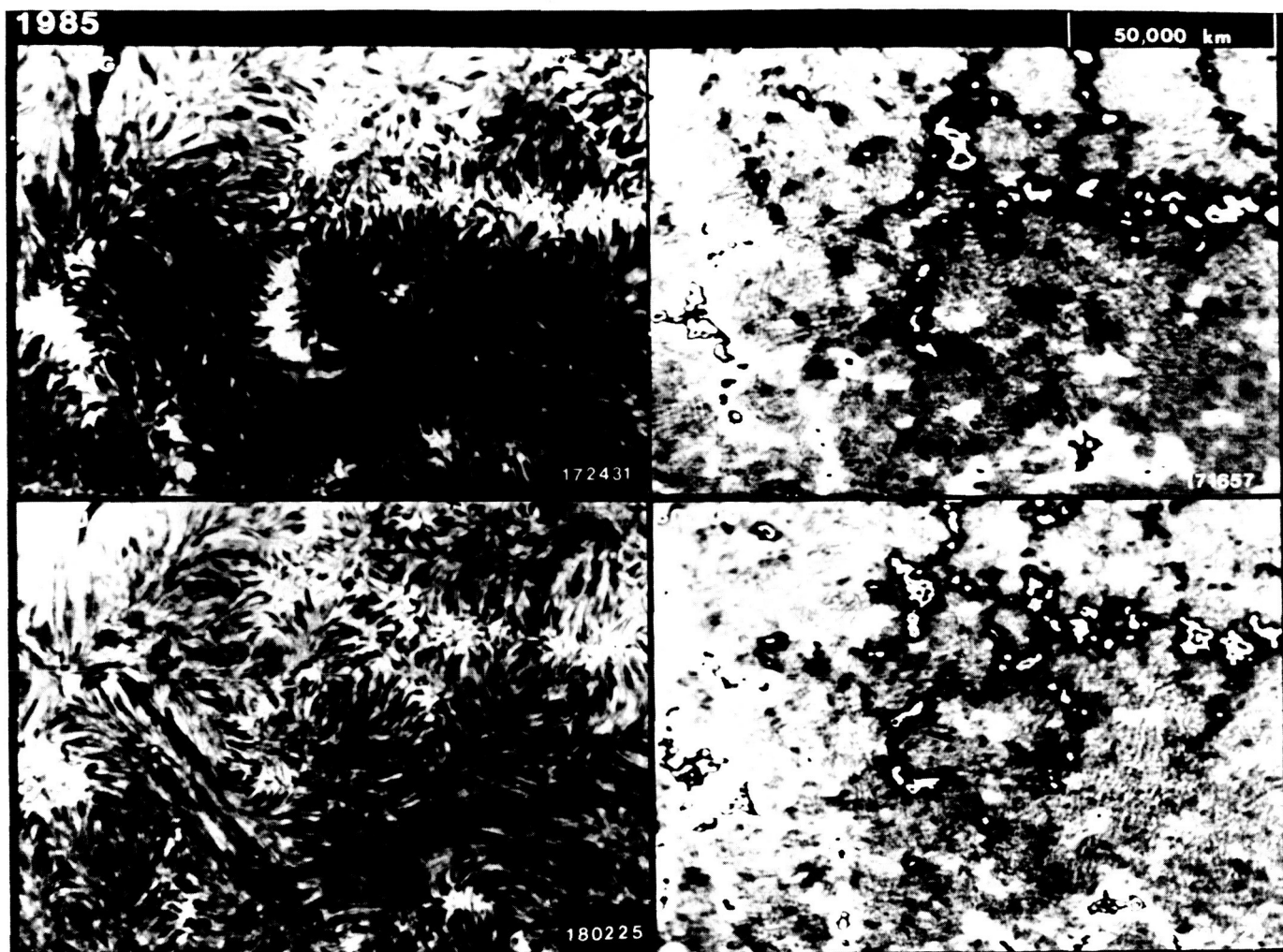


Fig. 3. Comparison of the structure of a filament in $H\alpha$ (left) with the line-of-sight magnetic flux under and adjacent to the filament (right). At the left end of the filament opposite polarity fragments of magnetic flux move together and cancel. Sporadic cancellation of similar small fragments of magnetic flux typically occurs under filaments such as this one. Note that the filament becomes very narrow or breaks into segments where opposite polarity fragments are close together. Negative flux is black and positive flux is white except within the contours. These are areas of stronger magnetic field where each successive inner contour represents an increase in the field by a factor of 2 but the polarity is the same as around the periphery of the contours.

H α observations seem only to confirm previous coronal observations in which the filament mass appears to condense out of the corona. A new clue to the mass supply for filaments is suggested from our observations of cancelling magnetic flux at the ends of filaments or filament segments. The relative orientation of filaments to the cancellation sites is suggestive of a possible link between the field lines of the filament and the magnetic fields of the cancelling features. Because the true magnetic field geometries of both are yet unknown, this linkage is purely hypothetical and no specific magnetic field geometry is proposed in this paper.

It is important to establish more definitively whether the formation of filaments and the cancellation of magnetic flux are: (1) unrelated, (2) indirectly related, or (3) directly related. If directly related, we need to learn whether cancellation is a necessary condition for the formation of filaments.

From the observations described herein, I suggest that cancellation sites might relate to the formation and structure of filaments in the following ways:

- (1) As an evolutionary precondition
- (2) As an environmental influence on the width and path of a filament where it crosses a cancellation site
- (3) As specific locations where ionized mass from the chromosphere could conceivably enter the path of filaments and subsequently condense to form the strands of a filament.
- (4) As locations where the line-of-sight magnetic flux may be changing to horizontal components within filaments because of magnetic reconnection (Zwaan 1978).

Acknowledgments

W. Kershaw prepared the photographic illustrations. The H α observations were obtained under NASA grant NGL 05 002 034 and the magnetic field observations were supported by partially by NSF grant ATM 8211002 and AFOSR grant AFOSR-82-0018. The analysis was performed under NASA SMM Guest Investigator Grant NAG 5-766.

References

- Forbes, T.G. 1986, these proceedings.
- Hagyard, M., R.L. Moore and A.G. Emslie 1984, *Adv. Space Res.*, **4**, 71.
- Hermans, L.M. and Martin, S.F. 1986, these proceedings.
- Smith, S.F. 1968, *Structure and Development of Active Regions*, (ed.) K.O. Kiepenheuer, p. 267.
- Livi, S.H.B., Wang, J. and Martin, S.F. 1985, *Australian J. Phys.*, **38**, 855.
- Martin, S.F. 1973, *Solar Phys.*, **31**, 3.
- Martin, S.F. 1984, *Small-scale Dynamical Processes Stellar Atmospheres*, (ed.) S. Keil, National Solar Observatory, Sunspot, New Mexico, USA, p. 30.
- Martin, S.F., Livi, S.H.B., and Wang, J. 1985, *Australian J. Phys.*, **38**, 929.
- Tang, F. 1986, submitted to *Solar Phys.*.
- Zwaan, C. 1978, *Solar Phys.*, **60**, 213.

ON THE FORMATION OF ACTIVE REGION PROMINENCES ($H\alpha$ FILAMENTS)

Bogdan Rompolt¹

and

Thomas Bogdan

High Altitude Observatory, National Center
for Atmospheric Research²

ABSTRACT: Analysis of sequential $H\alpha$ images of active region prominence formation suggests that simple large-scale photospheric mass-motions may play a key role in the formation of these long, thin, $H\alpha$ filaments.

INTRODUCTION

Detailed investigations by one of us (B.R.) of the temporal evolution of the fine structure of active region prominences has prompted us to explore the possible influence of hypothetical large-scale photospheric velocity fields on the formation of active region filaments.

Our observations are based upon sequences of $H\alpha$ images of active regions taken by the Big Bear Solar Observatory, Holloman and Ramey US Air Force Base Observatories, and the Sacramento Peak National Solar Observatory. In addition, a number of high resolution $H\alpha$ limb photographs from the Astronomical Observatory of Wroclaw University has been employed.

The striking feature of these observations is that the formation of $H\alpha$ filaments appears to be consistent with the presence of a hypothetical large-scale shear flow in the vicinity of the (eventual) filament axis (see e.g., Fig. 1). In some cases, the observations would further suggest a smaller converging velocity component directed towards the filament axis or line of magnetic field polarity reversal (hereafter called the neutral line). While direct evidence for shear flows in active regions has been reported (Martres et al., 1971, 1974, 1977; Harvey and Harvey, 1976, 1980; Athay et al., 1985a,b, 1986a,b), so far as we know, simultaneous $H\alpha$ and ve-

¹ On leave from the Astronomical Observatory of Wroclaw University, Poland.

² The National Center for Atmospheric Research is sponsored by the National Science Foundation.

locity field observations of active region filament formation have not been obtained, so our conjectures are so far unsubstantiated.

OBSERVATIONS

In well developed active regions, one generally observes a hierarchy of dark $H\alpha$ filaments radiating outward from the main sunspots. Beyond the penumbra is a system of fine chromospheric filaments forming the superpenumbra (Loughead, 1968). These filaments usually begin within the penumbra and run outwards, in a more or less radial direction, for a distance on the order of the sunspot diameter. Another set of shorter filaments (fibrils) is found beyond the superpenumbral filaments (see Fig. 1a). It appears that active region prominences are formed from these outlying systems of filaments.

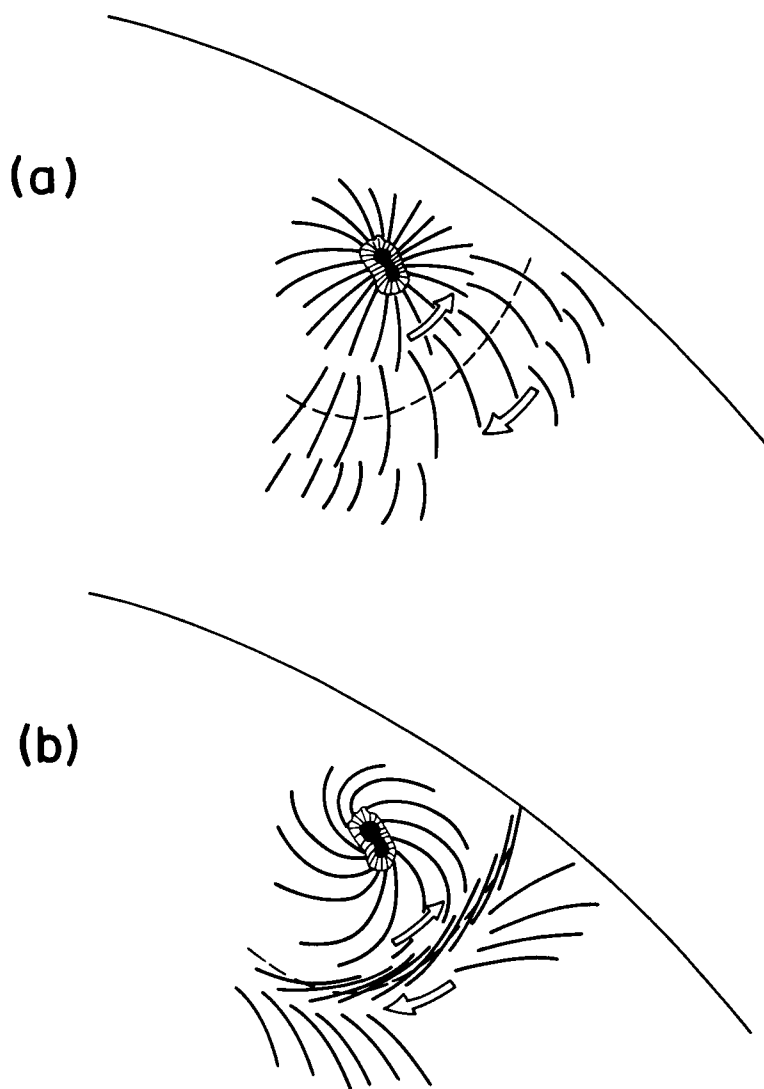


Fig. 1. $H\alpha$ filament formation in anti-parallel converging mass motions.

Figures 1 and 2 illustrate two fairly typical sequences, and the concomitant hypothetical photospheric mass motions, by which active region prominences form.

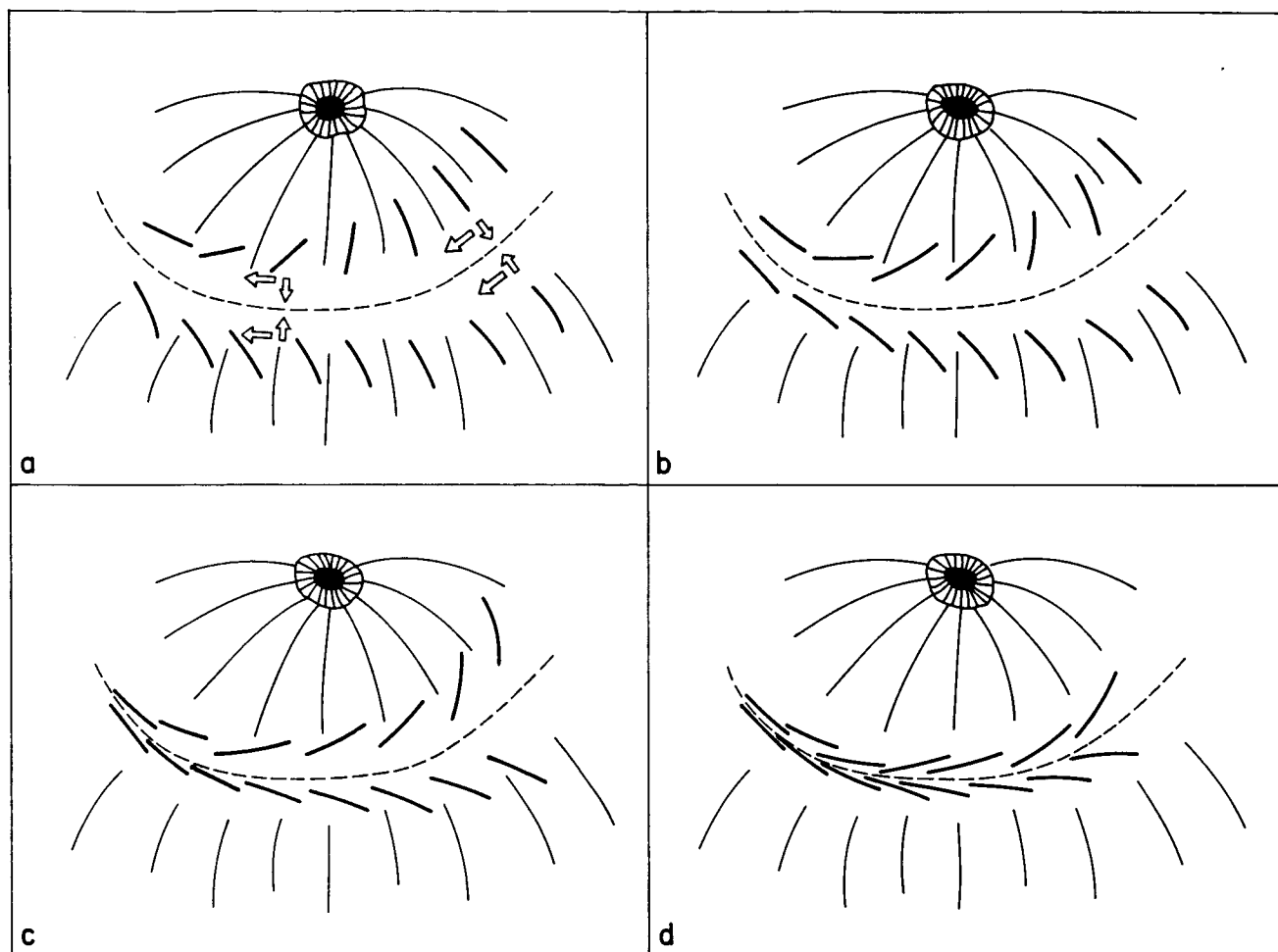


Fig. 2. $H\alpha$ filament formation in parallel converging mass motions.

In Figure 1 a system of fibrils, initially oriented approximately perpendicular to the magnetic neutral (dashed) line, is sheared by mass motions (indicated by arrows) at the photospheric level forming a long $H\alpha$ filament consisting of tightly packed fibrils. In Figure 2, two series of fibrils are sheared and then merged and tightly packed by a flow with a velocity component directed towards the neutral line. Note the difference in the arrangement of fibrils between Figures 1b and 2d, which results from hypothetical mass motions being anti-parallel (Fig. 3a), or parallel (Fig. 3b) on either side of the neutral line.

Our analysis of sequential $H\alpha$ images so far indicates that the majority of active region prominence formation is typical of Figure 1, and by inference, the mass motions of Figure 3a. Figure 4 is an example of an $H\alpha$ filament formed by the sequence of Figure 1, whereas Figure 5 is representative of the Figure 2 formation scenario.

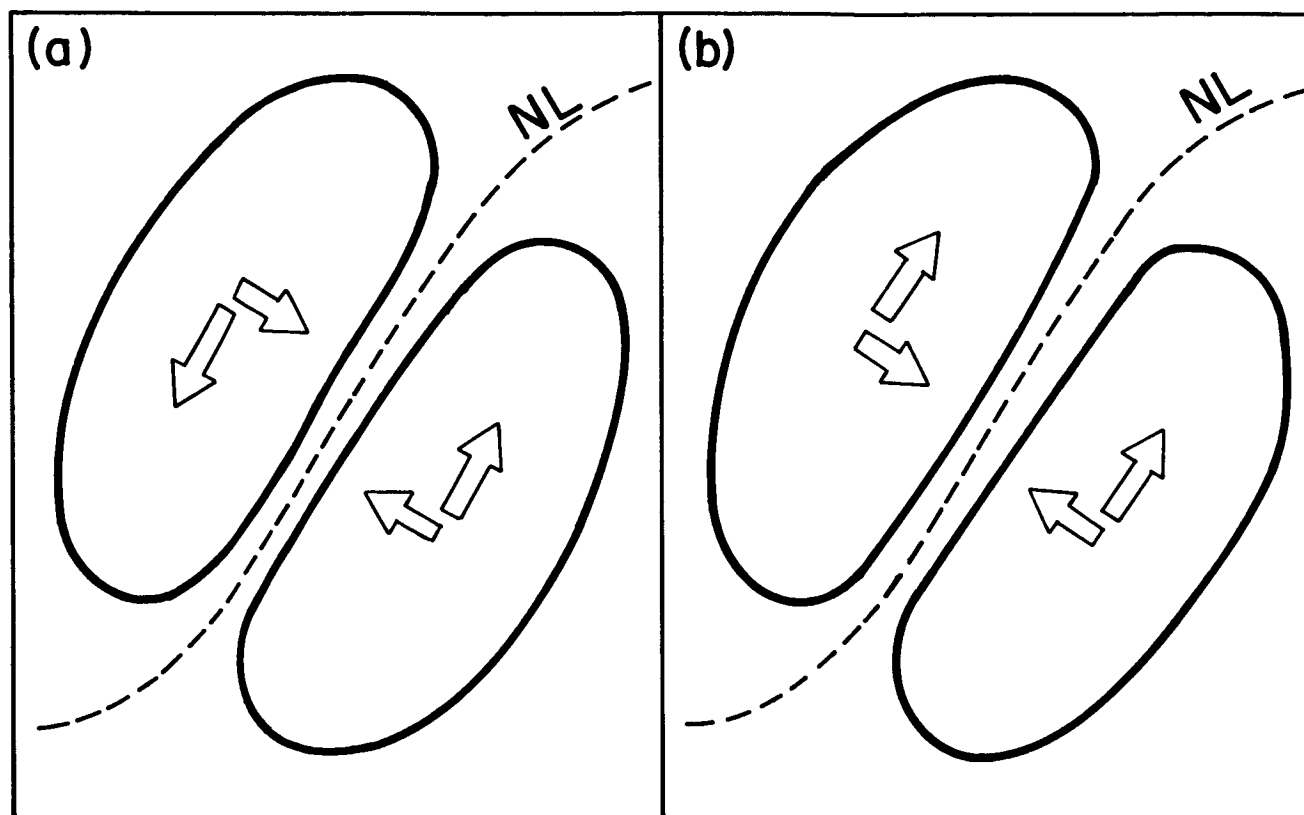


Fig. 3. Two types of converging mass motion about the magnetic neutral line (NL).

DISCUSSION

Investigation of sequential $H\alpha$ images suggests that the observed evolution and subsequent formation of active region prominences from outlying systems of fibrils about sunspots may be the result of some simple photospheric mass motions.

While following evolutionary changes of individual fibrils during formation of $H\alpha$ filaments we often found some fibrils to disappear for several tens of minutes to hours. After some time these fibrils reappeared again displaying changes in location and inclination with respect to the neutral line. Sometimes new fibrils, not seen earlier, abruptly became visible in the region of filament formation. This peculiar behaviour of fibrils made the observation of their evolutionary changes difficult.

The fine structure of some of the $H\alpha$ filaments, especially of those well developed, consists not only of normal fibrils but also of quite long thin filaments, twice and/or three times as long as the average length of fibrils. These filaments may be formed by the reconnection of two or more fibrils tightly packed in an $H\alpha$ filament. One possibility is schematically explored in Figure 6.

While the hypothetical photospheric mass motions of Figure 3 have not yet been observed, such motions at the transition region level have been reported (Athay et al. 1985a,b, 1986a,b). It will be useful to obtain direct photospheric velocity measurements in the vicinity of forming $H\alpha$ filaments. If such flows are indeed present,

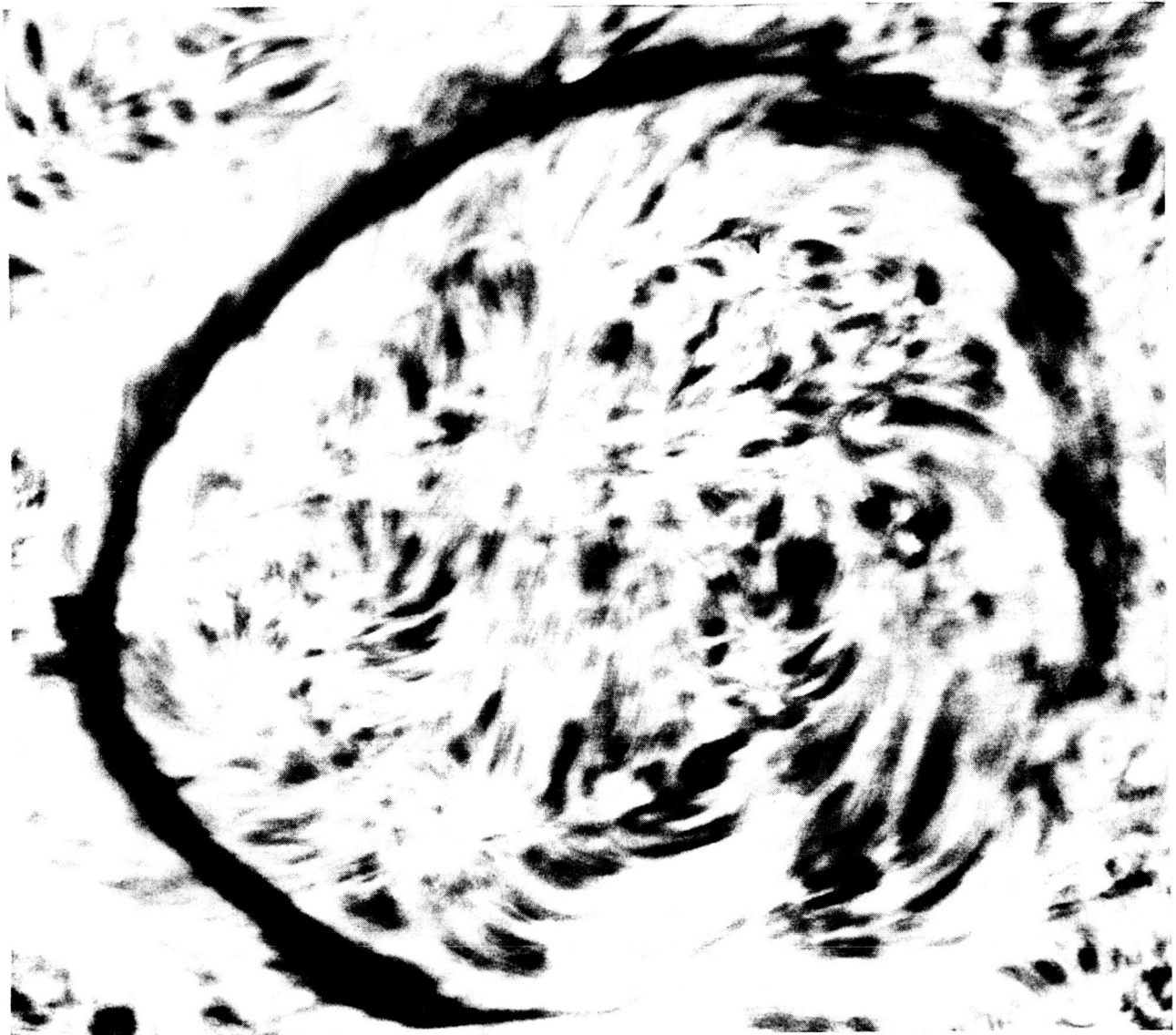


Fig. 4. An H α filament perhaps formed by anti-parallel motions - see Figure 3a (photo courtesy of Dr. R.B. Dunn and Dr. R.N. Smartt, Sacramento Peak National Solar Observatory).

they may provide a unifying principle behind the diversity of H α filament structures and formation.

ACKNOWLEDGEMENTS

One of us (B.R.) would like thank Dr. R.M. MacQueen and the High Altitude Observatory for the privilege of taking part in the Observatory's Visiting Scientist Program.

We would like to express our sincere thanks to Dr. R.B. Dunn and Dr. R.N. Smartt, Sacramento Peak National Solar Observatory, to Dr. H. Zirin, Big Bear Solar Observatory, and to Holloman and Ramey US Air Force Base Observatories for kindly

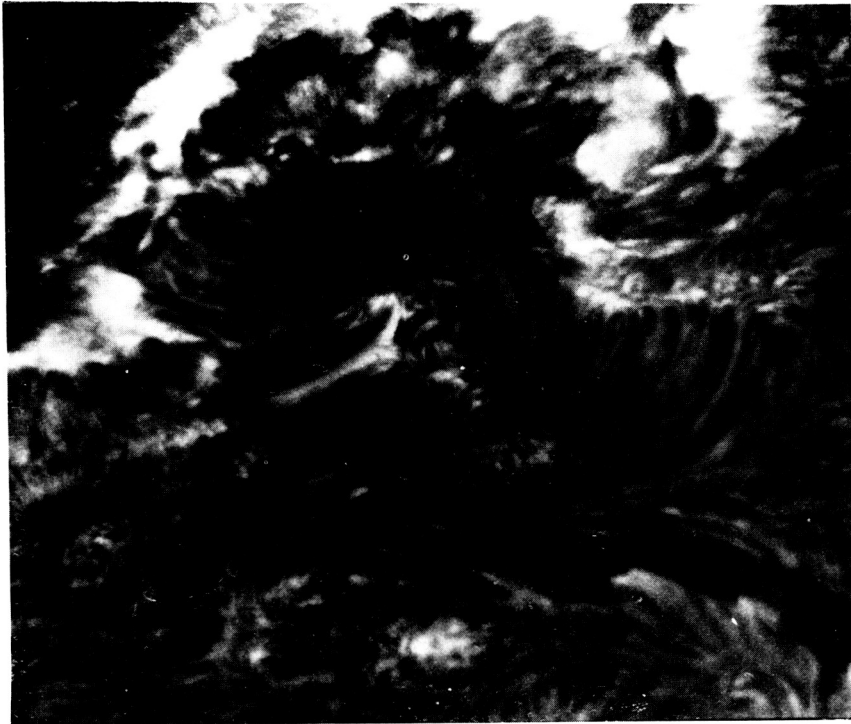


Fig. 5. An $H\alpha$ filament perhaps formed by parallel motions - see Figure 3b (photo courtesy of Dr. H. Zirin, Big Bear Solar Observatory).

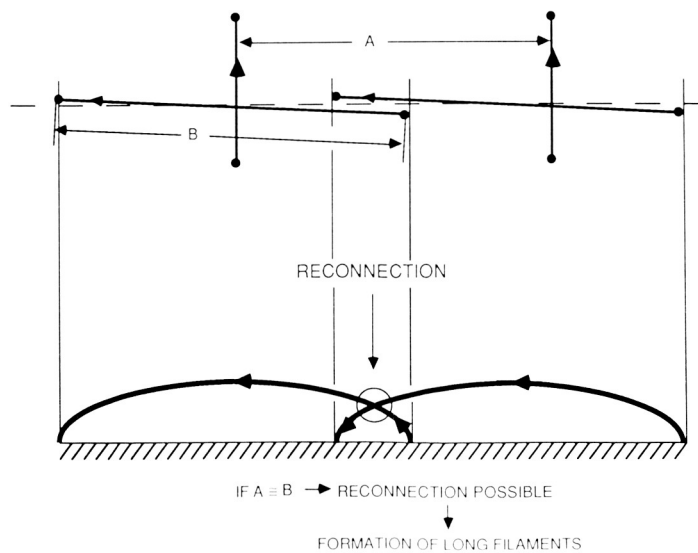


Fig. 6. Scheme for the formation of long, fine filaments in an active region prominence.

placing their observational material at our disposal.

Finally we wish to thank Dr. R.G. Athay for his comments on the manuscript.

REFERENCES

- Athay, R.G., H.P. Jones, and H. Zirin, 1985a, "Magnetic Shear. I. Hale Region 16918", *Astrophys. J.* 288, 363.
- Athay, R.G., H.P. Jones, and H. Zirin, 1985b, "Magnetic Shear. II. Hale Region 17244", *Astrophys. J.* 291, 344.
- Athay, R.G., H.P. Jones, and H. Zirin, 1986a, "Magnetic Shear. III. Hale Region 17255", *Astrophys. J.* 303, 877.
- Athay, R.G., J.A. Klimchuk, H.P. Jones, and H. Zirin, 1986b, "Magnetic Shear IV. Hale Regions 16740, 16815, and 16850", *Astrophys. J.* 303, 884.
- Harvey, K.L. and J.W. Harvey, 1976, "A Study of the Magnetic and Velocity Fields in an Active Region", *Solar Phys.* 47, 233.
- Harvey, K. and J. Harvey, 1980, "Photospheric Velocity Fields as Indicators of Flare Activity", in "Solar-Terrestrial Predictions Proceedings", ed. R.F. Donnelly, Boulder, NOAA Environmental Research Laboratory, Vol. 3, C-41.
- Loughead, R.E., 1968, "High-Resolution Photography of the Solar Chromosphere. V. The Fibrils around Isolated Sunspots", *Solar Phys.* 5, 489.
- Martres, M.J., J. Rayrole, E. Ribes, M. Semel, and I. Soru-Escout, 1974, "On the Importance of Photospheric Velocities in Relation to Flares", in "Flare Related Magnetic Field Dynamics", ed. Y. Nakagawa and D.M. Rust, Boulder, NCAR, 334.
- Martres, M.J. and I. Soru-Escout, 1977, "The Relation of Flares to 'Newly Emerging Flux' and 'Evolving Magnetic Features'", *Solar Phys.* 53, 225.
- Martres, M.J., I. Soru-Escout, and J. Rayrole, 1971, "An Attempt to Associate Observed Photospheric Motions with the Magnetic Field Structure and Flare Occurrence in an Active Region", in IAU Symposium 43, "Solar Magnetic Fields", ed. R. Howard, Dordrecht-Riedel, 435.

DIAGNOSTICS AND STRUCTURE

J.C. Vial

Laboratoire de Physique Stellaire et Planetaire
B.P. 10-F-91371, Verrieres le Buisson Cedex
France

The papers in this section discuss the structure of prominences and the diagnostic techniques used to evaluate their physical parameters. These include electron temperature, various densities (n_p , n_e , n_h), ionization degree, velocities, and magnetic field vector. UV and radio measurements have already evidenced the existence of different temperature regions, corresponding to different geometrical locations, e.g. the so called Prominence-Corona (P-C) interface. Velocity measurements are important for considering formation and mass balance of prominences but there are conflicting velocity measurements which have led to the basic question: what structure is actually observed at a given wavelength; what averaging is performed within the projected slit area during the exposure time? In optically thick lines, the question of the formation region of the radiation along the line of sight is also not a trivial one. The same is true for low resolution measurements of the magnetic field. Although already reasonably well understood, we have made significant progress with the C.P.P. workshops. Coupling diagnostics with structure is now a general preoccupation as it reflects in the title of this section.

I. TEMPERATURE DETERMINATION

New results are presented by Engvold and Brynildsen (1986) who used the Fourier Transform Spectrometer (Kitt Peak) to observe 3 prominences between 7740 and 14000 Å. After a careful subtraction of the sky emission, Paschen lines are calibrated and provide directly the excitation temperature (8000 K). Line profiles of different ions or atoms help to separate the kinetic temperature T from the non-thermal velocity V . T slightly increases from 6200 K (central region) to 7000 K (edge) and V remains around 6 km s⁻¹ with no edge variation.

Low temperatures are also obtained in radio wavelengths with some additional geometry information. Observations of Hiei et al. (1986) at 8.3 and 3.1 mm show that (radio) depression regions correspond to the position of magnetic field neutral lines but not always to H α filaments (the reciprocal being always true). An H α filament appears at a pre-existing depression channel, a phenomenon quite similar to the disappearance brusque where the EUV flux remains after the total disappearance of the H α filament. From the measured depression, the temperature is estimated at about 6600 K. The opacity at 8.3 mm (computed with an assumed electron density of $10^{10.5}$ cm⁻³) is larger than 1, which makes possible radio observations at the limb.

II. TRANSITION REGION (P-C)/ENERGY INPUT

At longer wavelengths, radio observations have been performed with the V.L.A., the resolution of which (2" at 15 GHz) is now rather competitive with optical instruments. Kundu (1986) reports brightness temperatures of $4 \cdot 10^4$ K at 20 cm and $1.5 \cdot 10^4$ K at 6 cm, and depressions well correlated with H α and He (10830 Å) filaments. The width of the radio depression is larger than the H α filament but comparable to the He dark feature. Kundu concludes that the emission arises from the transition sheath surrounding the prominence. The modelling of the transition region indicates some pressure gradient. Similar features are shown by Gary (1986): depressions at 2, 6 and 20 cm, a good superposition with H α filaments but structures appear larger at 6 and 20 cm than in H α . Interestingly the 2 cm width is quite similar to the optical one and Gary notes bright "rims", about 2" (or less) wide, on each side of the filament. He concludes that it corresponds to the sheath between the cool and hot material, although footpoint emission is not discarded. Gary suggests a center to limb observational test.

In the UV, Skylab observations are revisited by Schmahl and Orrall (1986) who computed the differential emission measure from 10^4 to $10^{6.4}$ K. They compare the observed low absorption in the Lyman continuum at high temperatures with the results of modelling sets of threads. They try 3 different geometries:

- 1) hot sheaths around cool cores
- 2) isothermal threads (a reference to Poland and Tandberg-Hanssen's SMM results, 1983)
- 3) threads with longitudinal temperature gradients along the magnetic field.

They find no solution with #2, and a rather improbable one with #1. Geometry #3 allows for a balance between radiative losses and conductive flux. The low absorption at high temperature is explained by the lower temperature gradient here, and the minimum of the Differential Emission Measure (DEM) around 10^5 K is recovered for a coronal pressure of $N.T \sim 10^{14.2}$. However the strong absorption requires, either a geometrical explanation (such as a wrapping around cool cores of threads) or some non-LTE mechanism where emission is allowed from cooler regions.

The problem of the shape of the DEM between $10^{4.5}$ and 10^6 K, in particular its commonality between the P-C and C-C interface, is attacked from a theoretical point of view by Rabin (1986). He recalls how classical models determined by thermal conduction along the magnetic field fail because the very thin transition region around $T \sim 10^{4.5}$ does not radiate enough to provide the (observed) increase of DEM toward lower temperatures. The cool "coronal" loops proposed by Antiochos and Noci (1986) are not compatible with the great vertical extension of prominences. Heating-cooling cycles, suggested by Athay (1984) for spicules, could work for prominences only if the heating function is carefully chosen and is remarkably similar in widely

different environments. The current-heating model of Rabin and Moore (1984) faces a similar question: why its proposed fine-scale electric currents should be present with comparable properties in prominences and in the chromosphere. In response to these difficulties, he advances the idea that the shape of the DEM can be produced by the combined action of longitudinal and transverse thermal conduction, even in the absence of internal heating, if the transition plasma is highly fragmented. The orthogonal conduction is also taken into account in the thermal equilibrium study of a 2 D structure by Demoulin et al. (1986). Here the energy input also includes some wave heating proportional to the density. Instability takes place for longitudinal length scales greater than about one arc minute. Orthogonal length scales smaller than 5 km enable the transverse conduction to stabilize the structure. Larger scales lead to an instability time of about 10^4 s, comparable to the lifetime of prominences fine structure.

III. DENSITIES AND IONIZATION DEGREE

These quantities were well established a few years ago (see Hirayama's review in the proceedings of the 1978 Oslo Colloquium): typical values of electron density (about 10^{10} to 10^{11} cm^{-3}) and ionization degree ($n_p/n_1 \sim 1$ to 3) were confirmed by Skylab, OSO 8 and eclipse results. Later on, they were questioned by Landman (1984): from the ratio of metallic lines (e.g. MgI/SrII), he derived electron densities larger than 10^{11} cm^{-3} , ionization degree as low as 0.09 and (neutral) hydrogen densities as high as $4.5 \cdot 10^{12}$ cm^{-3} . Such values imply a very large amount of material (a prominence mass close to the corona's) and a β ratio higher than 1. Hirayama (1986) compares Stark determinations of the electron density with measurements of MgI/SrII emissions. Contrary to Landman, he finds that electron densities range between 10^{10} and $10^{11.4}$ cm^{-3} and the Mg/SrII ratio is independent of density. This point is crucial since massive prominences found by Landman (partly) resulted from high electron densities. Combining with the emission measure information, Hirayama derives an effective length of about 80 km and a filling factor of about 0.3. Thread diameters of, say, less than 300 km, spaced every 1000 km would have an ionization degree fixed by the full illumination of the Lyman continuum.

As shown above, emission measure and density determinations require a strong filamentation at low and high temperatures. However, any undisputable diagnostic must be established from the agreement of all possible observations. In this respect, the resonance UV lines, with their large range of formation "depths", seem appropriate although they need much care in their non-LTE treatment.

IV. MODELLING

Heinzel et al. (1986) repeat the 1 D non-LTE computations of Heasley, Milkey and Mihalas (see Heasley and Mikley, 1983, and previous papers)

for the hydrogen atom, implementing new features such as the exact chromospheric incident line profiles and partial frequency redistribution (PRD). They find the usual wing lowering and also some frequency coherence in the near wings which explains why emergent prominence profiles mimic the incident ones (e.g. for $L\alpha$). A low pressure and density model fits the OSO 8 observed profiles quite well, except for the $L\beta$ line (which requires more studies in redistribution and multidimensionality). In these computations, 5 atom levels are involved which demonstrates strong non-LTE interlocking. This is also well evidenced in the work of Heinzel and Romport (1986) who evaluate the influence of radial velocities on hydrogen lines in moving prominences. The $L\alpha$ line shows a Doppler dimming (lower intensity) increasing with the velocity. On the contrary, $H\alpha$ and $H\beta$ have a Doppler brightening of about 3 peaking at velocities of 160 km s^{-1} . The $L\beta$ line follows a complex behaviour. Such results, which apply for low density plasmas, may be used not only for transient phenomena but also for lower velocity structures such as loops. Permanent velocities are systematically studied in order to assess the mass, momentum and energy budgets and help to establish prominence models.

V. VELOCITIES AND MASS FLOW

Some contradiction has been found in the past between (apparent) downflows observed at the limb (Dunn's thesis, 1960) and upflows derived from Dopplershifts in $H\alpha$ (Meudon Group, see for instance, Martres et al. 1981). Since then, more evidence has been accumulated for both flows in cool and hotter regions, as detected in C IV by the UVSP experiment on SMM. From HeI (10830Å) observations at Sac Peak, Engvold and Keil (1986) conclude that blue shifts dominate redshifts, the former reaching 3 km s^{-1} in darkest areas, the latter being common in edges. They question the existence of such persistent flows on the basis of the insufficient spatial (and temporal) resolution which mixes different upward and downward structures. The already observed $H\alpha$ and C IV blueshifts are confirmed by Simon et al. (1986) but they seem to be more systematic in an active region filament (between foot points) than in a quiescent one. Moreover, downflows (comparable in $H\alpha$ and C IV) exist in the foot points of the active region filament. Simon et al. suggest a long magnetic rope rising while material drains at the foot points. 21 active region filaments have been studied also in C IV by Klimchuk (1986) with UVSP/SMM observations. A majority of them are associated primarily with relative blueshifts, however local deviations exist and some filaments coincide with lines of apparent velocity reversal. Klimchuk discusses the problem of absolute velocity calibration in C IV Dopplergrams and proposes a procedure relying on velocities previously measured in quiet and active regions by Skylab, OSO 8, etc. His center to limb study leads to small velocity magnitudes ($< 3 \text{ kms}^{-1}$) in filaments. Directions of flow are still uncertain.

Evidently, more studies are necessary and the UVSP/SMM database should be used extensively for center limb, quiescent/active/eruptive

filament comparisons. Thompson (1986) gives the key to this data base consisting of Dopplergrams, Rasters through the line and Profile Matrix observations. Certainly the addition of simultaneous ground based measurements will increase the interest of such studies.

In this respect, a sequence of simultaneous H α and C IV observations of active region filaments has been analyzed by Schmieder *et al.* (1986). No significant power is found in H α and C IV velocities around 200 s, except for regions identified as foot points where some oscillations in C IV exist, dominated by a systematic upward flow. The authors conclude that the energy input is probably due to convective motions rather than pressure oscillations.

Velocities may also help to discriminate between possible models (KS, KR, Hiriyama..) but magnetic fields are prime and necessary ingredient of these models.

VI. MAGNETIC FIELD

Important recent progress has been achieved with the use of the Hanle effect ie. the depolarization by local magnetic field. Broad band polarimetry in D3 performed on 256 prominences at Pic du Midi by Leroy, Bommier and Sahal (see for instance, Leroy *et al.* 1984 and previous papers) has shown that the average field is horizontal, at an angle of about 20° with the filament axis and is lower than 30 G. From a statistical study, it appears that low altitude prominences have potential field (KS type) and high ones a non-potential field (KR). A review and a comparison with other Zeeman and Hanle (Sac Peak) measurements are given by Landi (1986). He shows how the polarization has been computed in an optically thick line such as H α and how the use of thin and thick lines may help to solve the ambiguity in the direction of the magnetic vector. Simultaneous observations of circular and linear polarization in several spectral lines would be a significant step. Such an improvement is in progress with the computations of the hydrogen H β line (along with He D₃) which are compared to previous observations (Bommier, 1986). When depolarizing collisions with electrons are taken into account, not only the 3 coordinates of the magnetic field vector are unambiguously determined, but also the electron density can be derived. Out of 14 prominences, some 8 have a magnetic field significantly inclined to the horizontal plane. The electron density ranges from 10^9 to $4 \cdot 10^{10}$ cm⁻³. Such a diagnostic, although difficult because of transfer problems, seems very promising.

CONCLUSIONS

Since a complete review exists (Hiriyama, 1985), we shall only discuss the results from these workshops. Although the observed range of temperatures probably reflects the range of situations in different prominences, mean values lower than 7000 K have been presented which may indicate the existence of thick structures. Such a tendency somewhat contradicts other

results concerning significant ionization degree and low densities. All electron density determinations, for instance, are in the low range of values ($\leq 10^{11} \text{ cm}^{-3}$) as compared to Landman's higher values. An agreement for low pressure around $10^{-1} \text{ dyn cm}^{-2}$ (and sometimes lower) was achieved through the different contributions. With typical magnetic values of, say, 15G in prominences, we arrive at a picture where the noise gas pressure is lower in prominences than in the corona while the contrary stands for magnetic pressure. Classical models that could take these features into account have been questioned in terms of geometrical structure. Observed differential emission measures, velocities and computed energy budgets certainly require some degree of material filamentation. Much progress is occurring in transfer problems also (see e.g. Fontenla and Rovira, 1985). But such analysis should also rely on direct observations. It is our feeling that such work should be supported by spectroscopic observations with a subarcsecond resolution (0.1"), necessary for velocity (and magnetic field ?) measurements, and a good temporal resolution. Perhaps very high resolution images coupled with lower resolution spectroscopy in many different lines would be a first realistic step. Such an effort is certainly worthwhile in view of the important progress evidenced by these workshops.

REFERENCES

- Antiochos, S.K. and Noci, G. 1986, *Ap.J.*, 301, 440.
 Athay, R.G. 1984, *Ap.J.*, 287, 412.
 Bommier, V. 1986, this proceedings.
 Demoulin, P., Malherbe, J.M., Schmieder, B., and Raadu, M.A. 1986, this proceedings.
 Dunn, R.B. 1960, Ph.D. Thesis, Harvard University.
 Engvold, O. and Brynildsen, N. 1986, this proceedings.
 Engvold, O. and Keil, S.L. 1986, this proceedings.
 Fontenla, J.M. and Rovira, M. 1985, *Solar Phys.*, 96, 53.
 Gary, D.E. 1986, this proceedings.
 Heasley, J.N. and Milkey, R.W. 1983, *Ap.J.*, 268, 398.
 Heinzel, P., Gouttebroze, P., and Vial, J.C. 1986, this proceedings.
 Heinzel, P. and Rimpolt, B. 1986, this proceedings.
 Hiei, E., Ishiguro, M., Kosugi, T., and Shibasaki, K. 1986, this proceedings.
 Hiriyama, T. 1979, *IAU Colloq.* 44, 4.
 Hiriyama, T. 1985, *Solar Phys.*, 100, 415.
 Hiriyama, T. 1986, this proceedings.
 Klimchuk, J.A. 1986, this proceedings.
 Kundu, M.R. 1986, this proceedings.
 Landi Degl' Innocenti, E. 1986, this proceedings.
 Landman, D.A. 1984, *Ap.J.*, 279, 438.
 Leroy, J.L., Bommier, V., and Sahal-Brechot, S. 1984, *Astron. and Astrophys.* 131, 33.
 Martres, M.J., Mein, P., Schmieder, B., and Soru-Escut, I. 1981, *Solar Phys.*, 69, 301.
 Poland, A.I. and Tandberg-Hanssen, E.A. 1983, *Solar Phys.*, 84, 63.
 Rabin, D. 1986, this proceedings.

Schmahl, E.J. and Orrall, F.Q. 1986, this proceedings.
Schmieder, B., Malherbe, J.M., Mein, P., and Tandberg-Hanssen, E.A. 1986,
this proceedings.
Simon, G., Schmieder, B., Demoulin, P., Malherbe, J.M. and Poland, A.I.
1986, this proceedings.
Thompson, W. 1986, this proceedings.

TEMPERATURES OF QUIESCENT PROMINENCES MEASURED FROM HYDROGEN PASCHEN AND CaII IR LINES

Oddbjørn Engvold and Nils Brynildsen

Institute of Theoretical Astrophysics
University of Oslo, P.O.Box 1029
Blindern, N-0315 Oslo 3, Norway

INTRODUCTION

Prominence temperatures and non-thermal velocities are most commonly determined from emission line widths from elements of different atomic weight. It is assumed that the lines are optically thin. The average temperature for the main part of quiescent prominences is 6500 K (5000-8000 K) according to Hirayama (1985). The corresponding velocities are $3 \text{ km s}^{-1} < V < 8 \text{ km s}^{-1}$. The lowest value recorded from the combined widths of H, He, and metallic lines is $4300 \pm 200 \text{ K}$ (Hirayama 1978). A tendency of increasing temperature towards the periphery of prominences was first noticed by Hirayama (1964, 1971). The results from a number of studies give $8000 \text{ K} < T < 12000 \text{ K}$ and $8 \text{ km s}^{-1} < V < 20 \text{ km s}^{-1}$ in the outer parts of prominences (Hirayama 1971; Engvold 1978; Landman et al. 1977).

Analysis of the hydrogen excitation-ionization equilibrium (e.g. Chultem and Yakovkin 1974) indicates that the excited levels of the hydrogen atoms in quiescent prominences are near thermodynamic equilibrium, i.e. $T_{\text{exc}} \approx T_{\text{kin}}$. The gas temperature will then be reflected in the relative intensities of hydrogen lines. Earlier measurements of hydrogen Balmer lines in prominence spectra are incomplete (Jefferies and Orrall, 1962; Nikolsky et al. 1971) and show large variations from case to case in terms of excitation temperature. Stellmacher (1969) finds $T_{\text{exc}} = 6000 - 6250 \text{ K}$ from the brightness variation of the lines $H\beta$ through H_9 , and Morozhenko (1974) gets $T_{\text{exc}} \approx 7300 \text{ K}$ using the lines from $H\alpha$ to H_{20} .

Measurements by Landman and Mongillo (1979) gave still a substantial scatter in the H I Balmer decrement which represented excitation temperatures ranging from 3450 K to 11000 K. This quite large variation in T_{exc} was ascribed partly to measurement errors, and to the low spectral resolution in the observation which did not permit the authors to correct properly for line-blends. Very recent observations in the far infrared (10 - 20 μm) of prominence hydrogen lines have been analysed by Zirker (1985) who finds a Boltzmann distribution corresponding to $T_{\text{exc}} = 3800$ K. The author points out that the IR hydrogen lines span a narrow range of energy and the result is therefore highly sensitive to errors in the measured line intensities. The value of T_{exc} is nevertheless uncomfortably low when compared to $T_{\text{kin}} \approx 10\,000$ K which is derived from the widths of the same lines and an infrared line of He.

Observations of continuum emission near the Balmer jump at 3646 Å have been used to derive prominence temperature and density (cf. Jefferies and Orrall 1962). The results are quite uncertain since they depend on the assumed thickness of the emitting volume. The H I Lyman continuum of nine hedgerow prominences observed with the EUV spectrometer on Skylab could be represented by color temperatures between 6122 K and 8669 K with a mean of 7524 ± 739 K (Orrall and Schmahl 1980). Considering the large optical thickness of the Ly C these values presumably equal the electron temperatures.

The temperature of prominence gas is a function of the incident radiation from the corona, chromosphere and photosphere (c. Heasley and Mihalas 1976). One notices that an equilibrium temperature will also be a function of the Ly C opacity. The concept of an actual equilibrium situation may however be debated. The relatively short lifetimes of the small scale structures of quiescent prominences could suggest that the gas is subjected to rapid changes in temperature and/or density (Engvold 1980)

The noted centre-to-edge effect evidently represents a real variation in prominence temperature. But generally, the notable variations in the result quoted above may largely reflect deficiencies in the method used. Different combinations of line widths are often found to give different temperatures (Jefferies and Orrall 1962; Hirayama 1978; Landman 1979). This clearly illustrates problems with the 'line width'-method. For instance unresolved filamentary structures may affect the profiles of various lines differently and thus lead to slightly erroneous temperatures. The excitation temperature

determined from hydrogen line intensities is highly sensitive to photometric errors and to effects of line opacities.

New and high quality observations of infrared prominence lines of hydrogen, calcium and other species have been obtained. We have compared temperatures derived from line widths and from hydrogen line intensities in an attempt to assess the reliability of the two methods discussed above.

OBSERVATION, INSTRUMENTATION AND DATA REDUCTION

During 12-17 September 1983 a number of prominences were observed with the McMath solar telescope of National Solar Observatories, using the Fourier transform spectrometer with a InSb detector (Brault 1979). The present study refers to three prominences observed 13 and 14 september.

Prominence A: Large quiescent prominence at S28 E90

Prominence B: Stable prominence in weakly enhanced magnetic region at about N08 E90

Prominence C: Quiescent prominence at N30 E90

Spectra were obtained at a total of 15 different locations in the three prominences in the wavelength range $\lambda\lambda 7740\text{--}14000\text{\AA}$. The aperture covered an area of 80 arcsec^2 on the solar image. The light reflected off the aluminium coated aperture plate was imaged through a narrow band $H\alpha$ filter. This system allowed us to select the pointing within a prominence and to maintain aperture position during a scan. The integration time for individual spectra was 17 minutes. Spectral resolution was typically $\Delta\nu = 0.005\text{ cm}^{-1}$ ($\lambda/\Delta\lambda = 2\,000\,000$).

The spectrum of the sky background is bright in comparison to all infrared prominence emission lines, with the exception of the He I $\lambda 10830\text{\AA}$ line, and it needs to be subtracted from the data. For this purpose we made separate spectral scans of the sky background close in time to the prominence observations and at corresponding distances from the solar limb. The incident solar spectrum is modified by absorption in the terrestrial atmosphere and by the spectral responses of the beamsplitter and the detector. In order to establish an absolute intensity scale we made spectral scans of the solar disk center with the same instrument setting except for a necessary gain adjustment of the detector system.

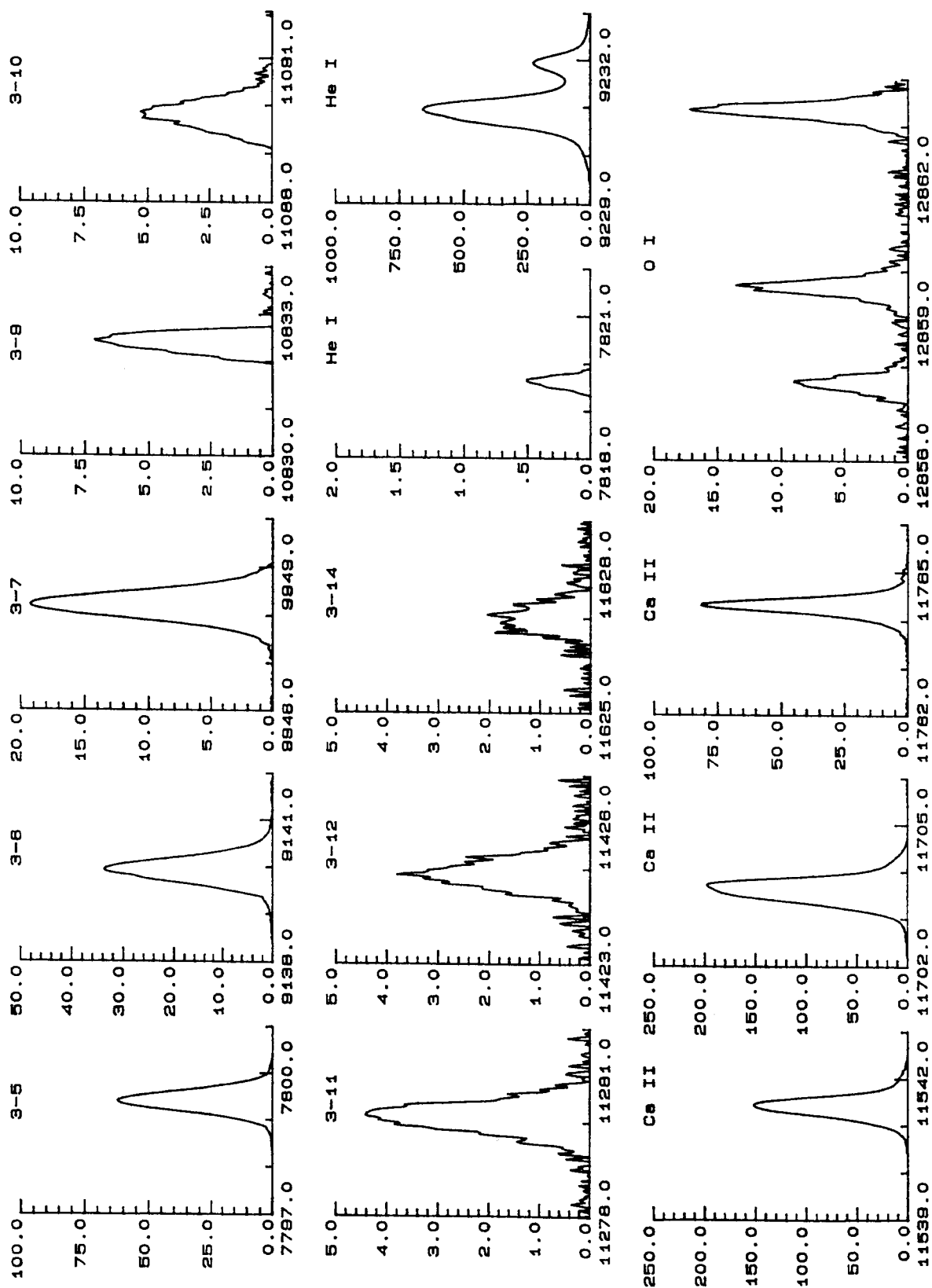


Figure 1. Emission lines from edge of Prominence A observed on 14 September 1983. The intensities x250 are in units of $\text{erg cm}^{-2} \text{s}^{-1} \text{sr}^{-1} \text{\AA}^{-1}$.

The first step in the data reduction was to subtract the appropriate sky background emission from each of the prominence spectra. The intensities were then transformed to an absolute scale via the solar disk spectra and the corresponding continuum intensity values given by Labs and Neckel (1968). Further details of the data reduction procedures are given in Engvold and Brynildsen (1986).

Figure 1 shows an example of emission lines recorded in a medium bright portion of prominence A. In the spectrum of particularly bright prominence structures the hydrogen line from up to levels $n = 23$ could be observed.

ANALYSIS

Excitation temperature

The line intensities reflect the relative upper state populations. In the case that the population of the excited levels is determined basically by the balance of ionizing collisions and recombinations the population will obey a Boltzmann distribution. The intensity variation with level quantum number is then a function of temperature only and may be represented by the relation

$$\frac{1}{kT} (\chi_0 - \chi_i) = \ln (E\lambda/g_i A_{ij}) + \text{const.}$$

where the observed line emission is E , and all the other parameters have their usual meaning. The indices 0, i and j denote respectively ionization energy from ground level, the upper and lower energy level.

Figure 2 shows a plot of the right hand side of the equation versus ionization energy from level i divide by Boltzmann's constant, $\Delta\chi/k$. The slope of the best fitting yields excitation temperature, which in the present case becomes $8\,000 \pm 700$ K. The solution is sensitive to photometric accuracies, to statistical noise in the data, and to effects of line saturation. Terrestrial line absorption disturbs the observations of H_{3-8} and H_{3-9} and reduce the total line emission relative to its true value. (The H_{3-8} line is severely disturbed and is not measured at all.) The deviation of the line profile from a best Gaussian fit (r^2) is a good measure of the quality of the data in terms of signal/noise and it indicates effects of saturation in

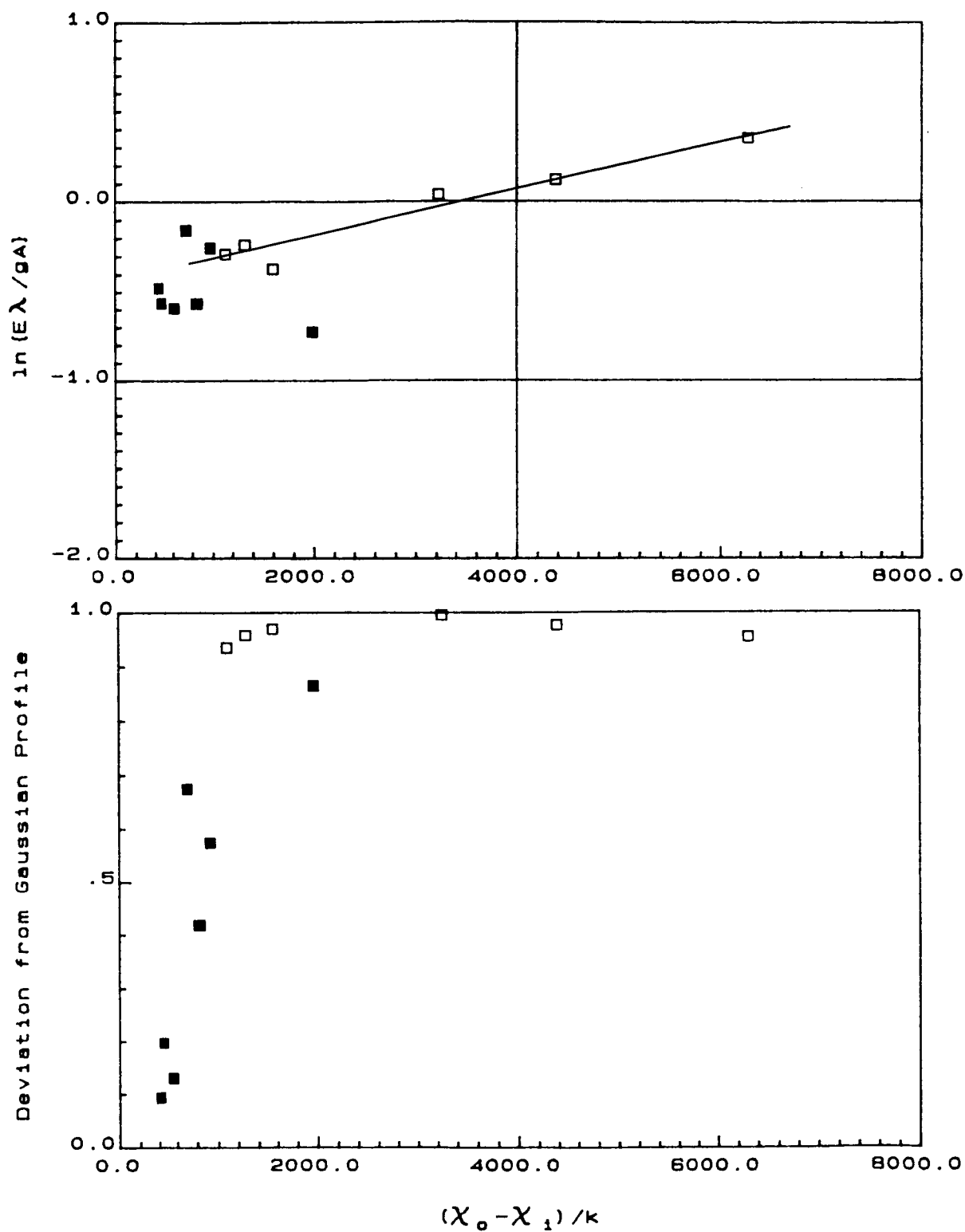


Figure 2a. The Boltzmann graph of the hydrogen Paschen lines shown in Figure 1. The slope of the distribution corresponds to $T_{\text{exc}} = 8000 \pm 700$ K.
 b. The deviation of line profiles from a best Gaussian fit.

the profile of the earliest lines in the series. Figure 2a shows the deviation from Gaussian profile of the lines given in the Figure 2b. The value $r^2 = 1$ means that the profile is Gaussian. The excitation temperature is determined from the slope through lines for which $r^2 > 0.95$.

Table 1

Temperature and non-thermal velocities of three quiescent prominences. The kinetic temperatures and velocities are derived from H I and Ca II lines.

Date	Prom.: Location	T_{exc} (K)	T_{kin} (K)	V (km s ⁻¹)
13 Sep-84	A: Edge	8000 ± 700	6300	6.3
	A: Central part	8000 ± 700	6850	5.9
	A: Top part	7000 ± 500	6430	5.3
	A: Central part	8000 ± 700	5540	5.9
	B: " "	7200 ± 500	12200	7.7
	B: " "	8000 ± 500	9010	6.8
	B: " "	6000 ± 500	6470	11.1
	B: Edge	8000 ± 500	5530	12.2
14 Sep-84	A: Edge	8000 ± 700	7270	6.3
	A: "	10000 ± 1000	5900	6.0
	B: Central part	10000 ± 1000	6340	4.8
	C: " "	6500 ± 500	7100	6.9

Kinetic temperature.

The line widths are determined from the best fit Gaussian profile for each line. If we assume that lines of different elements are formed in the same volume we may separate and obtain the kinetic temperature (T_{kin}) and the non-thermal velocity (V) according to standard procedure (cf. Zirker 1985). We may apply the 'line width'-method to various combinations of lines from the present data, such as H-Ca, H-O, H-He, and in principle even Ca-O. The tripple compo-

nent He I $\lambda 10830\text{\AA}$ is generally strongly saturated and cannot be used to determine T_{kin} except in a very few cases of weak emission. The hydrogen Paschen lines are basically optically thin in the prominence spectra, and the widths are measured from the most Gaussian shaped profiles ($r^2 \approx 1$) in each case. The same profile criterion was used to derive non-saturated widths from the Ca II lines ($\lambda 8498\text{\AA}$, $\lambda 8542\text{\AA}$ and $\lambda 8662\text{\AA}$) and from O I ($\lambda 7772\text{\AA}$, $\lambda 7774\text{\AA}$, and $\lambda 7775\text{\AA}$). The relative strength and width of the lines of Ca II and of O I provide additional informations on the line opacities. See Engvold and Brynildsen (1986) for further detail.

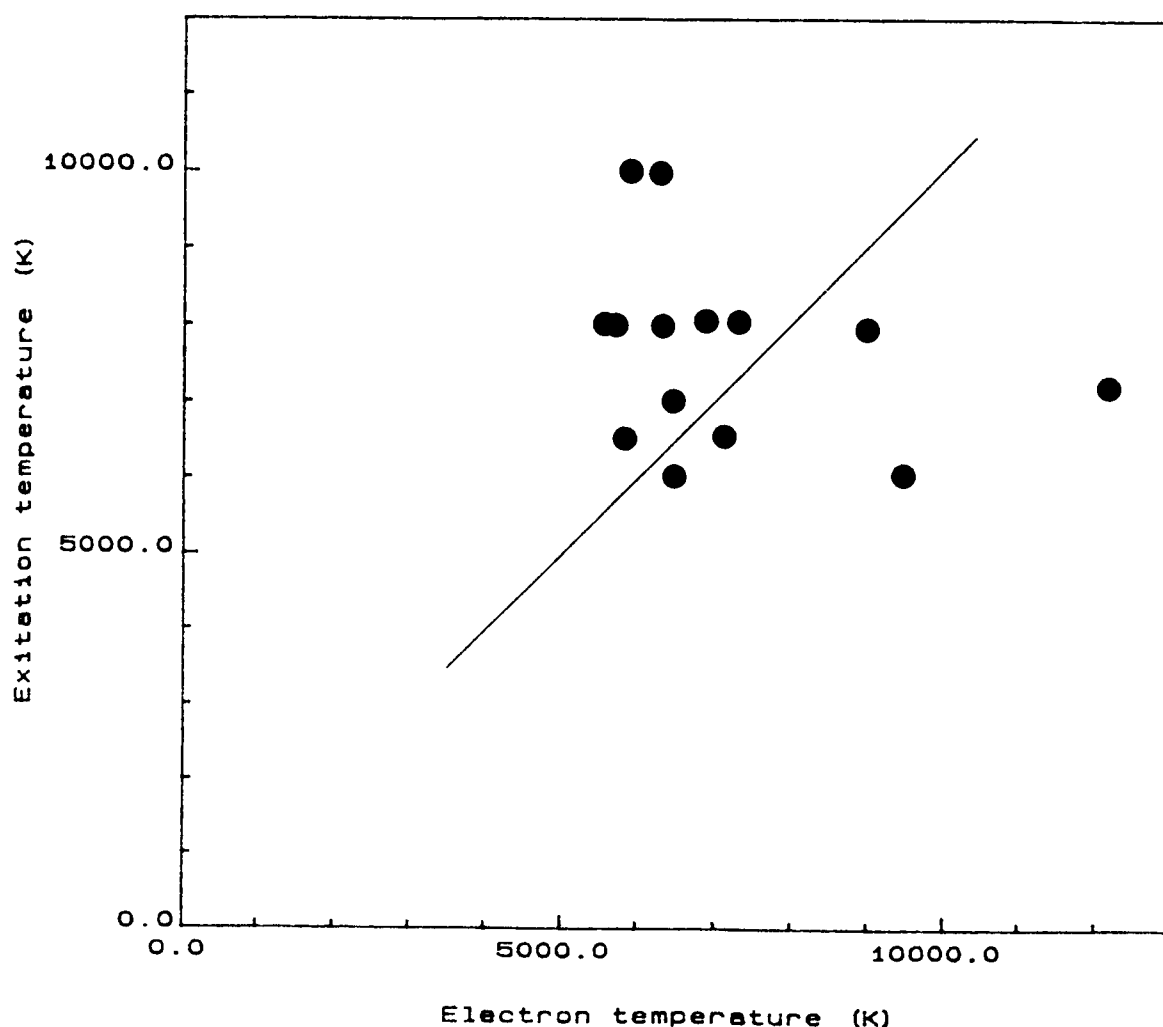


Figure 3. A plot of T_{exc} versus T_{kin} .

Table 2

Averaged temperatures and non-thermal velocities
in two quiescent prominences.

	Prominence A		Prominence B
	Central region	Edge and top	Central region
T_{kin} (K)	6200 ± 900	7000 ± 900	8500 ± 2700
T_{exc} (K)	8000 ± 700	8250 ± 1200	7800 ± 1700
V (km s ⁻¹)	5.9	6.0 ± 0.5	7.6 ± 2.6

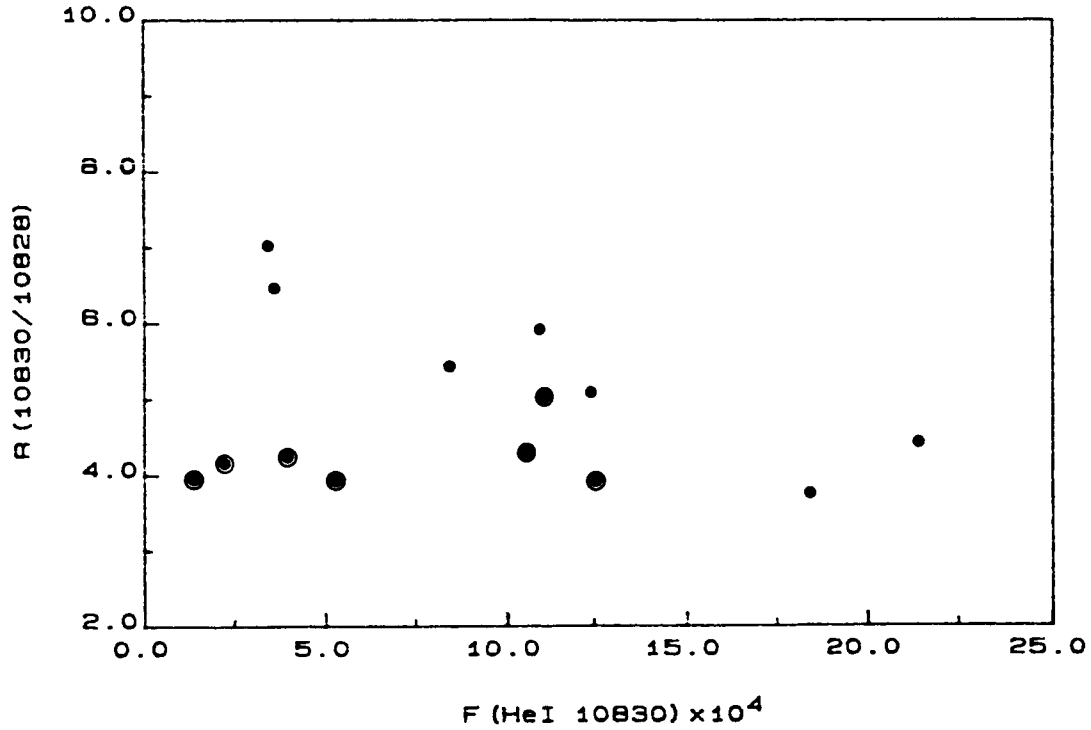


Figure 4. A plot of the He I line ratio $\lambda 10830\text{\AA}/\lambda 10828\text{\AA}$ versus total flux of the He I line. The optical thin line ratio is 8:1. Small dots represents central parts of the prominence and circles with dots are from prominence edges.

Comparison of T_{exc} and T_{kin}

Table 1 gives T_{exc} , T_{kin} and the non-thermal velocity (V) determined from 13 positions in the prominences A, B and C. (In two of the positions observed the line profiles were irregular and strongly asymmetric and were therefore not measured.) The tabulated kinetic temperatures have been derived from H I and Ca II line widths. The result from H I and O I is not substantially different from H I and Ca II. Figure 3 shows a plot of excitation temperature versus kinetic temperature ($T_e = T_{\text{kin}}$).

CONCLUDING REMARKS

The observed differences between T_{exc} and T_{kin} are hardly significant and can be attributed to data noise which is partly unresolved filamentary structure, and partly measurement errors. We conclude that the two methods for temperature determination when applied to optically thin lines give reasonably consistent results, i.e. the population of the excited levels of hydrogen is collisionally controlled.

The well known increase in T and V towards the edge of quiescent prominences (Hirayama 1964) is not corroborated by the present data. One explanation for this could be that prominence A is atypical. The optical thickness of prominence emission lines tends to increase from center to edges as demonstrated by the case of He I $\lambda 10830 \text{ \AA}$ in Figure 4. If line opacity plays a significant role in earlier centre to edge determinations of T and V , a smaller variation would be expected from measurements in optically thin lines, such as in the present case.

Acknowledgements

We thank Rob Hubbard, Jeremy Wagner, and Greg Ladd for invaluable assistance with observations and preparation of the data tapes. Pål Brekke helped with preparation of the figures.

Travel grant (K.Nr. 14.10.08.43) for the study was given by the Norwegian Research Council for Sciences and the Humanities.

References

- Brault, J.W.: 1979, "Proceedings of the 1978 JOSO Workshop", Eds.:
G. Godoli, G. Noci, A. Righini, in Oss. Mem. Arcetri, 106, 33.
- Chultem, T. and Yakovkin, N.A.: 1974 Solar Phys. 34, 133.
- Engvold, O.: 1978, Solar Phys. 56, 87.
- Engvold, O.: 1980, Solar Phys. 67, 351
- Engvold, O. and Brynildsen, N.: 1986, (In preparation)
- Heasley, J.N. and Mihalas, D.: 1976, Astron. J. 205, 273.
- Hirayama, T.: 1964, Publ. Astron. Soc. Japan 16, 104.
- Hirayama, T.: 1971, Solar Phys. 19, 384.
- Hirayama, T.: 1978, "Physics of Solar Prominences", IAU Colloq. 44,
Proceedings eds.: E. Jensen, P. Maltby, F.Q. Orrall., p.4.
- Hirayama, T.: 1985, Solar Phys. 100, 415.
- Jefferies, J.T. and Orrall, F.Q.: 1962, Astrophys. J. 135, 109.
- Labs, D. and Neckel, H.: 1968, Z. Astrophys., 69, 1.
- Landman, D.A. and Mongillo, M.: 1978, Solar Phys. 63, 87.
- Landman, D.A. Edberg, S.J. and Laney C.D.: 1977, Astrophys. J.
218, 888.
- Morozhenko, N.N.: 1974, Solar Phys. 35, 395.
- Nikolsky, G.M., Gulayev, R.A., and Nikolskaya, K.I.: 1971, Solar
Phys. 21, 332.
- Orrall, F.Q. and Schmahl, E.J.: 1980, Astrophys. J. 240, 908.
- Stellmacher, G.: 1969, Astron. Astrophys. 1, 62.
- Stellmacher, G.: 1979, Solar Phys. 61, 61.
- Zirker, J.B.: 1985, Solar Phys. 102, 33.

DARK FILAMENTS OBSERVED AT 8.3mm AND 3.1mm WAVELENGTHS

E. Hiei, M. Ishiguro, T. Kosugi, and K. Shibasaki*

Tokyo Astronomical Observatory, Mitaka, Tokyo 181

*Research Institute of Atmospherics, Nagoya University,
Toyokawa, Aichi 442

ABSTRACT

Mapping of the sun was made at 3.1mm (98 GHz) and 8.3mm (36 GHz) wavelengths with a 45m dish radio telescope at the Nobeyama Cosmic Radio Observatory. The depressions associated with large $H\alpha$ filaments are derived to be -0.2 at 8.3mm and -0.05 at 3.1mm, which are darker than the values inferred by Raoult et al. (1979).

INTRODUCTION

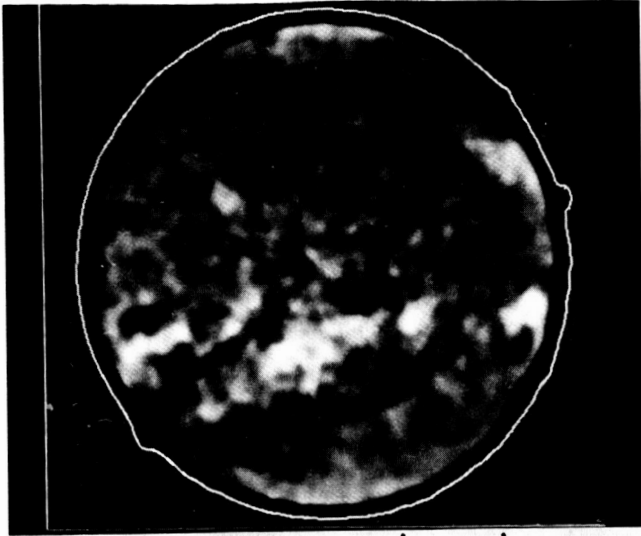
The radio observations of the filaments are valuable for studying the physical conditions in and surrounding the prominences. The spatial resolutions of the radio observations, however, are worse than those in the optical ones, and the determinations of the size and the brightness temperature of the filaments are more or less affected by the antenna beam-width.

Many dark filaments have been observed at millimetric and centimetric wavelengths as brightness depressions on the disk. These observations are summarized in Table 1. Raoult et al. (1979) made a synthesis of the millimetric and centimetric observations of the quiescent prominences on the disk by correcting the instrumental beam-width and derived a spectrum of the brightness temperature of the radio filaments between 3.5mm and 6cm wavelengths. Apushkinskii and Topchilo (1976 a) presented the brightness temperatures of 70 filaments, selected from 300 radio filaments observed at the Lebedev Physics Institute and 70 at the Crimea Astrophysical Observatory, and derived the height dependence of the temperature in the prominences. The prominence-corona transition region was studied by Chiuderi-Drago et al. (1975), Lantos and Raoult (1980), and Schmahl (1979). The weakening in the brightness depression after disappearance brusque was observed (Kundu and Lantos, 1977). A radio observation of a prominence at mm-wavelength during a solar eclipse was carried out in order to obtain the structure and physical parameters of the prominence (Simon and Wickström 1971, Apushkinskii et al. 1976). Radio flux enhancements associated with the filaments were observed at 169 MHz (Axis et al., 1971)

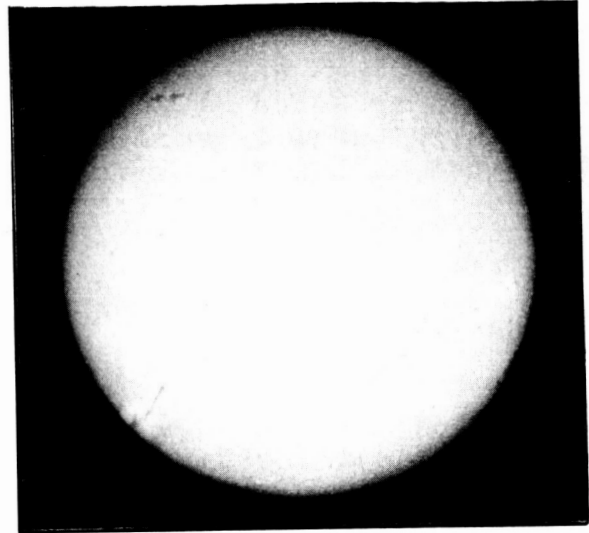
TABLE 1 OBSERVATION OF FILAMENTS

Wavelength	HPBW (arc min)	Telescope	Reference	
1.2 mm	1.2	36ft NRAO	Kundu	1970
2.0	1.2	22m Crimea	Efanov	1972
2.0		22m Lebedev	Apushkinskii et al.	1976a
2.25		22m Crimea	Efanov et al.	1969
3.1	0.28(17")	45m Nobeyama	Hiei et al.	1986
3.2	3.0	15ft Aerospace C.	Simon	1965
3.3	2.8	15ft Aerospace C.	Simon & Wickström	1971
3.5	1.2	36ft NRAO	Kundu	1970, 1972b
			Kundu & Lantos	1977
3.5	1.2	36ft NRAO	Buhl & Tlamicha	1970
4.0	1.0	22m Crimea	Efanov	1972
4.0		22m Lebedev	Apushkinskii & Tsyganov	1973
4.0	1.2	13.7m Helsinki	Kundu et al.	1978
6.0		22m Crimea	Efanov et al.	1972
6.0		22m Lebedev	Apushkinskii et al.	1976a
7.0	0.9	120ft Haystack	Schmahl et al.	1971
8.0	1.7	22m Lebedev	Khangil'din	1964
8.0	1.6	22m Crimea	Efanov	1972
8.0		22m Lebedev	Apushkinskii	1976a, 1976c
8.15		22m Crimea	Efanov et al.	1969
8.3	0.77(46")	45m Nobeyama	Hiei et al.	1986
8.5		22m Lebedev	Apushkinskii et al.	1976a
9.0	3.5	36ft NRAO	Kundu	1970
9.5	1.5	85ft NRL	Kundu & McCullough	1972a
1.2 cm	0.67	100m Effelsberg	Kundu et al.	1978
1.3	2.4	22m Crimea	Efanov	1972
1.35	1.5	120ft Haystack	Pramesh et al.	1977
1.36	1.4	120ft Haystack	Schmahl et al.	1971
1.6	3.0	22m Crimea	Efanov	1972
1.95	2.1	140ft NRAO	Chiuderi-Drago & Felli	1970
2.0	2.0	140ft NRAO	Tlamicha	1969
2.0	2.2	120ft Haystack	Schmahl et al.	1971
2.0	1.0	100m Effelsberg	Butz et al.	1975
2.0	2.2	120ft Haystack	Pramesh et al.	1977
2.8	1.25	100m Effelsberg	Fürst et al.	1973
2.8	1.25	100m Effelsberg	Kundu et al.	1978
3.8	4.4	120ft Haystack	Pramesh et al.	1977
3.8	4.1	120ft Haystack	Schmahl et al.	1981
3.8	4.4	120ft Haystack	Straka et al.	1975
6.0	2.6	100m Effelsberg	Chiuderi-Drago et al.	1975
6.0	2.5	100m Effelsberg	Kundu et al.	1978
6.0	0.25(15")	WSRT	Rao & Kundu	1980
6.0		VLA	Kundu	1985
11	5.0	100m Effelsberg	Kundu et al.	1978
20		VLA	Kundu	1985
1.78 m		Nanfay	Axisa et al.	1971
1.88		Culgoora	Dulk & Sheridan	1974
3.75		Culgoora	Dulk & Sheridan	1974

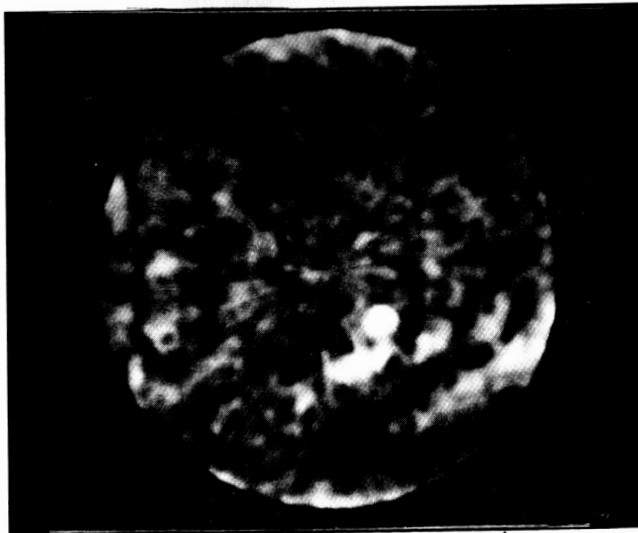
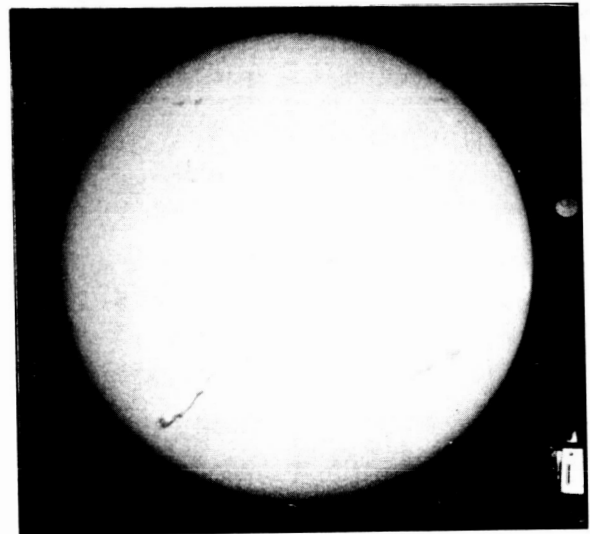
ORIGINAL PAGE IS
OF POOR QUALITY



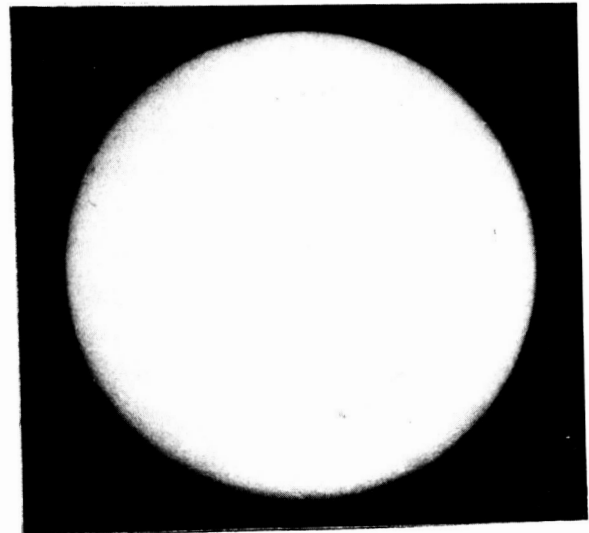
1984 JULY 17 (36GHz)



1984 JULY 18 (36GHz)



1984 JULY 22 (36GHz)



and at 80 and 160 MHz (Dulk and Sheridan, 1974). Recent understanding of the radio observations of the filaments are reported by Kundu (1979, 1985).

High quality maps at 36 GHz (8.3mm) and 98 GHz (3.1mm) were obtained with a 45-m radio telescope at the Nobeyama Cosmic Radio Observatory from 16 July to 22 July 1984. Their brightness temperature and its time change are discussed.

OBSERVATION AND ANALYSIS

The radio telescope and observation were described in detail by Kosugi et al. (1985) and only a short description is made here.

The angular resolutions of the 45-m dish telescope is of 46 arcsec (36 GHz) and 17 arcsec (98 GHz) at a half-power beam-width. The whole disk of the Sun were radially scanned in order to minimize the variation of the atmospheric attenuation due to the change of the weather condition during the observation. One scan length of 0.9° was made in 25 sec and the increment in the scan angle is 0.75° . Total 240 scans per 180° were carried out in 2 hours. In this radial-scan method the sudden change in the atmospheric attenuation within 25 sec is unavoidable, but the slow variation is corrected by using the brightness at the disc center.

The observations at 36 GHz were made at 5-7h UT on 16th, 0.5-2.5h UT on 17th, 0.5-2.5h UT on 18th, 1-3h UT on 19th, 23h on 21st - 1h UT on 22nd, 1-3h UT on 22nd, and 3-5h UT on 22nd July 1984, and the observations at 98 GHz at 6-8h UT on 17th, 1-3h UT on 19th, 23h on 21st - 1h UT on 22nd, 1-3h UT on 22nd, and 3-5h UT on 22nd July 1984. Simultaneous observations at 36 GHz and 98 GHz were made by using a beam splitter on 19th and 22nd July 1984.

Figures 1 show the radio maps and $H\alpha$ filtergrams observed at Mitaka.

The comparison between the radio (36 GHz) and $H\alpha$ features of the dark filaments shows the following results.

- 1) all $H\alpha$ filaments correspond to the depressions on the disk, but not all depressions correspond to $H\alpha$ filaments,
- 2) the positions of enhanced regions and the depressions move from east to west day by day. No systematic difference in the positions between the radio maps and $H\alpha$ filtergrams is found. Therefore the height of the depression is about the same as $H\alpha$ filaments within the accuracy of the observation,
- 3) depression becomes deep when the size of $H\alpha$ filament becomes large. This suggests that the instrumental dilution still affects the depression,
- 4) radio filaments, that can not be seen in $H\alpha$ filtergrams, exist along the neutral line of the magnetic field,
- 5) there were three filaments, which could be seen at $H\alpha$ filtergrams only in 1-2 days. The depression seems to be appeared simultaneously with its corresponding $H\alpha$ dark

- filament, and the depression became weak but still seen after the disappearance of the $H\alpha$ dark filament,
- 6) sometimes the depression appeared earlier than the $H\alpha$ dark filament. On the depression in north-west disk on July 17, no $H\alpha$ filament is seen, and on July 18, an $H\alpha$ filament appeared there and the depression become darker than that on July 17. On July 19 the $H\alpha$ filament was seen near the limb. Another example is seen at the depression near the disk center (south) on July 19. On July 18, the $H\alpha$ filament is not seen, and the depression is also weaker than that on July 19,
 - 7) a contour line on the radio map of July 17 (Figure 1) shows $1/8$ level of the average brightness of the quiet Sun. The protuberances in east-south limb and in north-west limb are corresponding to the $H\alpha$ prominences (McCabe 1986),
 - 8) at 96 GHz (3.1mm), depression corresponding to an $H\alpha$ filament is seen but weaker than that at 36GHz.

These observations may suggest that an $H\alpha$ filament appear at a pre-existing depression channel. Therefore some depressions come from the prominences and the prominence-corona interface, and some appear before the appearance of an $H\alpha$ filament and are seen after its disappearance. The other depressions, which are not corresponding to the dark filaments, is due to the different physical conditions of the chromosphere-corona transition region.

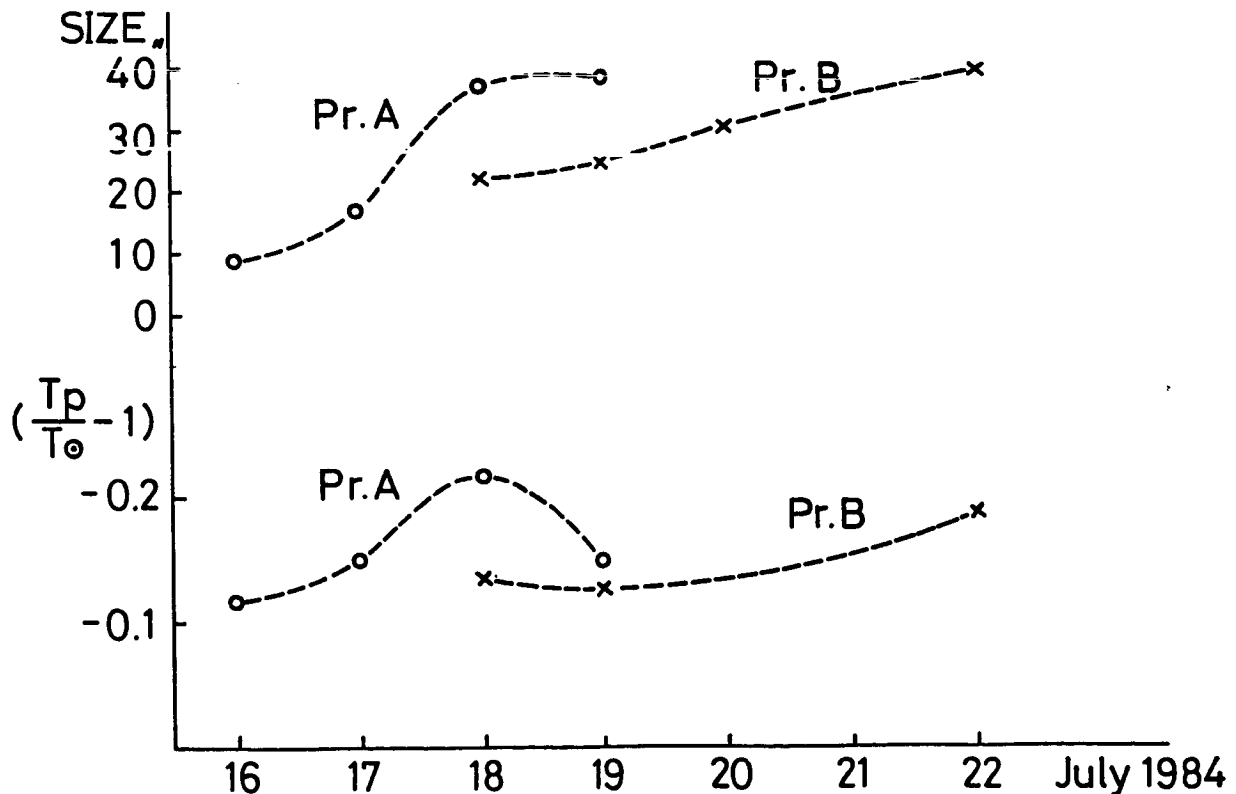


Figure 2

The diagram (Figure 2) shows the change of the value of depressions. The ordinate is $(T_p/T - 1)$, and the abscissa the day of July. The depression of prominence A (Pr. A) at 8.3mm becomes darker and darker, and again weaker. The depression of prominence B (Pr. B) becomes darker and darker. The above shows the width (size) of Pr. A and B. The size of Pr. A on 16 and 17 July is smaller than the antenna beam-width of 46 arcsec and the observed brightness is thought to be affected by the background quiet Sun. On 18 and 19 July, the size of Pr. A is about the same size as the beam-width, and the depression shows a value, not seriously affected by the quiet Sun. On July 19, the size of Pr. A is the same as that on July 18, but the depression becomes weak. Therefore, this depression is thought to be real. This will be due to the change of physical state in Pr. A, or to the change of the filling factor of the prominence.

The depression of -0.2 at 8.3mm for Pr. A and Pr. B is the lowest value at our observations.

The mean value of the depression at 8.3mm wavelength derived by Raoult et al. (1979) is about -0.1 , which still seems to be affected by the background bright disk due to the lack of the spatial resolution.

If we take 8000°K as the brightness temperature of the quiet Sun at 8.3mm, and the depression is to be -0.2 , then the temperature of the prominence is estimated to be $\sim 6600^\circ\text{K}$, which is consistent with the temperature derived from the spectroscopic study of the quiescent prominence. The temperature and electron number density, following Hirayama's review (1985) are $T_e \sim 6500^\circ\text{K}$, and $n_e \sim 10^{10.5}$. In this case the optical depth of the prominence at 8.3mm becomes 1 at only 40km depth, and therefore the optical depth at 8.3mm is quite large in quiescent prominences.

At 3.1mm, the depression is as small as -0.05 . If we take 6500°K as the electron temperature of the prominence, the brightness temperature is estimated to be 6200°K .

The optical depth at 3.1mm becomes 1 at 280km depth. If the width of the filamentary structures of the prominence is about 300km, the each filament has $\tau = 1$ at 3.1mm.

If the optical depth of the filament is large, then the residual brightness of the depression and the peak brightness above the limb should be the same. But if there exists some difference between them, it means that filling factor must be taken into account in order to explain the difference.

CONCLUDING REMARKS

- 1) A group of the depressions on the radio map is larger than that of $H\alpha$ filaments. The depressions are due to $H\alpha$ filaments, or pre/après-filament state, or different physical state at the transition region between the

- chromosphere and the corona.
- 2) T_p/T ratio is equal or smaller than 0.8 at 8.3mm and about 0.95 at 3.1mm.
 - 3) If we adopt the prominence model of $T_e=6500K$ and $n_e=10^{10.5}$, then $\tau=1$ at 8.3mm corresponds to 40km length, and at 3.1mm to 280km length.

REFERENCES

- Apushkinskii, G.P., and Tsyganov, A.N.: 1973, *Radio fizika*, 16, No. 9, 1973.
- Apushkinskii, G.P., Topchilo, N.A., and Tsyganov, A.N.: 1976 a, *Solnechnye Dannye*, No. 2, 56.
- Apushkinskii, G.P. and Topchilo, N.A.: 1976 b, *Sov. Astron.* 20, 323.
- Apushkinskii, G.P., Berulis, I.I., Losovskii, B. Ya., Sorochenko, R.L., Tsyganov, A.N., and Yasnov, L.V.: 1976 c, *Sov. Axisa*, F., Arignon, Y., Martres, M.J., Pick, M., and Simon, P.: 1971, *Solar Phys.* 19, 110.
- Buhl, D. and Tlamicha, A.: 1970, *Astron Astrophys.* 5, 102.
- Butz, M., Fürst, E., Hirth, W., and Kundu, M.R.: 1975, *Solar Phys.* 45, 125.
- Chiuderi-Drago, F. and Felli, M.: 1970, *Solar Phys.* 14, 171.
- Chiuderi-Drago, F., Fürst, E., Hirth, W., and Lantos, P.: 1975, *Astron. Astrophys.* 39, 429.
- Dulk, G.A. and Sheridan, K.V.: 1974, *Solar Phys.* 36, 191.
- Efanov, V.A., Kislyskov, A.G., Moiseev, I.G., and Naumov, A.I.: 1969, *Solar Phys.* 8, 331.
- Efanov, V.A. and Kislyskov, A.G.: 1972, *Solar Phys.* 24, 142.
- Efanov, V.A., Kislyakov, A.G., Lebskii, Yu. V., Moiseev, I.G., and Naumov, A.I.: 1972, *Izv. Krym. Astofiz. Obs.* 10, 137.
- Fürst, E., Hachenberg, O., Zinz, W., and Hirth, W.: 1973, *Solar Phys.* 32, 445.
- Hiei, E., Ishiguro, M., Kosugi, T., and Shibasaki K.: 1986, this paper.
- Hirayama, T.: 1985, *Solar Phys.* 100, 413.
- Khangil'din, U.V.: 1964, *Sov. Astron.* 8, 234.
- Kosugi, T., Ishiguro, M., and Shibasaki, K.: 1986, *Publ Astr. Soc. Japan.* 38, 1.
- Kundu, M.R.: 1970, *Solar Phys.* 13, 348.
- Kundu, M.R. and McCullough, T.P.: 1972 a, *Solar Phys.* 24, 133.
- Kundu, M.R.: 1972 b, *Solar Phys.* 25, 108.
- Kundu, M.R. and Lantos, P.: 1977, *Solar Phys.* 52, 393.
- Kundu, M.R., Fürst, E., Hirth, W., and Butz, M.: 1978, *Astron. Astrophys.* 62, 431.
- Kundu, M.R.: 1979, *IAU Colloq.* 44, 122.
- Kundu, M.R.: 1985, *Solar Phys.* 100, 491.
- Kundu, M.R., Melozzi, M., and Shergoonkar, R.K.: 1986, *Astron. Astrophys.*

- Lantos, P. and Raoult, A.: 1980, Solar Phys. 66, 275.
- McCabe, M.: 1986, private communication.
- Pramesh, A., Rao, A.P., and Kundu, M.R.: 1977, Solar Phys. 55, 161.
- Rao, A.P. and Kundu, M.R.: 1980, Astron. Astrophys. 86, 373.
- Raoult, A., Lantos, P., and Fürst, E.: 1979, Solar Phys. 61, 335.
- Schmahl, E.J.: 1979, IAU Colloq. 44, 102.
- Schmahl, E.J., Bobrowsky, M., and Kundu, M.R.: 1981, Solar Phys. 71, 311.
- Simon, M.: 1965, Astrophys. J. 141, 1513.
- Simon, M. and Wickström, B.: 1971, Solar Phys. 20, 122.
- Straka, R.M., Papagiannis, M.D., and Kogut, J.A.: 1975, Solar Phys. 45, 131.
- Tlamicha, A.: 1969, Solar Phys. 10, 150.

VLA OBSERVATIONS OF SOLAR FILAMENTS AT 6 AND 20 CM WAVELENGTHS

M. R. Kundu
Astronomy Program,
University of Maryland
College Park, MD 20742

ABSTRACT

Using the Very Large Array we have observed several solar filaments at 1.5 and 5 GHz. The brightness temperatures of the filaments are $4-5 \times 10^4$ K at 20 cm and $1.5-1.6 \times 10^4$ K at 6 cm. The maximum temperature depressions appear to be associated with $H\alpha$ filaments. Comparison with He 10830Å spectroheliogram shows that 20 cm temperature depressions correspond to the regions of reduced intensity in the He 10830Å around filaments, which correspond to coronal cavities. We have studied the temperature and density structure of the transition sheath between the filament and the surrounding corona assuming that the energy radiated away is balanced by the energy conducted from the corona. We find that the observations can be better explained by a model having a pressure gradient in the transition sheath around the filament.

OBSERVATIONS

At millimeter and centimeter wavelengths quiescent prominences appear as temperature depressions well correlated with $H\alpha$ filaments (Kundu, 1972; Rao and Kundu 1977; Kundu et al 1978). Both radio and ultraviolet observations have suggested the existence of a transition sheath around the prominence where the electron temperature increases from the filament temperature to coronal values. Since microwave radiation originates in the transition region and the low corona, centimetric observations can provide a useful diagnostic on the coronal environment of a filament (Rao and Kundu, 1977). Most of the previous studies were limited to frequencies > 5 GHz. We carried out high resolution radio observations of filaments at 5 and 1.4 GHz, using the Very Large Array (VLA). The radio maps were compared with $H\alpha$ and He 10830Å spectroheliograms. The observations were made on September 27 and 28, 1984 using the VLA in the D configuration (Kundu, Melozzi and Shevgaonkar, 1986). The array was used in a time sharing mode, alternately at 6 and 20 cm.

RESULTS

Figure 1 shows the 6 cm map superposed on the $H\alpha$ picture of the region for September 27. The error in the superposition is estimated to be $\sim 8''$. Radio temperature depressions are observed in the northern and southern part of the microwave active region associated with an $H\alpha$ plage. The southern depression runs along an $H\alpha$ filament. The width of the temperature depression is $\sim 30''-40''$ and is larger than the $H\alpha$ width ($\sim 10''-15''$). The depression peaks are clearly associated

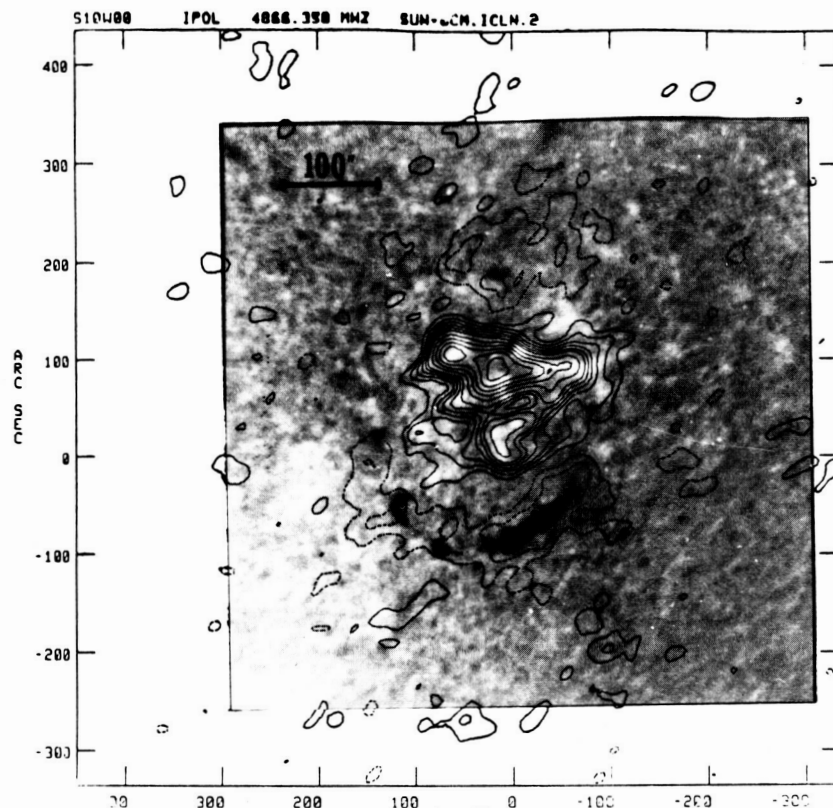


Fig. 1 6 cm map superimposed on the H α picture of September 27, 1984 (courtesy of Scaramento Peak Observatory). The temperature contours indicate levels ranging from -970 K to 3.9×10^3 K with respect to the quiet Sun temperature.

with the H α cold material. In the northern part of the H α plage, the radio depression is $\sim 100''$ wide. Although the maximum depression is located above the H α filamentary structure on both September 27 and 28, a large part of the radio structure is not associated with any H α feature.

In Figure 2, the radio map of September 28 is compared with the He 10830Å spectroheliogram. The 20 cm intense regions correspond well to the dark region of He 10830Å spectroheliogram; the regions of reduced intensity around the filaments are the filament channels which correspond to low density coronal regions (Harvey and Sheeley, 1977). Temperature depressions at 20 cm match these regions remarkably well. It is worth noting that although some radio emission voids are not associated with any particular H α feature, they appear to overlie regions of reduced intensity in He 10830Å.

In Figures 1 and 2, we have identified a number of sources for which we have computed the brightness temperatures (T_b) on both days of observations. At 20 cm the average T_b 's are 5.1×10^4 and 4×10^4 K on September 27 and 28 respectively. The main cause of uncertainty in these estimates is the assumed value for the average T_b of the quiet sun, T_{qs} . At 6 cm the observed T_b 's are fairly constant and are consistent with previous observations (e.g. Chiuderi et al, 1975; Kundu et al, 1978).

ORIGINAL PAGE IS
OF POOR QUALITY

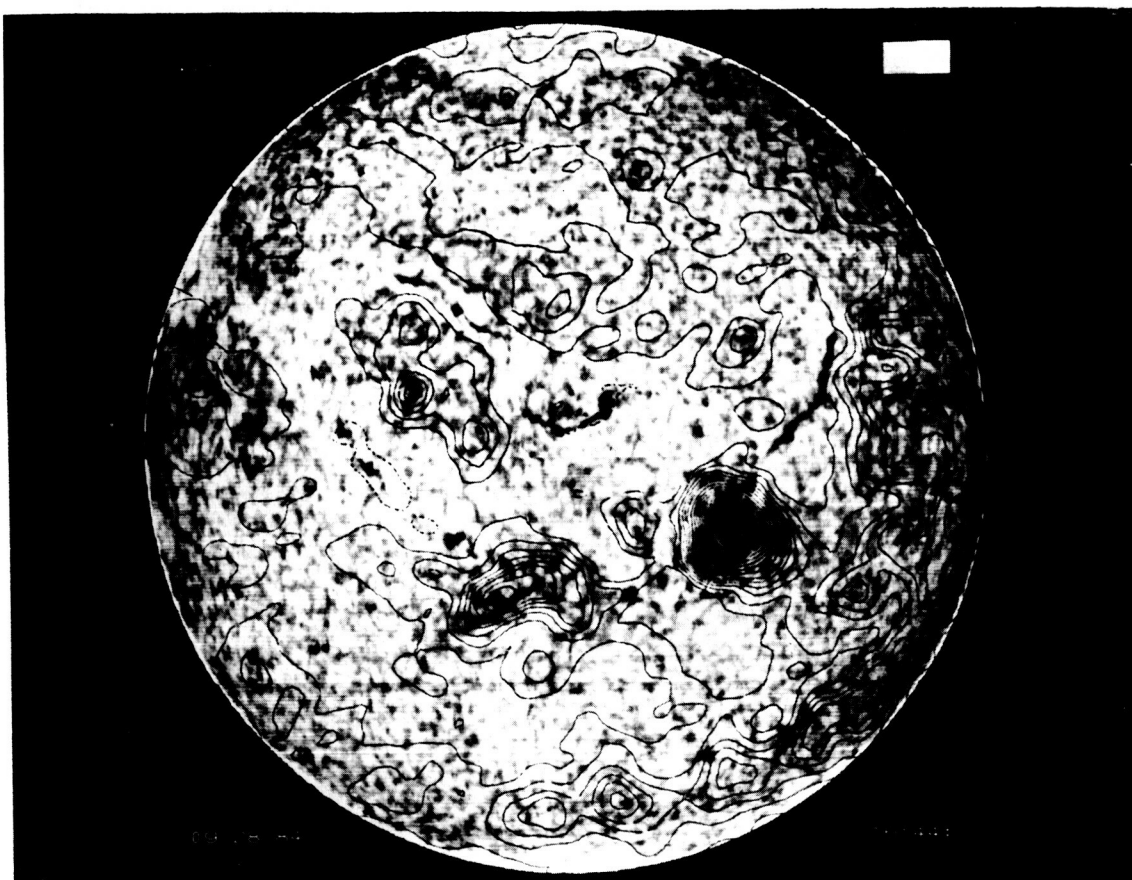


Fig. 2 Radio Sun at 20 cm of September 28, 1984, superimposed on the He 10830Å spectroheliogram (courtesy of J. Harvey). The temperature contours indicate levels ranging from -8.5×10^3 to 6.7×10^4 K with respect to the quiet sun temperature.

DISCUSSION

Our observations indicate that the radio filaments are larger in size than their optical counterparts. This implies that coronal cavity surrounding the filament leads to a broadening of the $H\alpha$ filament in the radio band (Kundu 1972; Kundu et al 1978). The 20 cm temperature depressions coincide with the He 10830Å regions of reduced intensity, suggesting that the radio depressions are also related to regions of lower density and/or temperature in the corona. Indeed, the observed radio depression around a filament can be interpreted as due to reduced emission of a coronal cavity surrounding the filament. The observed difference in brightness temperature ΔT_b between T_{qs} and T_{cav} (the brightness temperature associated with the cavity) is $4-6 \times 10^3$ K at 20 cm and 150-450 K at 6 cm.

We have attempted to study the physical conditions in the transition sheath following the method first used by Rao and Kundu (1977). Following them we have assumed that the variation of temperature with height is determined by a balance between the thermal energy conducted in from the corona and the energy radiated away.

We find that our VLA observations can be fitted by assuming a constant pressure, $P \approx 1-3 \times 10^{14} \text{ cm}^{-3} \text{ K}$, confirming the previous optical estimates as well as the radio results of Rao and Kundu (1977). However, the fit is relatively poor at higher frequencies. A better fit at higher frequencies is obtained if we assume that in the transition sheath the pressure has a power law relation with the temperature (see Kundu, Melozzi and Shevgaonkar 1986 for details).

SUMMARY

1. The observed brightness temperature of filament cavities at 20 cm has an average value $\sim 5.1 \times 10^4 \text{ K}$ and at 6 cm it is $\sim 1.5 \times 10^4 \text{ K}$.
2. The radio depressions have maximum values above $H\alpha$ filaments. However the radio filaments are broader than their optical counterparts. At 20 cm the radio filaments coincide with lighter He 10830Å regions which probably correspond to filament cavities.
3. Although every $H\alpha$ filament can be associated with a radio depression, the reverse is not true. However in the latter case, the radio depression seems to be associated with light He 10830Å regions.
4. In modelling the transition sheath between a filament and the corona, we have found that the energy conducted through the sheath is radiated away and no energy is conducted into the main body of the filament, confirming previous results of Rao and Kundu (1977). It seems that a model in which the pressure varies in the transition sheath reproduces the observations more accurately than in the case of constant pressure.

This research was supported by NSF grant ATM 84-15388, NASA grant NGR 21-002-199, and NASA contract NAG 5511.

REFERENCES

- Chiuderi-Drago, F., E. Flüst, W. Hirth, and P. Lantos, 1975, *Astron. and Astrophys.* 39, 429.
- Harvey, J.W., and N.R. Sheeley, 1977, *Solar Phys.* 54, 343.
- Hiei, E., 1985, private communication.
- Kundu, M.R., 1972, *Solar Phys.* 25, 108.
- Kundu, M.R., E. Flüst, W. Hirth, M. and Butz, 1978, *Astron. Astrophys.* 62, 431.
- Kundu, M.R., M. Melozzi, and R.K. Shevgaonkar, 1986, *Astron. Astrophys.*, in press.
- Rao, A.P. and M.R. Kundu, 1977, *Solar Phys.* 55, 161.

THE MICROWAVE STRUCTURE OF QUIESCENT SOLAR FILAMENTS AT HIGH RESOLUTION

Dale E. Gary
Solar Astronomy 264-33
California Institute of Technology
Pasadena, California

ABSTRACT

We present high resolution VLA maps of a quiescent filament at three frequencies. The spatial resolution ($\sim 15''$ at 1.45 GHz, $\sim 6''$ at 4.9 GHz, and $\sim 2''$ at 15 GHz) is several times better than previously attained. At each frequency, the filament appears as a depression in the quiet Sun background. The depression is measurably wider and longer in extent than the corresponding $H\alpha$ filament at 1.45 GHz and 4.9 GHz, indicating that the depression is due in large part to a deficit in coronal density associated with the filament channel. In contrast, the shape of the radio depression at 15 GHz closely matches that of the $H\alpha$ filament. In addition, the 15 GHz map shows enhanced emission along both sides of the radio depression. A similar enhancement is seen in an observation of a second filament obtained 4 days later, which suggests that the enhancement is a general feature of filaments. Possible causes of the enhanced emission are explored.

I. INTRODUCTION

Quiescent solar filaments are clouds of relatively low temperature plasma (6500 K) suspended in and surrounded by plasma at coronal temperatures ($> 10^6$ K). The observed close proximity of cool and hot gas over a lifetime of many days requires very complete magnetic isolation of the filament plasma. Given this general picture, it seems necessary to postulate the existence of some structure (which we will call the "transition-sheath", in analogy to the chromosphere-corona transition region) that separates these regions of cool and hot gas (Butz et al. 1975; Schmahl et al. 1974). Radio observations at multiple frequencies should be sensitive to the presence of such a filament transition-sheath, especially when a portion of the sheath is seen edge-on.

Microwave observations of filaments with rather poor (a few arcmin) resolution (Rao and Kundu 1977; Raoult et al. 1979) consistently show filaments to be roughly the same size as the filament as seen in $H\alpha$, and depressed in brightness relative to the surrounding quiet Sun. The microwave observations of Rao and Kundu (1980), who obtained the best spatial resolution ($15''$ at 5 GHz) prior to the present work, again show the depression to be very similar in size and shape to the $H\alpha$ filament. In contrast, observations by Bracewell and Graf (1981) with $17''$ resolution at 10.7 GHz indicate a depression larger than the filament, with a central brightening corresponding to the filament itself. The latter authors suggest that the depression commonly seen at lower resolution is the filament cavity, and that observations at higher resolution would also have shown the filament as enhanced. A model by Straka et al. (1975) supports this suggestion, but observations of a filament depression over several days as it approached the limb (Schmahl, Bobrowsky, and Kundu 1981) were not consistent with the brightening Straka et al. predicted.

Observations in the most compact array configuration of the VLA have been made by Dulk and Gary (1983) at 1.45 GHz, and by Kundu, Melozzi, and Shevgaonkar (1986) at 1.45 and 4.9 GHz. These observations generally support the earlier observations of Rao and Kundu (1980). They show a depression that is somewhat larger than the $H\alpha$ filament, but do not show an enhancement. The resolution of these observations is still quite poor, however, and at significantly lower frequencies than the observations of Bracewell and Graf (1981).

Here we present new three frequency observations made with the VLA in its hybrid C/D configuration, which gives higher resolution than the D configuration used for previous VLA observations while retaining the short spacings necessary for high quality large-scale maps. In §II we present the observations of one quiescent filament for which the data quality is particularly high, and compare the maps to the corresponding $H\alpha$ image. A second filament was observed 4 days later, and the 15 GHz map is also presented, verifying that an observed enhancement along the edges of the filaments is a general feature at this frequency. In §III we consider the possible causes for the enhancement. We conclude in §IV with a discussion of the implications of these observations for the structure of the filament.

II. OBSERVATIONS

The Very Large Array of the National Radio Astronomy Observatory * was used in its C/D configuration to observe solar quiescent filaments on 1984 July 16 and 1984 July 20. The array was time-shared among three frequencies—1.45 GHz, 4.9 GHz, and 15 GHz—to produce 12 hour synthesis maps on 16 July, and 6 hour synthesis maps on 20 July. The data were amplitude calibrated against the standard calibrator 3C48. Regrettably, however, the on-line correction for system temperature was incorrect, yielding brightness temperature values that are untrustworthy. Since the required multiplicative factor is as yet undetermined, we will discuss only relative brightness variations in the maps.

The maps at three frequencies for 16 July are shown in Figure 1, along with the corresponding H α image from Caltech, all to the same scale. In the figure, positive contours are drawn with heavy lines, and negative contours with light lines. The filament is easily seen as a depression (that is, negative contours) at each frequency, where the lowest contours correspond well to the H α filament. Positive contours in the 1.45 and 4.9 GHz maps correspond to slight brightenings of plage in the H α image. In contrast, the 15 GHz map shows lanes of bright emission on either side of the filament that seem to have no counterpart in the H α image.

The observation of a second filament 4 days later gives us an opportunity to check whether these bright features at 15 GHz are structures generally associated with filaments, or are peculiar to the filament in Figure 1. The map of a quiescent filament, observed on 20 July, was synthesized over 6 hours, rather than the twelve hours used for the maps in Figure 1, but otherwise the observations are similar. A flare occurred in an active region to the north of the filament on 20 July, which adversely affected the observations at lower frequencies. The 15 GHz observations, however, were not affected due to the smaller field of view at the higher frequency. The map is shown in Figure 2, where the filament stretches diagonally across the map in nearly the same orientation as the filament in Figure 1. Again the filament appears as a depression similar in shape to the corresponding H α filament (not shown), and again the bright lanes of emission appear flanking the filament. We now turn to a discussion of the origin of these bright lanes of emission.

III. POSSIBLE CAUSES OF THE ENHANCED EMISSION AT 15 GHz

A. Instrumental Effects

There are two effects that could cause an apparent enhancement along the edges of a depression in VLA data. The first is the effect of bad or improperly calibrated data samples. In radio synthesis, a data sample from a pair of antennas represents a measurement of a single fourier component of the sky brightness distribution. An abnormally high amplitude measurement for a single antenna pair results in linear "stripes" of alternating bright and dark features in the map. From an examination of plots of amplitude versus baseline over the duration of the observations, we conclude that no abnormally high amplitudes are included in the maps.

The second instrumental effect is the VLA response to a sharp edged, broad-topped feature. Because the VLA does not measure low and zero spatial frequency fourier components, a depression shaped like a rectangle function (*cf.* Bracewell 1978) might appear with bright edges. However, since we know the smallest spacing of the VLA in the C/D configuration, we can predict how broad such spurious bright features would be. The smallest spacing corresponds to a spatial scale of more than $150''$, which implies that missing spacings can cause features only of order this size, whereas the features we are discussing are more than an order of magnitude smaller ($10''$ in size). We conclude that the bright emission features cannot be due to missing spatial frequencies.

We further note that the fidelity of the map is sufficiently high, as demonstrated by the comparison of the negative contours with the H α filament in Figure 1, that the bright features must be regarded as real solar features. Possible identification of these features is discussed in the next subsection.

* The National Radio Astronomy Observatory is operated by Associated Universities Inc., under contract to the NSF.

ORIGINAL PAGE IS
OF POOR QUALITY

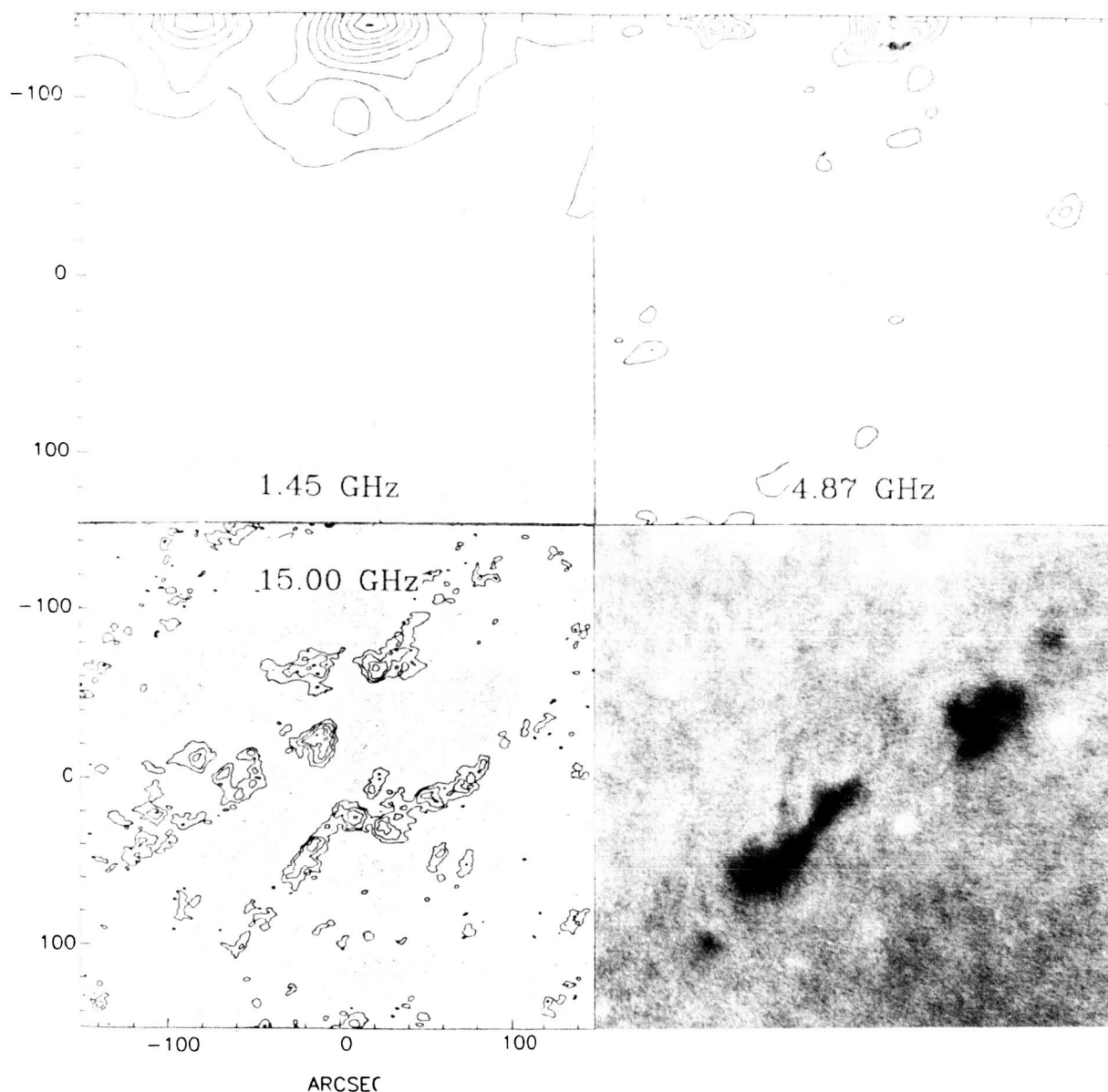


Figure 1. Contour plots of a filament observed on 1984 July 16 at three frequencies, together with an H α image obtained at Caltech, all to the same scale. The heavy contours outline regions enhanced relative to the background brightness, while light contours represent regions depressed in brightness. The 1.45 and 4.9 GHz maps show the typically observed depression associated with, but somewhat larger than the filament. The unique 15 GHz observation, however, shows a previously unreported feature, enhanced emission along the edges of the filament depression. See text for possible explanations of this phenomenon.

B. Solar Features

There are at least three possible solar origins for the emission: 1) emission from chromospheric plage, unassociated with the filament, that is coincidentally aligned with the filament axis, 2) emission from chromospheric plage that marks the footpoints of the magnetic loops that support the filament, and 3) emission arising well above the chromosphere, unassociated with plage, that marks the edges of the filament transition sheath. We discuss each of these possibilities in turn.

Coincidental Alignment of Plage

Undoubtedly some of the areas of enhanced 15 GHz radio emission arise from plage regions, since there is occasional correspondence between some of the bright radio features and slight enhancements in $H\alpha$ in Figure 1. However, it seems unlikely that the plage associated regions will appear *coincidentally* along the edges of the filament in such a way as to give the impression of a nearly continuous lane of emission, as appears especially along the lower edge of the filament in Figure 1. Further, there is a clear absence of enhanced emission away from the edges of the both filaments in Figures 1 and 2.

Enhanced Plage Associated with the Filament

The bright lanes of enhanced emission are reminiscent of the two ribbon flares sometimes seen associated with erupting quiescent filaments (Tang 1986). Certainly the supporting magnetic field lines required in any filament model will intersect the chromosphere somewhere along the edges of the filament channel, and perhaps be the site of local heating. However, this scenario would seem to require enhanced $H\alpha$ plage along the edges of filaments, whereas such plage is not generally seen, nor is it visible in Figure 1. In addition, the radio enhancement is not seen at lower frequencies, even though both the 1.45 and 4.9 GHz maps show bright features at the other sites of plage. It remains possible that some heating is taking place that is visible at 15 GHz, but does not affect the region of the chromosphere where the $H\alpha$ spectral line is formed. If this is the case, enhanced emission in some UV lines would be expected. Confirmation must await more complete observations, including UV observations of filaments at the required $10''$ resolution.

Emission From a Transition Sheath

If a transition sheath surrounds the cool filament material, it should be visible as optically thin emission at 15 GHz. This emission would be expected to be brightest where the line of sight depth of the transition sheath is greatest, i.e. along the edges of the filament, in agreement with the observations. The breadth of the lanes of emission in Figures 1 and 2 is about $10''$, or about 7000 km. This is probably much broader than the transition sheath itself, but increased breadth can be accounted for by irregularities in the shape of the sheath. This possibility also requires confirmation from more complete observations, however.

IV. IMPLICATIONS OF THE ENHANCED EMISSION AT 15 GHz

We have argued that the bright lanes of emission seen in the 15 GHz map of Figures 1 and 2 are solar features associated with the filament. We are left with two contending possibilities: emission either from the footpoints of the magnetic loops supporting the filament or from a transition sheath surrounding the filament. In either case, these new observations give an indication of a filament associated structure never before directly observed. (It is possible, however, that the report by Bracewell and Graf (1981) of a brightening associated with a filament at 10.7 GHz refers to the same phenomenon as shown here.)

The separation of the bright lanes is about $70''$ for both filaments, suggesting that this size scale is not uncommon. Comparing the 15 GHz map in Figure 1 with the 4.9 GHz map, it can be seen that the bright lanes at 15 GHz lie at the outer edges of the filament channel. Note that there is a gap in the $H\alpha$ filament, while the filament channel marked by the depression at 1.45 and 4.9 GHz shows no gap. While the depression at 1.45 and 4.9 GHz results partly from a deficit in coronal material in the filament channel (Kundu, Melozzi, and Shevgaonkar 1986), probably there is also some opacity contributed by the cool material within the $H\alpha$ filament itself, especially at higher frequencies.

The fact that the filament extends upward for some distance into the corona suggests an observational test of the two possible origins for the 15 GHz enhanced emission. If the emission is located at footpoints, the

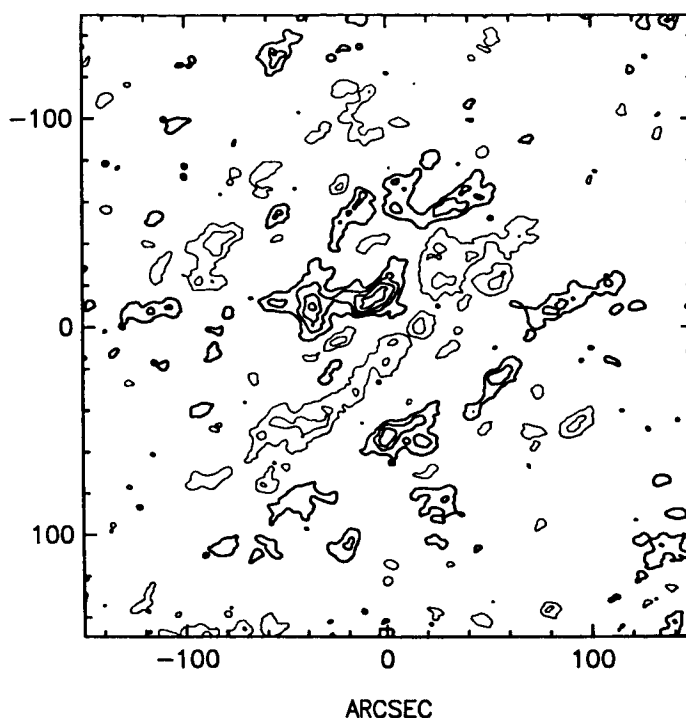


Figure 2. The 15 GHz map of a second filament observed on 1984 July 20. A comparison with the 15 GHz map in Figure 1 shows that the bright lanes of emission along the edge of the filament depression are similar in the two maps. This suggests that the phenomenon is a general one.

lane of emission on the limbward side of the filament will be occulted as the filament approaches the limb. If the emission arises from a transition sheath, on the other hand, the limbward edge of the filament should remain while the other edge becomes less apparent, reflecting a more irregular sheath on the underside of the filament. VLA observations over several days as a filament approaches the limb would allow this question to be resolved.

Acknowledgement: This work was supported by the National Science Foundation under grant ATM-8309955.

REFERENCES

- Bracewell, R. N. 1978 *The Fourier Transform and Its Applications*, McGraw-Hill, New York, p52..
- Bracewell, R. N. and Graf, W. 1981, *Nature*, **290**, 758.
- Butz, M., Fürst, E., Hirth, W., and Kundu, M. R. 1975, *Solar Phys.*, **45**, 125.
- Dulk, G. A. and Gary, D. E. 1983, *Astron. Astrophys.*, **124**, 103.
- Tang, F. 1986, *Solar Phys.* in press..
- Kundu, M. R., Melozzi, M., and Shevgaonkar, R. K. 1986 *Astron. Astrophys.* in press..
- Rao, A. P. and Kundu, M. R. 1977, *Solar Phys.*, **55**, 161.
- Rao, A. P. and Kundu, M. R. 1980, *Astron. Astrophys.*, **55**, 161.
- Raoult, A., Lantos, P., and Furst, E. 1979, *Solar Phys.*, **61**, 335.
- Schmahl, E. J., Foukal, P. V., Huber, M. C. E., Noyes, R. W., Reeves, E. M., Timothy, J. G., Vernazza, J. E. and Withbroe, G. L. 1974, *Solar Phys.*, **39**, 337.
- Schmahl, E. J., Bobrowsky, M., and Kundu, M. R. 1981, *Solar Phys.*, **71**, 311.
- Straka, R. M., Papagiannis, M. D., and Kogut, J. A. 1975, *Solar Phys.*, **45**, 131.

INTERPRETATION OF THE PROMINENCE DIFFERENTIAL EMISSION
MEASURE FOR THREE GEOMETRIES

E.J. Schmahl
Astronomy Program
University of Maryland
and
F.Q. Orrall
Institute for Astronomy
University of Hawaii

ABSTRACT

We have used prominence EUV line intensities observed from Skylab to derive the differential emission measure $Q(T)$ in the prominence-corona (PC) interface from 3×10^4 to 3×10^6 K, including the effects of Lyman Continuum absorption. Using lines both shortward and longward of the Lyman limit, we have estimated the importance of absorption as a function of temperature. The magnitude of the absorption, as well as its rate of increase as a function of temperature, place limits on the thread scales and the character of the interfilar medium. We have calculated models based on three assumed geometries: 1) Threads with hot sheaths and cool cores; 2) Isothermal threads; 3) Threads with longitudinal temperature gradients along the magnetic field. Comparison of the absorption computed from these models with the observed absorption in prominences shows that none of the geometries is totally satisfactory.

1.0 INTRODUCTION

Prominences have been observed in emission in EUV lines formed at temperatures between 10^4 and 10^6 K from the OSO-6 spacecraft (Noyes et al 1972) and rocket flights (Jones, Parkinson, Speer and Yang 1971; Orrall and Speer 1974, Yang et al 1975), Skylab (Schmahl et al 1974, Schmahl and Hildner 1977, Moe et al 1979, Mariska, Doschek and Feldman 1979, Feldman and Doschek 1977), OSO-8 (Bonnet et al 1978; Vial et al 1979, 1981) and Solar Max (Poland and Tandberg-Hanssen 1983). Orrall and Speer (1974) attributed the EUV emission to the prominence-corona interface, henceforth called the PC interface. Orrall and Schmahl (1976 Paper I) showed that the PC interface was similar to, but significantly different than, the chromosphere-corona transition region. This study showed that lines longward of the Lyman limit were more intense than those lines of similar formation temperature which lay shortward of the Lyman limit. Estimates of the amount of absorbing hydrogen in prominences were made in Paper I, but a subsequent analysis of the absolute intensities in prominences and the solar disk (Schmahl and Orrall 1979, Paper II) showed that the Lyman Continuum (LC) absorption had been underestimated. The absolute intensities of EUV lines can, in principle, provide well-determined models of density as a function of temperature in prominences, as has been done for the quiet and active disk (Withbroe 1976, 1977; Raymond and Doyle 1981). In this paper, we tabulate the intensities of EUV emission lines for a well-observed prominence, and compute the differential emission measure $Q(T) = N_e^2 d\lambda/dT$ including the effects of absorption, for two different thread geometries, and a class of magnetic orientations. We conclude with a discussion of the fit of the different model geometries to the data and other discriminating tests that could be made of the models.

2.0 DIFFERENTIAL EMISSION MEASURES

The line set for the prominences of Paper I was compared with the spectral data of Vernazza and Reeves (1978) and Noyes et al (1985) obtained for disk and coronal (non-prominence) pointings. Blends or spurious lines were deleted. The line intensities were determined using the calibration published by Reeves et al (1977).

A number of authors have computed differential emission measures of solar features (Withbroe 1977, Raymond and Doyle 1981; Noyes et al. 1985). In general one determines a function $Q(T)$ such that the intensities of a set of m lines approximately satisfy the relation:

$$I_{\lambda}^{(k)} = c_k \int Q(T) G_k(T) dT, \quad k = 1 \text{ to } m,$$

where $c_k = 1.74 \times 10^{-16} A_k g_{\text{eff}} f_{12}^{(k)}$, and the symbols have their usual meaning (cf Withbroe 1976).

We have obtained a least square fit $Q(T)$ to this equation for the prominence of 12 January 1974 (Figure 1). The two curves (1) and (2) for $Q(T)$ in Figure 1 ($Q_o(T)$ and $Q_{\text{abs}}(T)$, respectively), are for wavelengths longward and shortward of the Lyman limit. There is a considerable difference between the curves, and it is seen that the ratio Q_{abs}/Q_o increases from about 1/16 at $\log T = 5.0$ to about 1/3 at $\log T = 6.2$. This variation with temperature for the attenuation of lines by the Lyman continuum was noted in Paper I, but in a somewhat less quantitative way. We have included the changes in rate coefficients suggested by Doschek and Feldman (1982) and the changes (from Paper I) are denoted by arrows in the Figure.

In papers I and II, there were no coronal lines whose wavelengths were longward of the Lyman limit, and it was difficult to estimate the effect of absorption for formation temperatures above 10^6 K. We have therefore included the Fe XII $\lambda 1242.2$ line, using the emissivity computed by Flower (1977). (Feldman, Cohen and Doschek 1983 have confirmed his analysis). This provides information about $Q(T)$ for $T = 10^{6.2}$. For higher temperatures, we have incorporated the X-ray upper limit ($Q < 6.2 \times 10^{19} \text{ cm}^{-5} \text{ K}^{-1}$) reported by Serio et al (1978).

3. GENERAL CONSIDERATIONS

One of our objectives for determining the differential emission measure $Q(T)$ is to give information about the fine structure of prominences. It is clear, however, that there is no unique way in which the distributions of density $N_e(\lambda)$ and temperature $T_e(\lambda)$ as a function of path length (λ) may be unfolded from the function $Q(T)$. We must, instead, depend on more specific geometric models relating the temperature structure to the thread structure. The two main geometries proposed are: 1) Threads with cool cores and hot sheaths (Orrall and Speer, 1974, Yang, Nicholls and Morgan 1975, Orrall and Schmahl 1980), 2) Isothermal threads of various temperatures (Poland and Tandberg-Hanssen 1984). 3) Magnetically aligned threads with temperature and density varying only along the axis of the thread (e.g. Mariska 1985), or threads with lines of force not aligned (Low, 1982, Athay et al 1983, Leroy et al 1984).

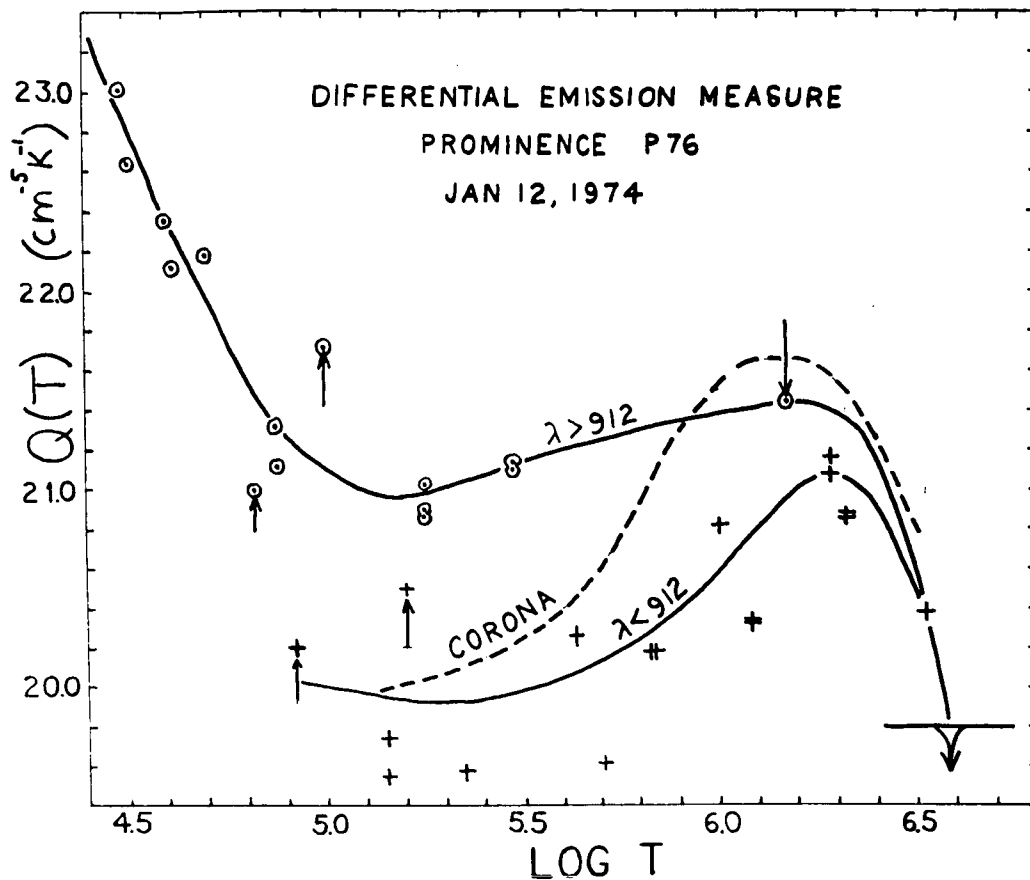


Figure 1. Emission measure data for 29 spectral lines in a limb prominence observed with the HCO spectroheliometer on SKYLAB. The bottom curve shows the differential emission measure function $Q_{\text{abs}}(T)$ fitted to lines with wavelengths $< 912\text{\AA}$. The top curve shows $Q_0(T)$ computed using only lines with wavelengths $> 912\text{\AA}$, including the emission of the ambient corona along the line of sight. The middle curve shows $Q(T)$ after deleting the estimated contribution not associated with the prominence. The dashed curve shows $Q_{\text{cor}}(T)$ for off-limb spectra (Vernazza and Reeves 1978).

4. APPLICATION OF GEOMETRIES TO $Q(T)$

Previous attempts to model threads have either used single slabs or regular arrays of cylinders. It seems more appropriate, however, to incorporate some degree of randomness in the arrays of threads, and this does not add any significant complexity to the problem. Our calculations apply mainly to average spectra or to spectra obtained with a wide slit which encompasses many structures. For the above geometries we shall take the threads to be cylinders parallel to the z axis, distributed randomly with uniform probability between the $y = 0$ plane and the $y = L$ plane. The radius r_i of the i^{th} thread is assumed to be $\ll L$, and its (random) position (x_i, y_i) is assumed to follow a rectangular probability distribution between $y = 0$ and $y = L$, and $x = 0$, and $x = L$. Thus we may compute the expectation value of the number of intersections, $\langle m(r) \rangle$, the expectation

optical depth, $\langle\tau\rangle$, and the expectation differential emission measure $\langle Q_0(T) \rangle$ with $\langle\tau\rangle = 0$, and $\langle Q_{\text{abs}}(T) \rangle$ with $\langle\tau\rangle \neq 0$. (For reasons of space, we cannot present these calculations. The details will be published elsewhere.)

4.1 GEOMETRY #1: COOL CORES/HOT SHEATHS

For the core/sheath geometry we have calculated the variation with temperature of the "absorption factor" $Q_{\text{abs}}(T)/Q_0(T)$. Figure 2 shows curves for a few values of the parameters: the total expectation optical depth, b (the pressure index, where $p \propto T^{b-1}$), r_0 (thread core radius) and N_0 (the electron density at $T = 20000$ K). In general, the absorption factor rises as a function of T , and shows the greatest difference between its low and high temperature values when $\tau(\text{total})$ is large.

It appears that core/sheath thread models (Geometry #1) can explain the observed variation of absorption as a function of temperature only if $b > 1.5$, which requires a large rate of increase in pressure through the PC interface.

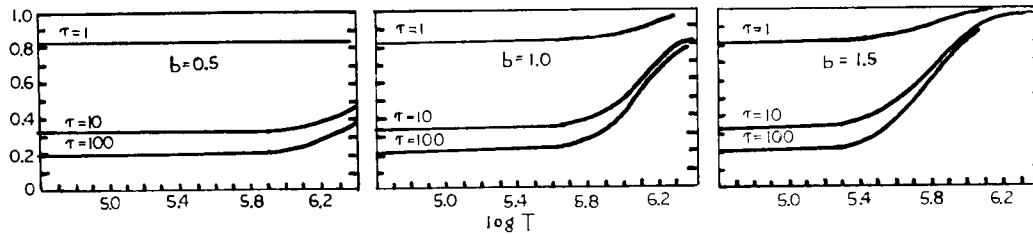


Figure 2. Computed curves of $Q_{\text{abs}}(T)/Q_0(T)$ for Geometry #1. The density, thread radius and expectation number of threads in the line of sight are the same in all three cases, while the parameter b in $N_e(T) = AT^b$ is varied: $b = 0, 1, 1.5$. It appears that $b > 1.5$ in order to get a variation similar to that observed (Figure 1).

4.2 GEOMETRY #2: ISOTHERMAL THREADS

The geometry suggested by Poland and Tandberg-Hanssen (1983) is one for which hot material appears displaced from cool material at distances greater than the thread radius. Thus we may model this as a set of isothermal threads of various temperatures with random positions uncorrelated in the x and y directions. Again we compute the expectation value of the emission measure from a random thread in the presence of cylindrical absorbing threads, each of optical depth τ_1 along a diameter ($2r_0$). The calculations yield: $\langle Q_{\text{abs}}(\tau) \rangle = \langle Q(0) \rangle (1 - \exp(-\pi m \tau_1)) / \pi m \tau_1$. The expectation absorption factor, a decreasing function of $m \tau_1$, is equivalent to that of a slab with uniform emissivity and absorptivity, having optical depth $\tau(\text{tot}) = \pi m \tau_1$ (the expectation optical depth.). In this geometry there is no explicit dependence of the absorption factor on temperature through a radial dependence $T(r)$, but instead the dependence is obtained by choosing m (the expectation number of threads) to be a function of T such that the computed and observed $Q(T)$ agree.

As previously, we assumed a density dependence of the form T^b . Then given $m(T)$ threads of temperature T , there must be $m'(T)dT$ threads in the range $T, T+dT$. Thus the emission measure distribution must satisfy: $Q(T)dT = N_0^2(T/T_e)^{2b} \pi r m'(T)dT$. We may as well assume that the threads are of the same diameter $r = R$, although variable $r(T)$ could be included in the same way as density ($N_e = N_0(T/T_e)^b$).

Integrating the expression for $m(T)$ gives:

$$m(T) = m_0 + \int_{T_0}^T \frac{Q(T) dT}{N_0^2 \pi R(T/T_0)^b}.$$

Clearly m is an increasing function of T , but the absorption factor Q_{abs}/Q_0 is a decreasing function of m . Hence no combination of parameters in this geometry will make the absorption factor increase as a function of temperature.

4.3 GEOMETRY #3: MAGNETIC FIELD PARALLEL GRAD T

A number of possibilities and problems become apparent if the temperature gradient in prominences is parallel to the magnetic field, (which may, or may not, be parallel to the axis of the threads). The most interesting consequence of this is that the emission from the PC interface may result mainly from the energy input by thermal conduction from the corona. In this case, the observed function $Q(T)$ must be derivable from the energy balance, and $Q_0(T)$ in Figure 1 provides a test for such a model.

The basic problems of energy balance in prominences have been summarized by Tandberg-Hanssen (1974) and others. We restrict ourselves to the case in which the radiative flux is balanced by the conductive flux from the corona. This case has been analyzed by Rosner et al (1978) for active region loops, and the same mathematical method may be applied to this prominence geometry. We assume that mechanical heating is restricted to the coronal domain $T > T_c$ where T_c is approximately 10^6 K. Then the balance of conductive and radiative flux may be expressed as: $T/Q(T)^2 = (8k^2/Kp^2) \int dT' T'^{-1/2} P(T')$.

There is essentially only one free parameter which may be varied to match the computed $Q(T)$ with the one derived directly from observations: the coronal pressure $N_0 T_0$. For any value of the pressure, the function $Q(T)$ is very flat. In fact, regardless of the (positive) radiative loss function assumed, $Q(T)$ may not rise faster than $T^{1/2}$. At a temperature of 10^5 K, a reasonable fit to the observed $Q(T)$ is given if $\log(N_0 T_0) = 14.2$. At higher temperatures, the $Q(T)$ derived from the conductive balance is reasonably close to curve 1 in Figure 1.

In the temperature domain $\log T = 5.0$ to 6.0 , $Q(T)$ varies roughly as a power law with index $a = 0.2 (\pm 0.2)$. Assuming constant pressure and integrating $Q(T)$, the distance s expressed as a function of temperature is:
 $s = s_0 + 10^{15} T_5^{3+a} Q(T_0)/N_0 T_0 (3+a).$

In our case, the ratio $Q(T)/N_0 T_0$ is approximately 1×10^{-8} . Thus the distance of the 5×10^5 K level from the 1×10^5 K level will be approximately 5" (the size of the Harvard slit). It has been shown that prominences start becoming more diffuse (at the 5" scale) at temperatures around 5×10^5 K (Paper I and Schmahl 1979). Thus if the PC interface wraps around (or curves into) the cool cores of threads, (assuming they are less than or of order 0.5" in diameter) then the radius must exceed 5" above half a million degrees. At higher temperatures, the radius would be greater still, and thus the hotter portions of the interface would be more exposed to view and less subject to absorption, much like Geometry #1. One would expect the ratio Q_{abs}/Q_0 to be an increasing function of temperature, but the rate of increase would depend strongly on the smallest geometrical scales, which are largely unknown.

5. DISCUSSION AND CONCLUSIONS

Both of the two thread geometries studied herein have certain shortcomings or difficulties, particularly with regard to the Lyman continuum absorption, and its apparent decrease at higher temperatures. Geometry #1, where cool threads are surrounded by hot sheaths, was advanced to explain the facts that emission appears thread-like and co-spatial (to 5") in lines formed at many temperatures. This geometry is not easily explained in terms of an energy budget, but it can explain the apparent decrease of absorption with temperature if the pressure is an increasing function of radius. However, the pressure must increase by at least two orders of magnitude ($b = 1$) in the range $10^5 < T < 10^6$ K and this seems rather improbable.

Geometry #2 (isothermal threads) has been invoked to explain the appearance of filamentary emission with little axial variation, but apparently uncorrelated (or variable) line emission from thread to thread. Because of the assumed lack of spatial correlation between temperature regimes, this geometry cannot explain the observed decrease of absorption as a function of temperature.

Geometry #3 ($\text{grad } T \parallel \vec{B}$) has the virtue that radiation losses (at least for $2 \times 10^4 < T < 10^6$ K) can be balanced by conductive flux from the corona. This geometry can be combined with geometry #1, as in Low's (1982) model. The classical absorption (LTE) mechanism, however, cannot readily explain the observed amount of absorption, unless there are multiple threads or sheets along the line of sight (see geometry #1 and Paper II). On the other hand, the radiative-conductive flux balance cannot be maintained if there are multiple enfilades (sheets) of threads hanging on the same magnetic field lines, since the conductive flux will be used up by the outermost sheets.

The non-LTE mechanism proposed by Shoub (1983) might explain the existence and variation of absorption. However, it should be noted that there seems to be little positive evidence in terms of line widths (Feldman and Doschek 1977) or temperature diagnostics (Doyle et al 1985), that hot emission occurs in cool media, as required by Shoub. Further, in the absence of a simple analytic approximation for Shoub's mechanism, we are unable to estimate its importance for different thread geometries in prominences.

The observations of more EUV lines with better statistics, more pressure and density diagnostics, particularly at high temperatures, combined with improved resolution at wavelengths spanning the Lyman limit, may be required to decide the final issue of the appropriate geometry for the PC interface.

REFERENCES

- Athay, R.G., Querfeld, C.W., Smartt, R.N., Landi degl'innocenti, E. and Bommer, V., *Solar Phys.* 89, 1983.
Bonnet, R., Lemaire, P., Vial, J., Artzner, G., Gouttebroze, P., Jouchou, A., Leibacker, J., Skumanich, A. and Vidal-Madjar, A., *Ap.J.*, 221, 1032, 1978.
Doschek, G.A., and Feldman, U., *Ap.J.*, 254, 371, 1982.
Doyle, J.G., Raymond, J.C., Noyes, R.W. and Kingston, A.E., *Ap. J.* 297, 816, 1985.
Feldman, U., Cohen, L. and Doschek, G.A., *Ap.J.*, 1983.
Feldman, U. and Doschek, G.A., *Ap.J. (Letters)* 216, L119, 1977.
Flower, D.R., *Astron. Astrophys.* 54, 163, 1977.
Hirayama, T., *Solar Phys.* 100, 415, 1986.

- Jones, T., Parkinson, W., Speer, R., and Yang, C., Solar Phys. 21, 372, 1971.
- Kjeldseth Moe, O., Cook, J.W. and Mango, S.A., Solar Phys. 61, 319, 1979.
- Leroy, J.L., Bommier, V. and Sahal-Brechot, S.: 1964, Astron. Ap. 131, 33.
- Low, B.C., Solar Phys. 75, 119, 1982.
- Mariska, J.T., Doschek, G.A. and Feldman, U., Ap.J., 232, 929, 1979.
- Mariska, J.T., 1985: presented at first CPP workshop, Airlie, VA.
- Noyes, R.W., Raymond, J.C., Doyle, J.G., and Kingston, A.E., Ap. J. 297, 805, 1985.
- Noyes, R.W., Dupree, A., Huber, M.C.E., Parkinson, W., Reeves, E.M. and Withbroe, G.L., Ap.J. 176, 515, 1972.
- Orrall, F.Q. and Speer, R., Chromospheric Fine Structure (ed. R.G. Athay), Reidel, 1974, 193.
- Orrall, F.Q., and Schmahl, E.J. (Paper I), Solar Phys. 50, 365, 1976.
- Orrall, F.Q. and Schmahl, E.J., Ap.J. 240, 908, 1980.
- Poland, A.I., and Tandberg-Hanssen, E.A., Solar Phys. 84, 63, 1983.
- Raymond, J.C., and Doyle, J.G., Ap.J. 247, 686, 1981.
- Reeves, E.M., Timothy, J.G., Huber, M.C.E., and Withbroe, G.L., Applied Optics, 16, 849, 1977.
- Rosner, R., Tucker, W.H., and Vaiana, G.S., Ap.J., 220, 643, 1978.
- Schmahl, E.J. and Orrall, F.Q. (Paper II), Ap. J. Letters 231, L41, 1979.
- Schmahl, E.J., I.A.U Colloq. 44, 102, 1979.
- Schmahl, E.J., Foukal, P.V., Huber, M.C.E., Noyes, R.W., Reeves, E.M., Timothy, J.G., Vernazza, S.E. and Withbroe, G.L., Solar Phys. 39, 337, 1974.
- Schmahl, E.J. and Hildner, E., Solar Phys. 55, 473, 1977.
- Serio, S., Vaiana, G.S., Godoli, G., Motta, S., Pirronello, V. and Zappala, R., Solar Phys. 59, 65, 1978.
- Shoub, E.C., Ap.J. 260, 339, 1983.
- Tandberg-Hanssen, E.A., Solar Prominence, D. Reidel. Publ. Co., Dordrecht, Holland, 1974.
- Vernazza, J.G. and Reeves, E.M., Ap.J. Suppl. 37, 485, 1978.
- Vial, J.C., Lemaire, P., Artzner, G. and Gouttebroze, 1981
- Vial, J.C., Gouttebroze, P., Artzner, G. and Lemaire, P., Solar Phys. 61, 39, 1979.
- Withbroe, G.L., C.F.A. Preprint No. 524, 1976 (unpublished).
- Withbroe, G.L., Proc. of the Nov. 7-10, 1977 OSO-8 Workshop, Univ. of Colo., 1977
- Yang, C., Nicholls, R., and Morgan, F., Solar Phys. 45, 351, 1975.

THE PROMINENCE-CORONA INTERFACE AND ITS RELATIONSHIP TO THE CHROMOSPHERE-CORONA TRANSITION

Douglas Rabin

National Solar Observatory, National Optical Astronomy Observatories*

ABSTRACT

The classical model of the chromosphere-corona transition does not account for the observed behavior of the differential emission measure for $T \lesssim 10^5$ K. Several models have been proposed to resolve this discrepancy in physically different ways. Because the observed differential emission measure at the prominence-corona interface is on average nearly the same as in the chromosphere-corona transition, prominences offer a fresh testing ground for models tailored to the chromosphere-corona transition. I consider three such models and conclude that none extends in a natural way to the environment of prominences. I advance a simple idea involving thermal conduction both along and across the magnetic field from the corona into cool threads.

1. Introduction

The transition between chromospheric (or prominence) plasma and coronal plasma may be broadly defined as all gas in the temperature range $10^4 < T < 10^6$ K. Throughout most of this range ($T \gtrsim 3 \times 10^4$ K), the plasma radiates mainly through optically thin permitted transitions in ions that exist with significant abundance only in relatively narrow intervals of temperature ($\Delta \log T \lesssim 0.3$). For such a transition, the power radiated from a volume of plasma is

$$P = \beta \int G(T) n_e^2 dV \approx \beta G(T_{\max}) \int n_e^2 dV. \quad (1)$$

Here $G(T)$, which expresses the relative population of the upper level, is sharply peaked near T_{\max} and β is an amalgam of atomic parameters and abundances.

It is clear from this that the basic information observations provide about the thermal structure of the transition plasma is contained in the behavior of the differential emission measure (DEM),

$$\epsilon(T) = n_e^2(T) \frac{dV(T)}{d \ln T}, \quad (2)$$

where $dV(T)$ is the volume of plasma in the logarithmic temperature interval $d \ln T$.

In Figure 1, curve A represents the "average" behavior of the solar DEM, as compiled from many sources in the literature. The precise shape of the curve should not be taken too literally. There are variations from region to region, the spectroscopic diagnostics effectively smooth the curve to a resolution $\Delta \log T \approx 0.3$, and it is difficult to quantify all the sources of uncertainty in a given determination of the DEM. However, the basic shape is well established: a broad minimum in the range $5.0 \lesssim \log T \lesssim 5.4$ with a steeper rise to lower temperatures than to higher temperatures. The same curve can characterize the spatially-averaged emission from quiet regions, active regions (if the curve is shifted upward by about a factor of ten), and coronal

* Operated by the Association of Universities for Research in Astronomy, Inc., under contract with the National Science Foundation.

holes (*cf.* Chambe 1978; Raymond and Doyle 1981; Dere 1982). For the present purpose, the key observation is that this property extends to the spatially-averaged emission from prominences: the DEM curve of the prominence–corona interface is essentially similar, in shape and in strength, to the DEM curve of the quiet chromosphere–corona transition (Schmahl and Orrall 1979; Yang, Nicholls and Morgan 1975).¹ Below, we explore some of the consequences of this uniformity.

2. Models of the Chromosphere–Corona Transition

In the standard picture (Giovanelli 1949; Athay 1966), the thermal structure of the transition is determined mainly by thermal conduction along the magnetic field. The temperature dependence of classical thermal conductivity, $\kappa(T) \propto T^{5/2}$, leads in a plane-parallel model to the familiar thin transition layer with a steep temperature gradient. The cooler part of the transition ($4.3 < \log T < 5.0$) is so thin ($\lesssim 200$ km) that it cannot radiate enough to account for the rise in DEM below $T \approx 10^5$ K.

The standard model has been refined to allow for nonplanar magnetic geometry and steady flows. The result is that the basic thermal structure is little changed (Athay 1981, 1982). To date, no variant of the standard model has reproduced the observed low-temperature rise in the DEM. This failure has led to several recent models, three of which are next described.

The three models share one feature: the cooler transition plasma occupies volumes separated in space or time from the volumes containing hotter transition plasma, and the hot branch of the DEM curve ($\log T \gtrsim 5.3$) is assumed to arise in the manner described by the standard model. Otherwise the models are quite different. Because each (by design) can reproduce the cool branch of the DEM curve for the chromosphere–corona transition, other information must be brought to bear — *e.g.*, observations of velocities, time dependence, or spatial structure (or other stars; see Section 4). Here we shall be concerned with the similarity between the DEM curves for the chromosphere–corona transition and the prominence–corona interface. Our brief treatment of the models is directed toward that end and is not intended to review all the advantages and disadvantages of each.

a) Cool "Coronal" Loops

The most recent model (Antiochos and Noci 1986) is in some ways the most natural. It also appears to be the least tenable as a model for the prominence–corona interface.

In this model, the cooler transition plasma resides in low-lying magnetic loops that are nowhere hotter than a few times 10^5 K (see Feldman 1984; Rabin and Moore 1984). A pleasing feature of the model is that cool loops arise as a solution of the standard "coronal loop equations" on an equal footing with familiar hot-loop solutions. No additional mechanism is invoked to produce the cooler transition plasma.

The equation of static energy balance, $\nabla \cdot \mathbf{F}_c = H - C$, where \mathbf{F}_c is the thermal conductive flux and H and C are the volumetric heating and cooling, admits an isothermal solution in the absence of gravity. To see this, one may picture the "loop" as a horizontal cylinder held at the same temperature on both ends (the chromosphere). The minor influence of gravity introduces a mild temperature gradient. Antiochos and Noci show that such near-isothermal solutions cannot exist if gravity is important, for then hydrostatic equilibrium dictates a rapid decrease in density with height. The radiative cooling,

$$C(T) = n_e^2 \Lambda(T), \quad (3)$$

¹ Systematic differences in detail do show up in a plot of the intensity ratio between prominence and quiet Sun for lines at various temperatures (Orrall and Schmahl 1976; Mariska, Doschek and Feldman 1979).

where $\Lambda(T)$ is the radiative loss function, will also tend to decrease rapidly, whereas there is no reason to suppose that the heating is a similarly rapid function of height. Therefore, T must increase in order to increase $\Lambda(T)$. However, beyond $T \approx 10^5$ K, $\Lambda(T)$ becomes a *decreasing* function of T , and the demands of energy balance are incompatible with hydrostatic equilibrium. Therefore, the vertical extent of the cool loops must be less than the gravitational scale height at 10^5 K, about 5000 km.

Antiochos and Noci show that the DEM curve produced by a single cool loop has negative slope, as is required by observations; but the value of the slope is sensitive to the characteristics of the heating function. The DEM from an assemblage of loops will also depend on the relative numbers of loops of different heights (different maximum temperatures) and the variation of the maximum heating rate in a loop, H_{\max} , with the height of the loop. Antiochos and Noci use an *ad hoc* heating function parameterized as a function of magnetic field strength, which is in turn parameterized as a function of height. The heating function that gives a good match to the observed DEM is a steep function of loop height, $H_{\max} \propto h_{\text{loop}}^{-4}$. In effect, the rise in DEM below 10^5 K is secured by preferentially heating the lowest loops.

The sensitivity of this model to the distribution of assumed heating is unappealing, but the chromosphere–corona transition may nonetheless choose to meet the proper conditions. By the same token, however, it is hard to see why the heating in a prominence should conduct itself in the *same* way to produce the *same* DEM curve.

There is a more fundamental objection to this model as applied to prominences. Quiescent prominences typically extend to heights of 30000 km or so, far beyond the limit of 5000 km set by the gravitational scale height at $T \approx 10^5$ K. Yet emission from cooler transition plasma is observed over the entire prominence, not just near the footpoints. It is possible to imagine that cool-loop solutions exist high above the chromosphere by being trapped within vertical undulations of the magnetic field (Antiochos, personal communication). The undulations would have to have a characteristic peak-to-peak amplitude of less than 5000 km and would have to be an essential feature of prominence geometry. In the absence of independent evidence, this must be considered artificial.

b) Heating–Cooling Cycles in Spicules

This model (Athay 1984) builds on two observations. First, spicules usually disappear from view while still rising, presumably because they are being heated and get too hot to radiate $H\alpha$. Second, a mean downflow is observed at $T \approx 10^5$ K, and the mass flux is approximately the same as the upward mass flux in spicules (which must in any case return, since it is far greater than the mass flux in the solar wind). The model envisions three types of regions in the solar atmosphere: heating up; cooling down; and near equilibrium. It is assumed that the latter two regions are adequately described by conventional models of the chromosphere–corona transition and therefore suffice to produce the hot branch of the DEM curve. The cooler branch arises from spicules in the process of heating.

The principal attraction of this model is that it explicitly recognizes the kinematic and time–dependent nature of the atmosphere. The principal disadvantage is that the slope of the cooler branch of the DEM curve is sensitive to the (unspecified) nature of the heating.

In the simplest nonstationary model, with thermal conduction ignored, the DEM is determined by how long a given volume of gas remains in each interval of temperature, which is in turn determined by the excess of heating over cooling,

$$\frac{dT}{dt} \approx \frac{T}{4.5p} (H - C), \quad (4)$$

where p is the gas pressure (taken to be constant during the heating). This leads to the following expression for the DEM:

$$\epsilon(T) = 9k(n_e T)^2 F_p \frac{1}{T(H-C)}, \quad (5)$$

where F_p is the upward proton flux.

It is evident that the emission measure directly reflects the temperature-dependence of the heating, $\epsilon(T) \propto H(T)T^{-1}$, except at temperatures for which $H(T)$ only slightly exceeds $C(T)$. Athay (1984, Fig. 1) secures agreement with observation by choosing $H = \text{constant}$ and $H = 1.07C$ at $\log T = 4.5$ (the lowest temperature considered). Because $C(T)$ (at constant pressure) is also nearly constant in the range $4.5 \leq \log T \leq 4.9$, the behavior of the small difference $H - C$ is able to influence the DEM (steepening it, since $C(T)$ decreases slightly). Note that both a close match between H and C at $\log T = 4.5$ and the constancy of H are essential to this result. The match at $\log T = 4.5$ itself presents a problem. Athay restricts his analysis to temperatures above the peak of $L\alpha$ radiation at $\log T \approx 4.25$ on the reasonable grounds that not all $L\alpha$ radiation need arise in spicules and that radiative transfer in $L\alpha$ should not be neglected. However, unless one begs the question of how spicules are heated to $\log T = 4.5$, the heating rate must be sufficient to surmount the $L\alpha$ cooling peak, which is about 50 percent stronger than the cooling at $\log T = 4.5$. If H is so chosen, $H - C$ (for constant H) varies by less than a factor of two over the range $4.5 \leq \log T \leq 5.0$.

In summary, this model agrees with observation only for special choices of the heating rate. As in the model of Antiochos and Noci, this cannot be ruled out. But it is also clear how remarkable it would be if this attractive heating-cooling picture, inspired by spicules, were not only to carry over *qualitatively* to structures as different from spicules as are quiescent prominences, but were to be characterized by the same *quantitative* behavior of the volumetric heating.

c) Heating by Filamentary Electric Currents

The key to producing the cooler branch of the DEM curve in this model (Rabin and Moore 1984) is the temperature dependence of cross-field thermal conductivity. At constant pressure,

$$\kappa_{\perp} \propto T^{-5/2} \quad (6)$$

whereas

$$\kappa_{\parallel} \propto T^{5/2}; \quad (7)$$

so it is not surprising that cross-field conduction leads to a negative slope in the DEM.

The model postulates that the cool transition plasma is internally heated by field-aligned electric currents. The current density must be high,

$$j \gtrsim 10^7 \text{ statamp cm}^{-2}, \quad (8)$$

in order to balance radiative losses, but the current filaments (or sheets) must be thin,

$$d \lesssim 1 \text{ km}, \quad (9)$$

or else the magnetic field associated with the current itself will be unreasonably strong ($B > 100$ gauss). If the characteristic thickness of the filament is less than the cross-field conduction length,

$$d \lesssim d_c = \left(\frac{\kappa_{\perp} T}{n_e^2 \Lambda} \right)^{1/2} \approx 0.1 B^{-1} \text{ km}, \quad (10)$$

then cross-field conduction dominates the thermal structure, and the DEM curve has a slope in good agreement with observations [see equation (11) and Fig. 1].

None of the models considered here physically incorporates the heating mechanism. The previous two models simply include it as a parameter. The filamentary-current model specifies the mechanism (ohmic dissipation) but does not explain how the necessary currents are

produced. In the context of prominences, the present model has the further shortcoming that it does not predict the *amount* of cooler transition plasma. That is, although the shape of the cooler DEM curve is specified, its magnitude at a given temperature, and therefore the temperature at which it crosses the hot branch of the DEM curve, is determined by the number of current filaments per unit area. Why should this number be comparable in low-lying loops and in quiescent prominences? [However, as illustrated in Fig. 1, the steepness of the cool branch of the DEM means that it may be substantially displaced in magnitude (vertically) without much changing the temperature of its intersection with the hot branch.]

3. Thermal Conduction Across and Along the Magnetic Field

It is instructive to analyze the models considered above because each has interesting (but different) physics and each has a tantalizing set of strong and weak points. Yet, in the final analysis, the close correspondence between the DEM curves for the chromosphere–corona transition (which itself encompasses everything from active regions to coronal holes) and the prominence–corona interface serves as much as anything to draw attention to the most attractive feature of the *original* conception of the transition region: that thermal conduction “does everything” — provides the energy, determines the thermal structure, and is there whenever and wherever needed. In contrast, the cool-coronal-loop model and the heating-spicule model rely on the detailed behavior of an unspecified heating mechanism to match the cool branch of the DEM — they must be “fine-tuned.” The filamentary-current model requires that the current elements be present, in comparable numbers, in widely different environments.

One possibility for recovering a unified treatment of the transition plasma is that nonclassical electron transport influences the structure of the transition (Roussel-Dupre 1980*a,b*; Shoub 1983). It appears that streaming by fast electrons in the enhanced (non-Maxwellian) tail of the distribution function has only a minor effect on the excitation and energy balance of ions used as transition-plasma diagnostics (Keenan 1984; Owocki and Canfield 1986). The importance of the nonclassical heat flux, both in terms of magnitude and distribution over temperature, is not yet clear. The nonclassical flux depends sensitively on the temperature structure of the transition, which has thusfar been assumed rather than calculated self-consistently (Owocki and Canfield 1986).

Here I consider a different idea, not yet developed to the stage of a “model.” Any cool magnetic structure that protrudes into the corona will receive heat both along and across field lines.² Classical cross-field conduction is usually ignored at coronal temperatures because it is much weaker than along-field conduction. At $T \approx 10^5$ K, the disparity is smaller but still substantial. An analytic model with planar geometry, including conduction and radiation (in power-law segments) gives the following expressions for the DEM per unit area exposed to the corona:

$$\epsilon_{\perp}(T) = 10^{22.7} (n_e T)_{15}^2 B^{-1} T_{\text{low}}^{3/2} \left[1 - (T_{\text{low}}/T)^3 \right]^{-1/2} T_5^{-7/2} \text{ cm}^{-5} \quad (11)$$

$$\epsilon_{\parallel}(T) = 10^{26.2} (n_e T)_{15} \left[1 - (T_{\text{low}}/T)^{1/2} \right]^{-1/2} T_5^{5/4} \text{ cm}^{-5}, \quad (12)$$

where T_{low} is the cool temperature at which the conductive flux goes to zero and T_5 means T in units of 10^5 K. The magnitude of $\epsilon_{\parallel}(T)$ is about right to match observations at $T = 10^5$ K. Therefore, to turn up the DEM below 10^5 K, we must increase the area exposed to cross-field conduction. In Figure 1, curves *B–D* show the results of simple area-weighted superpositions with the cross-field area increased by factors of $10^{3.5}$, $10^{4.0}$, or $10^{4.5}$ (the curves have been displaced upward one decade from the mean observed curve). Clearly, a typical ratio $\sim 10^4$ is

² Appropriately, it seems to have been in the context of prominences that cross-field thermal conduction was first considered in the solar atmosphere (Orrall and Zirker 1961; Doherty and Menzel 1965).

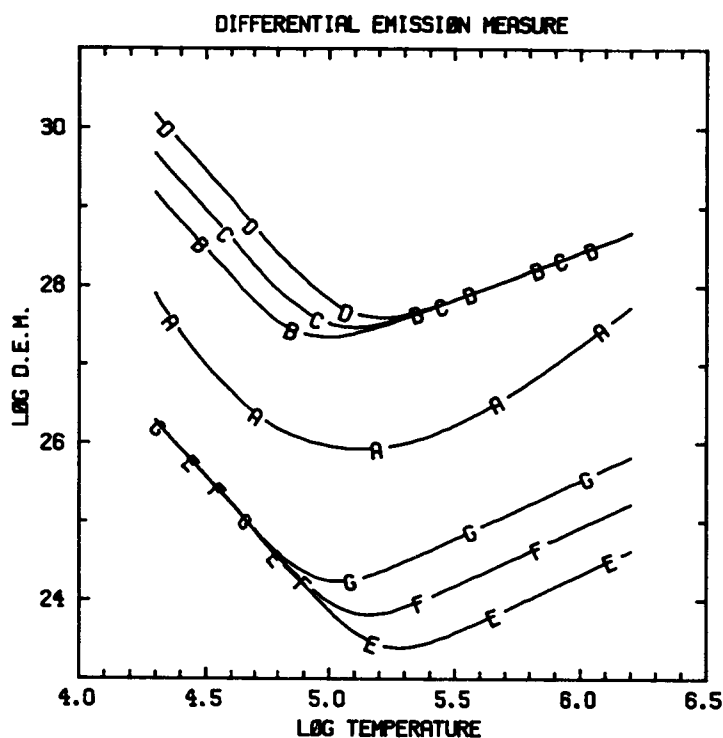


Fig. 1. Observed and computed DEM curves. A: "average" observed curve for non-active areas; a mean curve for active regions would be higher by about a factor of ten. B-D: area-weighted superpositions of transverse and longitudinal thermal conduction, with the area exposed to cross-field conduction increased by factors of $10^{3.5}$, $10^{4.0}$, and $10^{4.5}$ respectively; the curves have been displaced upward by one decade. E-G: mixtures of transverse and longitudinal conduction for magnetic field inclined to the isotherms by 0.05, 0.1 and 0.2 degrees respectively; the curves have been displaced upward by two decades. In the computations, $n_e T = 10^{15}$, $T_{\text{low}} = 10^4$, and $B = 3$.

needed to match the observed curve, but, because the cool branch of the DEM is steep, the ratio can vary by more than an order of magnitude from place to place without moving the minimum of the DEM curve out of its observed range, $\log T \approx 5.0-5.4$. It may be noted that the slope of the hotter branch of the DEM in curves B-D (as well as E-G) is shallower than the observed slope. This is a consequence of the simplified radiation law and planar geometry adopted in the present treatment, which does not attempt to model the hotter transition *per se* (cf. Athay 1981, 1982).

If magnetic field lines characteristically leave cool structures at a small angle to the isotherms, transverse conduction and longitudinal conduction are physically blended rather than superposed. By rotating the conductivity tensor, one may still solve the planar problem analytically. The result is shown for three angles by curves E-G in Figure 1; the curves have been displaced upward by two decades. The shape of the observed curve is reasonably well-matched for an angle of 0.1 or 0.2 degrees. As in the previous example, the area exposed to the corona must be increased by about four orders of magnitude in order to reach the proper normalization.

The necessary area exposed to cross-field conduction will be smaller if the cross-field transport is nonclassical. For Bohm-type diffusion, the emission measure is increased over its classical value by

$$\frac{\epsilon_{\perp B}}{\epsilon_{\perp c}} \approx 10^{0.8} B^{1/2} (n_e T)_{15}^{-1/2} T_{\text{low}}^{-5/4} T_5^{5/2}, \quad (13)$$

about an order of magnitude at $T = 10^5$ K. However, the slope of the DEM curve produced by Bohm conduction is approximately -1 , shallower than the observed curve. And, where the wave-particle interactions that lead to Bohm-like conduction are active, *parallel* thermal conduction will be inhibited (and changed in temperature dependence) at the same time that perpendicular conduction is enhanced.

4. Discussion

Although they are too simple, the analytic models considered in the previous section illustrate the basic idea: thermal conduction can determine the slopes of both branches of the DEM, without adjustable parameters. The principal attraction of a single microphysical mechanism is that it can operate basically unchanged in a variety of settings, from prominences to plages. Other stars may now be added to the list of environments. Observations with *IUE* and with the *Einstein Observatory* have produced DEM curves broadly similar in shape (although not necessarily in strength) to the solar curve among stars from a range of spectral types (late F to early M) and gravities (e.g., Zolcinski *et al.* 1982; Linsky *et al.* 1982). This again suggests a process without too many "knobs."

The price exacted for the idea considered here is a willingness to contemplate transition plasmas that are highly fragmented, such that the area exposed to the corona is three or four orders of magnitude greater than the projected surface area. Is this reasonable?

Historically, whenever the resolution of our observations has improved, we have seen finer structure (prominences are a good case in point). There is no observational evidence to suggest that this process is nearing an end. There is far to go from the internal viewpoint of the transition plasma: its fundamental scales (such as Debye length and proton gyroradius) are often centimeters or less. We must rely on indirect diagnostics.

Schmahl and Orrall (1979) have presented evidence that Lyman continuum absorption affects EUV spectra everywhere on the Sun, from network cells to active regions to quiescent prominences (also see Withbroe 1977; Kanno 1979; Nishikawa 1983). The inferred attenuation, about a factor of six, is remarkably constant from place to place. Orrall and Schmahl (1980) have analyzed the Lyman continuum data in more detail for nine hedgerow prominences. They find that there must be at least 4–10 cool threads or sheets along a typical line of sight, but an upper limit is not determined. Further information on the distribution of absorbing material may come from the observation that the Lyman continuum absorption is smaller at 10^6 K than at 10^5 K (Schmahl and Orrall 1986).

Recently, Fontenla and Rovira (1985) have constructed NLTE models of prominence threads and have computed profiles and absolute intensities of $L\alpha$, $L\beta$, $H\alpha$ and the Lyman continuum from an ensemble of threads (observations are discussed by Vial 1982). They infer that the minimum number of threads along a line of sight ranges from 10 to over 100, depending on the model; but again, no upper limit is placed on the number of threads.

Such studies show promise for constraining the degree of filamentation in prominences. Already it is clear that imagining thousand-fold filamentation along the line of sight is not as far-fetched as it might first appear.

There are good opportunities for progress in at least two other directions. First, we need *spatially and temporally resolved* ($\sim 1''$, ~ 1 min) determinations of the DEM in various structures. It will not be easy to collect enough photons! Still, it is vital to progress beyond "average" DEM curves now that several models vie to reproduce them. The fact that *Skylab* and *SMM* observations sometimes show differences in spatial structure between various transitional and coronal lines should alert us to expect dramatic departures from the mean curves (Cheng 1980; Poland and Tandberg-Hanssen 1983). It may be possible to test whether the DEM depends on pressure and magnetic field strength in the manner indicated by Equations 11 and 12.

A second fruitful direction will be further analysis of stellar DEM curves. Here the complete spatial averaging is offset by the opportunity to sample a wide range of coronal and chromospheric parameters. For example, β Dra (G2 Ib-II), which shows strong chromospheric and transition emission in conjunction with a relatively weak and extended corona, poses difficulties for models of the transition plasma based on thermal conduction and points toward internal heating (Brown *et al.* 1984).

References

- Antiochos, S. K., and Noci, G. 1986, *Ap. J.*, **301**, 440.
- Athay, R. G. 1966, *Ap. J.*, **145**, 784.
- _____. 1981, *Ap. J.*, **249**, 340.
- _____. 1982, *Ap. J.*, **263**, 982.
- _____. 1984, *Ap. J.*, **287**, 412.
- Brown, A., Jordan, C., Stencel, R. E., Linsky, J. L., and Ayres, T. R. 1984, *Ap. J.*, **283**, 731.
- Chambe, G. 1978, *Astr. Ap.*, **70**, 255.
- Cheng, C.-C. 1980, *Solar Phys.*, **65**, 347.
- Dere, K. P. 1982, *Solar Phys.*, **77**, 77.
- Doherty, L. R., and Menzel, D. H. 1965, *Ap. J.*, **141**, 251.
- Feldman, U., 1983, *Ap. J.*, **275**, 367.
- Fontenla, J. M., and Rovira, M. 1985, *Solar Phys.*, **96**, 53.
- Giovanelli, R. G. 1949, *M.N.R.A.S.*, **109**, 372.
- Kanno, M. 1979, *Pub. Astr. Soc. Japan*, **31**, 115.
- Keenan, F. P. 1984, *Solar Phys.*, **91**, 27.
- Linsky, J. L., Bornmann, P. L., Carpenter, K. G., Wing, R. F., Giampapa, M. S., Worden, S. P., and Hege, E. K. 1982, *Ap. J.*, **260**, 670.
- Mariska, J. T., Doschek, G. A., and Feldman, U. 1979, *Ap. J.*, **232**, 929.
- Nishikawa, T. 1983, *Solar Phys.*, **85**, 65.
- Orrall, F. Q., and Schmahl, E. J. 1976, *Solar Phys.*, **50**, 365.
- _____. 1980, *Ap. J.*, **240**, 908.
- Orrall, F. Q., and Zirker, J. B. 1961, *Ap. J.*, **134**, 72.
- Owocki, S. P., and Canfield, R. C. 1986, *Ap. J.*, **300**, 420.
- Poland, A. I., and Tandberg-Hanssen, E. 1983, *Solar Phys.*, **84**, 63.
- Rabin, D. M., and Moore, R. L. 1984, *Ap. J.*, **285**, 359.
- Raymond, J. C., and Doyle, J. G. 1981, *Ap. J.*, **247**, 686.
- Roussel-Dupre, R. 1980a, *Solar Phys.*, **68**, 243.
- _____. 1980b, *Solar Phys.*, **68**, 266.
- Schmahl, E. J., and Orrall, F. Q. 1979, *Ap. J. (Letters)*, **231**, L41.
- Schmahl, E. J., and Orrall, F. Q. 1986, these proceedings.
- Shoub, E. C. 1983, *Ap. J.*, **266**, 339.
- Vial, J. C. 1982, *Ap. J.*, **253**, 330.
- Withbroe, G. L. 1977, in *Proceedings of the OSO-8 Workshop*, ed. E. Hansen and S. Schaffner (Univ. of Colorado), p. 1.
- Yang, C. Y., Nicholls, R., and Morgan, F. 1975, *Solar Phys.*, **45**, 351.
- Zolcinski, M.-C., Antiochos, S. K., Stern, R. A., and Walker, A. B. C. 1982, *Ap. J.*, **258**, 177.

THERMAL STABILITY ANALYSIS OF THE FINE STRUCTURE OF SOLAR PROMINENCES.

Pascal Démoulin

Jean - Marie Malherbe

Brigitte Schmieder

Observatoire de Paris - Section de Meudon
92 195 Meudon Cedex - France

and

Mickael A. Raadu

Royal Institute of technology
Department of plasma physics
S- 100 44 Stockholm - Sweden

SUMMARY

We analyse the linear thermal stability of a 2D periodic structure (alternatively hot and cold) in a uniform magnetic field. The energy equation includes wave heating (assumed proportional to density), radiative cooling and both conduction parallel and orthogonal to magnetic lines. The equilibrium is perturbed at constant gas pressure. With parallel conduction only, it is found to be unstable when the length scale l_{\parallel} is greater than 45 Mm. In that case, orthogonal conduction becomes important and stabilizes the structure when the length scale l_{\perp} is smaller than 5 km. On the other hand, when l_{\perp} is greater than 5 km, the thermal equilibrium is unstable, and the corresponding time scale is about 10^4 s : this result may be compared to observations showing that the lifetime of the fine structure of solar prominences is about one hour ; consequently, our computations suggest that the size of the unresolved threads could be of the order of 10 km only.

FUNDAMENTAL EQUATIONS OF THERMAL EQUILIBRIUM.

We use the 2D "chessboard" of figure 1, which displays a periodic hot (T_1) and cold (T_2) structure in a uniform magnetic field (this could be the case in the central parts of prominences, see Leroy et al., 1983). We write equations for thermal equilibrium of hot and cold cells, as :

$$\begin{cases} \rho_1 h - \rho_1^2 Q(T_1) - 2 \frac{F_{\parallel}}{l_{\parallel}} - 2 \frac{F_{\perp}}{l_{\perp}} = 0 \\ \rho_2 h - \rho_2^2 Q(T_2) + 2 \frac{F_{\parallel}}{l_{\parallel}} + 2 \frac{F_{\perp}}{l_{\perp}} = 0 \end{cases}$$

$$\text{Where } F_{\parallel} = \frac{k_{o\parallel}}{3.5} \frac{T_1^{3.5} - T_2^{3.5}}{l_{\parallel}} \quad \text{and } F_{\perp} = - \frac{k_{o\perp}}{1.5} \frac{T_1^{-1.5} - T_2^{-1.5}}{l_{\perp}}$$

are respectively the heat flux parallel and orthogonal to the magnetic field. ρ_1 and ρ_2 are the densities of respectively hot and cold cells. $k_{o\parallel}$ and $k_{o\perp}$ are conduction coefficients ; $k_{o\perp}$ depends on the strength of the magnetic field B.

We assume that the gas pressure remains constant ($\rho_1 T_1 = \rho_2 T_2 = \rho T = \text{constant}$) and use the cooling function $Q(T)$ given by Hildner (1974). Unknown quantities are h , T_1 , T_2 . The equilibrium state (h , T_2), when T_1 is fixed, is given by the set of 2 equations above. Possible solutions are shown in figure 2 (top).

ANALYSIS OF THERMAL STABILITY

We perturb the equilibrium at constant gas pressure P and heating h ($T \rightarrow T + \delta T$). Equations are linearized assuming that $\delta T \propto e^{\beta t}$, where β is a growth rate. We assume also that there is no motion in a direction perpendicular to the magnetic field, so that $l_{\perp} = \text{constant}$. Hence, mass conservation gives $1/\rho = \text{constant}$. We get two solutions for β : the first one is always negative (stable solution), but the second one can either be positive (unstable) or negative (stable). It depends on the values of equilibrium parameters $1//$, l_{\perp} and T_1 . The magnetic field strength B was kept constant (1 Gauss).

RESULTS

Figure 2 (bottom) gives the growth rate as a function of l_{\perp} and hot temperature T_1 (parallel conduction was neglected there). The thermal equilibrium is unstable when $\beta > 0$: this is always the case when l_{\perp} is too large ($> 10^6$ m). When l_{\perp} is smaller than 10^5 m, the equilibrium may be stable if T_1 does not exceed a critical value T_{max} ($T_{\text{max}} = 10^6$ K for $l_{\perp} = 10^4$ m).

Figure 3 gives β as a function of l_{\perp} and $1//$ for a 2 D model (T_1 was kept constant). It shows that, when $1// < 45$ Mm, the thermal equilibrium is stable; when $1// > 45$ Mm, it is unstable, unless $l_{\perp} < 5$ km. When $l_{\perp} > 5$ km, the time scale for instability is approximately equal to 10^4 s and corresponds to the observed life time of the fine structure in solar prominences. This result suggests that the size of thin threads could be as small as 10 km. The temperature of hot cells (T_1) used in the computations was 10^6 K.

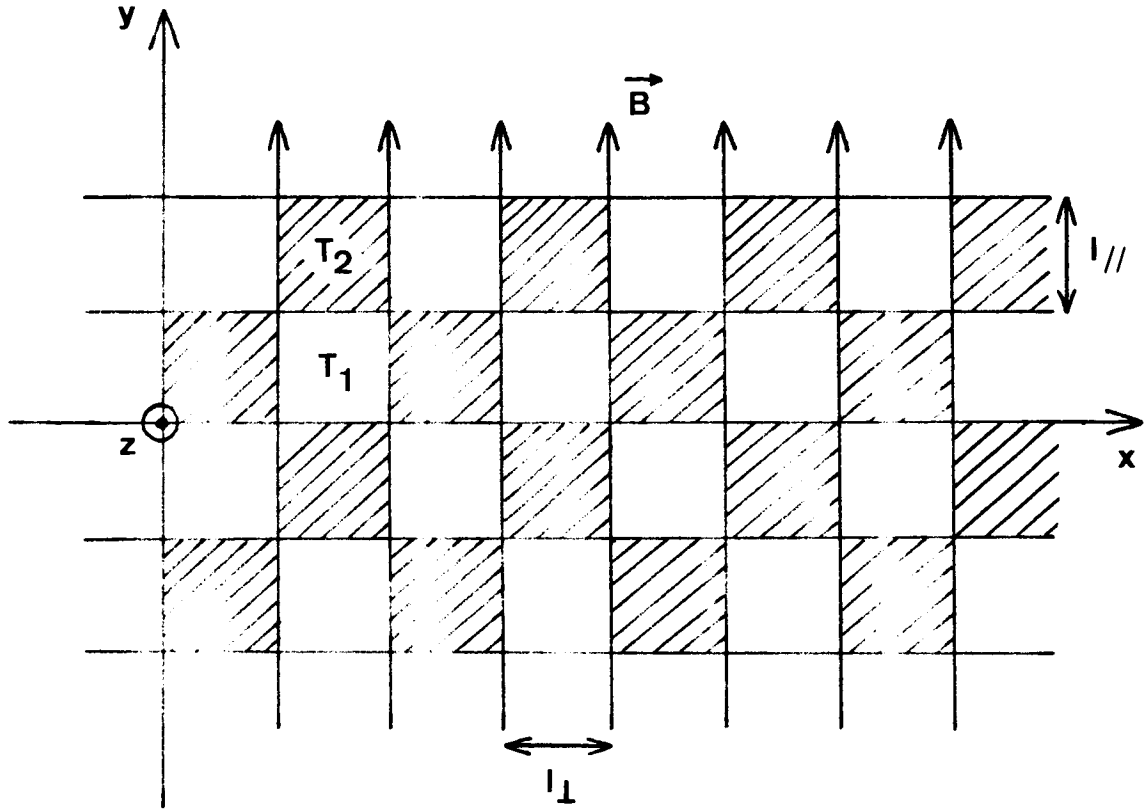


figure 1 : the geometry of the model : the structure is periodic in x direction (length scale l_{\perp}) and y direction (length scale $l_{//}$). The magnetic field B is parallel to y. z is the vertical axis. White areas are hot (T_1) and tenuous (ρ_1) ; dashed cells are cold (T_2 and dense (ρ_2)).

figure 2 : next page

top : $\log Q(T) + (\text{orthogonal conduction}) / \rho^2$ as a function of $\log(T)$ for different values of the length scale l_{\perp} (1D calculation with $l_{\perp} = 10^3, 10^4, 10^5, 10^6$ and 10^7 m). Equilibrium solutions are located at points A, B, C (intersection with the straight line $\log(T) + \log(\frac{k h}{\rho m})$). When the heating becomes too large, the cold solution A does not exist any more.

bottom : the growth rate as a function of hot temperature T_1 (1 D calculation) The function $\text{sgn}(\beta) / \log|\beta|$ is displayed for different values of l_{\perp} (same as above).

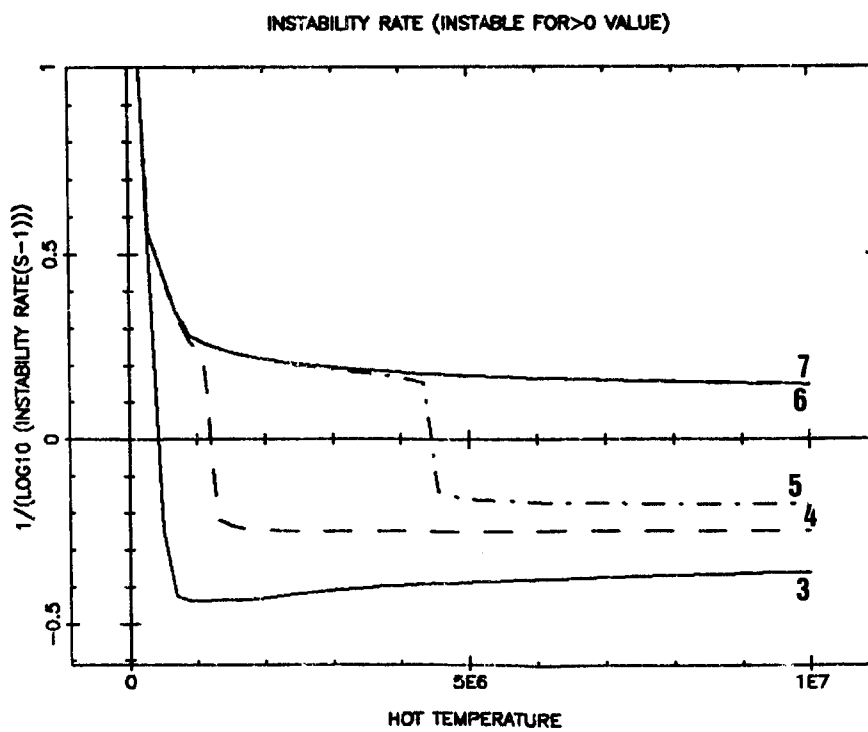
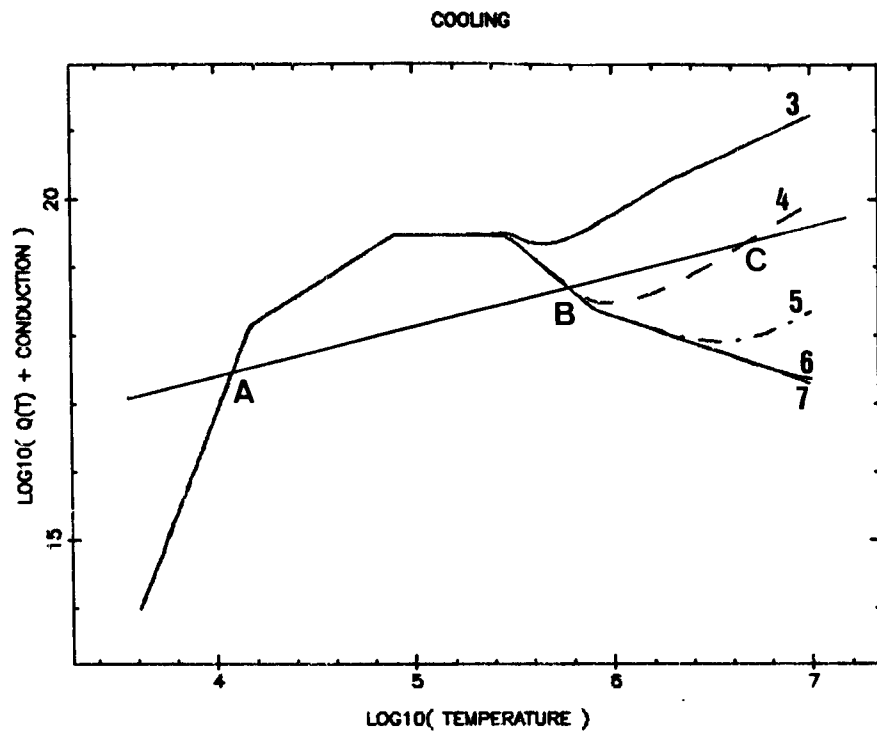


figure 2

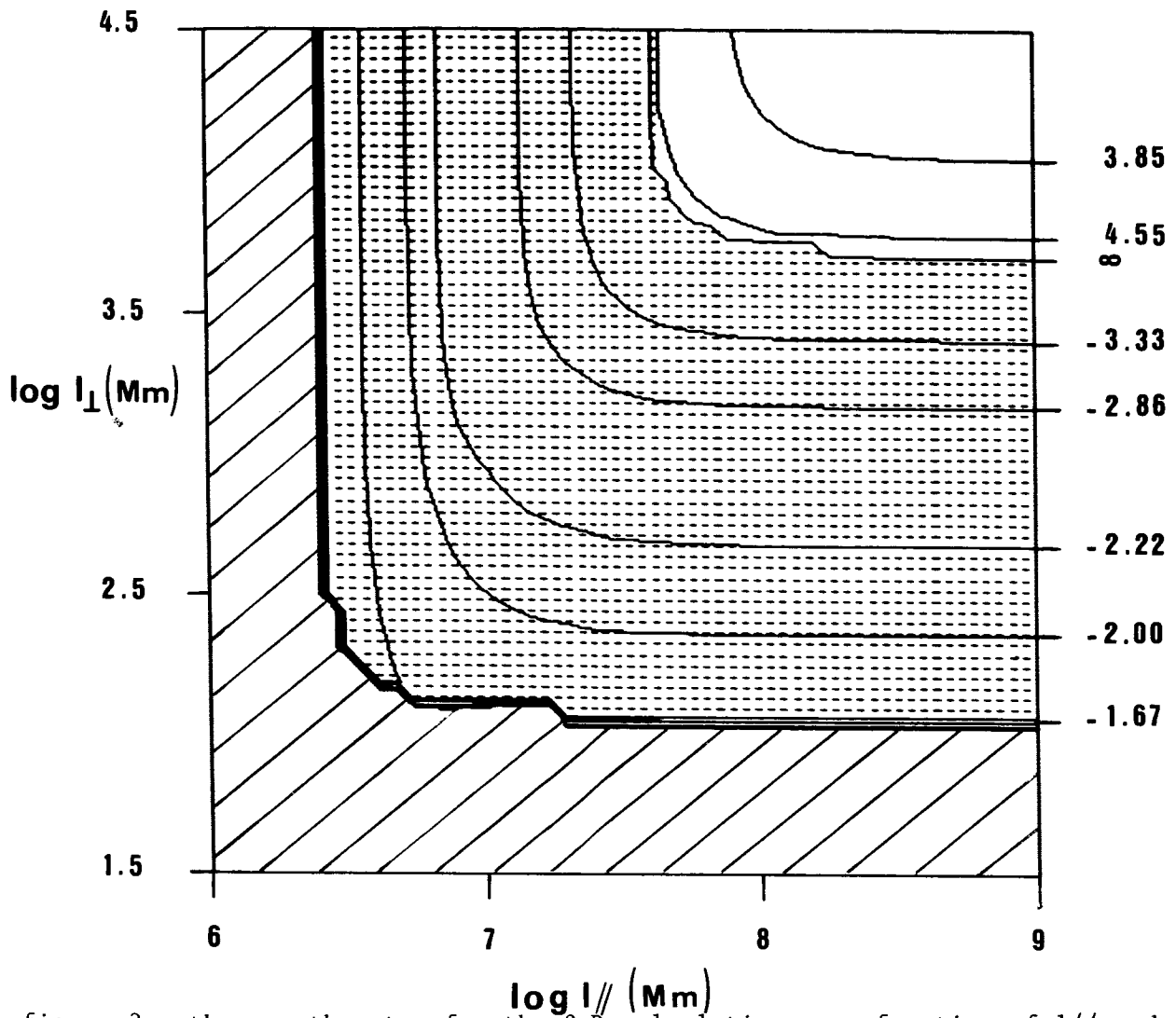


figure 3 : the growth rate for the 2 D calculation as a function of I_{\parallel} and I_{\perp} . Isocontours of $\text{sgn}(\beta) \log|\beta|$ are displayed. The dotted area is stable ($\beta < 0$); the white one (top) is unstable ($\beta > 0$). The dashed region (left and bottom) represents the domain where a cold equilibrium does not exist (see figure 2).

REFERENCES

- Dunn, R.B. : 1960, Thesis Ph.D, Harvard University
- Engvold, O. : 1976, Solar Phys., 49, 283
- Hildner, E. : 1974, Solar Phys., 35, 123
- Leroy, J.L., Bommier V., Sahal S. : 1983, Astron. Astrophys., 83, 135
- Maltby, P. : 1976, Solar Phys., 46, 149.

The Density and Thickness of Quiescent Prominences

Tadashi Hirayama

Tokyo Astronomical Observatory

Mitaka, Tokyo 181, JAPAN

[Abstract] The electron density was determined for a number of quiescent prominences at various positions from the Stark effect. It was found that the intensity ratio of MgI emission lines to SrII lines is independent of the observed electron density in the range of $10^{10.2}-10^{11.4}\text{cm}^{-3}$. This contrasts with Landman's (1984) theoretical expectation that the ratio is proportional to the electron density. From the intensity of Balmer lines and the electron density, it is inferred that the true diameter of a thread in prominences of high electron density may be smaller than $0.2''$. The averaged total number density of hydrogen N_H was found to be $3-6 \times 10^{11}\text{cm}^{-3}$, leading to a total gas pressure P_g of 0.6 dyn cm^{-2} and a total density of $\sim 1 \times 10^{-12}\text{gcm}^{-3}$. Landman's large value of $N_H \sim 6 \times 10^{12}$ and $P_g \sim 6$ may have resulted either from the fact that he has treated very bright prominences and/or from the derivation of the high electron density for all prominences he studied.

Recently Landman (1983, 1984, and 1985) has shown from intensity ratios of various lines that the mean electron density of quiescent prominences is $N_e \sim 10^{11.3}\text{cm}^{-3}$ and the total gas pressure of $3-6\text{ dyn cm}^{-2}$ with the total number density of hydrogen $N_H \sim 5 \times 10^{12}\text{cm}^{-3}$ and with the ionization ratio of hydrogen (N_{HII}/N_{HI}) of ~ 0.09 (see also Nikaido and Kawaguchi, 1983). The Landman's values of N_H and the gas pressure are more than one order of magnitude larger than the previous values (Hirayama, 1979, p.14). See also discussions on the older values by Landman (1983).

In order to inspect this problem, first I have determined the electron density from the hydrogen-Stark effect using an unpublished extensive table of line intensities and widths of prominences (32000 lines in total) which I observed with the 40cm coronagraph at Sacramento Peak Observatory in 1969 (Hirayama, 1972, Paper I). The method of determining the electron density, which takes the ion contribution to the broadening into account, is described in Hirayama (1971). Figure 8 of Paper I shows examples, where $1/e$ -widths of Balmer lines are plotted against principal quantum number, and it is easy to

distinguish, say, between $N_e = 10^{10.3}$ and $10^{11.2}$. In the case of a post-flare loop, a high electron density of $N_e = 10^{12} \text{ cm}^{-3}$ was obtained with the same method (see Fig. 9 of Paper I).

The result is the following (Hirayama, 1985): the average electron density was found to be $10^{11.02} \text{ cm}^{-3}$ for five hedgerow quiescent prominences at 57 different positions, and $10^{10.48} \text{ cm}^{-3}$ for two curtain-like old quiescent prominences at six different positions. The maximum value was $10^{11.4} \text{ cm}^{-3}$, and if $N_e \leq 10^{10.0}$ the determination becomes difficult. If lines up to H28 are observed, the electron density can be derived when $N_e \geq 10^{10.2}$.

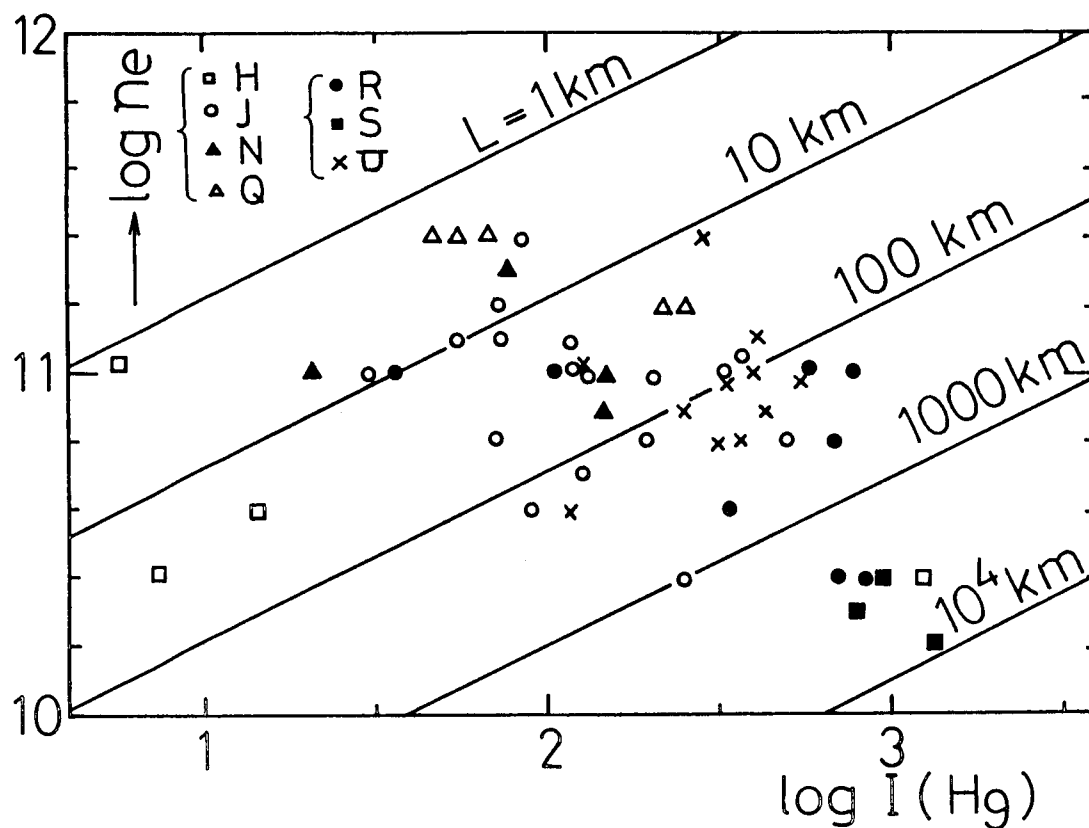


Fig. 1. The electron density from the Stark effect vs. the intensity of hydrogen Balmer line H9 ($\text{erg cm}^{-2} \text{s}^{-1} \text{sr}^{-1}$). Full lines: lines of constant effective geometrical length L .

Figure 1 shows the electron density, N_e , thus determined vs. the intensity of an optically thin Balmer^e line of H9, $I(\text{H9})$. Letters H, J, N, ... refer to prominences listed in Table II of Paper I, and data from various heights and portions of each prominence were utilized. Using the average value of the whole sample of $N_e = 8.4 \times 10^{10}$, and with $T = 7000 \text{ K}$, the emission measure $N_e^2 L$ and the effective length L can be determined from the average intensity of $I(\text{H}_9) = 240$: $N_e^2 L = 6.3 \times 10^{28} \text{ cm}^{-5}$ and $L = 80 \text{ km}$.

If one uses values from 6 points in the lower right corner of Figure 1, L becomes 4600km, and from 4 points having high N_e of $10^{11.4}$, one obtains an extremely low value of the effective length: $L=2.4$ km. Larger L 's are obtained for stable big quiescents, and low values of L are from low height, rather young quiescents, which lie perpendicular to the solar equator. Note that there are not many data points of lower intensity with lower electron density in Figure 1. This is simply because the electron density cannot be determined for these prominences.

Now we discuss the implications of the value of the effective geometrical length integrated along the line of sight, L . We assume that prominences consist of a number of long threads of a diameter ϕ of 300km (Dunn, 1960), and that they are, for simplicity, suspending vertically. Then $L=10$ km means that the number of threads in a distance of 10" along the solar limb, n , is about unity: $n\pi(\phi/2)^2=L\times 10''$. Since the average L is 80km, n should be 8, the filling factor of $n\phi/10''$ being 0.3. However if $L>200$ km, overlapping of threads in the line of sight must be occurring: $n\phi>10''$. If $L\leq 10$ km as derived before in some cases, it means that the thread diameter should be smaller than 300km. This comes from the following consideration: we measured spectra with a 10" length of the microphotometer slit, and with a 10" step of raster scan. And the distribution of the total intensity of emission lines along the spectrograph slit which was placed parallel to the limb is found to be rather smooth. Since the seeing was probably better than 10", it means that there should be at least one thread within a distance of 10": $n\geq 1$. This requires that $\phi\leq 2(L\times 10''/\pi)^{1/2}$. For example $\phi\leq 150$ km, if $L=2.4$ km as found above. It is hoped to observe the thread diameter of less than 150km from the direct imaging.

Next we derive the total number density of hydrogen N_H by using the intensity ratio of H9 and MgI 3838. Since the ionization potential to MgIII is rather large (15.0eV), Mg is expected to be mostly in MgII, so that the intensity $I(\text{Mg}3838)$ is proportional to $N_e N(\text{MgII}) L \propto N_e N_H L$. With the average observed value of $I(3838)=55 \text{ erg cm}^{-2}\text{s}^{-1}\text{sr}^{-1}$ and with the above values of N_e and L , N_H is found to be $6\times 10^{11}\text{cm}^{-3}$ if one uses non-LTE calculations by Landman (1984, Table 2). $N_H=3\times 10^{11}$ is obtained, if one adopts Vernazza et al.'s computation (1981, Table 21, VALIII) near 7000K. Here we note that Mg3838 line is optically thin because the ratio of $I(\text{Mg}3838)/I(\text{Mg}3832)$ was found to be independent of a wide range of values of $I(\text{Mg}3838)$, and that the intensity ratio of $I(\text{Mg}3838)/I(\text{H}9)(\sim 0.23)$ is also independent of $I(\text{H}9)$. $N_{\text{HII}}/N_{\text{HI}}$ then becomes ~ 0.2 (from Landman's Table), or ~ 0.4 (VALIII), and the optical depth at the head of the hydrogen Lyman continuum becomes ~ 30 (Landman) or ~ 10 (VALIII). These are not too far from older values (Hirayama, 1979). A factor of two difference in $N_{\text{HII}}/N_{\text{HI}}$ from the Landman's value of 0.09 mainly comes from the difference of the observed intensity ratio of $I(3838)/I(\text{H}9) \sim 0.49$. Landman's data are from very bright (or

large thickness) prominences, and Landman's large N_e value simply comes from a rather large N_e of 2×10^{11} for every prominence he studied, which, in turn, may or may not be true (see below).

Landman claims that the intensity ratio of $[I(\text{Mg}3838) + I(\text{Mg}3832)] / [2 \times I(\text{SrII}4077)]$ (abbreviated as $I(\text{Mg})/I(\text{Sr})$) is proportional to N_e in the range of $10^{10.5} - 10^{12.0} \text{ cm}^{-3}$. Although it may be that $I(\text{Mg})/I(\text{Sr}) \propto N_e$ holds for post-flare loops of high N_e (Foukal et al., 1986), quiescent prominences do not show this behavior as shown in Figure 2. Here

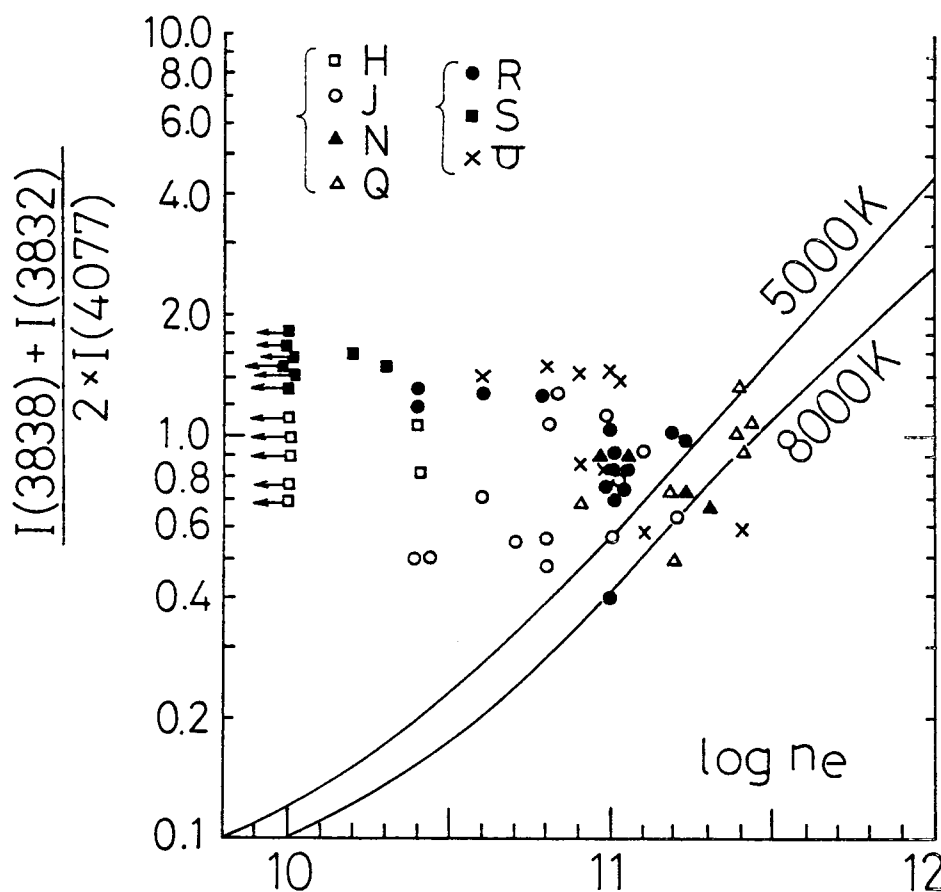


Fig. 2. Intensity ratio of metallic lines vs. electron density from the Stark effect. Full lines: Landman's calculation. Various symbols refer to prominences listed in Hirayama (1972).

$I(\text{Mg})/I(\text{Sr})$ is plotted against the observed N_e obtained from the Stark effect, each data point being from a single exposure, and full lines are from Landman's calculation (Foukal et al., 1986, Fig. 4). If photoionizations of SrII to SrIII, which do not seem to be well-founded (see Landman, 1985), were much more effective, it may in principle be possible to obtain a constancy of the intensity ratio against N_e . The electron density may well be

lower than 10^{10}cm^{-3} for much fainter portions of prominences (Bommier et al., 1986). I inspected the relation between $I(\text{Mg})/I(\text{Sr})$ and $I(\text{Mg}3838)$ to see if the ratio becomes lower when $I(\text{Mg}3838)$ becomes very small. Here I included faint portions where the electron density cannot be determined from the Stark effect. While $I(\text{Mg}3838)$ ranged from about 2-3 to 300 $\text{erg cm}^{-2}\text{s}^{-1}\text{sr}^{-1}$ (Landman's averaged value was 2800), the ratio changed only by a factor of 3: $I(\text{Mg})/I(\text{Sr})=[I(\text{Mg}3838)/10^2]^{0.22}$. So I would guess that something might be wrong with the calculation (probably of SrII), although low intensities do not necessarily ensure the low electron density. But it is difficult to doubt the existence of $N_e \sim 10^{10.0}$.

In conclusion, two points are worth mentioning. First the effective thickness L of quiescent prominences of low height is found to be only 10km or less, which is surprising. However this effective thickness can be converted to a thread diameter of 150km or less. On the other hand big, high altitude quiescent prominences showed $L=5000\text{km}$ or so. This is not surprising, since the apparent length in the line of sight will easily exceed 10^5km . Second, there is a discrepancy between the electron density found from the Stark effect and the intensity ratio of metallic lines. Further observations and calculations are needed to clarify this point.

The average physical quantities for the present data are $N_e=8.4 \times 10^{10}$, $N_H=3-6 \times 10^{11}$, $N_{\text{HII}}/N_{\text{HI}}=0.2-0.4$, and a filling factor of ~ 0.3 , which implies that one 300km-diameter thread can be found every 1000km along the long axis of a quiescent prominence. Since the optical depth of the head of HI Ly α becomes less than 10 for a 300km thread, the maintenance of the temperature of 7000k by the incoming UV radiation below 912A will not be difficult. The average total gas pressure is found to be 0.6 dyn cm^{-2} , and the average total density of $1 \times 10^{-12} \text{ g cm}^{-3}$ is derived by adopting the helium-to-hydrogen ratio of 10%.

References

- Bommier, V., Leroy, J.L., and Sahal-Br  chot. S.: 1986, *Astron. Astrophys.* **156**, 90.
Dunn, R.B.: 1960, Thesis, Harvard Univ.
Foukal, P., Hoyt, C., and Gilliam, L: 1986, *Astrophys. J.* **303**, 861.
Hirayama, T.: 1971, *Solar Phys.* **17**, 50.
Hirayama, T.: 1972, *Solar Phys.* **24**, 310, referred to as Paper I.
Hirayama, T.: 1979, *IAU Colloquium* **44**, p.4.
Hirayama, T.: 1985, *Solar Phys.* **100**, 415.
Landman, D.A.: 1983, *Astrophys. J.* **270**, 265.
Landman, D.A.: 1984, *Astrophys. J.* **279**, 438.
Landman, D.A.: 1985, *Astrophys. J.* **290**, 369.
Nikaido, Y. and Kawaguchi, I.: 1983, *Solar Phys.* **84**, 49.

PARTIAL REDISTRIBUTION EFFECTS IN THE FORMATION OF HYDROGEN LINES IN QUIESCENT PROMINENCES

P. Heinzel¹, P. Gouttebroze², and J.C. Vial²

1. Astronomical Institute of the Czechoslovak Academy of Sciences
25165 Ondrejov, Czechoslovakia
2. Laboratoire de Physique Stellaire et Planétaire
B.P. 10 - F-91371 Verrières-le-Buisson Cédex, France

ABSTRACT

Departures from complete frequency redistribution (CRD) in hydrogen lines are investigated for solar prominences. Partial redistribution effects (PRD) are found both in the wings (their already known lowering) and in the central part of the $L\alpha$ line; a new feature is evidenced here: the partially coherent scattering in the near wings of the line leads to a double-peaked profile mirroring the incident solar radiation. With a low density model, we obtain a good agreement with OSO 8 observed profiles. On the contrary, the PRD computed $L\beta$ profile (lower density, no reversal) departs from the observed one, a result which calls for more progress in terms of non l.t.e. transfer and modelling.

1. INTRODUCTION

During the last decade, several highly-sophisticated partial-redistribution techniques (PRD) have been applied to the analysis of the strong resonance lines formed in the solar chromosphere, plages or sunspots. Being low-density structures, solar prominences are also very good candidates for possible departures from complete redistribution (CRD), at least for most opaque lines like hydrogen $L\alpha$ or $L\beta$. As reported by Vial (1982a), various high-resolution $L\alpha$ and $L\beta$ line profiles of a quiescent prominence have been recorded by the LPSP spectrometer on board of OSO-8 satellite. Applying the two-dimensional radiative transfer code of Mihalas et al. (1978), Vial (1982b) has simulated theoretical $L\alpha$ profiles (using a two-level atom and CRD) and made a comparison of their basic parameters with those corresponding to OSO-8 data. The agreement was satisfactory, but no direct comparison between the shapes of the theoretical and measured profiles was presented in this study. It is the aim of the present paper to make possible a first comparison of OSO-8 $L\alpha$ and $L\beta$ profiles with theoretical PRD computations in order to assess the real importance of departures from CRD. Moreover, we investigate the behaviour of the total CRD and PRD intensities of the hydrogen lines and compare our results with those of Milkey et al. (1979) and with the data presented by Heinzel and Vial (1983).

2. PROMINENCE MODELS

Since our principal interest is to estimate PRD effects on hydrogen lines, we start here with simple one-dimensional (1D) isothermal-isobaric prominence models. These models are of the (a - c) type of Heasley and Milkey (1976) or perhaps more realistic low-pressure ones of Heasley and Milkey (1978, 1983). The quiescent prominence as seen on the limb is represented by a vertically-standing slab of finite thickness with all model parameters being depth-independent. As basic input parameters we use the set (M , T , p , v_t , y) -see Tab. 1- where M is the total column mass along the line of sight, T is the kinetic temperature, p represents the total

gas pressure and v_t characterizes the mean microturbulent velocity. The prominence plasma is assumed to be composed of hydrogen and helium atoms, the abundance ratio of helium to hydrogen being $y = 0.1$.

MODEL	M (g/cm ²)	T (°K)	p (dyn/cm ²)	v_t (km/sec)	y
a3	1.2-5	7500	0.065	0	0.1
a5	3.0-5	7500	0.065	0	0.1
LP1	1.2-5	7500	0.010	0	0.1
LP2	3.0-5	7500	0.020	0	0.1
LP3	3.0-5	7500	0.020	6	0.1

Table 1. - Parameters of the prominence models used in this paper.

Since the prominence slab is irradiated symmetrically from both sides by the incident solar radiation, we treat only one half of it. The corresponding second-order boundary conditions for the radiative transfer equation (RTE) are used in the same manner as in Mihalas et al. (1975), but are properly modified for the finite symmetrical slabs (see also Heasley and Mihalas, 1976). The surface boundary condition requires the knowledge of the mean incident radiation field in all lines and continua. For Balmer lines we use the limb-darkened profiles of David (1961), P_α , P_β and B_α line profiles are taken from Zelenka (1976). All these profiles are subsequently adjusted to limb-darkened continuum level. Disc-center intensities of L_α and L_β lines were obtained by OSO-8 (see, e.g., Vial, 1982a). To obtain the intensity profiles of L_γ and L_δ , we scaled the profile of L_β by the ratios of total intensities L_γ/L_β and L_δ/L_β , respectively. Integrated intensity of L_β is taken from OSO-8, L_γ and L_δ from Vernazza and Reeves (1978). In order to obtain the most realistic mean-intensity profiles required in the surface boundary condition, we integrated numerically the above incident intensities, using the geometry and technique as discussed by Heinzel (1983). For all models we use the height 4000 km which corresponds to OSO-8 observations used here for a comparison. By the same procedure we also precomputed all fixed rates for optically thin lines. The continua are treated in two different ways: optically thick Lyman continuum transfer is solved in detail at several frequency points for which we specify the incident radiation temperatures equivalent to intensities measured on OSO-6. For all subordinate continua we simply use one "mean" T_{rad} which defines the corresponding fixed rates ($T_{rad} = 5480, 5900, 6200, 6400$ K (without dilution) for Balmer, Paschen, Brackett and Pfund continua, respectively).

3. FORMATION OF HYDROGEN LINES WITH PARTIAL REDISTRIBUTION

The laboratory-frame redistribution function (LRF) used in the present computations takes generally the form (Heinzel and Hubeny, 1982)

$$R(\nu', \nu) = \gamma R_I(\nu', \nu) + (1 - \gamma) R_{III}(\nu', \nu) \quad (3.1)$$

with R_I being either R_{II} for the case of the resonance lines or R_V for the lines of subordinate series. While the functions R_{II} and R_V contain certain degree of coherence of the scattering in the line wings, the function R_{III} can be simply replaced by complete redistribution in the observer's frame.

The branching ratio γ is defined as :

$$\gamma = \frac{P_j}{P_j + Q_E} \quad (3.2)$$

where P_j is the total depopulation rate of the upper level j , while Q_E represents the elastic collision rate.

Strictly speaking, Eq. (3.1) has been derived assuming the impact approximation and isolated lines and, therefore, is not applicable to hydrogen lines. However, as demonstrated by Yelnik et al. (1981), the correct ARF (atomic-frame) for hydrogenic $L\alpha$ line is formally the same as that corresponding to LRF (3.1), but the elastic collision rate Q_E is now frequency-dependent. Consequently, the atomic profile function is no longer Lorentzian in the wings and, moreover, the branching ratio is also frequency-dependent (Q_E in (3.1) is replaced by $Q_E(\nu)$).

For $L\beta$ we apply the same procedure with $Q_E(\nu)$ taken from Gouttebroze et al. (1978). For higher members of the Lyman series, we simply use CRD. Moreover, Heinzel (1983) has shown that for quiescent prominences observed on the limb, the subordinate lines exhibit negligible departures from CRD when applying LRF R_V . Anticipating this result, we use in the present computations CRD instead of complicated LRF (3.1) for all subordinate lines.

As a basic procedure to solve the non-LTE transfer problem with PRD we use a combination of an equivalent-two-level-atom approach (ETA) and partial-linearization technique. In the frame of the so-called standard PRD problem (see below), ETA was modified by Hubeny (1985) to account directly for PRD in one line at a time. The resulting source function is

$$S(\nu) = \frac{\bar{J} + \lambda(\bar{R}_{II}(\nu) - \bar{J}) + \eta}{1 + \epsilon_\nu} \quad (3.3)$$

where \bar{J} is the integrated mean intensity and $\bar{R}_{II}(\nu)$ is the redistribution integral. The parameters η and ϵ_ν in (3.3) have the similar meaning as in standard ETA (for details see Hubeny, 1985). A very important parameter appearing in Eq. (3.3) is the parameter λ

$$\lambda = \frac{A_{ji}}{P_j} \cdot \frac{P_j}{P_j + Q_E} = \frac{A_{ji}}{P_j} \cdot \gamma \quad (3.4)$$

where A_{ji} is the spontaneous emission rate for the given transition. For strong resonance lines like $L\alpha$ or $L\beta$, λ in form (3.4) reflects the coherence properties of the transition $i \leftrightarrow j$. Equations (3.3) and (3.4) are valid if all multilevel cross-redistributions lead to a natural population of the upper level j - this is exactly what we call the standard PRD problem, i.e. we consider here no PRD multilevel interlocking.

Simply speaking, γ alone is the branching ratio derived for a two-level-atom, while λ accounts for multilevel processes. From (3.4) we get for $L\alpha$ $\lambda \approx \gamma$ since $P_2 = A_{21}$. On the other hand, for $L\beta$ we have $P_3 = A_{31} + A_{32}$ so that $\lambda = 0.56\gamma$. Since the ratio γ for both $L\alpha$ and $L\beta$ is nearly equal to unity (for low-density media), the importance of the redistribution term $\bar{R}_{II}(\nu)$ in (3.3) is significantly reduced for $L\beta$ due to the scattering process $2 \rightarrow 3 \rightarrow 1$ which is assumed to contribute to the emission in $L\beta$ as a CRD process.

The numerical procedure for solving the full non-LTE problem is the following: the basic iteration loop uses the linearization scheme as described by Mihalas et al. (1975) to solve simultaneously RTE (by Feautrier method), equations of statistical

equilibrium, particle and charge conservation equations. Hydrostatic equilibrium is treated iteratively, the temperature structure is given from the model. We use 5-level hydrogen atom with continuum and explicitly treat all Lyman lines, Lyman continuum and H α line. Other transitions are assumed to be optically thin and their radiative rates are fixed by the external radiation field. The linearization loop ensures the global convergence of this highly non-linear problem. Between each two linearization iterations, we perform several ETA iterations, accounting directly for PRD in L α and L β lines. In this way, we obtain fast convergence (within 2 - 3 linearization iterations) in all 50 depths and for all transitions and level populations. We use most important opacity sources for hydrogen spectrum formation in low-density prominences, both ETA and linearization schemes use variable Eddington factors (Auer and Mihalas, 1970) to minimize the computer time. Inelastic collisional rates for hydrogen are taken from Mihalas et al. (1975). The redistribution matrices are used as depth-independent since $P_j \gg Q_E$ and the electron and proton densities vary only slowly with depth. On the other hand, the branching ratio $\gamma(\nu)$ is computed for all depths.

4. DISCUSSION OF NUMERICAL RESULTS AND COMPARISON WITH OBSERVATIONS

In Fig. 1 we display typical L α profiles for both PRD and CRD approaches (for the model LP1).

Drastic differences between CRD and PRD profiles can be explained in the following manner. Around line center, PRD behaves similarly as CRD and the emergent radiation is saturated at the level of diluted incident chromospheric intensity. However, when the scattering takes place in the near wings, we can observe an interesting effect:

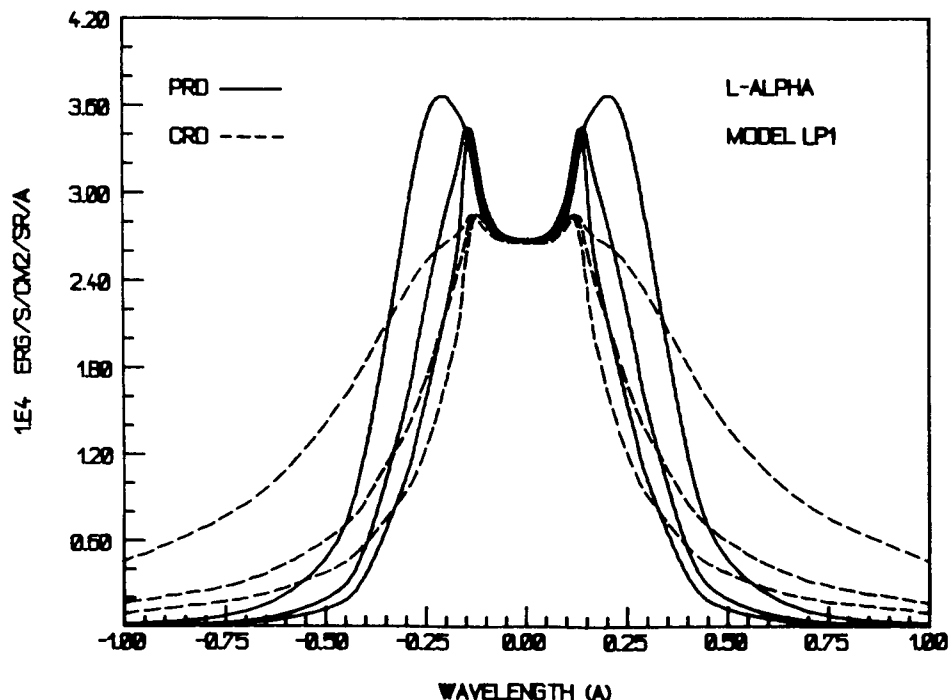


Fig. 1 - L α intensities emergent from a prominence slab (model LP1). Both PRD (—) and CRD (---) profiles are displayed for three outgoing angles with $\mu = 1.$, 0.6 and 0.2 (broader profiles correspond to lower values of μ).

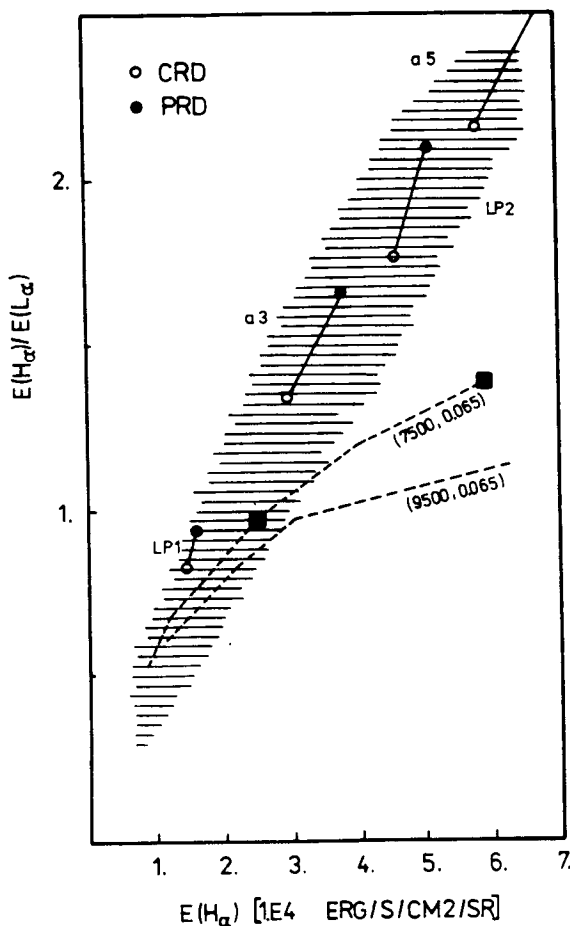


Fig. 2 - Dependence of the ratio $E(H\alpha)/E(L\alpha)$ on $E(H\alpha)$, E being the integrated intensity in units $\text{ergs s}^{-1} \text{cm}^{-2} \text{sr}^{-1}$. Hatched region contains the observed ratios taken from Heinzel and Vial (1983), dashed lines correspond to CRD intensity-ratios as obtained by Heasley and Milkey (1976) for the models indicated in parentheses (labeled by kinetic temperature and total gas pressure). Our theoretical ratios for models a3 and a5 are to be compared with squares on the dashed curve (7500, 0.065). Our CRD (o) and PRD (•) computations are presented for $\mu = 1$.

Milkey et al. (1979): their CRD intensity ratios are shown in Fig. 2 as two dashed lines, a1 - a5 models lie on the curve (7500, 0.065). For models a4 - a5, this curve is significantly below the (hatched) region of observed values as taken from Heinzel and Vial (1983) - this discrepancy is caused probably by adopting unrealistic incident $L\alpha$ radiation field. The theoretical $L\alpha$ profiles of Milkey et al. (1979) exhibit only the second PRD-feature, i.e. the low wing intensities. These authors obtained no difference between CRD and PRD for the line core and near wings and, subsequently, their integrated $L\alpha$ intensities are a factor two lower for PRD as compared with CRD which leads to an apparent agreement with Skylab data. Furthermore, we note that LP1 is the model with lower M and, therefore, for $\mu = 1$ and 0.6 the incident peak is not fully reproduced due to lower optical thickness of $L\alpha$ (see Fig. 1). However, for thicker models like LP2 (Fig. 3), LP3 or a5, the incident peak is nicely reproduced and its position agrees well with that for the original peak. It seems that the observed $L\alpha$ peak-to-peak distance (PTPD) in quiescent

for CRD, the photons absorbed in this region can freely diffuse into the wings which become broad and intense; PRD is, on the other hand, represented by partially-coherent scattering in the wings so that the incident chromospheric $L\alpha$ peaks (centered at $\Delta\lambda \approx \pm 0.2 \text{ \AA}$) are partly "reproduced" for the PRD case. The photons absorbed in the core or in the near wings cannot freely penetrate into the wings as in the CRD case and, as a consequence, far-wing intensities are sufficiently below the CRD values. Very low PRD wings follow from the well-known behaviour of the redistribution function R_{II} . Partial reproduction of the strong incident $L\alpha$ peaks has the following consequences. First, due to quasi-coherent penetration of these peak photons into the slab center, we arrive at higher excitation of hydrogen, i.e. the populations of the excited levels are higher for PRD. As a consequence, the lines of subordinate series are more intense for PRD than for CRD, which is demonstrated for $H\alpha$ line in Fig. 2.

In this figure, $L\alpha$ integrated intensities are nearly the same for both PRD and CRD (for PRD, the low intensities in the far wings are compensated by the two peaks), but $H\alpha$ is shifted in PRD case. In this way we can also explain the results obtained by

prominences is simply a measure of partially-coherent reproduction of the incident chromospheric peaks and the actual value of PTPD depends on the coherence ratio λ and on the total opacity in $L\alpha$.

Finally, PRD leads also to higher electron densities inside the slab, simply due to higher excitation of the second level which controls the photoionization by the Balmer continuum.

For a direct comparison with OSO-8 observations (Vial, 1982a) we used the model LP2.

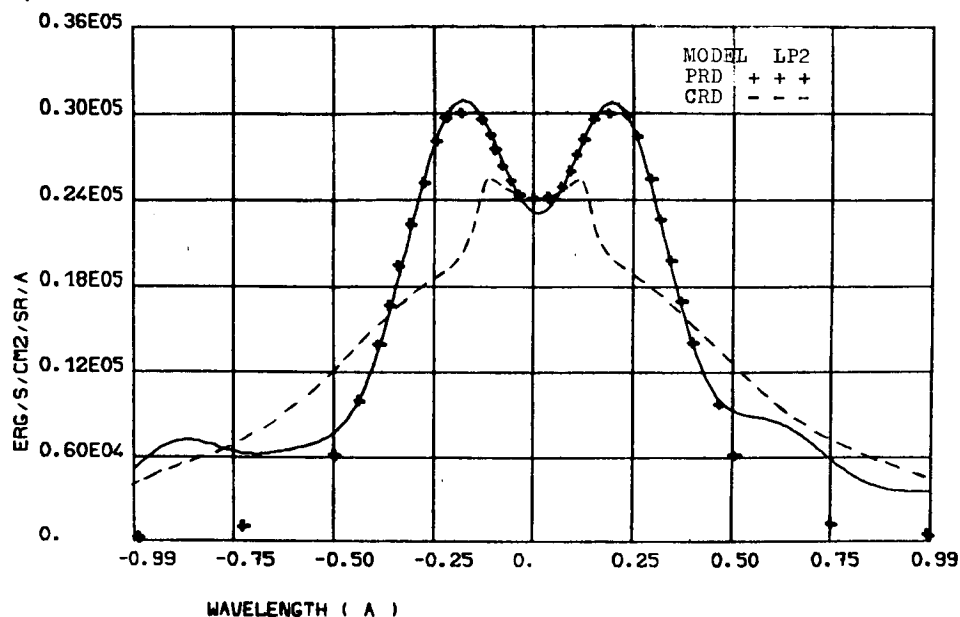


Fig. 3 - Comparison of the observed $L\alpha$ profile (full line) with theoretical PRD and CRD intensities for model LP2 ($\mu = 0.6$). For details and discussion see the text.

In Fig. 3 we display the observed $L\alpha$ profile, together with corresponding theoretical PRD and CRD profiles. PRD profile has been smoothed to account schematically for the finite spectrometer resolution (0.02 Å) and for small line-of-sight velocities of the order of 5 km/s (see Jensen, 1982). While CRD profile is in no case capable of explaining the observed shape, our PRD $L\alpha$ profile leads to a reasonable fit. However, there are certain differences to be discussed. First, the difference in the central dip can be due to either small inaccuracies in the geocoronal-absorption removing, or simply to inappropriate value of the incident radiation used in the computations. Secondly, the observed peaks are somewhat higher than computed. In fact, for thicker models like LP2 we arrived at rather flat peaks and these can be slightly modified when the deconvolution procedure is applied (this is also valid for the flat core). Finally, a wavelike character of the far wings is due to deconvolution so that we can rely on the intensities up to approximately ± 0.5 Å from the line center. As we have found from the computations, the central intensity of $L\alpha$ is determined mainly by the value of the diluted incident radiation and is insensitive to variations of the model parameters. On the other hand, the peak value is somewhat lowered for non-zero v_t (model LP3).

The profile parameters, corresponding to Fig. 3, are summarized in Table 2. We see

that our PRD values reproduce quite well the observations, possibly except for the total intensity corrected for the filling factor (note that the actual observed value of E can be lower with respect to data-reduction effects discussed above). The 2D total intensity is too low even when CRD is used. Note also a satisfactory agreement between $H\alpha$ intensities. Finally, the electron density as obtained for LP2 model ($n_e = 7 \times 10^9 \text{ cm}^{-3}$) is in good agreement with the values recently obtained from polarimetric observations (Bommier, present volume). The geometrical thickness of the prominence is somewhat large - 11 500 km -, but this corresponds to a low gas pressure 0.02 dyn/cm^2 .

	$L\alpha$				$L\beta$			$H\alpha$		
PARAMETERS	LP2 PRD	LP2 CRD	2D CRD	OBS. FPO	LP2 PRD	LP2 CRD	OBS. FPO	LP2 PRD	LP2 CRD	OBS.
FWHM (A)	0.76			0.74	0.26	0.23	0.61			
PTPD (A)	0.37	0.23	0.32	0.37	(no reversal)		0.33			
$I(\text{peak})/I_0$	1.25	1.06	1.3	1.33	(no reversal)		1.85			
$E_1(\times 10^4)$	2.70	3.03	1.61	2.84	0.007	0.005	0.044	7.51	6.76	5.-9.
$E_2(\times 10^4)$				3.55			0.055			
PTPD - peak-to-peak distance - I_0 - central intensity (prominence) E_1 (ergs $\text{s}^{-1} \text{ cm}^{-2} \text{ sr}^{-1}$) - integrated intensity E_2 - as E_1 but corrected for filling factor (see Vial, 1982a)										

Table 2.

Comparison of basic profile parameters of $L\alpha$, $L\beta$ and $H\alpha$. LP2 is the model from Table 1, 2D model corresponds to the computations of Vial (1982b), FPO means "first part of orbit" (see Vial, 1982a). $H\alpha$ intensity was estimated using OSO-8 CaII intensities and the relation between CaII and $H\alpha$ as given by Stellmacher (1979). $L\alpha$ parameters correspond to the profiles in Fig. 3. Theoretical $L\alpha$ profiles for the model LP2 have been corrected for the actual value of the calibration disc-center intensity ($6.5 \times 10^4 \text{ ergs s}^{-1} \text{ cm}^{-2} \text{ sr}^{-1}$), for LP2 we used the values for $\mu = 0.6$.

As we have found during the course of our investigation, $L\beta$ line presents, on the other hand, a complicated and so far unresolved problem. Looking at Table 2, we see immediately that the basic $L\beta$ profile-parameters differ significantly from the observed ones and, moreover, the theoretical integrated intensity is also a factor 5 - 10 lower than the observed value (for both CRD and PRD). This surprising result needs further verifications and more sophisticated calculations are to be done to resolve this discrepancy.

Our knowledge of the $L\beta$ radiation field inside the prominence is also essential for estimating the degree of $H\alpha$ line polarization (from which we can deduce the magnetic-field topology via the Hanle effect -see Bommier, present volume-) and, therefore, PRD-interlocking as well as various multidimensional effects are to be properly accounted for in the future computations.

5. CONCLUSIONS

We have demonstrated the most important effects of PRD in the formation of hydrogen L_α line in quiescent prominences. Except for the well-known lowering of the far wings as compared to CRD, we have found a new PRD feature for L_α prominence line: strong peaks of the incident solar radiation are partly reproduced due to quasi-coherent scattering in the near wings of L_α and, as a consequence, we obtain typical prominence L_α profiles with significant central reversal and PTPD comparable to the solar one. All features we have found are actually observed as our comparison with OSO-8 data shows. However, for L_β line we arrived at a substantial discrepancy between the theoretical and observed intensities. Having estimated the differential PRD effects for L_α , future computations should try to establish the proper interplay between PRD and multidimensional radiation-transport influences on the prominence spectral diagnostics. Our present report should serve as a starting point in developing more sophisticated non-LTE techniques which will be capable of explaining new data from UVSP/SMM or other planned space experiments.

ACKNOWLEDGEMENTS

One of us (P.H.) highly appreciates the possibility to stay at LPSP in 1984, where this work was originated. P.H. and J.C.V. would like to thank NASA for its financial support which enabled them to present this report during the CPP-workshop. All numerical computations were performed using the facilities of the Ondrejov Observatory Computing Center and the Cray-1 computer of the "Centre de calcul Vectoriel pour la Recherche".

REFERENCES

- Auer, L.H., Mihalas, D.: 1970, M.N.R.A.S. 149, 60.
David, K.H.: 1961, Z. für Astrophys. 53, 37.
Gouttebroze, P., Lemaire, P., Vial, J.C., Artzner, G.: 1978, Astrophys. J. 225, 655.
Heasley, J.N., Mihalas, D.: 1976, Astrophys. J. 205, 273.
Heasley, J.N., Milkey, R.W.: 1976, Astrophys. J. 210, 827.
Heasley, J.N., Milkey, R.W.: 1978, Astrophys. J. 221, 677.
Heasley, J.N., Milkey, R.W.: 1983, Astrophys. J. 268, 398.
Heinzel, P.: 1983, Bull. Astron. Inst. Czechosl. 34, 1.
Heinzel, P., Hubeny, I.: 1982, J. Quant. Spectrosc. Radiat. Transfer 27, 1.
Heinzel, P., Vial, J.C.: 1983, Astron. Astrophys. 121, 155.
Hubeny, I.: 1985, Bull. Astron. Inst. Czechosl. 36, 1.
Jensen, E.: 1982, Sol. Phys. 77, 109.
Mihalas, D., Heasley, J.N., Auer, L.H.: 1975, NCAR Technical Note NCAR-TN/STR-104, NCAR, Boulder.
Mihalas, D., Auer, L.H., Mihalas, B.R.: 1978, Astrophys. J. 220, 1001.
Milkey, R.W., Heasley, J.N., Schmahl, E.J., Engvold, O.: 1979, in Physics of Solar Prominences, IAU Coll. 44, Eds. Jensen, E., Maltby, P., Orrall, F., Inst. Theor. Astrophys., Oslo, 53.
Stellmacher, G.: 1979, Sol. Phys. 61, 61.
Vernazza, J.E., Reeves, E.M.: 1978, Astrophys. J. Suppl. 30, 1.
Vial, J.C.: 1982a, Astrophys. J. 253, 330.
Vial, J.C.: 1982b, Astrophys. J. 254, 780.
Yelnik, J.B., Burnett, K., Cooper, J., Ballagh, R.J., Voslamber, D.: 1981, Astrophys. J. 248, 705.
Zelenka, A.: 1976, Astron. Astrophys. 48, 75.

NON-LTE HYDROGEN-LINE FORMATION IN MOVING PROMINENCES

P. Heinzel

Astronomical Institute, 251 65 Ondřejov, Czechoslovakia

B. Rompolt *

High Altitude Observatory, NCAR, Boulder, CO 80307, U.S.A.

ABSTRACT

We investigate the behaviour of hydrogen-line brightness variations, depending on the prominence-velocity changes. By solving the non-LTE problem for hydrogen we determine quantitatively the effect of Doppler brightening and/or Doppler dimming (DBE, DDE) in the lines of Lyman and Balmer series. It is demonstrated that in low-density prominence plasmas, DBE in $H\alpha$ and $H\beta$ lines can reach a factor of three for velocities around 160 km/sec, while the $L\alpha$ line exhibits typical DDE. $L\beta$ brightness variations follow from a combined DBE in the $H\alpha$ and DDE in $L\alpha$ and $L\beta$ itself, providing that all relevant multilevel interlocking processes are taken into account.

INTRODUCTION

In the present paper we investigate the problem of hydrogen emission emergent from prominence structures moving in the corona. In fact, there exists a vast literature concerning the formation of emission lines in quiescent prominences (see the review by Hirayama, 1985 or Heinzel et al., 1986), but the influence of the prominence macroscopic motions on the amount of the emitted line radiation has not been studied yet in greater detail. Considering the hydrogen spectrum, only Rompolt (1980 a, b) has made some calculations of brightness variations in Balmer lines caused by velocity changes, assuming a two-level atom undergoing radiative transitions. Since there exist several observational indications of, at least, $H\alpha$ brightness variations in different moving structures, which can be explained in terms of the so-called Doppler brightening and/or Doppler dimming effect (DBE, DDE) (see Rompolt, 1967; Hyder and Lites, 1970; Labonte, 1979; Kawaguchi et al., 1984), we address this study to a detailed non-LTE treatment of hydrogen-line formation in moving prominences. We try to assess the prominence brightness variations caused by the macroscopic-velocity changes, keeping other prominence parameters fixed for the moment. As a result, we present here the first quantitative estimates of DBE and DDE in hydrogen lines and briefly discuss the influence of various prominence-plasma parameters on such brightness variations.

* On leave from the Wroclaw University Observatory, Poland

NON-LTE RADIATIVE TRANSFER IN A MOVING PROMINENCE

For the purpose of this rather exploratory work we use a simplified one-dimensional geometry where the prominence is represented by a plane-parallel slab of finite thickness and its motion is simply simulated by determining the velocity-dependent boundary conditions. This schematic approach avoids complicated multidimensional solutions, still keeping the basic non-LTE physics of the problem. For a five-level model atom of hydrogen we solve simultaneously the radiative transfer equations in all Lyman transitions and in the H α line (the radiation field in the remaining transitions is fixed by the external solar radiation), together with the equations of statistical equilibrium and particle and charge conservation equations. The corresponding numerical procedure is the same as that applied by Heinzel et al. (1986) for quiescent prominences. As the basic iteration loop we use a linearization scheme similar to that of Mihalas et al. (1975), supplemented by several equivalent-two-level-atom iterations in order to accelerate the convergence. Hydrostatic equilibrium is treated iteratively. We use all hydrogen opacity sources which are important in low-density prominence plasmas; the hydrogen atomic data were compiled from different sources (inelastic collisional rates are computed according to Mihalas et al., 1975).

As a result, we obtain the overall excitation and ionization balance for hydrogen in the moving prominence, depending on the velocity v , height H above the solar surface and on the basic input parameters M , T , p , v_t . M is the total column mass along the line of sight, T is the kinetic temperature of the plasma, p represents the total gas pressure and v_t characterizes the mean microturbulent velocity. To obtain the correct gas density structure, the prominence is assumed to be composed of helium and hydrogen with the abundance ratio equal to 0.1 (a contribution of helium ionization to the total electron density is negligible under typical prominence conditions).

Photospheric and chromospheric line radiation fields incident at the prominence at a given height determine (i) the velocity-dependent radiative rates for all optically-thin lines, and (ii) the velocity-dependent surface boundary conditions for all line transitions treated explicitly (i. e. Lyman lines and H α). Both these quantities have been precomputed for a given grid of velocities using the method described by Heinzel (1983). The incident radiation fields used here are identical to those described in Heinzel et al. (1986) and also the continua are treated in a similar way.

In this paper we use the complete frequency redistribution for all lines, but we cannot rule out possible effects of quasi-coherent scattering in L α and L β line wings on the velocity-dependent level populations (for higher velocities, most of the incident L α and L β radiation is absorbed in the wings).

NUMERICAL RESULTS AND DISCUSSION

From the velocity-dependent level populations we computed the emergent integrated intensities for all lines of interest and for radial velocities in the range of 0 - 240 km/sec. To demonstrate the effect of the prominence motion on the hydrogen-line emission, we define here the relative intensity or brightness $W = E(v)/E(0)$, where E is the velocity-dependent integrated intensity. For the sake of illustration, we have selected one representative isothermal-isobaric model with parameters $H=50000$ km, $M=1.2 \times 10^{-5}$ g/cm², $T=6500$ K, $p=0.1$ dyn/cm², $v_t=0$ km/sec (the geometrical thickness amounts about 650 km).

The resulting electron density n_e generally depends on the velocity, but for velocities up to about 200 km/sec this dependence is very weak and n_e can be regarded as nearly constant - this fact allows us to estimate the importance of various MHD-processes leading to density variations.

The behaviour of W for our schematic model is displayed in Fig. 1 for Lyman and Balmer lines.

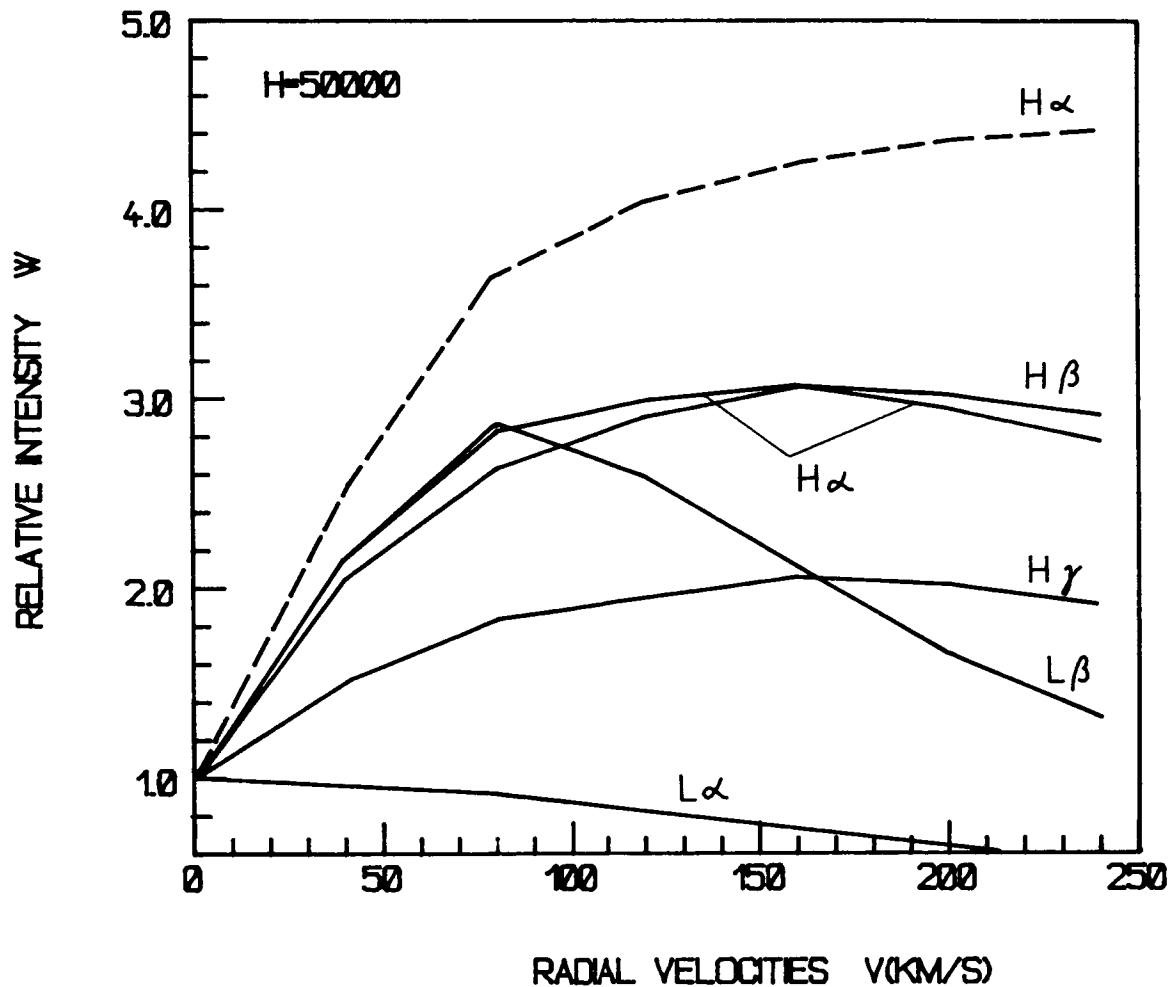


Figure 1

Brightness variations for Lyman and Balmer lines as computed for the model described in the text. Full lines correspond to multilevel non-LTE solution, dashed line corresponds to a two-level model atom without collisions.

Due to a decrease of the second-level population for higher velocities, the $L\alpha$ brightness decreases as demonstrated in Fig. 1 - this decrease represents typical DDE. A more complicated situation occurs for third level, the population of which depends on three factors: DDE in $L\alpha$, a similar effect in $L\beta$ and an important DBE in $H\alpha$ line. The rate of radiative excitation in these lines is roughly proportional to velocity-dependent incident line radiation so that the third-level population inside the prominence body remarkably increases for velocities up to about 160 km/sec (DBE in $H\alpha$ is dominant), and then decreases due to the action of DDE in $L\alpha$ and $L\beta$ itself. Since the third level of the hydrogen atom represents a common upper state for both $L\beta$ and $H\alpha$ lines, the behaviour of the brightness variations in these two lines is similar except for higher velocities, where the optically-thin $H\alpha$ line still exhibits DBE while the surface emission of $L\beta$ is strongly affected by DDE in $L\beta$ itself (see Fig. 1). DBE in $H\alpha$ takes place for velocities up to about 160 km/sec which is in qualitative agreement with the results of Hyder and Lites (1970). A similar behaviour was also found for the $H\beta$ line, while $H\gamma$ exhibits a less pronounced DBE, reaching only a factor of two. Finally, in Fig. 1 we compare our "exact" $H\alpha$ brightness variations with those following from a two-level-atom approximation without collisions (see Rompolt, 1980 a, b). The significant difference between these two curves is the consequence of the multilevel interlocking (including the effect of continua) and the appropriate DDE in $L\alpha$ and $L\beta$ which are not accounted for by the two-level-atom model.

To obtain a more complete picture of the various interdependences, we have also computed some examples using other values of T , v_t and p . An increase of T or v_t generally leads to a prominence brightening, namely for lower velocities. For high velocities, the changes in T or v_t do not affect DBE significantly. Gas pressure p determines the plasma density and, consequently, also the electron density which controls the rate of collisional transitions. As could be expected, for higher n_e we arrived at much less pronounced DBE in Balmer lines since the source function becomes collisionally-dominated. For n_e of the order 10^{13} we observe practically no velocity effects on the line source functions (the model discussed above led to $n_e = 2.43 \times 10^{10} \text{ cm}^{-3}$).

Our non-LTE modelling of a moving prominence can equally be applied to other coronal structures like limb flares, cool coronal loops, various types of prominence ejecta and transient $H\alpha$ - phenomena. If the hydrostatic equilibrium used here is replaced by more realistic MHD-equilibria, the present approach can serve as a basis for further development of adequate spectral diagnostics of the prominence plasma and deeper understanding of the relevant radiation-hydrodynamical processes.

The authors are indebted to NASA for its financial support which enabled them to participate in the CPP-Workshop.

REFERENCES

- Heinzel, P., 1983, "Resonance Scattering of Radiation in Solar Prominences", Bull. Astron. Inst. Czechosl., **34** (1).
- Heinzel, P., Gouttebroze, P., Vial, J. C., 1986, "Partial Redistribution Effects in the Formation of Hydrogen Lines in Quiescent Prominences", this volume.
- Hirayama, T., 1985, "Modern Observations of Solar Prominences", Sol. Phys., **100** (415).
- Hyder, Ch. L., Lites, B., 1970, "H α Doppler Brightening and Lyman- α Doppler Dimming in Moving H α Prominences", Sol. Phys., **14** (147).
- Kawaguchi, I., Nakai, Y., Funakoshi, Y., Kim, K. P., 1984, "Brightening Phenomena in Prominences at the Center of the H α line", Sol. Phys., **91** (87).
- Labonte, B., 1979, "Activity in the Quiet Sun", Sol. Phys., **61** (283).
- Mihalas, D., Heasley, J. N., Auer, L. H., 1975, "A Non-LTE Model Stellar Atmosphere Computer Program", NCAR Technical Note, NCAR-TN/STR-104.
- Rompolt, B., 1967, "The H α Radiation Field in the Solar Corona for Moving Prominences", Acta Astron., **17** (329).
- Rompolt, B., 1980 a, "Doppler Brightening Effect in H α Line for Optically Thin Moving Prominences", Hvar Obs. Bull., **4** (39).
- Rompolt, B., 1980 b, "Doppler Brightening of Active Prominences in Hydrogen Balmer Lines", Hvar Obs. Bull., **4** (49).

VERTICAL MOTIONS IN QUIESCENT PROMINENCES
OBSERVED IN THE He I $\lambda 10830\text{\AA}$ LINE

Oddbjørn Engvold
Institute of Theoretical Astrophysics
University of Oslo
P.O.Box 1029, Blindern
N-0315 Oslo 3, Norway

and

Stephen L. Keil
AFGL
Sacramento Peak Observatory
Sunspot, New Mexico 88349

INTRODUCTION

Movies of quiescent prominences seen in $H\alpha$ show apparent downflow of matter (Dunn, 1960; Menzel and Wolbach, 1960; Engvold, 1976; Anzer 1978). The effect is confirmed by observations of downflows in the Ca II K line from large filaments/prominences (Kubota 1978). Several recent studies show evidence for the opposite case from observations in $H\alpha$, i.e. that there is a predominantly upward directed flow in prominences seen on the disk (Mein, 1977; Martres et al. 1981; Malherbe et al. 1981). The quoted results are slightly ambiguous because the observed Ca II K and $H\alpha$ line shifts can be severely influenced by displacements of the chromospheric component of the line and by the line opacity and source function which generally are not well known. This problem is discussed by Beckers (1962), 1968) and Cram (1975) in connection with measurements of chromospheric velocities.

The implications of systematic vertical motions in and around prominences are important for understanding their formation and existence.

Pikel'ner (1971) proposed a siphon-type model in which hot matter is sucked up along the magnetic field lines into the 'cool' prominence region. Similar types of dynamic models have been investigated by Priest and Smith (1979), Uchida (1980), and Ribes and Unno (1981). Malherbe and Priest (1983) suggest that vertical motion is a result of lateral motion in the footpoints of the supporting magnetic fields. Recent studies by Jensen (1983, 1986) show that prominence matter may be supported by Alfvén-wave dissipation. This support mechanism is a stochastic process which will result in a local re-shuffling rather than a net transfer of prominence matter.

It is difficult to choose between the various dynamic models because the observational picture from H α and the Ca II K line is still rather unsettled. We have therefore undertaken an observational program of prominences on the disk using the $\lambda 10830\text{\AA}$ line of He I. The He I line is weak in the chromosphere but quite strong in prominences (Giovannelli et al. 1972) and Doppler shifts can be interpreted indubitably in terms of line-of-sight motions. Some conclusions from the study are reported here. A more detailed account of the work is given in Engvold and Keil (1986).

OBSERVATIONS

The observations contain two-dimensional spectral scans of a total of 17 different prominences on the solar disk from the period 3-9 May 1981, using the main spectrograph of the solar vacuum telescope at Sacramento Peak. A 100 x 100 CCD camera in the spectral focus covered 100 arcsec along the slit and 6.0\AA in the spectral direction. When properly adjusted the He I $\lambda 10830.330\text{\AA}$ and $\lambda 10829.088\text{\AA}$, the Si I $\lambda 10827.109\text{\AA}$, and the atmospheric (H_2O) $\lambda 10832.109\text{\AA}$ lines were recorded simultaneously. The water vapor line and the solar Si I line were used for calibration of the wavelength scale (cf. Breckinridge and Hall 1973). Each series of scans consists of 60 spectral frames recorded in rapid succession and stored on magnetic tape while the solar image drifted across the entrance slit of the spectrograph. Each series of spectral frames covered $60 \times 99 \text{ arcsec}^2$ area on the Sun. The individual CCD frames were corrected for variable pixel sensitivity and large scale noise pattern, and subsequently used to generate images of continuum intensity, intensity and velocity in the He I and Si I lines. For more details on the observations and image processing the reader is referred to Engvold and Keil (1986).

VERTICAL MOTION IN QUIESCENT PROMINENCES

Figures 1, 2 and 3 show contour plots of three typical cases in our data. The upper frames are He I line center intensity. The darkest parts of the filament correspond to line depression of 18 per cent relative to continuum. The lower frames give the line-of-sight. Dotted contour lines are upward and solid lines to downward motions. No line shift is measured where the He I line is less than 4 percent deep, which is the case in the regular chromosphere.

The following conclusions may be drawn from the data:

1. Blue shifts are much more common than red shifts. In many cases more than 90 per cent of the projected prominence area is associated with blue shifts.
2. The darkest prominence regions show the largest blue shift ($v < 3 \text{ km s}^{-1}$)
3. Red shifts are most commonly seen at prominence edges.
4. The general pattern of prominence velocity persists for several hours. On the scale of about 10 arcsec and less changes are detectable in the course of 2-5 minutes.

CONCLUDING REMARKS

The observed predominance of the blue shifts is largely in agreement with earlier results from H α (cf. Martres et al. 1981).

It cannot, however, be concluded definitely that the observed shift really represents a net flow of matter. The situation could possibly be analogous to that of the solar transition region where lines such as C IV $\lambda 1548\text{\AA}$ seem to indicate a net inflow, which can hardly be true, at velocities $> 4 \text{ km s}^{-1}$ in the quiet Sun (Athay et al. 1983; Gurman and Athay 1983). If the typical structure element of the prominence is sub-resolution, i.e. 2-3 arcsec or worse, as in the present case, an apparent net shift could result if the ascending and the descending elements have different temperature and/or pressure. Different lines could then indicate different flow velocities and even opposite directions. The stochastic support mechanism of Jensen (1986) could provide such conditions in prominences. The

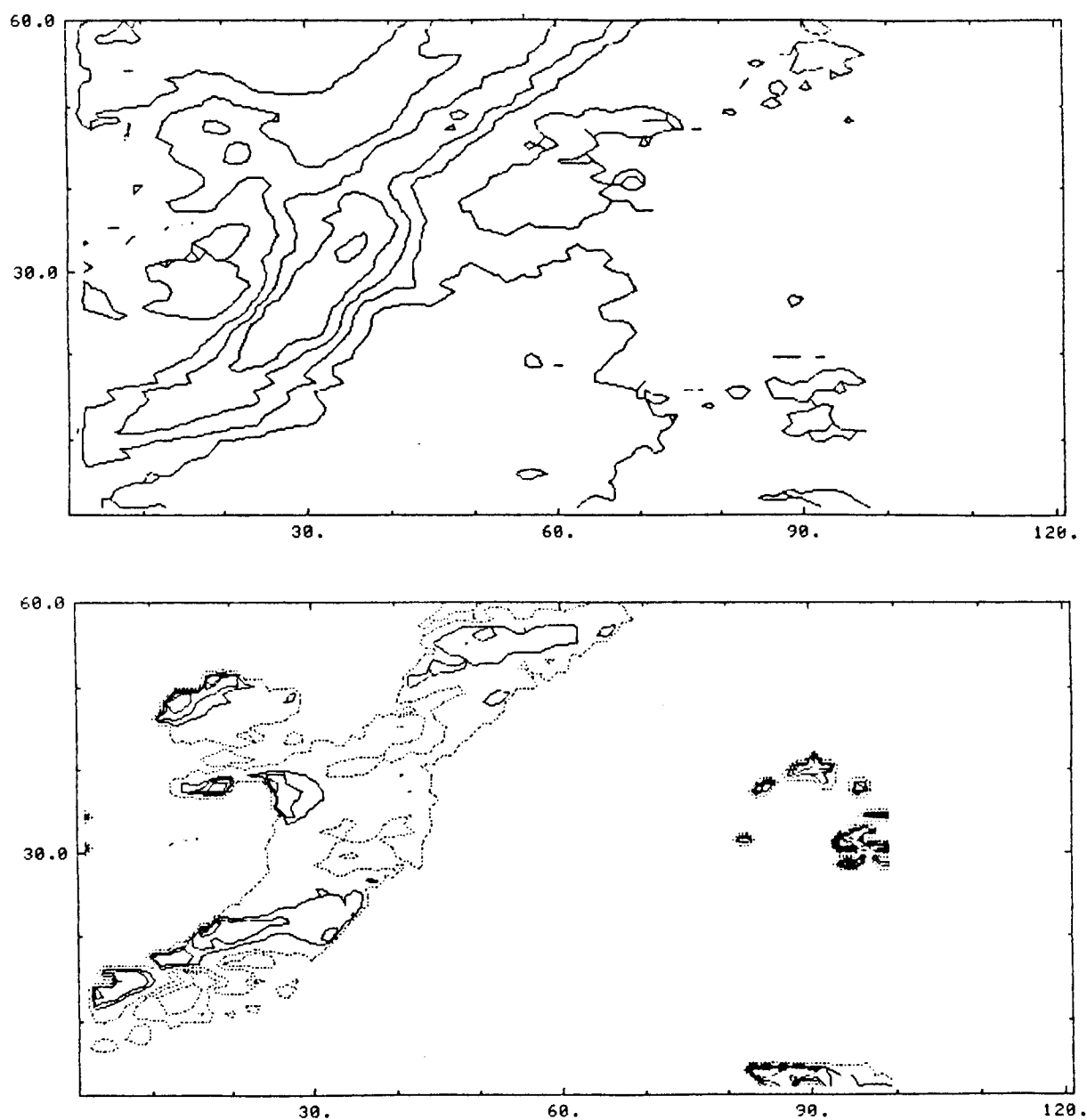


Figure 1. Contour plots of large quiescent prominence at S20 E24 observed May 4 1981 at 14:51 UT. The position of the prominence is seen in the image of He I central line intensity (upper frame). The lower frame shows the line shift. Dotted contour lines are blue and solid lines are red shift ($\Delta v = 0.5 \text{ km s}^{-1}$). The numbers on the axes are in arcseconds.

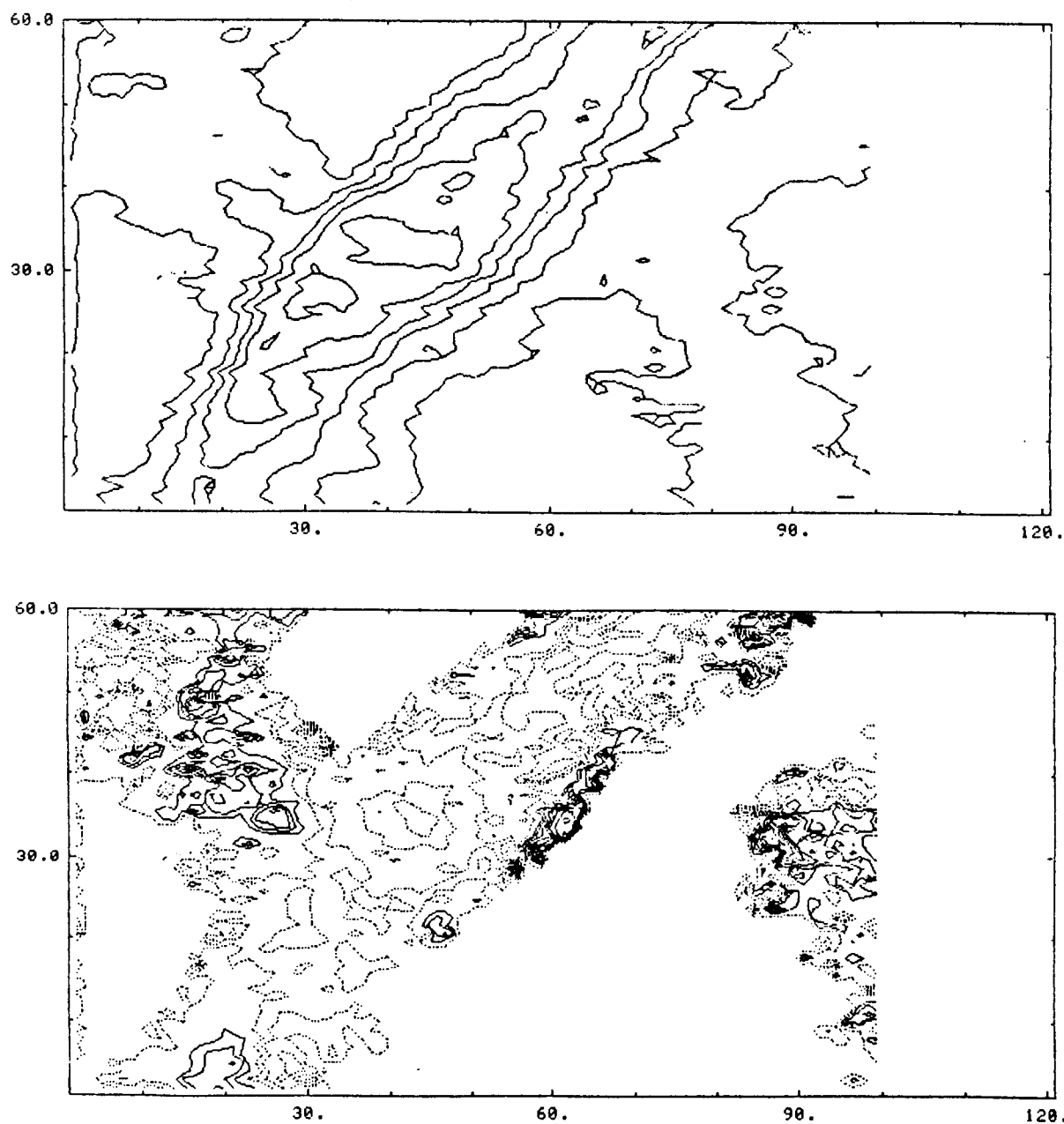


Figure 2. Same prominence as in Figure 1 observed at S20 W47 on May 9 1981 at 15:17 UT.

apparently conflicting results from the Ca II K and H α and He I λ 10830 could possibly be explained as an effect of spatially unresolved moving structures. More detailed and simultaneous observations in many lines are needed to settle the question.

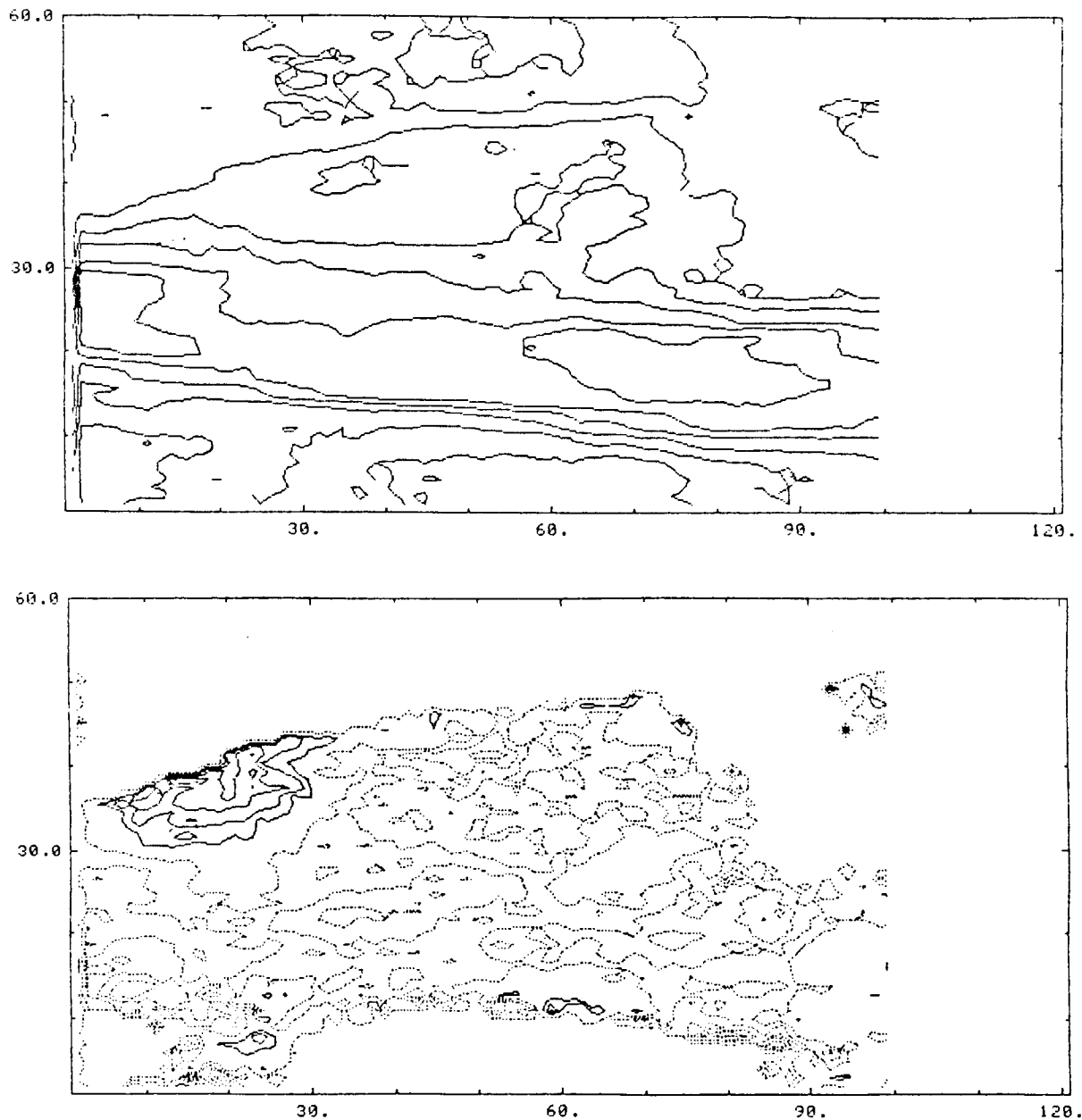


Figure 3. Contour plots of quiescent prominence at position N05 W22 observed May 9 1981 16:37 UT.

Acknowledgements

We are grateful to Phil Wiborg, Horst Mauter and Richard Mann for their enthusiastic support with the observations.

References

- Anzer, U.: 1978, in "Physics of solar prominence", IAU Colloq. 44,
Eds.: E.Jensen, P.Maltby, F.Q.Orrall, p. 322.
- Athay, R.G., Gurman, J.B., Henze, W., and Shine, R.A.: 1983,
Astrophys. J. 265, 219.
- Beckers, J.M.: 1962, Austr. J. Phys. 15, 327.
- Beckers, J.M.: 1968, Solar Phys. 3, 367.
- Breckinridge, J.B. and Hall, D.N.B.: 1973, Solar Phys. 28, 15.
- Cram, L.E.: 1975, Solar Phys. 42, 53.
- Dunn, R.B.: 1960, Ph.D. Thesis, Harvard University.
- Engvold, O.: 1976, Solar Phys. 49, 283.
- Engvold, O. and Keil, S.L.: 1986, (In preparation).
- Giovanelli, R.G., Hall, D.N.B., and Harvey, J.W.: 1972, Solar Phys.
22, 53.
- Gurman, J.B. and Athay, R.G.: 1983, Astrophys. J. 273, 374.
- Jensen, E.: 1983, Solar Phys. 89, 275.
- Jensen, E.: 1986, This proceedings.
- Kubota, J.: 1980, in Proceedings of "The Japan-France Seminar on
Solar Physics", Eds.: F. Moriyama and J.C. Henoux, p. 178.
- Malherbe, J.M., Schmieder, B., Ribes, B., Mein, P.: 1983, Astron.
Astrophys. 119, 197.
- Malherbe, J.M. and Priest, E.: 1983, Astron. Astrophys. 123, 80.
- Martres, M.-J., Mein, P., Schmieder, B., and Soru-Escaut, I.: 1981,
Solar Phys. 69, 301.
- Mein, P.: 1977, Solar Phys. 54, 45.
- Menzel, D.H., and Wolbach, J.G.: 1960, Sky and Tel. 20, 252 and
330.
- Pikel'ner, S.B.: 1971, Solar Phys. 17, 44.
- Priest, E. and Smith, E.A.: 1979, Solar Phys. 64, 217.
- Ribes, E. and Unno, W.: 1981, Astron. Astrophys. 91, 129.
- Schmieder, B., Malherbe, J.M., Poland, A.I., and Simon, G.: 1985,
Astron. Astrophys. 153, 64.
- Uchida, Y.: 1980, in Proceedings of "The Japan-France Seminar on
Solar Physics" Eds.: F.Moriyama and J.C. Henoux, p. 169.

CONSTRAINTS ON FILAMENT MODELS DEDUCED FROM DYNAMICAL ANALYSIS

G. Simon, B. Schmieder, P. Demoulin, and J.M. Malherbe
Observatoire de Paris, Section de Meudon

DASOP, F-92195 Meudon Cedex, France

and

A.I. Poland

Laboratory for Astronomy and Solar Physics,
NASA Goddard Space Flight Center, Greenbelt, Md. USA

I. Introduction

The problems of prominence structure, support, and stability are of fundamental importance in understanding solar plasmas. The original theoretical work in this area was done by Kippenhahn and Schluter (1957), who theorized that prominence material was supported by a magnetic loop with a dip in the middle. A more recent model by Kuperus and Raadu (1973) envisions the prominence as being supported by an X type magnetic configuration with material condensing from coronal material. While there are several variations on these theories they represent the two basic concepts for prominences and both are treated basically as static, although the Kuperus and Raadu model could be extended to a dynamic concept.

The dynamic studies of prominences have been largely observational. Both upflows and downflows have been reported by various authors (see for example: Dunn, 1960; Engvold, 1976; Kubota, 1980; Martres et al., 1981; Malherbe et al., 1981 and 1983; Schmieder et al., 1985; Engvold et al., 1985; and Simon et al., 1986).

We present here the conclusions deduced from simultaneous observations obtained with the Ultra-Violet Spectrometer and Polarimeter (UVSP) on the Solar Maximum Mission satellite, and the Multichannel Subtractive Double Pass (MSDP) spectrographs at Meudon and Pic du Midi observatories. The observations were obtained in 1980 and 1984. All instruments have almost the same field of view and provide intensity and velocity maps at two temperatures (approximately 1×10^5 K for CIV with the UVSP, and 1×10^4 K for H α with the MSDP). The resolution is ~ 0.5 to $1.5''$ for H α and $3''$ for CIV. The high resolution and simultaneity of the two types of observations allow us to more accurately describe the flows in prominences as functions of temperature and position. The results put some constraints on the models and show that dynamical aspects must be taken into account.

II. Active Region Filaments

An active region filament, located in NOAA region 2697, was observed continuously on September 29 and 30, 1980 (see Schmieder et al., 1985). The filament was located near disk center appeared to consist of three extended, low lying loops limited by the footpoints marked A, B, C, and D in figure 1a. The filament lies along a neutral line of photospheric magnetic field, with the "footpoints" anchored in regions of enhanced positive magnetic field. The Dopplergrams obtained in H α and CIV (figure 1b and 1d) show that material in the filament between the "footpoints" is blueshifted while at the "footpoints" material is redshifted.

The measured values of velocity are presented in tables 1 and 2. We note that during seven hours of observation on September 29, a particularly high steady flow was observed at "footpoint" A. These types of motions seem to be

fairly typical of other motions observed in active region filaments.

Table 1 - Redshifts at the Footpoints (km/s)

Point	A	B	C	D
H α	-9 to -12	-1 to -3	-1 to -6	-3 to -6
CIV	-2 to -10	-2 to -8	0 to -2	-3 to -6

Table 2 - Blueshifts between the Footpoints (km/s)

	A-B	B-C	C-D
H α	2	1.5 to 3	0 to 2
CIV	5 to 10	5 to 10	10 to 25

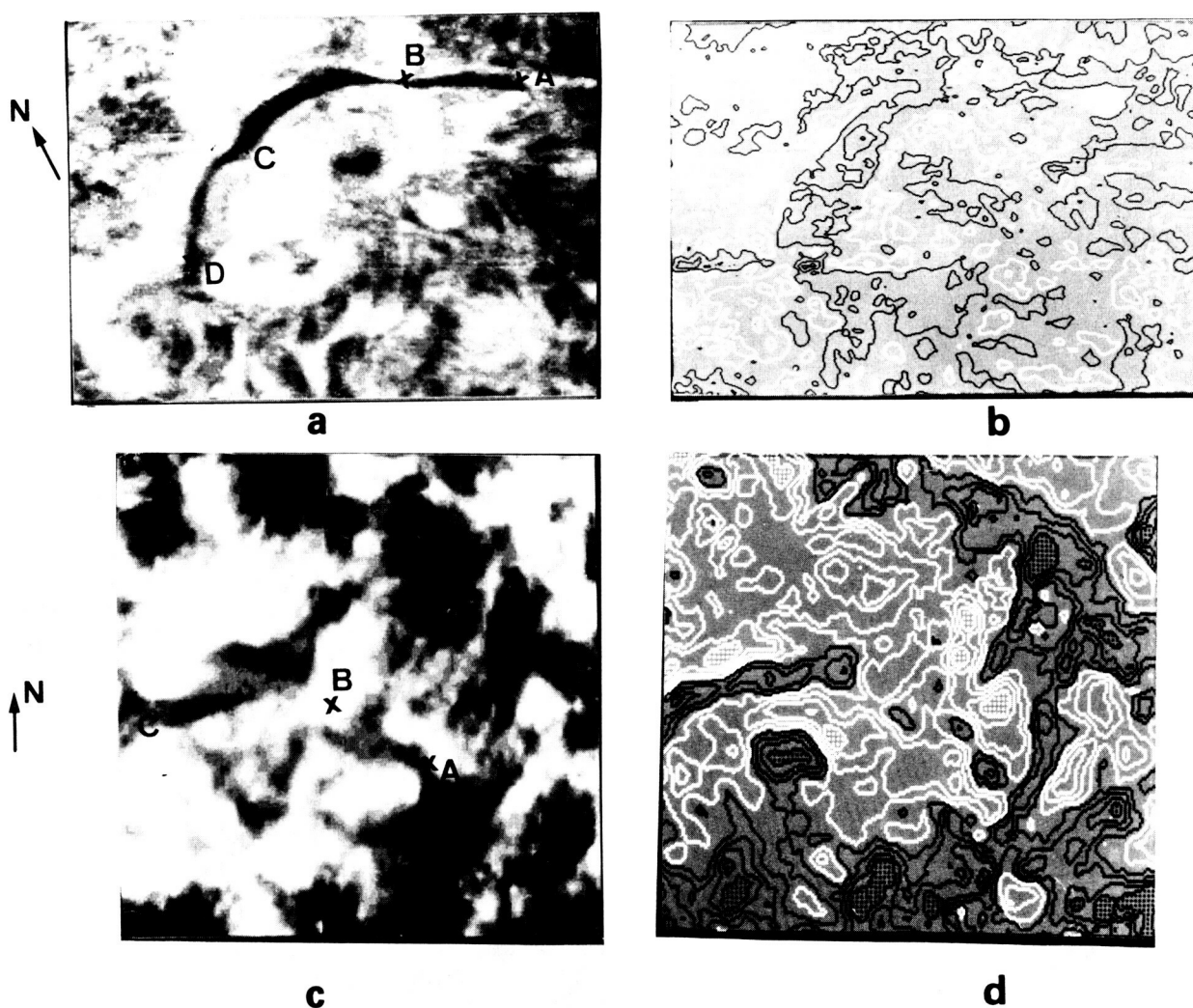


Figure 1. Intensity maps in H α (a) and in CIV(c) lines, Velocity maps in H α (b) and in CIV(d) of an active region filament (white contours correspond to red shifts)

ORIGINAL PAGE IS
OF POOR QUALITY

ORIGINAL PAGE IS
OF POOR QUALITY

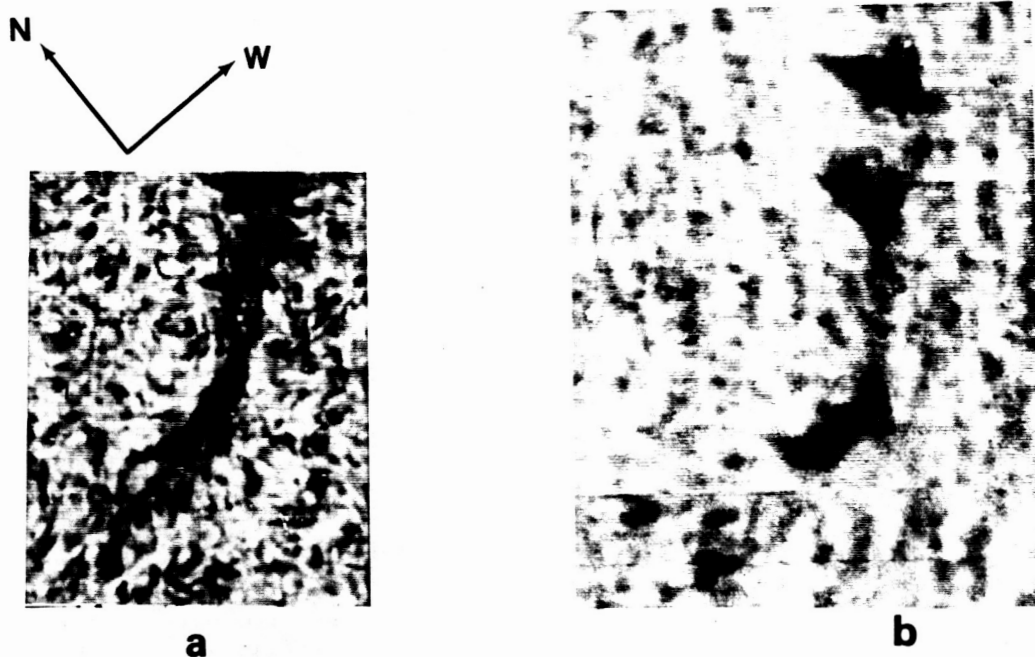


Figure 2: $H\alpha$ images of a quiescent filament on October 15 (a),
and October 17, 1984 (b).

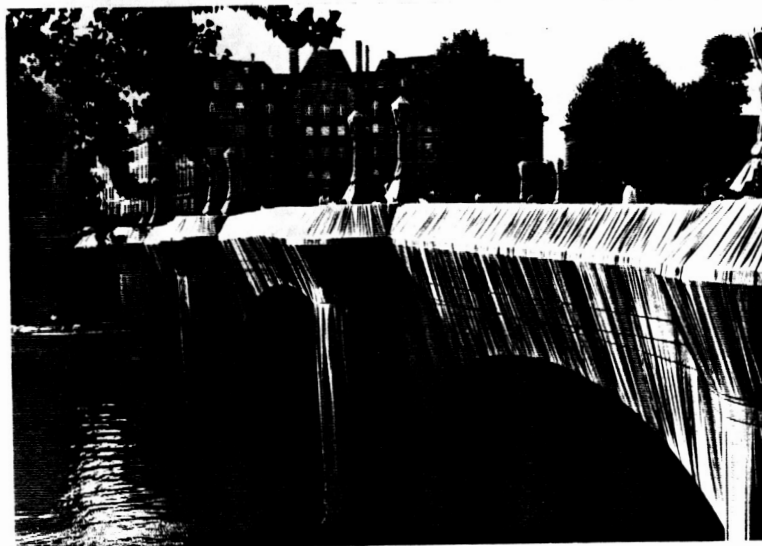


Figure 3: The Pont Neuf in Paris, wrapped by Christo in June, 1985.

III. Quiescent Filament

Similar intensity and velocity measurements were made on a quiescent filament from October 15 through October 18, 1984. The objective of the study was to determine the three dimensional nature of the flows in H α and CIV using the center-to-limb perspective effects.

Observations in H α on October 17 (figure 2b) and later show a classical quiescent filament structure with footpoints connected by a large arch. This structure has an appearance similar to the Pont Neuf wrapped by Christo (figure 3). The fine structure of the filament could be seen with the very good seeing available at Pic du Midi on October 15, 1984. This revealed that the large loops were actually composed of many small scale loops with typical radii of 1000km. These small scale loops seemed to be arranged in a cluster at the footpoints, and somewhat better aligned between them.

Velocity measurements showed that there was no coherent velocity pattern along the filament. The velocities in H α ranged from 2 to 5km/s on October 15 and were smaller on the other days. However, the reduced velocities are most likely due to the smearing effect from bad seeing. The comparison of H α and CIV velocities was also inconclusive.

A statistical study of the velocities in the field of view in and near the filament gives an idea of the structure of the velocity. The standard deviations of the velocities in the filament are compared to the whole field of view (2'x2') as functions of time. These are presented in figure 4 for several different satellite orbits over several days. Near disk center the values are greater in the filament than in the mean transition region around it, while the opposite situation occurs near the limb (see figure 5), although both values decrease. Measurements of the Doppler broadening of the line show the same effect, which indicates that the large scale (>3") and the small scale (<3") velocity structure have the same behavior. From these measurements we deduce that the vertical velocities are greater than the horizontal ones by a factor of 3 in the filament and 2.5 outside (Simon et al., 1986).

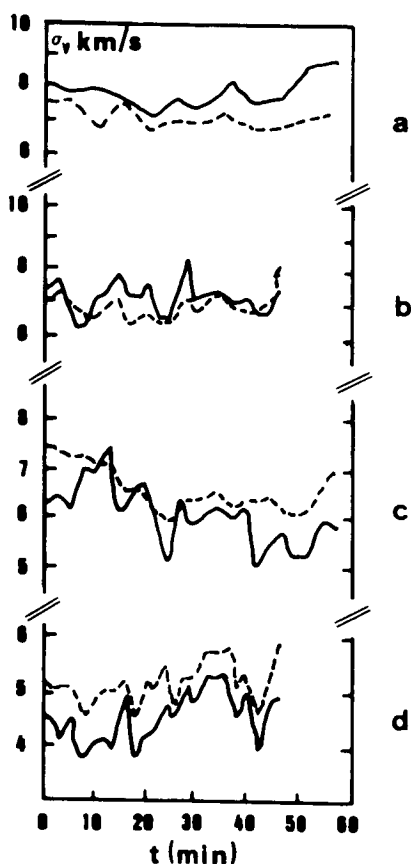


Figure 4. Velocity standard deviation calculated for each frame during the SMM orbit, on October 15, 16, 17, and 18, 1984 (resp. a,b,c, and d). solid lines are for the filament area data and the dashed ones for the 2'x2' area dat.

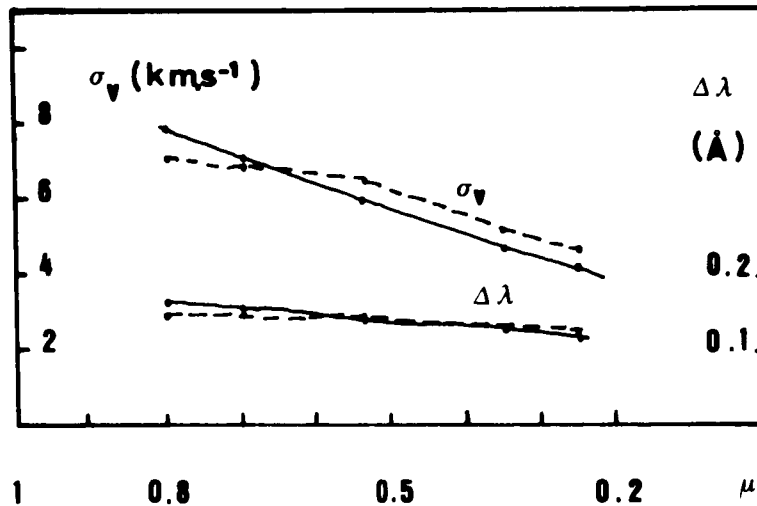


Figure 5. Variation of the velocity standard deviations (σ_v) and of the Doppler linewidth ($\Delta\lambda$) of the CIV line versus μ .

IV. Conclusion

The observations of the active region filament pointed out a reasonable model for this type of prominence. The downward velocity at the footpoints with the upward velocity between suggests a model with a long magnetic flux rope with material slowly draining out at the footpoints. As the total mass in the loop decreases it allows the central part to rise. The problem with this model is that the small pressure scale height should make the prominence drain much more rapidly than is observed.

The quiescent filament observations do not seem to provide any insight into the validity of either the Kippenhahn-Schluter or Kuperus-Raadu models for prominences. The observations seem to indicate that there are no really significant flows, and the structure consists of many small scale loops. Time observations seem to indicate that dynamic models may be more appropriate for describing prominences. Although a dynamic model has been presented by Poland and Mariska (1986), the time scales indicated by the calculations seem to be too long for the observations.

References

- Dunn, R.B., 1960, Thesis Harvard University AFCRL 65-398.
- Engvold, O., 1976, Solar Phys. 49, 283.
- Engvold, O., Tandberg-Hanssen, E., and Reichmann, E., 1985, Solar Phys. 96, 36.
- Kippenhahn, R., and Schluter, A., 1957, Z. Astrophys. 43, 36.
- Kubota, O., 1980, Proceedings of the Japan-France Seminar on Solar Physics, Moriyama and Henoux Ed., 178
- Malherbe, J.M., Schmieder, B., and Mein, P., 1981, Astron. Astrophys. 102,

- 124.
- Malherbe, J.M., Schmieder, B., Ribes, E. and Mein, P., 1983, *Astron Astrophys.* 119, 197.
- Martres, M.J., Mein, P., Schmieder, B., and Soru-Escout, I., 1981, *Solar Phys.* 69, 301.
- Poland, A.I., and Mariska, J.T., 1986, *Solar Phys.* (in press).
- Raadu, M., and Kuperus, M., 1973, *Solar Phys.* 28, 77.
- Schmieder, B., Malherbe, J.M., Poland, A.I., and Simon, G., 1985, *Astron. Astrophys.* 153, 64.
- Simon, G., Schmieder, B., Demoulin, P., and Poland, A.I., 1986, *Astron. Astrophys.* (in press).

C IV DOPPLER SHIFTS OBSERVED
IN ACTIVE REGION FILAMENTS

J.A. Klimchuk*
E.O. Hulburt Center for Space Research
Naval Research Laboratory
Washington, DC 20375-5000

*NRC-NRL Cooperative Research Associate

ABSTRACT

The Doppler shift properties of 21 active region filaments have been studied using C IV Dopplergram data. Most are associated with corridors of weak magnetic field that separate opposite polarity strong fields seen in photospheric magnetograms. A majority of the filaments are relatively blue shifted, although several lie very close to the dividing lines between relative blue and red shift. Only one filament in our sample is clearly red shifted. A new calibration procedure for Dopplergrams indicates that sizable zero point offsets are often required. The center-to-limb behavior of the resulting absolute Doppler shifts suggests that filament flows are usually quite small (< 3 km/s). It is possible that they vanish.

INTRODUCTION

In recent years there have been several studies of the dynamics of solar filaments observed in EUV emissions (e.g., Orrall *et al.* 1983, Schmieder *et al.* 1984, 1985, Engvold *et al.* 1985, Athay *et al.* 1986). The Kippenhahn-Schluter theory of prominence support suggests that upflows should be present, while the Kuperus-Raadu theory suggests downflows (Schmieder *et al.* 1984). A major goal, therefore, has been to test these theories and to otherwise guide the theoretical efforts.

An unambiguous description of filament dynamics is, unfortunately, still lacking. One difficulty is the considerable variety in the observational results. Both red and blue shifts have been reported, and it is not yet clear what, if any, Doppler shift properties are typical. A second, more fundamental difficulty is that all of the Doppler shifts measured to date have been relative to an assumed and somewhat arbitrary zero point. Without knowing the absolute Doppler shifts it is impossible to determine either the directions or the magnitudes of the flows.

In this contribution we add to the data base on relative Doppler shifts by presenting new results for 21 active region filaments. The relationship of these filaments to the photospheric magnetic field is discussed. We then describe a method of calibrating the Dopplergrams, and thereby obtain estimates of the absolute Doppler shifts. This allows us to infer some simple properties of the flows.

The reader is reminded that active region filaments may be substantially different from quiescent filaments and prominences discussed elsewhere in these proceedings. Active region filaments are well defined, low-lying features, whereas quiescent prominences are often diffuse and can extend to great heights above the solar surface. It is not obvious that the two should have similar flow properties.

OBSERVATIONS

The data used in this study consist of C IV (1548) Dopplergrams from the Ultraviolet Spectrometer and Polarimeter on SMM, photospheric magnetograms from Kitt Peak National Observatory, and H α filtergrams from Big Bear Solar Observatory. Typical examples can be found in Figure 1. Frame (a) is a 4' x 4' Dopplergram with a pixel resolution of 3". As described by Simon *et al.* (1982), it is derived from intensities measured simultaneously in the red and blue halves of the line. Doppler shifts are inferred from these intensities by assuming a shape and a width for the profile. In this grey scale display light shades correspond to relative red shifts and dark shades correspond to relative blue shifts. The rms value is near 8 km/s, which is about average for Dopplergrams that contain active regions. Individual Doppler shifts are only accurate to a few kilometers-per-second, however, due to unknown variations in the profile.

The Dopplergram in frame (a) has been normalized in the traditional manner whereby the average Doppler shift vanishes across the raster. In frame (b) we present the same data, but with a much more realistic calibration. The Doppler shifts shown here are believed to be the true, absolute Doppler shifts of C IV. A discussion of the calibration procedure is postponed until later.

The middle row of Figure 1 contains two photospheric magnetograms having the same field-of-view as the Dopplergrams. On the left is a ± 100 Gauss filled in contour plot, and on the right is a continuous plot with a ± 100 Gauss dynamic range. Light and dark shades now correspond to positive and negative magnetic fields, respectively. The grey areas of the contour plot contain weak fields that are mostly less than 20 Gauss in magnitude. Recall that only the line-of-sight component of the field is measured by the magnetograph. In this case it corresponds approximately to the vertical component, since the active region is not far from disk center.

Completing the figure at the bottom is an on-band H α filtergram to the left and an Fe I (8688) "wing spectroheliogram" to the right. The latter was obtained by summing, instead of differencing, the left and right circular polarization signals from Kitt Peak. It is useful for identifying sunspots, which show up as dark areas. All of the observations in this figure were made within a period of three hours.

The images of Figure 1 have been carefully coaligned to an accuracy of about 5". Doppler zero lines (DZLs), which separate areas of relative red and blue shift in uncalibrated Dopplergrams, have been marked in frame (a) and transferred to the other frames as a spatial reference. The transfer was made only after the DZLs were first corrected for distortions caused by solar rotation during the time lapse between observations. In this instance the distortions are minimal, but in other cases they can be important. A detailed description of the correction and alignment procedures can be found in Klimchuk (1985). We simply state here that the alignments do not depend solely on the SMM spacecraft pointing coordinates, which are uncertain by at least 12".

RELATIVE DOPPLER SHIFTS

Figure 1 reveals some rather striking spatial correlations between features seen in the different images. With the exception of sunspots, regions of strong magnetic field tend to be bright in H α and red shifted in C IV. Areas of weak field, on the

AR 2418

7 MAY 1980

0 47

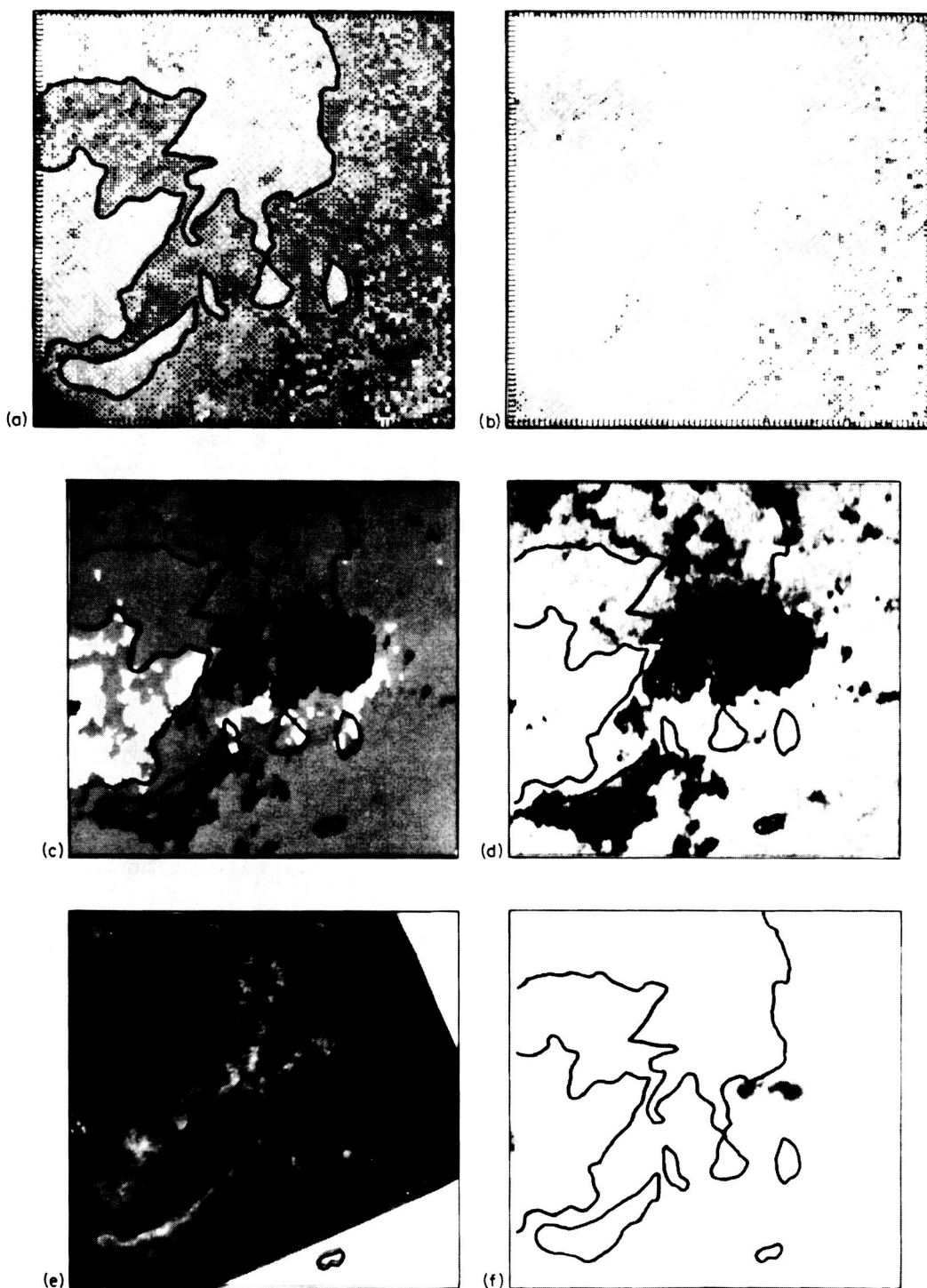


Figure 1. Six different images of Active Region #2418 observed on 7 May 1980: (a) C IV Dopplergram (uncalibrated), (b) calibrated C IV Dopplergram, (c) ± 100 Gauss contour plot, (d) continuous magnetogram plot, (e) H_{α} filtergram, (f) Fe I wing spectroheliogram. See text for details.

Table 1 Relative CIV Doppler Shifts of Active Region Filaments (number of occurrences)				
	Blue	Red	DZL	Mixed
Disk*	11	0	3	1
Limb*	2	1	3	0
Total	13	1	6	1

* $\rho < 0.5$ for disk cases, $\rho > 0.7$ for limb cases.

other hand, are dark and mostly blue shifted. Notice the narrow yet distinct corridor of weak field that separates the opposite polarity strong fields of the active region. It corresponds closely with a band of blue shift, even down to some of the smaller details. Lying within this corridor, extending all the way from the lower left corner to near the center of the raster, is a long and thin active region filament.

These spatial relationships are not unique to this particular active region. In fact, they are common to a great majority of the 37 active regions we have examined. Most of the active region filaments we identified are associated with corridors of weak fields similar to the one shown here. Some occur in the middle of the corridor, and others lie near the boundary. Only rarely, however, is a filament seen to stray far into a region of strong field.

It is important to stress that corridors have a finite width. Because the measured fields are so weak, it is often not possible to precisely locate the neutral line. Furthermore, the position of the neutral line changes with the angle of observation in a manner that is consistent with horizontal fields in the upper photosphere (Klimchuk 1985). The commonly held notion that filaments are situated along neutral lines therefore has ambiguous meaning.

Since corridors are mostly blue shifted, so too are a majority of active region filaments. Many filaments are completely surrounded by blue shifts, while others, especially those that lie near a boundary, appear to coincide closely with DZLs - they have blue shifts on one side and red shifts on the other. Table 1 lists the relative Doppler shift properties of the 21 filaments comprising our study. Roughly two-thirds are clearly blue shifted, as indicated in the bottom row. A smaller number coincide with DZLs (to within about 5"), and only one is unambiguously red shifted. The filament listed as "mixed" passes through both a large area of blue shift and a large area of red shift. Although each of the filaments is assigned to a single category, local deviations in the Doppler shift may be present. Schmieder *et al.* (1985) have discussed a filament with a blue shifted body and red shifted "feet", for example.

The results of Table 1 are in good agreement with the blue shifts reported by Orrall *et al.* (1983) and Schmieder *et al.* (1984, 1985). They seem to differ, however, with the findings of Engvold *et al.* (1985), who identified just as many active region filaments with red shifts as with blue shifts (there are three of each kind, with two additional filaments that coincide with DZLs and one that is mixed). These results must be treated with some caution, however, as uncertain spacecraft pointing coordinates were used to coalign most of the Dopplergram/filtergram image pairs. A majority of the filaments examined by Athay *et al.* (1986) are reported to be associated with DZLs. Since those authors used relatively relaxed association criteria, it is likely that some cases would be classified as blue or red shifted in our analysis.

The first two rows of Table 1 give separate results for two subgroups of the 21 filaments - disk filaments, observed within $0.5 R_{\odot}$ of sun center, and limb filaments, observed within $0.3 R_{\odot}$ of the limb. Doppler shifts are most sensitive to vertical motions in the first group, but to horizontal motions in the second. Furthermore, limb observations are susceptible to projection effects when the C IV and H α emissions do not originate at exactly the same height in the atmosphere. We see that the results are not obviously different for the two groups. The ratio of DZL to blue shift cases is higher near the limb, but the statistics are too small to know whether this is significant.

ABSOLUTE DOPPLER SHIFTS

To begin to really understand the flows in filaments it is necessary to first put the Doppler shift measurements on an absolute scale. This is a non-trivial task, since the UVSP instrument, like others of its kind, does not have an internal wavelength calibration. We have therefore attempted to calibrate the data after the fact using a procedure that is now described.

A limited number of "absolute" Doppler shift measurements have already been made in both active and quiet regions on the sun. From data collected by instruments such as the NRL slit spectrograph on Skylab, the CU spectrometer on OSO-8, the HRTS rocket experiment, and UVSP, a variety of authors have determined Doppler shifts of C IV (or similar lines) relative to nearby lines formed in the lower chromosphere (active regions: Feldman *et al.* 1982, Dere 1982, Brueckner 1981; quiet regions: Roussel-Dupre and Shine 1982, Dere *et al.* 1984, Doschek *et al.* 1976, Brueckner *et al.* 1978, Shine 1985). It is generally assumed that the lower chromosphere is a good zero point reference, since densities are very large there and velocities must be correspondingly small to maintain a reasonable mass flux.

On the basis of these results we conclude that low spatial resolution observations of the quiet sun should, on average, yield Doppler shifts that are represented by an 8 km/s vertical downflow. Low spatial resolution observations of active regions should yield average red shifts ranging from 15 km/s at disk center to 10 km/s near the limb (which is not consistent with vertical flow). We have therefore calibrated our Dopplergrams by artificially degrading their resolution and forcing them to agree with the expected values. Since the quiet sun values are believed to be more reliable, we place most of the emphasis on those areas.

For Dopplergram rasters that include part of the limb, an independent calibration can be used as a check. Under the assumption that horizontal motions average to zero, we force the average Doppler shift at the limb to vanish. Vertical motions are normal to the line-of-sight at the limb and therefore do not contribute to the

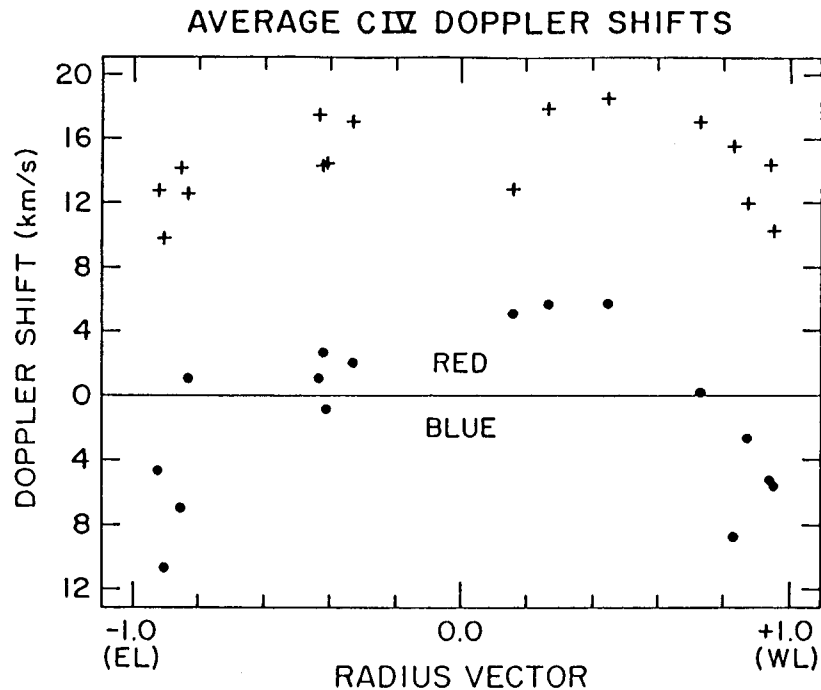


Figure 2. Absolute C IV Doppler shifts averaged over the weak field corridors (dots) and strong field plages (crosses) of 12 active regions. Four regions were observed twice. The points are plotted as a function of radius vector, or fractional distance to the limb from sun center. The east and west limbs are at -1.0 and $+1.0$, respectively. Corridor values are representative of the Doppler shifts in and around a majority of active region filaments. Their uncertainties are roughly ± 8 km/s.

Doppler shift there. The calibrations obtained in this way are able to confirm those obtained by the previous method.

Calibrated Dopplergrams are offset to the red by typically 4-11 km/s relative to their uncalibrated counterparts. This results in a large excess of absolute red shifts, as is clearly evident in frame (b) of Figure 1. The blue shifts that do remain are mostly very small in magnitude. Notice, in particular, how the Doppler shifts approximately vanish in the weak field corridor, where the filament is located.

Average Doppler shifts have been determined for the weak field corridors in several other active regions. They are plotted as dots in Figure 2 as a function of the radius vector of the observation. (Crosses indicate the average Doppler shifts in strong field regions and do not concern us here.) Not all of the corridors of Figure 2 contain filaments, but the observed Doppler shifts do not seem to depend on whether a filament is present. The values are thus representative of filament Doppler shifts.

An obvious trend in Figure 2 is for the Doppler shifts to be blue near both of the limbs and red near the center of the disk. This is difficult to understand in terms of simple, resolved flows. The symmetry about central meridian suggests that the motions are vertical, but vertical motions would produce Doppler shifts with a constant sign, contrary to the result. Perhaps a more involved interpretation is necessary. Before resorting to this, however, we note that the uncertainties in the plotted points are perhaps as large as ± 8 km/s. Given this, we see that the data is consistent with simple flows of very small magnitude ($\lesssim 3$ km/s). No other interpretation is obvious, even allowing for the sizable error bars. We conclude, therefore, that high temperature mass motions are probably minimal in a majority of active region filaments. Their directions cannot be determined at this time.

This research was conducted while the author was a graduate assistant at the High Altitude Observatory of the National Center for Atmospheric Research. NCAR is sponsored by the National Science Foundation.

REFERENCES

- Athay, R.G., J.A. Klimchuk, H.P. Jones, and H. Zirin, 1986, "Magnetic Shear IV. Hale Regions 16740, 16815, 16850," Ap. J., 303 (884).
- Brueckner, G.E., J.-D.F. Bartoe, and M.E. VanHoosier, 1978, "High Spatial Resolution Observations of the Solar EUV Spectrum," Proceedings of the OSO-8 Workshop, November 7-10, 1977, ed. E. Hansen and S. Schaffner, Lab. for Atmos. and Space Physics, Boulder (380).
- Brueckner, G.E., 1981, "The Dynamics of Active Regions," Solar Active Regions, ed. F.Q. Orrall, Colorado Associated Univ. Press, Boulder (113).
- Dere, K.P., 1982, "Extreme Ultraviolet Spectra of Solar Active Regions and Their Analysis," Solar Phys., 77 (77).
- Dere, K.P., J.-D.F. Bartoe, and G.E. Brueckner, 1984, "High Resolution Telescope and Spectrograph Observations of the Quiet Solar Chromosphere and Transition Zone," Ap. J., 281 (870).
- Doschek, G.A., U. Feldman, and J.D. Bohlin, 1976, "Doppler Wavelength Shifts of Transition Zone Lines Measured in Skylab Solar Spectra," Ap. J., 205 (L177).
- Engvold, O., E. Tandberg-Hanssen, and E. Reichmann, 1985, "Evidence for Systematic Flows in the Transition Region Around Prominences," Solar Phys., 96 (35).
- Feldman, U., L. Cohen, and G.A. Doschek, 1982, "Doppler Wavelength Shifts of Ultraviolet Spectral Lines in Solar Active Regions," Ap. J., 255 (325).
- Klimchuk, J.A., 1985, "Large-Scale Structure and Dynamics of Solar Active Regions Observed in the Far Ultraviolet," Ph.D. thesis, Univ. of Colorado (printed by the National Center for Atmospheric Research).
- Orrall, F.Q., G.J. Rottman, and J.A. Klimchuk, 1983, "Outflow From the Sun's Polar Corona," Ap. J. (Lett.), 266 (L65).

- Roussel-Dupre, D., and R.A. Shine, 1982, "Average Solar Line Profiles of C IV and Si IV from OSO-8 Observations," Solar Phys., 77 (329).
- Schmieder, B., J.M. Malherbe, P. Mein, and E. Tandberg-Hanssen, 1984, "Dynamics of Solar Filaments. III. Analysis of Steady Flows in H α and C IV Lines," Astron. Ast., 136 (81).
- Schmieder, B., J.M. Malherbe, A.I. Poland, and G. Simon, 1985, "Dynamics of Solar Filaments. IV. Structure and Mass Flow of an Active Region Filament," Astron. Ast., 153 (64).
- Shine, R.A., 1985, "Absolute C IV Doppler Shifts Measured with UVSP," private communication.
- Simon, G., P. Mein, J.C. Vial, R.A. Shine, and B.E. Woodgate, 1982, "Measurements of Solar Transition Zone Velocities and Line Broadening Using the Ultraviolet Spectrometer and Polarimeter on the Solar Maximum Mission," Astron. Ast., 115 (367).

Searching the UVSP database, and a list of experiments showing mass motions.

William Thompson
Applied Research Corporation
8201 Corporate Drive
Landover, MD

Since the Solar Maximum Mission (SMM) satellite was launched in February of 1980, a large database has been built up of experiments using the Ultraviolet Spectrometer and Polarimeter (UVSP) instrument. Access to this database can be gained through the SMM Vax 750 computer at Goddard Space Flight Center. One useful way to do this is with a program called USEARCH. This program allows one to make a listing of different types of UVSP experiments. As an example, one could make a list of all Dopplergram experiments made during the month of April in 1980. It is evident that this program is useful to those who would wish to make use of UVSP data, but who don't know what data is available. Therefore it was decided to include a short description of how to make use of the USEARCH program in these proceedings. Also described here, but not included due to space limitations, is a list of all UVSP experiments showing mass motions in prominences and filaments. This list was made with the aid of the USEARCH program.

There are at the time of this writing four telephone numbers that will connect to the Vax. These are (301)-344-5596, 7951, 7952 and 7074. Each is connected to a Hayes modem capable of operating at rates of either 300 or 1200 baud. The baud rate is set automatically by entering a carriage return after connecting with the modem. (Be careful, entering any other character has the potential of setting an incorrect baud rate.) At that point one should get the "Username:" prompt, followed by the "Password:" prompt. If all four of the modem lines are in use at once, however, the user will be automatically logged off with an apology and a suggestion to try again later. If users have trouble logging on they can try calling me at (301)-344-8619, Art Poland at (301)-344-6991, or Joe Gurman at (301)-344-7599.

Unfortunately, the Goddard Space Flight Center telephone system is undergoing a change in the near future, and all the telephone numbers will be different than they are now. For most telephone numbers the change will be limited to the digits 344 changing to 286 (e.g. (301)-344-8619 will become (301)-286-8619), but the situation is more complicated in regard to computer modems. The details of this changeover are not precisely clear to us yet.

After logging on, you should get a dollar sign (\$) prompt. At that point, you can type in the command USEARCH. From that point on, the USEARCH program will ask a series of questions designed to tailor the output to your requirements. Sample sessions are shown in figures 1 and 2. Figure 2 shows the process using the extended search mode, while figure 1 shows the process without it. The first question in either case concerns where the output will be sent. If the letter "D" (either upper or lower case) is entered, then the output will be saved as a disk file. Otherwise it will be sent directly to a printer. The printer formats ("V" or "L") differ only in the number of lines per page (61 for "V" or 53 for "L"). Normally a blank space is inserted between experiments made

during different orbits, but this can be inhibited to save space. If a question is not answered, then the default ("NO" unless otherwise specified) is assumed.

The program next asks for the range of the search. This can be expressed either in experiment numbers, or in terms of day-of-year (DOY) for a given year. The values must be separated by commas. The range 1,32000 would include all the data up to the failure of the UVSP wavelength drive. All questions after that can be ignored except for those which are of particular interest to the user. If no answer is given, then that option has no effect on the output. Among the possible options used to tailor the output is entering the first several letters of the experiment definition name. One can request a certain file type, either "PB" for playback or "FD" for final data, or one can request both types. This only pertains to experiment numbers after 16800. The different experiment type numbers are shown in table 1 which is reproduced from Henze (1979). The radial distance from the center of the sun's disk is measured in units normalized to unity at the solar limb. The selection of "NOAA Active Region No. or Code" is only moderately useful. For instance, selecting code 6 ("Limb") only selects out those experiments which have been marked as limb experiments, not all those taken at the limb. The remainder of the questions should be self explanatory.

The output provided by the USEARCH program gives the following information about each experiment [Gurman, 1986]: the experiment number, the date, start time (UT), and day-of-year of the observation, the duration in minutes, the spacecraft roll in degrees clockwise from north, the NOAA active region number or code, the radius vector of the center of the UVSP field of view in units of the solar radius, the position angle of the center of the UVSP raster pattern measured counterclockwise (eastward) from north, the x and y coordinates of the center of the UVSP raster pattern in arc seconds, the x and y step sizes in arc seconds, the x and y extents of the raster pattern in arc seconds, the slit set number [Woodgate et al., 1980], the detector(s) used, the approximate wavelength in Angstroms of the first detector listed, the wavelength drive step size in motor steps (about 5 mA second order), the number of wavelengths sampled, the polarimeter position (A, B or OUT), the number of polarimeter positions, the loop order (explained below), the wavelength drive calibration shift, the number of repetitions of the outmost active loop started, the detector gating time in seconds, the reformatting status (P for playback, F for final data, B for both), the number of logical records in the data file, the experiment type [Henze, 1979], and the experiment definition name.

The nesting or loop order for the instrument mechanisms are given as a four letter code. X and Y refer to rastering in the X (south to north) and Y (west to east) directions, P to the rotation of the polarimeter, and W to the stepping of the wavelength drive. The innermost loop is given first, and then in order outward. For instance, if the order were WXYZ then the instrument would step through wavelength at each X and Y position before stepping to the next pixel position, while if the order were XYZW then the instrument would step through every X and Y position at each wavelength position before stepping to the next wavelength position. All mechanisms are listed even if some or all are unused. The unused mechanisms are listed last, and the default order is XYZW.

The USEARCH program was used to make a list of all observations taken UVSP instrument showing mass motions in solar prominences and filaments. This list pointed to some several thousand experiments in total. These data were then

analyzed to determine when significant changes in pointing were done, so as to reduce the list to a more manageable size. Once this was done, the list of pointings was compared to the H-alpha synoptic charts published in the Solar--Geophysical Data prompt reports. Although this sort of comparison is crude, as conditions on the sun will change over the period of one Carrington rotation, it is still possible to get some idea of the probability of finding a filament in many of the particular pointing sets. However, it was not judged possible to accurately determine if a limb observation would show a prominence based on the synoptic charts.

The data are organized into three tables in a separate document [Thompson, 1986]. The first table presents the data for all UVSP dopplergram experiments. Table 2 presents the raster through the line (RTL) experiments and table 3 presents the profile matrix (PM) experiments. The RTL experiments differ from the PM experiments in that in the latter a scan through wavelength is made at each pixel position before moving to the next pixel, while in the RTL mode a complete image is made in each wavelength before moving to the next wavelength. Included in the tables is a numerical code for each pointing set which represents the judged probability of finding a filament in the field of view, where 0 represents "probably not", 1 represents "possibly", 2 represents "probably", and 3 represents a limb observation. Only the first two tables were distributed at the meeting. Contact me for a copy of this document.

REFERENCES

- Gurman, J., UVSP catalog description. (1986), unpublished.
Henze, W., The Ultraviolet Spectrometer and Polarimeter experiment on the Solar Maximum Mission: A general description. (1979), unpublished.
Solar-Geophysical Data, 428-490 Part I, April 1980 to June 1985, U. S. Department of Commerce (Boulder, Colorado, U.S.A. 80303)
Thompson, W.T., A comprehensive list of UVSP experiments showing mass motion. (1986), unpublished.
Woodgate, B.E. et al., The Ultraviolet Spectrometer and Polarimeter on the Solar Maximum Mission. (1980), Solar Physics 65, 73.

**ORIGINAL PAGE IS
OF POOR QUALITY**

Table 1. UVSP experiment types. (Reproduced from Henze, 1979).

NUMBER	NAME	EXPLANATION
1	SPECTROHELIOGRAM	Raster
2	DOPPLERGRAM	Raster with velocity slits, periodic recentering of lines, and wavelength offsets to calibrate
3	POLARGRAM	Raster using polarimeter
4	MAGNETOGRAM	Raster with velocity slits and polarimeter, periodic recentering of lines, and wavelength offsets to calibrate.
5	I-MAX	Performs raster and finds position of maximum intensity.
6	I-MIN	Performs raster and finds position of minimum intensity.
7	FLASH WATCH	Repeats rasters until maximum intensity exceeds threshold.
8	RED-MAX	Performs Dopplergram raster and finds position of maximum redshift of line (maximum velocity away from spacecraft).
9	BLUE-MAX	Performs Dopplergram raster and finds position of maximum blue shift of line (maximum velocity toward spacecraft).
10	SPECTROGRAM	Spectral scan.
11	LAMBDA-MAX(GLOBAL)*	Performs spectral scan and finds wavelength at which intensity is maximum.
12	LAMBDA-MAX(LOCAL)*	
13	LAMBDA-MIN(GLOBAL)*	Performs spectral scan and finds wavelength at which intensity is minimum.
14	LAMBDA-MIN(LOCAL)*	
15	SPECIAL	Anything, parameter block completely specified by experimenter.
16	PROFILE MATRIX	Raster of spectrograms over a single line profile with raster step changes after complete profile is observed.
17	MULTI-LINE PROFILE MATRIX	Raster of spectrograms over several line profiles; after all line profiles are scanned at one position, then raster step changes.
18	RASTER THROUGH THE LINE	Set of rasters at different wavelengths in line profile; after raster is completed at one wavelength, then wavelength drive steps to new wavelength.
19	POLARIZED PROFILE MATRIX	Same as No. 16 except using polarimeter.
20	POLARIZED MULTI-LINE PROFILE MATRIX	Same as No. 17 except using polarimeter.
21	POLARIZED RASTER THROUGH THE LINE	Same as No. 18 except using polarimeter.

*if global, then the wavelength is stored in a wavelength register and the previous value is destroyed. If local, then the previous value in the wavelength register is not destroyed.

Figure 1. USEARCH sample session without the extended search menu.

```
$ usearch
  CATALOG SEARCH AND PRINTOUT:
For DISK FILE instead of spooling, enter D           d
Printer format [V for Versatec or Printronix,
                L for LaserGrafix; default = V]
Inhibit space between orbits in output? [Y,N]
Extended search menu? [Y,N]

Answer any of the following: (Defaults are ALL possibilities
    except for experiment nos. or DOYs.)

Experiment Nos.: First,Last
Enter DOY limits & Year [DOY1,DOY2,YR]
Must specify experiment number or DOY range. Try again.

Experiment Nos.: First,Last           1,100
Experiment Name, or part of [e.g.,C4CON]

Hope you made no mistakes! Do you want to try again? [Y/N]
More? [Y/N]

  Output to Disk File PRNTR.LIS --    97 EXPS.
$
```


Figure 2. USEARCH sample session with the extended search menu.

```

$ usearch
  CATALOG SEARCH AND PRINTOUT:
For DISK FILE instead of spooling, enter D                      d
Printer format [V for Versatec or Printronix,
                  L for LaserGrafix; default = V]
Inhibit space between orbits in output? [Y,N]
Extended search menu? [Y,N]                                     y

Answer any of the following: (Defaults are ALL possibilities
                              except for experiment nos. or DOYs.)

Experiment Nos.: First,Last                                     1,100
Experiment Name, or part of [e.g.,C4CON]
File type (exps. after 16800): 1=PB, 2=FD, 3=both
Wavelength limits in Angstroms (Integers)
Slit No.
Detector No. (more than one entry will
              search for a combination of detectors)
Experiment Type No.
Polarimeter A, B, or O for OUT
Lower, upper limits on radial distance from sun center
Image size in pixels [NX,NY]
Resolution desired in arcsec/pixel [DX,DY]
Lower limit on Duration in minutes
NOAA Active Region No. or Code:
  (1=Sun Center, 2=Coalignment, 3=Star, 4=Coronal Hole,
   5=Filament, 6=Limb, 7=Bright Point, 8=Prominence,
   9=Door Closed, 10=Night, 11=N or S Pole,
   12=Plage, 13=Quiet Sun, 14=Sun Center with Tracking)
Spectra only (including PM's and RL's)? [Y/N]

Hope you made no mistakes!   Do you want to try again? [Y/N]
More? [Y/N]

Output to Disk File PRNTR.LIS --      97 EXPS.
$

```

ON THE EXISTENCE OF OSCILLATIONS IN SOLAR FILAMENTS
OBSERVED IN H_{α} AND C IV LINES

Schmieder B, Malherbe J.M., Mein P.
Observatoire de Paris - Section de Meudon
92 195 - Meudon Cedex - France

and
Tandberg - Hanssen E.
NASA, Marshall Space Flight Center, AL. 35812, USA

ABSTRACT

Time sequence observations of filaments in both the H_{α} line and the 1548 A C IV line were analyzed with the Fourier transform technique in the frequency range (1 - 10 mHz). No oscillation is detected in filaments except at the footpoints where a steady velocity gradient is large. The energy is probably due to convective motions rather than pressure oscillations.

INTRODUCTION

Studies on the heating mechanisms of the solar corona have pointed out the importance of the inhomogeneities in the atmosphere. The observations of filaments which are structures located inside the corona and connected with the photosphere can make understandable the transport of energy through magnetic structures.

Time sequences of filament observations were made simultaneously in the H_{α} line and in the C IV line in 1980 using respectively the Multichannel Subtractive Double Pass spectrograph (MSDP) operating on the Meudon Solar Tower and the Ultra - Violet Spectrometer and Polarimeter (UVSP) on board the SMM satellite. Table 1 gives the characteristics of the observations.

Table 1 Filament observations

instrument	MSDP (Meudon)	UVSP (SMM)
line	H_{α}	C IV
wavelength	6563 A	1548 A
number of sequences	3	5
time duration	15 - 25 min	25 - 35 min
time step	60 sec	30 sec
spatial resolution	1"	3"
field of view	1' x 3'	1' x 1'

ORIGINAL PAGE IS
OF POOR QUALITY

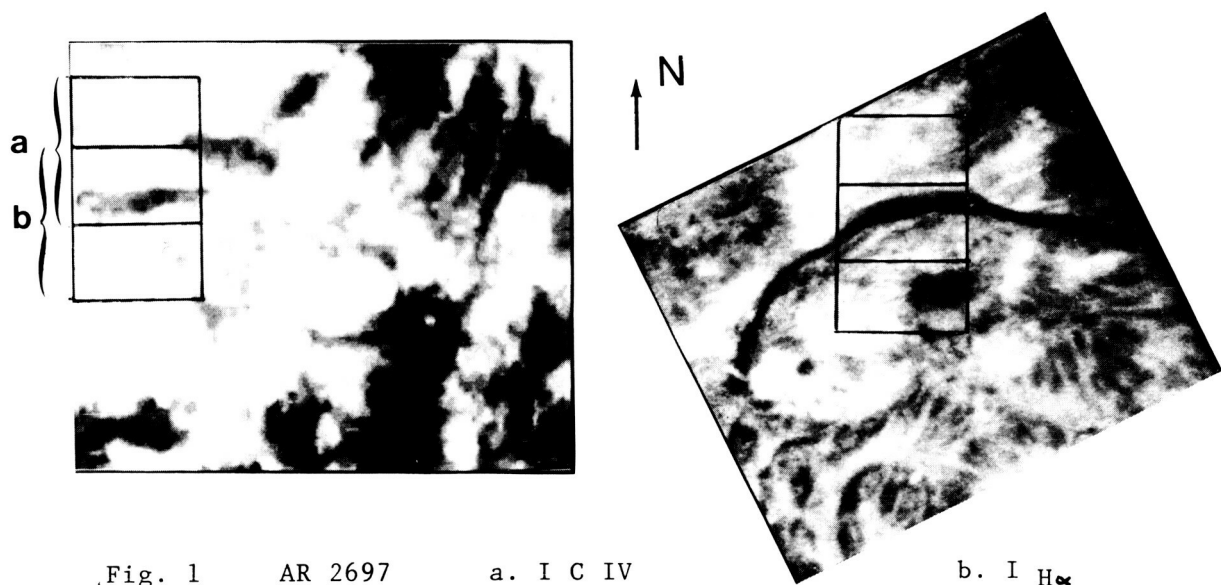


Fig. 1

AR 2697

a. I C IV

b. I H α

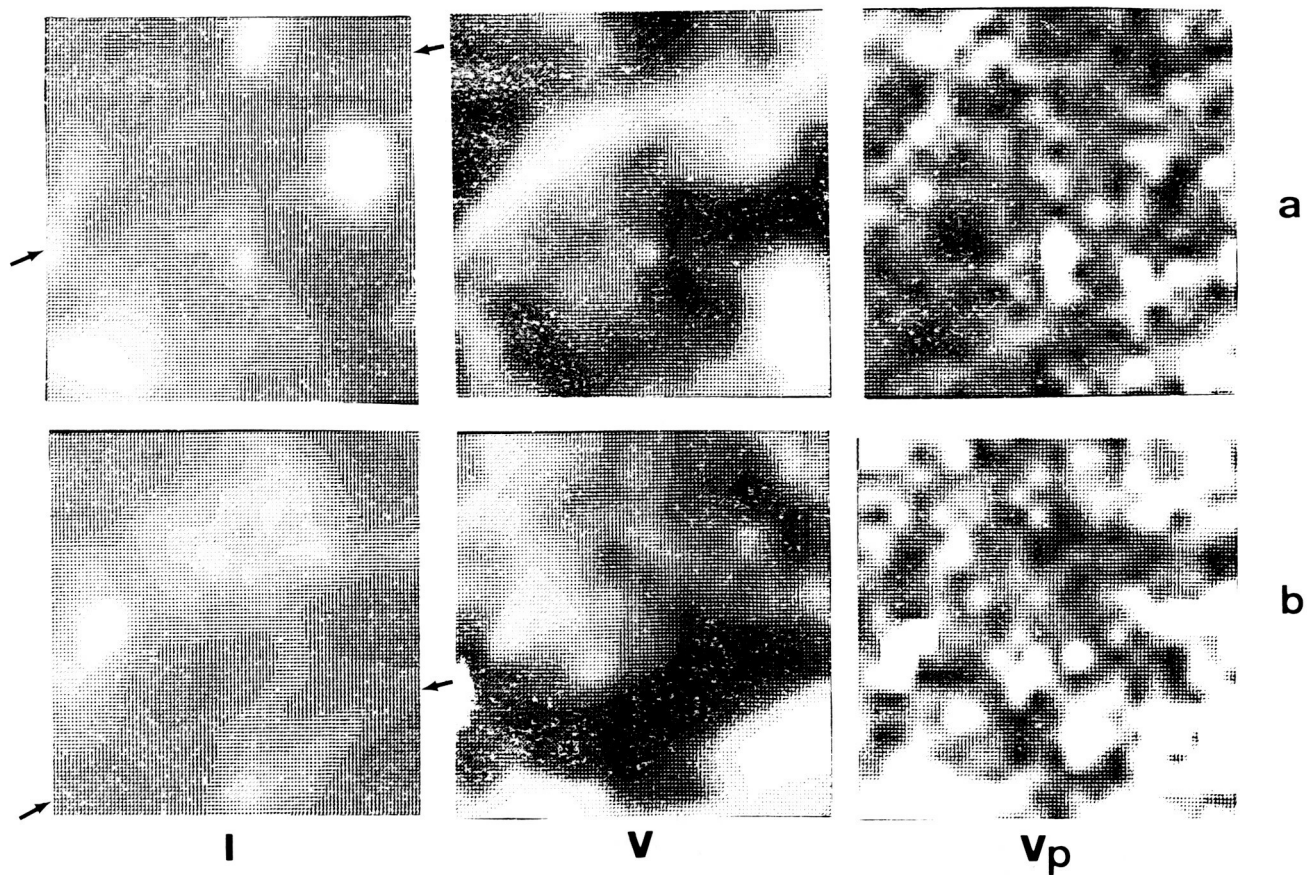


Fig. 2 CIV observations a: case 1- Sept 30 1980, b: case 2-Sept 28 1980

These observations concern two different active regions named by NOAA : AR 2701 and AR 2697 (Fig. 1). Boxes a and b in figure 1 indicate the C IV field of view ($1' \times 1'$) represented on the figure 2, respectively 2a and 2b. The arrows show the filament region (Fig. 2 I).

Stationary velocity fields

For almost all the time sequences, the stationary velocity field is upward in the filament (Fig. 2a V : white zone) but in case 2 we observe a strong horizontal gradient of velocity at the location of the filament (Fig. 2b V) suggesting a loop (Engvold et al. 1985). The mean values over the time reach $+10 \text{ km s}^{-1}$ and -14 km s^{-1} in C IV, and 2.5 and -3.5 km s^{-1} in H_{α} . Such regions have been interpreted as foot points of filaments (Schmieder et al. 1985).

Velocity power spectrum

These sequences of observations were analyzed by the Fourier transform technique. We obtain velocity maps at different frequencies. In figure 2 Vp, we present results for periods around 200 s. The oscillations in filaments are not detected in H_{α} line in the frequency range ($1\text{-}10 \text{ mHz}$) ; they have no significant amplitudes in C IV lines (case 1 - Fig. 3ab). This result is consistent with the efficient reflection of acoustic waves at the top of the chromosphere confirming a previous result (Malherbe et al. 1981). Outside the filament, the well known chromospheric oscillations around 200s are present (Fig. 3a). In the transition region no oscillation is detected outside sunspots and bright points. As that concerns only a few points, the power spectrum is weak (Fig. 3b). For the case 2 we observe energy located principally in the loop region corresponding to upflows (Fig. 2b Vp - white zones correspond to energetic regions). The power spectrum (Fig. 3c) presents a low decay towards high frequencies. The observed peaks do not seem significant, because the variations of intensity and velocity versus time at oscillating points show no particular enhanced frequencies.

No present filament model is valid to interpret the existence and the stability of the footpoints of the filaments: siphon mechanism (Ribes and Unno 1980), magnetic flux rope (Schmieder et al. 1985). The existence of energy power in the footpoints during activation of the region can be due to photospheric convective motions rather than oscillations (Malherbe et al. 1986).

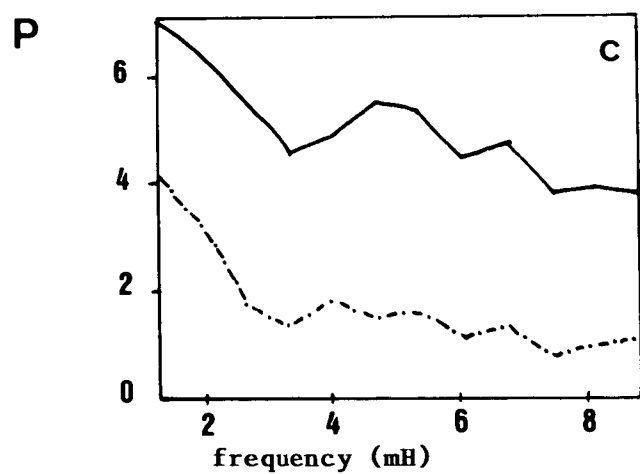
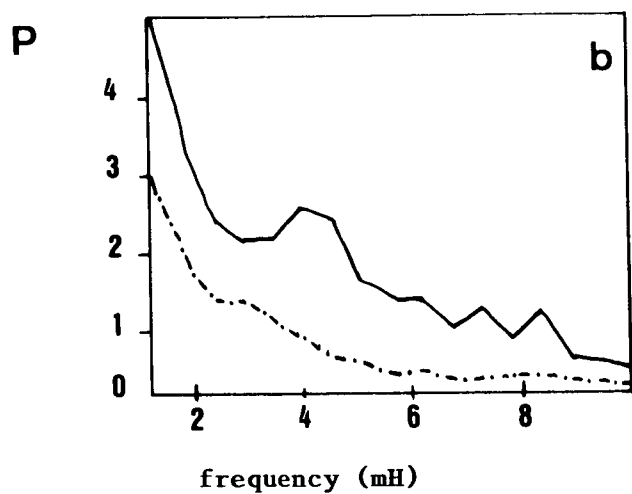
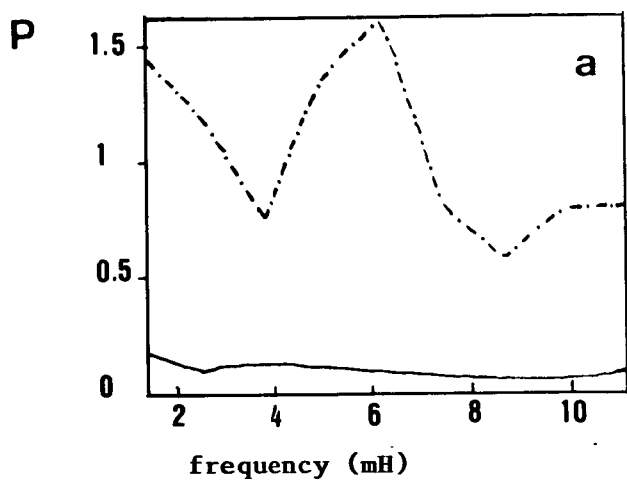


Fig. 3 Velocity Power Spectrum

- a. H_{α} (Sept 30. 80)
- b. C IV. case 1 (Sept 30. 80)
- c. C IV. case 2 (Oct 2. 80)

(dashed line bright regions
solid line dark regions)

REFERENCES

Engvold, O., Tandberg-Hanssen, E., Reichman, E., 1985, "Evidence for systematic flows in the transition region around prominences", Solar Phys. 96, 36.

Malherbe, J.M., Schmieder, B., Mein, P. 1981, "Dynamics in filaments : I oscillations in a quiescent filament", A & A 102, 124.

Malherbe, J.M., Schmieder, B., Mein, P., Tandberg-Hanssen, E. 1986, "Dynamics of solar filaments : V oscillations in H and C IV lines", A & A, to be published

Schmieder, B., Malherbe, J.M., Mein, P., Poland, A. 1985, "Dynamics of solar filaments : IV Structure and mass flow of an active region filament" Astron. and Astrophys. 153, 64.

Ribes, E., Unno, W. 1980, "Steady flow models of dark filaments" Astron. and Astrophys. 91, 129.

MEASUREMENTS OF MAGNETIC FIELDS IN SOLAR PROMINENCES

Egidio Landi Degl'Innocenti

Istituto di Astronomia, Università di Firenze, Firenze, Italy

INTRODUCTION

It is well known that the magnetic field vector plays a fundamental role in the physics of solar prominences, being the main agent in determining their geometrical forms, their motions, and, eventually, their existence itself. For this reason, any attempt of measuring magnetic field vectors in prominences has to be considered as an extremely important contribution to the understanding of the physical picture of these structures.

Magnetic fields can be measured, in solar prominences, by means of two different basic mechanisms that are responsible for the introduction (or the reduction) of a given amount of polarization in spectral lines: these are the Zeeman effect and the Hanle effect.

Through the splitting of the magnetic components of a spectral line, the Zeeman effect is able of introducing a certain amount of circular polarization across the line profile. This circular polarization results in being of the order of

$$\bar{g} \nu_L \cos \psi / \Delta \nu$$

where \bar{g} is the effective Landé factor of the line, ν_L is the Larmor frequency that is proportional to the magnetic field, ψ is the angle between the magnetic field and the line of sight and $\Delta \nu$ is the line-broadening in frequency units. For typical magnetic fields that are believed to be present in prominences (≈ 10 -20 G), the circular polarization results in being of the order of few tenths of a percent or lower, and can then be measured by means of high-sensitivity magnetographs or spectropolarimeters. With this technique, however, only the longitudinal component of the field can be obtained and the real structure of the vector magnetic field configuration remains highly undetermined.

The Hanle effect consist in a modification of the linear polarization that is induced in spectral lines by the anisotropic illumination of the prominence plasma by the photospheric radiation field. In the absence of magnetic fields, emission lines from prominences are, in general, linearly polarized along the solar limb direction, with polarization values typically of the order of a fraction of a percent. The presence of a magnetic field acts through the combination of a depolarization mechanism and a rotation of the direction of maximum polarization that both depend on the intensity and direction of the field. As a result, the magnetic field vector can be conveniently recovered through the measurement of linear pola-

rization in suitable emission lines from prominences, although a twofold degeneracy, typical of the Hanle effect, avoids an unambiguous determination of \vec{B} from optically thin lines. The aim of this paper is to present an updated review of the work that has been done on this subject and to point out some of the perspectives that are still open for future work.

MEASUREMENTS OF MAGNETIC FIELDS THROUGH THE ZEEMAN EFFECT

The first quantitative observations based on this technique were obtained in the late 60's by means of standard solar magnetographs. The main results, due to Rust (1966, 1967), Harvey (1969), and Tandberg-Hanssen (1970) were obtained with the Climax magnetograph of HAO and are reviewed in Tandberg-Hanssen (1974). They show a distribution of the longitudinal component of the magnetic field vector, as observed in $H\alpha$ for 135 quiescent prominences, ranging from 0 to 26 G, with a peak value at approximately 5 G, and an overall mean of 7.3 G. It was also shown by these investigators that, even if the measured field strength may vary from point to point (with a slight trend for $B_{||}$ to increase with height), the polarity of the field does not change for a given prominence. Similar observations have been reported more recently by Kim et al. (1982) and by Nikolsky et al. (1984). These observations, obtained with the spectrally scanning magnetograph installed at the 53 cm coronagraph of the Kislovodsk Station, show a broad distribution of observed field strengths with two peaks for $B_{||}$ close to 8 and 20 G. Moreover, it has been found by these authors, from a statistical analysis of the behavior of the observed field strength with the angle between the line of sight and the prominence long axis, that the magnetic field vector is inclined of approximately 25° with respect to the prominence long-axis itself.

In spite of the good results that have been obtained through the Zeeman-effect method, it has to be pointed out here that, according to theoretical calculations (Landi Degl'Innocenti, 1982) and to observations (Athay et al., 1983, Nikolsky et al., 1984), the V-profile of a typical emission line from prominences (like $\text{HeI } D_3$, $H\alpha$, or $H\beta$) has a characteristic signature that results from the superposition of a symmetric component (due to atomic polarization) and an antisymmetric component (due to the Zeeman effect). The determination of the longitudinal component of the field requires the separation of the antisymmetric component from the observed profile. This procedure has been actually followed in the reduction of the observations by Nikolsky et al., whose results can then be considered as fully reliable.

MEASUREMENTS OF MAGNETIC FIELDS THROUGH THE HANLE EFFECT

In recent years, extensive series of linear polarization observations in prominence emission lines have been obtained through the Pic-du-Midi coronagraph polarimeter (Leroy et al., 1977, 1984; Leroy, 1981) and through the HAO Stokes polarimeter (House and Smartt, 1982; Athay et al., 1983; Querfeld et al., 1985). At the same time, our theoretical understanding of the physical mechanisms underlying the appearance of polarization in prominence emission lines has grown considerably. While Landi Degl'Innocenti (1983) has attacked in full generality the problem of the generation and transfer of polarized radiation in spectral lines, more specific contributions have been brought by several authors. Bommier and Sahal-Brechot (1978) have developed a formalism of the quantum theory of the Hanle effect to obtain the theoretical expectations for the integrated linear polarization of the $\text{HeI } D_3$ line in optically thin prominences in the presence of weak magnetic fields ($B < 10$ G).

This formalism has been subsequently generalized by Bommier (1980) to allow for larger values of the magnetic field and by Landi Degl'Innocenti (1982) to interpret the fine structure of the D_3 line not only in linear but also in circular polarization. Further theoretical progress has been achieved by Landolfi and Landi Degl'Innocenti (1985) who have computed the expected polarization of the NaI D lines in optically thin prominences for arbitrary values of the magnetic field vector, by Bommier et al. (1986 a,b) who have performed analogous computations on H β taking properly into account the depolarizing effect of electron collisions, and, finally, by Landi Degl'Innocenti et al. (1986) who have attacked the more involved problem of H α polarization in optically thick prominences.

The theory developed in the papers quoted above have been successfully applied to a conspicuous set of data with the aim of determining the configuration of the magnetic field vector in prominences. Athay et al. (1983) report on the interpretation of the D_3 polarization observed in 13 prominences with the HAO Stokes-polarimeter. The main result of this investigation concerns the inclination of the magnetic field vector with respect to the solar radius that shows a pronounced preference to be close to 90° ; in other words, the field appears to be horizontal. The values obtained for B range from 6 to 27 G while the azimuth angle α with respect to the prominence long-axis does not show any systematic trend. It must be emphasized at this point that, due to the fact that it is impossible to discriminate (for optically thin lines) between two magnetic fields symmetric with respect to the plane containing the line of sight and the solar radius, the azimuth angle determination has an intrinsic ambiguity. In the observations of Athay et al. (1983) it was impossible to ascertain, in most cases, whether the field was crossing the prominence in the same sense of the underlying photospheric field or in the opposite sense. More recently, Leroy et al. have presented very interesting results on the interpretation of the (unresolved) D_3 line observed with the Pic-du-Midi coronagraph polarimeter in 120 prominences of the polar crown (Leroy et al., 1983) and in 256 quiescent prominences of medium and low latitude (Leroy et al., 1984). In these investigations, that complete previous results obtained by Leroy (1977, 1978), the azimuth α of the magnetic field vector is retrieved by means of a detailed statistical analysis that is based, however, on the assumption of the horizontality of the field itself. The main results of the analysis by Leroy et al. are summarized in the following: a) for polar crown prominences a mean value of 6 G is obtained at the beginning of solar cycle XXI, and a mean value of 12 G is reached just before maximum; b) the azimuth of the magnetic field vector, α , makes a small angle (25°) with the long axis of the prominence and shows a marked preference to be directed from the negative to positive photospheric polarity, thus supporting the Kuperus-Raadu (KR) family of models (Kuperus and Raadu, 1974) and contradicting the Kippenham-Schlüter (KS) one (Kippenham and Schlüter, 1957); c) for quiescent prominences of medium and low latitude, there is strong evidence that they can be grouped in two different types, those having maximum height smaller than 3×10^4 km, and those having maximum height larger than 3×10^4 km; d) prominences of the first type are found to have a magnetic structure consistent with the KS type of models with $\alpha \sim 20^\circ$ and $B \sim 20$ G; e) prominences of the second type are found to have a magnetic structure consistent with the KR type of model with $\alpha \sim 25^\circ$ and $B \sim 5$ to 10 G.

Finally, some new results have been published by Bommier et al. (1986a) on the magnetic field vector determination in a reduced number of quiescent prominences observed quasi-simultaneously in D_3 and H β at Pic-du-Midi. Apart from the independent determination of electron densities (a subject that is not covered in this paper), the use of two different lines allows, in principle, to obtain the inclination of

the field with respect to the solar radius. (Similarly to the case where the two fine-structure components of D_3 are observed, as in Athay et al., 1983). The results obtained from the joint D_3 and H_β observations are found to be in general good agreement with previous diagnostics based solely on D_3 observations, although the field inclination appears to scatter significantly from the 90° value, being in the range between 70° and 110° . These tilt angles with respect to the horizontal are interpreted by Bommier et al. assuming a V-shaped depression of the lines of force in the prominence material.

PERSPECTIVES FOR FUTURE WORK

The results that have been summarized in the former sections clearly show the potentiality of polarimetric observations as diagnostic tools for our understanding of the magnetic configuration of solar prominences. A further point where some progress can be achieved in the near future concerns the resolution of the ambiguity intrinsic to circular and linear polarization observations. Indeed, from circular polarization observations only the projection of the magnetic field along the line of sight can be determined (once the antisymmetric component is extracted from the V-profile), while, from linear polarization observations of optically thin lines, a twofold ambiguity remains between a magnetic field determination and its specularly symmetric image with respect to a plane containing the line of sight and the local solar radius (for prominences observed in the plane of the sky). For optically thick lines like H_α , the situation changes dramatically, as the possibility of multiple scattering inside the prominence body introduces a further physical direction into the problem and changes the simple specular symmetry previously outlined. Polarization diagrams for the expected polarization in H_α from optically thick prominences have been obtained by Landi Degl'Innocenti et al. (1986). Their results show that an ambiguity is still present in the field determination, but this ambiguity doesn't have the simple behavior of the specular symmetry typical of the optically-thin case. Simultaneous observations in optically thin and optically thick lines are then able, in principle, of solving the azimuth ambiguity. In concluding we want to stress the fact that the theory of the Hanle effect is nowadays established to such a degree of sophistication that it could provide the actual determination of the magnetic configuration of prominences with improved accuracy with respect to the present situation. To this aim simultaneous observations of the circular and linear polarization in several spectral lines ($\text{HeI } D_3$, NaID , H_α , H_β) are needed. We hope that a new instrument, capable of performing similar observations with high spatial resolution, will be soon available to the solar scientific community in order to unravel in further details one of the most puzzling problems in the physics of solar prominences, namely the problem of their magnetic configuration.

REFERENCES

- Athay, R.G., Querfeld, C.W., Smartt, R.N., Landi Degl'Innocenti, E. and Bommier, V.: 1983, *Solar Phys.* 89, 3.
 Bommier, V.: 1980, *Astron. Astrophys.* 87, 109.
 Bommier, V., Leroy, J.L. and Sahal-Brechot, S.: 1986a, *Astron. Astrophys.* 156, 79.
 Bommier, V., Leroy, J.L. and Sahal-Brechot, S.: 1986b, *Astron. Astrophys.* 156, 90.
 Bommier, V. and Sahal-Brechot, S.: 1978, *Astron. Astrophys.* 69, 57.
 Harvey, J.W.: 1969, Ph. D. Thesis, University of Colorado.
 House, L.L. and Smartt, R.N.: 1982, *Solar Phys.* 80, 53.

- Kim, I.S., Koutchmy, S., Nikolsky, G.M. and Stellmacher, G.: 1982, *Astron. Astrophys.* 114, 347.
- Kippenham, R. and Schlüter, A.: 1957, *Z. Astrophys.* 43, 36.
- Kuperus, M. and Raadu, M.A.: 1974, *Astron. Astrophys.* 31, 189.
- Landi Degl'Innocenti, E.: 1982, *Solar Phys.* 79, 291.
- Landi Degl'Innocenti, E.: 1983, *Solar Phys.* 85, 3.
- Landi Degl'Innocenti, E., Bommier, V. and Sahal-Brechot, S.: 1986, *Astron. Astrophys.* (submitted).
- Landolfi, M. and Landi Degl'Innocenti, E.: 1985, *Solar Phys.* 98, 53.
- Leroy, J.L.: 1977, *Astron. Astrophys.* 60, 79.
- Leroy, J.L.: 1978, *Astron. Astrophys.* 64, 247.
- Leroy, J.L.: 1981, *Solar Phys.* 71, 285.
- Leroy, J.L., Bommier, V. and Sahal-Brechot, S.: 1983, *Solar Phys.* 83, 135.
- Leroy, J.L., Bommier, V. and Sahal-Brechot, S.: 1984, *Astron. Astrophys.* 131, 33.
- Leroy, J.L., Ratier, G. and Bommier, V.: 1977, *Astron. Astrophys.* 54, 811.
- Nikolsky, G.M., Kim, I.S., Koutchmy, S. and Stellmacher, G.: 1984, *Astron. Astrophys.* 140, 112.
- Querfeld, C.W., Smartt, R.N., Bommier, V., Landi Degl'Innocenti, E. and House, L.L.: 1985, *Solar Phys.* 96, 277.
- Rust, D.M.: 1966, Ph. D. Thesis, University of Colorado.
- Rust, D.M.: 1967, *Astrophys. Journ.* 150, 313.
- Tandberg-Hanssen, E.: 1970, *Solar Phys.* 15, 359.
- Tandberg-Hanssen, E.: 1974, "Solar Prominences", D. Reidel Publ. Co., Dordrecht.

MAGNETIC FIELD VECTOR AND ELECTRON DENSITY DIAGNOSTICS
FROM LINEAR POLARIZATION MEASUREMENTS
IN 14 SOLAR PROMINENCES

V. Bommier

Laboratoire de Physique Atomique et Moléculaire
et d'Instrumentation en Astrophysique
DAPHE, Observatoire de Paris-Meudon
92195 Meudon Principal Cédex

ABSTRACT

The Hanle effect is the modification of the linear polarization parameters of a spectral line due to the effect of the magnetic field. It has been successfully applied to the magnetic field vector diagnostic in solar prominences. The magnetic field vector is determined by comparing the measured polarization to the polarization computed, taking into account all the polarizing and depolarizing processes in line formation and the depolarizing effect of the magnetic field. The method has been applied to simultaneous polarization measurements in the Helium D₃ line (5876 Å, 3d³D → 2p³P) and in the Hydrogen Hβ line in 14 prominences. Four polarization parameters are measured (two polarization degrees and two polarization directions), which lead to the determination of the three coordinates of the magnetic field vector and the electron density, owing to the sensitivity of the Hβ line to the non-negligible effect of depolarizing collisions with electrons and protons of the medium. A mean value of $1.3 \times 10^{10} \text{ cm}^{-3}$ is derived in 14 prominences.

1. INTRODUCTION

The prominences emission lines observed at the solar limb with a coronagraph are linearly polarized by Rayleigh scattering of the underlying anisotropic photospheric radiation. In zero magnetic field the polarization direction would be parallel to the solar limb. The magnetic field modifies the linear polarization of the emitted line, leading to a depolarization and to a rotation of the polarization direction: these are the two main features of the Hanle effect. This effect has been successfully used for determining the prominence magnetic field from polarization measurements of the Helium D₃ line (5876 Å, 3d³D → 2p³P) (Leroy *et al.*, 1983, 1984; Athay *et al.*, 1983; Querfeld *et al.*, 1985). The diagnostic is achieved by matching the observed polarization parameters and the computed ones. The computation of the polarization of the Helium D₃ line has been achieved using a quantum formalism of matter radiation interaction (Bommier and Sahal-Bréchet, 1978; Bommier, 1980; Landi Degl'Innocenti, 1982), and leaning on the recent works on Helium line formation in prominences (Heasley *et al.*, 1974).

The Hydrogen Hα and Hβ line polarization in prominences has been measured at the Pic-du-Midi (Leroy, 1981). The interpretation of polarization measurements requires further investigation because, owing to the large dipole interaction between the Hydrogen atom and the surrounding electrons and protons, the depolarizing effect of collisions between fine structure levels (n, ℓ, j) and (n, ℓ', j') cannot be ne-

glected. This lead to a new method of diagnostic of the electron density, which has been applied to 14 prominences observed in Helium D_3 and Hydrogen $H\beta$ simultaneously (Bommier *et al.*, 1986). By measuring the polarization parameters of two lines, one gets four measured quantities, because two parameters are measured for each line, which are the polarization degree and direction. Four quantities can be determined from interpretation, which are the three coordinates of the magnetic field vector and the electron density in the case of D_3 and $H\beta$. The radiative transfer problem is avoided because these lines are optically thin in prominences; this is not the case of $H\alpha$ which is not optically thin and for which the radiative transfer problem for polarized radiation in the presence of a magnetic field has to be solved before interpreting the observations (Landi Degl'Innocenti, these proceedings).

In Section 2 we present the main steps and physical hypothesis of the $H\beta$ polarization computation; the results of interpretation of polarization measurements are given in Section 3.

2. CALCULATION OF THE LINEAR POLARIZATION OF THE $H\beta$ EMISSION LINE OF SOLAR PROMINENCES

The computation of the linear polarization of prominences Helium and Hydrogen Balmer lines requires firstly a quantum formalism of matter-radiation interaction : the master equation for the atomic density matrix, which describes the evolution of the atom coupled to the bath of photons and perturbers, is solved at the stationary state. The emitted photons density matrix and the polarization parameters of the emitted line are derived straightly from the atomic populations and coherences computed at the stationary state. (Bommier and Sahal-Br  chot, 1978; Bommier, 1980).

The atomic density matrix has been expanded over a basis which diagonalizes the fine-structure and the magnetic field interaction. The validity of the computation is then extended up to field strengths of 100 Gauss. In the case of Hydrogen, the hyperfine structure also has been taken into account in a preliminary calculation, but turns out to be negligible with respect to the measurement inaccuracies.

The resolution of the master equation at the stationary state requires the knowledge of the line formation processes. These are known from the work of Heasley *et al.* (1974) for Helium lines, Heasley and Mihalas (1976), Heasley and Milkey (1976, 1978) for Hydrogen lines, by solving the coupled problem of radiative transfer and statistical equilibrium. In the case of Hydrogen lines, the first atomic model (Heasley and Mihalas, 1976) assumed five bound levels and a continuum for statistical equilibrium computations. Heasley and Mihalas (1978) have shown that radiative cascades from upper levels up to $n = 20$ must be included in the statistical equilibrium equations for obtaining correct Balmer line intensities. In fact that effect, together with that of radiative recombinations, is much less important for the atomic polarization. Owing to measurements inaccuracies, it can be neglected in the present problem : thus statistical equilibrium equations have been solved for the levels $n = 1$ to 4 for the computation of the $H\beta$ polarization.

The alignment of the Zeeman sublevels is due to the absorption of the anisotropic incident photospheric and chromospheric radiation field. However, radiative transfer and statistical equilibrium should be solved consistently for optically thick transitions. In fact very high optical thickness for the Lyman lines are derived in Heasley's series of models ($\tau_{Ly\alpha} \sim 10^6$). Thus, owing to the trapping of the Lyman radiation in the prominence material, we have considered that their anisotropy is completely lost, and we have used the local intensities at the bottom of the pro-

minence, taken from recent quiet sun intensity measurements at the center of the disk. For the Balmer lines, their optical thickness has been obtained by Landman and Mongillo (1979) from line profile measurements : $\tau_{H\alpha} \sim 2.2$; $\tau_{H\beta} \sim 0.3$. Nevertheless, in our computations, the prominence has been assumed to be optically thin in the Balmer lines ($H\alpha$ and $H\beta$) and in the Paschen line $P\alpha$. With the exception of the $H\alpha$ line, our model is thus consistent with that of Heasley and Milkey (1978), where the Lyman lines and $H\alpha$ are optically thick and the Balmer, Paschen and all other lines between excited levels are optically thin.

The computation of line polarization must also take into account the non-magnetic polarizing or depolarizing effects. In the case of Hydrogen lines, the statistical equilibrium results from radiative transitions and also from transitions between fine structure levels n, ℓ, j and $n, \ell \pm 1, j'$ due to collisions, owing to the large dipole interaction between the Hydrogen atom and the surrounding electrons and protons. The corresponding collisional rates are of the same order of magnitude as the radiative rates, for typical electronic densities of prominences. We have computed the collisional transition probabilities using a semi-classical description of the collision and assuming the impact approximation, which means that the collision duration is very small with respect to the mean time between collisions, or, in other words, that collisions are well-separated in time. The impact approximation is valid at typical electron densities in prominences. The effect of collisions with protons has been found to be 10 times larger than the effect of collisions with electrons. Owing to the isotropic distribution of electrons and protons, the effect of collisions is to decrease the anisotropy of the Zeeman sublevels which is responsible for the polarization of the emitted radiation.

3. DIAGNOSTIC OF THE MAGNETIC FIELD VECTOR AND OF THE ELECTRON DENSITY

The diagnostic of the magnetic field vector and of the electron density is achieved by matching the observed polarization parameters and the computed ones for each observed line. This leads to the determination of a series of field vector solutions and density values for which the computed polarization parameters are equal to the observed ones for each line. The final determination is achieved by looking at the common field vector solutions in the two series.

In fact, in most of cases, multiple solutions are obtained, which are grouped two by two owing to the fundamental degeneracy of the solutions : two field vector symmetrical with respect to the line of sight have the same effect on the line polarization and cannot be distinguished.

In the multiple solutions (up to 8), a selection has been done based on several criteria determined from results obtained in previous works on the prominence magnetic field vector determination from polarization measurements in the D_3 line resolved in two components (Athay *et al.*, 1983; Querfeld *et al.*, 1985) or unresolved (Leroy *et al.*, 1984) :

- 1 - Though rather vertical solutions should be valuable a priori, they can be discarded on account of the statistical analysis of the polarization degree and the direction of polarization observed in the Helium D_3 line, for which the depolarization is of magnetic origin only : the observed average depolarization is too large to be consistent with rather vertical fields (Sahal-Br  chot *et al.*, 1977; Leroy, 1978).
- 2 - Field strengths higher than 30 Gauss are highly improbable in quiescent prominences : such derived field strengths are very probably parasitic solutions due to level-crossings effects in the D_3 line (Bommier, 1980).
- 3 - The angle between the magnetic field vector and the prominence long axis is clo-

se to 25° (Leroy et al., 1983, 1984).

4 - The field component that is along the long axis of the filament shows a general organization which forms over the Sun's Surface a regular pattern well defined and consistent. (Fig. 13 of Leroy et al., 1984).

5 - For the high prominences ($h > 30\,000$ km), which show filamentary or curtain-like structures, the lines of force cross the prominence in the opposite direction with respect to the polarity of the adjacent photospheric field (Leroy et al., 1984) as in the Kuperus-Raadu model type. This is the case of all the prominences of our sample, with the exception of prominence n° 12.

All these criteria have been used for solving the ambiguities of the diagnostic. It is very interesting and important to notice that all these criteria do not contradict one another : it has been possible in all cases to select one field vector and only one, among the multiple solutions of our sample, which agrees with all the above criteria.

However, if we compare our sample to that analyzed by Athay et al. (1983), it contains a greater number of cases where the field lines of force are not exactly horizontal, but somewhat aslant. The angle of deviation of the lines of force from the horizontal plane is more than 25° in seven prominences of our sample. Therefore one must consider that the magnetic field in quiescent prominences should be less horizontal than currently admitted. Such a geometry is difficult to admit in quiescent prominences where the cold material is observed hanging on the support made by the lines of force, either motionless, or hardly moving; a 30° slope of the

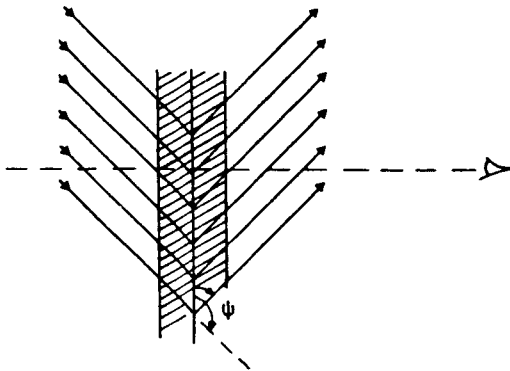


Fig. 1 - the simple geometry of field lines used in this work : the polarization degree and direction of the H β line have been computed assuming that two field works with inclination ψ and $180^\circ - \psi$, and the same azimuth θ , are present along the line-of-sight.

interpretation of polarization measurements has been undertaken again, assuming V shaped lines of force (see Fig. 1), in order to schematize by this mean the shape of lines of force in the prominence models (Kippenhahn and Schluter, 1957; Kuperus and Raadu, 1974), in which a magnetic through is assumed, where the cold material can be supported against gravity.

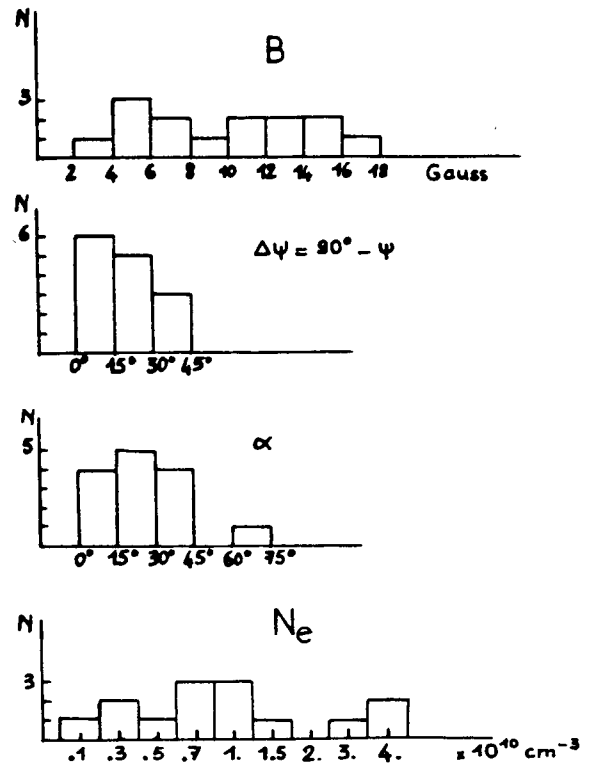


Fig. 2 - Histograms of the magnetic field vector and electron density determined in 14 prominences observed at the Pic-du-Midi. The three coordinates of the field vector are : the field strength B, the inclination angle with respect to the horizontal plane $\Delta\psi$, the angle α between the field vector projected on the horizontal plane and the prominence long axis.

The result on the magnetic field vector and electron density determination is given on the histograms of Fig. 2, which give the three coordinates of the magnetic field vector (field strength, angle of inclination of the lines of force with respect to the horizontal plane, angle between the field vector projected on the horizontal plane and the prominence long axis) and the electron density in the 14 prominences. The mean value of the determined electron density is $1.3 \times 10^{10} \text{ cm}^{-3}$ in the 14 prominences.

The sensitivity of the H β polarization to electron and proton collisions is in the range $10^9 - 10^{11} \text{ cm}^{-3}$: this is very favourable for using this density diagnostic method in quiescent prominences. For densities larger than 10^{11} cm^{-3} the collisional depolarization becomes very effective, and the polarization degree of H β becomes too small to be measured (less than 10^{-3}). Densities higher than 10^{11} cm^{-3} in prominences are therefore not compatible with the observed polarization of the H β line.

4. CONCLUSION

The collisional depolarization of Hydrogen lines provides a method for determining the electron density in a density range where the Stark broadening becomes too small to be interpreted, these two methods being therefore complementary.

The method has been applied to magnetic field vector and electron density diagnostic in 14 prominences and has led to a mean value of $1.3 \times 10^{10} \text{ cm}^{-3}$ for electron density.

RÉFÉRENCES

- Athay, R.G., Querfeld, C.W., Smartt, R.N., Landi Degl'Innocenti, E. and Bommier, V.: 1983, *Solar Phys.* 89, 3.
- Bommier, V., and Sahal-Bréchot, S.: 1978, *Astron. Astrophys.* 69, 57.
- Bommier, V.: 1980, *Astron. Astrophys.* 87, 109.
- Bommier, V., Leroy, J.L., and Sahal-Bréchot, S.: 1986, *Astron. Astrophys.* 156, 79 and 90.
- Heasley, J.N., Mihalas, D., and Poland, A.I.: 1974, *Astrophys. J.* 192, 181.
- Heasley, J.N., Milkey, R.W.: 1976, *Astrophys. J.* 210, 827.
- Heasley, J.N., Milkey, R.W.: 1978, *Astrophys. J.* 221, 677.
- Heasley, J.N., Mihalas, D.: 1976, *Astrophys. J.* 205, 273.
- Kippenhahn, R., and Schlüter, A.: 1957, *Z. Astrophys.* 43, 36.
- Kuperus, M., and Raadu, M.A., 1974, *Astron. Astrophys.* 31, 189.
- Landi Degl'Innocenti, E.: 1982, *Solar Phys.* 79, 291.
- Landman, D.A., and Mongillo, M.: 1979, *Astrophys. J.* 230, 581.
- Leroy, J.L.: 1978, in *Physics of Solar Prominences*, IAU Coll. 44, eds. E. Jensen, P. Maltby, F.Q. Orrall, p. 56.
- Leroy, J.L.: 1981, *Solar Phys.* 71, 285.
- Leroy, J.L., Bommier, V., Sahal-Bréchot, S.: 1983, *Solar Phys.* 83, 135.
- Leroy, J.L., Bommier, V., Sahal-Bréchot, S.: 1984, *Astron. Astrophys.* 131, 33.
- Querfeld, C.W., Smartt, R.N., Bommier, V., Landi Degl'Innocenti, E., and House, L.L.: 1985, *Solar Phys.* 96, 277.
- Sahal-Bréchot, S., Bommier, V., Leroy, J.L.: 1977, *Astron. Astrophys.* 59, 223.

FILAMENT DISAPPEARANCES

William J. Wagner

Space Environment Laboratory, NOAA, Boulder, CO, USA 80303

INTRODUCTION

The phenomenon of the sudden filament disappearance (Disparition Brusque) is a familiar one to observers at H-alpha telescopes. Nevertheless, the importance in Disparition Brusques (DB) continues to grow for several reasons which are cited below. We must report that the Coronal and Prominence Plasmas Workshop was a very "constructive" one--that is, there seemed to be more emphasis on building and maintaining filaments than in destroying them. As a consequence, this sub-group is smaller than most of the others. All the same, progress in this area of filament disappearances seems steady and assured, based on results and programs reported during the Workshop.

THE IMPORTANCE AND INTEREST OF DBs

Disappearing filaments engender interest for two principal reasons. They offer a temptingly simple challenge for various theoretical solar work. DBs also provide a surrogate or marker for still other solar effects whose occurrence is more difficult to discern: the support mechanism for prominences, the changing magnetic fields over a sunspot cycle, and geoeffective coronal mass ejections.

The DB phenomenon seems analogous in many respects to the chromospheric flare process. However, DBs are easier to observe and analyze because they offer a target which pre-exists. Filaments apparently pass from equilibrium into a situation which finds reconnection of magnetic field taking place. Similarly, the pertinent time scales for the DB process are much slower than those in flares, making filament disappearances prime candidates for studies of solar activity/flares.

DBs are important further because in their mode of disappearing, filaments seem to give information (beyond simple feasibility arguments) on how they were originally formed and, especially, on their support mechanism. We must discern what agent intervened (or what process was turned off) when the filament became unstable. The critical thresholds in mass, flux, or field twist that had previously been satisfied may be revealed in eruptions. As a help in answering these questions, Bommier (1986b) offered an interesting paper. Her observations (Bommier et al, 1986a; Leroy et al, 1984) of prominence magnetic fields indicate that tall polar crown filaments appear to be suspended by the Kuperus-Raadu (1974) mechanism, lower-lying active region filaments by the Kippenhahn-Schluter (1957) model. This would be an

important result to verify because it implies at what altitude and in what configuration the neutral point existed in each case prior to eruption. Surely, the DB or accompanying coronal mass ejection must exhibit different behavior when starting from the K-R or K-S (or from the Hirayama, 1986) configurations.

Information may be available from DBs on the general solar cycle variation of magnetic fields. I note that during the present years of solar cycle minimum, huge filaments may erupt accompanied by only minimal (A-class) soft X-ray emission. In 1980, the same spacecraft instrumentation typically recorded M-class Long Duration Events in soft X-rays with peak intensities 1000 times greater. Is this a function of generally decreased fields, or a predominance during the current phase of the activity cycle of one prominence support mechanism over others?

Finally, in the past few years, solar-terrestrial physicists have grown increasingly aware of DBs (see, for example, Joselyn and McIntosh, 1981). Filament disappearances are now known to be as geophysically important as flares for their geomagnetic storm, ionospheric, and thermospheric heating effects. The reason for this, of course, lies in the coronal mass ejection which invariably accompanies the eruptive (dynamic) DB but is more difficult to detect (Wagner 1984).

It was observations from space that taught us that coronal mass ejections encircle erupting filaments. Space science has also shown us the need to distinguish between true dynamic DBs and thermic DBs which seem to be a temporary heating of the filament to EUV temperatures--not really what had been classically regarded as an eruptive disappearance. Lastly, the advantage of space observations is also apparent in their ability to reveal in soft X-rays the magnetic arches which exist with and after a DB.

Most of the papers in this group use data taken from space. When the American space science program is re-established, we expect that many more of the questions posed here will be answered.

WORKSHOP CONTRIBUTIONS TO DB UNDERSTANDING

Coronal and Prominence Plasmas workshop participants learned the results of one theoretical investigation and three observational studies concerning prominence disappearances. Mouradian, Martres, and Soru-Escout (1986) provided new details on Disparition Brusques of the thermic type (DBt). With data from Skylab, these workers report that filaments fade and reappear in neutral hydrogen spectral lines in as little as 30 minutes. This could be an important result for prominence formation theory. The heat flux necessary to accomplish this is apparently very high. Certain segments of the filaments were seen to pass through the cycle of recombination-ionization-recombination four times in as many days. Heating appears to progress from the outside of the prominence to the inside.

Malherbe and Forbes (1986) offer work which suggests that extreme temperatures (not unlike those of a flare) in the vicinity of a prominence can cause the prominence to

go unstable and disappear. These investigators consider wave, Joule, viscous, and conduction modes of energy transfer to occur in addition to radiative in affecting the target filament.

The trigger mechanism for dynamic Disappearance Brusques (DBd) is not well understood currently. Simon, Gesztelyi, Schmieder, and Mein (1986) provided evidence that reconfiguration of magnetic field on a small scale can trigger filament activations. Examples include a case wherein two pores (manifestations of emerging flux knots) move together, leading to the destabilization of a filament and the start of a two-ribbon flare. Another filament activation was marked by the birth of a new pore very close to the filament which was subsequently seen to twist. These authors were of the opinion that such pore-destabilizations are a common feature of the DBd.

Kopp and Poletto (1986) are using the Altschuler-Newkirk (1969) method on line-of-sight magnetic field data over a limited region of the sun (the data are assumed to repeat over the rest of the solar surface). They calculate the 3-dimensional potential field topology in the corona over the location of flares and DBs which are presumed to undergo reconnection processes. Work is in progress to map the coronal field at the time of the 21 May 1980 flare, after which high X-ray arches were observed by the HXIS experiment on the NASA Solar Maximum Mission spacecraft. Results of the calculations will be compared to the observed arches to determine if the post-event coronal field seems to have relaxed to a potential-like configuration. Another interesting comparison will be the estimate of energy represented in the arch formation to the observed thermal energy of the arch. Kopp and Poletto also hope to determine whether the arches represent reconnection at high altitude or simply disconnected loops.

The evolution of a filament through a sequence of magnetostatic equilibria, non-equilibrium phase, and finally eruption as the line current through the filament builds up, can be traced by Kuin and Martens (1986) with their addition of precise energy balance equations to those of force balance. Footpoint field motions increase fields in the filament and simultaneously electric current. The filament rises to find a new equilibrium. Eventually, no more equilibria configurations exist which will allow a balance of forces. The filament undergoes a dynamic disappearance and at the same time induces large currents in the neutral sheet far below the erupting filament. These lead to H-alpha flaring action below the eruptive. These authors suggest various data sets which, if obtained, would test this DB-flare model.

More extensive discussions of recent work on disappearing filaments may be found in the excellent reviews by Tandberg-Hanssen (1974) and Martin (1980).

FUTURE DIRECTIONS

The Workshop group on disappearing filaments discussed a number of interesting questions for further consideration or work. Of very basic importance for constraining models that address filament support and/or eruption is an increase in

our knowledge of coronal magnetic field configurations. Thus, the analytic work which compares calculated potential configurations to observations of field structure should be supported (perhaps by offers of computer time). Likewise, an X-ray instrument such as that on the Japanese HESP satellite or planned U.S. soft X-ray telescopes will provide valuable data for this purpose. These data are unobtainable from ground-based observatories. In addition, such instruments promise to yield time-dependent studies of magnetic field evolution. Our present solar "atmospheric sounding" is limited to the very modest range of heights represented by visible wavelength magnetograms and the tracings of white light pores.

It would help us to describe why a filament's "disparition brusque" occurs if we could state with certitude that magnetic fields along a neutral line cannot erupt without the presence of a filament. Are there such things as spontaneous erupting non-prominences, or are these simply called "flares"?

Finally, much can probably be learned from disappearing filaments about the way they are originally formed and supported. For example, it was not clear to the group that the Kippenhahn-Schluter mechanism, for the suspension of low-lying active region filaments, can permit thermic DBs. Yet, the DBt seems to be an active region event, rather than a high latitude phenomenon. Also, progress would be made if the process of the unwinding of a DBd were better understood. Is unwinding more common in active region filament eruptions than in polar, high altitude filament eruptions? Is this unwinding process related to the respective support mechanisms?

The disappearing filament group looks forward to answers to at least some of these problems. The group hopes it served to aid the formulation of these questions if not their resolution.

REFERENCES

- Altschuler, M. D., and Newkirk, G., Jr. 1969, Solar Phys., **9**, 131.
- Bommier, V. 1986, this Proceedings.
- Bommier, V., Leroy, J. L., and Sahal-Brechot, S. 1986, Astron. Astrophys., **156**, 79.
- Hirayama, T. 1986, this Proceedings.
- Joselyn, J. A., and McIntosh, P. S. 1981, J. Geophys. Res., **86**, 4555.
- Leroy, J. L., Bommier, V., and Sahal-Brechot, S. 1984, Astron. Astrophys., **131**, 33.
- Kippenhahn, R., and Schlutter, A. 1975, Z. Astrophysik, **43**, 36.
- Kopp, R. A., and Poletto, G. 1986, this Proceedings.
- Kuin, N. P. M., and Martens, P. C. H., 1986, this Proceedings.

- Kuperus, M., and Raadu, M. A. 1974, Astron. Astrophys., **31**, 189.
- Malherbe, J. M., and Forbes, T. G. 1986, this Proceedings.
- Martin, S. F. 1980, Solar Phys., **68**, 217.
- Mouradian, Z., Martres, M. J., and Soru-Escut, I. 1986, this Proceedings.
- Simmon, G., Gesztelyi, L., Schmieder, B., and Mein, N. 1986, this Proceedings.
- Tandberg-Hanssen, E. 1974, Solar Prominences, D. Reidel Publ. Co., Dordrecht, Holland.
- Wagner, W. J. 1984, Ann. Rev. Astron. Astrophys., **22**, 267.

THE HEATING OF FILAMENTS AS A DISAPPEARANCE PROCESS

Z. MOURADIAN
M.J. MARTRES
I. SORU - ESCAUT

Observatoire de Paris
Section de Meudon
DASOP - UA 326
F-92195 Meudon Principal CEDEX

FRANCE

INTRODUCTION

The sudden disappearance of filaments, commonly called "Disparition Brusque" (DB) is of two types : i) the well known ejection of cool prominence material into the corona, i.e., a dynamic process (DBd) and ii) the heating of the prominence plasma (Mouradian et al., 1981). When the hydrogen of the filament becomes ionised, then the filament start to be visible in EUV lines keeping the same shape and position as the cool one. This process which is a thermic disappearance was named DB thermic (DBt). In Mouradian et al., (1986) a complete description of this phenomena is given. Successive disappearances and condensations of a quiescent filament from 1973 june 13 to 17 was studied. This observation was provided by two instruments Skylab ATM aboard satellite : the Harvard College Observatory polychromator and X ray telescope of the American Science and Engineering Co. (2-32, 44-55 Å).

The heating of filaments was confirmed by Malherbe et al., (1982) who observed a partial DBt consequently to a flare. In Schmahl et al., (1982), it was pointed out that before a DB, filaments are spanned by hot arches emissive in OVI or/ and Mg X or in soft X rays. Many DBs obey to this scenario.

THE HEATING OF THE FILAMENT OF JUNE 1973

The heating of the studied filament may be explained -as seen above- by a hot arch which span it. This arch is well visible in soft X rays. It is close to the part of the filament which shows several DBs. The intensity of different EUV lines ($7 \cdot 10^3$ to 10^6 K) was studied by the spatial variation following the transition from cool to hot prominence.

The figure 1 shows us the ratio of the filament integrated intensity over the line profile and the quiet surrounding sun. At the right site of the filament observed on June 15th at 17:22, a hot filament is visible. Note that the cool filament is in absorption ($I/I_0 < 1$) in regard to the surrounding,

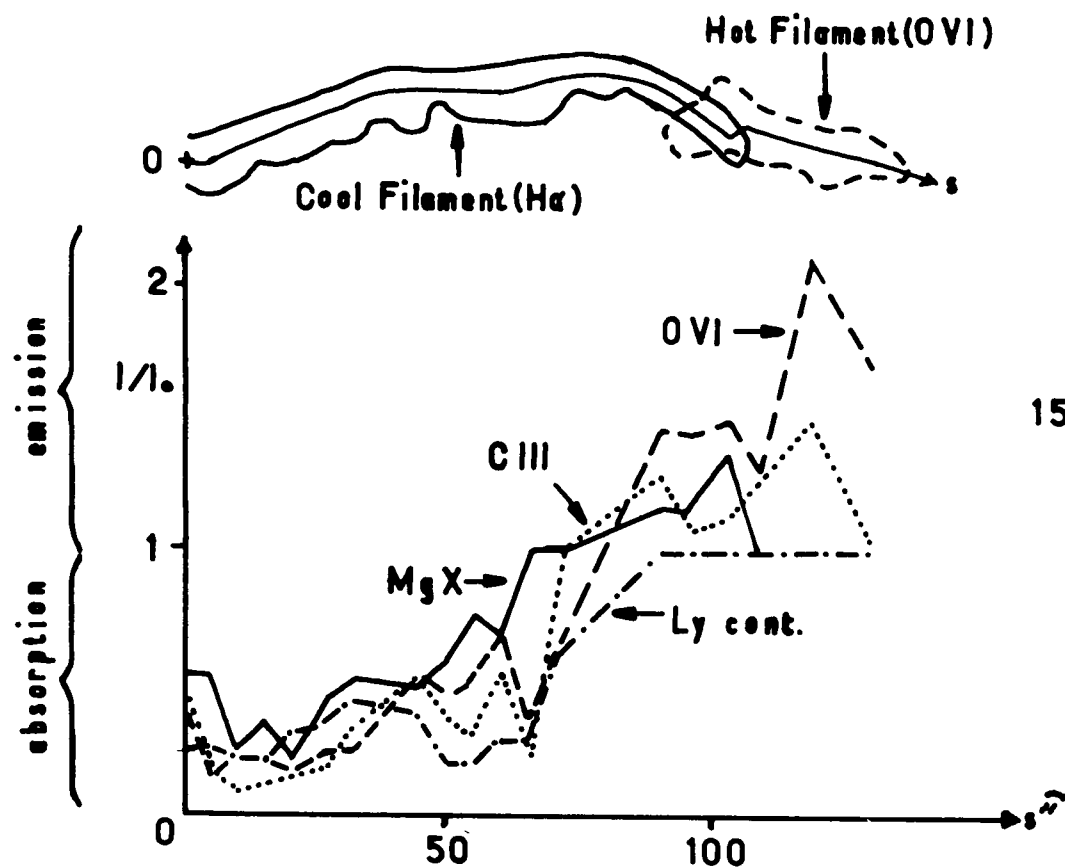


FIG.1
15 JUNE 1973
17:22

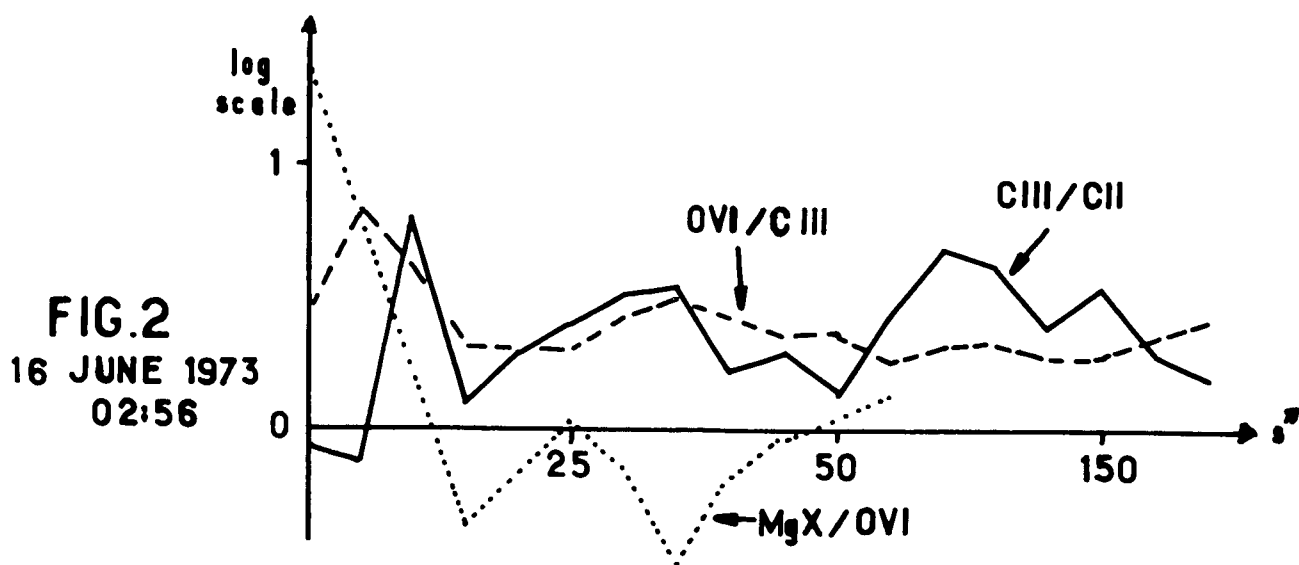


FIG.2
16 JUNE 1973
02:56

whereas the hot filament is in emission ($I/I_0 > 1$). In figure 2 we show that the intensity ratio of three lines formed at three different temperatures (CIII/CII, OVI/CIII and MgX/OVI) gives a similar result. We see that peaks appear at the end of the hot filament where is also the transition to the cool filament. These peaks (on the left of the figure) show that the heating is propagated toward the filament by conduction, because the energy transport is more efficient for the higher temperatures than for the lower ones. On the right side of the peaks the body of the filament seems to be in thermal equilibrium. Concerning the energy transport from the hot X arch to the filament, it cannot be provided by thermal conductivity because the lines of force between the hot X arch and the prominence, are about perpendicular. In conclusion we can say that the only likely heating mechanism is the irradiation of the filament by overspanning hot X ray emissive arches.

ENERGY INCREASE DURING THE HEATING PROCESS

It can be seen in figure 2 that the hot filament has reached an equilibrium state between the input and the lost of energy. The energy input is function of the radiation field of the X source and of the dilution factor. Using the density values (Mouradian et al., 1986) we are able to compute the thermic energy stored by the hot prominence, which is defined as :

$$E_k = \frac{3}{2} K \int_0^{\infty} [(n_e T)_H - (n_e T)_C] dT = 7 \cdot 10^3 \text{ erg cm}^{-3}$$

where the indexes H and C mean hot and cool.

The transition between the hot and cool parts of the filament must be studied with better time resolution than that of our sample, in order to understand the energy transport mechanism.

REFERENCES

- Malherbe, J.M., Simon, G., Mein, P., Mein, N., Schmieder, B., and Vial, J.C., 1983, *Adv. Space Res. Vol.2, N° 11*, p.53
- Mouradian, Z., Martres, M.J., and Soru - Escout, I., 1981
Proceed. of the Japan - France Seminar on Solar Physics
 eds. F. Moriyama and J.C. Hénoux, p. 195.
- Mouradian, Z., Martres, M.J., and Soru - Escout, I., 1986
 in preparation.
- Schmahl, E.J., Mouradian, Z., Martres, M.J., and Soru - Escout, I., 1982, *Solar Phys.* 81, 91.

ON THE THERMAL DURABILITY OF SOLAR PROMINENCES,
OR HOW TO EVAPORATE A PROMINENCE ?

J.M. Malherbe
Observatoire de Paris - Section de Meudon
92195 Meudon Principal Cedex - France

T.G. Forbes
University of New Hampshire
Space Science Center, Durham, NH 03824 USA

ABSTRACT

We investigate the thermal disappearance of solar prominences under strong perturbations due to wave heating, Ohmic heating, viscous heating or conduction. Specifically, we calculate how large a thermal perturbation is needed to destroy a stable thermal equilibrium, and find that the prominence plasma appears to be thermally very rugged. Its cold equilibrium may most likely be destroyed by either strong magnetic heating or conduction in a range of parameters which is relevant to flares.

I. INTRODUCTION

The thermal equilibrium of a prominence may be modeled using the approximate equation:

$$h\rho - \rho^2 Q(T) + j^2/\sigma + \eta v^2/\ell^2 + k_o T_c^{7/2}/L^2 = 0$$

where

$h\rho^2$ is the magnetic heating, assumed constant per unit of mass.

j^2/σ is the Ohmic heating. We will assume $\sigma = \sigma_o T_o^{3/2}$ with σ_o being a constant.

$\eta v^2/\ell^2$ is the viscous heating with $\eta = \eta_o T_o^{5/2}$, η_o being a constant.

$k_o T_c^{7/2}/L^2$ is the thermal conduction with T_c the coronal temperature and k_o a constant.

$\rho^2 Q(T)$ is the radiative cooling.

The quantities ρ , T , v , j have their usual meaning. Here L corresponds to the thermal length-scale along a magnetic field line from the photosphere to the prominence, and ℓ corresponds to the prominence thickness. $Q(T)$ is the piecewise cooling function given by Hildner (1974) in the form $Q(T) = \chi T^\alpha$ with:

Temperature (K)	χ (MKSA)	α
$T < 1.5 \times 10^4$	1.759×10^{-13}	7.4
$1.5 \times 10^4 < T < 8 \times 10^4$	4.290×10^{10}	1.8
$8 \times 10^4 < T < 3 \times 10^5$	2.860×10^{19}	0
$3 \times 10^5 < T < 8 \times 10^5$	1.409×10^{35}	-2.5
$T > 8 \times 10^5$	1.970×10^{24}	-1.0

We now consider separately the balance between radiative losses and magnetic heating, Ohmic heating, viscous heating, or conduction.

II. WAVE HEATING VS. RADIATION

This equilibrium is described by the following set of equations:

$$h_p \rho_p = \rho_p^2 Q(T_p) \text{ in the prominence (subscript p)}$$

$$h_c \rho_c = \rho_c^2 Q(T_c) \text{ in the corona (subscript c).}$$

Hence $Q(T_p)/Q(T_c) = \rho_c/\rho_p$, if $h_p = h_c$.

With $T_p = 10^6$ K and a ratio $\rho_p/\rho_c = 100$, we get a reasonable temperature of $T_p = 8425$ K for the prominence. Now for heating at constant gas pressure, this equilibrium is:

$$[Q(T)/Q(T_c)] (T_c/T) = h/h_c.$$

Thus, new equilibrium temperatures are given by $Q(T)/T = \text{constant} \times h$. For a given heating rate there are generally two solutions, a cold one and a hot one. The cold one does not exist anymore above $T_p = 8 \times 10^4$ K, due to the behavior of $Q(T)$, and the prominence disappears when

$$h > h_m = h_c Q(T_m) T_c / [Q(T_c) T_m].$$

With $T_m = 8 \times 10^4$ K, we get $h_m/h_c = 213.7$. Hence, a strong magnetic heating is necessary to evaporate a prominence. Such a heating could be produced by enhancement of the ambient coronal heating mechanism or by magnetic energy released during a flare.

III. JOULE HEATING VS. RADIATION

This balance results from the following equation:

$$j^2/\sigma = \rho^2 Q(T), \quad \text{with } \sigma = \sigma_0 T^{3/2}.$$

The current density j can be expressed in terms of the transverse magnetic field B_\perp by using the mechanical equilibrium condition:

$$\rho g = j B_{\perp}.$$

where g is the solar gravity. The equilibrium temperature is then given

$$T_p = [g^2 / (B_{\perp}^2 \chi \sigma_0)]^{1/(\alpha + 3/2)}.$$

With a transverse magnetic field B_{\perp} of 7G (Leroy et al. 1983), and a classical conductivity of $\sigma_0 = 8 \times 10^{-4}$ MKSA, we get an unusually low value of $T_p = 1092$ K. In order to obtain a realistic prominence temperature we need to increase the resistivity by a factor of 10^6 , and then we obtain a more reasonable temperature of 5157 K. Disrupting a prominence by current dissipation requires an even larger anomalous resistivity. With the same analysis as above, it is necessary to increase the anomalous resistivity yet further by a factor of 5×10^5 or 5×10^{11} altogether. Alternatively, one could also decrease the magnetic field by a factor of 700.

IV. VISCOUS HEATING VS. RADIATION

This equilibrium may be described by the following equation:

$$\eta v^2 / \rho^2 = p^2 Q(T) \quad \text{with } \eta = \eta_0 T^{5/2}.$$

Let us compare viscous and Ohmic heating. The viscous and magnetic Reynolds numbers R_e and R_m are given by:

$$R_e = v l \rho / \eta, \quad R_m = v l \mu_0 \sigma,$$

In prominence conditions ($T = 8000$ K, $\rho = 10^{-12}$ g cm $^{-3}$, $l = 3000$ km, and $v = 2$ km s $^{-1}$, Schmieder et al. 1984), we obtain with classical coefficients σ_0 and η_0 :

$$R_m \sim 4 \times 10^6 \text{ and } R_v \sim 10^8.$$

Therefore, viscous dissipation is smaller than ohmic heating. Note that this is not true in the corona (Hollweg 1985). The equilibrium temperature is given by

$$T_p = [(\eta_0 v^2) / (L^2 \rho^2 \chi)]^{1/(\alpha - 5/2)} = 870 \text{ K}.$$

In order to get a realistic prominence temperature on the order of 5700 K, we need to increase the viscous resistivity by a factor of at least 10^4 . Perturbing the equilibrium at constant gas pressure ($\rho T = \text{constant}$), and constant mass flux ($\rho v = \text{constant}$), we obtain the expression

$$Q(T) / T^{13/2} = \text{constant} \times \eta_0.$$

for the new temperature. A cold solution does not exist above $T_m = 1.5 \times 10^4$ K due to the behavior of $Q(T)$. Consequently, the prominence disappears when

$$\eta_0 > \eta_{om} = \eta_{op} [Q(T_m) / Q(T_p)] (T_p / T_m)^{3/2}.$$

With $T_p = 5700$ K we obtain an extra anomalous factor $\eta_{om} / \eta_{op} = 2.4$. This means that anomalous viscosity is a possible candidate to evaporate a prominence.

V. CONDUCTION VS. RADIATION

When conduction balances radiation, we have the following equilibrium:

$$\rho^2 Q(T) = k_0 T_c^{7/2} / L^2, \quad (k_0 = \text{constant}).$$

L is the thermal length-scale along magnetic lines coming from the photosphere to the prominence. With $\rho = 10^{-12}$ g cm⁻¹ and $T_c = 10^6$ K, this equation provides $T_p = 3556$ K with $L = 3 \times 10^4$ km, or $T_p = 4786$ K with $L = 10^4$ km or $T_p = 8917$ K with $L = 10^3$ km, so conduction is important in the energy budget of prominences. Now if we perturb this equilibrium at constant gas pressure and constant L , we obtain

$$Q(T)/T^2 = \text{constant} \times T_c^{7/2}.$$

A cold solution does not exist above $T_m = 1.5 \times 10^4$ K, and so the prominence disappears when

$$T_c > T_{cm} = T_c [Q(T_m)/Q(T_p)]^{2/7} (T_p/T_m)^{4/7} = T_c (T_m/T_p)^{2(\alpha-2)/7}.$$

With $L = 3 \times 10^4$ km, we get $T_{cm}/T_c = 9.21$. Hence, the appearance of a hot region in the neighborhood of a prominence is a possible mechanism to heat and evaporate a prominence. Such a hot temperature region could be the consequence of a flare.

ACKNOWLEDGEMENTS

This work was partially supported by the Observatoire de Paris, and by NASA Grant NAGW-76 to the University of New Hampshire.

REFERENCES

- Hildner, E., 1974, Solar Phys., **35**, 123.
 Hollweg, J., 1985, J. Geophys. Res., **90**, 7620.
 Leroy, J.L., Bommier, V., Sahal, S., 1983, Solar Phys., **83**, 135.
 Schmieder B., Malherbe, J.M., Mein P., Tandberg-Hanssen E., 1984, Astron. Astrophys., **136**, 81.

FILAMENT ERUPTION CONNECTED TO PHOTOSPHERIC ACTIVITY.

¹G.SIMON, ²L.GESZTELYI ¹B.SCHMIEDER AND ¹N.MEIN

1. Observatoire de Paris, DASOP (UA 326),
F-92195 Meudon Principal Cedex, France.
2. Debrecen Observatory, H-4010 Debrecen, Hungary.

I-INTRODUCTION

The solar prominences are known to be supported by a "stable" magnetic structure, with respect to the usual lifetime of the prominences. The continuous evolution of the structure may change suddenly into an activation or an eruption which are generally explained by the effect of reconnection processes in the magnetic structure.

The different types of activation of filaments have been well studied (see reviews from Tandberg-Hanssen (1974) and Martin (1980), but there is a lack of observations that can explain the origin of that activation.

We have studied two cases of activation of filaments that occurred in regions of intense magnetic activity (Martin et al., 1983, and Gesztelyi, 1984). The simultaneous observations from Debrecen (white light and H-alpha filtergrams), and from Meudon (Magnetograms, MSDP Dopplergrams and intensity maps in H-alpha) gave us a complementary set of data from which we can produce evidence of the influence of the photospheric magnetic field on the destabilization process of the filaments. On June 22, 1980, the eruption of the filament is associated to the motion of pores, which are the manifestations of emerging flux knots (Malherbe et al., 1983, Simon et al., 1984). On September 3, 1980, the twisting motions in the filament are associated to the birth of a pore in its neighbourhood (Schmieder et al., 1983, Gesztelyi et al., 1983, Schmieder et al., 1985).

II-RELATION WITH THE MOTIONS OF PORES.

Located in the Hale active region 16918, the observed filament lies along a neutral line roughly directed East-West, near the disk center on June 22, 1980. It crosses a region of enhanced magnetic field to which corresponds a bright plage in the H-alpha line. Two pores have been observed at Debrecen Observatory (Martin et al., 1983) on each side of the filament

The activity of the region may be summarized by these main features (Simon et al., 1984) :

- The southern pore began to move toward the filament (northwards) at approximatively 1230 UT, at a velocity of 0.2 km/s (figure 1) ;

- The brightest point in the southern plage, corresponding to the moving pore location, began the same motion at 1259 UT, with a velocity of 20 km/s (figure 2) ;

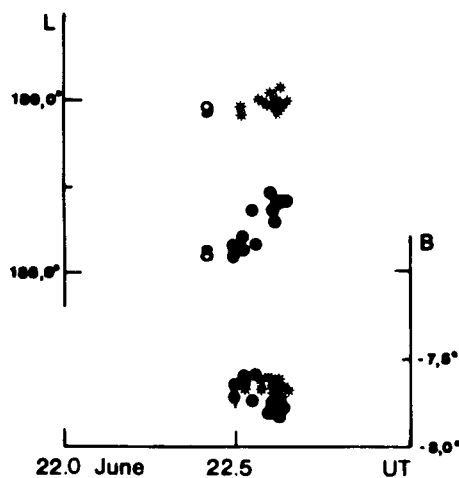


Fig.1 Carrington coordinates versus time of the pores 8 and 9 on June 22, 1980

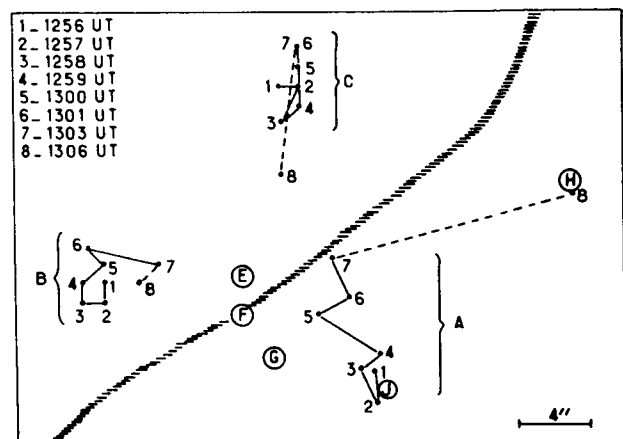


Fig.2. Location of the maxima of brightness in plage near filament. The maximum A is related to the pore 8.

- A two-ribbon flare occurred at 1305 UT on each side of the filament ;

- The prominence material continues to travel through the corona with a velocity projected on the disk of 120 km/s.

The history of these events leads to think that the evolution of the photospheric magnetic field is at the origin of the destabilization of the filament and of the onset of the two-ribbon flare, by the reconnection processes that are involved.

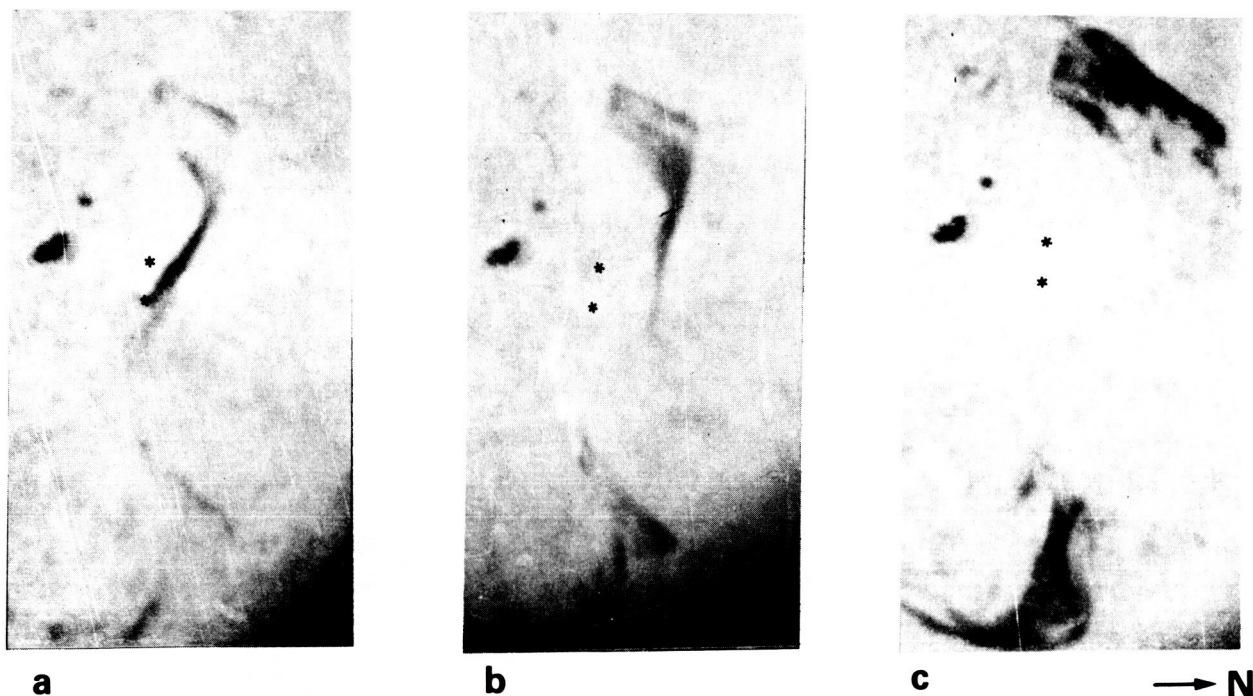


Fig.3. Debreceen filtergrams (H-alpha +1A) at 1302 UT (a), 1305 UT (b), and 1312 UT (c) on June 22, 1980, showing the motion of the absorbing material. Stars give the position of the pores.

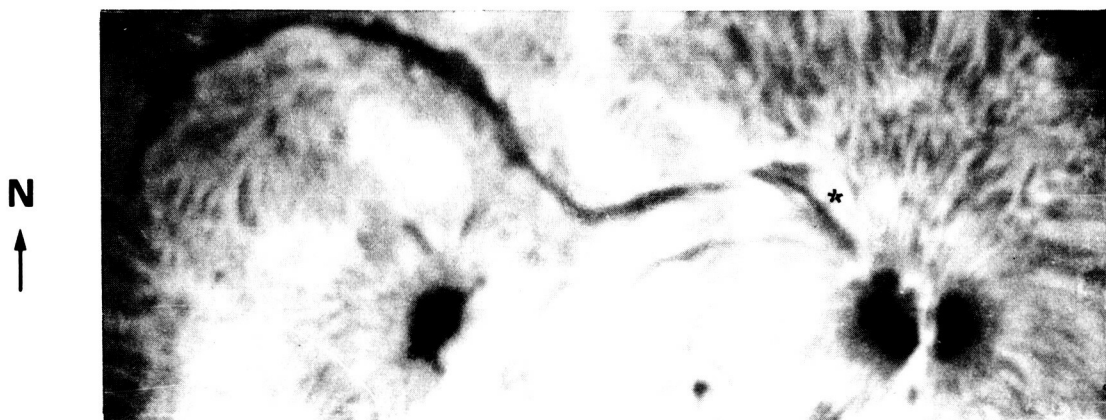


Fig.4. Debreceen H-alpha filtergram at 0750 UT on Sept.3, 1980. The position of the pore is indicated by a star.

ORIGINAL PAGE IS
OF POOR QUALITY

III-RELATION WITH THE BIRTH OF A PORE.

In the Hale active region 17098, the filament lies at North of the sunspots, at the location 10N-10W on September 3, 1980. Gesztelyi and Kondas (1983) observed the birth of a pore, at approximately 6 arc seconds north of the filament, by 0743 UT. (figure 4). They report that the filament was activated at 0753:54 UT, as the filament began to be visible on H-alpha + 1A filtergrams.

Schmieder et al. (1985) have analysed this activation that was observed at Meudon observatory in the H-alpha line with the MSDP. They report that the H-alpha line began to broaden in the filament by 0748 UT. At 0752:19 UT, a subflare, southwards close to the filament, was accompanied by a disturbed velocity field in the filament with parts rising (+10km/s) and other ones falling (-7km/s) (figure 5). Later on, the filament was disturbed by twisting motions. In that case, the activation may be related to the emergence of flux near the filament.

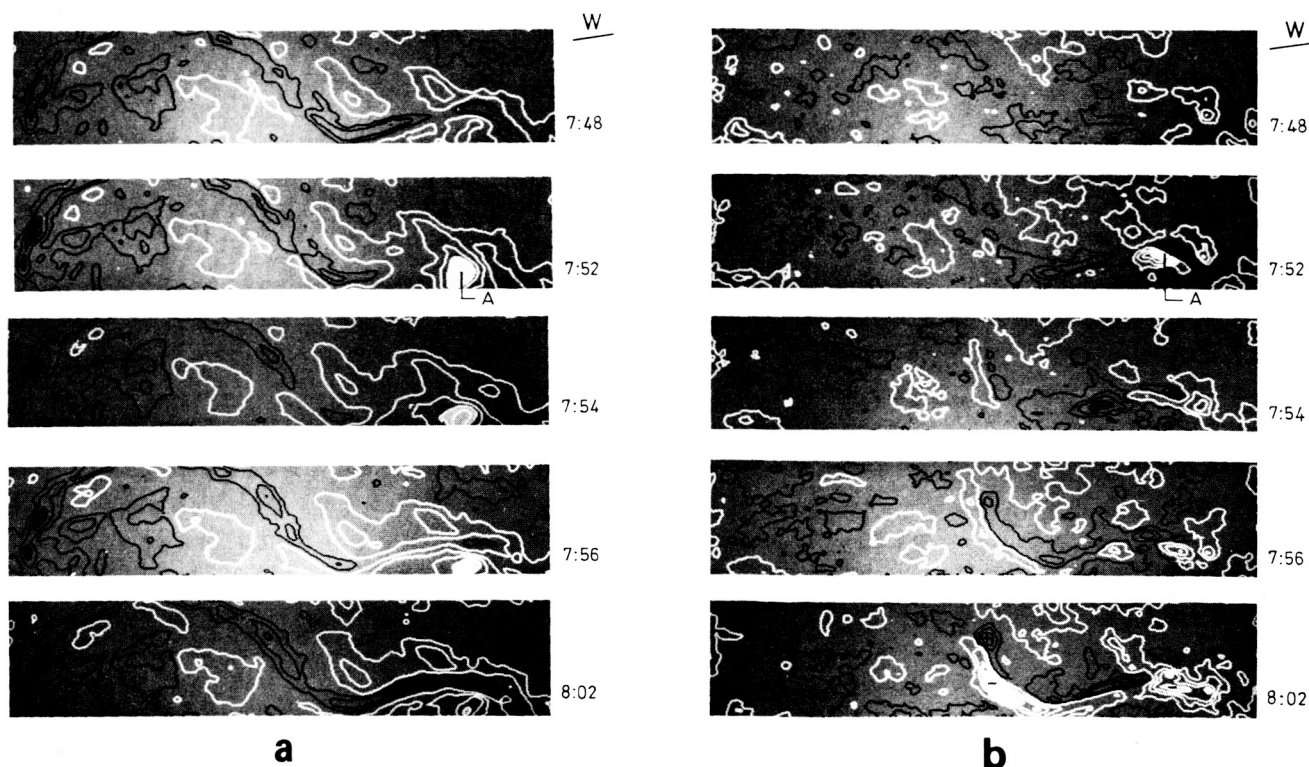


Fig.5. H-alpha intensity (a) and velocity (b) at different times on Sept.3,1980. Black lines correspond to the filament in (a) and to upward velocity in (b). Point A is the subflare kernel.

IV-CONCLUSION

These observations give evidence of the direct influence of the emerging flux evolution on the activation of these filaments and the onset of flares. They may be well described by the theoretical models built upon the interaction of a growing dipole with a "stable" magnetic structure. The type of activation (eruption and ribbon flare like on the first case, or twisting motions and subflare like on the other one) may depend on the structure of the local magnetic field. It is necessary to develop simultaneous observations of the photosphere and the chromosphere with very good time and space resolution to determine the initial conditions that may be used in modelling problems.

REFERENCES

- Gesztelyi, L., 1984, "Consecutive homologous flares and their relation to sunspots motions", *Adv. Space Res.*, 4, n°7(19).
- Gesztelyi, L., and Kondas, L., 1983, "The development of activity in Hale region 17098", *Publ. Debrecen Obs.*, 5(133).
- Malherbe, J.M., Simon, G., Mein, P., Mein, N., Schmieder, B., and Vial, J.C., 1983, "Preflare heating of filaments", *Adv. Space Res.*, 2, n°11(53).
- Martin, S.F., 1980, "Preflare conditions, changes and events", *Solar Phys.*, 68 (217).
- Martin, S.F., Deszo, L., Gesztelyi, L., Antalova, A., Kucera, A., and Harvey, K.L., 1983, "Emerging magnetic flux, flares and filaments - FBS interval 16-23 June 1980", *Adv. Space Res.*, 2, n°11(39).
- Schmieder, B., Malherbe, J.M., and Raadu, M.A., 1984, "Magnetic instabilities in solar filaments : models of twisting motions and ejecta". *Proceedings of Fourth European meeting on Solar Physics*, ESA SP-220 (273).
- Schmieder, B., Raadu, M.A., and Malherbe, J.M., 1985, "Twisting motions in a disturbed solar filament", *Astron. Astrophys.*, 142 (249).
- Simon, G., Mein, N., Mein, P., and Gesztelyi, L., 1984, "Preflare activity of solar prominences", *Solar Phys.*, 93 (325).
- Tandberg-Hanssen, E., 1974, "Solar prominences", D.Reidel Publ. Co., Dordrecht, Holland.

MAGNETIC FIELD RE-ARRANGEMENT AFTER PROMINENCE ERUPTION

R.A. Kopp

Los Alamos National Laboratory, Los Alamos, NM 87545

G. Poletto

Osservatorio Astrofisico di Arcetri, Firenze, Italy

INTRODUCTION

It has long been known that magnetic reconnection plays a fundamental role in a variety of solar events. Although mainly invoked in flare problems, large-scale loops interconnecting active regions, evolving coronal hole boundaries, the solar magnetic cycle itself, provide different evidence of phenomena which involve magnetic reconnection. A further example might be given by the magnetic field rearrangement which occurs after the eruption of a prominence. Since most often a prominence reforms after its disappearance and may be observed at about the same position it occupied before erupting, the magnetic field has to undergo a temporary disruption to relax back, via reconnection, to a configuration similar to the previous one.

The above sequence of events is best observable in the case of two-ribbon (2-R) flares but most probably is associated with all filament eruptions. Even if the explanation of the magnetic field rearrangement after 2-R flares in terms of reconnection is generally accepted, the lack of a three-dimensional model capable of describing the field reconfiguration, has prevented, up to now, a thorough analysis of its topology as traced by H α /X-ray loops. The purpose of the present work is to present a numerical technique which enables one to predict and visualize the reconnected configuration, at any time t , and therefore allows one to make a significant comparison of observations and model predictions throughout the whole process.

THE 3-D MODEL

Some years ago, Altschuler and Newkirk (1969) and Altschuler et al. (1977) developed a method to calculate the global magnetic structure of the corona, assumed to be potential, from the measured line of sight component of the photospheric magnetic field. These authors solved Laplace's equation $\nabla^2 \psi = 0$ for the scalar potential ψ , in spherical coordinates, assuming as boundary conditions the observed values of the magnetic field. In the domain between $r = R_\odot$ and $r = R_w$, which represents the height at which $\psi = 0$ (or, equivalently, where the magnetic field becomes radial) ψ is given by

$$\psi(r, \theta, \phi) = r_{\odot} \sum_{n=1}^{\infty} \sum_{m=0}^n P_n^m(\theta) \left\{ \left[c_n^m \left(\frac{r}{r_{\odot}} \right)^n + (1 - c_n^m) \left(\frac{r_{\odot}}{r} \right)^{n+1} \right] g_n^m \cos(m\phi) \right. \\ \left. + \left[d_n^m \left(\frac{r}{r_{\odot}} \right) + (1 - d_n^m) \left(\frac{r_{\odot}}{r} \right)^{n+1} \right] h_n^m \sin(m\phi) \right\}$$

where $c_n^m = d_n^m = - \left[\left(\frac{r_1}{r_{\odot}} \right)^{2n+1} - 1 \right]^{-1}$; $P_n^m(\theta)$ are the Legendre functions of degree n , order m , and g_n^m, h_n^m must be determined from measurements. Once ψ is known, the magnetic field components at any point (r, θ, ϕ) are given by

$$B_r = - \frac{\partial \psi}{\partial r} \quad B_{\theta} = - \frac{1}{r} \frac{\partial \psi}{\partial \theta} \quad B_{\phi} = - \frac{1}{r \sin \theta} \frac{\partial \psi}{\partial \phi}$$

We refer the reader to the above-quoted references for more details on the method. Although traditionally used to derive global coronal fields from photospheric fields measured over a solar rotation, in principle nothing prevents the application of this technique to the study of the temporal variation of the coronal field topology above limited solar areas, provided that, for each field calculation, boundary conditions are taken from single observations. Moreover, varying the height R_w where the magnetic field becomes radial provides a means of representing a reconnection process where fields have reconnected only below R_w . A time-dependent situation may therefore be simulated, even if the $R_w = R_w(t)$ profile can be determined only a posteriori, matching the observed with the analytically derived topology.

The practical application of the method meets however with severe problems whenever a high resolution magnetic field representation is required, due to the dramatic increase of computing time with the size of the input data matrix and the value $n = N$ at which the harmonic series is truncated. To alleviate these difficulties we consider data from a limited sector of the Sun and fill the outside regions with periodic repetition of the field pattern within the sector. With this procedure both the number of input data and the number of coefficients g_n^m, h_n^m is smaller, and as a consequence the computing time is drastically shortened. For example, fields given with about 30 arcsec resolution over a sector 30° wide can be reconstructed with $N = 63$ in about 10^h , using a VAX 750.

MAPPING CORONAL FIELDS

Despite the time reduction achieved by the above-mentioned procedure, the overall computing time still remains rather long. However, much insight into the reconnecting topology can be obtained from model fields, given with coarse resolution and easily reconstructed in shorter times. Figures 1 and 2 show the magnetic field topology of such a model field whose negative and positive polarities are oppositely stretched along the East-West direction. Individual maps within each figure differ in the source surface height: the two figures differ in the criterion adopted for fieldline selection. Figure 1 shows maps with fieldlines originating from randomly chosen photospheric footpoints; in Figure 2 only those fieldlines which close at the height of the source surface are shown.

The two representations complement each other: although no observed configuration will at any time look like any maps of Figure 2, a comparison of the two kinds of

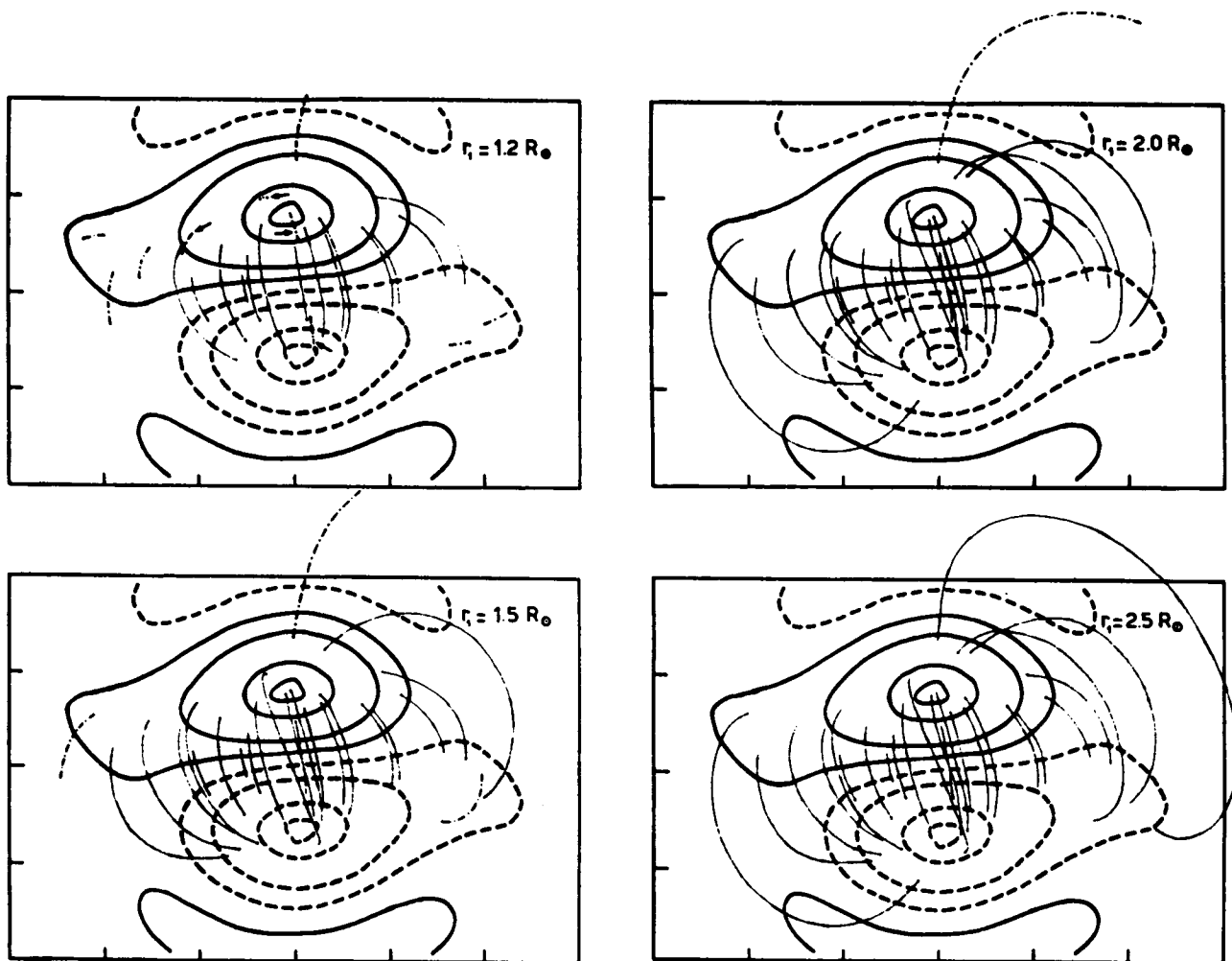


Figure 1. Randomly chosen field lines for the bipolar model field described in the text, superimposed on isogauss contours of the surface field. Dot-dashed fieldlines are open.

representation is necessary to ensure that no relevant structure is missing from the more realistic topologies of Figure 1.

Examination of Figures 1 and 2 shows that field lines bridging directly across the neutral line and closing at relatively low heights, connect footpoints located at about the same longitude, whereas peripheral field lines, which close at much greater altitudes may connect widely separated longitudes. When analyzing observed configurations this behavior may be interpreted erroneously as evidence for a non-potential, or sheared, field, since field lines appear not to cross the neutral line at right angles. However taking into account the height shift in the orientation of the neutral line, one can easily verify that this is not the case.

The May 21, 1980 flare - accompanied by a coronal transient and a growing system of post-flare loops (de Jager and Švestka, 1985), providing diverse evidence for field disruption - constitutes an ideal case to test the model capabilities. At the time of this writing a coronal field mapping, at a number of different source heights, has not yet been completed. Therefore, in Figure 3 we give only a map of the ob-

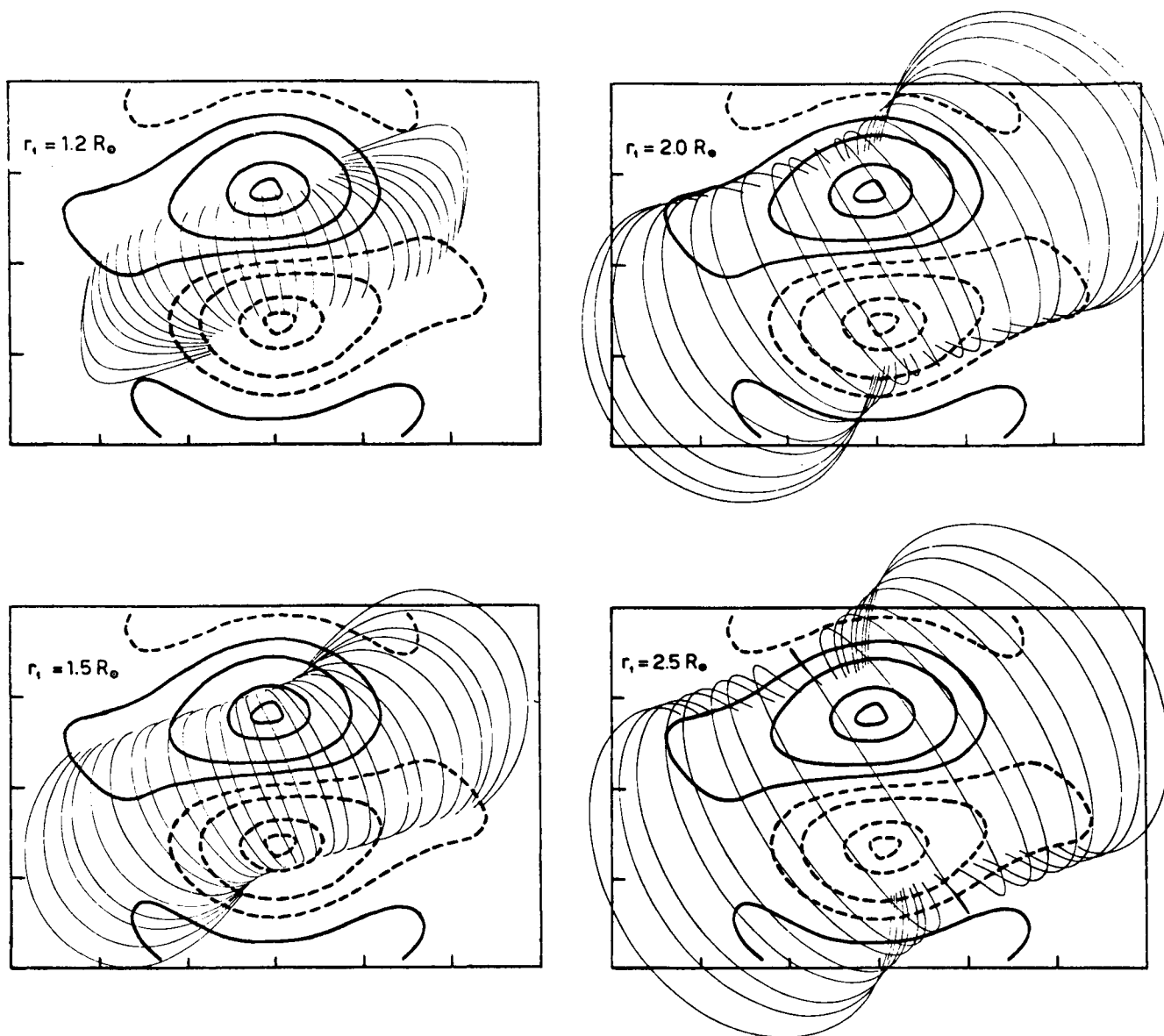


Figure 2. Arcade of loops which form just as the source surface reaches the indicated height, for the same model field as was used in Figure 1.

served and reconstructed photospheric field. Magnetograph observations, originally taken with a 2 arcsec resolution, have been averaged to yield data with 32 arcsec resolution. The surface field obtained using Legendre functions up to $N = 87$ yields nearly a perfect representation of this input field configuration.

FUTURE PERSPECTIVES

The main area of applicability of the method lies in the comparison between observed and computed reconnecting configurations. Usually a filament erupts more than once in its lifetime; thus the question arises whether after each eruption the reconnected configuration is potential and only afterwards energy starts building up

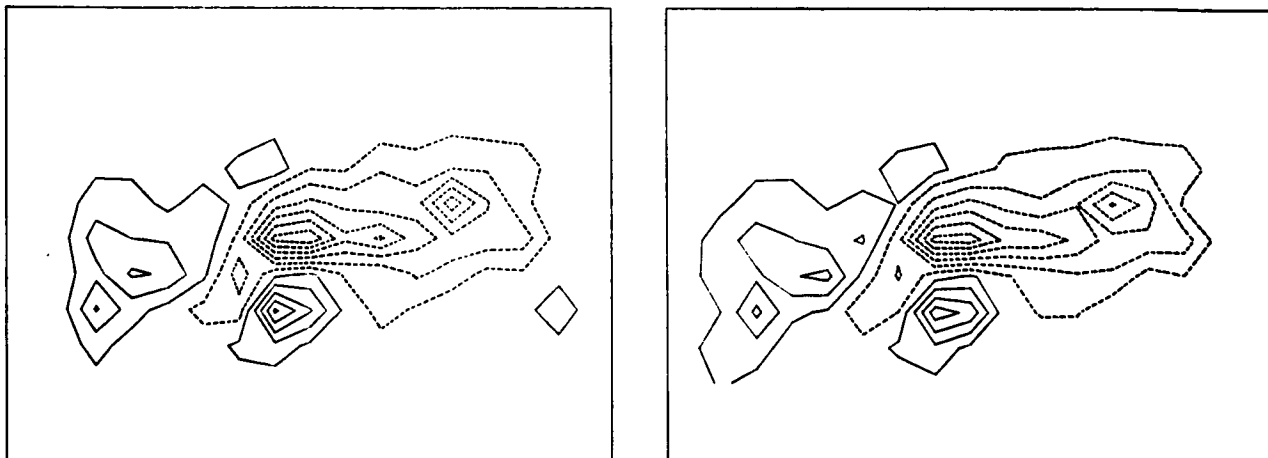


Figure 3. Contour plots of the observed (left) and reconstructed (right) line-of-sight surface magnetic field for the active region of the 21 May 1980 flare.

again, or whether reconnection occurs to a non-potential field, thus not releasing all of the stored energy in any single event. To ascertain which of the above hypotheses is correct, it will suffice to check the observed time history of magnetic field topologies against the potential ones.

Closely related to the above topic is the possibility of identifying the nature of the giant arches repeatedly observed by the HXIS instrument onboard SMM (Švestka, 1982, 1984). These gigantic structures, observed in association with 2-R flares, could result either directly from reconnection at high altitudes (as the topology of the model field shown in Figures 1 and 2 might suggest) or from the upper disconnected loops which overlie the reconnecting arcade (Švestka, 1982). Future observations of the magnetic field rearrangement after filament eruptions, possibly in the absence of flares, will help to establish whether giant arches are characteristic of all such events or only of the most energetic ones.

Finally, the method allows one to estimate the amount of energy released by relaxation towards a potential configuration. This liberated energy has to be at least of the same order of magnitude as the thermal energy content of the loops, if reconnection is the sole energy source of the newly formed closed structures. Estimates of this sort have already been performed in idealized 2-D configuration, but have never been applied to real 3-D topologies.

REFERENCES

- Altschuler, M.D. and Newkirk, G., Jr.: 1969, *Solar Phys.* 9, 131.
 Altschuler, M.D., Levine, R.H., Stix, M. and Harvey, J.: 1977, *Solar Phys.* 51, 345.
 De Jager, C. and Švestka, Z.: 1985, *Solar Phys.* 100, 435.
 Švestka, Z., Stewart, R.T., Hoyng, P., van Tend, W., Acton, L.A., Gabriel, A.H., Rapley, C.G. and 8 co-authors: 1982, *Solar Phys.* 75, 305.
 Švestka, Z.: 1984, *Solar Phys.* 94, 171.

A DYNAMIC MODEL OF FILAMENT ERUPTIONS AND TWO RIBBON FLARES

N. Paul M. Kuin (SASC Technologies Inc)
Piet C. H. Martens (NRC research associate)
NASA-Goddard Space Flight Center
L.A.S.P., CODE 682,
Greenbelt, MD 20771

INTRODUCTION

Two basically different models for the filament equilibrium by Kippenhahn and Schluter (1957) and Kuperus and Raadu (1974) have appeared in the literature. In both models the filament is considered to carry a current. The force balance in the Kippenhahn and Schluter model is between the downward force of gravity and the upward Lorentz force between the filament current and the horizontal component of the background field due to bipolar regions close to the filament. The way the current circuit is closed in the photosphere is not considered in this model. In the Kuperus and Raadu model the downward gravitational force is balanced by the upward Lorentz force on the filament current from the magnetic field of a virtual mirror current of opposite sign. The mirror current is situated below the photosphere and closes the circuit in their model.

A further analyses by van Tend and Kuperus (1978) added the force due to the horizontal component of the background field to the Kuperus and Raadu model. The background magnetic field is assumed to be due to bipolar regions near the filament, and has the opposite sign to the field in the Kippenhahn and Schluter model. An interesting argument is presented by van Tend and Kuperus, in which they show that in the magnetic field configuration they present the currents tend to merge above the neutral line. Van Tend and Kuperus also showed that there is a maximum current above which non-equilibrium of the filament exists. They argue that once the filament surpasses this maximum value for the current, an eruption results. They suggest that this is related to the mass ejection in a solar flare, filament disappearance before a flare and the disappearance brusque of the filament.

In order to obtain a better model which actually describes these phenomena, the evolution of the filament has to be considered in detail. A first attempt was recently presented by Kaastra (1985). Kaastra did not formulate the precise energy balance equations for the problem, as is done in the present work. He used the a semi-empirical velocity law for filaments, where he assumes a negligible acceleration of the filament. Kaastra closed his equations by using an assumption about the relation between the height and the current of the filament. Thus he was able to model the eruption of the filament itself. He further included the existence of a current sheet at the neutral point. In the absence of magnetic field, as is the

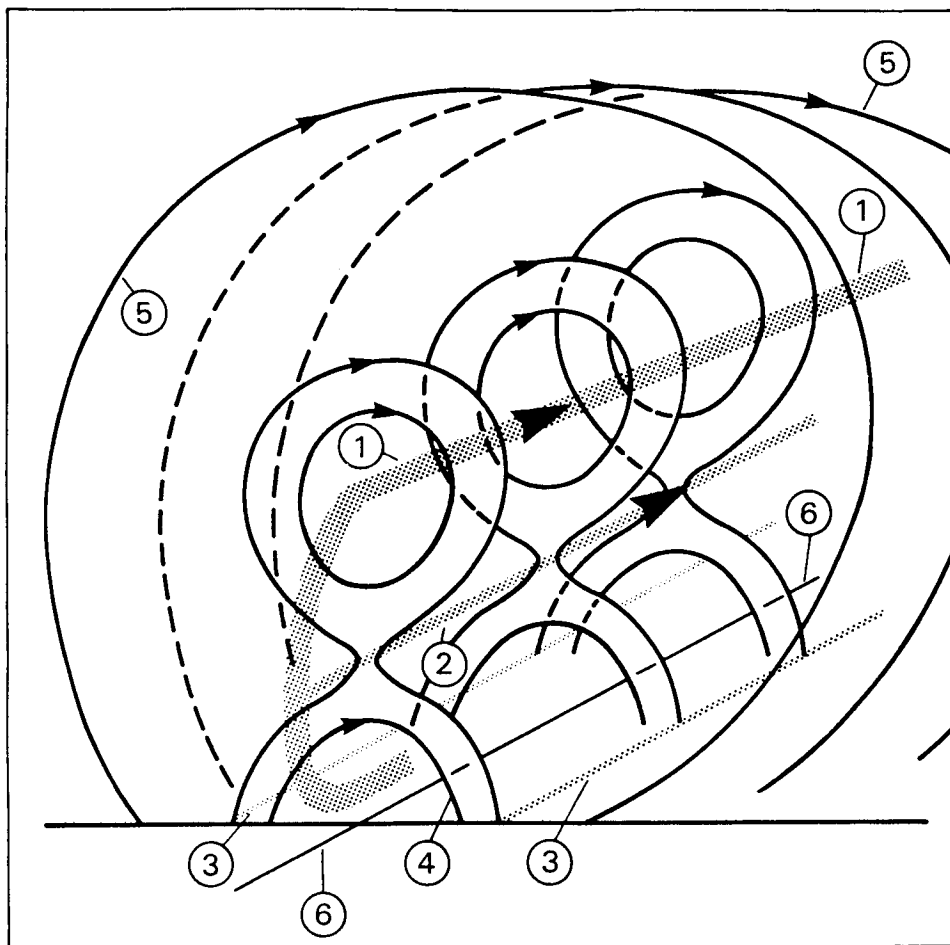


Fig. 1 A schematic of the field and current configuration during the filament eruption. 1. Filament current. 2. X-type neutral line. 3. Flare ribbons. 4. Closed fieldlines. 5. Background field. 6. Line of polarity reversal.

case at the neutral point, the rise of the current carrying filament induces a large electric field at the neutral point during the eruption. The resulting electron acceleration may then cause the hard X-rays observed during the flare. Kaastra compared his model to the May 16, 1981 flare, and found a good agreement with the observations.

In the present model not only the force balance, but also the energy balance of the filament is taken into account. Thus a fully closed system of equations is obtained, that describes the evolution of the filament, first in force equilibrium during the current build-up phase, then in the non-equilibrium phase before the eruption, and the eruption itself. A neutral point appears above the photospheric surface in the non-equilibrium phase, but long before the eruption. We find that although the filament itself may be in non-equilibrium, the evolution may still be slow up to the height where the eruption takes place. The eruption of the filament itself causes a large induced electric field at the neutral point which leads to the observed flare phenomena (see also Kaastra, 1985, for a detailed description)

THE DYNAMIC FILAMENT ERUPTION MODEL

We consider the filament as a line current, because the thickness of the filament is much smaller than its length or height above the photosphere.

Before the emergence of the X-type neutral point above the photosphere three forces act on the filament: gravity, the Lorentz force on the filament current due to the background field, and the Lorentz force on the filament current from the field generated by the chromospheric return current. After the emergence of the X-type neutral point above the photosphere two additional forces are present: the Lorentz force on the filament current from the field generated by the current located at the X-type neutral point, and Lorentz force due to the field generated by its return current in the chromosphere. Hence the force balance equation is:

mass filament \times acceleration = sum of Lorentz forces on the filament + gravity.

We assume that the mass of the filament is conserved, so that we do not have to solve the continuity equation.

It is suggested by observations that photospheric footpoint motions increase the shear of the field over the polarity-reversal line during the build-up phase. The stretching of field lines by footpoint motions gives rise to energy input into the filament, reflected in an increase in its current. Since the photospheric resistivity is high compared to that in the corona, we model the energy supply to the filament as an applied voltage with a large internal resistance in the circuit of the filament and return current. (For a discussion of the details of conversion of observed parameters to these circuit parameters, see Martens, 1986). The energy input into the filament circuit results in work done against the magnetic and gravitational forces acting on the filament, a change in its kinetic energy, and

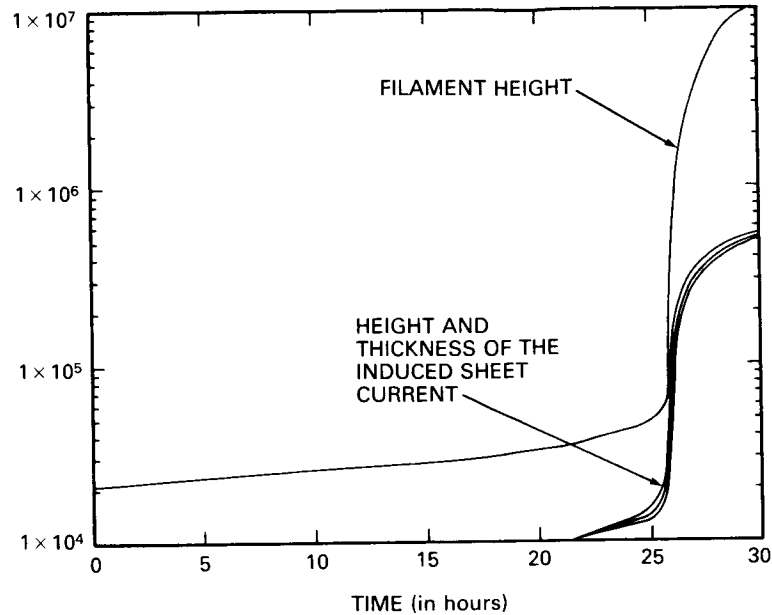


Fig. 2. The height of the filament and current sheet (in km) as a function of time (in hours). Zero time is the moment of emergence of the X-type neutral point above the photosphere, and lies in the non-equilibrium regime (no static solution).

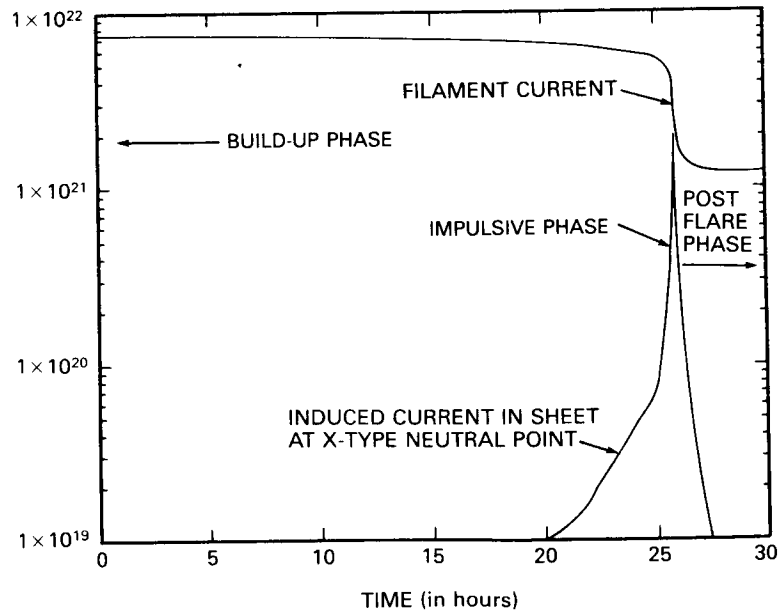


Fig. 3. The current of the filament and the induced current at the X-type neutral line (in units of statamp).

compensates for the resistive losses in the filament circuit.

The current sheet equations are 1. the force balance which determines the height of the sheet, 2. the energy equation describing the current induced by a change in the flux through the current sheet circuit. 3. the continuity equation which relates the induced current and the width of the current sheet (Syrovatskii, 1971, Kaastra, 1985). A detailed discussion will be published by Martens and Kuin (1986).

The equations describing the evolution of the filament are a sixth order system of ordinary non-linear equations, and are solved numerically. The initial filament height, velocity and current are found by assuming force-equilibrium. The parameters in the problem are the thickness of the filament, the depth and strength of the dipole representing the background field, the mass of the filament, and the resistivity in the filament and sheet circuit. Values derived for the May 16, 1981 flare were used.

RESULTS

In Figs. 2 and 3 the results for the May 16, 1981 flare are shown. The build-up of the filament current at earlier times was very slow. At $t=-40$ hours the current is at 0.96 of the current at $t=-10$ hours. Notice that the slow evolution continues, even when the filament is already in the non-equilibrium regime (past $t=-10$ hours). A neutral sheet is formed below the filament far before the eruption. The current induced by the change in flux through the current sheet circuit, due to the rising filament, is large enough for acceleration of the whole electron distribution (Kaastra, 1985), and this is the cause of the hard X-ray flare.

In order to make a comparison with the observations of a two-ribbon flare we need: -a magnetogram, -the height of the filament as a function of time, -an observational estimate of the energies in the mass ejection, the interplanetary blastwave, and the electromagnetic energy radiated away during the flare, -an estimate of the mass of the filament.

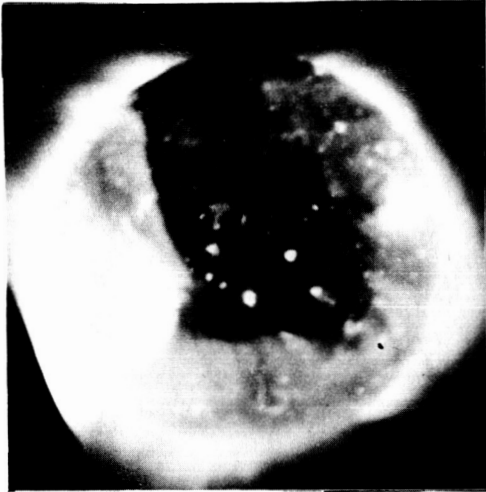
REFERENCES

- Kaastra, J.S., 1985, "Solar Flares: An Electrodynamic Model", thesis, University of Utrecht.
- Kippenhahn, R., and Schluter, A., 1957, *Z. Astrophysik* 43, 36.
- Kuperus, M., and Raadu, M.A., 1974, *Astron. Astrophys.* 31, 189.
- Martens, P.C.H., and Kuin, N.P.M., 1986, in preparation.
- Martens, P.C.H., 1986, submitted to *Solar Phys.*
- Syrovatskii, S.I., 1971, *Sov. Phys. J.E.T.P.* 33, 933.
- van Tend, W., and Kuperus, M., 1978, *Solar Phys.* 59, 115.

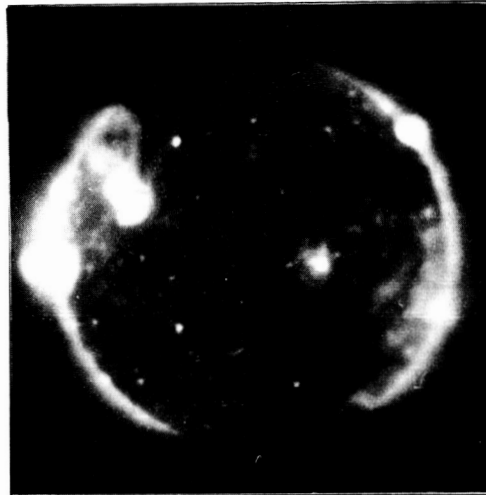
CORONA

ORIGINAL PAGE IS
OF POOR QUALITY

CORONAL X-RAY OBSERVATIONS 1974 - 1981



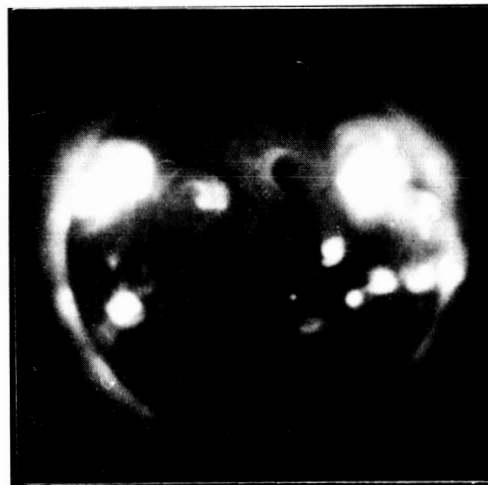
27 JUNE 1974



17 NOVEMBER 1976



31 JANUARY 1978



13 FEBRUARY 1981

High spatial resolution images of the solar corona obtained with an X-ray grazing incidence rocket payload. The images are representative of the variations in coronal structure and emission over the solar cycle. They were obtained near the end of the decline of Cycle 20 (1974), at activity minimum (1976), during the rise of Cycle 21 (1978), and just after the recent activity maximum (1981). Courtesy of the Solar Physics Group, American Science and Engineering, Inc.

PRECEDING PAGE BLANK NOT FILMED

Photo Courtesy of

D. Webb

American Science and Engineering
Cambridge, Mass.

LARGE SCALE STRUCTURE OF THE CORONA

M.R. Kundu
 Astronomy Program
 University of Maryland
 College Park, MD 20742

INTRODUCTION

Studies of large scale structures of the sun's corona are best done from synoptic observations. For the latter, we need dedicated imaging instruments. At the present time, we have two such instruments in the radio domain, both at meter-decameter wavelengths. The first one is the Nançay (France) one-dimensional radioheliograph at 169 MHz which produces two-dimensional solar images in about 10-12 hours by earth rotation aperture synthesis. The second one is the Clark Lake Radio Observatory multifrequency radioheliograph which produces two-dimensional images of the sun in the frequency range 15-125 MHz with a time resolution of $\sim 1/2$ second by aperture synthesis technique in the same manner as does the Very Large Array (VLA). We do not have any dedicated imaging instrument in microwaves, although at 20 cm wavelength some isolated studies of the large scale structure of the sun's corona can be made with the VLA.

In the optical domain, studies of large scale structure are done with several instruments: (1) Groundbased white light K-coronameter at Mauna Loa; (2) Solwind white light coronagraph on the satellite P78-1; (3) coronagraph polarimeter on Solar Maximum Mission satellite; (4) Kitt Peak magnetograph; (5) Kitt Peak He I spectroheliograph; and (6) H α filtergrams.

In this chapter we present a brief description of some radio results obtained with meter-decameter radioheliographs (M.R. Kundu, 1986 and P. Lantos and C.E. Alissandrakis, 1986). An optical study based upon synoptic data of pB, H α filtergrams and large scale B-fields is presented by M. McCabe. This is followed by two theoretical papers by R. Wolfson (1986) and T.J. Bogdan and B.C. Low (1986) on the interpretation of CME's and modeling of three-dimensional corona.

The studies of Kundu (1986) and Lantos and Alissandrakis (1986) are primarily concerned with a comparison of radio maps with white light pictures and He 10830Å spectroheliograms. These maps exhibit coronal streamers and coronal holes, and their evolution. The streamers appears as elongated lobes of enhanced brightness; the coronal holes appear as brightness voids in the radio-heliograms. The combined data (in radio and optical domains) can lead to determinations of electron temperatures and densities as a function of altitude in both streamers and coronal holes. When transient burst activity takes place, such as type III or type II bursts, one can trace the path of exciting electron streams or shock waves with respect to the streamer. Synoptic charts produced both from radio and optical data permit us to follow the evolution of streamers and holes, and to detect any abnormal feature when a transient, such as a coronal mass ejection (CME) event or radio burst, takes place.

McCabe used synoptic data during 18 solar rotations (1982-83): (1) daily polar plots of pB distribution (Mauna Loa); (2) low resolution synoptic B-field

maps (Stanford); (3) H α synoptic maps with inferred neutral lines; and (4) H α filtergrams. The objective of her study was to investigate the relationship between the large scale photospheric magnetic field structure and the coronal polarized brightness (pB) distribution. The results obtained show a fairly good association between coronal structures and global photospheric neutral lines, which relate to heliospheric current sheets. However she finds that there are other neutral lines on a smaller scale which have no coronal counterparts. These neutral lines generally lie at the boundaries of unipolar field areas containing coronal holes or of mid-latitude unipolar regions within such areas.

Wolfson studied quasistatic evolution of magnetostatic coronal structures by developing a series of models that describe global magnetostatic equilibrium of an axisymmetric corona including gravity, gas pressure, and the Lorentz force. These models are based on the equation of Hundhausen, Hundhausen and Zweibel (1981) that includes a free function describing the distribution of coronal current. These models contain a parameter representing a deviation from a potential field and therefore related to amount of excess mass loaded into the corona. Wolfson (1986) studied four different models, and found interesting agreement between models and observations in several cases, in terms of the predicted amount of excess mass in the corona prior to a mass ejection.

Bogdan and Low (1986) worked on modeling three-dimensional corona by constructing a class of magnetostatic atmosphere in a $1/r^2$ gravity. Their solutions possess electric currents distributed continuously in space in the lower atmosphere and directed perpendicular to the gravitational force. They treat the problem in a fully 3-dimensional geometry, allowing for an arbitrary prescription of normal magnetic flux at the lower boundary of the atmosphere. The latter feature allows them to use KPNO magnetograms as observational inputs into their models. The coronal density structures predicted by the models can be compared with those given in the HAO C/P data.

FUTURE PROBLEMS

Several future problems have been identified by the group.

(1) Development of three-dimensional theoretical models including current distribution and prediction of density values and their comparison with the observed ones.

(2) Detailed comparison of synoptic radio and white light pictures; and determination of temperature distribution in the corona. Such comparison will also lead to detection of transients such as CME's and radio emission for which energetic electrons are of coronal origin (for example, as a result of streamer disruption phenomena).

(3) Synoptic soft X-ray and radio imaging of the corona and white light coronagraph measurements. Any other measurements that pertain to temperature and density structure of the corona should be undertaken.

REFERENCES

Bogdan, T.J. and Low, B.C., "Three-Dimensional Magnetostatic Model of the Large-Scale Corona", 1986 (This proceedings).

Hundhausen, J.R., Hundhausen, A.J., and Zweibel, E.G., 1981, J. Geophys. Res., 86, 1117.

Kundu, M.R., "Large Scale Study of the Sun's Radio Corona", 1986 (This proceedings).

Lantos, P. and Alissandrakis, C.E., "Synoptic Study of the Corona at Meter Wavelengths", 1986 (This proceedings)

McCabe, M.K., "The White Light Corona and Photospheric Magnetic Fields", 1986 (This proceedings).

Wolfson, R., "Quasistatic Evolution of Magnetostatic Coronal Structures", 1986 (This proceedings).

LARGE SCALE STRUCTURE OF THE SUN'S RADIO CORONA

M. R. Kundu
Astronomy, Program
University of Maryland
College Park, MD 20742, USA

ABSTRACT

We present results of studies of large scale structures of the corona at long radio wavelengths, using data obtained with the multifrequency radioheliograph of the Clark Lake Radio Observatory. We show that features corresponding to coronal streamers and coronal holes are readily apparent in the Clark Lake maps.

INTRODUCTION

The Clark Lake multifrequency radioheliograph, which has been operating for several years, produces 64×64 pixel solar images (of 0.5 HPBW \times 0.5 HPBW per pixel) within the frequency range 20 – 125 MHz. The field of view and the angular resolution of the telescope are both frequency dependent. The field of view is approximately $2.3^\circ \times 1.9^\circ$ at 80 MHz, when observing at the zenith. It scales inversely with frequency (in both dimensions), and is larger because of foreshortening when observing away from the zenith. The angular resolution ranges from 2.7 arc min at 125 MHz, to 17 arc min at 20 MHz. The telescope is electronically steered for pointing in different sky directions, and is continuously tunable across the entire frequency range. In practice, one is restricted to observe within interference-free bands. Several such bands are available. In this paper we shall concentrate on the results obtained at 38.5 , 50.0 and 73.8 MHz. The sensitivity of the system is about 1 Jy (10^{-4} solar flux units) at all frequencies. At the present time we have the capability of producing two-dimensional images of the Sun at the rate of one picture every 0.6 seconds. We use this fast rate of imaging only when the Sun is active. For synoptic studies of the Sun, we use much slower time resolution (~ 1 to 3 minutes). The array receives lefthanded (LH) circularly polarized radiation (Kundu et al 1983). In this paper we present results obtained by the Clark Lake instrument on large scale structures of the corona.

1. Large Scale Structures of the Corona

We obtain representative "daily" maps of the Sun at several frequencies in the 25 to 110 MHz range. The maps as presently obtained during periods of low and moderate activity permit us to study the large scale structure of the corona in the height range 1.5 – 3.0 R_\odot . Figure 1 shows a sequence of CLRO maps at 50 MHz. The cross in the center of each map gives the disk center position, with bar lengths equal to the solar photospheric diameter, and the north arrow indicates the direction of solar north. The sequence of maps covers nearly one solar rotation (Carrington No. 1754), with the exception of a few days of absent data. The letters "A-I" indicate longlived sources, "a" and "b", shortlived ones, and "CH" a coronal hole. All of the sources except G appear to rotate with

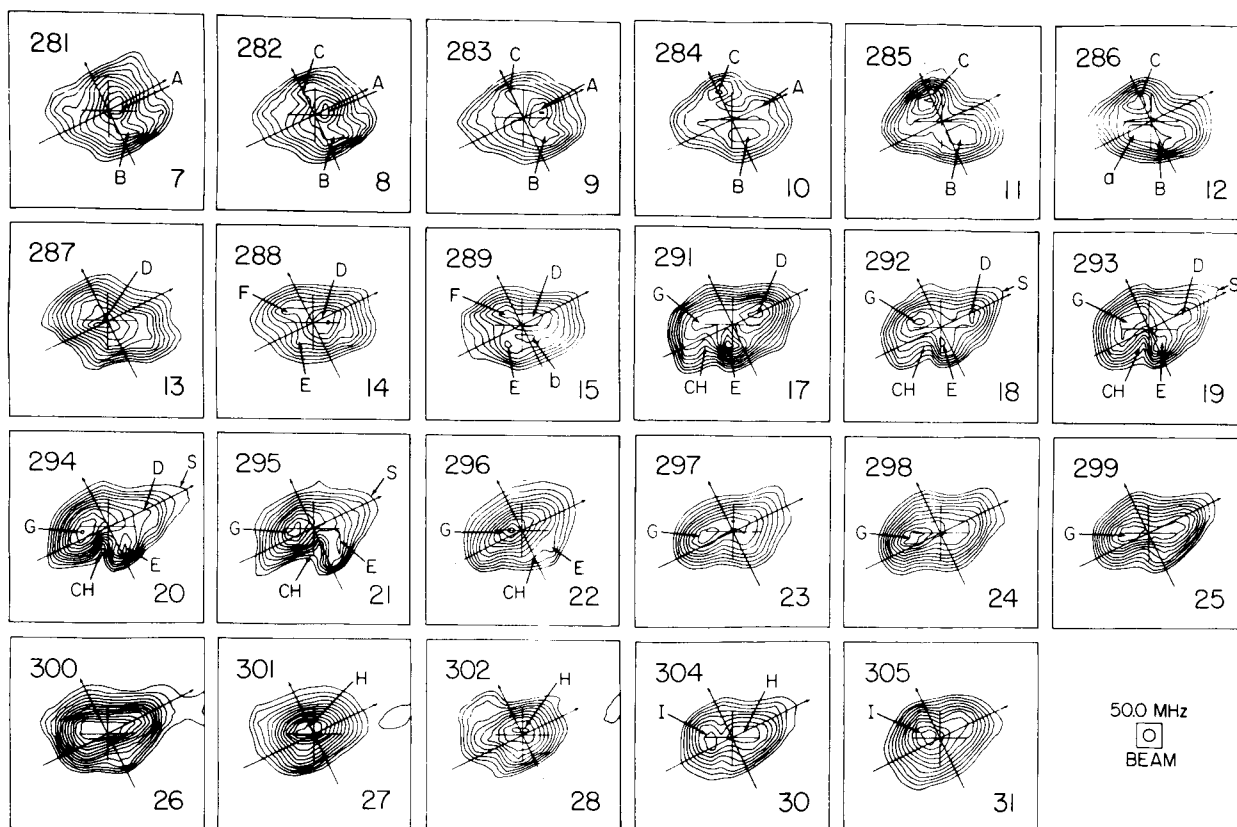


Figure 1. CLRO maps at 50 MHz for October 7-31, 1984. The central cross shows sun center; its arms extend out to one solar radius. The beam size is shown by the ellipse in the upper left corner of the first map. The arrow on each map points to solar north (see text for details).

the solar rotation rate. The letter S points to one of the extended lobes that is strongly associated with a streamer seen in SOLWIND coronagraph images.

One of the most striking features of the radio maps seen at 50 MHz and also at 73.8 and 30.9 MHz is a coronal hole on the disk, whose central meridian passage occurred on day 295 (October 21). Fig. 2 shows He 10830Å maps of the "footprint" of the coronal hole at the chromospheric level along with 30.9, 50 and 73.8 MHz maps. The He 10830Å "hole" is also sketched on the radio maps. Note the excellent agreement of the He 10830Å and 73.8 MHz "holes" on October 19-21. This might imply that the 73.8 MHz hole extends down close to the chromospheric level. However, at 50 MHz, the hole appears further east, and still further east at the lowest frequency (30.9 MHz). Since the source heights at the lower two frequencies are (roughly) 1.5 and 1.7 solar radii, the maps show that the coronal hole bends eastward through ~ 30-45 degrees of longitude at heights ranging from 1.0 to 1.7 radii. This backward bending of the hole is in the same sense as the "garden hose" Archimedian spiral suggested for the solar wind (Kundu et al 1986).

In general, lobe-like structures in the radio maps show spatial association with persistent white light streamers in the coronagraph images and the minima (contours drawn toward the sun center) correspond to coronal holes. The radio coronal holes have excellent correspondence with the coronal holes depicted on He 10830Å images.

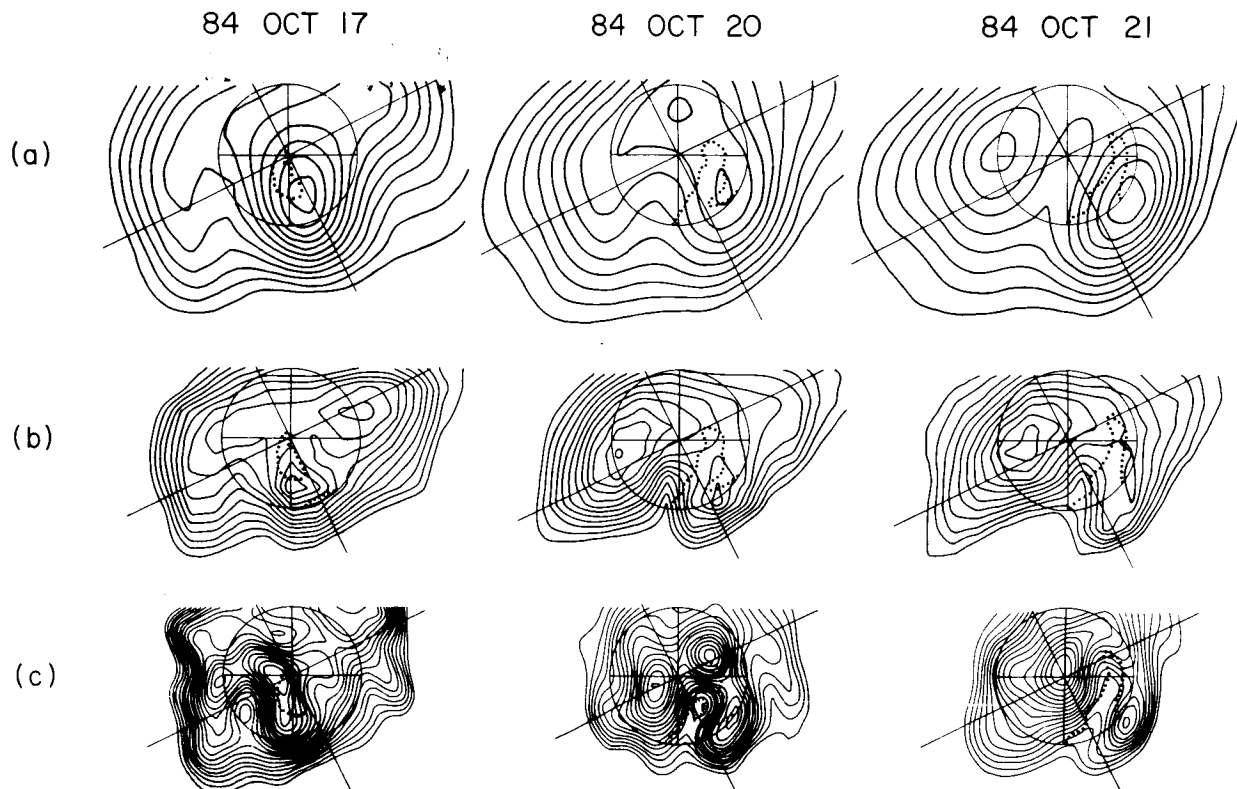


Figure 2. CLRO maps on October 17, 19 and 21, 1984 showing the coronal hole at a) 30.9, b) 50 and c) 73.8 MHz. The 10830Å hole boundary is shown by the dotted curves on each of the radio maps. On October 19 and 21, the correspondence is excellent between the 73.8 MHz contours and 10830Å, which may mean that at this frequency the hole extends down close to the chromospheric level. However, the hole appears displaced eastward as one moves to lower frequencies (greater heights), indicating a backward bending of the hole.

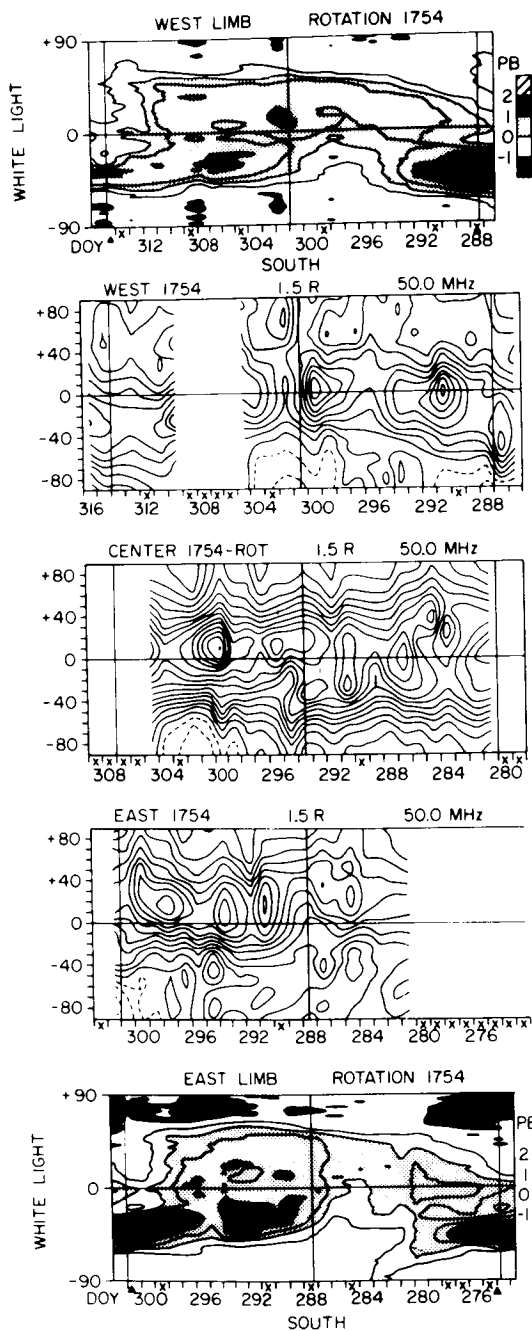
Taking constant radius scans on the "daily" maps at each observed frequency we produce synoptic contour charts of both limbs during successive Carrington rotations. An example is shown in Figure 3. Such charts permit us to easily recognize large scale rearrangements and evolution of the corona on long time scales and to perform the following studies.

(i) Study and identify the long term changes in the global coronal structure that take place due to the occurrence of transients.

(ii) Follow the evolution of coronal holes for long periods of time, at several heights corresponding to different frequencies.

ACKNOWLEDGEMENTS.

This research was supported by Air Force grant F1962883K004 and NASA contract NAG 5752.



ORIGINAL PAGE IS
OF POOR QUALITY

Figure 3. Synoptic charts from 50 MHz map data at (b) West limb, (c) Central Meridian, (d) East limb, at radius $1.3 R_{\odot}$. Mauna Loa coronagraph synoptic charts made from west and east limb data are shown in (a) and (e). There is a general correspondence between the maxima of the 50 MHz west limb charts and the brighter regions of the white light west limb charts, although the maxima do not have a one-to-one association. The coronal hole at the south pole is apparent in both the 50 MHz and white light data.

REFERENCES

- Kundu, M.R., W.C. Erickson, T.E. Gergely, M.J. Mahoney, and P.E. Turner, 1983, *Solar Phys.* **83**, 385.
- Kundu, M.R., T.E. Gergely, E.J. Schmahl, A. Szabo, R. Loiacono, Z. Wang, R.A. Howard, 1986, *Solar Phys.* submitted.

SYNOPTIC STUDY OF THE CORONA AT METER WAVELENGTH

P. Lantos
Observatoire de Paris
Meudon, France

C.E. Alissandrakis
University of Athens
Athens, Greece

The Mark III Nançay Radioheliograph (Radioheliograph Group, 1983) is used to observe the Sun at 169 MHz ($\lambda=1.77$ meter) with a time resolution of 25 East-West and North-South images per second. When the brightness distribution of the Sun is stable during the eight hours of daily observation, a two dimensional map can be produced using the technique of earth rotation synthesis (Alissandrakis et al., 1985). The best images are obtained during the period April-August, when the declination of the Sun is high to give a good coverage in the uv plane and a reasonable North-South resolution. The spatial resolution is 1.5' East-West and, in summer, 3.5' North-South (half power beam width). The maps are calibrated using Cygnus A as reference.

An example of a radio map is shown in Figure 1. A large coronal hole is observed as a depression (hatched contours) in the North-West quadrant. Its brightness temperature is 400-500,000 K. This value is to be compared with the quiet sun brightness temperature of about 600-700,000K in North-East quadrant. Bright sources in the southern hemisphere are nonthermal noise storm continua and bright arch systems (Alissandrakis et al., 1985).

On the disk the meter wavelength emission originates from the low corona with contribution from the chromosphere-corona transition region. On the limb, the corona is observed at higher altitude with integration along line of sight. To summarize the daily maps over the entire solar surface, synoptic charts are plotted after a Mercator projection, either on the disk or on the limb. Because of the radio center to limb effect, the data are limited, on the disk, to the regions close to central meridian, taking into

ORIGINAL PAGE IS
OF POOR QUALITY

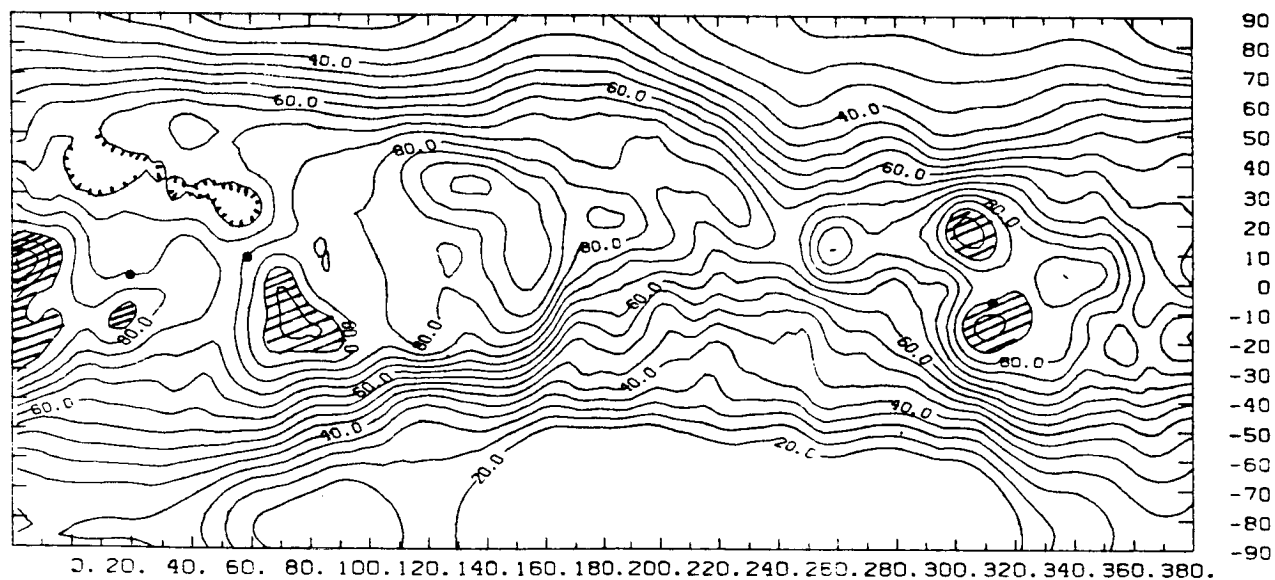
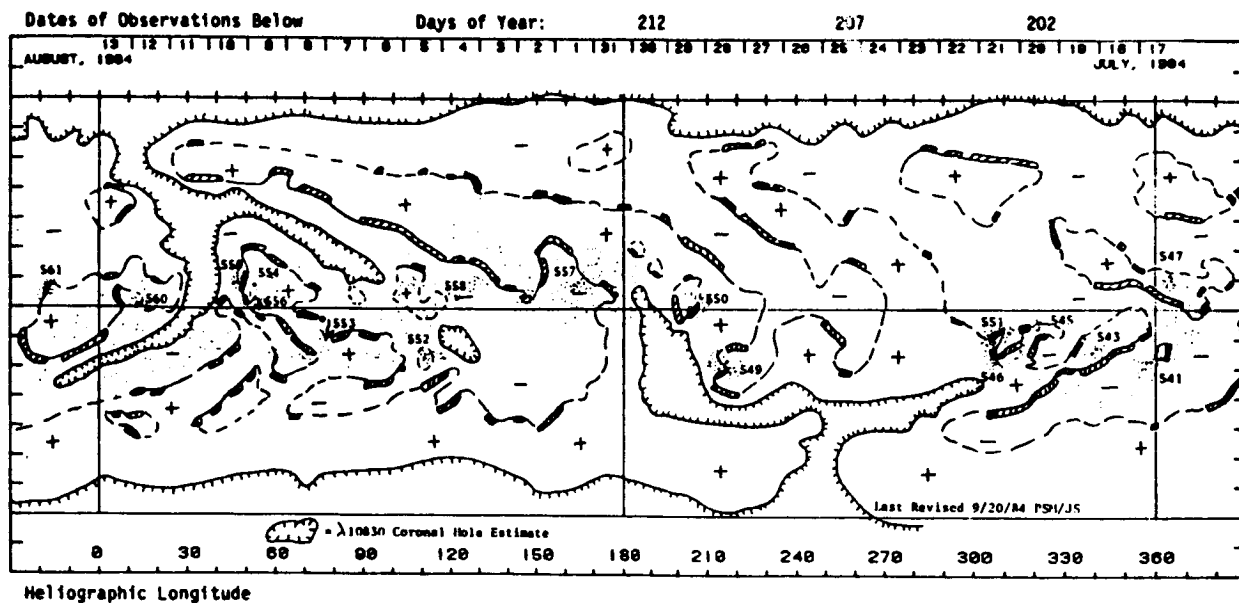


Figure 2

Comparison of synoptic charts on the disk for Carrington Rotation 1751

2a- Boulder synoptic chart

2b- Nançay synoptic chart (unit= 10^4 K)

ORIGINAL PAGE IS
OF POOR QUALITY

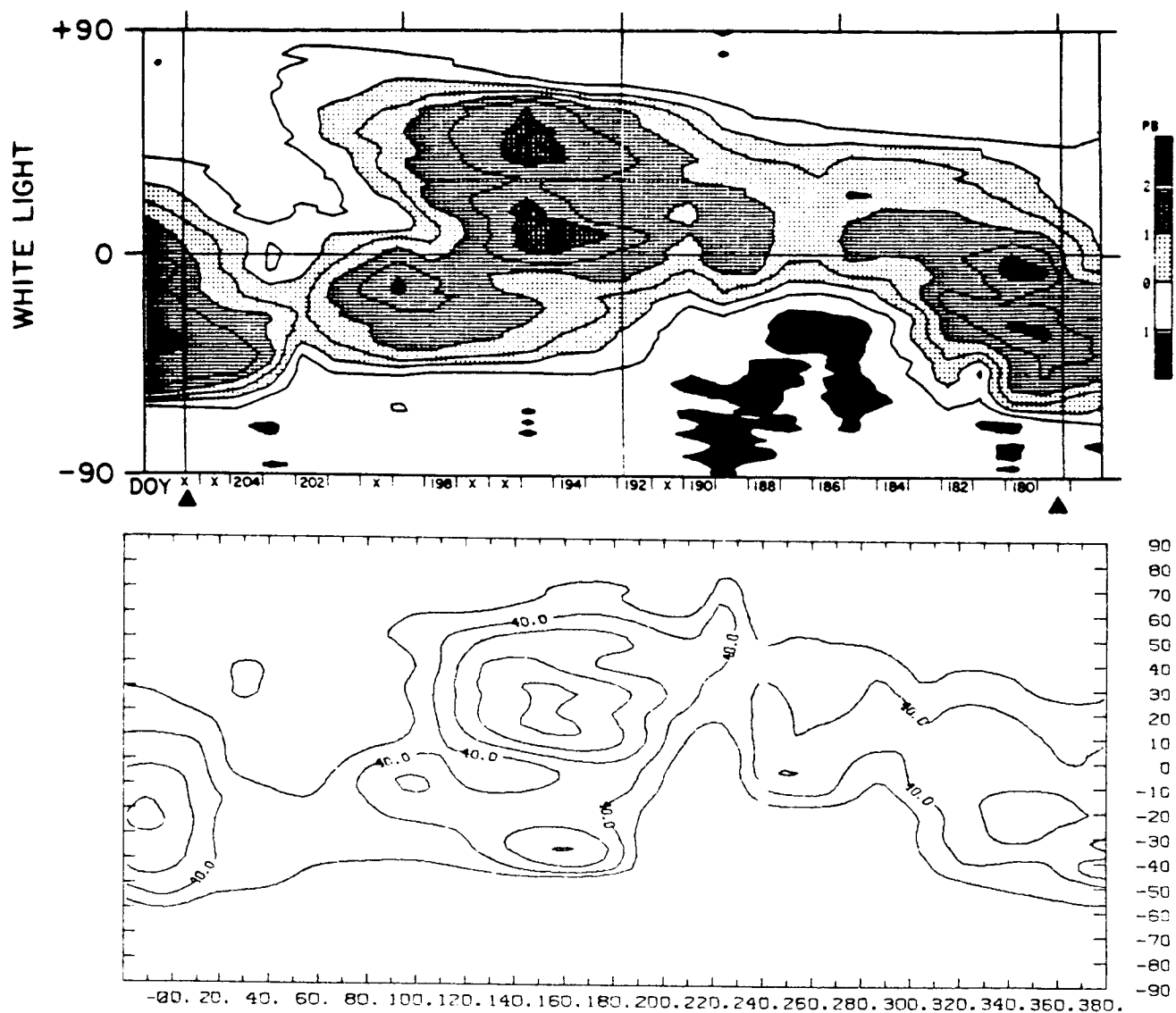


Figure 3

Comparison of synoptic charts on the limb for Carrington Rotation 1750

3a- Chart on the west limb with HAO Mark III K-coronameter.

3b- Chart with Nançay Radioheliograph at 169 MHz for the same limb
(unit= 10^4 K)

gives densities of the order of 10^9 cm^{-3} (Davies and Krieger, 1982) while density limit for wave propagation at 169 MHz is $3.5 \cdot 10^8 \text{ cm}^{-3}$.

The other radio sources are generally located close to inversion line of longitudinal magnetic field. Sometimes they are related to $H\alpha$ filaments (as suggested by Axisa et al., 1973), and sometimes not. Only 10% of $H\alpha$ filaments of the Boulder or Meudon synoptic charts are associated with meter wavelength enhancements, while 60% are not related to localized sources brighter than 50,000K above the quiet regions. The remaining 30% are ambiguous because of noise storms in the vicinity.

Figure 3 represents a comparison of limb synoptic charts obtained with the HAO Mark III K-coronometer (3a) and with the Nançay Radioheliograph (3b) both produced for a distance of 1.3 solar radius. The high density region oscillating between southern and northern hemispheres is well observed on both charts. At higher altitude, it gives rise to the heliosheet which separates interplanetary sectors. As K-corona is only sensitive to electron density while radio brightness is sensitive to both density and temperature, a detailed comparison of both observations opens a new method of coronal temperature diagnostic.

REFERENCES

- Alissandrakis C.E., Lantos P., Nicolaïdis E., 1985, *Solar Physics* 97, 267
Axisa F., Avignon Y., Martres M.J., Pick M., Simon P., 1971, *Solar Physics* 19, 110
Davis J.M., Krieger A.S., 1982, *Solar Physics* 80, 295
Le Squeren A.M., 1963, *Annales d'Astrophysique*, 29, 171
Radioheliograph Group, 1983, *Solar Physics* 88, 383
Sime D.G., Fisher R.R., Altrock R.C., 1985, NCAR Technical Note 251
Solar Geophysical Data Report n°481, NOAA, Boulder, 1984

THE WHITE LIGHT CORONA AND PHOTOSPHERIC MAGNETIC FIELDS

Marie K. McCabe
Institute for Astronomy
University of Hawaii
Honolulu, Hawaii

INTRODUCTION

It is recognized that the structure of the heliospheric current sheet, as computed from the observed photospheric magnetic field using a potential field approximation and as inferred from synoptic maps of the observed coronal polarized brightness (pB), gives essentially the same results (Wilcox and Hundhausen, 1983; Burlaga et al., 1981; Pneuman et al., 1978). Thus, white light observations of the corona are often interpreted as indicating the overall structure of the coronal magnetic field, where bright regions of the corona generally lie over neutral line positions (Sime et al., 1984). It might then be expected that inspection of the coronal brightness distribution would allow inference of the large-scale photospheric field structure and vice versa. To test this hypothesis, Garcia et al. (1984) carried out a statistical study of three solar rotations comparing synoptic maps of the longitudinal component of the photospheric magnetic field at $\lambda 6303$ with maps showing the pB at heights above $1.3 R_{\odot}$. Their analysis revealed that no particular type (i.e., active region or quiet) or orientation of neutral line lay predictably below a bright feature, nor was there any hemispheric preference for a particular sense of polarity across the neutral line. Many coronal features were associated with specific neutral lines, but the conditions necessary and sufficient to establish the correspondence were not found.

In this paper some results are presented from a continuing investigation of the coronal structure vs. the photospheric magnetic field relationship. Two approaches to the problem are considered. First, the individual coronal features recorded at each limb were located on a chart of the magnetic field measured with low spatial resolution, depicting the large-scale or global field configuration. Second, the characteristics of neutral line segments--defined by the presence of $H\alpha$ filaments--with no associated coronal structure were investigated. Preliminary results will be discussed.

DATA

The inconclusive results of Garcia et al. (1984) suggested the following approach to the problem:

1. The data base was expanded from 3 to 19 solar rotations commencing in January 1982. During this period, the interplanetary magnetic field showed a simple two sector structure for several months, but it was more complex at other times.
2. Instead of using synoptic maps of the coronal polarized brightness (pB) distribution for correlation with neutral lines, coronal features were individually

identified from K-coronameter polar scans at $1.3 R_{\odot}$ (for details of Mauna Loa Solar Observatory data products, see Rock and Seagraves, 1982). The heliographic coordinates for each feature were determined from the latitude of maximum brightness and the longitude of the limb at the time of the scan. The positions were plotted as shown in Figure 1, on a chart representing the particular rotation, where the circle sizes indicate three ranges of brightness and the filled and open circles indicate measures of the relative height of each streamer.

3. On the global scale, the solar magnetic field is made up of magnetic cells defined by the large-scale neutral lines, which are also marked by filaments, filament channels, etc. (see Levine, 1977). For the present study, the Stanford Solar Magnetic Field Synoptic Charts (SGD, 1982-83) were used to identify large-scale neutral lines. The relatively low spatial resolution-- 180 arcsec^2 --of the maps more nearly matches that of the coronal measurements, which are one day (13°) apart; further, this avoids the small-scale bipolar regions with field lines that are closed at heights in the corona below those used in this study. The Stanford Magnetic Field Chart for Carrington Rotation 1723 (June 15-July 12, 1982) is shown in Figure 1a on which the positions of the coronal features identified as above are also plotted. The heavy black line designates the large-scale or global neutral line that winds around the Sun.
4. $H\alpha$ synoptic charts published in Solar Geophysical Data Reports include solar magnetic neutral lines inferred from $H\alpha$ structures (McIntosh, 1972); they also show where filaments have been observed along the neutral lines. This chart for Carrington rotation 1723 appears in Figure 1b with the coronal features plotted as in Figure 1a. The filled-in filaments are those that were clearly visible on $H\alpha$ filtergrams as they crossed the disk but had no coronal counterpart, for example, streamers, at either limb.

RESULTS

Coronal Features vs. Neutral Line

As seen in Figure 1, the large-scale magnetic field of the Sun at that time was basically a bipolar system. The neutral line appeared to be tilted with respect to the equator for the greater part of the rotation and then completed the cycle with a convoluted path going north near 360° of longitude and through a rapidly developing active region. This pattern had become established by rotation 1720 (March-April 1982) and was maintained through rotation 1725 (August 1982), after which it became much more complex. By inspection, it appears that coronal features are associated with the large-scale neutral line, even when the pattern is complex. To quantify the results for the 19 rotations, the criterion for a positive association of a coronal structure with the neutral line was that it be no more than 10° distant from the line. This was chosen by considering the 1 day interval between K-coronameter measurements and the unknown projection effects at the limb. The results are shown in Table 1 for two selected rotations--1723 and the more complex system of 1729--with the totals given for all 19 rotations. The number and percentage of associations are shown separately for the streamers--where the $pB = 1 \times 10^{-8}$ contour reaches a height above $1.8 R_{\odot}$ --and for the bright features, where $pB > 15 \times 10^{-8}$ disk center brightness. The last column indicates the number of structures that were both bright and streamer-like.

ORIGINAL PAGE IS
OF POOR QUALITY

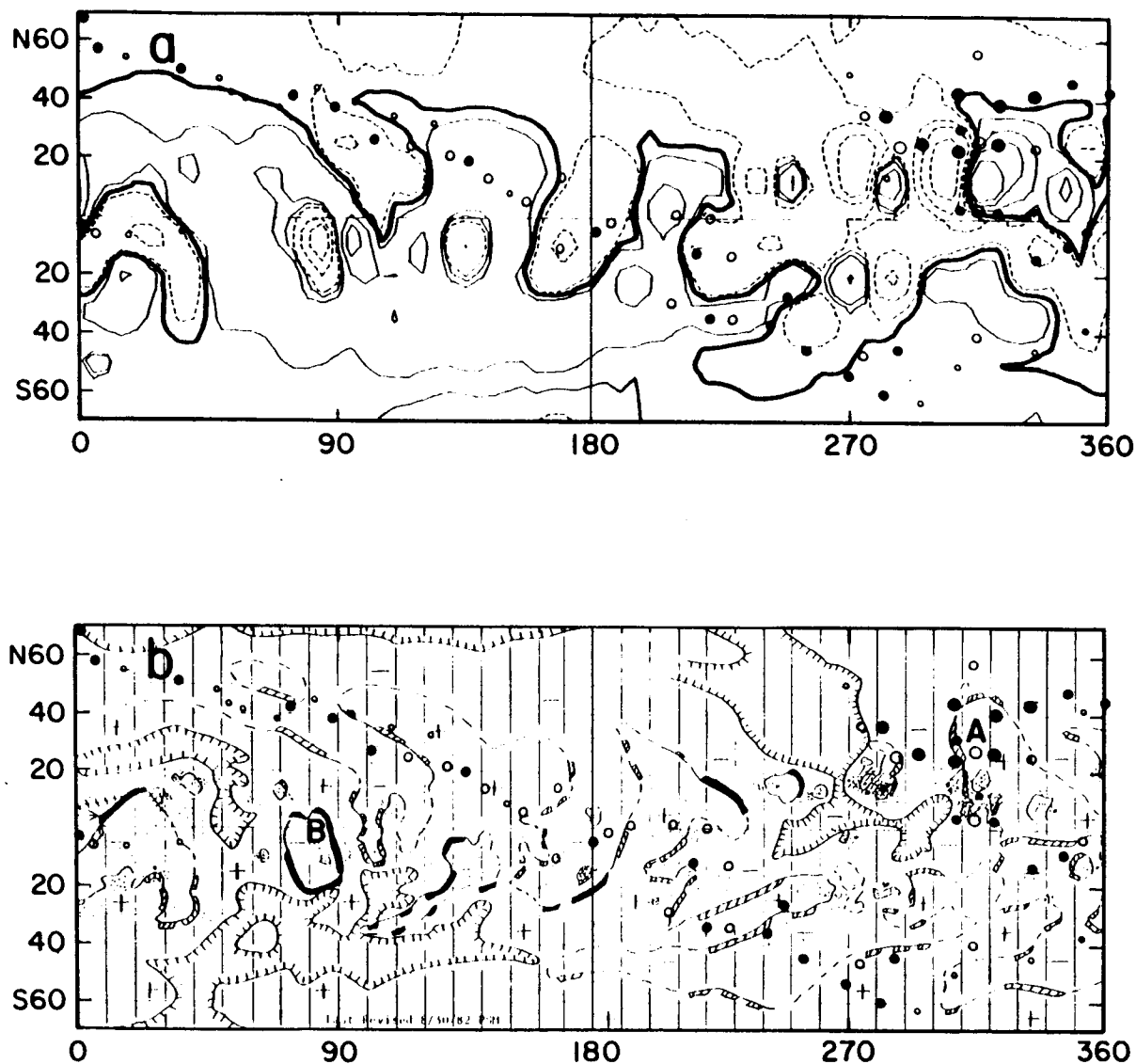


Figure 1. Position of K-coronameter features from East and West limb observations during Rotation 1723 (June 15-July 12, 1982) superimposed on (a) the Stanford Magnetic Field and (b) H α synoptic charts (SGD, 1982). The circle sizes-large to small-represent $pB \geq 15$, $8 \leq pB < 15$, $pB < 8$ in units of 10^{-8} center disk intensity. The filled and open circles indicate the $pB = 1$ contour reaches heights of at least 1.96 or 1.80 R_{\odot} respectively. The broad line in (a) marks the neutral line of the large scale magnetic field and the filled in filaments in (b) do not have any associated K-corona features.

Table 1

Rotation	Streamers Total	NL Assoc. %	Bright Struc. Total	NL Assoc. %	Streamers with pB > 15
1723	33	82	10	90	7
1729	50	92	45	93	26
1717-35	751	82	296	92	213

Magnetic Neutral Lines vs. Coronal Features

The presence of an $H\alpha$ filament provides a definite indication of the position of a photospheric neutral line on the solar disk (McIntosh et al., 1972). For 11 rotations in the series above, we have, to date, checked all stable filaments, that is, those observed on daily $H\alpha$ filtergrams all the way across the disk, and we have recorded whether they were accompanied by coronal feature at one limb or the other. When this test was applied to the well-defined filaments marked A and B in Figure 1b, they were found to be in contrast because of the presence and absence, respectively, of any overlying coronal feature; the same situation was true during adjacent rotations.

A total of 47 $H\alpha$ filaments were found to exist without associated coronal features, and the magnetic field properties at these neutral lines were investigated with the following results:

1. Nineteen percent showed the direction of polarity reversal in the direction corresponding to the Hale law for the particular hemisphere, and 43% showed the opposite direction, while for the remainder there was uncertainty due to the lines being almost parallel to the solar equator.
2. Forty percent lay on neutral lines enclosing mid-latitude unipolar regions.
3. Ninety-one percent occurred where the field gradient was low, that is, in conditions typical of the quiet Sun, while only 2% were through active regions where the field gradient is usually stronger.
4. Eighty-five percent showed some association with coronal holes, with 62% lying on the neutral line bounding a coronal hole region and close to the hole, and the other 23% forming a closed boundary within the large unipolar region containing a coronal hole.

CONCLUSIONS

The preliminary results of this study on the relationship between coronal structures and photospheric neutral lines lead to two tentative conclusions. First, white light features detected with the K-coronameter tend to be associated with the large-scale global neutral line of the low-resolution (180 arcsec^2) photospheric magnetic field, which changes gradually during a period of several rotations. Second, there are neutral lines that exhibit no coronal enhancement above $1.3 R_{\odot}$; they tend to be at the borders of coronal hole unipolar areas or at boundaries of small unipolar regions within them. Thus, by application of a

quantitative test, the impression that magnetic field structures are important in ordering the distribution of coronal brightness has been verified. Further, it has been shown that the most important organization is that impressed by the large-scale, global neutral sheet.

There are, of course, other neutral lines identifiable in the photospheric magnetic field, even in the low-resolution description in the Stanford maps. For this epoch, these neutral lines do not lie under bright features in the corona. When the characteristics of the most stable, long-lived set of these (i.e., those bearing filaments) are examined, a particular property is found. They are almost all neutral lines at or near the boundaries of coronal holes or the neutral lines enclosing mid-latitude unipolar regions, often within much larger unipolar regions containing coronal holes. Thus, if an attempt is made to infer anything but the largest scale features of the photospheric magnetic field from the distribution of white light polarized brightness in the corona, it will fail at least by missing these unipolar regions.

This work will be continued by covering more rotations to include periods during which the large-scale magnetic field changes from a simple dipole to a more complex arrangement and other phases of the solar cycle.

Acknowledgments. D. G. Sime and C. J. Garcia have made important contributions to this work. Support was provided by NASA under grant NGL 12-001-011.

REFERENCES

- Burlaga, L. F., Hundhausen, A. J., and Zhao, X. P., 1981, J. Geophys. Res., 86, 8893.
- Garcia, C. J., Sime, D. G., and McCabe, M. K., 1984, B.A.A.S., 16, 533.
- Levine, R. H., 1977, in J. Zirker (ed.), Coronal Holes and High Speed Wind Streams, Colorado Assoc. Univ. Press, Boulder, Ch. 4.
- McIntosh, P. S., 1972, Rev. Geophys. Space Phys., 11, 837.
- Pneuman, G. W., Hansen, S. F., and Hansen, R. T., 1978, Solar Phys. 59, 313.
- Rock, K., and Seagraves, P., 1982, Technical Note NCAR/TN-200 + STR, NCAR, Boulder, Colorado.
- Sime, D. G., Fisher, R. R., McCabe, M. K., and Mickey, D. L., 1984, Astrophys. J., 278, L123.
- Solar Geophysical Data, 1982, 456 Part I 53, 55, August, 1982, U.S. Department of Commerce (Boulder, CO, USA 80303)
- Wilcox, J. M., and Hundhausen, A. J., 1983, J. Geophys. Res., 88, 8095.

QUASISTATIC EVOLUTION OF MAGNETOSTATIC CORONAL STRUCTURES

Richard Wolfson
 Department of Physics
 Middlebury College
 Middlebury, VT 05753

INTRODUCTION

This paper reviews four separate but related studies of coronal magnetostatic equilibria under a variety of boundary conditions and distributions of coronal current. Physically, all four studies assume an axisymmetric corona whose radial magnetic field at the coronal base is dipolar. Electric currents in the model coronas are assumed to flow in the azimuthal direction, giving rise to Lorentz forces that must be balanced by pressure gradients and gravity. Mathematically, such coronas are described by the equation of magnetostatic force balance and Ampere's law; under the model assumptions these equations combine to give a single equation for the effective potential $AR\sin\theta$:

$$\frac{1}{\sin\theta} \frac{\partial^2 (AR\sin\theta)}{\partial R^2} + \frac{\partial}{\partial \theta} \frac{1}{R^2 \sin\theta} \frac{\partial (AR\sin\theta)}{\partial \theta} = -4\pi R \sin\theta e^{-\int [g(R)/C^2] dR} F(AR\sin\theta) \quad (1)$$

(Hundhausen, Hundhausen, and Zweibel 1981; hereafter HHZ), where F is a free function. The case $F=0$ corresponds to a potential magnetic field decoupled from an atmosphere whose pressure varies only with radius. HHZ obtained analytic solutions to the linear problem arising when the function F is a constant. This case corresponds to a corona inflated with excess material throughout its entire volume, with pressure varying from pole to equator at any fixed radius. The studies reported here involve nonlinear functions $F(AR\sin\theta)$ and/or more elaborate boundary conditions, with the aim of providing more realistic models for observed coronal structures. Since all the models contain adjustable parameters related to the amount of excess mass loading in the corona, variation of these parameters can be used to study the quasistatic evolution of a model corona in response to mass addition.

CURRENT SHEET BOUNDARY CONDITIONS

The solar wind is a dominant influence on the coronal magnetic field, drawing some field lines into open configurations where they merge with the interplanetary field. Describing this situation in the context of a static model requires an artificial boundary condition that forces field lines to open. A common approach employs a source surface, beyond which the field lines are assumed radial (Altschuler and Newkirk 1969). In the present model, we assume instead that a current sheet exists in the equatorial plane, beginning at some height R_1 and extending to infinity. This approach models more realistically the observed behavior of the solar magnetic field in crossing the equatorial

plane. Mathematically, the current sheet is incorporated by forcing the field component B_θ to zero for points in the equatorial plane with $R > R_1$. With this boundary condition, and with the function F in equation (1) being a constant, the solution may be written in terms of Legendre polynomials (Wolfson 1985). Increasing the constant value of the function F gives a series of model coronas that deviate increasingly from the potential field corona (Fig. 1).

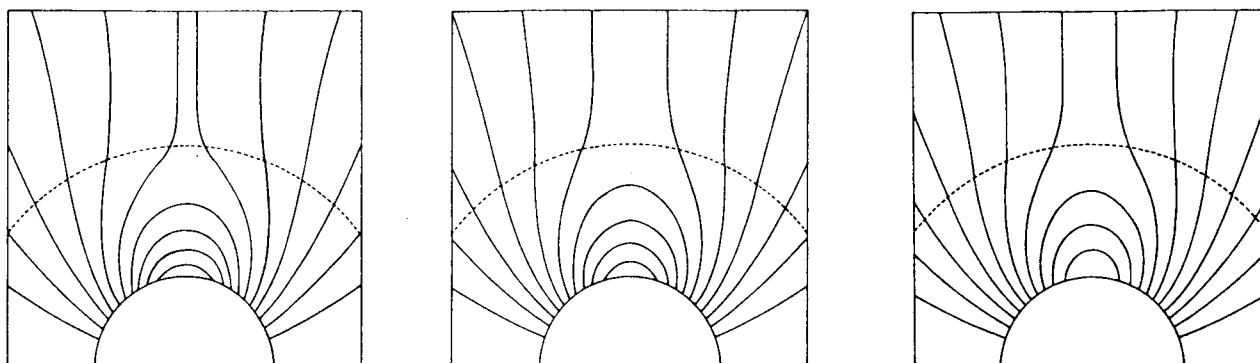


Fig. 1: Field lines for model coronas with increasing excess mass (from Wolfson 1985).

Analysis of the coronal current distribution in the open-field region shows that the current density decreases slightly from pole to equator at a fixed radius, then undergoes an abrupt reversal at the current sheet. This feature, along with flexibility in treating nonpotential fields, makes the present model a more realistic approach than the spherical source surface model.

A LIMITED CORONAL INFLATION

Choosing the function F in equation (1) to be a step function gives a model corona inflated with excess mass only below a particular field line. Fig. 2 shows the position of the field line that bounds the inflated region, for a variety of inflation parameters.

An interesting feature of the nonlinear model arising from a step function F is that solutions cease to exist, or undergo a dramatic and discontinuous change in morphology, above a certain value of the inflation parameter. We have suggested that this lack of nearby equilibrium solutions corresponds to the onset of dynamical processes which our quasistatic model cannot describe. For realistic coronal parameters, the mass associated with this loss of equilibrium is on the order of 10^{16} g--comparable to the mass ejected in a coronal mass ejection (CME).

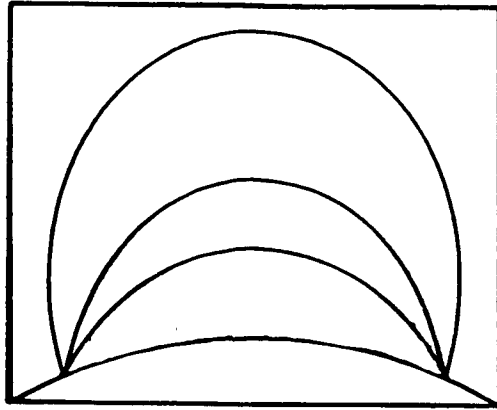


Fig. 2: Expansion of the field line bounding a region of inflated corona. Lowest field line shown is that of a potential field.

THE INFLATED CORONAL FLUX TUBE

Specifying the function F to be zero everywhere except for a limited region where it is a bipolar function gives a model corona whose magnetic field is everywhere potential except for a narrow tube (actually a torus in the axisymmetric geometry), which constitutes a high-pressure, high-density region surrounded by lower pressure corona. The resulting model may then provide a description of a white-light coronal loop. Increasing the amplitude of the function F corresponds to loading more mass into the tube. Fig. 3 shows that the result is an increase in the width of the tube coming almost entirely from an expansion of its outer bounding field line.

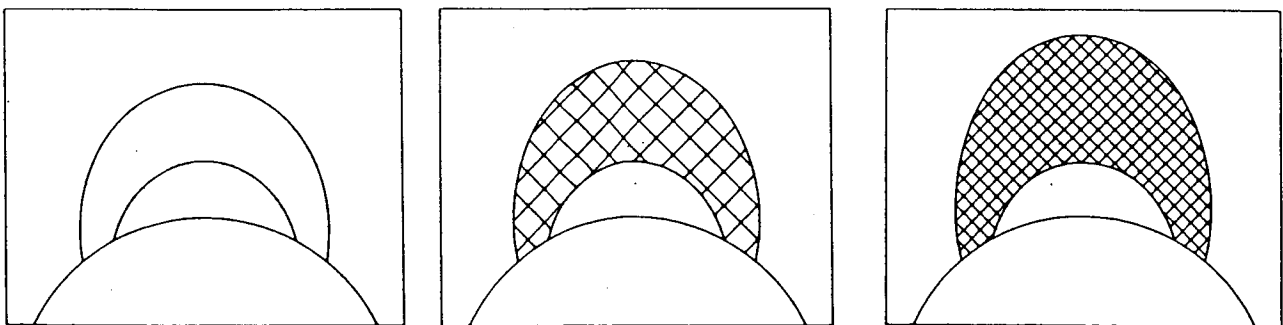


Fig. 3: Changing configuration of a "flux tube" as excess mass is added between specified field lines. Hatching indicates relative amount of excess mass (from Wolfson and Conover 1986).

That the tube top rises instead of falling as mass is added is a result of the increased Lorentz forces associated with the increasing coronal currents.

This nonlinear model exhibits the same loss of equilibrium as the previously described model; again, the excess mass involved is on the order of that ejected in a CME.

QUASISTATIC EVOLUTION OF A CORONAL STREAMER

The final and most ambitious calculation in this series attempts to model the quasistatic evolution of a coronal streamer prior to its disruption by an eruptive prominence and associated coronal mass ejection. Such an evolution occurred over a two-day period in August, 1980, as the closed-field region of a large and well-defined helmet streamer appeared to bulge and brighten before being disrupted by the eruption of the underlying prominence on August 18 (Illing and Hundhausen 1986). The model calculation involves inflating the coronal region below a specified field line, while applying current-sheet boundary conditions above that line. Total flux in the closed-field region is held constant, and the top height of the closed region adjusted accordingly as excess mass is added. Fig. 4 shows a sequence of model equilibria, beginning with a best fit to the initial observations of the streamer and ending with the greatest value of coronal inflation for which equilibrium solutions can be found.

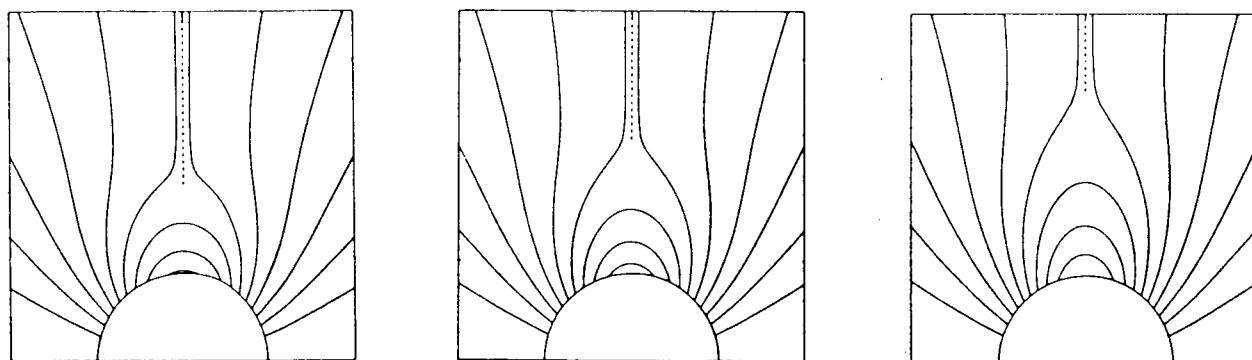


Fig. 4: A sequence of model equilibria describing the quasistatic evolution of a coronal helmet streamer (from Conover, Wolfson, and Illing, in preparation).

The calculated top heights and corresponding excess masses are consistent with measurements taken from coronagraph images (Conover, Wolfson and Illing, in preparation). Furthermore, the equilibrium sequence terminates at about the maximum top height and excess mass observed before the slow evolution gives way to the prominence eruption and mass ejection.

CONCLUSION

Although highly idealized, the axisymmetric magnetostatic models described in this paper provide insights into the behavior of a variety of coronal structures. The models show how more realistic current-sheet boundary conditions and coronal density variations may be modeled. And the nonlinear models invariably cease to have equilibrium solutions as the excess coronal mass is increased--just as the corona itself may undergo a transition to the dynamic behavior of a coronal mass ejection.

This work was supported by NSF grant AST-8311338 to Middlebury College.

REFERENCES

- Altschuler, M.D. and Newkirk, G. 1969, Solar Phys., 9, 131.
- Conover, C., Wolfson, R., and Illing, R.M.E. "The Evolution of a Coronal Helmet Streamer," in preparation.
- Hundhausen, J.R., Hundhausen, A.J., and Zweibel, E.G. 1981, J. Geophys. Res., 86, 11117.
- Illing, R.M.E. and Hundhausen, A.J. 1986, J. Geophys. Res., in press.
- Wolfson, R. 1985, Astroph. J., 288, 769.
- Wolfson, R. and Conover, C. 1985, "The Inflated Flux Tube: a Model for White-Light Coronal Loops," submitted.
- Wolfson, R. and Gould, S.A. 1985, Astroph. J., 296, 287.

THREE-DIMENSIONAL MAGNETOSTATIC MODELS OF THE LARGE-SCALE CORONA

T. J. Bogdan
B. C. Low

High Altitude Observatory
National Center for Atmospheric Research¹

INTRODUCTION

There is a relatively stable component of the large-scale corona that persists for periods of the order of a solar rotation. This component is captured in the synoptic charts constructed from the daily coronagraph observation of the density structures visible in Thomson-scattered light from the photosphere (e.g., Fisher and Sime 1984). The Thomson-scattered light is optically thin and the coronagraph images correspond to electron densities integrated along the line of sight. A long standing need therefore exists for the development of theoretical models of the corona capable of relating the observed integrated density to the actual three-dimensional coronal structures. It is the magnetic field and electric current in the highly conducting medium of the corona that order the density into various structures. Unfortunately, the coronal magnetic field cannot be measured to any useful spatial resolution. Only the longitudinal component of the magnetic field in the photosphere can be measured routinely with a magnetograph. An obvious approach for a theoretical model to adopt is to use the measured photospheric magnetic field as an input and extrapolate for both the magnetic field and density in the corona. Until recently, this approach has been feasible only with the potential field model (e.g., Newkirk and Altschuler 1970). The disadvantage, as is well known, is that a potential magnetic field does not interact with the plasma and the model predicts no density structure. The idea to use linear force-free magnetic fields with a constant α , proposed by Nakagawa (1973), has difficulties of nonuniqueness and infinite total magnetic energy when applied to coronal models in spherical geometry (Seehafer 1978). Non-constant α force-free magnetic fields and general non-potential magnetic fields in static equilibrium have so far proved to be mathematically intractable in three-dimensional geometry. In this paper, we describe a special class of magnetostatic equilibria, which are mathematically simple and yet sufficiently versatile so as to fit any arbitrary normal magnetic flux prescribed at the photosphere. With these solutions, the corona can be modeled with precisely the same mathematical procedure as has previously been done with potential fields. The magnetostatic model predicts, in addition to the coronal magnetic field, the three-dimensional coronal density which can be compared with coronagraph observations. This is an ongoing project being conducted at the High Altitude Observatory (HAO), using data from the Kitt Peak Magnetograph and several coronagraphs operated by HAO.

THREE-DIMENSIONAL MAGNETOSTATIC MODELS

The corona is in a state of expansion (Parker 1963, Hundhausen 1972). The expansion is believed to be negligible in the low corona, and, as a first approximation, the low corona is taken to be in static equilibrium and described by

$$\frac{1}{4\pi} \left(\vec{\nabla} \times \vec{B} \right) \times \vec{B} - \vec{\nabla} p - \frac{\rho G M_{\odot}}{r^2} \hat{r} = 0, \quad [1]$$

¹The National Center for Atmospheric Research is sponsored by the National Science Foundation.

$$\vec{\nabla} \cdot \vec{B} = 0, \quad [2]$$

where \vec{B} , p and ρ are, respectively, the magnetic field, pressure and density, G is Newton's gravitational constant, M_\odot the solar mass and r the heliocentric distance. To close the equations, we may relate the temperature to p and ρ through the ideal gas law and specify an equation for steady energy balance. The balance of energy in the corona plays an important role in determining coronal structures. The detailed processes are complicated and our current knowledge about them is very incomplete. In any case, to account for these processes would render the magnetostatic problem quite intractable. It therefore seems reasonable, as a first step, to ignore the energy equation and seek solutions to equations (1) and (2) with no further constraints. Even within such an artificial consideration, the magnetostatic problem is not readily tractable (see the review by Low (1985a)). Equations (1) and (2) have not been treated in fully three-dimensional geometry except for the cases of the potential magnetic field and the constant- α force-free magnetic field.

In a recent development, Low (1985b) showed that equations (1) and (2) can be reduced to a simpler problem without assuming any special geometry if the electric current density \vec{J} is assumed to flow everywhere perpendicular to the solar gravity. In this case, employing the usual spherical coordinates, we can express the magnetic field and electric current density as

$$\vec{B} = \Psi \hat{r} + \frac{1}{r} \frac{\partial \Phi}{\partial \theta} \hat{\theta} + \frac{1}{r \sin \theta} \frac{\partial \Phi}{\partial \phi} \hat{\phi}, \quad [3]$$

$$\vec{J} = \frac{c}{4\pi} \frac{1}{r \sin \theta} \frac{\partial}{\partial \phi} \left(\Psi - \frac{\partial \Phi}{\partial r} \right) \hat{\theta} - \frac{c}{4\pi} \frac{1}{r} \frac{\partial}{\partial \theta} \left(\Psi - \frac{\partial \Phi}{\partial r} \right) \hat{\phi}, \quad [4]$$

where Ψ is an arbitrary function of $\frac{\partial \Phi}{\partial r}$ and r . The magnetostatic problem reduces to solving

$$\frac{\partial}{\partial r} \left(r^2 \Psi \left(\frac{\partial \Phi}{\partial r}, r \right) \right) + \frac{1}{\sin \theta} \frac{\partial}{\partial \theta} \left(\sin \theta \frac{\partial \Phi}{\partial \theta} \right) + \frac{1}{\sin^2 \theta} \frac{\partial^2 \Phi}{\partial \phi^2} = 0, \quad [5]$$

for Φ as a boundary value problem given $\Psi(\frac{\partial \Phi}{\partial r}, r)$. The freedom to choose the form of Ψ arises from our not imposing an energy equation. From the solution Φ , the magnetic field is given by equation (3) and the equilibrium pressure and density are given by

$$p = p_0(r) - \frac{1}{8\pi} \Psi \left(\frac{\partial \Phi}{\partial r}, r \right) + \frac{1}{4\pi} \int^{\frac{\partial \Phi}{\partial r}} dv \Psi(v, r), \quad [6]$$

$$\rho = \rho_0(r) +$$

$$\frac{r^2}{GM_\odot} \left(\frac{1}{4\pi} \frac{1}{r^2 \sin^2 \theta} \frac{\partial \Phi}{\partial \phi} \frac{\partial \Psi}{\partial \phi} + \frac{1}{4\pi r^2} \frac{\partial \Phi}{\partial \theta} \frac{\partial \Psi}{\partial \theta} - \frac{1}{8\pi} \frac{1}{r^2 \sin^2 \theta} \frac{\partial}{\partial r} \left(\frac{\partial \Phi}{\partial \phi} \right)^2 - \frac{1}{8\pi r^2} \frac{\partial}{\partial r} \left(\frac{\partial \Phi}{\partial \theta} \right)^2 \right), \quad [7]$$

where p_0 and ρ_0 are the pressure and density of an arbitrary spherically symmetric hydrostatic atmosphere. The familiar case of a potential magnetic field is recovered if we set $\Psi = \frac{\partial \Phi}{\partial r}$, and then only the hydrostatic components in equations (6) and (7) remain. In general, equation (5) is

nonlinear and suitable numerical methods need to be developed to solve it. If we set

$$\Psi = \eta(r) \frac{\partial \Phi}{\partial r}, \quad [8]$$

where η is given, equation (7) is linear in Φ and standard numerical methods for elliptic equations can be employed to solve the boundary value problem. Bogdan and Low (1986) considered several cases of given η for which the boundary value problem is soluble analytically in terms of classical functions. In particular if

$$\eta(r) = \left(1 + \frac{a}{r}\right)^2, \quad [9]$$

where a is a constant, equation (7) admits the series solution

$$\Phi(r, \theta, \phi) = \sum_{n=1}^{\infty} \sum_{m=-n}^n \left(A_{mn} (r + a)^{-n-1} + B_{mn} (r + a)^n \right) Y_n^m(\theta, \phi), \quad [10]$$

where A_{mn} and B_{mn} are constant coefficients and Y_n^m are the usual spherical harmonics. As to be expected, the classical spherical-harmonic expansion for the potential field is obtained if $a = 0$. In fact, equation (9) shows that $\Psi \rightarrow \Phi$ in the limit of $r \rightarrow \infty$ so that in that limit, the magnetic field is potential. In other words, the electric current is confined to the low corona within a heliocentric distance of the order of a . For a given non-zero a , equation (10) can be fitted with a prescribed radial magnetic field at an inner spherical surface identified with the solar surface, using $B_r = \Psi$. An outer boundary condition is needed to determine the coefficients A_{mn} and B_{mn} uniquely. This outer condition may take the form of requiring the magnetic field to vanish as $r \rightarrow \infty$ or that the magnetic field becomes purely radial at some outer spherical surface (e.g., Newkirk and Altschuler 1970). The procedure follows essentially the same steps as that of the classical potential field model. However, the magnetic field is not potential for a non-zero with the equilibrium pressure and density is given by equations (6) and (7).

DISCUSSION

We plan to generate three-dimensional magnetospheric models of the corona based on equations (9) and (10), with an input of the photospheric normal magnetic flux from the Kitt Peak Magnetograph. This is a first opportunity for constructing a three-dimensional magnetostatic corona which is based on photospheric magnetograms and can be tested against coronagraph observations. By varying the free parameter a , it will be interesting to see if we can achieve a reasonable agreement between the density predicted by the model and the observed line-of-sight integrated density. The model is based on several artificial assumptions and we do not have *a priori* reasons to expect excellent agreement. The assumption of the electric current flowing perpendicular to gravity is not as severe as it may appear. Such a distribution of the electric current may result from stretching a magnetic field radially outward, starting from a potential state, as demonstrated by the solutions described by equation (10) for $a > 0$ (Bogdan and Low 1986). The outward stretch of the magnetic field may result from the buoyancy of magnetic structures. The assumption of equation (9) is more restrictive. It requires that the presence of electric current can be characterized by a single parameter, namely, a . The illustrative examples in Bogdan and Low (1986) look promising, but it remains to be seen from actual modelling with data if this is a workable hypothesis.

REFERENCES

Bogdan, T. J., and Low, B. C. 1986, "Three Dimensional Structures of Magnetostatic

Atmospheres. II. Modelling the Large-Scale Corona" , *Ap.J.* , in press.

Fisher, R., and Sime, D. G. 1984, "Rotational Characteristics of the White-Light Corona: 1965 - 1983" , *Ap.J.* **287**, 959.

Hundhausen, A. J. 1972, "Coronal Expansion and the Solar Wind" (Springer-Verlag).

Low, B. C. 1985a, "Some Recent Developments in the Theoretical Dynamics of Magnetic Fields" , *SolarPhys.* **100**, 309.

Low, B. C. 1985b, "Three-Dimensional Structures of Magnetostatic Atmospheres. I. Theory" , *Ap.J.* **293**, 31.

Nakagawa, Y. 1973, "A Practical Representation of the Solar Magnetic Field" , *Astron.Astrophys* **27**, 95.

Newkirk, Jr., G., and Altschuler, M. D. 1970, "Magnetic Fields and the Solar Corona. III. The Observed Connection between Magnetic Fields and the Density Structures of the Corona" , *Solar-Phys.* **13**, 131.

Parker, E. N. 1963, "Interplanetary Dynamical Processes" (Interscience).

Seehafer, N. 1978, "Determination of Constant α Force-Free Solar Magnetic Fields from Magnetograph Data" , *SolarPhys.* **58**, 215.

CORONAL DIAGNOSTICS

KENNETH R. LANG

Department of Physics and Astronomy
 Tufts University
 Medford, MA 02155

INTRODUCTION

The relatively recent development of satellite-borne X-ray telescopes and ground-based aperture synthesis radio telescopes has led to an examination of the solar corona with unprecedented resolution in space, time and frequency. The high spatial and spectral resolution of the X-ray instruments aboard Skylab and the Solar Maximum Mission (SMM) satellite have, for instance, showed that coronal loops dominate the structure of the Sun's lower corona [see Vaiana and Rosner (1978) for a review]. Strong magnetic fields hold a hot, dense plasma within the ubiquitous coronal loops.

Observations of soft X-ray spectral lines indicate that the quiescent, or non-flaring, coronal loops have electron temperatures $T_e \sim 2$ to 4×10^6 K and electron densities $N_e \sim 10^9$ to 10^{11} cm⁻³ with total extents $L \sim 10^9$ to 10^{10} cm. Similar temperatures are inferred from radio-wavelength brightness temperatures that are comparable to the local electron temperatures.

The detailed temperature and magnetic structure of the quiescent, or non-flaring, coronal loops has been inferred from radio wavelength synthesis observations. Synthesis maps describe the two-dimensional distribution of source brightness and the two-dimensional structure of the magnetic field [see Kundu and Lang (1985) for a review]. The unique ability to specify the strength and structure of the coronal magnetic fields is an important aspect of the radio wavelength synthesis maps.

Our current understanding of coronal loops is summarized in this chapter. It includes observations from ground-based radio telescopes and from X-ray telescopes lofted above the atmosphere, as well as theoretical interpretations of these observations.

The remaining sections of this introductory overview highlight both the observational and theoretical results that are discussed in greater detail in the following papers. We begin by discussing the three-dimensional structure of coronal loops. Alternative radiation mechanisms are then described within the context of both the radio and X-ray emission. Various methods of determining the strength and structure of the coronal magnetic field are then described. The final sections of

this introduction include the corone of nearby stars and future prospects for radio diagnostics of coronal loops.

THREE DIMENSIONAL STRUCTURE OF CORONAL LOOPS

Observations at different radio wavelengths generally sample different levels within coronal loops, with longer wavelengths referring to higher levels. The heights of the radio structures can be inferred from their angular displacements from underlying photospheric features, and the two-dimensional maps at different radio wavelengths can be combined to specify the three-dimensional structure of coronal loops. The accuracy of these height determinations depends on the geometry of the magnetic field, and the accuracy is greatest near the limb.

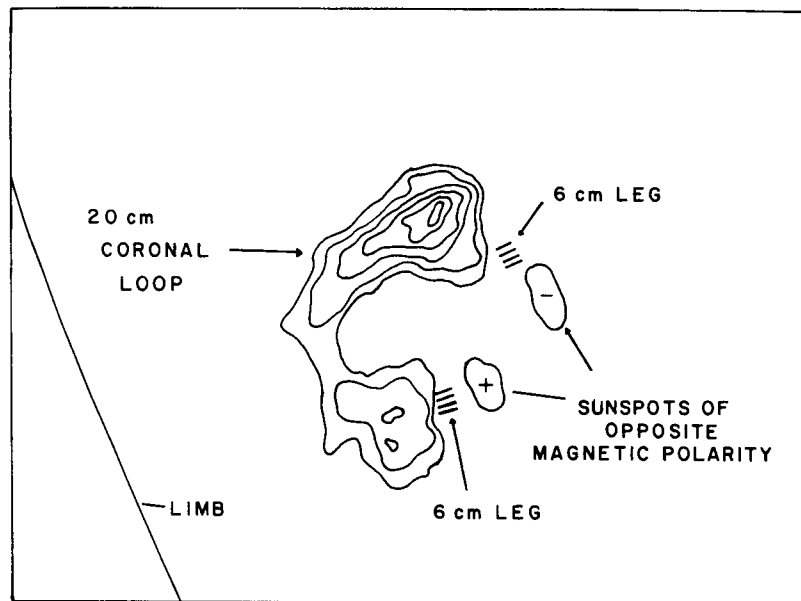


Figure 1. A VLA synthesis map of the total intensity, I , of the 20 cm emission from a coronal loop. The contours mark levels of equal brightness temperature corresponding to 0.2, 0.4, ...1.0 times the maximum brightness temperature of $T_B = 2 \times 10^6$ K. A schematic portrayal of the 6 cm emission, which comes from the legs of the magnetic loops, has been added together with the underlying sunspots that are detected at optical wavelengths.

Multiple-wavelength synthesis observations with the Very Large Array (VLA) have been carried out at wavelengths $\lambda = 20, 6$ and 2 cm (see Figure 1). The radiation at 20 cm can originate at both the apex and legs of coronal loops, and sometimes delineates the hot, dense plasma detected at X-ray wavelengths. The 20-cm coronal loops have brightness temperatures $T_B = 1 \times 10^6$ to 4×10^6 K and extents of $L = 10^9$ to 10^{10} cm. Magnetic field strengths of $H \sim 145$ G have been inferred from cyclotron lines at the apex of the 20-cm loops. Bright, highly polarized 6-cm cores often mark the legs of dipolar loops with $T_B = 2 \times 10^6$ to 5×10^6 K and heights $h \approx 10^9$ cm above the underlying sunspots. Values of H of ~ 600 to 900 G are inferred from the fact that these cores emit gyroresonance at the second or third harmonic of the gyrofrequency. The 2-cm emission has brightness temperatures of $T_B \approx 10^5$ K and often overlies sunspots at heights $h \approx 5 \times 10^8$ cm where H is $\approx 10^3$ G.

The 20-cm coronal loops have been discussed by Velusamy and Kundu (1981), Lang, Willson and Rayrole (1982), Dulk and Gary (1983), and McConnell and Kundu (1984). Multiple-wavelength VLA observations at 2, 6 and 20 cm have been presented by Lang, Willson and Gaizauskas (1983), Shevgaonkar and Kundu (1984), Kundu and Lang (1985) and Kundu (1986 - this proceedings). Most recently, Gary and Hurford (1986) have used microwave spectroscopy during a solar eclipse to delineate the physical conditions at a variety of levels within the legs and apex of a coronal loop (see Figure 2).

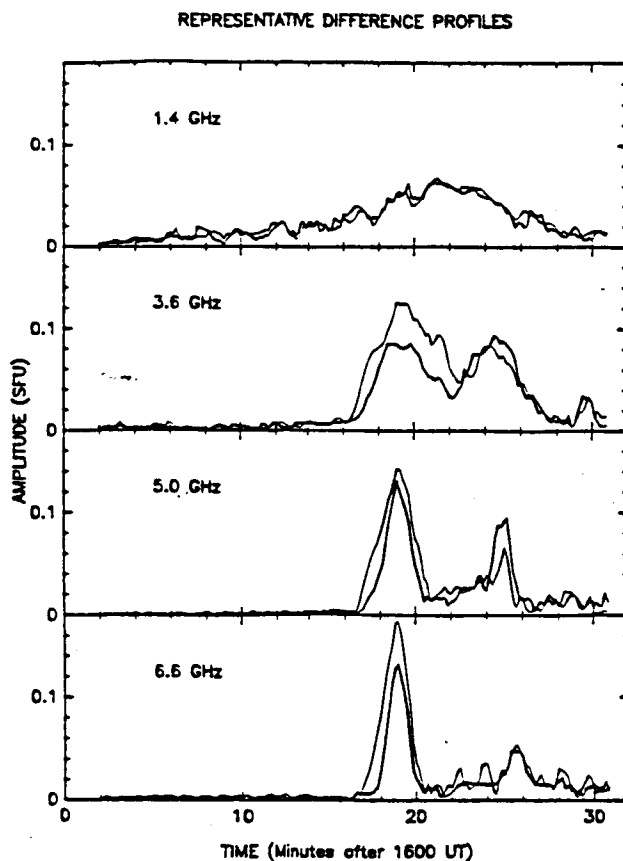


Figure 2. Differenced OVRO time profiles at four representative frequencies. Right hand circular (RH) polarization is shown by the heavy lines, and left hand (LH) polarization by the light lines. Below 3 GHz, the active region appears as a single board source. At higher frequencies, the region bifurcates into two main sources, becoming more localized to the sunspots as the observing frequency increases. The sense of polarization in the two spot sources is consistent with gyroresonance emission.

RADIATION MECHANISMS OF CORONAL LOOPS

The quiescent, or non-flaring, radiation of coronal loops is usually thermal in nature. The soft X-ray radiation is, for example, attributed to the thermal bremsstrahlung of hot million-degree electrons. However, at centimeter wavelengths there are two different thermal mechanisms: the bremsstrahlung of thermal electrons accelerated in the electric field of ions and the gyroresonant radiation of thermal electrons accelerated by magnetic fields can contribute to the emission. While the thermal bremsstrahlung emission is sensitive to the electron temperature and emission measure, gyroresonant emission is sensitive to the local magnetic field and electron temperature. It is this gyroresonant radiation which provides a sensitive measure of coronal magnetic field strength. Thus, it is important to distinguish which of these mechanisms is responsible for the emission from any given source at these wavelengths.

Strong evidence for thermal gyroradiation at coronal levels above sunspots has been provided by comparing the soft X-ray and centimeter-wavelength radiation of active regions [Kundu, Schmahl and Gerassimenko (1980); Pallavicini, Sakurai and Vaiana (1981); Schmahl et al. (1982)]. Although there is intense X-ray emission from the apex of coronal loops, the X-ray radiation often falls to undetectable levels in the legs of coronal loops above sunspots. Yet, intense radio radiation has sometimes been observed from both the apex and the legs of coronal loops. At other times radio emission has been detected from just the apex or just the legs of the loops, depending on the wavelength and observing conditions.

The near equality of the radio brightness and electron temperatures indicates that the radio emission from coronal loops is usually thermal. But the low electron densities inferred from the X-ray data above sunspots indicate that thermal bremsstrahlung is too weak to account for the intense radio radiation. The extra source of opacity has been attributed to gyroresonance absorption at the second or third harmonic of the gyrofrequency.

GYRORESONANT EMISSION



Figure 3. A Westerbork Synthesis Radio Telescope synthesis map of circular polarization at $\lambda = 6$ cm overlaid on an H α photograph obtained from the observatory at Athens. The contours are in steps of 1.5×10^5 K. The circularly polarized horseshoe structure that rings the sunspot umbra is due to gyroresonant emission in the curved magnetic fields of the sunspot penumbra.

Thermal gyroradiation at coronal levels above sunspots has been additionally confirmed by the detection of circularly polarized ring-shaped or horseshoe structures at 6 cm wavelength [Alissandrakis and Kundu (1982); Lang and Willson (1982)]. The highly-polarized (up to 100 percent) structures were predicted by the theory of gyroradiation in the curved magnetic fields above sunspot penumbrae [Gel'freikh and Lubyshev (1979)]. There is no detectable circular polarization above the central sunspot umbrae where the magnetic fields project radially upward into the hot coronal regions (see Figure 3). Depressions in the radio brightness temperature above sunspot umbrae have been attributed to cool material in these regions [Strong, Allisandrakis and Kundu(1984)].

At the longer, 20 cm, wavelength, emission is detected sometimes from both the apex and the legs of coronal loops (Lang, Willson, Strong, and Smith, 1986, and see Figure 4), and sometimes from just the apex (Webb et al., 1986). In the latter case, the electron densities and temperatures inferred from the X-ray spectral lines indicate that the plasma is optically thick at 20 cm, and hence that the observed brightness temperature should be equal to the electron temperature. However, the observed brightness temperature is a factor of 2 - 3 lower than the local electron temperature. Brosius and Holman (1986--this proceedings) and Holman (1986--this proceedings) explain this low brightness temperature in terms of a relatively cool, $<10^5$ K external plasma around the hot 2.5×10^6 K loops. Such material absorbs emissions primarily from the loop footpoints, where the optical depth along the line of sight is greatest. The loops and the external plasma are separated by a thin transition zone. The emission measure distributions for such models have been calculated, and have been found not only to agree well with recent observational emission measure curves for solar active region loops, but also to rise on both the cool and the hot side of the emission measure minimum. This is the first time that a theoretical emission measure curve for a single active region loop has been found to do this (cf. Antiochos and Noci, 1986).



Figure 4. A comparison of the soft X-ray (S.M.M.-left), H (SOON-middle) and 20 cm (V.L.A.-right) emission of an active region on the same day. The most intense soft X-ray emission is well correlated with intense 20 cm and H emission; but the 20 cm emission also extends across the areas near the sunspots where it is also intense. The angular spacing between fiducial marks on the axes is 60 arc-seconds.

Alternative radiation mechanisms may be required for intense radio emission from regions overlying weak photospheric magnetic fields. Observations of these regions have been reported by Akmedov et al. (1986), Lang (1986a-this proceedings), Lang and Willson (1986a-this proceedings), Webb, Davis, Kundu and Velusamy (1983), and Willson and Lang (1986). A possible explanation, first studied in detail by Chiuderi, Drago and Melozzi (1984), is the nonthermal synchrotron emission of mildly relativistic electrons; but some currently-unspecified mechanism must be accelerating the electrons. An equally plausible explanation is that currents amplify the magnetic field in the low solar corona to strengths that are a factor of ten larger than those inferred from magnetograms of the underlying photosphere. The observed radio emission might then be attributed to the gyroradiation of thermal electrons at the second and third harmonic of the gyrofrequency.

SPECIFYING THE CORONAL MAGNETIC FIELD

Measurements of the spectrum, polarization and angular size of active region sources at centimeter wavelengths have been pioneered by Soviet astronomers using the RATAN 600 [Radio Astronomy Telescope of the Academy of Sciences (Nauk)-see Akmedov et al. (1986)], and further developed and extended using the frequency-agile interferometer at the OVRO [Owens Valley Radio Observatory-see Hurford and Gary (1986) this proceedings]. By measuring both the angular size and the flux density at a variety of wavelengths, one can uniquely determine the brightness temperature spectrum of the sources. Circular polarization data can additionally be used to specify the magnetic field strength. Hurford and Gary (1986-this proceedings) have used this technique of microwave spectroscopy to measure the field distribution in the lower corona above sunspots.

In fact, both the strength and structure of the coronal magnetic field can be specified along the legs of coronal loops where gyroradiation dominates. The observations indicate that the magnetic fields systematically diverge and decrease in strength at higher heights (longer wavelengths) above single sunspots [see Hurford and Gary (1986) - this proceedings].

The magnetic field strength can also be inferred from individual cyclotron lines when gyroradiation dominates the emission. The observations at a single wavelength refer to a predetermined height where the radiation frequency is at one of the low harmonics of the gyrofrequency. Multiple-frequency observations provide information at a fixed height, regardless of field strength.

Holman and Kundu (1985) and Holman (1986 - proceedings) have pointed out that the emitting layers might be spatially resolved when a thin loop is observed. The magnetic field strength within each layer can then be inferred from the observing wavelength and the relevant harmonic. However, the cyclotron lines may overlap when the loop is thick or when a thin loop is observed along its legs.

The spectrum of an individual cyclotron line may also be obtained when observing at several wavelengths. For example, the spectra of individual cyclotron lines have been observed at wavelengths near 20 cm when the apex of a coronal loop is resolved [Willson (1985), Lang (1986a-this proceedings), Lang, Willson, Strong and Smith (1986)]. This is because the magnetic field strength is relatively constant near the loop apex; the cyclotron lines would merge into a continuum along the loop legs where the magnetic field strength decreases uniformly with height. Neutral current sheets might also play a role, leading to intense radio emission from a thin layer near the loop apex. Both a uniform field and a steep temperature gradient in the uniform region are probably required to detect the cyclotron lines. In any event observations of individual cyclotron lines indicate magnetic field strengths of $H = 145 \pm 5$ G at the apex of some coronal loops.

Solar bursts might also be used to infer the strength and configuration of coronal magnetic fields. Roberts, Edwin and Benz (1984) and Roberts (1984, 1986 - proceedings) have shown that bursts can impulsively generate magneto-acoustic oscillations in a coronal loop. These oscillations may be observed as quasi-periodic radio variations whose onset, duration and periodicity can be used to infer the height, size and magnetic field strength of the emitting region.

THE CORONAE OF NEARBY STARS

Nearby main-sequence stars of late spectral type exhibit quiescent, or non-flaring, X-ray emission whose absolute luminosity may be as much as 100 times that of the Sun [Vaiana et al. (1981)]. This suggests that these stars have hot stellar coronae with large-scale coronal loops and strong magnetic fields. The solar analogy suggests that these coronae might also be detected at radio wavelengths.

Nearby dwarf M flare stars do, in fact, exhibit slowly varying radio emission at 6 and 20 cm wavelength that is analogous to that of solar active regions. However, the X-ray observations rule out detectable thermal bremsstrahlung at radio wavelengths; the temperatures and emission measures inferred from the X-ray data indicate that the radio bremsstrahlung would be at least two orders of magnitude below detection thresholds. Moreover, thermal gyroradiation is an unlikely source of the intense 20 cm radiation from some of these stars; implausibly large coronal loops would have to be up to 10 times larger than the star with magnetic field strengths larger than 100 G at these remote distances. The most likely source of this slowly varying radiation in M-dwarf stars is gyrosynchrotron radiation from nonthermal electrons (Holman, 1986; Lang and Willson, 1986b).

In other words, the fact that we detect radio emission from these stars means that something unusual is happening on them. As an example, radio bursts from the dwarf M, stars have been attributed to coherent emission mechanisms like electron-cyclotron masers or coherent plasma radiation [Melrose and Dulk (1982); Dulk (1985)].

Quasi-periodic and individual spikes have been detected from the dwarf M star AD Leonis at 20 cm wavelength [Lang et al. (1983), Lang and Willson (1986a), Lang (1986a)-this proceedings]. These spikes are up to 100% circularly polarized with rise times less than 5 milliseconds. The rapid rise time indicates that the emitter's size is less than 0.005 of the star's radius, and that a symmetric emitter has a brightness temperature in excess of 10^{16} K. Such a high brightness temperature requires a coherent radiation mechanism. Similar high brightness temperature spikes

have been observed during solar flares. Unlike solar flares, however, the underlying nonspiky emission from the AD Leonis flare is probably also coherent [Holman, Bookbinder and Golub (1985)].

Coherent emission is also suggested by the narrow-band, slowly varying, 20-cm emission from the dwarf M star YZ Canis Minoris [Lang and Willson (1986)], as well as narrow-band 20 cm flares from the red dwarf stars AD Leo and UV Ceti [White, Kundu and Jackson (1986)]. The narrow-band structure cannot be explained by continuum emission processes such as thermal bremsstrahlung, thermal gyroradiation, or nonthermal gyrosynchrotron radiation. Coherent radiation processes seem to be required.

If the radiation is emitted by an electron-cyclotron maser at the second harmonic of the gyrofrequency, then the magnetic field strength is $H = 250$ G, and constraints on the plasma frequency imply an electron density of $N_e \approx 6 \times 10^9 \text{ cm}^{-3}$. Coherent plasma radiation at the first or second harmonic of the plasma frequency respectively require $N_e = 2 \times 10^{10} \text{ cm}^{-3}$ and $H \ll 500$ G or $N_e = 6 \times 10^9 \text{ cm}^{-3}$ and $H \ll 250$ G. Thus, the coherent burst mechanisms suggest that the coronae of dwarf M stars have physical parameters similar to those of solar active regions.

FUTURE PROSPECTS FOR CORONAL DIAGNOSTICS

Probable observations of coherent radiation processes on nearby stars are stimulating further searches for coherent signatures in the Sun's radio radiation. In fact, narrow-band structure has been observed in a solar burst [Lang and Willson (1984): Lang (1986b)], and rapid spikes during some solar bursts have been interpreted in terms of electron-cyclotron masers [Holman, Eichler and Kundu (1980); Holman (1983)]. Future observations with high resolution in time and frequency at the VLA, OVRO and Nancay will help determine the role that coherent radiation processes play in solar active regions.

The next decade will also include detailed comparisons of radio and X-ray observations with model coronal loops that include both thermal bremsstrahlung and thermal gyroradiation. Coronal magnetic fields may be directly inferred from observations and models in which the expected radio emission is computed as a function of wavelength, polarization and viewing angle. A comparison of the observed radiation with theoretical expectations will determine magnetic field strengths, electron densities and electron temperatures.

The evolution of coronal loops has strong future potential. Of special interest are the preheating and magnetic changes that trigger solar bursts [see Kundu and Lang (1985) for a review]. Emerging coronal loops and the magnetic interaction of existing coronal loops will be particularly interesting topics.

Future studies of the evolution of the three-dimensional magnetic and plasma structure of coronal loops will lead to valuable new insights to the nature of solar active regions and eruptions on the Sun and nearby stars. Such insights can only be fully realized by the development of a solar-stellar synthesis radiotelescope. Such an instrument would be dedicated to solar and stellar observations with high angular, temporal and frequency resolution.

ACKNOWLEDGEMENTS

Radio astronomical studies of the Sun at Tufts University are supported under Air Force Office of Scientific Research grant AFOSR-83-0019 and contract N0014-86-K-0068 with the Office of Naval Research. Our simultaneous VLA and Solar Maximum Mission satellite observations of the Sun are supported under NASA grant NAG 5-501.

REFERENCES

- Akhmedov, S.B., et al., 1986, "Structure of a Solar Active Region from RATAN 600 and Very Large Array Observations," *Astrophys. J.*, 301, 460-464.
- Alissandrakis, C.E. and M.R. Kundu, 1982, "Observations of Ring Structure in a Sunspot Associated Source at 6 Centimeter Wavelength," *Astrophys. J. (Letters)*, 253, L49-L52.
- Alissandrakis, C.E. and M.R. Kundu, 1984, "Center-to-Limb Variation of a Sunspot-Associated Microwave Source," *Astron. Astrophys.*, 139, 271-284.
- Antiochos, S.K. and G. Noci, 1986 "The Structure of the Static Corona and Transition Region," *Astrophys. J.*, 301, 440-447
- Brosius, J.W. and G.D. Holman, 1986, "Theoretical Models of Free-Free Microwave Emission from Solar Magnetic Loops," this Proceedings.
- Chiuderi-Drago, F. and M. Melozzi, 1984, "Non-Thermal Radio Sources in Solar Active Regions," *Astron. Astrophys.* 131, 103-110.
- Dulk, G.A., 1985, "Radio Emission from the Sun and Stars," *Ann. Rev. Astron. Ap.*, 23, 169-180.
- Dulk, G.A. and D.E. Gary, 1983, "The Sun at 1.4 GHz: Intensity and Polarization," *Astron. Astrophys.* 124, 103-107.
- Gary, D.E. and G.J. Hurford, 1986, "Multi-Frequency Observations of a Solar Active Region During a Partial Eclipse, BBSO 259, submitted to *Astrophys. J.*
- Gel'frikh, G.B. and B.I. Lubyshv, 1979, "Structure of Local Sources of the S Component of Solar Radio Emission," *Sov. Astron. A.J.*, 23, 316-322.
- Holman, G.D., 1983, "Some Recent Results in the Interpretation of High Brightness Temperature Microwave Spike Emission," *Adv.Space Res.*, 2, No.11, 181-183
- Holman, G.D., 1986, "Coronal Heating and the X-ray and Microwave Emission from M-Dwarf Flare Stars," in *Proceedings of the Fourth Cambridge Workshop on Cool Stars, Stellar Systems, and the Sun*, eds. M. Zeilik and D.M. Gibson (Springer-Verlag), in press.
- Holman, G.D., 1986, "High-Spatial-Resolution Microwave and Related Observations as Diagnostics of Coronal Loops," - this Proceedings.
- Holman, G.D., J. Bookbinder and L. Golub, 1985, "Implications of the 1400 MHz Flare Emission from AD Leo for the Emission Mechanism and Flare Environment," in *Radio Stars*, ed. R.M. Hjellming and D.M. Gibson, (Dordrecht: Reidel), 35-37.
- Holman, G.D., D. Eichler and M.R. Kundu, 1980, "An Interpretation of Solar Flare Microspikes as Gyrosynchrotron Maser Emission," in *Radio Physics of the Sun - I.A.U. Symposium No. 86*, ed. M.R. Kundu and T.E. Gergely, (Dordrecht: Reidel), 457-459.
- Holman, G.D. and M.R. Kundu, 1985, "The Microwave Structure of Hot Coronal Loops," *Astrophys. J.*, 292, 291-296.
- Hurford, G.J. and D.E. Gary, 1986, "Measurement of Coronal Fields Using Spatially Resolved Microwave Spectroscopy," - this Proceedings.
- Kundu, M.R., 1986, "Three Dimensional Structures of Solar Active Regions," this Proceedings."

- Kundu, M.R. and C.E. Alissandrakis, 1984, "Structure and Polarization of Active Region Microwave Emission," *Solar Phys.*, 94, 249-283.
- Kundu, M.R. and K.R. Lang, 1985, "The Sun and Nearby Stars," *Science*, 228, 9-15.
- Kundu, M.R., E.J. Schmahl and M. Gerassimenko, 1980, "Microwave, EUV and X-ray Observations of Active Region Loops: Evidence for Gyroresonance Absorption in the Corona," *Astron. Astrophys.* 82, 265-271.
- Kundu, M.R. and T. Velusamy, 1980, "Observation with the VLA of a Stationary Loop Structure in the Sun at 6 cm Wavelength," *Astrophys. J. (Letters)*, 240, L63-L65.
- Lang, K.R., 1986a, "Coronal Plasmas on the Sun and Nearby Stars," this Proceedings.
- Lang, K.R., 1986b, "Flare Stars and Solar Bursts: High Resolution in Time and Frequency," *Solar Phys.*, in press.
- Lang, K.R., J. Bookbinder, L. Golub and M. Davis, 1983, "Bright, Rapid, Highly Polarized Radio Spikes from the M Dwarf AD Leo," *Astrophys. J. (Letters)*, 272, L15-L18.
- Lang, K.R. and R.F. Willson, 1982, "Polarized Horseshoes Around Sunspots at 6 Centimeter Wavelength," *Astrophys. J. (Letters)*, 255, L111-L117.
- Lang, K.R. and R.F. Willson, 1983, "Multiple Wavelength Observations of Flaring Active Regions," *Adv. Space Res.* 2, No. 11, 91-100.
- Lang, K.R. and R.F. Willson, 1984, "V.L.A. Observations of Flare Build-Up in Coronal Loops," *Adv. Space Res.* 4, No. 7, 105-110.
- Lang, K.R. and R.F. Willson, 1986a, "Compact, Variable, Moving Sources on the Sun at 2 Centimeters Wavelength," this Proceedings.
- Lang, K.R. and R.F. Willson, 1986b, "Narrow-Band, Slowly Varying Decimetric Radiation from the Dwarf M Flare Star YZ Canis Minoris," *Astrophys. J. (Letters)*, 302, L17-L21.
- Lang, K.R. and R.F. Willson, 1986c, "Millisecond Radio Spikes from the Dwarf M Flare Star AD Leonis," *Astrophys. J.*, in press.
- Lang, K.R., R.F. Willson and V. Gaizauskas, 1983, "Very Large Array Observations of Solar Active Regions III. Multiple Wavelength Observations," *Astrophys. J.*, 267, 455-464.
- Lang, K.R., R.F. Willson and J. Rayrole, 1982, "Very Large Array Observations of Coronal Loops at 20 Centimeter Wavelength," *Astrophys. J.*, 258, 384-387.
- Lang, K.R., R.F. Willson, K.T. Strong and K.L. Smith, 1986a, "Physical Parameters of a Solar Active Region Inferred from Thermal Cyclotron Lines and Soft X-Ray Spectral Lines," *Astrophys. J.*, to be submitted.
- Lang, K.R., R.F. Willson, K.T. Strong and K. L. Smith, 1986b, "Simultaneous Solar Maximum Mission and Very Large Array Observations of Solar Active Regions," *Astrophys. J.*, to be submitted.
- McConnell, D. and M.R. Kundu, 1983, "VLA Observations of a Solar Active Region and Coronal Loops," *Astrophys. J.*, 269, 698-705.
- Melrose, D.B. and G.A. Dulk, 1982, "Electron-Cyclotron Masers as the Source of Certain Solar and Stellar Bursts," *Astrophys. J.*, 259, 844-858.
- Pallavicini, R., T. Sakurai and G.S. Vaiana, 1981, "X-Ray, EUV and Centimetric Observations of Solar Active Regions: an Empirical Model for Bright Radio Sources," *Astron. Astrophys.*, 98, 316-327.
- Roberts, B., 1984, "Waves in Inhomogeneous Media," in *The Hydrodynamics of the Sun*, ESA SP-220, November.
- Roberts, B., 1986, "Guided MHD Waves as a Coronal Diagnostic Tools," this Proceedings.
- Roberts, B., P.M. Edwin and A.O. Benz, 1984, "On Coronal Oscillations," *Astrophys. J.*, 279, 857-865.
- Schmahl, E.J., et al., 1982, "Active Region Magnetic Fields Inferred from Simultaneous VLA Microwave Maps, X-Ray Spectroheliograms, and Magnetograms," *Solar Physics* 80, 233-249.

- Shevgaonkar, R.K. and M.R. Kundu, 1984, "Three-Dimensional Structures of Two Solar Active Regions from VLA Observations at 2, 6 and 20 Centimeter Wavelengths" *Astrophys. J.*, 283, 413-420.
- Strong, K.T., C.E. Alissandrakis and M.R. Kundu, 1984, "Interpretation of Microwave Active Region Structures Using SMM Soft X-Ray Observations," *Astrophys. J.*, 277, 865-873.
- Vaiana, G.S. and R. Rosner, 1978, "Recent Advances in Coronal Physics," *Ann. Rev. Astron. Ap.* 16, 393-405.
- Vaiana, G.S., et al., 1981, "Results From An Extensive Einstein Stellar Survey," *Astrophys. J.*, 245, 163-182.
- Velusamy, T. and M.R. Kundu, 1981, "VLA Observations of Postflare Loops at 20 Centimeter Wavelength," *Astrophys. J. (Letters)*, 243, L103-L107.
- Webb, D.F., J.M. Davis, M.R. Kundu and T. Velusamy, 1983, "X-Ray and Microwave Observations of Active Regions," *Solar Phys.* 85, 267-283.
- Webb, D.F., G.D. Holman, J.M. Davis, M.R. Kundu and R.K. Shevgaonkar, 1986, "The Plasma and Magnetic Field Properties of Coronal Loops Observed At High Spatial Resolution," submitted to *Astrophys. J.*
- White, S.M., M.R. Kundu and P.D. Jackson, 1986, "Narrowband Radio Flares from Red Dwarf Stars," *Astrophys. J.*, submitted.
- Willson, R.F., 1983, "Possible Detection of Thermal Cyclotron Lines from Small Sources Within Solar Active Regions," *Solar Phys.*, 89, 103-113.
- Willson, R.F., 1985, "VLA Observations of Solar Active Regions at Closely Spaced Frequencies: Evidence for Thermal Cyclotron Line Emission," *Astrophys. J.*, 298, 911-917.

THREE DIMENSIONAL STRUCTURES OF SOLAR ACTIVE REGIONS

M. R. Kundu
Astronomy Program
University of Maryland
College Park, MD 20742

ABSTRACT

Three-dimensional structure of an active region is determined from observations with the Very Large Array (VLA) at 2, 6, and 20 cm. This region exhibits a single magnetic loop of length $\sim 10^{10}$ cm. The 2 cm radiation is mostly thermal bremsstrahlung and originates from the footpoints of the loop. The 6 and 20 cm radiation is dominated by low-harmonic gyroresonance radiation and originates from the upper portion of the legs or the top of the loop. The loop broadens toward the apex. The top of the loop is not found to be the hottest point, but two temperature maxima on either side of the loop apex are observed, which is consistent with the model proposed for long loops. From 2 and 6 cm observations it can be concluded that the electron density and temperature cannot be uniform in a plane perpendicular to the axis of the loop; the density should decrease away from the axis of the loop.

INTRODUCTION

The three dimensional structure of magnetic fields above active regions in the low corona and chromosphere-corona transition zone can be determined from multiwavelength radio observations. Radio methods of measuring magnetic fields in active regions are based upon the measurement of total intensity (I) and circular polarization (V) and the use of precise knowledge of the generating mechanisms of radio emission in active regions. The circular polarization in the gyroresonance absorption process which is relevant for sunspot associated sources is due to the fact that for typical conditions in the corona, the extraordinary mode becomes optically thick at the levels where $f = 3 f_H$ or $2 f_H$ ($f_H =$ gyrofrequency), whereas the ordinary mode becomes optically thick at the level $f = 2 f_H$ which is located at a lower level in the sun's atmosphere; the circular polarization in the extraordinary mode then results as a consequence of the temperature structure above active regions. In the free-free process, the circular polarization results from the fact that in the presence of a magnetic field the absorption coefficient in the extraordinary mode is higher than that in the ordinary mode; consequently, the $\tau = 1$ level in the e-mode occurs higher in the solar atmosphere than in the o-mode. Both these processes have been used to estimate magnetic field strengths at centimeter and millimeter wavelengths (Alissandrakis et al. 1980; Kundu et al. 1977; Kundu and McCullough, 1972). The circular polarization maps can be used as chromospheric and coronal magnetograms provided there is no radio wave propagation effect, which can be verified from the correspondence of the radio polarities with those of the photospheric magnetic field.

Aside from the magnetic field structure, the knowledge of the structure of an active region as a function of height is important. This is especially so

when the active region appears in the form of a loop as is often the case at centimeter wavelengths. Three dimensional active region studies have been reported by Shevgaonkar and Kundu (1984) from multifrequency observations using the VLA. They studied a region that exhibited a single loop without any other interacting loop nearby.

OBSERVATIONS

Figure 1 shows the total intensity (I) and circular polarization (V) maps at 2, 6 and 20 cm wavelengths. The 2 cm radiation ($\sim 80\%$ polarized; $T_b \sim 1.5 \times 10^5$ K) comes from two isolated spots which are co-spatial with two strong magnetic regions with opposite polarities, the sense of polarization being of the same sign as the magnetic fields on the magnetogram. Thus, the 2 cm radiation appears to originate from the foot points of a magnetic loop. The 6 cm total intensity map again shows two regions ($T_b \sim 4.5 \times 10^6$ K; $p \sim 10-15\%$), approximately at the same positions as the 2 cm regions, but larger in size. The larger size of the two regions at 6 cm compared to that at 2 cm, indicates that, if the active region emission originates in a loop, the loop must be diverging towards its apex. The existence of two isolated regions at 6 cm, with $T_b \sim 4.5 \times 10^6$ K indicate that the two legs of the loop have not started closing, and that the 6 cm radiation originates from the upper part of the legs of the loop. At 20 cm, the two regions are almost merged into each other but still keep their identity as two regions. The centers of these two merging regions are again co-spatial with the 6 cm peaks within the errors of measurement. The size of the two 20 cm regions is larger than that at 6 cm, but the peak T_b has decreased to $\sim 2.5 \times 10^6$ K and p is $\sim 20\%$.

The maps at different wavelengths obviously give sectional views of a magnetic loop at different heights. The magnetic field diverges along the loop in the upward direction. The loop seems to start closing at a height of $\sim 50 \times 10^3$ kms, where the 20 cm radiation originates. The 2 cm polarization data indicate that the extraordinary mode is optically thick in the transition zone, with $T_e \sim 1.5 \times 10^5$ K, and the ordinary mode becomes optically thick at a lower level (i.e. for a lower harmonic), with $T_e \lesssim 10^5$ K or it is optically thin. Shevgaonkar and Kundu concluded that the 2 cm radiation is dominated by thermal bremsstrahlung and originates from a layer where $N_e \sim 10^{10} \text{ cm}^{-3}$ and $B \sim 2000$ G. The T_b at 6 cm is $\sim 4.5 \times 10^6$ K and polarization is $\sim 15\%$. Since polarization is low, the gyroresonance radiation has to be optically thick for both modes. Taking $\alpha \approx 45^\circ$, $L_B = 10^9$ cm, $N_e = 4 \times 10^9 \text{ cm}^{-3}$, the highest harmonic for which both modes are optically thick is 3, resulting in $B \sim 600$ G at a height of $\sim 10^4$ kms. Assuming that the same magnetic field diverges with height, the conservation of the magnetic flux requires that if B is ~ 600 G and 2000 G respectively at 6 and 2 cm, the ratio of the source sizes at 6 cm and 2 cm should be ~ 3.5 , in contrast to the observed ratio of ~ 24 . This difficulty was overcome by assuming that in the outer rim of the magnetic pole, the 2 cm T_b is $< 10\%$ of its peak value, which requires the optical depth to be $\gtrsim 0.1$. Shevgaonkar and Kundu showed that the observations could be explained if N_e decreases by a factor of 3 from the core to the outer rim and B decreases towards the edge of the loop by a factor of 1.76 if T is taken constant or even more slowly if a cool core model is assumed, consistent with the combined high resolution microwave and soft x-ray observations of Strong et al (1984). If the magnetic field remains constant over the outer rim, the conservation of flux gives magnetic pole size ~ 2.5 times that of the 2 cm region, the same as the pole size in the magnetogram.

ORIGINAL PAGE IS
OF POOR QUALITY

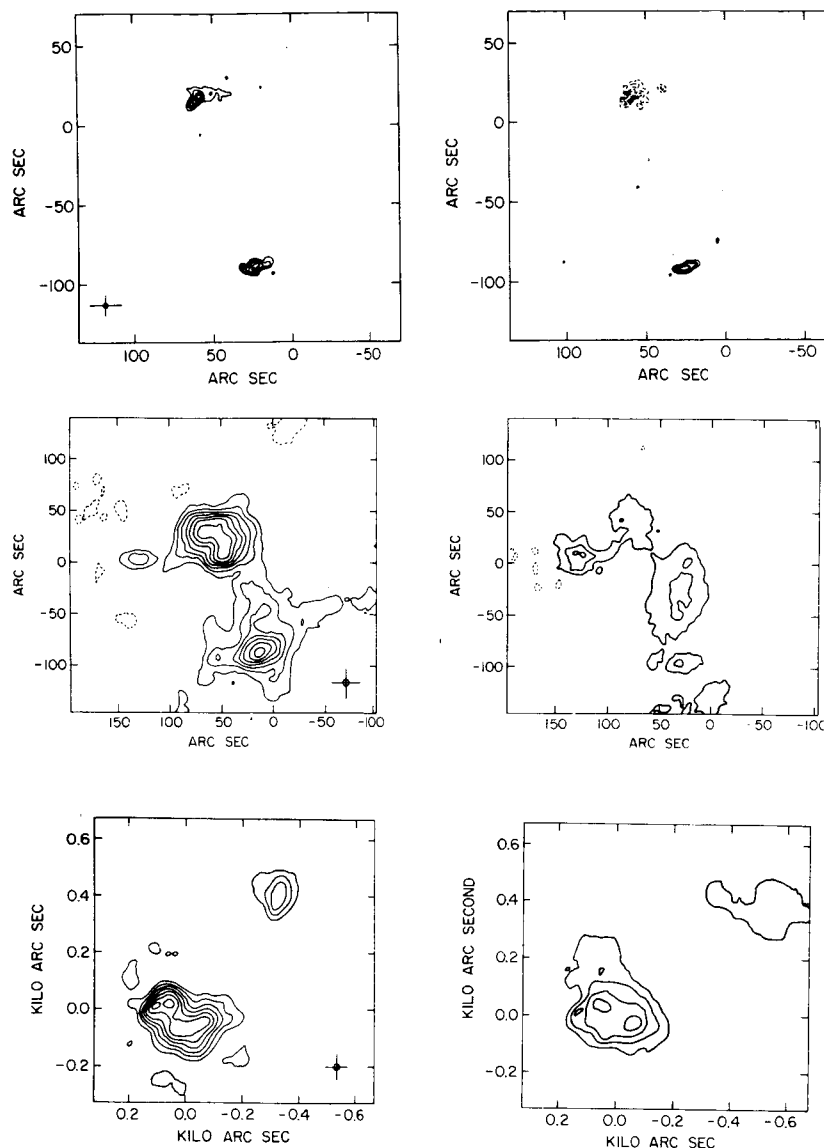


Fig. 1. Total intensity (left) and circular polarization (right) maps of an active region at 2 cm (top), 6 cm (middle) and 20 cm (bottom), made with the VLA with resolution of 2", 5" and 20" arc respectively. At 2, 6 and 20 cm, peak $T_b = 1.5 \times 10^5$ K, 4.6×10^6 K and 2.3×10^6 K respectively; the corresponding contour intervals are 2.9×10^4 K, 5.9×10^5 K and 3.1×10^5 K. For V-maps, the contour intervals are 1.9×10^4 K, 2.2×10^5 K and 1×10^5 K respectively.

At 20 cm, the radiation ($T_b \sim 2.5 \times 10^6$ K, $p \sim 20\%$) originates from the upper portion of the legs of the loop. According to the loop model with uniform energy deposition function along the loop (Rosner et al. 1978), the loop apex should be hottest and so T_b at 20 cm level must be at least 5×10^6 K, the same as the 6 cm T_b . But since the observed T_b is $\sim 2.5 \times 10^6$ K, the radiation must be optically thin with $\tau \sim 0.7$ to satisfy Rosner et al's model. For a source of

dimension 5×10^9 cm, N_e required to make $\tau \sim 0.7$ due to thermal bremsstrahlung should be $\sim 4 \times 10^9$ cm $^{-3}$, or an emission measure of $\sim 10^{29}$ cm $^{-5}$. This emission measure is higher by about one order of magnitude than that computed by Lang, Willson and Gaizauskas (1983) from VLA observations and by Vaiana and Rosner (1978) from X-ray observations. From magnetic flux conservation, the source size at 20 cm compared to that at 6 cm gives a magnetic field of ~ 150 G at 20 cm level, which is sufficient to generate the 3rd or 4th harmonic gyroresonance emission at 20 cm. Thus, the 20 cm radiation must be due to gyroresonance absorption. For $s=3$, $\tau_{\text{res}} \sim 10^3$ for both modes. By reducing N_e , it does not seem that the radiation can be made optically thin for $s=3$. Thus, T_e must be 2.5×10^6 K. For $N_e \sim 10^9$ cm $^{-3}$ or an emission measure of $\sim 10^{28}$ cm $^{-5}$ the region is optically thin due to thermal bremsstrahlung for $T_e \sim 2 \times 10^6 - 5 \times 10^6$ K, which can not explain the observed high T_b of $\sim 2.5 \times 10^6$ K. Lang, Willson and Gaizauskas (1983) concluded from their VLA observations that the 20 cm radiation ($T_b \sim 0.5 \times 10^6$ K) was optically thin bremsstrahlung, with $T_e \sim 2 \times 10^6$ K. However, to get $T_b \sim 2.5 \times 10^6$ K as observed by us, gyroresonance mechanism has to be invoked. Thus, the higher layer from which the 20 cm radiation originates is cooler than the lower layer from which the 6 cm radiation originates. This result does not support Rosner et al's model of uniform energy deposition along the loop, which gives maximum temperature at the apex of the loop. On the other hand, our observations provide evidence for Vesecky et al's (1979) model, according to which the temperature maximum need not necessarily occur at the apex of the loop but there could be two maxima, one on either side of it and a minimum at the apex of the loop.

CONCLUDING REMARKS

We have determined the three-dimensional structure of an active region from observations made with the Very Large Array (VLA) at 2, 6, and 20 cm. The region concerned is a single magnetic loop of length $\sim 10^{10}$ cm. The 2 cm radiation is found to be mostly thermal bremsstrahlung, originating from the footpoints of the loop. The 6 and 20 cm radiation is dominated by low-harmonic gyroresonance radiation, originating from the upper portion of the legs or the top of the loop. The loop broadens toward the apex. The top of the loop is not found to be the hottest point, but two temperature maxima on either side of the loop apex are observed, which is consistent with the model proposed for long loops. From 2 and 6 cm observations we conclude that the electron density and temperature cannot be uniform in a plane perpendicular to the axis of the loop; the density should decrease away from the axis of the loop.

REFERENCES

- Alissandrakis, C.E., M.R. Kundu, and P. Lantos, 1981, *Astr. Ap.* **82**, 30.
- Kundu, M.R., C.E. Alissandrakis, J.D. Bregman, and A.C. Hin, 1977, *Ap.J.*, **213**, 278.
- Kundu, M.R. and T.P. McCullough, 1972, *Solar Phys.* **27**, 182.
- Lang, K.R., R.F. Willson, and V. Gaizauskas, 1983, *Ap.J.*, **267**, 455.
- Rosner, R., W.H. Tucker and G.S. Vaiana, 1978, *Ap.J.* **220**, 643.

Shevgaonkar, R.K. and M.R. Kundu, 1984, Ap.J., 283, 413.

Strong, K.T., C.E. Alissandrakis, and M.R. Kundu, 1984, Ap.J., 277, 865.

Vaiana, G.S. and R. Rosner, 1978, Ann. Rev. Astr. Ap., 16, 393.

Vesecky, J.R., S.K. Antiochos, and J.H. Underwood, 1979, Ap.J., 233, 987.

HIGH-SPATIAL-RESOLUTION MICROWAVE AND RELATED OBSERVATIONS
AS DIAGNOSTICS OF CORONAL LOOPS

Gordon D. Holman
Laboratory for Astronomy and Solar Physics
NASA Goddard Space Flight Center
Greenbelt, Maryland

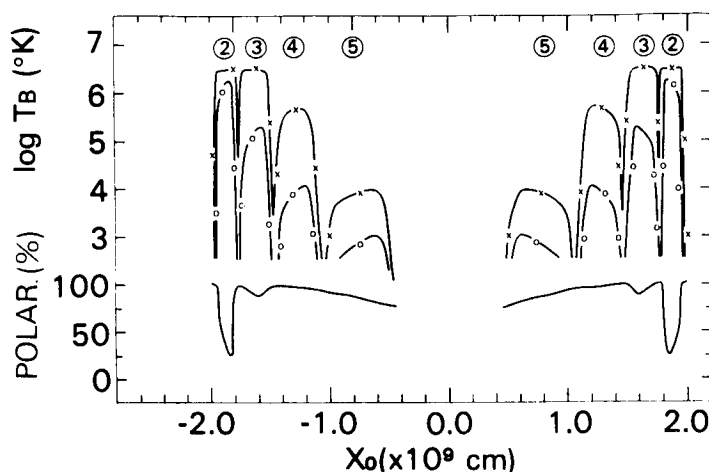
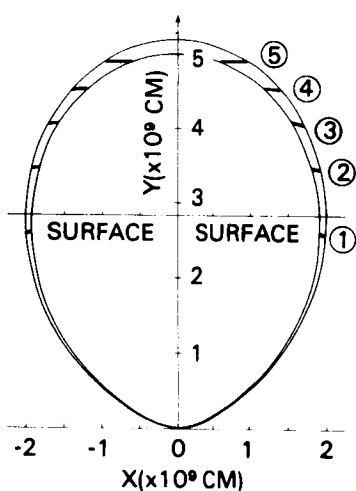
High-spatial-resolution microwave observations of coronal loops, together with theoretical models for the loop emission, can provide detailed information about the temperature, density, and magnetic field within the loop, as well as the environment around the loop. The capability for studying magnetic fields is particularly important, since there is no comparable method for obtaining direct information about coronal magnetic fields. Knowledge of the magnetic field strength and structure in coronal loops is important for understanding both coronal heating and flares. With arc-second-resolution microwave observations from the VLA, supplemental high-spectral-resolution microwave data from a facility such as the Owens Valley frequency-agile interferometer, and the ability to obtain second-of-arc resolution EUV or soft X-ray images, the capability already exists for obtaining much more detailed information about coronal plasma and magnetic structures than is presently available.

It has long been recognized by practitioners of solar radio astronomy that microwave observations provide a means of determining magnetic field strengths in the corona and transition zone (see Kundu and Lang, 1985, for a recent review). Early observations of the sun were encumbered by poor spatial resolution. Arc-second-resolution observations with the VLA, however, have clearly demonstrated that individual coronal loops and other structures can be resolved at microwave frequencies (see Kundu and Lang, 1985). Nevertheless, these single-frequency observations have not led to unambiguous determinations of coronal magnetic field strengths, since two different mechanisms, thermal bremsstrahlung (free-free) and thermal gyroresonance (cyclotron) emission, and possibly nonthermal gyrosynchrotron emission, can contribute to the microwave emission. Free-free emission is sensitive to electron temperature and emission measure, while gyroresonance emission is most sensitive to magnetic field strength (and direction) and electron temperature. Using gyroresonance emission to determine magnetic field strengths requires determining which of several possible harmonics of the electron gyrofrequency is responsible for the observed emission. Simultaneous VLA observations at 1.5 GHz, 5 GHz, and/or 15 GHz have not improved this situation much, since the emission mechanisms are also sensitive to frequency, and entirely different structures are typically observed at these widely-spaced frequencies. In order to confidently extract the desired physical information from these observations, additional observational data and more detailed theoretical modeling are required.

Computations of the microwave and related emissions from model coronal structures are important for obtaining an idea of what microwave signatures might be observed, for determining what combination of observational data is required to obtain the desired physical information, and are necessary for extracting complete information from the observational data. With these considerations in mind, the thermal gyroresonance emission from two-dimensional dipole loop models has been computed by Holman and Kundu (1985). These models were chosen as the simplest non-trivial, but potentially realistic, configuration from which the coronal microwave emission might arise. One of these loop models, and the corresponding 5 GHz

microwave emission, is shown in the figure below. An isothermal, 3×10^6 K plasma is confined between dipole magnetic field lines that cross the y axis at $y = 5.0$ and 5.2×10^9 cm (the dipole is at the origin). The footpoints of the loop are taken to be at the value of y where the outer magnetic field line becomes parallel to the y axis, marked "surface" in the figure. The field strength at the top of the loop is 300 G, and 1500 G at the footpoints. The loop density falls exponentially with height from 10^{10} cm $^{-3}$ at the footpoints to 10^9 cm $^{-3}$ at the top. The heavy curves indicate locations within the loop where a harmonic (circled number) of the local electron gyrofrequency is equal to the observation frequency, and, hence, locations from which gyroresonance microwave emission may be observed. For this model, thermal bremsstrahlung emission is not significant.

HARMONICS AT 5 GHz THIN LOOP

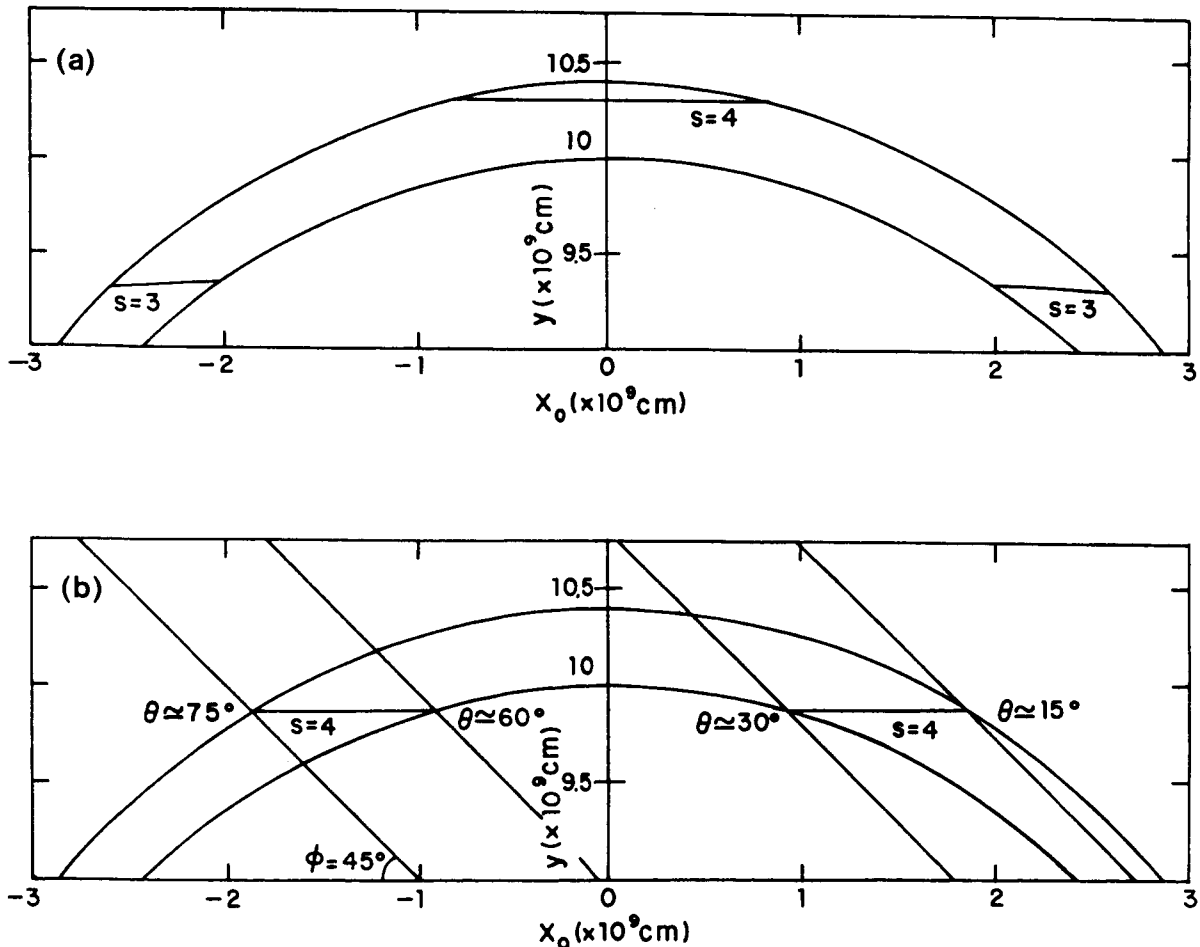


The figure on the right shows the 5 GHz brightness temperature and polarization plotted as a function of position for a scan along the length of the loop with the line of sight parallel to the y axis (the curve labeled with the symbol "x" shows extraordinary mode emission, and "o" denotes the ordinary mode of polarization). The important features are the high degree of spatial and polarization structure. The optically thick harmonics give the loop temperature, and determination of the harmonic number gives the local magnetic field strength. Computations of the loop emission at other nearby frequencies show that the microwave structure is very sensitive to observation frequency. It is also sensitive to the angle at which the loop is observed. This sensitivity can be used to remove the ambiguities present in a single frequency, single aspect angle observation. High-spatial-resolution observations at a series of closely spaced frequencies, such as those recently published by Willson (1985), are particularly valuable in this respect.

Although gyroresonance emission does not provide a sensitive diagnostic of plasma density, the gyroresonance optical depth is density dependent. Also, free-free emission is sensitive to emission measure and, therefore, density. For these reasons it is particularly valuable to have an independent measure of density or emission measure, such as can be provided by EUV or soft X-ray observations. Obtaining simultaneous images at microwave and EUV and/or soft X-ray frequencies provides the most direct means of obtaining detailed information about the magnetic and plasma properties of coronal structures. Simultaneous VLA and high-resolution (rocket) soft X-ray observations of active region loops have been obtained in a

series of papers by Webb, Davis, Kundu, and collaborators (Webb et al., 1983; Kahler et al., 1984; Webb et al., 1986). (References to other coordinated microwave and soft X-ray observations can be found in these papers.) These papers contain microwave observations of soft X-ray loops at 4.9 GHz (6 cm) and at 1.45 GHz (20 cm). Except for the hotter post-flare loop studied by Kahler et al. (1984), the X-ray loops had temperatures of $2.5 - 3 \times 10^6$ K, the X-ray temperature and emission measure did not vary significantly along the length of the loops, and the observations tended to show a relatively compact microwave source at or near the apex of the X-ray loop. These observations are studied in terms of microwave loop models in Webb et al. (1986).

Since the X-ray emission is primarily thermal bremsstrahlung, soft X-ray observations give direct information about the importance of thermal bremsstrahlung at microwave frequencies. For the active region loops observed by Webb et al. (1983, 1986), free-free emission was found to be important for the loops observed at 1.45 GHz, but was found to be unimportant for those observed at 4.9 GHz. The loops observed at 4.9 GHz were generally $>30\%$ polarized and had brightness temperatures slightly lower than the electron temperature deduced from the X-ray data. Since the highest optically thick harmonic was found to be the fourth, it was concluded that the 4.9 GHz emission was most likely 4th harmonic gyroresonance emission. This implies a magnetic field strength of 438 Gauss at the location of the microwave sources. Models for the loops observed at 4.9 GHz are shown in the figure below (from Webb et al. 1986).



The models in the figure, as in the previous figure, are dipole loop models, for which the magnetic field strength varies along the length of the loop. It was found that if the magnetic field did not vary along the length of the loop, too much of the loop would have been observed at 4.9 GHz. On the other hand, if the field strength varied as much as in the models of Holman and Kundu (1985), lower harmonic emission would have been observed from the legs of the loops. The requirement, then, is that the 3rd harmonic level not be present in the loop or, at least, in the hot, X-ray emitting part of the loop. This restricts the maximum field strength within the X-ray loop to a value less than 580 G. For the model in frame (a) of the figure, the (minimum) field strength at the top of the loop is 425 G and the X-ray emitting plasma terminates above the $s = 3$ level. The microwave emission is only seen from a region around the apex of the loop, as required by the observations.

An alternative possibility is illustrated in frame (b) of the figure. For this case the field strength at the apex of the loop is 375 G and a 4th harmonic level is present in each leg of the loop (the 3rd harmonic level is just below the x_0 axis). If the observer were to look directly down upon the loop ($\phi = 90^\circ$), two microwave source regions would be observed. For the line of sight inclined at an angle of $\phi = 45^\circ$, however, as shown, the source region in the left leg is observed near the center of the projected X-ray loop, while the region in the right leg of the loop would not have been observed. The latter occurs because for small angles θ between the line of sight and the magnetic field, the optical thickness of the 4th harmonic emission is too small for the microwave emission to have been observable. This model places less restriction upon the location of the 4th harmonic level within the loop than model (a). Like model (a), the maximum field strength within the X-ray loop must be less than 580 G.

The information inferred from the 1.45 GHz observations is rather different from the above, since the X-ray loops were found to be optically thick to free-free emission at 1.45 GHz. In order to understand why the entire X-ray loop was not observed down to the $\sim 2 \times 10^{-5}$ K sensitivity of the microwave observations, it was found that the X-ray loop must be enveloped by a cooler plasma with a temperature $\sim 10^5$ K or less. The compact microwave source could be explained if the external plasma ($T = 1 \times 10^5$ K) has a density $\sim 10^6$ cm $^{-3}$ at the top of the X-ray loop that falls off exponentially with height with the gravitational scale length. (The loop density was found to be $\sim 10^{10}$ cm $^{-3}$.) Most of the loop microwave emission, except for some emission from the top of the loop, is then masked by free-free absorption in the external plasma. This external plasma would have an emission measure $\sim 10^{26} - 10^{27}$ cm $^{-5}$. A "transition zone" or boundary layer might be expected to be present between the hot loop plasma and the cooler external plasma. The observational implications of, and restrictions upon, such a transition zone are discussed in the following paper (Brosius and Holman, these proceedings; also, Brosius and Holman, 1986).

An alternative model for the 1.45 GHz emission would be for the external absorption to be gyroresonance rather than free-free. This still requires an external plasma temperature of $\sim 10^5$ K or lower, but the plasma density above the loop can be as low as $\sim 10^6$ cm $^{-3}$. The absorption is most likely to be 2nd harmonic, since 3rd harmonic absorption requires an external plasma density as high as that required for free-free absorption. To obtain the microwave source, the 2nd harmonic level would have to graze the top of the X-ray loop (or graze a transition zone at the top of the loop). This implies a magnetic field strength of 260 G near the top of the X-ray loop. The microwave source would be a combination of gyroresonance and free-free emission.

Highly desirable future observations would be to have a set of high-spatial-resolution microwave maps at primarily closely spaced frequencies, together with high-spatial-resolution EUV or soft X-ray images of the same region. Coordinated high-spectral-resolution observations (with some spatial information so that brightness temperatures can be obtained) from an instrument such as the Owens Valley frequency-agile interferometer would also be desirable. A lot of information can be extracted from a good set of microwave observations alone, but coordinated EUV or soft X-ray observations provide a more direct route to conclusions that are less model dependent. E(or X)UV observations have some advantage over the soft X-ray observations, since a wider range of temperatures can be observed, and some direct density diagnostics can be obtained from line ratios. With either, however, important plasma information is obtained that could only be indirectly deduced from the microwave data alone. There is also much to be done in developing existing models, and in modeling different magnetic and plasma configurations. With more coordinated observations and theoretical modeling, it should be possible to obtain much new, reliable quantitative information about the magnetic and plasma properties of coronal structures.

REFERENCES

- Brosius, J. W., and Holman, G. D., 1986, in preparation.
 Holman, G. D., and Kundu, M. R., 1985, Ap. J., 292, 291.
 Kahler, S. W., Webb, D. F., Davis, J. M., and Kundu, M. R., 1984, Solar Phys., 92, 271.
 Kundu, M. R., and Lang, K. R., 1985, Science, 228, 9.
 Webb, D. F., Davis, J. M., Kundu, M. R., and Velusamy, T., 1983, Solar Phys., 85, 267.
 Webb, D. F., Holman, G. D., Davis, J. M., Kundu, M. R., and Shevgaonkar, R. K., 1986, Ap. J., submitted.
 Willson, R. F., 1985, Ap. J., 298, 911.

THEORETICAL MODELS OF FREE-FREE MICROWAVE EMISSION FROM SOLAR MAGNETIC LOOPS

Jeffrey W. Brosius

Laboratory for Astronomy and Solar Physics
NASA/Goddard Space Flight Center, Greenbelt, MD
and SASC Technologies, Inc., Lanham, MD
and

Gordon D. Holman

Laboratory for Astronomy and Solar Physics
NASA/Goddard Space Flight Center, Greenbelt, MD

We calculate the free-free microwave emission from a series of model magnetic loops. The loops are surrounded by a cooler external plasma, as required by recent simultaneous X-ray and microwave observations, and a narrow transition zone separating the loops from the external plasma. To be consistent with the observational results, upper limits on the density and temperature scale lengths in the transition zone are found to be 360 km and 250 km, respectively. The models which best produce agreement with X-ray and microwave observations also yield emission measure curves which agree well with observational emission measure curves for solar active regions.

As discussed by Holman (previous paper in these Proceedings), coronal loops are often optically thick to free-free emission at observational frequencies around 1 GHz. We deal primarily with a frequency of 1.45 GHz (20 cm), and include only thermal bremsstrahlung as the source of emission. In the present discussion we will expand on the thermal bremsstrahlung model of the previous paper--that of a semi-circular loop surrounded by a cooler, absorbing, external plasma--and consider the effects of a temperature/density "transition zone" (boundary layer) separating the loop and the external medium. We choose density and temperature functions which yield a smooth transition from the loop values ($N_L = 1.5 \times 10^{10} \text{ cm}^{-3}$, $T_L = 2.5 \times 10^6 \text{ K}$) to the external medium limiting values ($N_0 = 0$ at infinity, $T_0 = 5 \times 10^4$), and we incorporate the full Appleton-Hartree expression for the index of refraction in the evaluation of the optical depth and brightness temperature integrals. The density and temperature of the external plasma are taken to vary as

$$N = (N_s) \exp(-y/L_g) + \exp[-(r-r_0)/L_N] [(N_L) - (N_s) \exp(-y/L_g)]$$

$$T = (T_0) + (T_L - T_0) \exp[-(r-r_0)/L_T],$$

where $N_s = 2 \times 10^{13}$ is the base density, y is the vertical height, $L_g = 3000 \text{ km}$ is the gravitational scale length, r is the radial position (the center of curvature of the loop is at $r=0$), r_0 is the outer radius of the loop ($3 \times 10^4 \text{ km}$), L_N is the density scale length in the transition zone, and L_T is the temperature scale length in the transition zone. The inner radius of the loop is $2.5 \times 10^4 \text{ km}$.

To begin, we show a naked loop, i.e., one with no external absorbing plasma (Fig. 1). Since the loop is optically thick, the observer sees an essentially constant brightness temperature (equal to the loop temperature) as

the loop is scanned. When an external, cool plasma is provided (with a temperature/density discontinuity at the outer edge of the loop, i.e., $L_N=L_T=0$), a significant amount of the loop emission is absorbed (Fig. 2). The result is that one obtains a model which conforms to the recent observations of Webb et al. (1986), in which the microwave source covers about 1/3 the physical extent of the X-ray loop and is found to have a peak brightness temperature of $\sim 1.0 \times 10^6$ K.

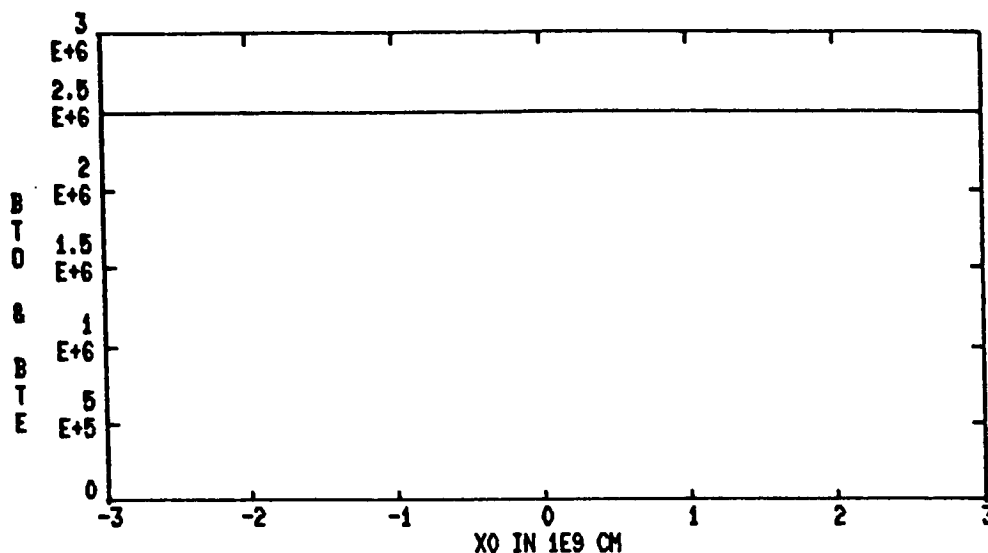


Fig. 1. Brightness temperature versus line-of-sight distance from loop center (in units of 10^9 cm) for a loop with no transition zone and no external plasma.

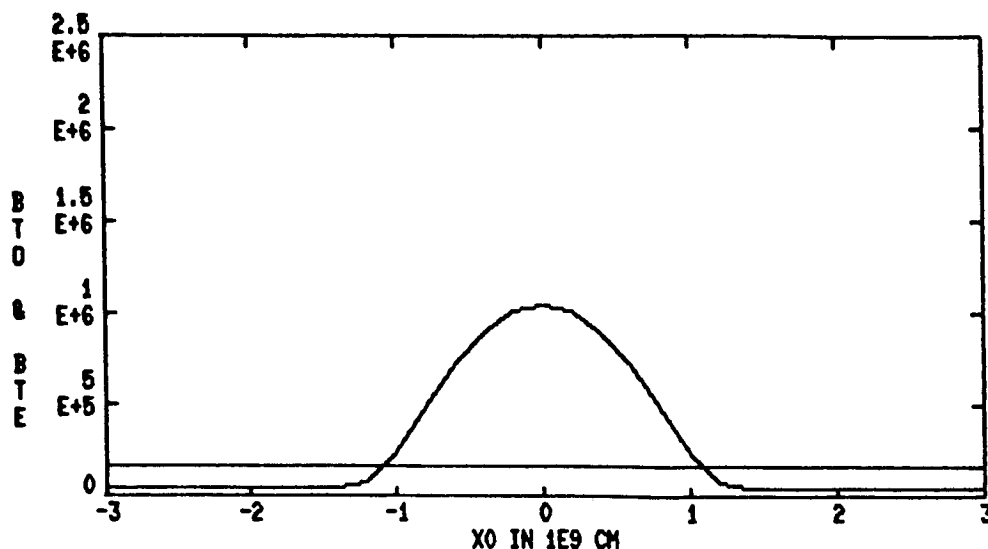


Fig. 2. Same as above for a loop surrounded by an external plasma and thin transition zone ($L_N=L_T=0$).

The presence of cool, external material in the corona is suggested by recent observational and theoretical work (Webb et al., 1986; Kanno and Suematsu, 1982; Schmahl and Orrall, 1979). In particular, Schmahl and Orrall find continuum absorption in EUV spectra from everywhere on the sun, whether in coronal holes, active regions, prominences, or elsewhere. They propose a "cloud" model to account for this neutral hydrogen absorption shortward of 912 Å, and this model is later confirmed by Kanno and Suematsu. Thus a cloud of cool (neutral) hydrogen is believed to overlie material at transition region temperatures. Kanno and Suematsu (1982) suggest that such clouds are the remnants of cool, chromospheric material jetted into the corona. In the present context, we suggest that cool ($T < 10^5$ K), plasma overlies hot, magnetic structures associated with the solar corona.

At the interface between the hot, dense loop and the cool, less dense external plasma, we introduce a "transition zone" boundary layer. This is reasonable primarily because a smooth transition is physically more appealing than a sharp discontinuity. Thus we have an essentially inverted solar atmosphere above magnetic loops, in which the coolest material overlies the narrow transition layer material, which overlies the hot, coronal plasma.

Now that we have argued for the presence of the cool external plasma and seen its effects, let us consider the effects of the density/temperature "transition zone" boundary layer separating the hot loop from this cool plasma.

The base density of the external plasma and the gravitational scale height (which depends upon T_0) both have a strong effect on the absorption by the external medium. For present purposes, therefore, it is advantageous to keep these parameters fixed and to allow only the "transition zone" density and temperature scale lengths, L_N and L_T , to vary. For a given base density and external temperature, one may estimate the density and temperature scale lengths which yield a peak brightness temperature of 1×10^6 K. A loop model may then be calculated for this set of parameters, and appropriate adjustments on the density and temperature scale lengths made until either (a) the peak brightness and loop width are made to conform to the simultaneous X-ray and microwave observations, or (b) it be shown that the brightness and width could not be made to conform to the simultaneous X-ray and microwave observations.

It was found that for temperature scale lengths greater than 250 km, no density scale length could be found which would satisfy both the loop width and peak brightness temperature conditions simultaneously. Furthermore, for this upper limit on the temperature scale length, 360 km was established as an upper limit on the density scale length. See Fig. 3.

We now briefly discuss some of our results.

There are two contributions overall to the observed brightness temperature: (a) the contribution from the loop, as seen through the external medium, and (b) the contribution from the boundary layer/external plasma itself. Varying the scale lengths performs two functions: (a) it varies the optical depth between the observer and the top edge of the loop, thus varying the contribution to the observed brightness temperature from the loop, and (b)

it varies the contribution to the observed brightness temperature from the boundary layer/external plasma itself. The percentage contribution to the total brightness temperature from each of these two regions ranges from 0% to 100%, depending on the optical depth of the external medium.

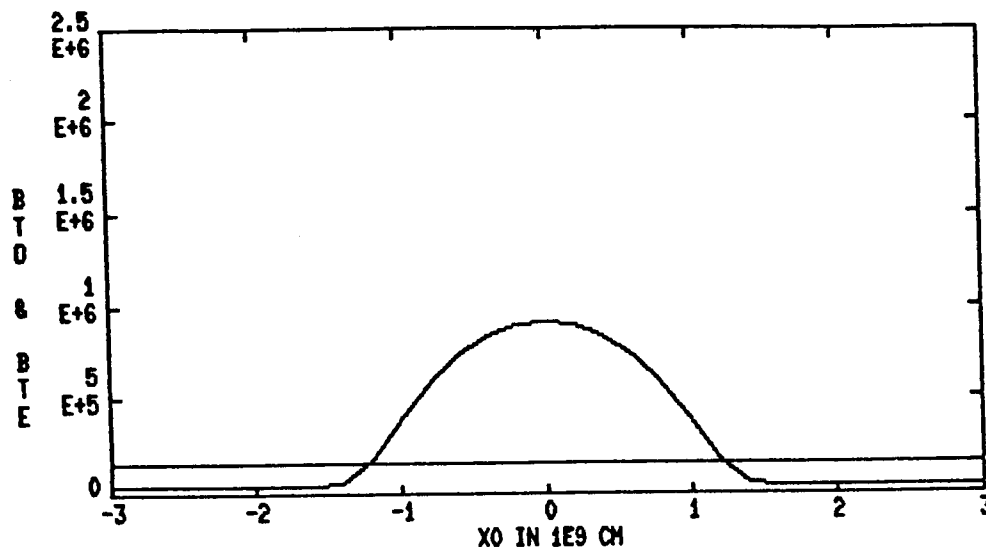


Fig. 3. Brightness temperature versus line-of-sight distance from loop center (in units of 10^9 cm) for a loop surrounded by an external plasma and transition zone with $L_N=360$ km, $L_T=250$ km.

For "base densities" less than that used here (2×10^{13}) the external plasma is insufficiently thick to absorb the required amounts of loop emission. Furthermore, for lower temperatures the gravitational scale length is smaller, so that the density drops off faster, also making the external medium less thick and less capable of absorbing the necessary loop emissions. Also, while raising the external temperature would tend to offset this, it should not be raised above the level of instrumental sensitivity (1.7×10^5 K), as the whole loop would then be visible at a temperature of 1.7×10^5 K, which it is not. (This last statement is true only if the external medium is optically thick. We know, however, that it must be at least partially thick, as it must absorb sufficient quantities of loop emission from the loop center.) Finally, for a magnetic field strength of 100 gauss or greater, the plasma at the "base" is field-dominated. If, however, the density were much larger, the gas pressure would exceed the field pressure, and the resulting pressure imbalance would be unrealistic.

Finally, we calculated the emission measure distribution, $EM=N^2T/(dT/dY)$, for the boundary layer/external plasma for several combinations of the density and temperature scale lengths (Fig. 4), and found that the model which best fits the recent simultaneous X-ray and microwave observations produces an emission measure curve which agrees well with recent observationally obtained emission measure curves for solar active regions (Noyes et al., 1985; Vernazza and Reeves, 1978). Notice that for the first time a theoretical emission

measure curve for a single active region loop has been found which rises sharply to both the cool and the hot side of the emission measure minimum (cf. Antiochos and Noci, 1986).

We are currently engaged in making theoretical predictions which will enable the validity of the present model to be further evaluated (Brosius and Holman, 1986).

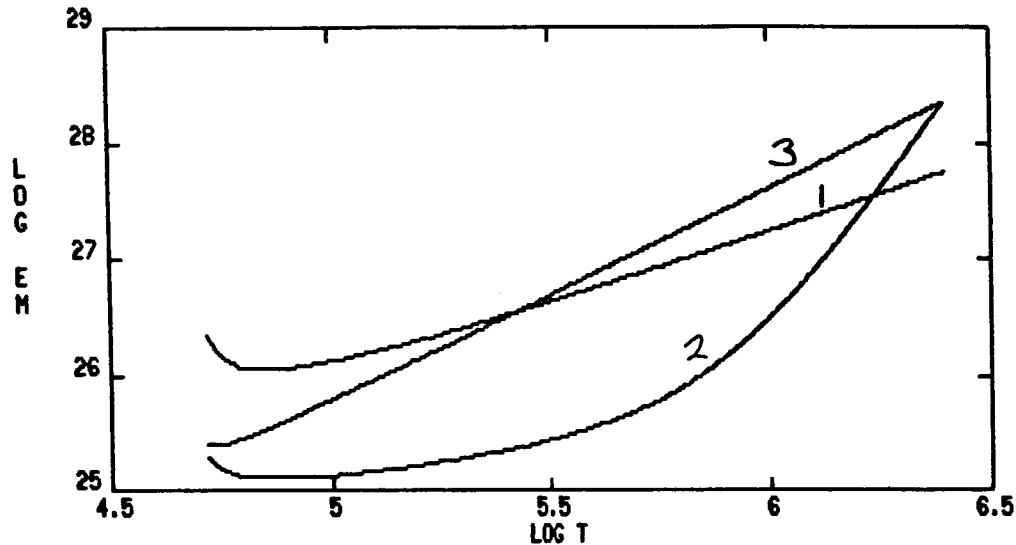


Fig. 4. $\log_{10} EM$ versus $\log T$. Emission measure is in units of cm^{-5} . Curve 1: $L_N=360$ km, $L_T=250$ km; curve 2: $L_N=360$ km, $L_T=1000$ km; curve 3: $L_N=L_T=1000$ km.

This work was supported in part by NASA Grant 188-38-53-01.

REFERENCES

- Antiochos, S. K., and Noci, G., 1986, *Ap.J.* **301**, 440.
 Brosius, J. W., and Holman, G. D., 1986, in preparation.
 Kanno, M., and Suematsu, Y., 1982, *Publ.Astron.Soc.Japan* **34**, 449.
 Noyes, R. W., Raymond, J. C., Doyle, J. G., and Kingston, A. E., 1985, *Ap.J.* **297**, 814.
 Schmahl, E. J., and Orrall, F. Q., 1979, *Ap.J.* **231**, L41.
 Vernazza, J. E., and Reeves, E. M., 1978, *Ap.J.Suppl.* **37**, 485.
 Webb, D. F., Holman, G. D., Davis, J. M., Kundu, M. R., and Shevgaonkar, R. K., 1986, *Ap.J.*, submitted.

CORONAL PLASMAS ON THE SUN AND NEARBY STARS

KENNETH R. LANG

Department of Physics and Astronomy
 Tufts University
 Medford, MA 02155

INTRODUCTION

The Very Large Array (VLA) has been used to observe solar microwave sources with second-of-arc angular resolution. Both the quiescent, or non-flaring, microwave sources and the flaring ones are usually resolved. They are often associated with the apex and/or legs of the ubiquitous coronal loops, which heretofore have been observable only with X-ray telescopes sent above the atmosphere. Multiple-wavelength VLA observations can specify the strength, evolution and structure of the magnetic fields in coronal loops, while also providing constraints on the electron density and electron temperature of the plasma trapped within the coronal loops.

VLA observations are providing new insights to the preburst heating and magnetic interaction that precede eruptions from solar active regions [Lang and Willson, (1983, 1984)]; but these interesting studies are not discussed here [see Kundu and Lang (1985) for a review]. We instead summarize our current understanding of the quiescent, or non-flaring, microwave emission from solar active regions. The next section briefly reviews the thermal radiation mechanisms that account for most of the quiescent emission, while also pointing out that current-amplified magnetic fields or non-thermal radiation may be required in some instances. This is followed by a discussion of the 20 cm radiation of coronal loops and the thermal cyclotron lines that accurately specify their magnetic field strength. The 20 cm and X-ray emission of the coronal plasma are then compared. We next discuss the coronae of nearby stars, where coherent radiation processes seem to prevail, and then conclude our summary with promising research opportunities for the future.

THERMAL RADIATION, CURRENTS AND NON-THERMAL RADIATION

The quiescent microwave emission of solar active regions has been attributed to the thermal radiation of hot electrons trapped within the strong magnetic fields of coronal loops. The microwave brightness temperature is then on the order of the million-degree electron temperature, and either thermal bremsstrahlung or thermal gyroresonant radiation dominate the emission. Bremsstrahlung, or braking radiation, is emitted when the thermal electrons are accelerated in the electric fields of ions and gyroresonant radiation is emitted when the thermal electrons are accelerated by magnetic fields.

Strong evidence for gyroresonant radiation at coronal levels above sunspots was provided by a comparison of microwave, EUV and X-ray observations [Kundu, Schmahl and Gerassimenko (1980); Pallavicini, Sakurai and Vaiana (1981)]. The near equality of the microwave brightness and electron temperatures indicated that the microwave emission was thermal, but the absence of detectable X-ray radiation above sunspots indicated a relatively low electron density there. This meant that the high microwave brightness temperature above sunspots could not be due to bremsstrahlung, but it could be explained by thermal gyroresonant radiation at the second or third harmonic of the gyrofrequency.

Thermal gyroradiation at coronal levels above sunspots was fully confirmed by the detection of circularly polarized ring-shaped or horseshoe structures [Allisandrakis and Kundu (1982); Lang and Willson (1982)] that were predicted using the theory of gyroresonant radiation in the curved magnetic fields above individual sunspots [Gel'freikh and Lubyshev (1979)]. These structures were observed at 6 cm wavelength where circular polarizations as high as 100% were detected. Bright sunspot-associated sources observed at 2 to 6 centimeters wavelength are now widely believed to be due to the gyroradiation of million-degree electrons spiralling about strong magnetic fields above sunspots.

But there is another class of compact, bright microwave sources in this wavelength range that are not associated with sunspots. They occur above regions of apparently-weak photospheric magnetic fields. For instance observations at 6 cm wavelength revealed sources with coronal brightness temperatures $T_B > 10^6$ K in regions away from sunspots [Schmahl et al. (1982); Webb, Davis, Kundu and Velusamy (1983)]. Force-free (potential) magnetic field extrapolations from the known photospheric values indicate that the magnetic field in the low solar corona is too weak to account for the observed emission by gyroradiation.

The situation is even worse at shorter wavelengths where stronger magnetic fields are required to produce gyroradiation at the first few harmonics of the gyrofrequency. (Higher harmonics produce insufficient optical depth to account for the high brightness temperatures.) Lang and Willson (1986a-this proceedings) and Willson and Lang (1986) report the presence of compact, bright 2-cm sources that require magnetic field strengths of $H \approx 2,000$ G in the low solar corona at regions away from sunspots if they are attributed to gyroresonance radiation.

Bright microwave sources in regions of apparently-weak photospheric fields can be explained by two different hypotheses. First, the emission could be thermal gyroradiation at the second or third harmonic of the gyrofrequency in strong magnetic fields. Currents might amplify the magnetic field in the low corona to values greater than those expected from extrapolations from the photosphere. Alternatively the photospheric magnetograms could be misleading, and strong magnetic fields could exist in isolated regions away from sunspots. Secondly, the emission could be nonthermal radiation in weak magnetic fields. Nonthermal synchrotron radiation from mildly relativistic electrons is one possibility, but some as yet unspecified mechanism must be continuously accelerating the electrons [Akhmedov et al. (1986), Chiuderi-Drago and Melozzi (1984); Willson and Lang (1986)].

Figure 1 provides the radiation spectra for the three types of sources usually detected at short centimeter wavelengths [see Akmedov et al. (1986) for greater details]. The most common type of source is the sunspot-associated component (A and C) that is attributed to thermal gyroresonance radiation in the legs of coronal loops that are connected to the underlying sunspots. Source D is a filament-associated component located above a magnetic neutral line in regions of apparently-weak magnetic field. Yet, this source has a steep radiation spectrum and high brightness temperature of $T_B > 7 \times 10^6$ K. It may be attributed to non-thermal radiation or to thermal gyroradiation in current-amplified magnetic fields. Then there is the filament-associated source B that has the flat spectrum of optically-thin thermal bremsstrahlung. Electron densities $N_e \approx 10^9$ to 10^{10} cm⁻³ are consistent with this interpretation, suggesting that in this case we are detecting the same thermal plasma that is observed at X-ray wavelengths from coronal loops. But this plasma is more commonly detected at the longer radio wavelength of 20 centimeters.

Individual cyclotron lines from AR 4398 are shown in Figure 3 together with the flat spectrum of the nearby active region AR 4399. The flat spectrum of AR 4399 is attributed to thermal bremsstrahlung, whereas the spectrum of AR 4398 can be explained by cyclotron line emission from a narrow layer of width $\Delta L \approx 10^8$ cm, electron density $N_e \approx 10^9$ cm⁻³ and a relatively high electron temperature $T_e \approx 4 \times 10^6$ K (solid line). Here the harmonic number $n = 4$ and the magnetic field strength $H = 145$ G. A key aspect of this discovery is the extraordinary precision in measuring the magnetic field strength; a change of only $\Delta H = 20$ G shifts the central frequency of the line by 170 MHz.

COMPARISON OF THE 20 CM AND X-RAY EMISSION

As previously mentioned, comparisons between the X-ray and short microwave (3 to 6 cm) radiation from solar active regions provided evidence for a new source of opacity at microwave wavelengths above sunspots. It has been attributed to gyroresonance effects in the legs of coronal loops connecting with underlying sunspots. Recent comparisons of the 6 cm radiation from the apex of coronal loops indicates that its brightness temperature is less than the electron temperature measured at X-ray wavelengths; this has been explained by a cool ($\approx 10^5$ K) external plasma [Holman (1986 - this proceedings); Webb, Holman, Davis and Kundu (1986)].

However, there have been no published comparisons of X-ray data with the 20 cm emission of the coronal plasma. In some instances, there is radiation at 20 centimeters wavelength near sunspots where no X-ray radiation is detected. The radio emission may be attributed to gyroresonant radiation of a low density plasma in magnetic fields of strength $H = 145$ to 290 G (harmonic $n = 4$ to 2), [see Lang, Willson, Strong and Smith (1986a) for greater details].

In other cases, the 20 centimeter radiation appears at the apex of coronal loops, but with a slightly lower brightness temperature, $T_B \approx 1.4$ to 1.7×10^6 K, than the electron temperature, $T_e \approx 3.0 \times 10^6$ K, inferred from the X-ray data. This may be explained by a low temperature plasma with $T_e \approx 10^5$ K that lowers the effective brightness temperature of the radio bremsstrahlung while not affecting the X-ray data that only detects the 10^6 K plasma [see Holman (1986 - this proceedings); Lang (1986 - this proceedings); and Lang, Willson, Strong and Smith (1986a) for greater details]. Because the line of sight through the low temperature plasma is greatest along the legs of coronal loops, it can reduce the size of the radio source below that of the X-ray emission. That is, the low temperature plasma can, under the right circumstances, confine the detectable radio radiation to the apex of coronal loops.

As illustrated in Figure 4, there are other instances in which the 20-cm radiation and the soft X-ray emission have the same angular extent. In this case, the maximum brightness temperature of the radio emission has the same value as the electron temperature, $T_e = 3 \times 10^6$ K, inferred from the X-ray data. At first sight it would seem that the 20-cm emission is the thermal bremsstrahlung of the X-ray emitting plasma (electron density $N_e = 2 \times 10^{10}$ cm⁻³), but in this instance we have also detected a cyclotron line. Preliminary modeling indicates a thin layer of $T_e \approx 4 \times 10^6$ K with a magnetic field strength of $H = 145$ or 187 G (harmonic $n = 4$ or 3). The thermal electrons that give rise to the X-ray radiation therefore also seem to produce strong gyroresonant radiation at 20 centimeters wavelength.

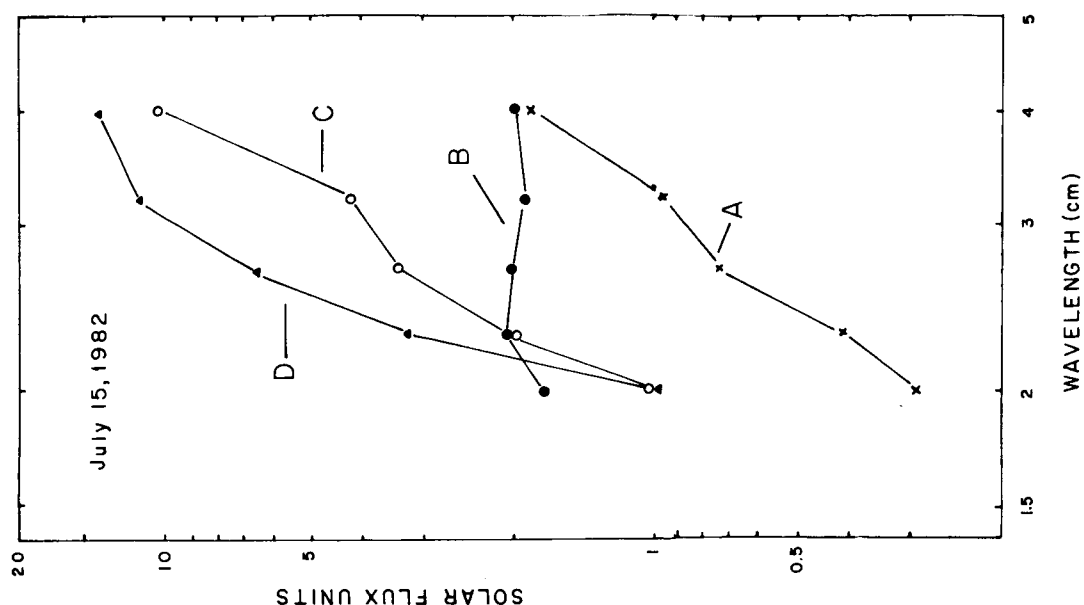


Figure 1. The radiation spectra of four sources associated with an active region. The steep spectrum of the filament-associated source D is attributed to the gyrosynchrotron radiation of mildly relativistic electrons whereas the flat spectrum of the source B is attributed to thermal bremsstrahlung. The sunspot-associated sources A and C are attributed to gyroresonance emission in the legs of coronal loops.

CORONAL LOOPS AT 20 CM WAVELENGTH AND THERMAL CYCLOTRON LINES

Radiation from a post-flare loop at 20 centimeters wavelength was reported by Velusamy and Kundu (1981); but there is a much more extensive literature regarding the quiescent 20-cm radiation of coronal loops [Lang, Willson and Rayrole (1982); Lang, Willson and Gaizauskas (1983); McConnell and Kundu (1983); Shevgaonkar and Kundu (1984); Kundu and Lang (1985); Kundu (1986 - this proceedings); Lang (1986 - this proceedings)]. The radiation at this longer wavelength often comes from the hot, dense plasma trapped within the coronal loop (see Figure 2 for a typical example). The 20-cm coronal loops have peak brightness temperatures of 1×10^6 to 4×10^6 K and extents of about 10^{10} cm. Their radio emission can be attributed to thermal bremsstrahlung or thermal gyroresonant radiation, or both.

Of special interest is the recent detection of thermal cyclotron lines near the apex of coronal loops at wavelengths near 20 centimeters [see Figure 3 and Willson (1985) for greater details]. These cyclotron lines are emitted at harmonics of the gyrofrequency, with a wavelength that depends only on the harmonic number and the magnetic field strength. However, because the magnetic field in the legs of coronal loops decrease uniformly with height, the individual cyclotron lines at short wavelengths will usually merge into a smooth continuum.

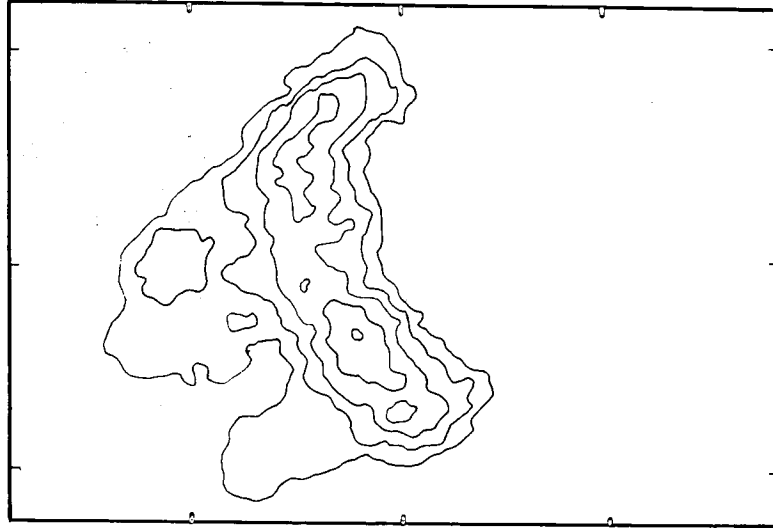


Figure 2. A typical radio wavelength (20 cm) V.L.A. map of the hot, million-degree plasma trapped in a coronal loop. The angular scale between fiducial marks on the axes is 60 arc-seconds.

At 20 centimeters wavelength we can observe the apex of coronal loops where the magnetic field is nearly constant and the spectrum of individual cyclotron lines can be resolved. This will be particularly true if currents or some other process confine the intense emission to a thin, hot layer within the loop apex.

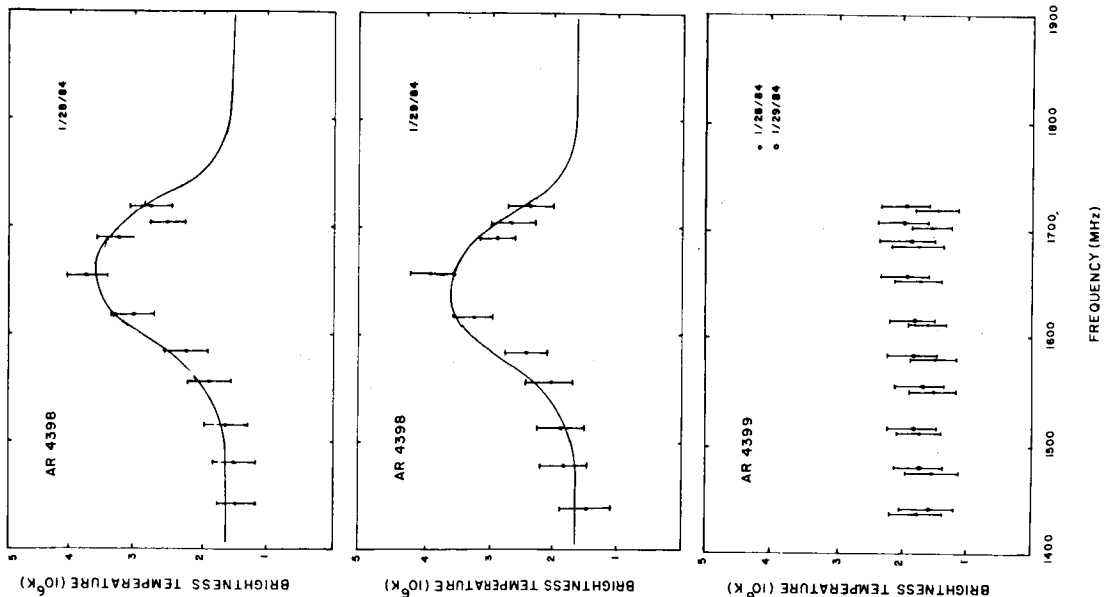


Figure 3. VLA data at ten closely-spaced frequencies near 1446 MHz (20 cm) showing thermal cyclotron line spectra from active region AR 4398 on successive days, together with optically-thick thermal bremsstrahlung spectra from active region AR 4399 on the same days.

ORIGINAL PAGE IS
OF POOR QUALITY

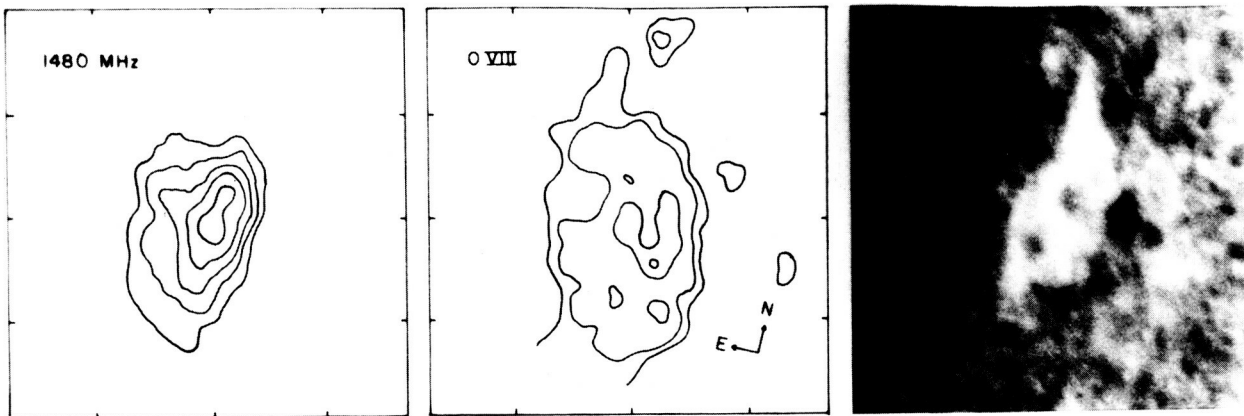


Figure 4. A comparison of the 20 cm emission (V.L.A.-left), soft-X-ray (S.M.M.-middle) and $H\alpha$ (SOON-right) emission of an active region on the same day. The angular spacing between fiducial marks on the axis is 60 arc-seconds.

CORONAE OF NEARBY STARS

Nearby dwarf M stars exhibit slowly-varying, quiescent microwave radiation and microwave bursts that have been detected with the Very Large Array (VLA) and the Arecibo Observatory. Observations with high resolution in frequency and time provide strong evidence for coherent radiation mechanisms in the coronae of these stars [Lang (1986b)]. Such mechanisms provide stringent constraints on the electron density and magnetic field strength in the stellar coronae.

Narrow-band, slowly varying radiation has been detected from the dwarf M star YZ Canis Minoris when using the VLA at wavelengths near 20 centimeters [Lang and Willson (1986b)]. White, Kundu and Jackson (1986) subsequently repeated this experiment, finding narrow-band bursts from the dwarf M stars AD Leonis and UV Ceti. The narrow-band structure cannot be explained by continuum emission processes such as thermal bremsstrahlung, thermal gyroresonant radiation or nonthermal gyrosynchrotron radiation. Although gyroresonant radiation can give rise to narrow-band cyclotron lines, it requires an implausibly large source that is hundreds of times larger than the star. The observations of narrow-band structure can apparently only be explained by coherent mechanisms like electron-cyclotron lines or coherent plasma radiation.

Independent evidence for coherent radiation mechanisms is provided by high-time-resolution observations of the dwarf M star AD Leonis at the Arecibo Observatory [Lang, Bookbinder and Golub (1983), Lang and Willson (1986c)]. As illustrated in Figure 5, quasi-periodic, highly polarized spikes are observed at 20 centimeters wavelength with rise times of less than 5 milliseconds. An upper limit to the linear size of the spike emitting region is $L \leq 1.5 \times 10^8$ cm, the distance

that light travels in 5 milliseconds. This size is only five hundredths of the estimated radius of AD Leonis. Provided that the emitter is symmetric, it has a brightness temperature greater than 10^{16} K. The high degrees of circular

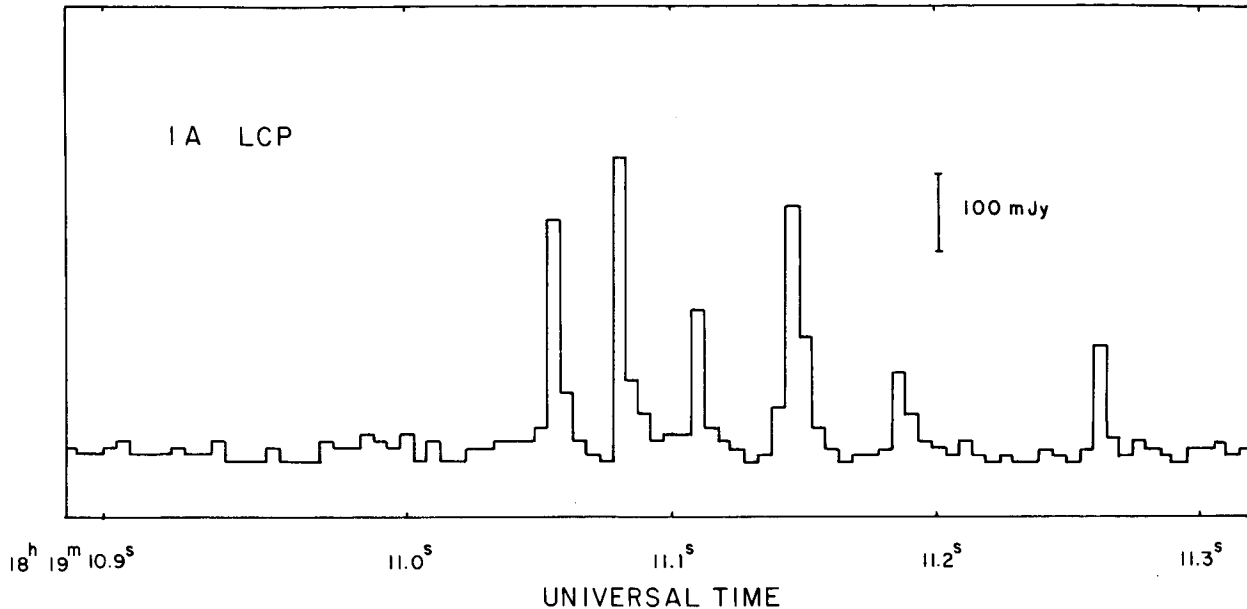


Figure 5. The total power detected at a frequency of 1415 MHz (21.2 cm) while tracking the dwarf M star AD Leonis. The left-hand circularly polarized (LCP) signal has been displayed with a 5 ms integration time. There are five quasi-periodic spikes with a mean periodicity of $T_D = 32 \pm 5$ ms and a total duration of $T_D = 150$ ms. Each of these spikes had a rise time of $\tau_R < 5$ ms, leading to an upper limit to the linear size $L < 1.5 \times 10^8$ cm for the spike emitter. A symmetric source of this size would have a brightness temperature of $T_B > 10^{16}$ K, requiring a coherent radiation mechanism.

polarization (up to 100%) indicate an intimate connection with the star's magnetic field, and the high brightness temperatures suggest a coherent radiation mechanism such as an electron-cyclotron maser or coherent plasma radiation.

The coherent process provides constraints on the electron density, N_e , and the magnetic field strength, H , in the stellar coronae [see Dulk (1985) for the relevant formulae]. If the electron-cyclotron maser emits at the second harmonic of the gyrofrequency, the longitudinal magnetic field strength $H = 250$ G and constraints on the plasma frequency imply an electron density of $N_e \approx 6 \times 10^9$ cm $^{-3}$. Coherent plasma radiation at the first or second harmonic of the plasma frequency respectively require $N_e = 2 \times 10^{10}$ cm $^{-3}$ and $H \ll 500$ G or $N_e = 6 \times 10^9$ cm $^{-3}$ and $H \ll 250$ G.

PROMISING DIRECTIONS FOR THE FUTURE

Future VLA observations at 20 centimeters wavelength will continue to provide diagnostic tools for the solar corona. Observations of thermal cyclotron lines offer a promising method of accurately determining the coronal magnetic field strength. Comparisons with soft X-ray spectral lines will help delineate the

electron density and temperature, while also specifying the radiation mechanisms. One promising approach that grew out of this conference involves simultaneous observations with the VLA and the Owens Valley Radio Observatory (OVRO). The OVRO will provide spectral information that is not obtainable with the VLA, whereas the high angular resolution of the VLA will remove ambiguities in the OVRO data. Future collaborations between the Tufts University group and the Observatoire de Paris - Nancay Radio Heliograph will provide new perspectives to coherent radiation processes on the Sun. The rapidly growing studies of the microwave radiation from dwarf M and RS CVn stars will continue to provide new insights to physical processes in stellar coronae. The full potential of these studies of the Sun and nearby stars will only be realized by the development of a solar-stellar synthesis radiotelescope. Such an instrument would be dedicated to solar and stellar observations with high angular, temporal and frequency resolution.

ACKNOWLEDGEMENTS

Radio astronomical studies of the Sun at Tufts University are supported under Air Force of Scientific Research grant AFOSR-83-0019 and contract N0014-86-K-0068 with the Office of Naval Research. Simultaneous VLA and Solar Maximum Mission observations of the Sun are supported by NASA grant NAG 5-501.

REFERENCES

- Akhmedov, S.B., et al., 1986, "Structure of a Solar Active Region from RATAN 600 and Very Large Array Observations," *Astrophys. J.*, 301, 460-464.
- Alissandrakis, C.E. and M.R. Kundu, 1982, "Observations of Ring Structure in a Sunspot Associated Source at 6 centimeter Wavelength", *Astrophys. J. (Letters)*, 253, L49-L52.
- Chiuderi-Drago, F. and M. Melozzi, 1984, "Non-Thermal Radio Sources in Solar Active Regions," *Astrophys.* 131, 103-110.
- Dulk, G.A., 1985 "Radio Emission from the Sun and Stars," *Ann, Rev. Astron. Ap.*, 23 169-180
- Dulk, G.A. and D.E. Gary, 1983, "The Sun at 1.4 GHz: Intensity and Polarization," *Astron. Astrophys.*, 124, 103-107
- Gel'frikh, G.B. and B.I. Lubyshev, 1979, "Structure of Local Sources of the S Component of Solar Radio Emission " *Sov. Astron. A.J.*, 23, 316.
- Holman, G.D., 1986, "Determining Magnetic and Plasma Structure of Coronal Loops from Microwave and Soft X-ray Observations", : this Proceedings.
- Kundu, M.R., 1986, "Three Dimensional Structure of Solar Active Regions," this Proceedings.
- Kundu, M.R. and K.R. Lang, 1985, "The Sun and Nearby Stars," *Science*, 228, 9-15.
- Kundu, M.R., E.J. Schmahl and M. Gerassimenko, 1980, "Microwave, EUV and X-ray Observations of Active Region Loops: Evidence for Gyroresonance Absorption in the Corona," *Astron. Astrophys.* 82, 265-271.
- Kundu, M.R. and T. Velusamy, 1980, " Observation with the VLA of a Stationary Loop Structure in the Sun at 6 cm Wavelength," *Astrophys. J. (Letters)*, 240, L62-L65.
- Lang, K.R., 1986a, "Coronal Diagnostics "-this Proceedings.
- Lang, K.R., 1986b, "Flare Stars and Solar Bursts: High Resolution in Time and Frequency," *Solar Phys.*, in press.
- Lang, K.R., J. Bookbinder, L. Golub and M. Davis, 1983, "Bright, Rapid, Highly Polarized Radio Spikes from the Dwarf AD Leo," *Astrophys. J. (Letters)*, 272, L15-L18.

- Lang, K.R. and R.F. Willson, 1982, "Polarized Horseshoes Around Sunspots at 6 Centimeter Wavelength.", *Astrophys. J. (Letters)*, 255 L111-L117.
- Lang, K.R. and R.F. Willson, 1983, "Multiple Wavelength Observations of Flaring Active Regions," *Adv.Space Res.* 2, No. 11, 91-100.
- Lang, K.R. and R.F. Willson, 1984, "V.L.A. Observations of Flare Build-Up in Coronal Loops," *Adv. Space Res.* 4, no. 7, 105-110.
- Lang, K.R. and R.F. Willson, 1986a, "Compact, Variable, Moving Sources on the Sun at 2 Centimeters Wavelength," *this Proceedings*.
- Lang, K.R. and R.F. Willson, 1986b, "Narrow-Band, Slowly Varying Decimetric Radiation from the Dwarf M Flare Star YZ Canis Minoris," *Astrophys. J. (Letters)*, 302, L17-L21.
- Lang, K.R. and R.F. Willson, 1986c, "Millisecond Radio Spikes from the Dwarf M Flare Star AD Leonis," *Astrophys. J.*, in press.
- Lang, K.R., R.F. Willson and V. Gaizauskas, 1983, "Very Large Array Observations of Solar Active Regions III. Multiple Wavelengths Observations," *Astrophys. J.* 267, 455-464.
- Lang, K.R., R.F. Willson and J. Rayrole, 1982, "Very Large Array Observations of Coronal Loops at 20 Centimeter Wavelength," *Astrophys. J.*, 258, 384-387.
- Lang, K.R., R.F. Willson, K.T. Strong and K.L. Smith, 1986a, "Simultaneous Solar Maximum Mission and Very Large Array Observations of Solar Active Regions", *Astrophys. J.*, to be submitted.
- Lang, K.R., R.F. Willson, K.T. Strong and K.L. Smith, 1986b, "Physical Parameters of Solar Active Regions Inferred from Thermal Cyclotron Lines and Soft X-ray Spectral Lines," *Astrophys. J.*, to be submitted.
- McConnell, D. and M.R. Kundu, 1983, "VLA Observations of a Solar Active Region and Coronal Loops," *Astrophys. J.*, 269, 698-705.
- Schmahl, E.J., et al., 1982, "Active Region Magnetic Fields Inferred from Simultaneous VLA Microwave Maps, X-ray Spectroheliograms, and Magnetograms", *Solar Phys.* 80, 233-249.
- Shevgaonkar, R.K. and M.R. Kundu, 1984, "Three-Dimensional Structures of Two Solar Active Regions from VLA Observations at 2, 6 and 20 Centimeter Wavelengths," *Astrophys. J.*, 283, 413-420.
- Strong, K.T., C.E. Alissandrakis and M.R. Kundu, 1984, "Interpretation of Microwave Active Region Structures Using SMM Soft X-ray Observations," *Astrophys. J.* 277, 865-873.
- Velusamy, T. and M.R. Kundu, 1981, "VLA Observations of Postflare Loops at 20 Centimeter Wavelength," *Astrophys. J. (Letters)*, 243, L103-L107.
- Webb, D.M. J.M. Davis, M.R. Kundu and T. Velusamy, 1983, "X-ray and Microwave Observations of Active Regions," *Solar Phys.* 85, 267-283.
- Webb, D.F., G.D. Holman, J.M. Davis and M.R. Kundu, 1986, "High-Spatial-Resolution Microwave and Soft X-ray Observations as Diagnostics of Solar Magnetic Loops", *Astrophys. J.*, submitted
- White, S.M., M.R. Kundu and P.D. Jackson, 1986, "Narrowband Radio Flares from Red Dwarf Stars," *Astrophys. J.*, submitted.
- Willson, R.F., 1985, "VLA Observations of Solar Active Regions at Closely Spaced Frequencies: Evidence for Thermal Cyclotron Line Emission," *Astrophys. J.*, 298, 911-917.
- Willson, R.F. and K.R. Lang, 1986, "VLA Observations of Compact, Variable Sources on the Sun," *Astrophys. J.*, in press.

MEASUREMENT OF CORONAL FIELDS USING SPATIALLY RESOLVED MICROWAVE SPECTROSCOPY

G. J. Hurford and D. E. Gary
Solar Astronomy 264-33
California Institute of Technology
Pasadena, California

INTRODUCTION

As large interferometers have become available for solar use, observation of active regions at microwave frequencies have been obtained with sufficient resolution to resolve the sources of interest. Such observations have shown that some of the active region emission is in the form of small sources with coronal brightness temperatures which are often (but not always) located near sunspots. The emission mechanism of gyroresonance opacity has been shown to account for such sources in most cases (*e.g.* Alissandrakis, Kundu and Lantos, 1980; Chiuderi-Drago et al. 1982; Lang, Willson and Gaizauskas, 1983). At intermediate microwave frequencies, ~ 5 GHz, where these sources are most readily observed, the corona is normally optically thin. However at the height and location where the observing frequency is a low harmonic of the local gyrofrequency, this mechanism can render the corona optically thick. The contrast between the 10^6 K brightness temperatures so achieved and the optically thin value of a few times 10^4 K is readily observable with interferometers. Such observations then identify the locations at which there is at least one height in the corona where the magnetic field has a value which can satisfy the resonance condition corresponding to the observing frequency.

An alternate approach to the study of active regions involves the use of microwave spectroscopy. From this perspective, gyroresonance opacity can be shown to introduce sharp breaks in the microwave spectra at frequencies corresponding to low harmonics of the gyrofrequency at the base of the corona. In this case, the magnetic field information refers to a specific height. Observations with relatively low spatial resolution but good spectral resolution have confirmed the expectations of such a picture (Hurford, Gary and Garrett, 1985, hereafter HGG).

In this paper, we consider the potential implications of observations which combine both high spatial and high spectral resolution. In particular, we will be interested in the ability to measure the magnetic field at the base of the corona on a point by point basis, as in a true magnetograph. In the next section, we present model calculations of the microwave brightness temperature spectrum along specific lines of sight near a sunspot. Subsequent sections will present corresponding observations.

MODELLING THE MICROWAVE SPECTRUM

To calculate the expected form of the microwave spectrum in the presence of strong magnetic fields, we assume a spherically symmetric solar atmosphere in which the temperature and density varies with height in accordance with a constant conductive flux model. The magnetic field was assumed to be a potential field generated by a vertically-oriented magnetic dipole buried below the photosphere. It is worth noting that the model is not formulated in terms of specific loops. Thus the spectral features that emerge below are a consequence of the convolution of the resonant character of gyroresonance emission, the steep temperature gradients at the base of the corona, and smoothly varying magnetic fields.

At each frequency and polarization, curves of growth were calculated along lines-of-sight using the MCMEM code (Magnetic Corona Microwave Emission Model) (HGG). The calculation took full account of free-free thermal bremsstrahlung (including magneto-ionic effects) and gyroresonance opacity. Combining results for integrations at different frequencies yielded brightness temperature spectra such as shown in Figure 1 for a typical line-of-sight.

Referring to Figure 1 we see that coronal temperatures are achieved at low frequencies. At high frequencies the resulting temperatures are much lower since the free-free optical depth of the corona is small and the gyroresonance condition is satisfied only in the chromosphere or below. Of most interest in the present context, however, are the sharp drops in brightness temperature at different frequencies in the two senses of circular polarization.

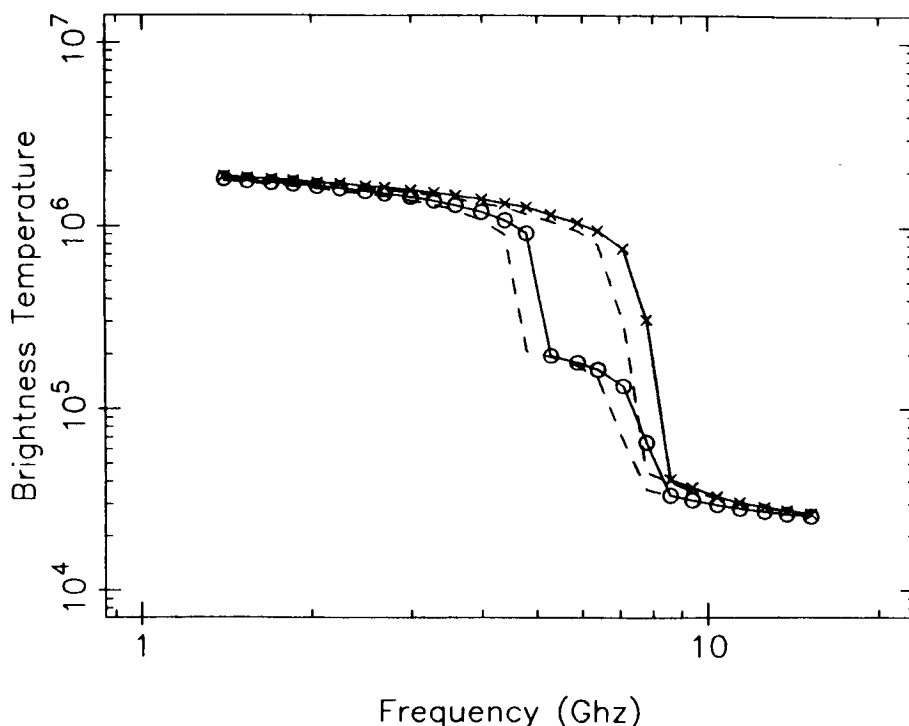


Figure 1. The crosses and circles show model spectra along a line of sight in extraordinary mode and ordinary mode respectively. The solid lines represent spectra for a magnetic field strength that is 10% larger than that assumed for the spectra shown by the dashed lines.

Under coronal conditions, the gyroresonance opacity at successively higher harmonics typically drops by at least an order of magnitude so that the coronal opacity at a given frequency/polarization is often dominated by emission at a single harmonic. Thus it is useful to think of this emission as coming from a single atmospheric layer (an isogauss surface) in which the field satisfies the resonance condition. As the frequency is increased, the magnetic field corresponding to this resonance layer must increase proportionately. For fields which decrease monotonically with height, this means that the height of emission decreases as frequency increases. Interpreting the frequency axis as a rough height scale, the sharp drop in brightness temperature occurs when the resonance layer reaches the transition zone.

The fact that the drop occurs at different frequencies in right- and left-circular polarization can also be explained by this picture. Since the opacity differs significantly between the ordinary and extra-ordinary propagation modes, the dominant harmonic is not necessarily the same in the two modes. Thus the resonance condition at the base of the corona is satisfied at different harmonics and so at different frequencies in right- and left-circular polarization.

Figure 1 also illustrates that the primary effect of enhancing the magnetic field strength by 10% is to shift the curves in frequency by 10%. Thus the frequency at which the discontinuity occurs (particularly in the extraordinary mode) can be interpreted in terms of the resonance condition at the base of the corona. This suggests that such spectra could be interpreted in terms of the magnetic field strength at the base of the corona. We now turn to the observations to judge whether these arguments are applicable in practice.

OBSERVATIONS

The Owens Valley frequency-agile interferometer (Hurford, Read and Zirin, 1985) was used to observe an isolated sunspot at 56 frequencies between 1.4 and 12 GHz in both right and left circular polarization. The observations, discussed in more detail elsewhere (Hurford, 1986) were obtained with the interferometer in its 3-element configuration which has sufficient resolution to enable the emission to be resolved at all frequencies. The single sunspot would be expected to provide a single, symmetric source of gyroresonance emission. Observations for which phase closure was not consistent with this expectation were rejected. In

practice, this procedure excluded the high and low frequency data for which free-free emission played a larger role. Given a single symmetric source, the ratio of amplitudes observed with different baselines could be directly interpreted in term of source size, which is defined as the FWHM of the equivalent gaussian. The availability of 3 baselines provided a redundant amplitude which helped confirm the appropriateness of a gaussian source profile. The ratio of flux to source size also yielded the brightness temperature at each frequency and polarization. Figure 2 shows the observed size and brightness temperature spectra.

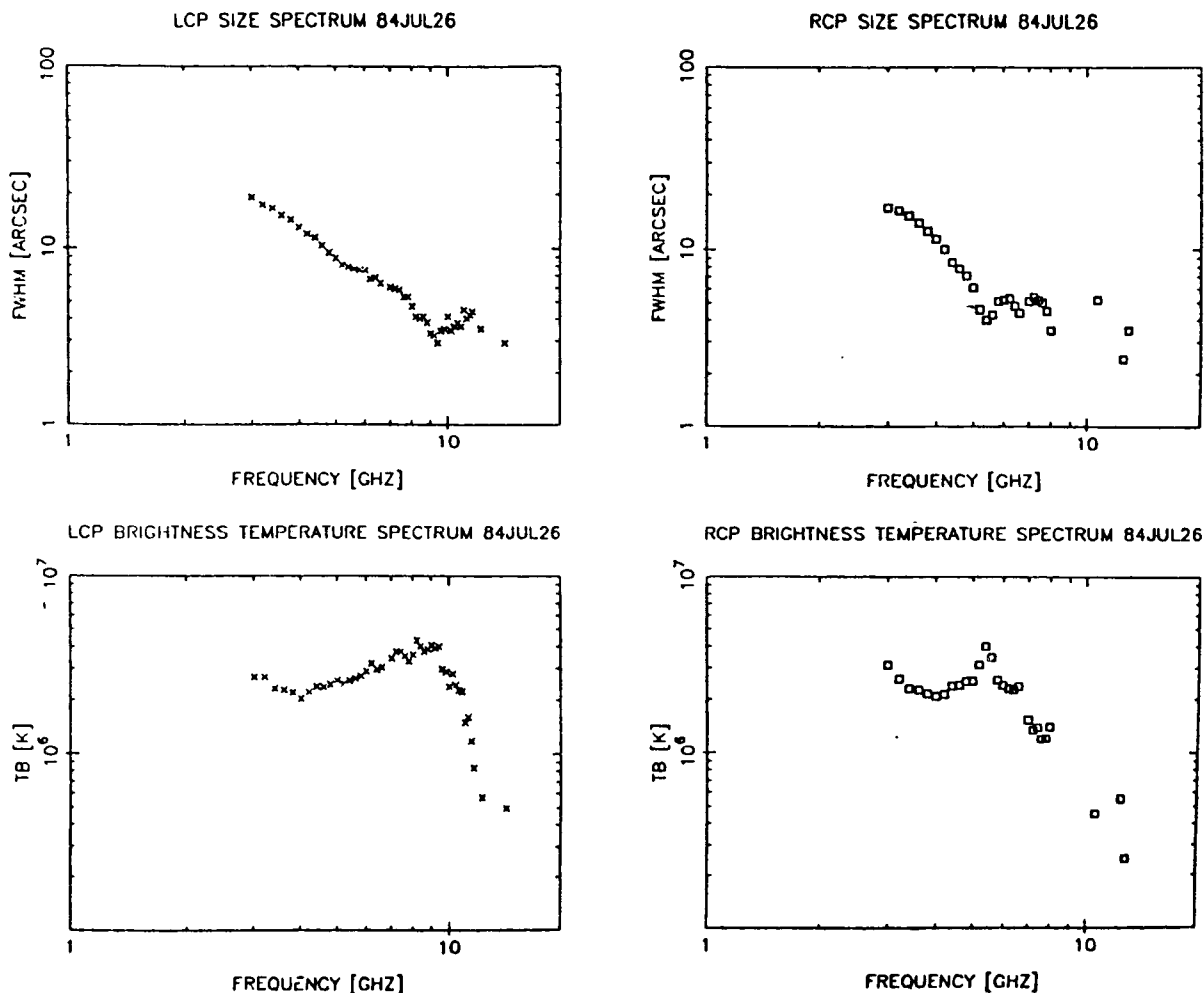


Figure 2. Size and brightness temperature spectra obtained for an isolated sunspot.

To compare the observations with the spectra in Figure 1, it is necessary to deduce the brightness temperature spectrum as it would be observed along specific lines of sight. Formally, the appropriate technique is to synthesize complete brightness temperature maps at each frequency. Then the brightness temperatures would be noted at a common location of interest in each map. In the present circumstance, we can use an abbreviated version of this procedure by exploiting the expected azimuthal symmetry of the source. We further assume that the centroid of each source is directly over the sunspot, an assumption that is reasonable given the isolated nature of the spot and its location near disk centre. These assumptions and the observations shown in Figure 2 define the source brightness temperature at each location. Following the procedure illustrated schematically in Figure 3, we can then deduce the brightness temperature spectrum at any desired radial displacement from the centre of the sunspot.

A typical spectrum is illustrated in Figure 4. It represents an observational determination of the microwave brightness temperature spectra along a specific line-of-sight, in this case toward a location 4000 km from the centre of the sunspot. As such, it can be directly compared to the model spectra in Figure 1.

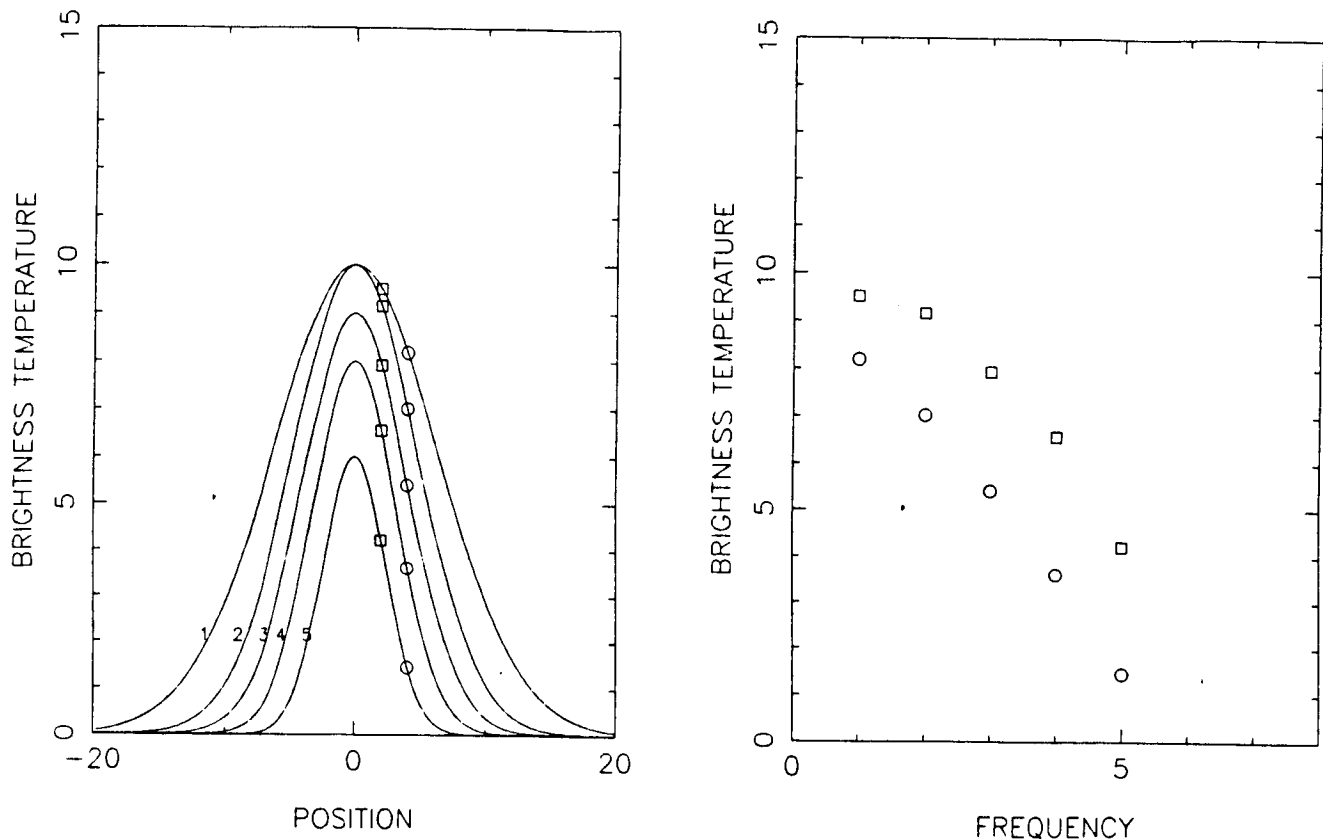


Figure 3. Schematic illustration of how size and brightness temperature spectra are converted to line-of-sight spectra in the case of a single gaussian source. In the left panel, spatial profiles based on size and brightness temperature parameters, are shown for 5 frequencies. At 2 positions of interest (squares and circles), such profiles then yield the line-of-sight spectra (at a single polarization) shown at right.

DISCUSSION

The comparison shows that the observed spectrum shares most of the principle features found in the model spectra. In particular the coronal brightness temperatures at low frequencies, the much lower values at high frequencies and the rapid dropoff in brightness temperature at different frequencies in right and left circular polarization. The observations even show the more complex form of the dropoff in the ordinary mode. Although there are quantitative differences between Figures 1 and 4, no attempt was made to adjust the model parameters to match this particular data set. Nevertheless, the correspondence provides confidence that such spectra can be interpreted to yield the value of magnetic field at the base of the corona. In the case illustrated, the magnetic field at the base of the corona at a radial displacement of 4000 km were found to be 900 g, to a precision of a few percent. Corresponding spectra yield the magnetic field at different radial displacements and so could provide the radial profile of the field at the base of the corona.

These considerations suggest that microwave spectroscopy can be used to deduce position dependence of the magnetic field at the base of the corona, much in the manner of a coronal magnetograph. Gary and Hurford (1986) have exploited a partial solar eclipse to apply microwave spectroscopy for a more complex region. They also found that in the absence of strong magnetic fields, the spectra of free-free emission could be interpreted in terms of loop temperature and density.

We believe that spatially resolved microwave spectroscopy provides a promising new coronal diagnostic. At present, however, a key limitation in its application is the lack of sufficient number of antennas with which to map complex active regions.

Acknowledgements: This work has been supported by the NSF under grants ATM-8309955, ATM-8610330 and AST-8315217 and by Air Force Contract F19628-84-K-0023.

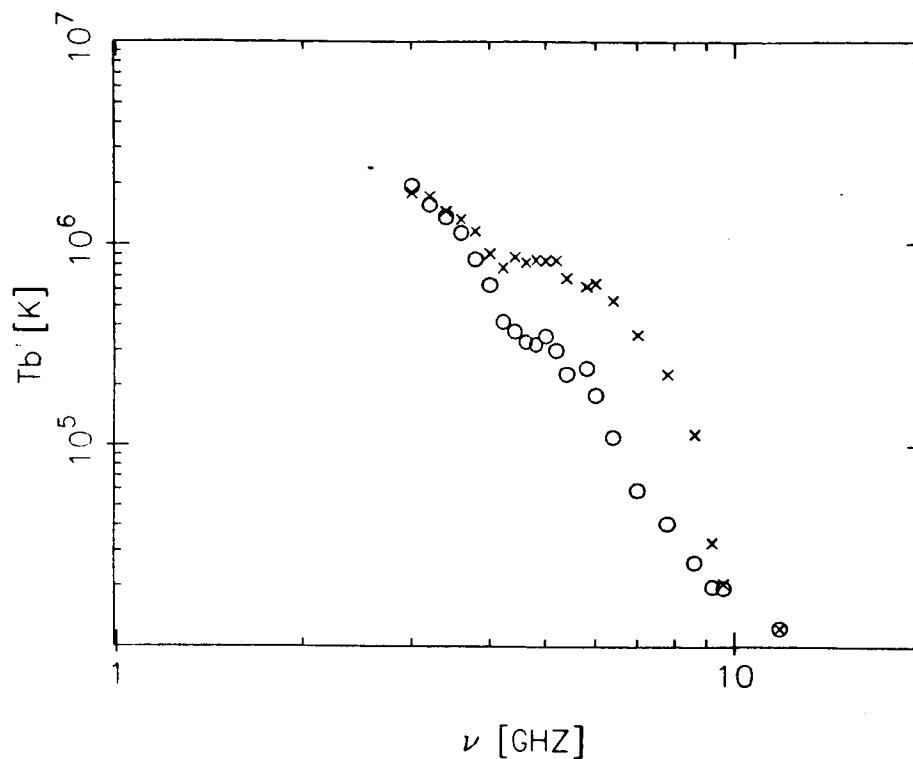


Figure 4. Typical line-of-sight brightness temperature spectra in left- and right-circular polarization (crosses and circles) deduced from the data shown in Figure 2 using the method illustrated in Figure 3.

REFERENCES

- Alissandrakis, C.E., Kundu M.R., and Lantos, P., 1980, *Astron. Astrophys.*, **82**, 30.
 Chiuderi-Drago, F., Bandiera, R., Falciani, R., Antonucci, E., Lang, K.R., Willson, R.F., Shibasaki, K., and Slottje, C., 1982, *Solar Phys.*, **80**, 71.
 Gary, D.E., and Hurford, G.J., 1986, *Astrophys. J.* (submitted), BBSO preprint 259.
 Hurford, G.J., 1986, *NASA Conf. Publ.*, **2421**, 191.
 Hurford, G.J., Read, R.B., and Zirin, H., 1984, *Solar Phys.*, **94**, 413.
 Hurford, G.J., Gary, D.E., and Garrett, H.B., 1985, *Radio Stars*, R.M. Hjellming and D.M. Gibson, eds. (Dordrecht: Reidel), , 379..
 Lang, K.R., Willson, R.B., and Gaizauskas, V., 1983, *Astrophys. J.*, **267**, 455.

GUIDED MHD WAVES AS A CORONAL DIAGNOSTIC TOOL

B. Roberts[†]

*Department of Physics and Astronomy
The University of Iowa
Iowa City, IA 52242*

INTRODUCTION

The coronal atmosphere is observed to be highly inhomogeneous with marked density and temperature variations; coronal loops abound. Magnetic forces dominate the atmosphere providing thermal insulation across field lines and almost rigid wave guides for the propagation of MHD waves. In a homogeneous low beta plasma, the slow magnetoacoustic wave gives one-dimensional propagation of sound whereas the fast magnetoacoustic wave gives isotropic propagation at the Alfvén speed. (See Weitzner (1983) and Roberts (1984, 1985) for recent discussions of the properties of MHD waves.) If, however, the low beta plasma is inhomogeneous in density, as with the corona, then fast magnetoacoustic waves are guided by regions of low Alfvén speed (Habbal, Leer, Leer, and Holzer 1979; Edwin and Roberts 1982, 1983; Roberts, Edwin, and Benz 1983, 1984; see also Newcomb 1957). For a general overview see Edwin and Roberts (1986a). Regions of low Alfvén speed occur in both coronal loops and in open field regions (coronal holes). We note, too, that current sheets (regions of the plasma where field reversal occurs) provide wave guides for fast magnetoacoustic waves (Edwin, Roberts, and Hughes 1986).

An important thing about such wave guides is that they preferentially select certain ranges of frequency and wavenumber for guided propagation. If a fast mode is generated impulsively, such as by a flare, it is guided along a region of low Alfvén speed and will exhibit frequencies of the order of the Alfvén speed divided by the width of the inhomogeneity. For typical coronal conditions, this will give rise to frequencies of about 1 Hz or higher.

The occurrence of preferred frequencies in an impulsively generated fast magnetoacoustic wave raises the interesting possibility that such distinctive signatures could be used as a seismological probe of the coronal atmosphere, allowing us to determine magnetic field strengths and/or spatial extents of density inhomogeneities. We discuss this possibility here (see also Edwin and Roberts 1986b).

[†]On leave from Dept. of Applied Mathematics, The University, St. Andrews, Fife, Scotland.

IMPULSIVELY GENERATED FAST WAVES

Consider a field-aligned cylindrical tube of dense gas embedded in a uniform magnetic field. In a low beta atmosphere, impulsively generated fast waves exhibit timescales (periodicities) of the general order (Roberts et al. 1984)

$$\tau = \frac{2.6a}{v_A} \left(1 - \frac{\rho_e}{\rho_0}\right)^{1/2}, \quad (1)$$

where ρ_0 and v_A are the gas density and Alfvén speed within the cylinder of radius a , and ρ_e is the gas density in the environment (where the Alfvén speed is v_{Ae} , with $\rho_0 v_A^2 = \rho_e v_{Ae}^2$). Ducting occurs provided $v_{Ae} > v_A$, which corresponds to $\rho_0 > \rho_e$. In a very dense region ($\rho_0 \gg \rho_e$), equation (1) reduces to

$$\tau = \frac{2.6a}{v_A}. \quad (2)$$

For example, with $a = 500 \text{ km}$ and $v_A = 10^3 \text{ km s}^{-1}$ we obtain, from (2), $\tau = 1.3 \text{ s}$.

In fact, the timescale τ is the maximum timescale that an impulsive event exhibits. Suppose that the source is located on the axis of the cylinder at $z = 0$, the impulse occurring at time $t = 0$. Then, at an observation point $z = h$ ($\gg a$) far down the axis of the cylinder, pressure and magnetic field variations, due to the passage of the impulsively generated fast magneto-acoustic wave (taken to be symmetric, sausage mode, oscillations within the cylindrical inhomogeneity), will exhibit three distinct phases (Roberts et al. 1984), analogous to sound waves in ocean layers (Pekeris, 1948). The first phase--called the periodic phase--begins at time $t = h/v_{Ae}$; in this phase the wave's amplitude is low and its period is given by (1). The second phase commences at a time $t = h/v_A$ when both the amplitude and the frequency of the wave undergo a substantial increase. This is the quasi-periodic phase. It lasts until the time $t = h/c_g^{\min}$, where c_g^{\min} is the minimum value of the mode's group velocity, when the amplitude of the wave begins to decline as the wave passes by the observation point $z = h$; this is the decay (or Airy) phase. A sketch of these three phases is given in Roberts et al. (1983, 1984).

DIAGNOSTICS

The distinctive theoretical profile of impulsively generated oscillations within a density enhancement (e.g., coronal loop) suggests that such oscillations might be used as a diagnostic probe of in situ coronal conditions. The periodic phase is of lower amplitude than the quasi-periodic phase. Thus, it is possible that the periodic phase of the motion be obscured by noise and so the fact that it is a precursor to the quasi-periodic phase may pass unnoticed. Considering the quasi-periodic phase, we note that its duration, τ_{dur} , is given by

$$\tau_{\text{dur}} = h \left(\frac{1}{c_{\text{g}}^{\text{min}}} - \frac{1}{v_{\text{A}}} \right) = \frac{h}{v_{\text{Ae}}} \left[\frac{v_{\text{Ae}}}{c_{\text{g}}^{\text{min}}} - \left(\frac{\rho_0}{\rho_e} \right)^{1/2} \right]. \quad (3)$$

Thus the duration depends both on the distance h between the source and the observation level and also on the magnitude of $c_{\text{g}}^{\text{min}}$, which in turn depends upon the magnitude of the density enhancement. In fact, τ_{dur} is related to the frequency ω^{min} within the quasi-periodic phase (strictly, the frequency at the end of the quasi-periodic phase): for fixed h , a and v_{Ae} , the higher the frequency ω^{min} the shorter the duration time τ_{dur} (Roberts et al. 1984). There is some observational support for this relation in Tapping's (1978) record of meter wavelength pulsating bursts, but further studies are needed. The greater the density enhancement (i.e., the larger the value of ρ_0/ρ_e), the lower the frequency ω^{min} and the lower the group velocity minimum, $c_{\text{g}}^{\text{min}}$, thus suggesting that very dense inhomogeneities have long quasi-periodic phases. By contrast, much smaller density enhancements ($\rho_0 \approx \rho_e$) have short quasi-periodic phases but extended decay phases, giving an event with the appearance of a decaying oscillation of extended duration. This may be an explanation of the gradually decaying wave train observed by McLean and Sheridan (1973).

A numerical illustration of equation (3) may be helpful. With $\rho_0 = 10 \rho_e$, inspection of Figure 4 in Roberts et al. (1984) gives $\omega^{\text{min}} a \approx v_{\text{Ae}}$ for which (from their Figure 7) $\tau_{\text{dur}} \approx h/v_{\text{Ae}}$. Thus, with $v_{\text{Ae}} = 2 \times 10^3 \text{ km s}^{-1}$ (so $v_{\text{A}} = 630 \text{ km s}^{-1}$), $a = 10^3 \text{ km}$ and $h = 5 \times 10^4 \text{ km}$, the quasi-periodic phase has a period of about 3s and a duration of 25s (or some 8 periods). Other choices of ρ_0/ρ_e , h and a will clearly give somewhat different numbers.

In summary, then, we have described how fast magnetoacoustic waves are ducted along regions of low Alfvén velocity (high density) in the corona, exhibiting a distinctive wave signature which may be used as a diagnostic probe of in situ coronal conditions (magnetic field strength, density inhomogeneity, etc.) Some observational knowledge of the start time of the impulsive wave source, possibly a flare, the start and end times of the generated wave event, and the frequency of the pulsations in that event permit a seismological deduction of the physical properties of the coronal medium in which the wave propagated. With good observations the theory offers a new means of probing the coronal atmosphere.

ACKNOWLEDGEMENTS

B.R. is grateful for support from the NASA Solar Maximum Mission Guest Investigator Program, and to Dr. Art Poland for his kind invitation to attend the CPP Workshop. B.R. was also supported by NASA through grant NGL-16-001-043. It is a pleasure to acknowledge the kind hospitality of Professor Donald Gurnett of the University of Iowa, and the efficient and helpful assistance from Kathy Kurth.

REFERENCES

- Edwin, P. M. and B. Roberts, 1982, "Wave Propagation in a Magnetically Structured Atmosphere; III: The Slab in a Magnetic Environment," Solar Phys., 76, 239.
- Edwin, P. M. and B. Roberts, 1983, "Wave Propagation in a Magnetic Cylinder," Solar Phys., 88, 179.
- Edwin, P. M. and B. Roberts, 1986a, "Guided Waves in Solar Magnetic Structures," in Proc. Second Intern. Conf. on 'Surface Waves in Plasmas and Solids,' Lake Ohrid, Yugoslavia (Sept. 1985).
- Edwin, P. M. and B. Roberts, 1986b, "Impulsively Generated Fast Coronal Pulsations," in Proc. SMM Workshop 'Rapid Oscillations in the Corona' (ed. B. R. Dennis), NASA, in press.
- Edwin, P. M., B. Roberts and W. J. Hughes, 1986, "Dispersive Ducting of MHD Waves in the Plasma Sheet: A Source of Pi2 Wave Bursts," Geophys. Res. Lett., 13, 373.
- Habbal, S. R., E. Leer and T. E. Holzer, 1979, "Heating of Coronal Loops by Fast Mode MHD Waves," Solar Phys., 64, 287.
- McLean, D. J. and K. V. Sheridan, 1973, "A Damped Train of Regular Meter-Wave Pulses from the Sun," Solar Phys., 32, 485.
- Newcomb, W. A., 1957, "The Hydromagnetic Wave Guide," in 'Magnetohydrodynamics' (ed. R. Landshoff), Stanford University Press, p. 109.
- Pekeris, C. L., 1948, "Theory of Propagation of Explosive Sound in Shallow Water," in 'Propagation of Sound in the Ocean,' Geol. Soc. Amer. Memoir, 27.
- Roberts, B., 1984, "Waves in Inhomogeneous Media," in 'The Hydromagnetics of the Sun,' European Space Agency SP-220, p. 137, Noordwijkerhout.
- Roberts, B., 1985, "Magnetohydrodynamic Waves," in 'Solar System Magnetic Fields' (ed. E. R. Priest), Reidel, p. 37.
- Roberts, B., P. M. Edwin and A. O. Benz, 1983, "Fast Pulsations in the Solar Corona," Nature, 305, 688.
- Roberts, B., P. M. Edwin and A. O. Benz, 1984, "On Coronal Oscillations," Ap. J., 279, 857.
- Tapping, K. F., 1978, "Meter Wavelength Pulsating Bursts During the May 21, 1972, Solar Noise Storm," Solar Phys., 59, 145.
- Weitzner, H., 1983, "Linear Wave Propagation in Ideal Magnetohydrodynamics," in 'Basic Plasma Physics,' (eds. A. A. Galeev and R. N. Sudan), North-Holland, Vol. 1, p. 201.

III. SMALL - SCALE CORONAL STRUCTURE

David F. Webb

Emmanuel College
Boston, Mass.

and

American Science and Engineering, Inc.
Cambridge, Mass.

BACKGROUND

This section is a review of recent observations and models pertaining specifically to solar coronal bright points (BPs) and more generally to small-scale coronal structure. We are primarily interested in addressing two questions: 1) What is the degree of correspondence among various alleged signatures of BPs at different levels of the atmosphere? and 2) What can BPs tell us about the emerging flux spectrum of the sun? In the following I first review older studies of BPs and then discuss the recent results presented at the Workshop.

BPs were first identified in coronal X-ray emission in 1969 (Vaiana et al., 1970), and their X-ray characteristics analyzed in detail during Skylab (see Golub, 1980 and Webb, 1981 for reviews). XBPs are compact (10-20 arc-sec) and short-lived (hours to a day), and at emergence are cooler ($\sim 1.8 \times 10^6$ K) than regions that will become active regions (Little and Krieger in Webb, 1981). XBPs have been correlated with bipolar structures that appear on photospheric magnetograms as ephemeral regions (ER) (Golub et al., 1977). Bright point-like features are also visible in the chromosphere and transition region but at lower contrast (Harvey and Martin, 1973; Bohlin et al., 1975; Habbal and Withbroe, 1981); at these levels they are difficult to distinguish from bright network elements.

Golub (1980) emphasizes that the distribution of the number of coronal features emerging as a function of either size or lifetime is a monotonically decreasing function. An arbitrary statistical distinction has been made that regions living less than about one day are called BPs, and those living more than four days are called active regions.

Golub et al. (1977) showed that the lifetime of an XBP was linearly correlated with the bipole separation and total magnetic flux of its associated magnetic feature, which had fluxes $< 10^{20}$ Mx. This single study, performed with Skylab-era data, was the basis for the argument that XBPs are the coronal signature of emerging flux in the quiet sun. This argument was based on the assumption that the bipoles associated with XBPs were ERs and, therefore, represented emerging flux. So, because XBPs are anticorrelated with the sunspot cycle such that the emerging flux spectrum is often dominated by small, short-lived structures (Davis, 1983), Golub (1980) has argued that the total average rate of flux emerging on the sun during the cycle is constant.

This suggestion has been disputed by Martin and Harvey (1979), Sheeley (1981), Harvey (1984), Martin et al. (1985) and Harvey (1985). Martin and Harvey (1979) and Harvey (1984) have shown that ERs tend to vary in phase with the solar cycle.

Martin et al. (1985) have suggested that there are two populations of XBPs, only one of which is associated with ERs and, therefore, emerging flux. Harvey (1984; 1985) suggests that HeI- λ 10830 dark points (DPs), which also are anticorrelated with the sunspot cycle, are XBP proxies. Therefore, since HeI DPs are not typically associated with ERs, then XBPs will not typically be associated with emerging flux. Finally, Tang et al. (1984) and Harvey (1984) suggest that ERs are not just small emerging active regions, because the number of ERs emerging over a solar cycle is $\sim 10^3$ more than expected from downward extrapolation of the size distribution of active regions.

BPs and active regions also differ in such properties as latitude distribution, rotation rate, and magnetic orientation. BPs, ERs and short-lived (1-3 days) CaK plages have more uniform latitude distributions than active regions (Harvey and Martin, 1973), but ERs tend to peak in the active region zones at solar maximum (Harvey, 1984). Magnetic pores, which live 10-60 hours, also are more broadly distributed in latitude than sunspots. The pores and Ca regions may represent an intermediate form of emerging flux. Golub and Vaiana (1978) measured the rotation rates of regions living from 1 to 7 days, and found that the rate was a function of lifetime (or size), such that XBPs rotated more slowly than active regions.

It is important to establish whether or not BPs are rooted in the network. Older studies indicated that XBPs (Howard et al., 1979) and ERs (Harvey and Martin, 1973) were not obviously spatially correlated with the Ca network, unlike active regions (EFRs) which tend to emerge at the boundaries of supergranular cells (Bumba and Howard, 1965). If true, this again implies fundamental differences between BPs and active regions. However, short-lived Ca plages (Harvey and Martin, 1973) and bright Ca network elements (Muller and Roudier, 1984) tend, like XBPs, to be anticorrelated with the cycle. Further, using Skylab data, Egamberdiev (1983) recently showed that XBPs are spatially associated with Ca network boundaries.

In the Skylab images BPs were typically unresolved. But using Skylab X-ray and EUV images, Sheeley and Golub (1979) were able to resolve a BP into two or three small loops, each 2500 km in diameter and 12,000 km long. Using fine-grain film, Davis and Webb (1981) observed a flaring XBP loop that was only one arc-sec across and 12 arc-sec long.

Finally, Nolte et al. (1979) found that a significant number of XBPs "flared" just before disappearing, and Golub et al. (1974) estimated that about 10% of all XBPs flared during their lifetime. Marsh (1978) identified small H α flares with ERs (i.e., "ER flares") and conjectured that they were associated with XBP flares. He demonstrated that the flares occurred when the ERs encountered the network boundary. Because some XBP flares are associated with macrospicules (Moore et al., 1977), or tiny filament eruptions, at least some XBPs may die following a catastrophic ejection of material. Hermans and Martin (1986 - this proceedings) suggest that small H α filament eruptions and accompanying "miniflares" may be common in the quiet sun. And Brueckner and Bartoe (1983) described high velocity jets and explosive events observed in the EUV. Although the correspondences of these features is unknown, their frequency and explosive nature led Ahmad and Webb (1978) and Brueckner and Bartoe to speculate that such small-scale structures could supply the entire mass flux of the solar wind.

It is apparent that we have no clear observational understanding of the bright small-scale structure of the quiet sun. However, important results based on new observations of BPs have been obtained recently. Therefore, in this section we are most concerned with observations relating to the correspondences of coronal BPs with other features at lower levels of the solar atmosphere. This bias is reflected in the papers which follow this review. Seven of the 11 papers on small-scale structure describe observations of the correspondences among bright quiet-sun features. I summarize these new results in the next part, which ends with a list of 5 outstanding questions on BP correspondences which were formulated at the end of the Workshop. Finally, in the last part I review several recent observations and models relating to the heating mechanism(s) of BPs and other small-scale structures, and the possible influence of these structures on coronal heating.

RECENT OBSERVATIONS OF CORONAL BRIGHT POINT STRUCTURE

Microwave Observations

In the three papers which follow, Habbal and Harvey (1986), Kundu (1986) and Lang and Willson (1986) describe recent, independent VLA radio observations of small coronal structures which appear to have characteristics typical of coronal BPs. The observations at 2, 6 and 20 cm reveal compact ($10 \sim 40$ arc-sec) sources with $T_b \approx 10^5 K$ and temporal variations over time scales of minutes. Emission at these wavelengths arises from the transition region and lower corona.

In the quiet sun at 6 cm (4.9 GHz) Marsh *et al.* (1980) found bright features associated with small bipoles and suggested that XBPs could account for a significant fraction of the quiet sun microwave signal. Recently, Habbal *et al.* (1986) observed with the VLA at 20 cm (1.45 GHz) three compact (20-40 arc-sec) structures which they considered to be coronal BPs. These structures exhibited spatial and temporal variations over time scales of minutes. Assuming free-free emission, Habbal *et al.* deduced magnetic field strengths of 50-100 G in the transition region - low corona of the BPs. However, their observations were somewhat compromised by the presence of several large active regions on the disk.

Habbal and Harvey (1986 - this proceedings) present preliminary results of an improved set of BP observations at 20 cm with the VLA on 8 September 1985. No large active regions impeded these observations and about 20 BPs were detected on the disk. Simultaneous observations were obtained in HeI- $\lambda 10830$, the photospheric magnetic field, H α , OVIII (SMM) and in microwaves from Owens Valley. All of the microwave BPs corresponded to HeI dark points (DP) and magnetic bipoles; there were, however, more HeI DPs and bipoles than microwave BPs. In their related paper, Harvey, Tang and Gaizauskas (1986 - this proceedings) report that 7 of 11 (64%) of the 20 cm BPs corresponded to cancelling magnetic bipoles (see below) and only two with emerging flux. Variations in the emission of BPs at 20 cm and in HeI DPs were often, though not always, correlated on time scales of minutes, similar to the behavior of EUV BPs in the Skylab data (Habbal and Withbroe, 1981).

Kundu (1986 - this proceedings) presents two VLA observations at 6 and 20 cm from a large set of data acquired before and during the Spacelab-2 mission. Several BPs were detected with $T_b = 1.0 - 3.6 \times 10^5 K$ and low degrees of polarization. In agreement with Habbal's results, the BPs corresponded to HeI DPs and bipoles. Kundu's

observations are important for the Spacelab collaboration discussed later as a test of the association between microwave BPs and EUV high velocity structures.

Finally, Lang and Willson (1986 - this proceedings) report on the first detections in the quiet sun at 2 cm (14.3 GHz) of small (5-25 arc-sec), variable, moving structures. Willson and Lang (1986) observed two highly polarized sources on 4 June 1984. More recently on 17 January 1986 2 cm sources with no measurable polarization were detected. One interesting possibility is that some of these sources arise from non-thermal gyrosynchrotron radiation. Such radio sources may be common, with a frequency of occurrence comparable to that estimated for XBPs, CIV jets and small eruptive filaments.

EUV and Visible Light Observations

Earlier I referred to the controversy surrounding the use of XBPs, ERs and HeI DPs as proxies of small-scale emerging flux on the sun. During the Workshop this subject was discussed in presentations by S. Martin, K. Harvey, L. Golub and myself. As reflected in the following papers, most of the present comparative studies of BPs involve the use of NSO-Kitt Peak HeI- λ 10830 DPs as a proxy for coronal BPs. Harvey *et al.* (1975) first noted that many coronal features seen in soft X-rays also appeared in HeI-D3 and 10830 images. Subsequently, lacking routine X-ray observations, many researchers have used λ 10830 images to detect coronal holes and BPs, which appear in HeI to be dark. This absorption is due to the enhanced population in the low corona of the triplet state of HeI, which absorbs the continuum radiation from below. However, the physical mechanism of this process is unknown. A popular suggestion is that excess XUV emission ($\lambda < 500 \text{ \AA}$) excites the underlying HeI from the ground state. Since HeI is a chromospheric line, chromospheric features, such as the network, contribute to the signal, lowering the contrast for coronal features. For example, using λ 10830 and X-ray rocket images, Kahler *et al.* (1983) showed that the detailed correspondence of the boundaries of coronal holes in the two data sets was poor. Such a comparison for XBPs and HeI DPs is being performed by L. Golub, K. Harvey and D. Webb, but has not been completed.

Harvey, Tang and Gaizauskas (1986 - this proceedings) report preliminary results of observations during six periods involving the simultaneous comparison of HeI- λ 10830 images and photospheric magnetograms with H α , CIV, SiII, CaII and microwave data (see above). HeI DPs are associated with microwave and CIV emission and CaII blueshifts, but not on a one-to-one basis. Like XBPs, He DPs are associated with apparent magnetic bipoles, but more often with cancelling, opposite-polarity flux than with emerging flux (ephemeral regions) (see also Harvey, 1984; 1985; Martin *et al.*, 1985). Also like XBPs, He DPs (Harvey, 1985) and mixed-polarity fields (Giovannelli, 1982) vary inversely with the solar cycle. Therefore, Harvey (1985) has suggested that coronal BPs are typically associated with chance encounters of existing flux (more mixed polarity) rather than with emerging flux.

This interpretation differs from that of Golub, Harvey and Webb (1986 - this proceedings). They compare near-simultaneous X-ray and magnetic data during four X-ray rocket flights, and find that XBPs were slightly more likely to be associated with emerging bipoles (ERs) than with chance encounters of existing flux. However, there was a less than 50% association between XBP and magnetic bipoles going in either direction; unfortunately only daily magnetograms were available to define the bipole evolutionary history.

Harvey, Tang and Gaizauskas (1986) also define two types of small-scale (10-30 arc-sec) HeI dark features: rapid darkenings with lifetimes of 10-30 min. associated with small ejecta, and longer lived (hours) darkenings which can exhibit large intensity variations over minutes. The ejecta are often associated with small surges and small filament eruptions (Hermans and Martin, 1986) and/or propagating "clouds". (Are these like the Skylab X-ray clouds described by Rust and Webb, 1977?)

During the Workshop, S. Martin reviewed the subject of small-scale magnetic fields with emphasis on recent observations at high spatial and temporal resolution obtained with the videomagnetograph (VMG) at Big Bear Solar Observatory (BBSO). The BBSO group has classified such structures by their place of origin (Martin, 1984) and by how they cancel or disappear (Livi *et al.*, 1985). Quiet sun magnetic fields are of three main categories: ephemeral regions, network fields and intra-network fields. We earlier discussed ERs; ERs appear to be the primary form of bipolar flux emergence in the quiet sun, but they have short lifetimes. Network fields are thought to be residual fields from decayed active regions which have clumped around the boundaries of supergranules. These fields are involved in the large-scale diffusion of the global magnetic field. Finally, intra-network magnetic fields are representative of the continuous generation of magnetic field in the network cell interiors. These field fragments are swept to the boundaries of the supergranules and may be associated with the small-scale velocity field of the sun.

Martin and colleagues have classified the disappearance of small-scale flux by the origin of their components in the above three categories. They observe flux disappearance only through "cancellation" of opposite polarity fragments which come into contact. Cancelling flux loss is gradual, equal for both polarities, and occurs most frequently at the boundaries of the network. They conclude that cancellation is the dominant form of magnetic flux disappearance in the quiet sun. However, the physical mechanism(s) causing this flux loss remains unknown. Martin *et al.* (1985) suggest that XBP could be associated with both ERs and cancelling flux, the latter arising from heating associated with field line reconnection.

Figure 1 presents fine examples of the emergence of flux in an ER (within the oval starting at 1735 UT) and the cancellation of flux (within the two rectangles at top and bottom of each frame). These are BBSO VMG images courtesy of S. Martin. Note the separation with time of the opposite poles of the ER. Due to this expansion, the negative pole (black) of the ER encounters and cancels a small fragment of opposite flux.

Hermans and Martin (1986) report on results of a study of a new class of quiet sun activity which they call small-scale eruptive filaments. Like large filaments, these are chromospheric absorption features, but the small eruptives are common (about 1000 on the sun per day) and short-lived (average 70 min.). They are often associated with tiny patches of emission ("mini-flares"), HeI dark features and possibly cancelling flux.

Holt *et al.* (1986 - this proceedings) describe results of a study to measure the radial velocity in the chromosphere under coronal BPs. Their procedure was to measure the CaII-K line profiles of HeI DPs within and outside of coronal holes. They find that DPs not in coronal holes exhibit small blue-shifts of $0.1-1.2 \text{ km s}^{-1}$,

ORIGINAL PAGE IS
OF POOR QUALITY

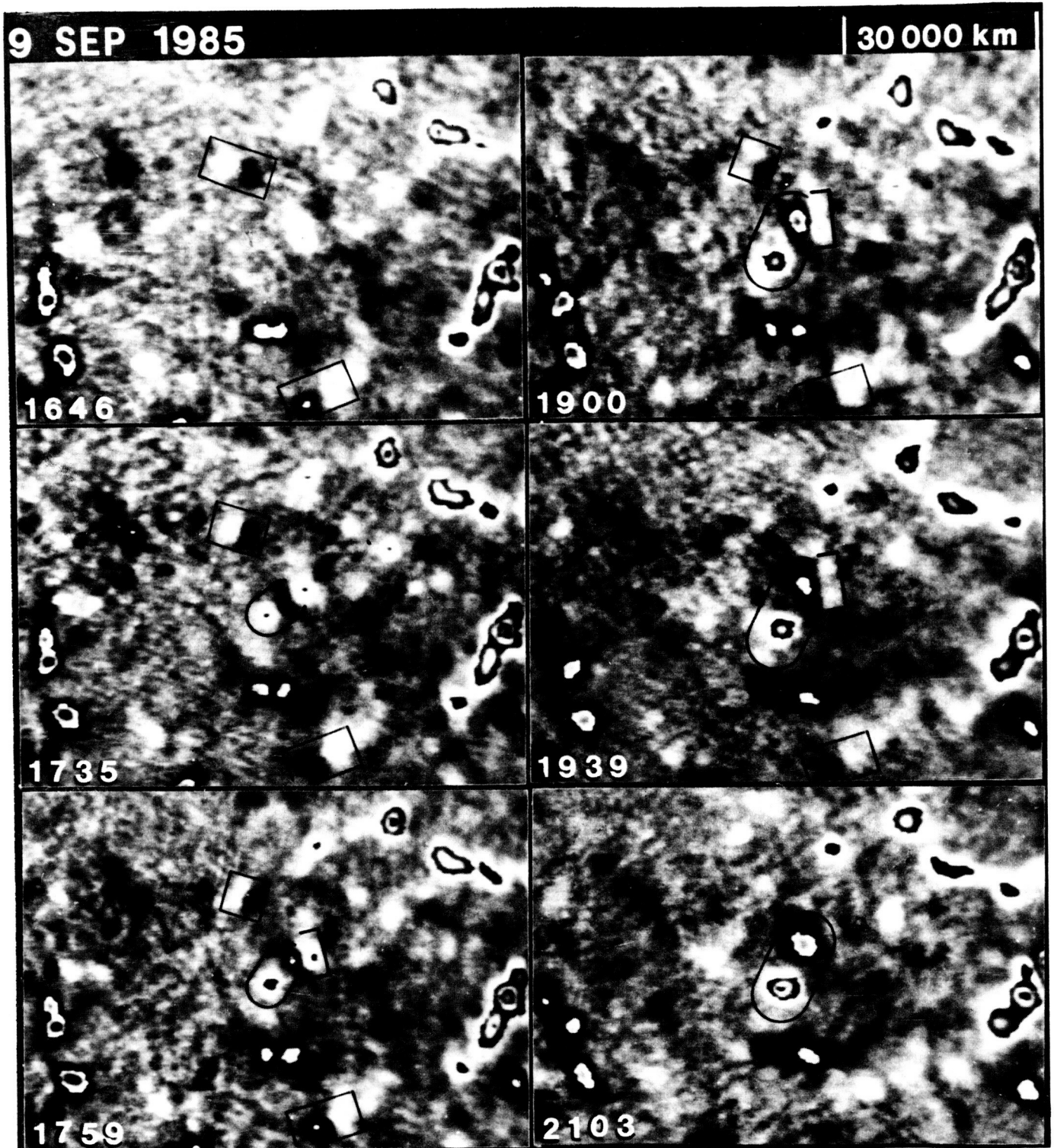


Figure 1

whereas 1/10 of the spectra of DPs within coronal holes have average blueshifts of 3.7 km s^{-1} . A collaborative study during the Spacelab-2 mission revealed that 4 of 5 HeI DPs had average blueshifts of about 1 km s^{-1} . These results lend some support to the speculation that coronal BPs and/or EUV jets might supply the mass flux in the solar wind. Small upward velocities in the chromosphere of a BP are not inconsistent with the observed velocities of $\sim 100 \text{ km s}^{-1}$ in the low corona for macrospicules (Moore *et al.*, 1977), XBP/polar plumes (Ahmad and Webb, 1978) and jets (Brueckner and Bartoe, 1983).

A wealth of high resolution EUV observations of the transition region, from experiments on Skylab, OSO-8, SMM, and HRTS, have become available in the last few years (e.g., Mariska, 1986). It is well known that the network in transition region lines is predominately redshifted. Using SMM CIV spectra, Gebbie *et al.* (1981) found a positive correlation between network intensity and redshift. Their plots showed a bimodal distribution, with the brightest sites having near-zero velocity. Toomre (private communication) speculated that these sites were the counterpart of coronal BPs. However, Athay *et al.* (1983) and Dere, Bartoe and Brueckner (1984) found no strong correlation between bright CIV network intensity and velocity.

Porter *et al.* (1986 - this proceedings) present recent results on temporal and spatial comparisons of similar SMM CIV images with magnetograms and HeI- $\lambda 10830$ images. They find frequent intensity fluctuations at many bright CIV sites. All CIV BPs correspond to magnetic bipoles, and the longest-lived to HeI DPs. A comparison of the HeI and CIV intensity variations and velocity profiles is being performed.

Finally, during the Workshop G. Brueckner presented early results on explosive events and jets observed in CIV with the NRL HRTS instrument on Spacelab-2. More complete results have been presented at later meetings (Cook *et al.*, 1986; Brueckner, Cook and Dere, 1986). CIV turbulent events and jets were first detected on HRTS rocket flights (Brueckner and Bartoe, 1983). These events were small (1-10 arc-sec), common, and Doppler-broadened to the blue, red or both by $\sim 100 \text{ km s}^{-1}$. To better establish the statistical importance of these events, 25% of the solar disk was surveyed in CIV during four orbits of the Spacelab-2 mission (see below). Initial examination of the film has revealed over 500 events with velocities $> 50 \text{ km s}^{-1}$. 35% of these events were blue-shifted (jets), 25% were red-shifted and 40% were both red and blue-shifted (turbulent or explosive events). The average velocity of each class was $\sim 80 \text{ km s}^{-1}$. Their average lifetime was 90 s, yielding a global birthrate of $\sim 40 \text{ s}^{-1}$. A global population of ~ 4000 events at any time has been estimated.

Spacelab-2 Collaboration

In 1985 a collaboration was organized to coordinate groundbased and Spacelab-2 observations of coronal BPs. Valuable coordinated observations were obtained, but few results are available at this time. The major emphasis of the collaboration is on comparative analysis of near-simultaneous observations of BPs at all levels of the solar atmosphere, especially during the HRTS survey from 3 August, 2127 UT to 4 August 1985, 0253 UT. During this period 13 rasters in CIV and in the $\lambda 1190$ - 1680 waveband were obtained; each CIV raster was about 1 arc-min N-S by 15 arc-min E-W, with 1 arc-sec step widths. Promising collaborative data obtained near or during this interval include photospheric magnetograms, HeI- $\lambda 10830$ and D3 spectro-

heliograms, VLA images at 2, 6 and 20 cm, H α images, CaK images and the CaK line profiles discussed by Holt et al. (1986). Although soft X-ray images were not obtained, this combination of data probably represents the best obtained to date for understanding the characteristics of BPs.

Summary of Observations of Bright Points

At the end of the Workshop we attempted to summarize our efforts by preparing a list of five questions which concern the correspondences of BPs, or other short-lived quiet sun features observed at all levels of the atmosphere. These questions are not comprehensive, but reflect our deliberations.

- 1) What is the relationship of BPs to emerging flux?
- 2) What is the correspondence of BPs, in the transition region and corona, to the network?
- 3) What is the correspondence of high velocity features, such as CIV jets, small eruptive H α filaments, H α and EUV macrospicules, XBP-polar plumes to BPs?
- 4) What is the correspondence of microwave BPs to other BPs?
- 5) Regarding the important HeI λ 10830 observations:
 - a. What is the correspondence of He DPs to other BPs?
 - b. What is the chromospheric influence on HeI line formation?

Table 1 is a listing of the BP or small-scale features that have been observed and are discussed here along with correspondences with other features which have been made or inferred. The table is intended only as a general listing of BP features and their possible associations.

So what are BPs? The Skylab observations showed that the small, compact features seen in the corona could be traced downward in temperature and height to bipolar magnetic structures in the photosphere. These structures fluctuate in size and intensity on short time scales (minutes) and their fluctuations are often correlated at different heights. Therefore, these BPs appear to be magnetically controlled and probably consist of one or more tiny loops.

The physical correspondence to specific small-scale features in the intermediate chromosphere and transition region is more confusing and uncertain. It is particularly important to determine if BPs are associated with the network. We have but a single study (Egamberdiev, 1983) in which XBPs are purported to be correlated with the network. Microwave and CIV BPs are correlated with HeI DPs which in turn are more often associated with magnetic flux cancellation which in turn occurs more often at the boundaries of the network. And there is evidence that the occurrence frequency of bright Ca network elements oscillates out of phase with the sunspot cycle, like XBPs and HeI DPs. Spicules are another common transient feature which is spatially correlated with the network. Are BPs associated with spicules? On the other hand, magnetic ERs appear randomly with respect to the network (Harvey and Martin, 1973; Martin, 1984), but are associated with at least some coronal BPs. It is possible that there are actually several physical classes

TABLE 1

OBSERVED BP FEATURES AND SUGGESTED CORRESPONDENCES

<u>Feature</u>	<u>Corresponding Features</u>
XBPs	Ephemeral regions (emerging flux) Cancelling flux (Ca network) EUV BPs Polar plumes
Flaring XBPs	H α and EUV macrospicules
HeI DPs	Cancelling flux Ephemeral regions Microwave BPs CIV BPs Ca II blueshifts
Microwave BPs	Cancelling flux Ephemeral regions HeI DPs
CIV BPs	Magnetic bipoles HeI DPs
CIV eruptives/jets	?
H α small-scale filament eruptions	Mini-flares HeI DPs Cancelling flux

of BPs on the sun. It is also possible that these classes are a function of size and/or lifetime. In this context, it is important to realize that we have not yet detected the turnover at the short end of the lifetime (and size?) distributions of XBPs, ERs, HeI DPs or CIV transients.

To a large degree our present confused situation is due to a wealth of spacecraft observations in X-rays and the EUV, and the lack of coordinated efforts to compare results at different wavelengths. Hopefully, our understanding of BP structure will soon improve sufficiently to permit the development of detailed theoretical models of their structure, heating and energy balance.

THE INFLUENCE OF SMALL-SCALE STRUCTURES ON CORONAL HEATING

We formulated a final question: What is the structure and heating mechanism(s) of small-scale solar structure? In this part I review two aspects of this question. First, I discuss observations and a model pertaining to heating mechanisms of BPs. Then I address the fundamental question of the relationship of these small-scale structures to the heating of the corona.

Heating Mechanisms of BPs

Using Skylab data, Sheeley and Golub (1979), Nolte et al. (1979), Little and Krieger (in Webb, 1981), and Habbal and Withbroe (1981) studied the temporal behavior of individual BPs. Nolte et al. and Little and Krieger observed both rapid variations and steady output (over tens of minutes) in the integrated flux from different XBPs, while Sheeley and Golub and Habbal and Withbroe found that the intensity variations in BP emission typically varied over several minutes. In the latter studies the temporal behavior of a BP was found to be the average of the more rapid variations of individual loops. Even during periods of relatively constant integrated emission, individual loops were observed to form and disappear. Habbal and Withbroe found that the intensity variations were often temporally correlated at different heights. Both Nolte et al. and Habbal and Withbroe attributed these variations to intermittent heating of individual loops, sometimes impulsively.

In agreement with these earlier results, Habbal et al. (1986) have found that microwave BPs exhibit spatial and temporal variations over time scales of > 2 min. Habbal and Harvey note that these microwave BP variations are often, though not always associated with HeI DP variations. Since the EUV and microwave BPs and the HeI DPs vary frequently in shape and emission and since they are associated with cancelling magnetic flux, Habbal and Harvey (1986) conclude that the magnetic field is fundamental to this dynamic behavior. Both Habbal and Harvey and Lang and Willson (1986) suggest that the BP variability might be caused by varying magnetic fields or density variations related to intermittent heating.

Porter et al. (1986) observed strong fluctuations in CIV intensity overlying magnetic bipoles. They considered this as evidence that small-scale impulsive heating is common in the quiet sun transition region and in active regions (Porter et al., 1984), but not always associated with coronal emission (BPs). They attributed this to a stochastic process involving the convective motion of loop foot-points which results in field line reconnection and impulsive heating events.

Klimchuk, Antiochos and Mariska (1986 - this proceedings) discuss a model of the heating of small-scale (i.e., low-lying) coronal loops, with implications for BPs. Recently, Antiochos and Noci (1986) demonstrated that low-lying static loops have both hot and cool solutions. Linear perturbation theory suggests that hot loops are thermally unstable while cool loops are thermally stable. This implies that small, cool loops should be more abundant than hot loops, and small coronal loops, like BPs, should be short-lived, even for steady-state heating. Klimchuk et al. (1986) extend this analysis by performing non-linear, numerical simulations of such structures and find that both hot and cool loops appear to be stable and, therefore, both may be common in the low corona.

Small-Scale Structure and the Heating of the Corona

It has been determined that the energy flux due to the upward propagation of acoustic waves is 2-3 orders of magnitude too small to heat the transition region and corona (Bruner, 1981). Since this result appeared, researchers have speculated on whether the energy in radiation and mass flows of small-scale structures is sufficient to heat the corona. Such features must be sufficiently common at all phases of the cycle, individually energetic and globally distributed

so as to meet the mass and energy input requirements at the base of the corona (e.g., $4 \times 10^5 \text{ erg cm}^{-2}\text{s}^{-1}$; Withbroe, 1977). Chromospheric spicules and EUV jets have been proposed as ubiquitous small-scale structures which meet these requirements. In addition, spicules, jets and XBP have been proposed as agents for providing the mass flux in the solar wind.

The upward mass flux in spicules exceeds the solar wind mass flux by about a factor of 100. Thus, infalling spicule material provides a large reservoir of potential energy that could heat the transition region and corona (Athay and Holzer, 1982). Brueckner and Bartoe (1983) suggested that EUV jets could heat the corona through shock wave heating or thermalization in confining magnetic fields. However, the recent Spacelab-2 data do not support the argument that the jets can provide sufficient energy flux to heat the corona.

Another approach to the coronal heating problem is suggested by the results of Orrall and Rottman (1986 - this proceedings). They examined the electron density "irregularity" of the inner corona by comparing EUV emission line intensity from coronal ions with K-coronal polarization brightness, pB. Since coronal emission depends on the square of the electron density and the scattered K-coronal brightness depends directly on the density, the combined observations constrain the density irregularity and include contributions from both resolved and unresolved structure along the line of sight. Orrall and Rottman develop models of the irregularity and find that it is too large to be explained by presently known inner coronal structures. They suggest that the irregularity might arise from unresolved small-scale structures possibly in instabilities or density fluctuations associated with coronal heating. It should be possible to pursue this question with two existing data sets of simultaneous AS&E soft X-ray ($f[N_e^{2d1}]$) and HAO white light ($f[N_e^{d1}]$) eclipse images (e.g., Krieger, 1977).

Finally, Schatten and Mayr (1986 - this proceedings) describe a model for coronal heating via spicules. Although they agree with others that spicules do not carry sufficient kinetic energy to heat the corona, they suggest instead that spicules are conduits which transport non-potential magnetic and wave energy into the solar atmosphere from the convection zone. This energy is then explosively released to heat the corona and possibly form an expanding solar wind.

REFERENCES

- Ahmad, I.A. and D.F. Webb, 1978, "X-ray Analysis of a Polar Plume", Solar Phys., 58 (323).
- Antiochos, S.K. and G. Noci, 1986, "The Structure of the Static Corona and Transition Region," Astrophys. J., 301 (440).
- Athay, R.G. and T.E. Holzer, 1982, "The Role of Spicules in Heating the Solar Atmosphere", Astrophys. J., 255 (743).
- Athay, R.G., J.B. Gurman, W. Henze and R.A. Shine, 1983, "Fluid Motions in the Solar Chromosphere-Corona Transition Region. I. Line Widths and Doppler Shifts for CIV", Astrophys. J., 265 (519).
- Bohlin, J.D., N.R. Sheeley, Jr, and R. Tousey, 1975, "Structure of the Sun's Polar Cap at Wavelengths 240-600Å", in (M.J. Rycroft, ed.) Space Research XV, Akademie-Verlag, Berlin (651).

- Brueckner, G.E. and J.-D. F. Bartoe, 1983, "Observations of High Energy Jets in the Corona Above the Quiet Sun, the Heating of the Corona, and the Acceleration of the Solar Wind", Astrophys. J., 272 (329).
- Brueckner, G.E., J.W. Cook and K.P. Dere, 1986, "Results From the HRST Experiment", Advances Space Res. (to be published).
- Bruner, E.C. Jr., 1981, "OSO-8 Observational Limits to the Acoustic Coronal Heating Mechanism", Astrophys. J., 247 (317).
- Bumba, V. and R. Howard, 1965, "A Study of the Development of Active Regions on the Sun", Astrophys. J., 141 (1492).
- Cook, J.W., P.A. Lund, G.E. Brueckner, J.-D. F. Bartoe, K.P. Dere and D.G. Socker, 1986, "Statistical Properties of Small High-Velocity Transition Region Events on the Sun Observed by HRTS on Spacelab-2", Bull. AAS, 18 (662).
- Davis, J.M., 1983, "X-ray Bright Points and the Sunspot Cycle: Further Results and Predictions", Solar Phys., 88 (337).
- Davis, J.M. and D.F. Webb, 1981, "The Radiative Instability as a Mechanism for Bright Point Flares", Bull. AAS, 13 (821).
- Dere, K.P., J.-D. F. Bartoe, and G.E. Brueckner, 1984, "High Resolution Telescope and Spectrograph Observations of the Quiet Solar Chromosphere and Transition Zone", Astrophys. J., 281 (870).
- Egamberdiev, Sh. A., 1983, "The Placement of X-ray Bright Points Relative to the Chromospheric Network", Sov. Astron. Lett., 9 (385).
- Gebbie, K.B. and 11 coauthors, 1981, "Steady Flows in the Solar Transition Region Observed with Solar Maximum Mission", Astrophys. J., 251 (L115).
- Giovanelli, R.G., 1982, "On the Relative Role of Unipolar and Mixed-Polarity Fields", Solar Phys., 77 (27).
- Golub, L., 1980, "X-ray Bright Points and the Solar Cycle", Phil. Trans. R. Soc. Lond., 297 (595).
- Golub, L. and G.S. Vaiana, 1978, "Differential Rotation Rates for Short-lived Regions of Emerging Magnetic Flux", Astrophys. J., 219 (L55).
- Golub, L., A.S. Krieger, G.S. Vaiana, J.K. Silk, and A.F. Timothy, 1974, "Solar X-ray Bright Points", Astrophys. J., 189 (L93).
- Golub, L., A.S. Krieger, J.W. Harvey, and G.S. Vaiana, 1977, "Magnetic Properties of X-ray Bright Points", Solar Phys., 53 (111).
- Golub, L., K.L. Harvey and D.F. Webb, 1986, "Magnetogram and Soft X-ray Comparisons of XBP and ER", this proceedings.
- Habbal, S.R. and K.L. Harvey, 1986, "Simultaneous Observations of Changes in Coronal Bright Point Emission at the 20 cm Radio and HeI $\lambda 10830$ Wavelengths", this proceedings.
- Habbal, S.R. and G.L. Withbroe, 1981, "Spatial and Temporal Variations of EUV Coronal Bright Points", Solar Phys., 69 (77).
- Habbal, S.R., R.S. Ronan, G.L. Withbroe, R.K. Shevgaonkar, and M. Kundu, 1986, "Solar Coronal Bright Points Observed with the VLA", Astrophys. J. (in press).
- Harvey, K.L., 1984, "Solar Cycle Variation of Emerging Active Regions", in The Hydromagnetics of the Sun, ESA SP-220, Noordwijkerhout, The Netherlands (235).
- Harvey, K.L., 1985, "The Relationship between Coronal Bright Points as Seen in HeI $\lambda 10830$ and the Evolution of the Photospheric Network Magnetic Fields", Aust. J. Phys., 38 (875).
- Harvey, K.L. and S.F. Martin, 1973, "Ephemeral Active Regions", Solar Phys., 32 (389).
- Harvey, J.W., A.S. Krieger, A.F. Timothy, and G.S. Vaiana, 1975, "Comparison of Skylab X-ray and Ground-based Helium Observations", Osserv. Mem. Oss. Arcetri, 104 (50).

- Harvey, K.L., F. Tang and V. Gaizauskas, 1986, "The Association of Chromospheric and Coronal Phenomena With the Evolution of the Quiet Sun Magnetic Fields", this proceedings.
- Hermans, L.M. and S.F. Martin, 1986, "Small-Scale Eruptive Filaments on the Quiet Sun", this proceedings.
- Holt, R.D., A.H. Park, J.C. Thompson, and D.M. Mullan, 1986, "Observations of the Ca II K Line in He10830 Å Dark Points on August 3, 1985", this proceedings.
- Howard, R., L. Fritzova-Svestkova, and Z. Svestka, 1979, "The Birthplace of Active Regions and X-ray Bright Points", Solar Phys., 63 (105).
- Kahler, S.W., J.M. Davis and J.W. Harvey, 1983, "Comparison of Coronal Holes Observed in Soft X-rays and HeI-10830 Å Spectroheliograms", Solar Phys., 87 (47).
- Klimchuk, J.A., S.K. Antiochos and J.T. Mariska, 1986, "A Numerical Study of the Thermal Stability of Low-Lying Coronal Loops", this proceedings.
- Krieger, A.S., 1977, "X-ray Observations of Solar Structural Features", in Proc. of the OSO-8 Workshop, Univ. of Colorado, Boulder, Colo. (98).
- Kundu, M.R., 1986, "VLA Observations of Coronal Bright Points at 6 and 20 Cm Wavelengths", this proceedings.
- Lang, K.R. and R.F. Willson, 1986, "Compact, Variable, Moving Sources Observed on the Sun at 2 Centimeters Wavelength", this proceedings.
- Livi, S.H.B., J. Wang, and S.F. Martin, 1985, "The Cancellation of Magnetic Flux. I. On the Quiet Sun", Aust. J. Phys., 38 (855).
- Mariska, J.T., 1986, "The Quiet Solar Transition Region", in (Burbidge, G., Lazer, D. and Phillips, J.G., eds.) Ann. Rev. of Astron. Astrophys., Vol. 24, Annual Reviews, Inc., Palo Alto, Calif. (to be published).
- Marsh, K.A., 1978, "Ephemeral Region Flares and the Diffusion of the Network", Solar Phys., 64 (93).
- Marsh, K.A., G.J. Hurford and H. Zirin, 1980, "VLA Observations of Spatial Structure in the Quiet Sun at 6 cm, During the 1977 October Eclipse", Astrophys. J., 236 (1017).
- Martin, S.F., 1984, "Dynamic Signatures of Quiet Sun Magnetic Fields", in (S.L. Keil, ed.) Proc. Symp. on Small-Scale Dynamical Processes in Quiet Stellar Atmospheres, NSO, Sacramento Peak, N.M. (30).
- Martin, S.F. and K.L. Harvey, 1979, "Emerging Active Regions During Solar Minimum", Solar Phys., 64 (93).
- Martin, S.F., S.H.B. Livi, J. Wang and Z. Shi, 1985, "Ephemeral Regions vs Pseudo Ephemeral Regions", in (M.J. Hagyard, ed.) Measurements of Solar Vector Magnetic Fields, NASA CP-2374, NASA Marshall Space Flight Center, Alabama (403).
- Moore, R.L., F. Tang, J.D. Bohlin and L. Golub, 1977, "H α Macrospicules: Identification with EUV Macrospicules and with Flares in X-ray Bright Points", Astrophys. J., 218 (286).
- Muller, R. and Th. Roudier, 1984, "Variability of the Quiet Photospheric Network", Solar Phys., 94 (33).
- Nolte, J.T., Solodyna, C.V. and M. Gerassimenko, 1979, "Short-Term Temporal Variations of X-ray Bright Points", Solar Phys., 63 (113).
- Orrall, F.Q. and G.J. Rottman, 1986, "Small Scale Structures and the Density Irregularity of the Inner Corona", this proceedings.
- Porter, J.G., J. Toomre and K.B. Gebbie, 1984, "Frequent Ultraviolet Brightenings Observed in a Solar Active Region with Solar Maximum Mission", Astrophys. J., 283 (879).

- Porter, J.G., E.J. Reichman, R.L. Moore, and K.L. Harvey, 1986, "Magnetic Location of CIV Events in the Quiet Network", this proceedings.
- Rust, D.M. and D.F. Webb, 1977, "Soft X-ray Observations of Large-Scale Coronal Active Region Brightenings", Solar Phys., 54 (403).
- Schatten, K.H. and H.G. Mayr, 1986, "Phlegethon Flow - A Proposed Origin For Spicules and Coronal Heating", this proceedings.
- Sheeley, N.R. Jr., 1981, "The Overall Structure and Evolution of Active Regions", in (F.Q. Orrall, ed.) Solar Active Regions, Colorado Assoc. Univ. Press, Boulder, Colo. (17).
- Sheeley, N.R. Jr. and L. Golub, 1979, "Rapid Changes in the Fine Structure of a Coronal Bright Point and a Small Active Region", Solar Phys., 63 (119).
- Tang, F., R. Howard and J.M. Adkins, 1984, "A Statistical Study of Active Regions 1967- 1981", Solar Phys., 91 (75).
- Vaiana, G.S., A.S. Krieger, L.P. Van Speybroeck, and T. Zehnpfenning, 1970, "The Structure of the X-ray Corona and Its Relation to Photospheric and Chromospheric Features", Bull. Am. Phys. Soc., 15 (611).
- Webb, D.F., 1981, "Active Region Structures in the Transition Region and Corona", in (F.Q. Orrall, ed.) Solar Active Regions, Colorado Assoc. Univ. Press, Boulder, Colo. (165).
- Willson, R.F. and K.R. Lang, 1986, "VLA Observations of Compact, Variable Sources on the Sun", Astrophys. J. (in press).
- Withbroe, G.L., 1977, "The Chromosphere and Transition Layers in Coronal Holes", in (J.B. Zirker, ed.) Coronal Holes and High Speed Wind Streams, Colorado Assoc. Univ. Press, Boulder, Colo. (145).

SIMULTANEOUS OBSERVATIONS OF CHANGES IN CORONAL BRIGHT POINT EMISSION AT THE 20 cm RADIO AND He λ 10830 WAVELENGTHS

Shadia R. Habbal
Harvard-Smithsonian Center for Astrophysics
Cambridge, Massachusetts 02138

and

Karen L. Harvey
Solar Physics Research Corporation
Tucson, Arizona 85718

INTRODUCTION

Coronal bright points are the smallest scale closed coronal structures that have been observed so far on the Sun (e.g. Golub *et al.*, 1974). They are associated with ephemeral magnetic bipolar regions (i.e. regions of opposite magnetic polarities) with lifetimes of hours (e.g. Harvey *et al.*, 1975). In x-ray spectroheliograms, coronal bright points appear to be collections of miniature loops or arches, typically 2500 km in diameter and 12,000 km in length (Sheeley and Golub, 1979). They are also characterized by significant changes over a few minutes in the intensity of emission from the plasma confined within the magnetic field forming these structures.

A detailed study of the extreme ultraviolet (EUV) data from Skylab (Habbal and Withbroe, 1981) showed that, over a period of 5 min, the shortest time scale available from the data, strong temporal and spatial variations in intensity of emission occur in the chromospheric through coronal layers of the bright points. Habbal and Withbroe (1981) attributed the changes in EUV emission to intermittent heating, possibly correlated with changes in magnetic field topologies over very small scales (few arcsec or less). More recently, Harvey (1985) has shown that, features which appear as "dark" absorption regions in the He I λ 10830 line (typically 15 to 20% darker than the average network) and believed to be the photospheric counterpart of coronal bright points, are often associated with encounters of existing opposite polarity magnetic regions rather than emerging magnetic flux. In He I λ 10830 they are also observed to be short lived ($<$ hours), often appearing and disappearing over a few minutes.

Recent radio observations acquired with the VLA at 20 cm wavelength showed that bright points appear as localized 20-40" radio sources, clearly distinguishable from the surrounding quiet sun (Habbal *et al.* 1986). At the 20 cm wavelength, the radio emission from bright points arises mainly from heights typical of the low corona-transition region. The bright points exhibit substantial spatial and temporal variations in radio emission over time scales as short as 2 minutes, very similar in nature to the variability observed in earlier studies at x-ray, EUV and optical wavelengths. Analysis of the data showed that the fluctuations observed in the radio emission are most likely due to intermittent heating.

OBSERVATIONS

We report here on preliminary results of observations of solar coronal bright points acquired simultaneously from ground based observatories at the radio wavelength of 20 cm and in the He I λ 10830 line on September 8, 1985. The impetus for obtaining simultaneous radio and optical data is (1) to identify correlations, if any, in changes of the low transition-coronal signatures of bright points with the evolution of the magnetic field, and (2) to distinguish between intermittent heating and changes in the magnetic field topology. Although simultaneous observations of H α emission and the photospheric magnetic field at Big Bear (S. Martin) were also made, as well as radio observations from Owens Valley Radio Interferometer (with G. Hurford) and SMM (O VIII line), we present here only a comparison between the He 10830 and VLA radio data.

The correspondence found between compact (20-40") radio sources observed at 20 cm with the VLA and the He I λ 10830 dark points is shown in Figure 1. The existence of an active region in the South East, and a smaller one close to Sun center made the superposition of the radio maps with a full disk He 10830 spectroheliogram particularly accurate. In the 512"x512" area around Sun center where the high temporal resolution He 10830 observations were made, the radio sources were found to coincide with He 10830 dark points. The spatial resolution is 1-2" in the He and 16" in the radio. There were, however, more He 10830 dark points than radio sources. The radio bright points with a dashed and a solid contour are those observed to last longer than 2 hours in the approximately 5 hours of simultaneous observations. The solid line contours represent shorter lived features (at least one hour). Comparison with high resolution magnetograms confirms that the radio bright points coincide with bipolar regions.

Shown in Figure 2 are the changes in time of the maximum radio brightness temperature and the absolute value of the maximum intensity of absorption in the He 10830 of one of the sources, source A. (0 min on the time axis corresponds to 16:00 UT). The time interval is 3 min, which is the time required to make a 512"x512" scan in the He line. Radio maps were made at the exact corresponding time intervals. The data gaps in the radio data correspond to the pointing of the antennas to the calibration source; also no radio maps were made in the He 10830 data gaps 17:56 - 18:23 and 20:15 - 20:41 UT. Sporadic variations in the emission (absorption) often occur at the shortest (3 min) time interval. (These variations are significant when greater than 10% in the intensity of absorption in the He λ 10830 and greater than 10^4 K in the radio brightness temperature). The temporal changes in the simultaneous observations are often correlated, but there are a few cases, for example between 19:00 and 19:30 or between 19:50 and 20:00, when the radio emission and He absorption are anticorrelated.

DISCUSSION

One of the striking features of bright points observed so far at different wavelengths is the spatial variation of the region of maximum emission (or absorption), i.e. the bright (dark) "patch" does not remain uniform but rather brightens in certain spots while others dim, also a bright point can completely fade and reappear rather suddenly at a later time (see, for example, Habbal and Withbroe 1981, and Habbal *et al.* 1986). Hence it is clear that these features are responding rather rapidly to dynamic effects. At the time of this writing a quick look at the magnetograms shows that at least 80 % of the radio sources correspond to areas of disappearing flux, i.e. where magnetic regions of opposite polarity approach each other and cancel. Very few are associated with new emerging flux. There are five bright points that overlie regions where some flux cancelling is occurring while new flux also emerges in the neighborhood. Hence this suggests that the magnetic field is playing an important role in the observed dynamic behavior of the bright points. On the other hand one of the plasma variables that can account for variations observed at the radio wavelength and the He 10830 absorption is the density. Density fluctuations caused by intermittent heating or from the interaction or roping around of the field lines could easily account for the sporadic nature of the variability in emission (absorption).

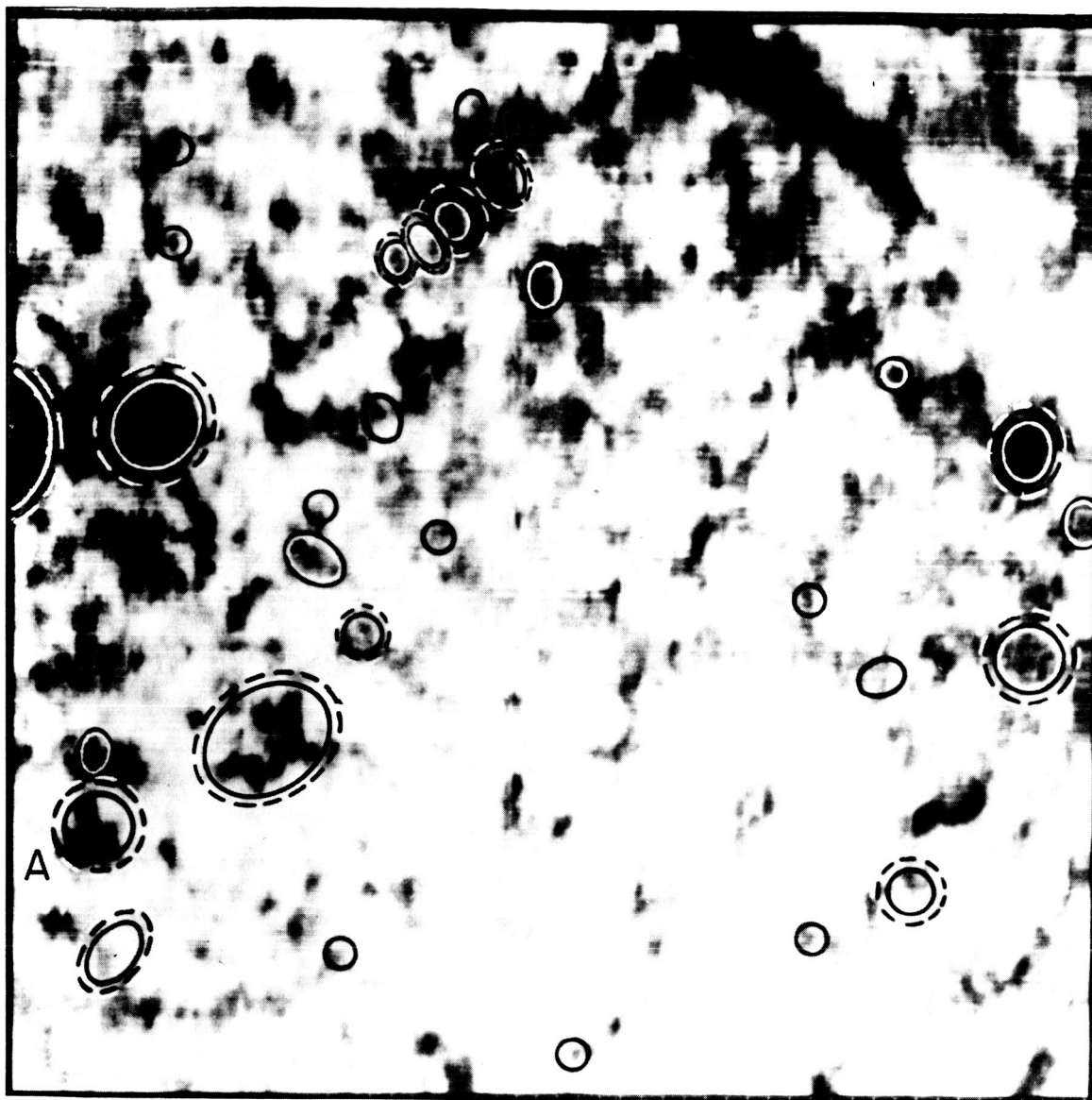


Figure 1: Overlay of radio sources, observed with the VLA at 20 cm, on a He λ 10830 spectroheliogram. The observations were made simultaneously on September 8, 1985. The field of view of the He λ 10830 spectroheliogram is $512'' \times 512''$, centered at Sun center at 16:00 UT. Radio sources indicated by two contours were present for at least 2 hours in the observing sequence of 5 hours. Shorter lived radio sources are indicated by one contour.

SOURCE A

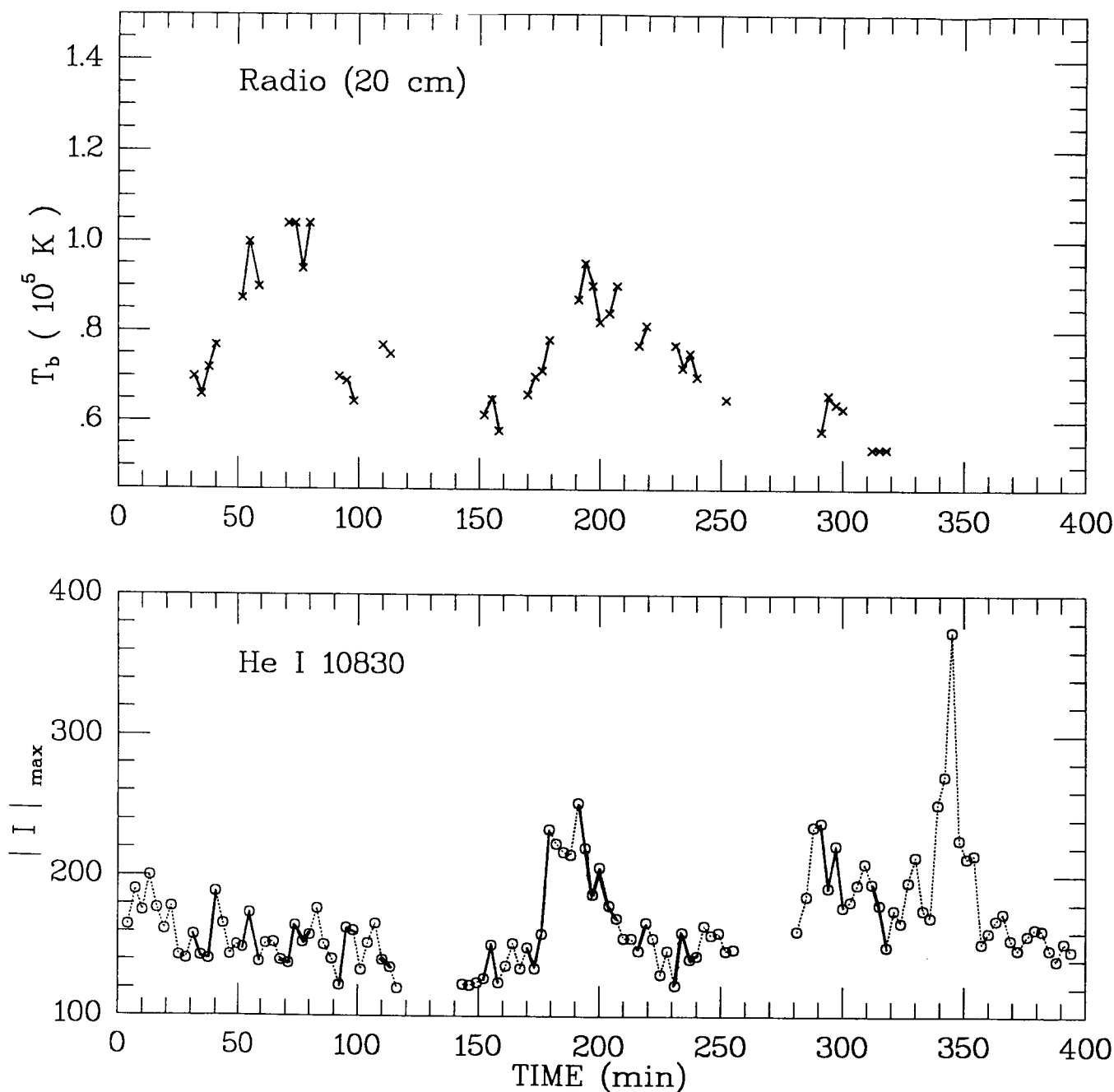


Figure 2: Changes in time of the absolute value of the maximum absorption ($|I|_{\max}$) in $\text{He } \lambda 10830$ and the maximum brightness temperature (T_b) of the radio emission at 20 cm for Source A. The solid lines at both wavelengths indicate simultaneous continuous observations with 3 min integration time. The dotted lines in the $\text{He } \lambda 10830$ connect data points with no corresponding radio data. The short data gaps in the radio correspond to the pointing of the antennas to the calibration source. Two data gaps exist in the $\text{He } \lambda 10830$ data: 116-143 (or 17:56-18:23 UT), and 255-281 (or 20:15-20:41 UT), when no radio data are shown either.

CONCLUSION

Radio observations are an important component in the study of coronal bright points because they are, at present, the only means to explore the transition region-corona heights from the ground with high temporal and spatial resolution. Furthermore, radio measurements can also be used to derive quantitative information regarding important solar plasma parameters such as the magnetic field strength, plasma density and electron temperature. For example, field strengths of the order of 50 to 100 G at the low corona-transition region height in bright points have been deduced for the first time from radio observations (Habbal *et al.* 1986). The radio observations will provide valuable quantitative information about the hot plasma in bright points while the optical data will provide information about the chromospheric and low chromospheric-coronal transition region and the photospheric magnetic field.

The intriguing questions that arise with respect to the behavior of bright points are directly related to the fundamental problem of coronal heating. If bright points are part of the same class of phenomena as active regions, but on a smaller scale, then the understanding of their behavior will shed light on the question of solar activity. Coronal bright points seem to offer an ideal candidate to explore the role of the magnetic field in the heating of the plasma, and the evolution of the field in time.

ACKNOWLEDGEMENTS

We thank R. Ronan for his help in the reduction of the radio data. The National Radio Astronomy Observatory is operated by Associated Universities, Inc., under contract with the National Science Foundation. This work was supported by NASA grants NGR 21-002-199 (S. R. Habbal) and NAS 5-28728 (K. L. Harvey).

REFERENCES

- Golub, L., Krieger, A. S., Vaiana, G. S., Silk, J. K., and Timothy, A. F. 1974, "Solar X-Ray Bright Points," *Astrophys. J.*, **189**, L93.
- Habbal, S. R. and Withbroe, G. L. 1981, "Spatial and Temporal Variations of EUV Coronal Bright Points," *Solar Phys.*, **69**, 77.
- Habbal, S. R., Ronan, R. S., Withbroe, G. L., Shevgaonkar, R., K. and Kundu, M. 1986, "Solar Coronal Bright Points Observed with the VLA," *Astrophys. J.* in press, July 15.
- Harvey, K. L., Harvey, J. W., and Martin, S. F. 1975, "Ephemeral Active Regions in 1970 and 1973," *Solar Phys.*, **40**, 87.
- Harvey, K. L. 1985, "The Relationship between Coronal Bright Points as seen in He I λ 10830 and the Evolution of the Photospheric Network Magnetic Field," *Australian J. of Physics*, **38**, 875.
- Sheeley, N., R. Jr., and Golub, L. 1979, "Rapid Changes in the Fine Structure of a Coronal Bright Point and a Small Active Region," *Solar Phys.*, **63**, 119.

VLA OBSERVATIONS OF CORONAL BRIGHT POINTS AT 6 AND 20 CM WAVELENGTHS

M.R. Kundu
 Astronomy Program
 University of Maryland
 College Park, MD 20742

Prior to and during Spacelab-2 operation, we made observations at 6 and 20 cm of solar coronal bright points, using the VLA in the C-configuration. The UV coverage ranged from 200 to 1.8×10^4 wavelengths. The maps were convolved with beams of $18'' \times 18''$ at 20 cm and $4'' \times 4''$ at 6 cm. Here we report only preliminary results from July 15 and July 31, 1985 observations.

Figure 1 shows the 20 cm results of July 15, 1985 observations. Our maps were compared with both KPNO He 10830Å spectroheliogram and magnetogram.

At the center of the disk a bipolar plage is present (the strongest region with several components). Near this plage region there is an H α filament along which runs a neutral line in the KPNO magnetogram. At 20 cm this filament is associated with a radio depression with $T_b \approx 1.8 \times 10^5$ K below the quiet sun T_b . The maximum depression is associated with a HeI dark feature, however the radio depression is much wider ($\sim 40''$) than the He counterpart ($\sim 20''$). Several bright points are present in the map. As mentioned above, they are identified from their association with dark points in the He spectroheliogram. Comparison with the KPNO magnetogram shows that the majority of these regions are bipolar. However the spatial resolution at 20 cm was not good enough to resolve the structures, and only one polarization was observed with very low degree of polarization. The brightness temperature of the sources 1, 2, 3 and 4 ranges from $\sim 1.0 \times 10^5$ K to 3.6×10^5 K above the quiet sun temperature. These values of the brightness temperature seem to indicate that the emission should be primarily due to an optically thin thermal plasma.

Figure 2 shows that the bright point No. 5 (see Fig. 1) at 20 cm is resolved into two components at 6 cm because of better resolution.

Figure 3 shows the results of July 31, 1986 observations. There are several bright point sources at 20 cm. The source A is associated with a dark point at He 10830Å and with a bipolar magnetic feature.

PRECEDING PAGE BLANK NOT FILMED

He I λ 10830

31 JULY 1985
20 cm
Intensity

MAGNETOGRAM

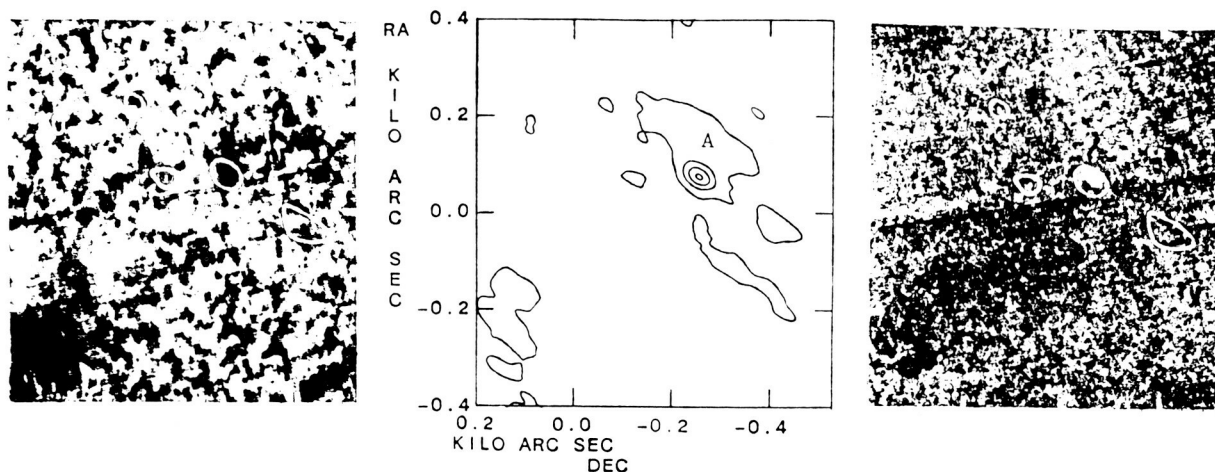


Figure 1. 20 cm (VLA) map and Kitt Peak He λ 10830 and Magnetogram (courtesy of J. Harvey) on 31 July, 1985. Source A is associated with bipolar magnetic feature and with dark point at He λ 10830. Other weak radio bright points are associated with weak bipolar regions and with faint dark points.

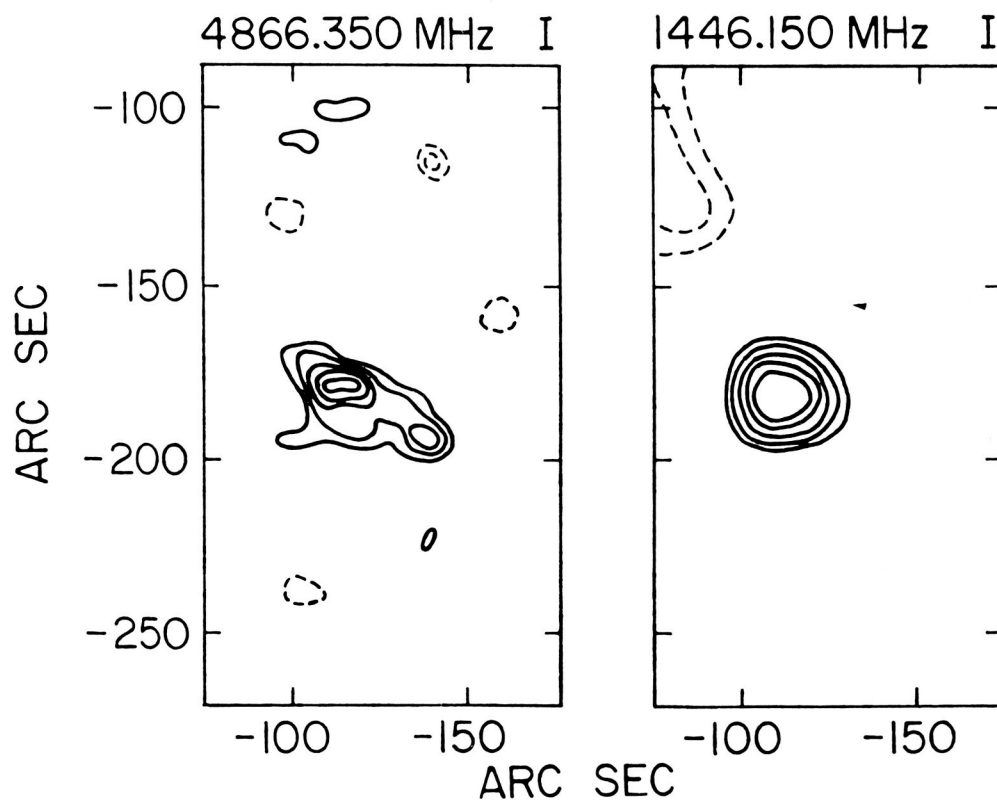


Figure 2. VLA maps of bright point No. 5 at 6 and 20 cm wavelength, July 31, 1985.

ORIGINAL PAGE IS
OF POOR QUALITY

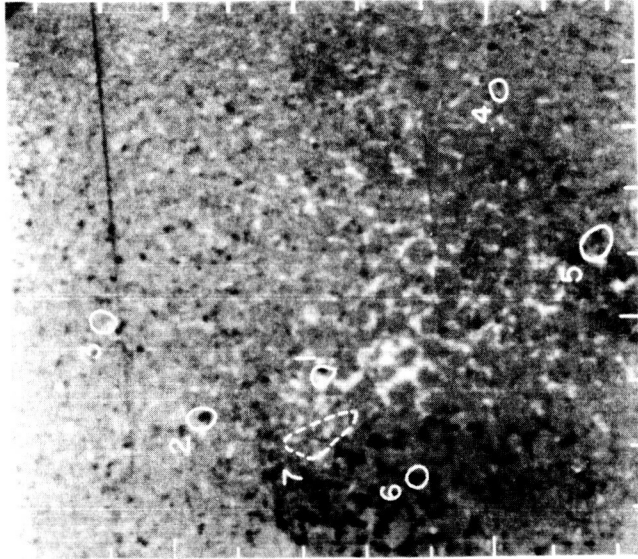
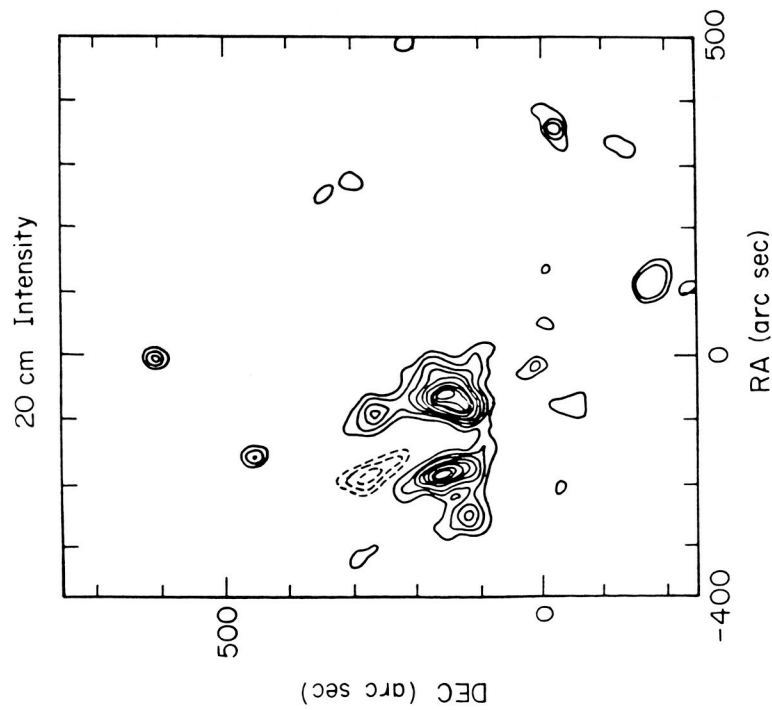


Figure 3. 20 cm (VLA map and Kitt Peak magnetogram (courtesy of J. Harvey). Five of the bright points (Nos. 1-5) are associated with bipolar magnetic features. For comparison, one of the bright points (No. 6) is shown to be lying in unipolar plage. The dashed curve (No. 7) is associated with an H α filament.

COMPACT, VARIABLE, MOVING SOURCES
OBSERVED ON THE SUN AT 2 CENTIMETERS WAVELENGTH

KENNETH R. LANG
ROBERT F. WILLSON

Department of Physics and Astronomy
Tufts University
Medford, MA 02155

INTRODUCTION

The high angular resolution provided by the Very Large Array (VLA) has permitted the spatial resolution of solar microwave sources and opened the way for comparisons with observations of similar angular resolution at optical and X-ray wavelengths. High-resolution VLA observations of solar active regions at relatively long wavelengths of 6 cm and 20 cm have, for example, led to the discovery of the microwave counterpart of the ubiquitous coronal loops that had previously only been observed by X-ray telescopes lofted above the Earth's atmosphere. The microwave emission of the coronal loops is attributed to the gyroresonant radiation and/or the bremsstrahlung of million-degree, thermal electrons trapped within the loops by strong magnetic fields; observations of this emission have provided valuable new insights into the nature of solar active regions and eruptions from the Sun and nearby stars [Kundu and Lang (1985); Lang (1986 a,b - this proceedings)].

In contrast, the short wavelength 2 cm emission of solar active regions is poorly understood. In spite of numerous VLA solar observations at 2 cm, there are only two published results [Lang, Willson and Gaizauskas (1983); Shevgaonkar and Kundu (1984)]. In both instances, compact (angular sizes $\theta \approx 15''$), highly polarized (degrees of circular polarization $\rho_c = 80\%$ to 90%) sources were found in regions of strong magnetic field (strength $H \approx 2,000$ G) above sunspots. The brightness temperatures of $T_B \approx 10^5$ K were characteristic of the electron temperature in the transition region.

Subsequent examination of the compact 2 cm sources in active regions indicated that they are variable over time scales of an hour or shorter. This probably explains the paucity of VLA results; synthesis maps averaged over 11 or 12 hours would not reveal several relatively-weak, time-variable sources.

To further complicate the matter, we have recently discovered compact, variable, highly-polarized 2 cm sources in regions of apparently-weak, photospheric magnetic field [Willson and Lang (1986)]. Our subsequent VLA observations have confirmed the existence of compact, variable 2 cm sources that are not associated with active regions, but these sources had no detectable circular polarization. In addition, both the unpolarized and polarized 2 cm sources were found to move laterally across the solar surface with velocities $V \approx 1$ km s⁻¹. In the next section we present observations of these compact, variable, moving sources. The concluding discussion mentions possible radiation mechanisms and implications for studies of the quiet Sun.

OBSERVATIONS

The VLA was used to observe the active region AR 4508 in the C configuration between 1530 and 2330 UT on June 4, 1984. The position of this region was NO6 E57 at 1300 UT on this day. Follow-up observations were made between 1500 and 2300 UT on January 17, 1986 in the D configuration. In this case, a region of bright plage and relatively-weak magnetic fields (no sunspots) was observed; its position was S10 W62 at 1300 UT on this day.

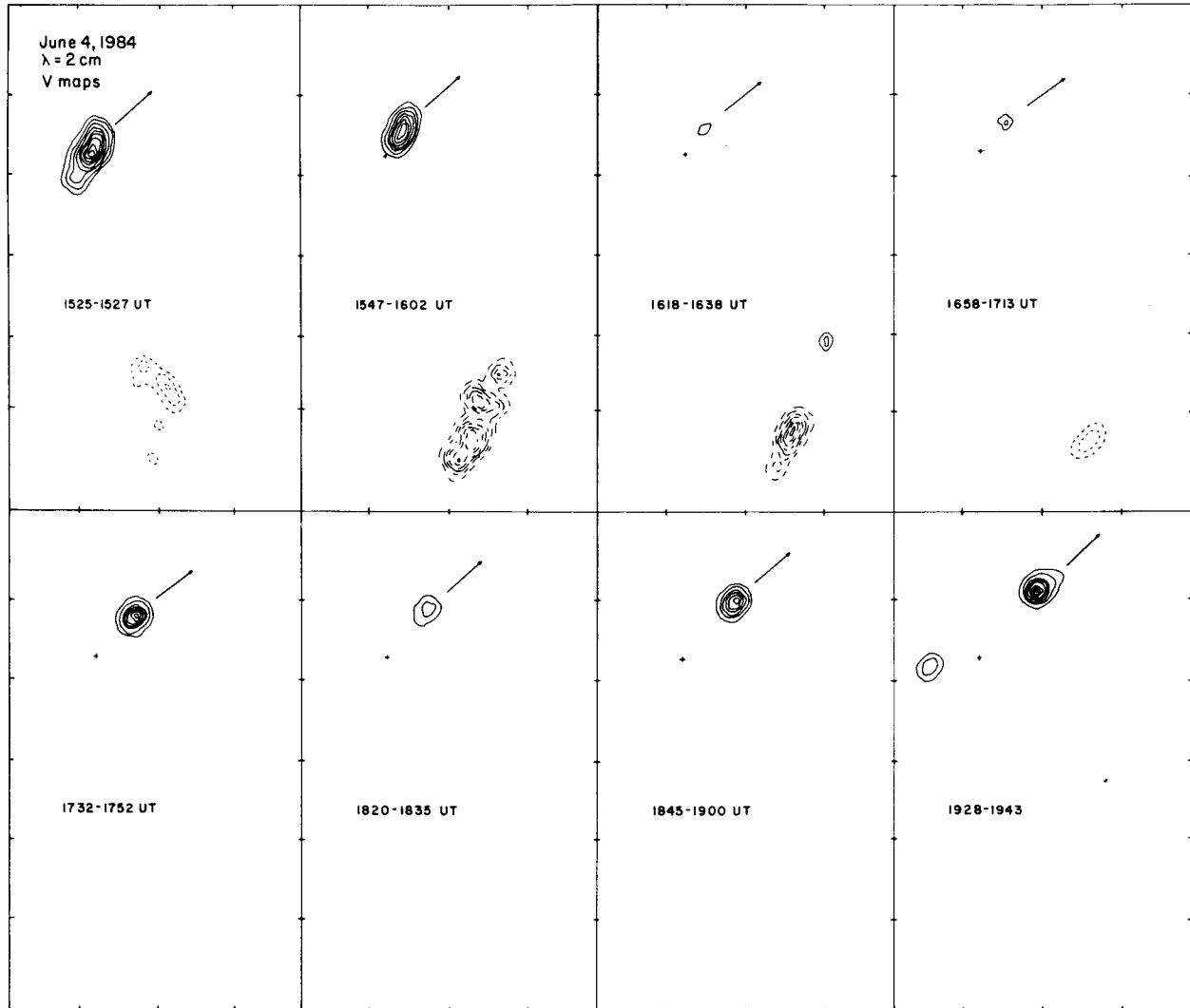


Figure 1. VLA synthesis maps of left circularly polarized (solid contours) and right circularly polarized (dashed contours) radiation at 2 cm wavelength. Here each box refers to the same area on the surface of the Sun, and the fiducial marks on the axes are separated by 10 arc-seconds. The northern source (top) varied over time scales of 30 minutes and moved laterally across the solar surface in the northwest direction a velocity of $\sim 1 \text{ km s}^{-1}$. The southernmost source varied over a time scale of about 60 minutes, and moved laterally towards the southwest at a velocity of $\sim 2 \text{ km s}^{-1}$. Here the contours mark levels of equal brightness with an outermost contour of 6.1×10^4 and a contour interval of $3.1 \times 10^4 \text{ K}$.

As illustrated in Figure 1, the 2 cm maps on June 4 showed two compact ($\theta \approx 5''$), highly circularly polarized ($\rho_c = 80$ to 90%) sources that vary on time scales of 30 to 60 minutes. The left circularly polarized source (solid contours) varied in maximum brightness temperature from $T_B = 2.0 \times 10^5$ K to $T_B < 0.5 \times 10^5$ K. Here each box refers to the same area of the Sun, and the arrows illustrate systematic motion to the northwest with a total motion of about $15''$ in three hours. The left circularly polarized source was therefore moving laterally across the surface of the Sun with a velocity of $V \approx 1 \text{ km s}^{-1}$. The right circularly polarized source (dashed contours) apparently moved towards the southwest at about twice this speed, but the motion is confused by the presence of more than one source.

Comparisons with Mt. Wilson magnetograms indicate that the two compact, variable, moving sources were located in regions of apparently-weak photospheric magnetic field ($H < 80$ G), and that they did not overlie sunspots. The high polarization of these sources is therefore somewhat enigmatic, for the polarization of thermal radiation requires strong magnetic fields of $H \approx 2,000$ G. We will return to this paradox in the discussion.

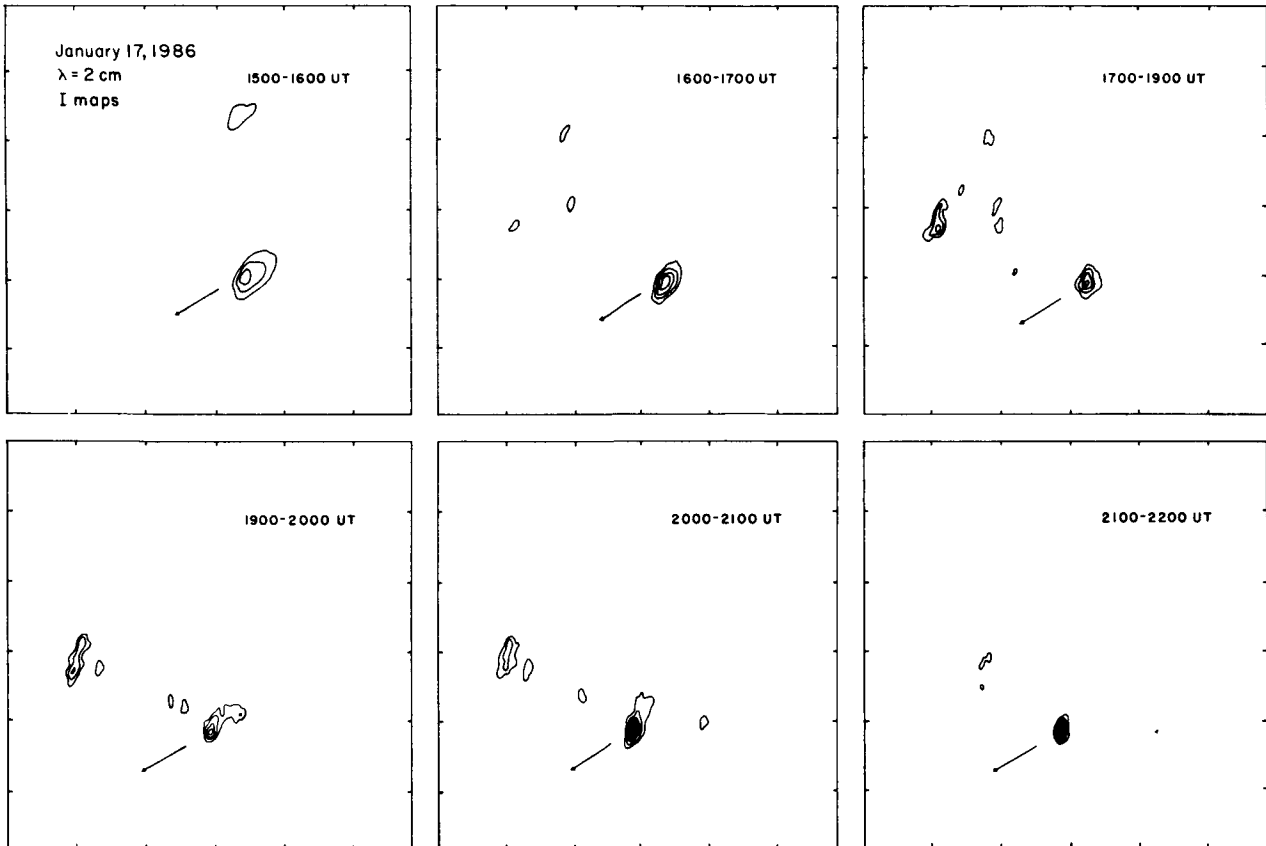


Figure 2. VLA synthesis map of the total intensity of the radiation at 2 cm wavelength. Here each box refers to the same area on the surface of the Sun, and the fiducial marks on the axes are separated by 60 arc-seconds. The southern source (bottom) increased slowly in brightness over a seven hour period while moving laterally across the solar surface in the southeast direction at a velocity of $\sim 1 \text{ km s}^{-1}$. The northern source (top) varied over a time scale of 180 minutes, but showed no detectable lateral motion. Here the contours mark levels of equal brightness with an outermost contour of 5.2×10^4 K and a contour interval of 1.8×10^4 K.

Our confirming observations on January 17, 1986 revealed compact 2 cm sources with angular sizes $\theta \approx 25''$ and maximum brightness temperatures of $T_B = 2.0 \times 10^5$ K. These sources were observed in plage regions with apparently-weak photospheric magnetic field and no sunspots, but in this case the compact sources had no detectable circular polarization ($\rho_C < 15\%$).

As illustrated in Figure 2, the compact unpolarized sources either varied substantially in intensity over time scales of hours (top sources) or slowly increased in brightness over a seven hour period (bottom source). Here each box refers to the same area on the surface of the Sun, and the arrows indicate a lateral motion at a velocity of $V \approx 1 \text{ km s}^{-1}$. Curiously, the relatively-unvarying source exhibited this motion, but the variable one showed no detectable motion.

DISCUSSION

We have discovered previously-unobserved sources at 2 cm wavelength in regions of apparently-weak photospheric magnetic field. The brightness temperatures of $T_B \sim 10^5$ K are characteristic of the transition region. The angular sizes are $\theta \sim 5''$ to $25''$, and they vary in intensity over time-scales of 30 minutes to more than 180 minutes. We have observed at least two of these compact, variable 2-cm sources within the $3'$ field of view every time we have observed the Sun; extrapolating to the $30'$ - wide Sun, we would expect hundreds of them on the visible surface of the quiet Sun. The compact, variable sources can either be highly circularly polarized ($\rho_C \approx 90\%$) or they can exhibit no detectable circular polarization ($\rho_C < 15\%$).

The enigmatic presence of highly polarized sources in regions of apparently-weak photospheric magnetic field may be explained by any one of three hypothesis. First, the photospheric field may have strengths of up to 2,000 G in compact regions that are not readily detected by the photospheric magnetograms. Alternatively, the magnetic field in the transition region or the low corona may be amplified by currents to a strength above that in the underlying photosphere. If either of these hypothesis is true, then the high circular polarization of the 2 cm sources can be attributed to either thermal gyroradiation or the propagation of thermal bremsstrahlung in the presence of a magnetic field of strength $H \approx 2,000$ G. A third hypothesis, developed by Willson and Lang(1985), is that the compact 2 cm sources are due to nonthermal gyrosynchrotron radiation of mildly relativistic electrons in relatively weak magnetic fields of strength $H \approx 50$ G.

But what accounts for the variability and lateral motion of both the polarized and the unpolarized sources? The source variability might be due to a variable magnetic field that comes and goes within the transition region and low solar corona. Alternatively, the variations could be interpreted in terms of thermal electron density variations related to heating changes or to non-thermal electron density variations resulting from a variable acceleration mechanism. The lateral motion can be attributed to an upward expansion of dipolar loops; the 2-cm observations detect the apparent lateral motion of the loop legs.

Finally, we would like to point out certain resemblances between the compact, variable 2-cm sources and other phenomena reported in this proceeding. These sources are resolved (they are not points) with angular sizes comparable to those of small erupting filaments [Martin (1986 - this proceedings)] and the 20 cm observations of so-called coronal bright points [Habbal (1986 - this proceedings)]. The time scale of the variations and the lateral motions of the 2-cm sources are

comparable to those of the small erupting filaments. The brightness temperatures of the 2-cm sources are the same as those of the 20-cm ones. Comparisons with features seen at the He I, λ 10830 transition are very misleading, for there are so many of these features that the statistical significance of a correlation has to be very low.

ACKNOWLEDGEMENTS

Radio astronomical studies of the Sun at Tufts University are supported under grant AFOSR-83-0019 with the Air Force Office of Scientific Research (AFOSR) and contract N0014-86-K-0068 with the Office of Naval Research (ONR).

REFERENCES

- Habbal, S., 1986, " Spatial and Temporal Observations of Coronal Bright Points" - this Proceedings.
- Kundu, M.R. and K.R. Lang, 1985, "The Sun and Nearby Stars: Microwave Observations at High Resolution, " Science 228, 9-15
- Kundu, M.R., 1986 a, "Coronal Plasmas on the Sun and Nearby Stars" - this Proceedings.
- Lang, K.R., 1986a "Coronal Plasmas on the Sun and Nearby Stars"- this Proceedings.
- Lang, K.R., 1986b, "Coronal Diagnostics - this proceedings.
- Lang, K.R., R.F. Willson and V. Gaizauskas, 1983, " Very Large Array Observations of Solar Active Regions III. Multiple Wavelength Observations," Astrophysical J., 267, 455-464.
- Martin, S., 1986, : Small Eruptive Filamentary Sources" - this Proceedings.
- Shevgaonkar, R.K. and M.R. Kundu, 1984 "Three Dimensional Structures of two Solar Active Regions from VLA Observations at 2,6 and 20 cm. Centimeter Wavelength", Astrophys. J., 283, 413-420.
- Willson, R.F. and K.R. Lang, 1986, "VLA Observations of Compact, Variable Sources on the Sun," Astrophysical Journal - to be published.

THE ASSOCIATION OF CHROMOSPHERIC AND CORONAL
PHENOMENA WITH THE EVOLUTION OF THE QUIET SUN
MAGNETIC FIELDS

Karen L. Harvey
Solar Physics Research Corporation
4720 Calle Desecada
Tucson, Arizona

Frances Tang
Solar Astronomy, 264-33
Caltech
Pasadena, California

Victor Gaizauskas
Herzberg Institute of Astrophysics
National Research Council of Canada
Ottawa, Canada

INTRODUCTION

Using daily full-disk magnetograms and He I 10830 spectroheliograms to study the count and surface distribution of ephemeral regions over the solar cycle, Harvey (1985) concluded that the small dark structures seen in 10830, thought to correspond to X-Ray bright points (Harvey *et al.*, 1975), were more often associated with magnetic bipoles that appeared to result from an encounter of already existing opposite polarity magnetic flux than with emerging small magnetic bipoles (ephemeral regions). Such encounters would be more likely to occur in areas of mixed polarity. The fractional area of the Sun covered by mixed polarity fields varies anti-correlated with the solar cycle leading to a possible explanation for the 180° out of phase solar cycle variation of X-ray bright points. To establish the validity of this suggestion, a detailed study of time-sequence magnetic field, He I $\lambda 10830$, H α , C IV and Si II observations of selected areas of the quiet sun was initiated about 2 years ago. The preliminary results of this study are presented in this summary. A more detailed report will be published elsewhere at a later date.

PRECEDING PAGE BLANK NOT FILMED

OBSERVATIONS

Eight observatories and instruments obtained a wide range of data during six observing efforts in 1983, 1984 and 1985, as follows: (1) National Solar Observatory: He I 10830 spectroheliograms (K. Harvey), (2) Big Bear Solar Observatory: longitudinal magnetograms and H α center-line filtergrams (F. Tang), (3) Ottawa River Solar Observatory: H α filtergrams through line (V. Gaizauskas), (4) Marshall Space Flight Center: longitudinal and transverse magnetograms (M. Hagyard), (5) Solar Maximum Mission, UVSP: C IV and Si II line profiles and He II spectroheliograms (A. Poland), (6) Solar Maximum Mission: FCS, O VIII spectroheliograms (J. Saba, K. Strong), (7) Very Large Array (VLA): 20 and 6 cm λ spectroheliograms (S. Habbal), (8) Swarthmore College: Ca II line profiles (R. Holt). Spatial resolution of these data was 1-3 arc-sec for the He I 10830, H α , and magnetic field data, and 10 arc-sec for the SMM UVSP and FCS data and the VLA observations. Temporal resolution was typically 3-5 minutes for the He I 10830, VLA cm λ and H α data and 5-7 minutes for the magnetograms and SMM data. Selected areas of the quiet sun and coronal holes were observed for periods of 4-10 hours each day during (1) 10-12 October 1983, (2) 28 November 1984, (3) 9 December 1984, (4) 25-28 May 1985, and (5) 25-27 June 1985, and (6) 8-9 September 1985.

RESULTS AND CONCLUSIONS

While the analysis and comparison of these data is still going on, there are several preliminary results and conclusions.

1. The network visible in He I 10830 displays a low level intensity variation over a spatial scale of the order of arc-seconds and a time scale of minutes. These intensity variations are somewhat oscillatory in appearance and decrease toward the limb, almost completely disappearing at longitudes $>45-50^\circ$. This suggests that the observed variations may be due in part to motions of network spicules and fibrils.
2. He I 'dark points' have a characteristic size of 10-30 arc sec and intensity variations that show a variety of time scales from minutes to several hours. Their observed behavior and size are similar to that seen in EUV (Habbal and Withbroe, 1981) and X-ray bright points (Nolte *et al.*, 1979; Sheeley and Golub, 1979). Two types of localized

darkening in He I 10830 are defined as dark points: (1) a rapid, almost flare-like, darkening. These events have a duration of about 10-30 minutes and often appear to be associated with ejecta, and (2) a longer lived darkening lasting hours, but which can show large amplitude intensity variations (50-120%) on a time scale of minutes.

Approximately 32% of the 10830 enhancements are associated with ejecta, a macrospicule, small-scale filament eruption, or a propagating disturbance of some type. The propagating disturbances are sometimes seen as a dark, front-like arch-shaped cloud in 10830 moving with horizontal velocities ranging from 16-140 kms^{-1} over distances from 20,000-70,000 km. (In a few cases, possible effects of these disturbances are detected out to distances of 200,000 km.) Also seen in the 10830 spectroheliograms are small (3-6 arc sec) bright structures that persist for one or two frames (~ 3 min). These are interpreted as a predominately vertical velocity structure. They occur at a rate of 2.6-3.9/hr/ 10^{10} km^2 . Comparisons with filtergrams taken at several positions through the $\text{H}\alpha$ line indicate no corresponding velocity structure associated for two such 10830 "velocity" points. Complex dynamics, however, are seen in an $\text{H}\alpha$ structure corresponding to a He I dark point overlying the site of disappearing magnetic flux.

3. Almost all of the 10830 dark points are spatially associated with magnetic bipoles. For 8 days of the 11 day data sample, a comparison has been made between the occurrence of He I dark points with the observed evolution of the underlying photospheric magnetic field. During the 8 days of observation, 477 He I dark points (both rapid and long-lived) occurred. 15% of these were co-spatial with ephemeral regions that have emerged during the observing period; 39% occurred at sites of disappearing flux that resulted from the encounter of existing, unrelated opposite polarity flux. The onset of the darkening seen in He I began when the approaching opposite polarity network elements are within 3-5 arc-sec or adjacent. In $\text{H}\alpha$, connecting fibrils or a small filament are seen to form between the approaching opposite polarity features. For 46% of the dark points no change was seen in the associated magnetic fields. Only 10% of the ejecta events occurred with ephemeral regions; 35% with encounters of opposite polarity magnetic flux.

In the reverse correlation considering magnetic field changes with He I dark points, about one-third of 307 identified ephemeral regions (31%)

were associated with a dark point; two-thirds (69%) were not. 57% of the 363 disappearing magnetic flux sites were associated with He I dark points, and 43% had no dark structure. 21% of the ephemeral regions were associated with ejecta events; 36% opposite polarity magnetic flux encounters were associated with ejecta.

We conclude that He I dark points and ejecta events are more likely (by a factor of 2-4) to be associated with encounters of existing opposite polarity flux than with the emergence of magnetic bipoles. Conversely, encounters of magnetic flux of opposite polarity are almost two times more like to result in an associated dark point in He I than ephemeral regions. Not all ephemeral regions and occurrences of encounters of unrelated opposite polarity magnetic network are correlated with He I dark points.

4. There is a good, though non one-to-one, correspondence between the locations of He I $\lambda 10830$ dark points and the bright structures observed in C IV. Most of the He I dark points have a bright C IV counterpart at some time during their lifetime. Though not all C IV bright points correspond to dark He I dark structures. A comparison of the intensity variations and velocity field between C IV and He I in the 10830 dark points is now being conducted and will be discussed in more detail in a later paper.

5. A good association has also been found between the positions of He I dark points and the bright points observed in 20 cm λ images with the VLA. For many of the He I and 20 cm structures, similar intensity variations are seen, both in the long and short time scales. Seven (7) of the 11 bright 20 cm points studied so far are located at sites of disappearing magnetic flux resulting from the encounters of existing opposite polarity magnetic flux; in two (2) 20 cm bright points, magnetic flux is both emerging and disappearing, and in the remaining two (2), there is no obvious change seen in the magnetic field. The results of this comparison are being presented separately in this workshop proceedings by S. Habbal and K. Harvey.

ACKNOWLEDGEMENTS

This work was funded for one of us (K.L.H) by NASA Grant NAS5-28728 and AFGL Project Order ESD84-611 through NOAA Project Order NA84RAA06789.

REFERENCES

- Habbal, S.R. and Withbroe, G.L., 1981, "Spatial and Temporal Variations of EUV Coronal Bright Points," *Solar Phys.* **69** (77).
- Harvey, J., Krieger, A.S., Timothy, A.F., and Vaiana, G.S., 1975, "Comparison of Skylab X-Ray and Ground-Based Helium Observations," *Osservazioni e Memorie Osservatorio di Arcetri*, **104** (50).
- Harvey, K.L., 1985, "The Relationship between Coronal Bright Points as seen in He I $\lambda 10830$ and the Evolution of the Photospheric Network Magnetic Fields," *Australian J. Phys.* **38** (875).
- Nolte, J.T., Solodyna, C.V., and Gerassimenko, M., 1979, "Short Term Temporal Variations of X-Ray Bright Points," *Solar Phys.* **63** (113).
- Sheeley, N.R., Jr. and Golub, L., 1979, "Rapid Changes in the Fine Structure of a 'Coronal Bright Point' and a Small Coronal 'Active Region'," *Solar Phys.* **63** (119).

Magnetogram and Soft X-ray Comparisons of XBP and ER

Leon Golub
Smithsonian Astrophysical Observatory

Karen L. Harvey
Solar Physics Research Corporation

David F. Webb
AFGL/PHP, Hanscom AFB

Introduction

The potential importance of the smallest emerging flux regions on the Sun has been discussed in numerous publications since the early 70's when the large number of such regions first became evident (Harvey, Harvey and Martin 1975; Golub *et al.* 1974; Golub *et al.* 1977; K. Harvey 1985). The association between the objects seen in ground-based data, such as high resolution magnetograms or H α and soft x-ray data has produced results which are often contradictory: the overlap in the two data sets is great enough as to leave no doubt that the same objects are *in general* seen by both techniques. However, there are significant numbers of cases in which a region is seen by one method but not by the other, and these discrepancies have never been fully explored.

Problems of this sort take on greater significance when we consider the role that small emerging flux regions assume in comparison to the larger active regions. A decade of work on this subject may be summed up as follows: x-ray studies indicate that bright points (XBP) represent the short-lifetime portion of a distribution which is continuous with active regions. The large number of XBP makes them the largest contributor to the total magnetic flux emergence from the Solar interior; moreover, XBP vary out of phase with the larger active regions, in such a way as to nearly conserve the total quantity of magnetic flux throughout the cycle. Similar studies done using magnetogram data offer very different results - ephemeral regions (ER) vary in phase with the cycle and are suggested to be primarily surface phenomena. XBP seem to be associated with chance encounters between opposite polarity network flux, arising from mixed polarity areas of diffusing fields from previously emerged active regions.

These studies are contradictory and the potential implications are too great to be ignored. In the hope of resolving the present impasse we have assembled as much *simultaneous* soft x-ray and magnetogram data as possible in order to test directly the above suggestions. These data have been obtained over the past decade during rocket flights of a soft x-ray telescope, with (weather permitting) same-day ground based observations.

The Data

Data from four flights of the AS&E x-ray rocket payload were used, along with the available magnetogram and He 10830 \AA observations. Dates and times are listed in Table 1. We also list the number of x-ray and magnetic features seen in each dataset; these will be explained in the next section. In the present study we have used only the x-ray and magnetic field data - the He observations will be included in the next stage of this work.

The x-ray features were selected by examination of enlarged transparencies, as described in our earlier papers (e.g. Golub *et al.* 1977). The magnetogram analysis entailed a somewhat more elaborate procedure than has been used in the past, with bipoles divided into several categories; ephemeral regions (i.e. emerging flux), chance encounters of opposite polarity field, and longer-lived bipoles visible on at least two days. Such identification was performed on the first magnetogram of the day and, if additional observations were available, subsequent magnetograms were compared with the first one in order to identify developing structures, encounters, and disappearing flux.

Table 1. Dates of Simultaneous X-ray and Magnetogram Data

Date	Type of Data	Time(s) [UT]	Feature	Number
13 Feb. 1981	X-ray	1916	XBP	5
	Magn.	1507	Encounter	19
	10830Å	1638	ER	22
			Bipole	11
16 Nov. 1979	X-ray	1703	XBP	14
	Magn.	1543, 1743, 1828,	Encounter	11
		1917, 2007, 2100.	ER	25
		10830Å	Bipole	10
16 Sept. 1976	X-ray	1803	XBP	90
	Magn.	1533	Encounter	31
		10830Å	ER	33
			Bipole	10
27 June 1974	X-ray	1948	XBP	58
	Magn.	1508, 1854	Encounter	30
		10830Å	ER	17
		1605, 1657, 1740 1804.	Bipole	6

Results

In view of the contradictory claims which have appeared in recent years, we anticipated that this more elaborate separation of magnetic features into emerging and "reconnecting" regions would clarify the situation. However, we find as the main result of the present study, that the separation makes very little difference. Our results are summarized in Table 1, which shows the number of each type of feature found in the x-ray and magnetogram images, the latter separated into the three classes mentioned above.

The comparison with x-ray data was done by first identifying the x-ray bright points, then correlating the XBP's with the three classes of magnetogram features which had been previously identified independent of the x-ray data. The major result of the comparison is that the three subgroups "encounters", "ephemeral regions" and "bipoles" provide an ordering having increasing probability of being seen in x-rays. That is, the reconnecting or chance encounters are less likely to coincide with an XBP than are the ephemeral regions, which are in turn less likely to overlap than are the old bipoles. The chance (averaged over the four observation days) of seeing an x-ray feature where a magnetic feature has been identified is:

encounters: 21%
ephemeral regions: 29%
bipoles: 50%

Note that these percentages represent identifications made from the magnetograms to the x-ray data. We have not attempted identifications in the other direction. However, the number of x-ray features seen in 1976 is greater than the number of magnetic features, in 1974 it is about the same and in 1979 and 1981 it is significantly lower.

We conclude that the separation of magnetic features into chance encounters and emerging flux makes some difference in the overlap with x-ray bright points, although the effect is not overwhelming. There is a slight tendency for a smaller fraction of the "encounters" to be visible in the corona. The difference in solar cycle dependence between XBP and ER is *not* explainable in terms of the results of this study.

This work was supported at SAO by NASA Grant NAGW-112.

References

- Golub, L., Krieger, A. S., Silk, J. K., Timothy, A. F. and Vaiana, G. S. 1974 *Ap. J.*, **189**, L93.
Golub, L., Krieger, A. S., Harvey, J. W. and Vaiana, G. S. 1977 *Sol. Phys.*, **53**, 111.
Harvey, K. L., Harvey, J. W. and Martin, S. F. 1975 *Sol. Phys.*, **40**, 87.
Harvey, K. L. 1985 *Proc. Ron Giovanelli Commem. Colloq.*, preprint.

SMALL-SCALE ERUPTIVE FILAMENTS ON THE QUIET SUN

Linda M. Hermans
 Infrared Processing and Analysis Center
 and
 Sara F. Martin
 Solar Astronomy
 California Institute of Technology
 Pasadena, California, USA

Abstract

We conducted a study of a little known class of eruptive events on the quiet sun. 61 small-scale eruptive filamentary structures were identified in a systematic survey of 32 days of $H\alpha$ time-lapse films of the quiet sun acquired at Big Bear Solar Observatory. When fully developed, these structures have an average length of 15 arc seconds before eruption. They appear to be the small-scale analog of large-scale eruptive filaments observed against the disk. At the observed rate of 1.9 small-scale eruptive features per field of view per average 7.0 hour day, we estimate the rate of occurrence of these events on the sun to be greater than 600 per 24 hour day. The average duration of the eruptive phase was 26 minutes while the average lifetime from formation through eruption was 70 minutes. A majority of the small-scale filamentary structures were spatially related to cancelling magnetic features in line-of-sight photospheric magnetograms. Similar to large-scale filaments, the small-scale filamentary structures sometimes divided opposite polarity cancelling fragments but often had one or both ends terminating at a cancellation site. Their high numbers appear to reflect the much greater number and mixture of small-scale than large-scale aggregates of opposite polarity magnetic flux on the quiet sun. From their characteristics, evolution and relationship to photospheric magnetic flux, we conclude that the structures described in this study are small-scale eruptive filaments and are a subset of all filaments.

1. INTRODUCTION

While surveying $H\alpha$ time lapse films of the quiet sun recorded at the Big Bear Solar Observatory, we have occasionally noted a small fibril or filament-like structure which would expand into an arch, break open at its top, and disappear. These phenomena appear similar to the eruptive phase of large-scale filaments photographed against the solar disk or large-scale prominences photographed at the limb. An example is illustrated in Figure 1. The event is the darkest feature in the middle of the frames from 19 56 20 until 20 08 44. It already is recognizable as a small loop in the first frame at 19 48 33. The loop breaks open at its top between 20 01 30 and 20 04 44. After that time, the ends of the loop slowly disappear; the event is over by the last frame at 20 18 31. In most small-scale eruptive events, the loop is not viewed as much from the side as in Figure 1. More typically, the events exhibit a small degree of lateral displacement before disappearing. Observations in the blue wing of $H\alpha$ confirm the lateral motion to be the plane of sky component of outward erupting mass.

ORIGINAL PAGE IS
OF POOR QUALITY

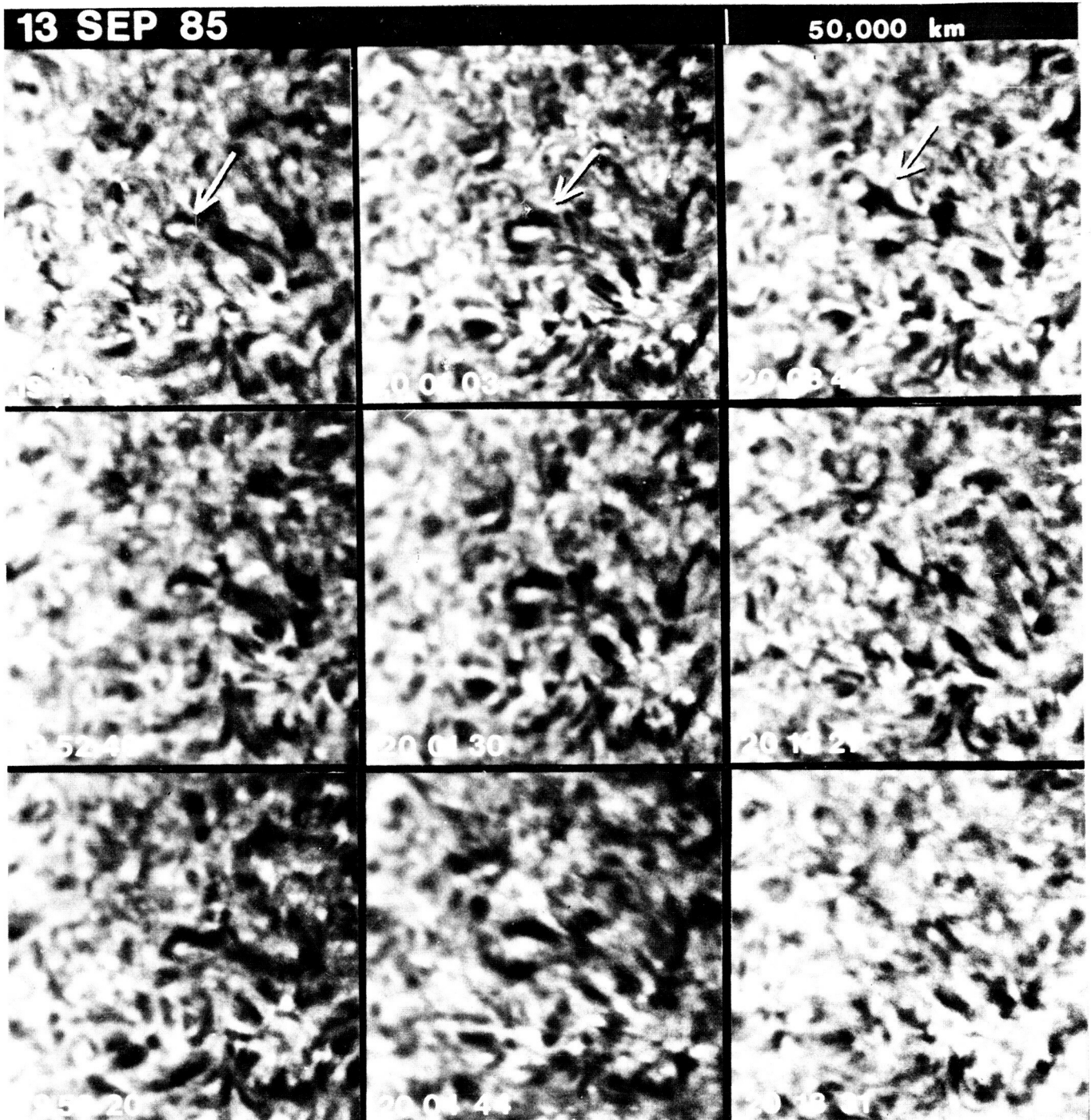


Fig. 1. Arrows on the upper image of each consecutive column of $H\alpha$ images point to the development and eruption of a small filamentary loop. In addition to exhibiting a pattern of motion common to many large-scale erupting prominences, the event also increases in absorption as it expands similar to pre-eruptive phase of large-scale filaments seen in projection against the solar disk. The loop breaks open at its top (between 20 01 30 and 20 04 44) where the Doppler shift is typically greatest. By 20 18 31, the legs of the loop have also disappeared.

After about 10 of these small-scale eruptive events had been noted, we decided to make a systematic survey of a selection of recent time-lapse films to study the properties of the small-scale eruptive events and to estimate their number on the quiet sun during solar minimum. In this paper we present the initial results of this analytical survey.

2. THE OBSERVATIONS

We initially chose to limit our systematic survey to $H\alpha$ films to a recent interval since 29 August 1985 when many quiet sun observations were made. We further limited the survey to conditions when: (1) concurrent long-integration videomagnetograms with increased sensitivity were recorded with a CCD television camera. (2) at least 1 hour of observations were acquired on a single area of the quiet sun in the center of the $H\alpha$ line, (3) the rate of filtergram acquisition was 2 or more frames per minute, and (4) the image quality for the majority of the day was visually estimated to be 2 or higher on a scale of 4. Between 29 August and 1 November 1985, observations made on 30 days met these criteria. We added to the survey, 2 and 3 August 1985, days which met the latter three criteria above and coincided with the Spacelab II flight.

The quiet sun observations on most of the days surveyed were biased towards observations near the center of the solar disk. It was a purposeful bias to obtain maximum signal in the videomagnetograms of the line-of-sight component of magnetic flux. The observations reported here were all acquired before this study was conceived. The field of view during the interval of this study was approximately 300×240 arc seconds.

3. RESULTS

3.1 Number of Events

During our survey, 63 conspicuous eruptive events were found in the 32 days of observations selected for this study. 61 of the 63 erupting filaments were considered to be small-scale; most of these are events that would not be easily recognized in full disk $H\alpha$ images. Usually the features initially resembled either filaments or fibrils in which the length of the feature is much longer than its width although occasionally an event, such as the one in figure 1, will have a loop shape when it first appears. Because our first objective is to clearly and accurately illustrate and describe these events as a class, we have restricted our analyses to only those events which revealed clear evidence of lateral displacement and expansion into an arch before its disappearance. This restriction eliminates any possible confusion with spicules, small surges and other events which show only mass motion along the length of the feature. However, this restriction also means that events which erupted primarily in our line-of-sight are excluded in this study. Hence, the numbers we report are a lower limit to the actual number of small-scale eruptive events that occur on the sun. Our counts of eruptive events could be low by a factor of 2 or more.

The average number of small-scale eruptive filamentary structures was 1.9 events per 7.0 hour average observing day per average field of view of 300×240 arc seconds. Except for the polar regions, which were not sampled above about 65 degrees, this number can be used to roughly estimate the number of events occurring per day of the sun. Even with the exclusion of the polar regions, we find that more than 600 small-scale eruptive events occur on the sun per 24 hour day.

3.2 Size of the Events

For each eruptive event we measured the linear distance in the plane of the sky between the end points of each feature. The measurement was made at the beginning of the lateral displacement and usually represents the maximum dimension of the feature at the top of the chromosphere. No correction was made for foreshortening. The distance between the ends of each feature ranged between 5 and 54 arc seconds with the average at 15 arc seconds.

3.3 Duration of the Events

30 of the 61 small-scale eruptive filamentary structures were observed from their formation through their complete disappearance. The range of lifetimes of these events was 15 and 201 minutes. The average lifetime was 70 minutes.

The eruptive phase, for the purposes of this study, is defined as beginning with our visual detection of the start of the lateral displacement and outward expansion of the small filaments and continuing until the structure completely disappeared. In a few cases, the lateral motion and expansion into a loop was already taking place while the filament was still developing. More often, however, the structure exhibited an earlier active phase that was longer than the eruptive phase. For 50 of the 61 events, the shortest observed eruptive phase was 6 minutes and the longest was 77 minutes with the average eruptive phase lasting 26 minutes.

3.4 Evolution of the Phenomenon

The small-scale filamentary structures spontaneously appear against the background of chromospheric fibrils without apparent association with pre-existing or underlying structures. Most are a single curvilinear structure similar in size to the surrounding chromospheric fibrils. Within minutes to tens of minutes after formation, they usually become distinguishable from other chromospheric structures by their motion, changes in shape, and increasing degree of absorption. They gradually evolve from this active phase to the eruptive phase. Like large filaments, the eruptive phase seems to be an irreversible process. The expansion into an arch or loop continues until the disappearance of the whole phenomenon as illustrated in Figures 1.

3.5 Association with Flares

75 percent of the small-scale eruptive structures were associated with very small flares. The flares occur during the eruptive phase similar to flares associated with large-scale erupting filaments. The event in Figure 1 is not flare-associated. In Figure 2, the associated small flare is seen in the last $H\alpha$ image at 2205 05 near the base of the right leg of the event.

3.6 Counterparts at Other Wavelengths

K. Harvey (1986) has identified dark features that correspond to the small-scale eruptive filaments in 10,830 Å spectroheliograms. In most cases, the 10,830 Å absorption is seen during the active and eruptive phases but does not necessarily correspond to the entire lifetime of an event. We would expect these small-scale eruptive events to be visible in any other chromospheric line that reveals filaments.

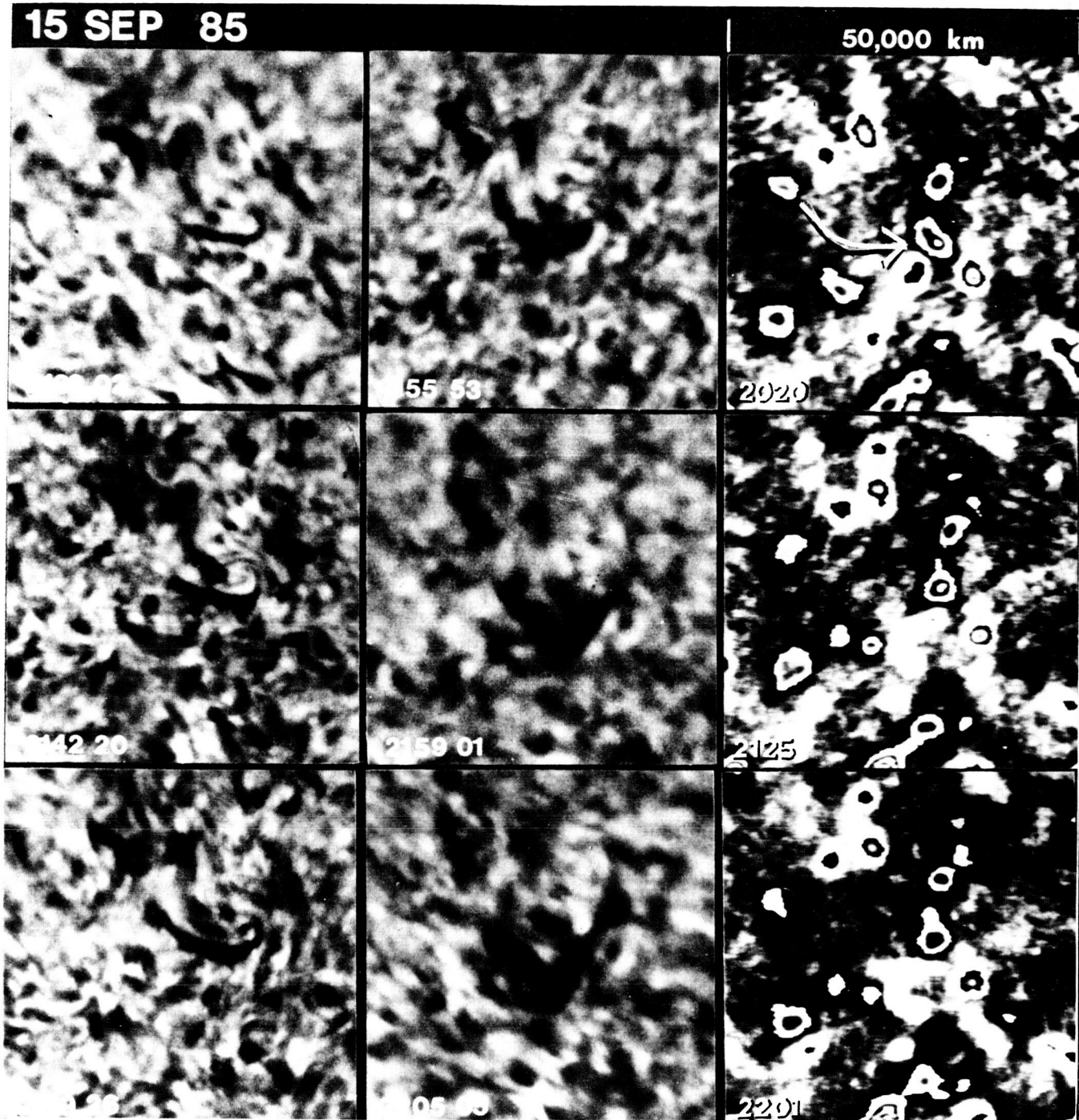


Fig. 2. The position of this small-scale eruptive filament relative to the line-of-sight component of the surrounding photospheric magnetic flux is marked the curved arrow in the top image of the column of magnetograms on the right. The filament lies between separated fragments of opposite polarity magnetic flux while the right end of the filament terminates at the junction between cancelling fragments of adjacent magnetic flux of opposite polarity. The decrease in the magnetic flux is seen from the reduction in area and contours. Negative fragments of flux are black and positive are white except within the contours where the polarity is the same as around the periphery.

We suggest the possibility that 'jets' observed in the ultraviolet (Brueckner 1984) are a coronal manifestations of the small-scale eruptive filaments. Both kinds of events are similar in scale, eruptive in nature, often identifiable as having a loop shape, and have high rates of occurrence. The 'jets' are identified in spectra which emphasizes their line-of-sight speeds whereas our sample of filtergrams of the small-scale eruptives emphasizes their motion in the plane of the sky. This hypothesized association could be tested by acquiring $H\alpha$ or 10,830 Å spectra concurrently with filtergrams of an adequate statistical sample of the small-scale eruptives at the same wavelengths or more directly by acquiring simultaneous observations of UV spectra and $H\alpha$ filtergrams, preferably at various wavelengths around line center.

Other possible associations between the small-scale eruptives, their associated flares, and various other small-scale coronal features such as coronal 'bright points', 'bright point' flares, 'dark points' in 10,830 Å spectroheliograms and compact radio sources are discussed by Webb (1986).

3.7 Association with Photospheric Magnetic Flux

We have begun a study of the correspondence of the positions of the small-scale filaments to photospheric magnetic flux seen in videomagnetograms of the line-of-sight component. Of the first 20 events examined for which there were corresponding magnetograms, 15 appeared to be spatially associated with cancelling magnetic features and for the other 5 no specific pattern has yet been recognized. Those associated with cancelling magnetic features are comprised of two variations. In 6 examples, the filament was coincident with the division between opposite polarities of the cancelling features and in 9 examples, one or both ends of the small filament terminated near the division between opposite polarities of the cancelling features.

An example of one of the small-scale eruptive events with one end terminating at cancelling magnetic fragments is shown in Figure 2. The magnetograms are the third column of images following the two columns of $H\alpha$ images to the left. An arrow on the first magnetogram denotes the path of the small filament; the head of the arrow points to the two adjacent opposite polarity cancelling fragments. Negative flux is black and positive flux is white for all areas outside of the contours. The area within the contours always has the same polarity as around the periphery of the contours. The contours enclose areas of higher magnetic flux in which the number of concentric contours, alternating from black to white or white to black, represents the number of times that the saturation level has been exceeded. The cancelling flux is recognized from the decrease in area and contours at the right of the arrow in contrast to other fragments of magnetic flux of similar size. The localized cancellation of magnetic flux begins before the initial appearance of the small filament.

4. DISCUSSION

The small-scale features described in this paper exhibit properties similar to large-scale filaments and prominences. Their formation, evolution, and eruptive character and association with flares during eruption are all similar to large-scale filaments. Their frequent relationship with cancelling fragments of magnetic flux is an association that has also just begun to be recognized as commonplace for large-scale filaments (Martin, 1986, these proceedings). The most obvious difference between these small-scale eruptive events and large-scale eruptive filaments is their much higher rate of occurrence. At present, we do not consider this to represent

a fundamental physical difference. In their pre-eruptive state, both the small-scale structures and large-scale filaments are associated with polarity inversion zones in magnetograms of only the line-of-sight component of magnetic flux. Because of the greater number and mixture of opposite polarity, small-scale magnetic features on the sun (Giovanelli 1982), there is also a correspondingly greater abundance of small-scale polarity inversion zones where small filaments have the opportunity to develop. We conclude that the structures described in this study are small-scale eruptive filaments. We recognize the small-scale eruptive filaments to be a subset of all filaments.

Acknowledgements

We appreciate the help of H. Zirin by providing temporary support for L.M.H. at the outset of this study. W. Kershaw and J. Nenow assisted in preparing the photographic illustrations. The observations used in this study were made possible partially by NSF grant ATM 8211002, NASA grant NGL 05 002 034, and AFOSR grant AFOSR-82-00118. Primary support for the data analyses came from the Air Force Office of Scientific Research on Grant AFOSR-82-0018.

References

- Brueckner, G.L. 1983, *Solar Phys.*, **86** 259.
- Giovanelli, R.G. 1982, *Solar Phys.*, **77** 27.
- Harvey, K.L. 1986, personal communication, also documented in final report on NASA grant NAS5-28728.
- Martin, S.F. 1986, these proceedings.
- Webb, D.F. 1986, these proceedings.

OBSERVATIONS OF THE Ca II K LINE
IN HeI0830A DARK POINTS ON AUGUST 3, 1985

Rush D. Holt, Albert H. Park,
Joseph C. Thompson
Swarthmore College
Swarthmore, Pennsylvania 19081

D. M. Mullan
Bartol Research Foundation
Newark, Delaware 19716

INTRODUCTION

In this paper we address the question: Is the velocity field of the solar chromosphere at the location of bright points (BP) different from that of the chromosphere in other regions of the sun? We have used dark points in HeI0830A spectroheliograms as ground-based proxy indicators of BP both in coronal holes and non-hole regions of the Sun, and we have obtained spectra of such points in the vicinity of the CaII K 3933A line. As a measure of differential chromospheric velocity, we have used the shift of the K line center relative to a nearby photospheric FeI line. We presume the K line center to be formed high in the chromosphere. We find that in helium dark points in general, the distribution of K line shifts is skewed towards the blue; in helium dark points which lie within coronal holes, the blueward skewing is more pronounced. Our results are of some interest in the context of spacecraft detections of outflows from BPs, and in the context of correlations of high speed solar wind streams from coronal holes.

On August 3, 1985 we observed five He-10830A dark points. Taken all together, the spectra of the five points that day show an average blue shift of 0.5 ± 0.3 km/s with respect to the spectra from random points on the Sun. Four of the five points showed blue shifts of approximately 1 km/s, and the fifth point (observed late in the day and less reliable than the others) showed a red shift of approximately 1 km/s. The CaII K spectra on August 3 show a pattern of blue shifts that is consistent with the overall pattern observed in helium dark points observed on 25 days over a 14-month period (Holt and Mullan, 1986). The overall pattern for the fourteen months shows a small blue shift between 0.1 and 1.2 km/s for average spectra from He 10830A dark points which are not within coronal holes. There is also greater dispersion of the wavelength shifts than for spectra from random points. The points on Aug 3 were not within coronal holes. For dark points within coronal holes a fraction of the spectra, one-tenth, show a more pronounced blueshift--about 3.7 km/s.

DATA ACQUISITION: TARGET IDENTIFICATION

To identify coronal holes and BP, we use spectroheliograms taken in the light of HeI 10830A at the National Solar Observatory Vacuum

Telescope on Kitt Peak (Livingston et al, 1976). The He 10830A image is relayed via telephone multiplexer (Colorado Video Expander 275) to the Swarthmore/Bartol Observatory, where the image is recorded digitally and also displayed on a video monitor. The resolution of the digital image is approximately 8 arcseconds per pixel.

On the He 10830A images, small dark points frequently are observed. Some lie within the coronal holes but their distribution is not obviously biased towards or away from coronal holes. During the Skylab mission, it was found that there was a close correlation between the He10830A dark points and BP (Harvey et al, 1974; Harvey and Sheeley, 1977). If Zirin's (1975) explanation of radiative pumping of the triplet level of HeI of weak He10830 absorption in coronal holes is correct, it would provide a natural explanation for enhanced absorption in He10830A in the chromosphere underneath a BP. However, even without knowing the details of the physical process, we adopt the empirical correlation (albeit imperfect) and assume that He10830A dark points are proxy indicators of BP. We use the He10830 images to identify not only BPs, but also to identify the coronal holes on any particular day.

The spectroheliograms are recorded once per day at Kitt Peak National Observatory, conditions permitting. Each spectroheliogram requires 45 minutes to complete. We receive the image within minutes after its completion. We identify the target points, calculate coordinates, and begin recording spectra usually within 30 minutes. The mean lifetimes of BPs are on the order of hours (Golub et al, 1977). The dark points on the HeI 10830 spectroheliograms have comparable lifetimes. On August 3, 1985 clouds delayed our observations for nearly three hours after we received the spectroheliogram. Spectra were recorded between 19:44 and 23:10 UT.

For each spectroheliogram, we find the center of the solar disk by triangulation from points on the circumference. We then locate our target points and determine their positions with respect to the center. Calculating from the solar tilt angles for each day, we then account for solar rotation at the latitude of each point during the time elapsed since that portion of the spectroheliogram was recorded. After scaling the image coordinates to match our telescope image guider, we position each point of interest on the entrance pinhole of our spectrometer. Our procedure for positioning the targets is uncertain by an amount which may be as large as about 10 arcsec. Most of the He 10830 dark points are of order 10-30 arcsec in size. We do not know whether or not the associated features in CaII K light would have the same size.

DATA ACQUISITION: CaK SPECTRA

The telescope is a 61-cm Cassegrain reflector mounted in a fixed equatorial position in a laboratory on top of a 50-foot building on the campus of Swarthmore College in Pennsylvania. The telescope is fed by a 91-cm polar heliostat mounted on the roof. This system provides a full solar image with a scale of 16 arcsec/mm, and the

stepping motors permit guiding movements as small as 0.1 arcsec in right ascension and 1 arcsec in declination.

The telescope feeds a high resolution spectrum scanner (Wyller and Fay, 1972). For our observations, the spectrometer is used in the Czerny-Turner configuration, and the echelle grating is rotated by a stepping motor so as to sweep the spectrum past an exit slit, where it is detected by a cooled photomultiplier tube (EMI 9789A). The spectrometer entrance pinhole (0.1 mm) is chosen to allow a spatial resolution of 1.6 arcsec on the solar surface. However, local seeing conditions usually degrade the resolution to worse than 2 arcsec. The exit slit size (0.007 mm) is chosen so as to allow spectral line positions to be determined to approximately 0.02 Å.

The spectrum is sampled by a PAR-SSR photon counter driven by a computer which also drives the grating motor. The spectrum is sampled at typically 100 points with an integration time of either 0.1 or 0.2 seconds per point, depending on light levels. The spectral scan covers about 2Å in the vicinity of CaK (3933Å). The FeI line at 3932.64Å serves as a photospheric reference line, with respect to which we measure the position of the central absorption (K3) of the CaK line. In addition to spectra of BP candidates, we also record spectra in the same wavelength region of random points on the solar disk. These "random disk points" provide the references to which we compare the wavelength separations of the FeI and CaK lines of BP candidates. The random disk points are generally chosen to be away from regions of strong magnetic activity (as determined from daily magnetograms, also received from Kitt Peak). Preceding and following the recording of the spectra of each target point, we record a number of spectra, usually 6 or more, at random points on the solar disk.

DISCUSSION

From each spectrum we calculate the difference in wavelength between the CaII K minimum and FeI reference line. This wavelength separation is compared to the average of the separations in five random-point spectra taken most recently before and the next five random-point spectra taken after the target point spectrum. If the separation is smaller than this 10-point average, we say that the K minimum has been shifted to the blue with respect to the spectrum of a random point. Conversely, we take a larger separation to be evidence of red shift.

We recorded 47 spectra of BP on August 3, 1985 (Table 1.). The histogram of the wavelength shifts shows a small average wavelength shift of 0.5 ± 0.3 km/s and also an asymmetry toward the blue. Four of the five points have spectra showing blue shifts of approximately 1km/s, which is between 1 and 3 standard deviations for the four points. (A different σ is calculated for the reference random point spectra for each BP spectrum.) The fifth point shows a red shift of about 1km/s which is greater than 2σ from the mean of zero. This fifth point was taken late in the

Table 1.
CaK Spectra of He 10830A Solar Dark Points Aug 3, 1985 Swarthmore

Dark Point Location	Time (UT)	Shift
A N5.3E14.7	19:44-19:56 (8 spectra) 22:44-23:10 (7 spectra)	-0.8km/sec \pm 0.3km/sec
B N18.1E20.2	20:11-20:19 (6 spectra)	-1 \pm 1km/sec
C N10.4E14.2	20:34-20:44 (5 spectra)	-1km/sec \pm 1km/sec
D N14.1W21	20:57-21:14 (10 spectra)	-1.0 \pm 0.8km/sec
E S5.2W11.1	21:31-21:54 (11 spectra)	+1 \pm 0.4km/sec

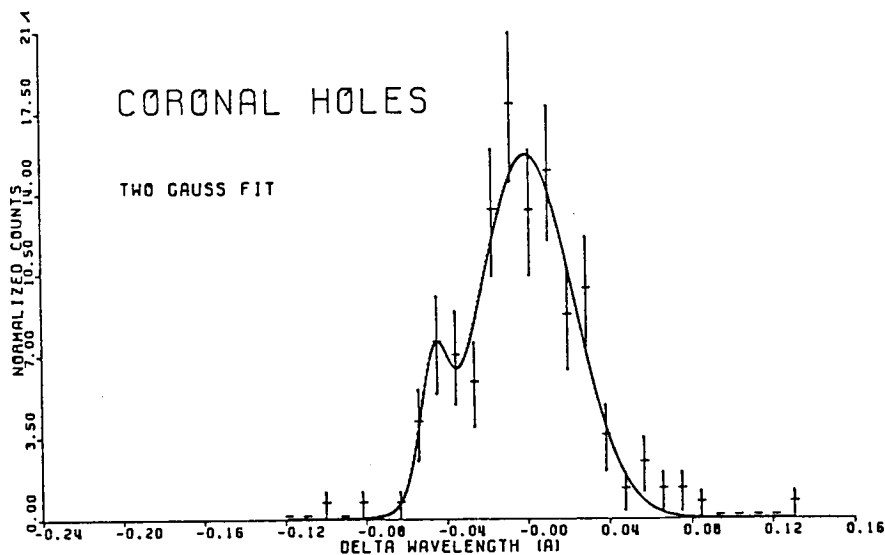


Fig. 1a. Wavelength shift of spectra of BP in coronal holes, relative to spectra of random points

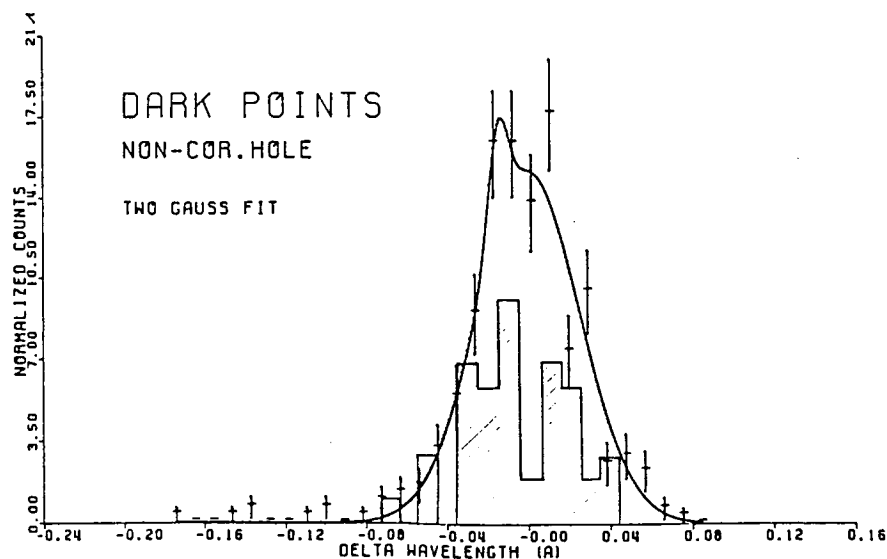


Fig. 1b. Wave length shift of spectra of BP not in coronal holes relative to spectra of random points. Superimposed is the histogram of the wavelengths from BP not in coronal holes observed Aug. 3, 1985

day, more than five and a half hours after the NSO 10830A spectroheliograms had been made, and it is less likely than the other points to have been a dark point.

In Fig.1a we show a two-gaussian curve fitted to the histogram of the wavelength shifts of the K minima of spectra taken of BP in coronal holes during the full 14-month observing program. In Fig. 1b we show a two gaussian fit to the histogram of wavelength shifts for BP not in coronal holes, and along with the smooth curve, we also show a histogram of K minima shifts for 47 spectra taken on August 3, 1985.

The skewness in the distributions is small. We are operating close to the limit of resolution of our system. However, it is noteworthy that the overall effect is a blueshift, especially in the BP's in coronal holes. For BP's not in coronal holes, like the samples of August 3, the blueshifts are less distinct. For BP's in coronal holes the amplitude of the blueshift is several kilometers per second. One should note that if material of chromospheric density moves outward at this velocity, it could supply the mass flux of the solar wind if this chromospheric flow were concentrated in a few dozen sources, each of diameter of a few arcsec.

ACKNOWLEDGMENTS

This work is supported in part by the National Science Foundation (ATM-82-10936) and by the Research Support Committee and the Lang Faculty Fellowship of Swarthmore College.

REFERENCES

- Gollub, L., Krieger, A.S., Vaiana, G.S., and Harvey, J.W., 1977, "Magnetic Properties of X-Ray Bright Points," *Solar Physics*, **53**, 111
- Harvey, J.W., , Krieger, A.S., Timothy, A.F., and Vaiana, G.S., 1974, "Comparison of Skylab X-Ray and Ground-Based Helium Observations," *Observ. Mem. Arcetri*, **104**, 50
- Harvey, J.W., and Sheeley, N.R., 1977, "Comparison of HeII 304A and HeII10830A Spectroheliograms," *Solar Physics*, **54**, 343
- Holt, Rush D., and D.M. Mullan, 1986, "Observations of the CaII K Line in HeI10830A Dark Points," submitted to *Solar Physics*
- Livingston, W.C., Harvey, J.W., Slaughter, C.D., and Trumbo, D., 1976, "Solar Magnetograph Employing Integrated Diode Arrays," *Applied Optics*, **15**, 40
- Wyller, A., and Fay, T.d., 1972, "URSIES: An Ultravariabe Resolution Single Interferometer Echelle Scanner," *Applied Optics*, **11**, 1152
- Zirin, H., 1975, "The Helium Chromosphere, Coronal Holes, and Stellar X-Rays," *Ap.J.Lett.*, **199**, L63

MAGNETIC LOCATION OF C IV EVENTS IN THE QUIET NETWORK

Jason G. Porter*, Ed J. Reichmann, Ronald L. Moore
Space Science Laboratory
NASA Marshall Space Flight Center
Huntsville, AL
and
Karen L. Harvey
Solar Physics Research Corporation
Tucson, AZ

INTRODUCTION

As observations of the quiet Sun have improved in spatial and temporal resolution, it has become increasingly apparent that the "quiet" solar atmosphere is in fact quite dynamic. The existence of at least one class of solar activity occurring outside major active regions has been well-known for some time; the localized sites of intense heating called coronal bright points or X-ray bright points (XBP) were first seen in 1969 (Vaiana et al. 1970).

The XBP correspond to small magnetic bipoles (Krieger et al., 1971; Harvey et al., 1975a; Golub et al., 1977), but not all bipoles have associated XBP. Golub et al. find no obvious coronal heating signature for half of their designated bipoles. A less rigorous definition of the amount of flux required to constitute a bipole would have resulted in an even larger fraction of non-XBP bipoles. Yet we might expect that the heating by loop activations observed at XBP-associated bipoles (Sheeley and Golub, 1979) is present at these other bipoles as well: Golub et al. (1976b) find that bipoles having lower flux are associated with XBP having shorter lifetimes, and Golub et al. (1976a) find that the number of XBP with lifetimes in a given range increases toward shorter lifetimes, down to the 2h lower lifetime cutoff for XBP included in their study. These shorter-lived bipoles might not all yield coronal brightenings of sufficient magnitude or longevity to appear on the relatively infrequent (one per hour) X-ray photographs examined by Golub et al. (1977). However, such activity could manifest itself in the transition region, perhaps as the turbulent events and jets recently observed with HRTS (e.g. Brueckner and Bartoe, 1983). Another class of jet-like events, the H-alpha and EUV macrospicules, has been identified with flares at XBP (Moore et al., 1977), and impulsive heating at XBP is apparent in the transition region observations discussed by Habbal and Withbroe (1981).

This sort of activity should be observable with the Ultraviolet Spectrograph and Polarimeter (UVSP) on the Solar Maximum Mission (SMM). We have examined UVSP observations of C IV intensity in the quiet Sun and

*NAS/NRC Resident Research Associate

compared them to magnetograms and He I 10830 Å spectroheliograms from Kitt Peak National Observatory (KPNO). The He I data have been shown to be a useful proxy for high-resolution soft X-ray data for purposes of locating coronal bright points (Harvey et al., 1975b). We find evidence that impulsive heating processes are common at small bipoles, and many of these are bipoles other than those having associated XBP.

THE OBSERVATIONS

The observations were made between 3 and 9 April 1985. Spatially rastered UVSP intensity measurements were obtained at 11 wavelength positions in the 1548 Å line of C IV. The wavelength positions were separated by 150 mÅ. Slit set 4 was used, combining a 3" x 3" entrance slit with a 300 mÅ exit slit. 120" x 120" rasters (40 x 40 pixels) were taken in a variety of quiet Sun regions including disk center, the equatorial limb, and the poles. Each raster took 2 m to complete, so successive rasters at the same position in the line were made 22 m apart. Two of the 11-position raster sets were typically obtained during a satellite orbit.

We see many fluctuations in C IV emission at sites throughout the network and in cell interiors, and so must set some arbitrary threshold for what we will call a "bright" point or event. The following criteria correspond fairly well to those intensity levels which are visually striking on linear gray-scaled images whose maxima are adjusted to yield dark cell interiors: for line center rasters, pixels which are at the 5σ level; for the two rasters adjacent to line center, 6σ ; for rasters farther in the wings, 7σ .

Some sites are bright throughout the typical 44m observing period and in all parts of the C IV line. Other bright points appear and disappear fairly rapidly, sometimes being notable in only 1 or 2 successive rasters. These are usually seen in the wings of the line, rather than at line center. Confinement of a bright event to so few of these rasters may be the result of either limited observable wavelength range or short lifetime. That is, these may be fairly long-lived sites of jet-like flows, or they may be events of arbitrary line profile whose intensities are above our assigned threshold values for less than 4 m. Previous observations of many short-lived brightenings in active regions (Porter et al., 1984) argue for lifetimes less than 4 m for most of the events defined by these thresholds. The jets observed by HRTS also have short lifetimes, typically 80 s or less. Since long-lived bright jets therefore seem unlikely, we shall refer to events occurring in only 1 or 2 of our C IV rasters as short-lived.

We superposed the C IV rasters on the magnetograms and He I spectroheliograms to within about 6" using solar coordinates derived from the Fine Pointing Sun Sensor onboard SMM. Within that limited range, we varied the colocation in order to find the best correspondence of C IV network to solar magnetic network or He I dark regions over the entire field of view.

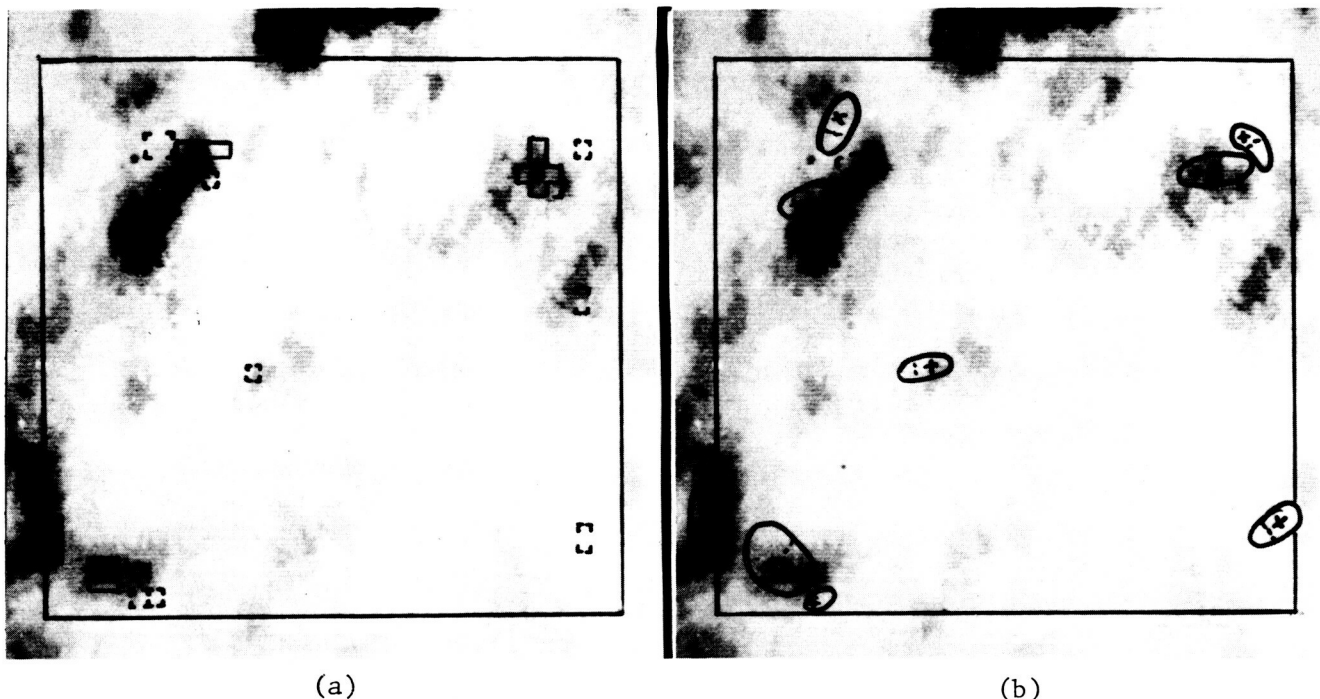


Figure 1. (a) A He I 10830 Å spectroheliogram taken 1 h after UVSP observations in the 1548 Å line of C IV. Long-lived C IV bright pixels are indicated by complete squares; transient events by corners. The long-lived sites are in the darkest He I areas, corresponding to XBP. Most sites of transient events are apparently heated too sporadically to display a He I (or coronal) signature. (b) Areas of magnetic bipoles underlying the C IV sites are superimposed on the He I spectroheliogram. All but one of the C IV sites overly bipoles. Note the correlation of bipole area with C IV brightness duration and He I darkness.

Figure 1a shows a KPNO He I 10830 Å spectroheliogram, obtained one hour after completion of two full scans through the C IV line by the UVSP on 7 April 1985. Complete squares indicate the locations of four long-lived bright C IV sites. Persistence of heating at these sites is well above our "longevity" criterion (intensities above threshold in 3 out of the 22 rasters comprising the double line scans), since even the weakest of them qualifies as "bright" in 5 rasters. Relative intensities do vary considerably in time at these sites, in some cases falling below threshold and then rising again, so the qualifying rasters are not necessarily consecutive. The variations may be multiple events in a single loop or the sequential activation of multiple loops within any given 3" x 3" pixel. Pixels which are the sites of short-lived events are denoted by corners alone. The spatial associations here are representative of those for all the C IV raster sets we have examined. All four of the long-lived C IV bright points are in very dark He I areas. These dark He I kernels almost certainly represent XBP (Harvey et al., 1975b). By contrast, locations of the short-lived C IV brightenings are generally unremarkable in He I, with most showing no darkening at all. The site near raster

center and the one below and to the left of the upper left long-lived site are exceptions, showing some moderate darkening.

The best fit of the C IV raster to the magnetogram places the brightest C IV features over the neutral lines of small magnetic bipoles. We find that the long-lived C IV sites correspond to the stronger bipoles (i.e., bipoles having more area and flux). The short-lived C IV bright points also overly bipoles, though the flux and area of these is much less than for the long-lived sites. The areas covered by the bipoles associated with all of these sites are drawn on the helium spectroheliogram in Figure 1b. The correlation of bipole area with C IV brightness duration and He I darkness is easily seen. The magnetic field underlying the long-lived site at the upper left is not a simple bipole; the positive patch enclosed within the dashed neutral line is surrounded by many small concentrations of negative field. Some of these are apparently halves of small bipoles in their own right--two of these associated with short-lived events are shown.

Only those bipoles associated with C IV bright sites are drawn here; there are others present on the magnetogram, so we cannot say whether all bipoles are sites of events such as these. In particular, there is one strong bipole about 15" - 20" below the long-lived site at the upper left area which we might also have expected to have an associated long-lived C IV bright point, but the C IV intensity at the site never rises above our threshold values. It does correspond to moderately bright network which exhibits several lesser brightenings (most notable in rasters near line center in both scans), and to a dark He I area. There may have been greater C IV events here (as well as at lesser bipoles) which escaped detection because of the sparse temporal sampling of the data.

For one short-lived site, the one at center right, we are unable to discern an underlying neutral line. This site lies on the edge of a positive unipolar patch, however, so it is possible that a small, unresolved region of negative polarity is present here.

DISCUSSION

We find strong fluctuations in C IV intensity at sites of magnetic bipoles throughout the network. The longer-lived C IV bright points overly the largest bipoles and correspond to He I dark points and thus presumably XBP; the shorter-lived sites are associated with bipoles lying near the limit of the magnetogram's sensitivity and usually have no long-lived coronal signature. Many smaller short-lived brightenings, perhaps associated with bipoles too small to detect, occur throughout the network. Time histories of intensity at the various sites shows that the heating is quite unsteady even at the long-lived sites; the impression is that some portion of the strong C IV emission at these sites is maintained by a series of small flare-like events similar to those which occur less frequently at the short-lived sites. This is in agreement with the interpretation of NRL EUV spectroheliograms by Sheeley and Golub (1979), who find that an XBP consists of a collection of small loops which

sequentially and independently brighten. Thus we conclude that the stochastic process whereby convective shuffling of loop footpoints leads to many topologically dissipative events in active regions and the larger bipoles treated here (see Porter et al., 1984 and references therein) continues to operate in regions of fewer, weaker flux loops, but the resulting events above threshold are less frequent.

REFERENCES

- Brueckner, G.E., and Bartoe, J.-D.F. 1983, Ap. J. 272, 329.
- Golub, L., Krieger, A.S., and Vaiana, G.S. 1976a, Solar Phys. 49, 79.
- Golub, L., Krieger, A.S., and Vaiana, G.S. 1976b, Solar Phys. 50, 311.
- Golub, L., Krieger, A.S., Harvey, J.W., and Vaiana, G.S. 1977, Solar Phys. 53, 111.
- Habbal, S.R., and Withbroe, G.L. 1981, Solar Phys. 69, 77.
- Harvey, K.L., Harvey, J.W., and Martin, S.F. 1975a, Solar Phys. 40, 87.
- Harvey, J.W., Krieger, A.S., Davis, J.M., Timothy, A.F., and Vaiana, G.S. 1975, B.A.A.S. 7, 358.
- Krieger, A. S., Vaiana, G. S., and Van Speybroeck, L. P. 1971, in Solar Magnetic Fields (R. Howard ed.), IAU Symp. 43, 397.
- Moore, R.L., Tang, F., Bohlin, J.D., and Golub, L. 1977, Ap. J. 218, 286.
- Porter, J.G., Toomre, J., and Gebbie, K.B. 1984, Ap. J. 283, 879.
- Sheeley, N.R. Jr., and Golub, L. 1979, Solar Phys. 63, 119.
- Vaiana, G.S., Krieger, A.S., VanSpeybroeck, L.P., and Zehnpfennig, T. 1970, Bull. A.P.S. 15, 611.

A NUMERICAL STUDY OF THE THERMAL STABILITY
OF LOW-LYING CORONAL LOOPS

J. A. Klimchuk, S. K. Antiochos, and J. T. Mariska

E. O. Hulburt Center for Space Research
Naval Research Laboratory
Washington, DC

INTRODUCTION

It has recently been shown that for low-lying loops with a maximum height of ≤ 5000 km there exists a "cool" solution to the static energy and force balance equations (Antiochos and Noci, 1986; Hood and Priest, 1979). In contrast to the well-known hot solution, with temperatures in the range of 10^6 K, the cool solution reaches a maximum temperature of only a few tens of thousands of degrees. Either of these solutions is possible for a given amount of energy deposited in the loop.

The existence of cool solutions has important implications for the interpretation of UV and X-ray observations, not only of the sun, but of all late-type stars that exhibit transition regions and coronae. The apparently universal rise in emission measure for decreasing temperature below 10^5 K might be explained by an unresolved mixture of both hot and cool loops, for example. In addition, certain kinds of solar features, such as fibrils and active region filaments, may be accurately described as cool loops. Other possible applications abound.

An important property of all static loops is their thermal stability. Even if a solution to the governing equations exists, it may not be physically realizable if it is unstable to small amplitude perturbations. Antiochos et al. (1985), among others, have performed detailed linear analyses of the stability of coronal loops. They find that for low-lying loops which admit both a hot and a cool solution, the hot solution is thermally unstable while the cool solution is thermally stable. This suggests that low-lying hot loops do not occur in abundance. Higher arching hot loops appear to be thermally stable, on the other hand, so their ubiquitous appearance on the sun is easy to understand.

One implication of the linear results is that the solar atmosphere should have a two component structure. For a dipole-like magnetic configuration, one envisions a set of small, cool loops nested inside an arcade of larger, hot loops, as indicated in Figure 1. The boundary between these two regions may be quite sharp, in which case there is a thin, secondary transition region several thousand kilometers above the photosphere. Another implication is that the compact X-ray bright points (bipolar regions) discussed elsewhere in these proceedings should be short lived, even for steady energy input.

Any linear stability analysis is, of course, only valid in the limit of small amplitude disturbances. It does not determine what happens to these disturbances when they grow into the non-linear, physically observable regime. If they continue to grow, then the system is truly unstable; however, if the

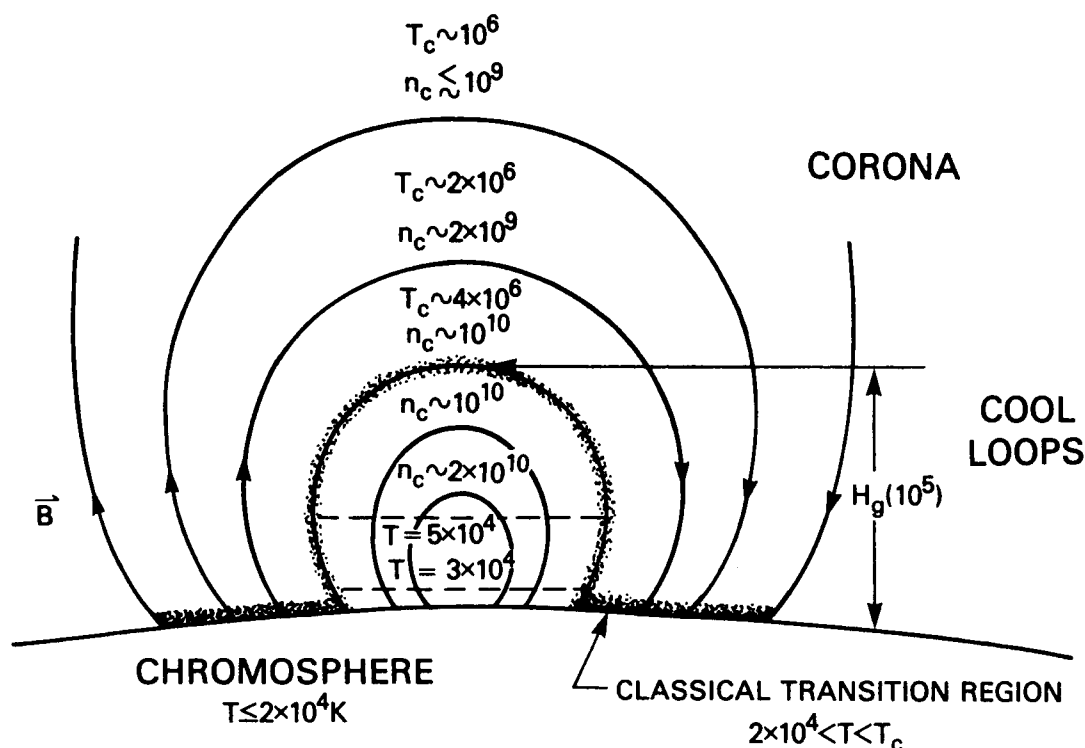


Figure 1. A hypothetical magnetic arcade consisting of cool inner loops surrounded by hot outer loops. Coronal temperatures and densities are given for a heating rate that is proportional to the square of the magnetic field strength. Notice that the cool loops have a maximum height on the order of the gravitational scale height at 10^5 K , or roughly 5000 km.

disturbances quickly saturate, then the system is for all practical purposes stable. We have therefore set out to study the non-linear evolution of loops that are subjected to a variety of small but finite perturbations. Only low-lying loops are considered, since the linear analysis suggests that higher loops are stable.

THE MODEL

We perform our analysis numerically using a one-dimensional hydrodynamic model developed at the Naval Research Laboratory. As described by Mariska *et al.* (1982), the computer code solves the time-dependent equations for mass, momentum, and energy transport. The radiation law of Raymond modified by a T^3 dependence below 10^5 K is employed, and uniform volumetric heating is assumed. The bottom of the loop atmosphere contains two scale-heights of chromosphere at 10^4 K , so the rigid wall boundary conditions should not be critical.

Our primary interest at this point is in active region filaments, hence we consider a geometry appropriate to those structures. The loop is a total of $6 \times 10^4 \text{ km}$ long and is quite flat. Its maximum height is approximately 10^3 km

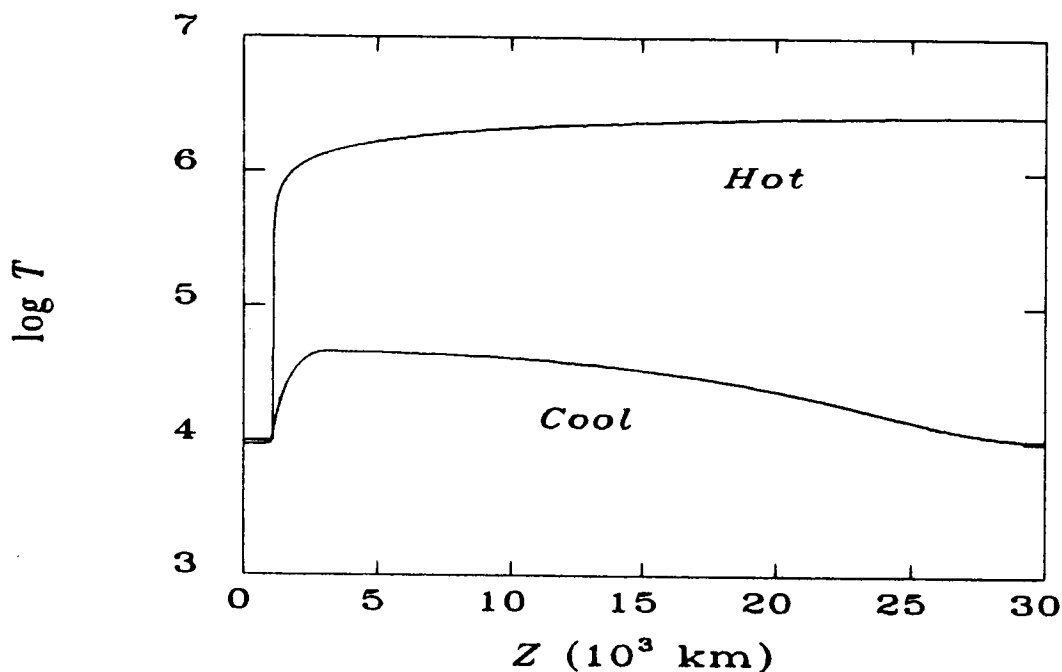


Figure 2. The temperature structure of the hot and cool solutions to the initial static loop. Only half of the symmetric loop is shown. The temperature differences at the end of each perturbation simulation are imperceptible on the scale of this plot.

above the chromosphere, so linear theory predicts it to be unstable. The loop has a very gradual dip in the center to form a gravitational well where dense prominence material could collect. Although a linear stability analysis has not been performed on loops with such a geometry, we expect that, if anything, the central dip will have a destabilizing influence.

The upper curve in Figure 2 shows the temperature profile of the hot solution in this geometry. Only half the loop is shown, as we assume at the outset that it is symmetric. The peak temperature is 2.6×10^6 K and occurs at the loop midpoint. The pressure at the top of the chromosphere is $2.6 \text{ dynes cm}^{-2}$.

The lower curve in the figure is the corresponding cool solution profile for the same energy input. It peaks near the loop apex (where the dip begins) at a value of only 4.7×10^4 K. The pressure of this solution is $0.2 \text{ dynes cm}^{-2}$, roughly an order of magnitude smaller than in the hot solution.

PERTURBATION SIMULATION

We have subjected both of these static solutions to moderate sized perturbations and allowed them to evolve for several thousand seconds (several cooling times and many sound travel times over the coronal portion of the loop). The first perturbation we considered was a 10 % change in the energy input rate--a decrease of 10 % for the hot solution, and an increase of 10 % for the cool solution. As expected, the temperatures begin to fall and rise, respectively, in response to the heating change. Fairly quickly, however, the

evolution slows and the atmosphere appears to settle into a new equilibrium state. This new state is very similar to the original one for both the hot and the cool cases. At the end of the calculations the temperature has changed by only a few percent at all locations. Therefore, the solutions appear to be stable to small perturbations in the heating.

A second perturbation we considered was an instantaneous sinusoidal velocity disturbance of $2\frac{1}{2}$ wavelengths across the half-loop. So as to remain well below the sound speed, the amplitude was chosen to be 10 km s^{-1} for the hot solution, but only 2 km s^{-1} for the cool solution. As before, the perturbation quickly saturates, and the final state of the loop is essentially identical to the original state. The hot and cool solutions are thus stable to this type of perturbation, as well.

DISCUSSION

These results suggest that both hot and cool loops of the geometry considered here are thermally stable against small amplitude perturbations of all kinds. Presumably low-lying loops of other geometries are also stable, but this remains to be shown. Just what causes the linearly unstable modes identified by Antiochos *et al.* (1985) to saturate is not clear. We are currently investigating this question.

If correct, our stability conclusion has important ramifications for the nature of low-lying coronal loops. It implies that the current state of a loop is strongly dependent upon the loop history. For example, a hot loop cannot spontaneously evolve into a cool one without some sort of a major event (e.g., a dramatic decrease in the heating rate, or an injection of copious amounts of cool material). In particular, active region filaments cannot spontaneously condense out of the hot corona, as has been suggested in the past. For further discussion of this point, see the contribution of Poland, Mariska, and Klimchuk in these proceedings.

Another implication of stability is that not all low-lying loops must be cool. The picture of Figure 1 may still be correct, but it need not be, as suggested earlier.

And finally, we end with a word of caution. The numerical results presented here must be considered only suggestive. A concern of ours is that the loop we modelled may not have been properly resolved; the grid size of 10 km in the transition region is only marginal. We are currently working on new simulations with a much improved resolution. In addition, we are exploring alternate geometries, such as the more traditional semi-circular loop. These results will be discussed in a future publication.

Portions of this work were supported by the NASA Solar Terrestrial Theory Program and by the Office of Naval Research. JAK is an NRC-NRL Cooperative Research Associate.

REFERENCES

- Antiochos, S.K., E.C. Shoub, C.-H. An, and A.G. Emslie, 1985, "Thermal Stability of Static Coronal Loops. I. Effects of Boundary Conditions," Ap. J., 298 (876).
- Antiochos, S.K. and G. Noci, 1986, "The Structure of the Static Corona and Transition Region," Ap. J., 301 (440).
- Hood, A.W. and E.R. Priest, 1980, "Are Solar Coronal Loops in Thermal Equilibrium?" Astron. Ast., 87 (126).
- Mariska, J.T., J.P. Boris, E.S. Oran, T.R. Young, Jr., and G.A. Doschek, 1982, "Solar Transition Response to Variations in the Heating Rate," Ap. J., 255 (783).
- Poland, A.I., J.T. Mariska, and J.A. Klimchuk, 1986, "Numerical Simulations of a Siphon Mechanism for Quiescent Prominence Formation," in these Proceedings.

SMALL-SCALE STRUCTURES AND THE DENSITY IRREGULARITY OF THE INNER CORONA

F. Q. Orrall

Institute for Astronomy

University of Hawaii

and

G. J. Rottman

Laboratory for Atmospheric and Space Physics

University of Colorado

ABSTRACT

We consider the observational evidence that the electron density irregularity factor $\langle N^2 \rangle / \langle N \rangle^2$ is much greater than unity in the inner corona, in particular, evidence derived from the photometric comparison of K-corona emission pB with the EUV emission from coronal ions. We develop a simple mathematical model for the irregularity having a minimum number of parameters. We use this model to explore some implications of the observations and to show that well-known resolved structures such as polar plumes and coronal loops as presently understood cannot alone explain the irregularity.

INTRODUCTION

C. W. Allen (1963) introduced the term "coronal irregularity factor" defined as $x = \langle N^2 \rangle / \langle N \rangle^2$ to describe the inhomogeneity of the solar corona. Here N (cm^{-3}) is the electron density. He compiled a table of estimates of x versus radial height based primarily on observed large scale structures such as streamers and condensations (Allen 1963, 1973). In this compilation $x = 1.1$ at R_0 , 1.6 at 1.5 R_0 , 2.5 at 2 R_0 , increasing outward. Later, Allen (1975) substantially increased his estimate of x in the inner corona to $x \sim 4$ at 1 R_0 increasing to ~ 30 at 1.5 R_0 . These revised estimates were based on a statistical study of the daily $\lambda 284$ FeXV intensity contour maps of the Sun obtained by the Goddard EUV spectroheliograph on the OSO-7 spacecraft. From a study of synoptic observations of the red and green forbidden lines and of the K-corona, Leroy and Trellis (1974) found the density irregularity to vary with the solar cycle. The coronal irregularity has been evoked in the interpretation of observed $\lambda 5303$ polarization (Arnaud 1982) and of radio bursts (see Bougeret and Steinberg 1977).

In this paper we consider the observational constraints set on the coronal irregularity in the inner corona by direct cospatial and cotemporal photometric comparison of the intensity of EUV emission lines from coronal ions with K-coronal brightness pB (the polarization times the brightness). The local emission of coronal resonance emission lines depends primarily on the electron density squared, the chemical abundance, and the electron kinetic temperature, while the K-coronal emission due to Thompson scattering by free electrons depends directly on the electron density and on the local radiation field. Hence, combined EUV/K-coronal observations set a constraint on the irregularity that includes the contribution of both resolved and unresolved structures. We discuss photometric comparisons of the EUV and K-coronas and develop a simple model of coronal density

irregularity based on structures embedded in the background corona. We use this as a basis for exploring the constraints set by observation on the irregularity and then consider whether the well-studied structures of the inner corona can account for it.

OBSERVATIONAL LIMITS ON THE IRREGULARITY

The first direct comparison of K-coronal brightness with the intensity of EUV emission lines was made by Withbroe (1970, 1971, 1972), who used EUV data from the Harvard spectrometer on the OSO-4 spacecraft and nearly cotemporal pB measurements made with the High Altitude Observatory's (HAO) Mark I K-Coronameter on Mauna Loa. Both sets of measurements were made at a fixed height of 2 arcmin ($1.125 R_{\odot}$) at all position angles around the limb. Withbroe found a strong correlation between pB and the EUV emission line intensities. He used the measurements of pB to put the EUV derived relative coronal abundances on an absolute scale relative to hydrogen and found them in reasonable agreement with the photospheric derived values. However, this derivation implicitly assumed that the coronal irregularity factor was unity.

More recently, a cotemporal and cospatial photometric comparison of the intensity of $\lambda 625$ MgX and pB has been carried out based on radial scans of the inner corona between 1.05 and $1.25 R_{\odot}$ (Orrall, Rottman, Fisher, and Munro 1986a, b). The $\lambda 625$ MgX intensities were obtained on rocket flights of the LASP EUV Coronal Spectrometer (Rottman, Orrall and Klimchuk 1982; Rottman 1986), and the pB measurements were made with the HAO Mark III K-Coronameter on Mauna Loa (Fisher, Lee, MacQueen and Poland 1981).

These new measurements show the same high correlation between $\lambda 625$ intensity and pB found by Withbroe (1972). The $\lambda 625$ intensities measured with the LASP EUV Spectrometer are in good average agreement with the Harvard measurements on OSO-4, OSO-6 and Skylab. However, a recent intercomparison of the HAO K-coronameters and eclipse cameras shows that the pB values provided by the Mark I K-coronameter (including those used by Withbroe) are too bright by about a factor of 4 (Fisher and Sime 1984; Fisher and Munro 1986). When the pB values used by Withbroe are corrected by this factor, they are in essential agreement with our more recent study.

Let E (ergs $\text{cm}^{-3} \text{s}^{-1} \text{sr}^{-1}$) be the local coronal emission of $\lambda 625$ MgX. With the assumptions of gravitational hydrostatic equilibrium and large-scale spherical symmetry, the $\lambda 625$ and pB measurements can be inverted to recover $\langle E \rangle$ and $\langle N \rangle$, respectively, as functions of height in the inner corona. Here we express E and N as average values, since the inner corona is to some unknown extent nonuniform or structured on scales short compared to the length of the observing column. For convenience we write the well-known and commonly used expression for the emission of a collisionally excited coronal resonance line (see Dere and Mason 1981) as $E = AN^2H(T)$. Here A is the coronal abundance of Mg relative to hydrogen. For Mg the coronal abundance is thought to be close to the photospheric value, $A \sim 4 \times 10^{-5}$ (see Meyer 1985). $H(T)$ contains all of the constant and temperature dependent terms. For $\lambda 625$ MgX it has a maximum between $T = 10^{6.0}$ and $10^{6.1}$ K (see Figure 1). We can then find from $\langle E \rangle$ and $\langle N \rangle$ derived from observation the quantity $\langle E \rangle / \langle N \rangle^2 = \langle AH(T)N^2 \rangle / \langle N \rangle^2$, assuming the photospheric abundance for Mg and using the upper limit to $H(T)$ yields a lower limit to the irregularity $x = \langle N^2 \rangle / \langle N \rangle^2$.

In a coronal hole near the south pole observed on 1983 July 25 this lower limit to x was found to be ~ 10 (Orrall et al. 1986a). Since the temperature implied by the observed scale height was $\sim 10^{6.0}$ K, the actual value of x was evidently close to this lower limit. Above an active region observed on 1980 July 15 the lower limit to x was found to be ~ 6 , but since the observed scale height implied $T \sim 10^{6.3}$ K, the actual value of x implied is ~ 30 (see Fig. 1). (The pB and EUV scale heights yielded the same temperature. This was also true in the coronal hole.) Similar large values of x are implied by Withbroe's data after correction as described above. Since Withbroe's data samples all position angles around the limb, this suggests that the inner corona has this large irregularity at all latitudes.

A MODEL FOR THE IRREGULARITY

Consider a two-component density model of the inner corona in which there are structures with electron density N_S filling a fraction α of the coronal volume. These are embedded in a background or ambient corona of density N_C . Then $\langle N \rangle = N_S \alpha + N_C (1 - \alpha)$ and $\langle N^2 \rangle = N_S^2 \alpha + N_C^2 (1 - \alpha)$. If we define $\beta = N_S/N_C$, then the coronal irregularity factor is given by $x(\beta; \alpha) = [\beta^2 \alpha + (1 - \alpha)] [\beta \alpha + (1 - \alpha)]^{-2}$. For a given value of β , $x(\beta, \alpha)$ has a maximum $x_{\max} = (\beta + 1)^2 / 4\beta$, which occurs at $\alpha = \alpha^*$, where $\alpha^* = (\beta + 1)^{-1}$. Thus, a given value of x implies a lower limit to β such that $\beta \geq (2x - 1) + [(2x - 1)^2 - 1]^{1/2}$, or if $x \gg 1$, then $\beta \geq 4x$. Since x approaches α^{-1} for large β , then $\alpha < x^{-1}$ (see Fig. 2).

The actual values of N_C and N_S are related to the observed mean density $\langle N \rangle$ by $N_C/\langle N \rangle = [\beta + (1 - \alpha)]^{-1}$ and $N_S/\langle N \rangle = \beta[\beta \alpha + (1 - \alpha)]^{-1}$, respectively. For the special case where β has the minimum value for a given value of x (that is where $\alpha = \alpha^*$) these ratios become $N_C/\langle N \rangle = (1 + \beta)/2\beta$ or $\sim 1/2$ for $\beta \gg 1$, and $N_S/\langle N \rangle = \beta(1 + \beta)/2\beta$ or $\sim \beta/2$ for $\beta \gg 1$. Thus even when β is large, the ambient density N_C need not be less than $1/2$ the mean observed value.

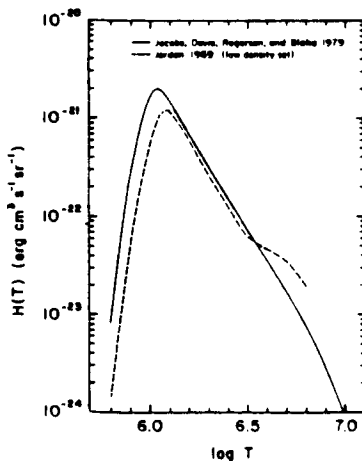


Figure 1. The function $H(T)$ for $\lambda 625$ MgX

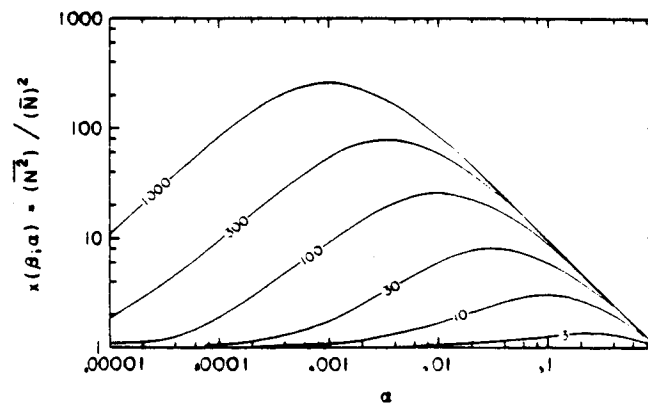


Figure 2. The coronal irregularity factor $x(\beta; \alpha)$ for several values of β .

CONTRIBUTIONS OF KNOWN CORONAL STRUCTURES

Using this model, we consider whether well-known coronal structures can account for the observed irregularity. The value of $x \sim 10$ inferred in the coronal hole observed in 1983 implies $\beta > 40$ and $\alpha < 0.1$. The minimum value $\beta = 40$ occurs at $\alpha^* = 0.024$. The best known structures in the inner polar corona are polar plumes (or rays) studied on white-light eclipse images. Saito (1965) found the average ratio of electron density in the plumes to that in the ambient corona (i.e., the quantity we have called β) to increase from 3 to 5 between 1.1 and $1.5 R_{\odot}$, respectively, and he compares this with previous published values ranging from 3 to 9. The temperature implied by the observed scale height was found to be 1.2×10^6 K and 1.0×10^6 K in the plumes and in the ambient corona, respectively.

Ahmad and Withbroe (1977) analyzed three well-defined plumes on $\lambda 625$ MgX and $\lambda 1032$ OVI images from the HCO/Skylab experiment. They found the plume density to be about three times greater than typical coronal hole models and $T \sim 1.1 \times 10^6$ K. Although plumes are too cool to be easily seen in soft X-rays, Ahmad and Webb (1978) studied plumes with bright points at their base on images from the S-054/Skylab experiment. Their pressure measurements in the plumes imply a density of about 10^8 cm^{-3} at $1.1 R_{\odot}$, roughly a factor of 2 less than that found by Saito (1965). Newkirk and Harvey (1968) studied plumes from white light eclipse observations made at three eclipses near sunspot minimum. They also found a core density in the plumes of about 10^8 cm^{-3} . They chose not to express plume densities in terms of the background density because of the observational difficulty in establishing the true density of the polar background corona (see Ney et al. 1961).

Thus most studies of plumes find values of β between 3 and 7 in the low corona. Unless these studies are incorrect (e.g., because of the difficulties of inferring the true density of the background polar corona as discussed by Newkirk and Harvey 1968), polar plumes cannot explain an irregularity as large as $x \sim 10$ in the polar corona.

The value of $x \sim 30$ inferred in the active region in 1980 July (near the edge of a nonflaring region) implies $\beta > 120$ and $\alpha < 0.033$. The minimum value $\beta = 120$ occurs at $\alpha^* = 0.0083$. Coronal loops are the most obvious and most studied structures that might produce this irregularity. The scaling law for quasistatic loops of Rosner et al. (1978), namely $T_m = 1.4 \times 10^3 (pL)^{1/3}$ can be used to estimate the density. We take for the maximum temperature $T_m = 2 \times 10^6$ K, and for the total length L of the loops, $0.3 R_{\odot}$. The resulting pressure p then implies an electron density $\sim 2.5 \times 10^8 \text{ cm}^{-3}$. This is about the density of polar plumes at this same height (see Saito 1965) and only slightly greater than the mean coronal density at this height. This suggests that quasistatic coronal loops do not produce the observed irregularity at these heights in the inner corona.

SUMMARY AND DISCUSSION

The coronal density irregularity inferred from comparison of the EUV and K-coronas is large at all latitudes and cannot easily be explained by the most obvious resolved structures of the inner corona as they are presently understood. One possibility is that it results from the small resolved and incipiently

resolved structures visible on high resolution coronal images in white light (see Newkirk 1967) and in the EUV (Brueckner and Bartoe 1974). On the other hand, it might arise in much smaller structures, possibly in instabilities or in density fluctuations associated with coronal heating.

Finally, it is necessary to point out that the value of the irregularity inferred from an EUV/pB comparison is sensitive to systematic errors in the absolute photometry--especially to errors in pB since it enters as the square into the determination of x . Additional observations are obviously needed. The density irregularity is clearly an important and basic physical parameter of coronal physics that can be quite directly estimated from observation.

We wish to thank Dr. A. N. McClymont for valuable discussion. This research was supported by NASA in part under grants NSG-5178 and NGL 12-001-011 and by a travel grant to one of us (FQO) to attend the Coronal and Prominence Plasmas Workshop.

REFERENCES

- Ahmad, I.A. and Webb, D.F., 1978, *Sol. Phys.* 58, 323.
 Ahmad, I.A. and Withbroe, G.L. 1977, *Sol. Phys.* 53, 397.
 Allen, C.W. 1963, *IAU Symposium*, 16, 1.
 Allen, C.W. 1973, *Astrophysical Quantities*, Athlone Press.
 Allen, C.W. 1975, *Mon. Not. R. Astron. Soc.* 172, 159.
 Arnaud, J. 1982, *Astron. Astrophys.* 112, 350.
 Bougeret, J.L. and Steinberg, J.L., 1977, *Astron. Astrophys.* 61, 777.
 Brueckner, G.E. and Bartoe, J.D., 1974, *Sol. Phys.* 38, 133.
 Dere, K.P. and Mason, H., 1981, in *Solar Active Regions*, ed. F. Orrall, Colorado Assoc. Univ. Press.
 Fisher, R.R. and Munro, R.H., 1986, in preparation.
 Fisher, R.R., Lee, R.H., MacQueen, R.M. and Poland, A.I., 1981, *Appl. Optics* 20 1094.
 Fisher, R.R. and Sime, D.G., 1984, *Ap. J.*, 285, 354.
 Jacobs, V. L., Davis, J., Rogerson, J. E. and Blaha, M., 1979, *Ap. J.* 230, 627.
 Jordan, C. 1969, *Mon. Not. R. Astr. Soc.* 142, 501.
 Leroy, J.L. and Trellis, M., 1974, *Astron. Astrophys.* 35, 289.
 Meyer, J.P., 1985, *Ap. J. Suppl.* 57, 173.
 Newkirk, G., Jr., 1967, *Ann. Rev. Astron. Astrophys.* 5, 213.
 Newkirk, G., Jr., and Harvey, J., 1968, *Sol. Phys.* 3, 321.
 Ney, E.P., Huck, W.F., Kellogg, P.J., Stein, W. and Gillett, F., 1961, *Ap. J.* 133, 616.
 Orrall, F.Q., Rottman, G.J., Fisher, R.R. and Munro, R.H., 1986a, *Cool Stars, Stellar Systems and the Sun*, Springer-Verlag, in press.
 Orrall, F.Q., Rottman, G. J., Fisher, R. R., and Munro, R. H., 1986b, *Ap. J.*, in preparation.
 Rosner, R., Tucker, W.H., and Vaiana, G.S., 1978, *Ap. J.* 220, 643.
 Rottman, G.J., 1986, *Sol Phys.*, in press.
 Rottman, G.J., Orrall, F.Q. and Klimchuk, J.A., 1982 *Ap. J.* 260, 326.
 Saito, K., 1965, *Publ. Astron. Soc. Japan* 17, 1.
 Withbroe, G.L., 1970, *Sol. Phys.* 11, 42.
 Withbroe, G.L., 1971, *Sol. Phys.* 18, 458.
 Withbroe, G.L., 1972, *Sol. Phys.* 25, 116.

PHLEGETHON FLOW - A PROPOSED ORIGIN FOR SPICULES AND CORONAL HEATING

Kenneth H. Schatten
 Hans G. Mayr
 Laboratory for Atmospheres
 NASA/Goddard Space Flight Center
 Greenbelt, Maryland

INTRODUCTION

We draw upon existing work to put together a model of the mass, energy and magnetic field transport into the corona. This transport originates, in our model, from a deep-seated flow issuing out of concentrated field structures. The fluid is ejected into the solar atmosphere with the help of magnetic forces on fibril field structures. We refer to the subsurface flow as a "phlegethon", named after the river of fire that flowed in Hades in Greek mythology. A new term to describe the gas is suggested because the flow appears to carry significantly greater amounts of energy in its non-potential magnetic fields than in its kinetic energy. As fire is a process which unleashes the stored (chemical) energy to create heat, the term is used here generically to describe heating through the unleashing of a magnetic form of stored energy. As with other models, the wave and current energy flux leads to the dramatic heating of the solar atmosphere. We shall concentrate on the flow below the photosphere (the phlegethon flow), which allows the energy to pass into, and be dissipated within, the solar atmosphere. We do not treat the details of the physical processes (wave breaking, heat conduction, etc.) above the photosphere, nor on the coronal field geometry, which usually forms loops in the solar atmosphere.

Network field structures are already considered good candidates for supplying coronal mass as they carry plasma jets, known as spicules (e.g., Beckers, 1972), having densities from 3×10^{10} to 3×10^{11} particles cm^{-3} (compared to $\sim 10^8$ particles cm^{-3} in the surrounding corona), with diameters of 500 to 1200 km, extending in height 10,000 to 20,000 km, with temperatures from 1 to 2×10^4 K. They contain material with upward supersonic flow velocities of 20 to 30 km s^{-1} with neither sign of material falling nor the upward velocity abated by gravity, make them ideal for supplying coronal material (Withbroe and Noyes, 1977). Thus we consider these structures as sources of material and energy for the solar atmosphere. A number of reviews have been written on the nature of spicules, with Beckers (1972) providing a comprehensive review of their observational and theoretical understanding.

THE ORIGIN OF SPICULES

We consider spicules to represent highly evacuated flux tubes from which gases pour supersonically into the solar atmosphere. Observationally, the high degree of evacuation of fluxtubes may manifest itself in the large nearly uniform field strength of 1400-2000 Gauss (Beckers and Schroter, 1968), comparable to the photospheric gas pressure, observed in nearly all photospheric magnetic features. This leaves little room for significant gas pressure on these field structures. Parker (1984) discusses theoretical

reasons how in a superadiabatic environment, free energy is utilized to concentrate the magnetic field into localized bundles of large field strength (fibrils), consistent with evacuated fluxtubes.

The differing behavior of magnetic buoyancy from gaseous buoyancy may play a major role in the evacuation of fluxtubes, since buoyancy is a critical force for the fluid dynamics within the convection zone. Buoyancy is required for this material to overturn since there is insufficient thermal energy (4×10^{-10} ergs per hydrogen ion) without buoyancy to allow the bulk of the material to rise from the convection zone base to the photosphere against the gravitational potential (-2×10^{-9} ergs per hydrogen ion). The magnetic buoyancy force differs from the thermal buoyancy force, because the latter is proportional to the weight of the displaced material and is therefore comparable to the actual weight of the material within a specific volume. The magnetic buoyancy force, however, originates from the non-potential field configuration, which the surrounding fluid pressures have contorted the magnetic field into. This bears little relation to the weight of material on the magnetic field, but rather is related to the external fluid pressures, modified by the Maxwell stress tensor. We envision a fibril fluxtube extending down to the base of the convection zone, decreasing in radius as it is examined at greater depths. At the lowest altitudes the magnetic field will no longer contract indefinitely, so that at some altitude the magnetic field lines will be nearly parallel. At these altitudes the magnetic buoyancy force will be much less than the gravitational or thermal buoyancy force. In the unmagnetized convection zone fluid, the buoyancy force balances the gravity force since the equations of stellar structure relate the gravitational force to the pressure gradient. Thus the gas density within a deep seated fluxtube decreases with altitude faster than the surrounding gas, where the thermally buoyant forces operate, and the fluxtube can achieve a relatively low density during its passage to the solar surface. Examining conditions higher in the convection zone, near the photosphere, for example, the magnetic stresses are near 10^{-2} dynes cm^{-3} for 300 km wide fibrils of field strength 2000 Gauss, with a 300 km scale height. This is comparable to the gravitational force of 10^{-2} dynes cm^{-3} for photospheric densities of 2×10^{17} particles cm^{-3} .

To summarize our view, for typical deep convection zone densities and fields, gravitational or buoyancy forces exceed magnetic forces for field aligned fluid flow. For shallow conditions or highly evacuated fluxtubes, the Maxwell stresses can exceed the gravitational force. This also can occur at any height, given a sufficiently low density on the fluxtube, because the Lorentz force is governed by the field geometry, not by the amount of material on the fluxtube. Thus, near the solar surface the vertical Lorentz force per unit mass is comparable to, or can exceed the gravitational or buoyant force. This can allow the high flow velocities observed in spicules to occur as a "solar wind" type solution to the Bernoulli equations including the Lorentz force.

ATMOSPHERIC HEATING AND ACCELERATION

We shall examine a treatment following the work of Bailyn et al.(1985). They have considered the solution topologies for polytropic winds associated with momentum deposition and find the general solution can have multiple critical points. Nevertheless, an integral of the motion can be obtained from the

magnetic Bernoulli equation as:

$$KE_p \equiv \frac{1}{2}v^2 + c_0^2 \ln\left(\frac{\rho}{\rho_0}\right) = E + \int_{r_0}^r D(r') dr' - \phi_G \quad (1)$$

where E is the constant of integration (which without the magnetic stress term would be the total energy per particle), $D(r) \equiv L_z/\rho = L_z/Nm$ is the rate of non-thermal momentum addition per unit mass; $c_0^2 \equiv \gamma P/\rho$, the square of the sound speed; KE_p , the kinetic energy per particle; ϕ_G , the gravitational potential; and where $E_B = \int_{r_0}^r D(r') dr'$ may be calculated for a known magnetic field and density structure, including the wave field.

Now, examining the terms of equation (1), for the spicule flow we have $\frac{1}{2}v^2 \sim 2 \times 10^{12} \text{ cm}^2 \text{ s}^{-2}$, and $c_0^2 \approx 10^{12} \text{ cm}^2 \text{ s}^{-2}$, both small compared with $\phi_G \approx 10^{15} \text{ cm}^2 \text{ s}^{-2}$, and $E_B \approx 10^{14} \text{ cm}^2 \text{ s}^{-2}$ for 10 Gauss twisted fields containing 10^{11} particles cm^{-3} integrated over a 1000 km height. Thus for spicule material a small distance above the photosphere, the terms on the left of equation (1) may be small, and the terms on the right, between 10^{14} and $10^{15} \text{ cm}^2 \text{ s}^{-2}$. Figure 1 shows these terms in the solar atmosphere for a simple field geometry.

The Maxwell stress, L_z includes not only the static component which cannot provide heating, but also contributions from waves (in particular, their decay). If we consider a small volume of space containing an arbitrary collection of Alfvén waves, one solution to the dynamical equations, as Parker showed, is for the plasma to travel along the field lines at the Alfvén speed. In this case the waves (in this reference frame) can remain stationary. Thus we can consider a damped set of waves travelling into a region of space, to add energy and momentum to the plasma within. A solution in which the plasma flow velocity equals the Alfvén velocity, we refer to as the "equipartition solution". For sinusoidal waves, the energy transport is divided equally between mechanical and electromagnetic terms. Above the photosphere, the magnetic contribution (per unit mass) to the vertical momentum equation, E_B , monotonically rises, until it exceeds all other physical contributors (eg. ϕ_G). The flow gradually accedes to the demands of this relentless magnetic force, until the flow rate approaches the local Alfvén velocity. This occurs at the "equipartition solution", when the wave energy and particle energy are comparable. At this point, the coronal plasma can no longer acquire energy or momentum from the waves (the curve KE_p approaches an asymptotic value) in the same manner that a sailboat "running with the wind" cannot surpass the wind speed.

Coronal heating problems are now considered. Kuperus, Ionson, and Spicer (1981) suggest that the quiet corona requires a heat source of about $3 \times 10^5 \text{ erg cm}^{-2} \text{ s}^{-1}$ and the quiet chromosphere, a heat source of $4 \times 10^6 \text{ erg cm}^{-2} \text{ s}^{-1}$ for global values of $2 \times 10^{28} \text{ erg s}^{-1}$ and $2.4 \times 10^{29} \text{ erg s}^{-1}$, respectively. The Maxwell stress may be transported at a flow rate of $S \approx V_A (B_0 B_1 / 4\pi)$. Taking spicule number densities at 10^{11} cm^{-3} , field strengths of $B_0 \approx B_1 \approx 10 \text{ G}$, we have V_A of order 100 km s^{-1} , yielding an energy flux of $S \approx 10^8 \text{ erg cm}^{-2} \text{ s}^{-1}$, providing for a global value of $2 \times 10^{28} \text{ ergs s}^{-1}$, when integrated over phlegethon structures with a total area of $2 \times 10^{20} \text{ cm}^2$. This value is sufficient for coronal heating, but 10 times too low for chromospheric heating. These flow energies appear also sufficient, when

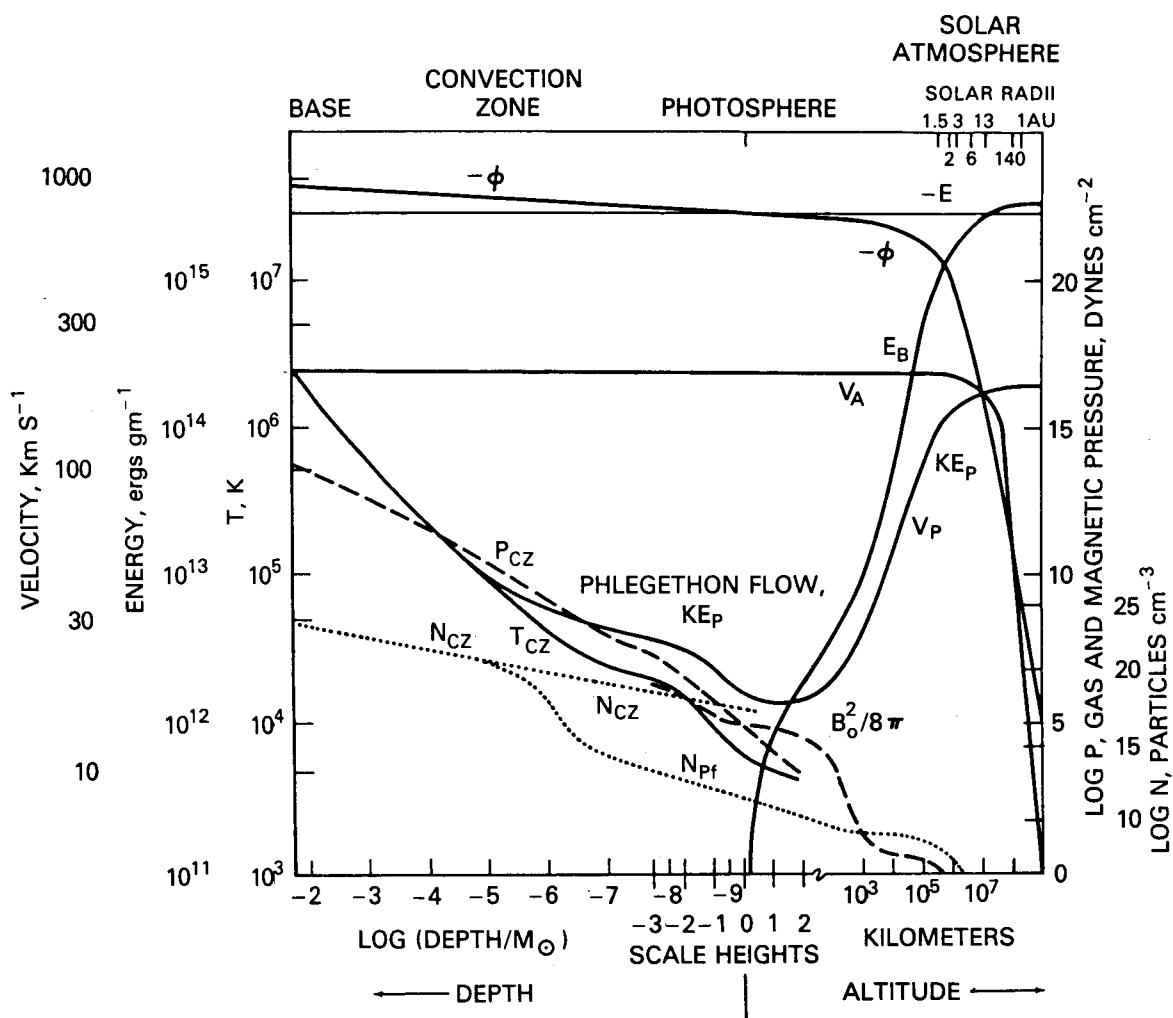


Figure 1. Shown are pressures, energies and densities in the convection zone and solar atmosphere. The subscript cz refers to normal convection zone fluid, and pf to "phlegethon flow" - material flow embedded on field structures. The magnetic pressure exceeds gas pressure above the photosphere. The kinetic energy per particle KE_p , related to the temperature and flow speed squared, the magnetic contribution to the flow energy, E_B , the constant, E , of the motion, and gravitational potential, ϕ , on fluxtubes are also provided in the convection zone and solar atmosphere. The Alfvén velocity, V_A , allows the base energy quality to reach the solar atmosphere. To allow for the rapidly changing conditions near the photosphere, doubly logarithmic abscissa scales are chosen which provide magnification within the region.

thermalized, to elevate spicule material to coronal temperatures. As the waves "break", they contain an energy flux of S and a mass flux of NV_F^{-1} . Dividing the former by the latter provides for 5×10^{-10} ergs particle $^{-1}$, or $\sim 2 \times 10^6$ K thermal energy per particle.

DISCUSSION

We have examined the following scenario for solar atmospheric heating. Fluid on rising fluxtubes deep within the convection zone obtains insufficient buoyancy to rise en masse to the photosphere. In this fashion, rising fluxtubes within the Sun's convection zone can become highly evacuated. Near the photosphere, the magnetic buoyancy force becomes large, ejecting material upwards in accordance with the magnetic Bernoulli equation. This leads to an outpouring of supersonic gases into the solar atmosphere. These gases contain insufficient kinetic energy to heat the corona or escape the gravitational pull of the Sun. In our view they are "wicked" into the solar atmosphere, where an energization of the material by concurrent wave field stresses occurs.

Examining these gases as they ascend on fluxtubes to greater altitudes, their density decreases, owing to gravity and the widening field channel that these gases flow along. On typical field geometries, when the fluid velocity exceeds a few km s^{-1} , hydromagnetic waves dominate the vertical momentum equation, relative to gravity ($L_z > \rho g$). This allows for the velocity to increase rather than decrease with altitude, consistent with the observed behavior of spicules rising supersonically into the solar atmosphere, with their motion unabated by gravity. Although the gases contain insufficient kinetic energy to supply coronal heating, they carry concurrent Maxwell stress and wave energy in their non-potential field configuration. With the explosive release of this energy, the gases erupt into the solar atmosphere to form a hot corona and a dynamically expanding wind. We find that these structures can provide the magnetic field, mass flow, and energy budget necessary to maintain the conventional solar atmosphere. Within the framework of this model, energy may dissipate at a temperature comparable to the temperature where the waves originated, allowing for an "equipartition solution" of atmospheric flow, departing the Sun at velocities approaching the maximum Alfvén speed.

REFERENCES

- Bailyn, C., Rosner, R. and Tsinganos, K., 1985, Ap. J., 296, 696.
 Beckers, J. M., 1972, Ann. Rev. Astron. Astrophys., 73.
 Beckers, J. M. and Schroter E. H., 1968, Solar Phys., 4, 142.
 Kuperus, M., Ionson, J. A., and Spicer, D. S. 1981, Ann. Rev. Astron. Astrophys., 19, 7.
 Landau, L. D., 1951, Classical Theory of Fields, (Addison-Wesley Reading, Mass.).
 Parker, E. N. 1984, Ap. J., 283, 343.
 Withbroe, G. L. and Noyes, R. W. 1977, Ann. Rev. Astron. Astrophys., 15, 363.

ENERGY CONVERSION IN THE CORONAL PLASMA

P.C.H. Martens

NAS/NRC Research Associate

Laboratory for Astronomy and Solar Physics

NASA-Goddard Space Flight Center

Greenbelt, Maryland 20771

INTRODUCTION

Solar and stellar X-ray emission is the observed waste product of the interplay between magnetic fields and the motion of stellar plasma.

The prevalent scenario these days is that stellar magnetic fields are generated and maintained by convective motions and differential rotation in the stellar interior (see Zeldovich et al., 1983 for a review on dynamo theory). Any stellar magnetic field will tend to concentrate in flux tubes and break out to the stellar surface because of its buoyancy (see Parker, 1979), and thus a magnetic link is established between the stellar interior, photosphere, and the outer layers, the so called corona. While in the convection zone and photosphere the magnetic field only has a minor influence on the plasma motions and energy flow, it completely dominates the dynamics and the energetics of the stellar corona.

For example, Parker (these proceedings) emphasizes the enormous differences in temperature, emission measure, and density between solar coronal holes and active regions. The basic difference between them, causing these discrepancies, is that in the former the magnetic field lines are open and find their way into the interstellar space, while in the latter the field lines are closed, i.e. reentrant into the photosphere.

Clearly then, the radiation signatures from stellar coronae, and probably also from chromospheres, as well as the wealth of phenomena they represent, like steady X-ray emission from loops and X-ray bright points, flares and winds, must find their explanation in the growth, evolution, and final dissipation of coronal magnetic fields. In particular, the constant high temperature of stellar coronae, both in open and closed coronal regions for the solar case, requires continuous non-thermal heating, which is the result of the dissipation of free magnetic energy that enters the corona in the form of currents or MHD waves. Theoretical understanding of the process of coronal heating is of the utmost importance, since the high temperature is what defines the corona in the first place. Most of the research described in this chapter deals with aspects of the several rivalling theories for coronal heating. The rest of the papers deals with processes of energy conversion related to flares.

GENERATION AND TRANSPORT OF ENERGY INTO THE CORONA

Before describing and contrasting the presently prominent theories of coronal heating, I will go several steps back and outline a scenario for the generation and transport of the energy that eventually gets dissipated in

stellar coronae. The theoretical description of the last part of this process, the conversion of energy in the corona, is the subject of the coronal heating theories.

As was mentioned above, magnetic fields are believed to be generated and maintained in the convection zone by the dynamo process. From the convection zone the field is buoyed upwards to form the photospheric and coronal field. The magnetic field that enters into the corona, is likely to carry currents from the onset, that can dissipate and contribute to the coronal heating. However, without much justification, these currents are generally ignored in coronal heating theories and it is assumed, often implicitly, that the field that enters the corona is potential (i.e. current free). It is then further surmised that part of the enormous amount of kinetic energy present in the plasma flows in the photosphere is converted into either MHD waves or field aligned currents by the interaction of these flows with the fields. This energy in the form of waves or currents propagates upwards along the field and enters the corona, where at least part of it is dissipated and results in coronal heating.

Both in the corona and the photosphere the time scale for the dissipation of magnetic fields is very long, so the field is essentially "frozen in", i.e. the plasma and the field move together. However, in the corona the magnetic forces completely dominate the thermal pressure gradient and therefore the coronal plasma has to follow the coronal field in its motion, while in the photosphere and below the situation is completely the opposite and the movement of the magnetic field lines is dominated by the plasma motions. Field aligned currents are then generated in the photosphere by **slow** motions of the footpoints of the coronal field lines, while the **faster** sloshing motions of the field lines generate the MHD waves that propagate upwards into the corona along the field lines. This leads to the generalized concept of the photospheric layers below the corona as the "driver" that generates the free energy that propagates into the corona (see Ionson, 1986, for a review). The "driver" represents the spectrum of photospheric motions over all timescales and all length scales. MHD waves and field aligned currents are simply the response of the coronal magnetic field to respectively the high-frequency and low-frequency part of the photospheric power spectrum.

A closed coronal structure, for example a loop, will evolve through a series of magnetostatic equilibria when its footpoints are moved on a timescale which is long compared to the time an Alfvén wave needs to travel along the structure. When the footpoints move on a timescale shorter than the Alfvén crossing time the field in the loop will not have the time to settle in a new equilibrium and the response will be a wave motion in the loop. Open coronal structures, such as coronal holes, always have a wave response to the photospheric driver, since their length, and hence their crossing time, is infinite.

Any coronal heating theory must explain how the corona responds to the energy input by the driver, and in particular, how the free energy is eventually dissipated. The essential input parameter for such a theory is the form of the photospheric energy spectrum (both its frequency and wave vector dependence) and this has to be established through careful observations of the motions of the photospheric magnetic field. Such observations have been made from Spacelab 2 (July 1985) and even better quality observations are expected

from the High Resolution Solar Observatory, the follow up of SOT. At this moment we do not know enough about this spectrum to rule out certain heating theories. However, it is reasonable to expect that most of the power will be within the 100-1000 seconds range. Within this range one finds the convective turn-over time, 800 seconds, the photospheric 5 minute oscillations and the chromospheric 3 minute oscillations. According to numerical estimates for length scales and Alfvén speeds given in **Parker's** contribution to these proceedings, such a power spectrum will generate a wave-like response in large coronal structures and field aligned currents in small structures. For example, on one hand, large coronal loops have Alfvén crossing times in excess of 200 seconds, while on the other hand X-ray bright points have a typical response time of 20 seconds. Therefore, a comprehensive theory of coronal heating should address the problem of the dissipation of both waves and currents.

THE BASIC PROBLEM OF CORONAL HEATING

So far I have discussed a scenario for the generation of free energy and the transport of it into the solar corona. Coronal heating theories take this process usually for granted, i.e. use it as an input parameter, and try to explain how and in what rate the energy that enters the corona is dissipated. This is by no means an easy task, and all theories for coronal heating run into the same basic problem in trying to explain the heating rates that are derived from observations of coronal X-ray emission. The problem is that given the classical coefficients for resistivity and viscosity (Spitzer, 1962), and reasonable estimates for current density and wave amplitude (see Parker's contribution to these proceedings for numerical values) the theoretical heating rates are orders of magnitude less than those required to balance the energy losses through conduction and coronal X-ray emission.

Any coronal heating theory has to explain how the dissipation is enhanced over the classical estimate, and different theories come up with different, often very ingenious and elegant ways of achieving this. The irreversible conversion of magnetic energy into thermal energy is found from the induction equation,

$$\frac{\partial \vec{B}}{\partial t} = \vec{\nabla} \times (\vec{v} \times \vec{B}) - \eta \nabla^2 \vec{B} \quad (1).$$

By taking the inner product of this expression with the magnetic field one finds the decay of magnetic energy into thermal energy from the last term. The second term describes the conversion between magnetic and flow kinetic energy and this process is reversible. In the derivation of Eq. (1) the spatial derivative of the resistive coefficient η has been neglected. It is clear that in order to enhance the resistive dissipation for a given magnitude of the field, either the coefficient of resistivity has to increase, or the spatial derivative of the field has to become large.

The irreversible conversion from flow kinetic energy into thermal energy is found in an analogous way from the Navier Stokes equation

$$\rho \frac{d\vec{v}}{dt} = -\vec{\nabla} p + \vec{j} \times \vec{B} + \rho \nu \left\{ \nabla^2 \vec{v} + \frac{1}{3} \vec{\nabla} (\vec{\nabla} \cdot \vec{v}) \right\} \quad (2).$$

Here ν is the kinematic viscosity coefficient (Spitzer, 1962). After taking the inner product with the velocity, the second term on the right hand side describes the work done against or by the Lorentz force, while the third term describes the irreversible decay of flow kinetic energy into thermal energy. This form of energy decay is relevant for the damping of MHD waves that consist of both particle motions and currents and thus are subject to both resistive and viscous damping. It is clear that in order to increase the viscous damping rate, either the coefficient of viscosity has to become much larger than its classical value, or the velocity amplitude of the MHD-waves has to be much larger than what the observations suggest, or the velocity shear has to become very large.

None of the theories described hereafter explores the possibility of an increase of many orders of magnitude of either viscosity or resistivity. The current heating theories of **Parker** (1979, 1986) and **Van Ballegooijen** (1986 and these proceedings) are based upon the development of very large field gradients, or equivalently, very large current densities. The resonance wave heating theory by **Ionson** (1982, 1985) relies on the development of large wave amplitudes in the resonant coronal loops. An extension and revision of this theory by **Davila** (these proceedings) is based on the development of large wave amplitudes in a very thin resonant layer. An alternative form of dissipation in resonantly heated coronal loops is investigated by **Heyvaerts and Priest** (1983). They describe the development of enormous velocity shears all over a loop due to a slow cross field variation of the Alfvén speed. Finally **Hollweg** (1984, 1986) hypothesizes a cascade of wave energy from (resonant) long wavelengths to short wavelengths, which implies the build up of large velocity gradients.

The question explored in those theories is then: what physical mechanism causes the build-up of strong gradients in the magnetic field or velocity field, or what causes the large wave amplitudes? The different theories give different answers and I will contrast those answers in the following. This comparison will at the same time serve as an introduction to the majority of the papers in this chapter.

THEORIES OF CORONAL HEATING

The most radical solution to the problem is given by **Parker** (1972, 1979, 1983, 1986, and these proceedings). Parker argues that a static coronal magnetic field that is smooth and force free everywhere, and satisfies the boundary conditions at the photosphere, simply cannot exist. The governing equations overdetermine the problem and therefore some sort of symmetry has to exist in force free fields. This symmetry is in general incompatible with arbitrary boundary conditions and the "frozen in" condition of the magnetic field and hence no regular and smooth solutions exist. Parker points out that instead the mathematical solutions to the problem will exhibit discontinuities, where the field gradients are infinitely large. In physical reality this means that current sheets will develop, where enough dissipation may take place to heat the corona. Hence the development of large field gradients is an **intrinsic** property of coronal magnetic fields, and there is no need to force the origin of current sheets by discontinuous motions of field lines in the photosphere. Specifically it is Parker's assertion that **continuous** footpoint motions of an originally **continuous** force free coronal field will create

discontinuities in the coronal magnetic field. This stands in contrast with the solutions for force free coronal fields with continuous boundary conditions: there is no doubt that these solutions will be continuous. The difference between the two situations is that in the former the history of the footpoint motions is an essential part of the problem. Knowledge of the photospheric power spectrum is still necessary to determine the amount of energy that is transported into the corona, but once the energy is there it will surely be dissipated. This process is called **topological heating**.

Three papers in this chapter deal with the problem of the existence of smooth force free fields in the solar corona. **Antiochos** presents evidence that in general force free coronal magnetic fields are **not** overdetermined by the constraints that the boundary conditions impose, and therefore that the formation of current sheets is not an intrinsic property of the coronal magnetic field (see also Antiochos, 1986). He finds that all the information of the wrapping of coronal field lines is contained in the boundary conditions to the field and hence there is no additional constraint on the field by the history of the footpoint motions. The problem then reduces to one that is very similar to a Dirichlet problem and the Dirichlet problem is known to have regular smooth solutions. Zweibel (1987) has recently derived similar results.

Berger in his contribution reaches exactly the opposite conclusion: he finds that thin current layers separating flux tubes will form in general. His argument is based on the nature of the magnetic field at the photospheric boundary. It is well known that in the photosphere the magnetic field is concentrated in flux tubes, with very little intertube flux. Arbitrary motions of these flux tubes in the photosphere necessarily create current sheets in the corona. Antiochos and Berger seem to agree that the photospheric footpoint motions in Berger's examples are discontinuous, and the formation of a current sheet is known to be trivial in that case. The real problem is to explain the formation of coronal current sheets by a continuous photospheric velocity field. However, this does not invalidate Berger's results: he shows quite convincingly that even a simple braiding pattern of three flux tubes is inconsistent with a smooth force free coronal field.

The last paper on the coronal magnetic field is by **Martens**. His basic approach is to try to determine the restrictions that the equations for force free fields impose on the geometry of these fields. For that purpose he derives the magnetohydrostatic equations in general non-orthogonal coordinate systems. The idea is then to find out what conditions the MHS equations impose on the metric tensor. This work is in a rather preliminary stage, but the first results do not seem to indicate the necessity of some sort of symmetry in force free fields, contrary to Parker's result (1986).

An alternative theory of coronal heating by **Van Ballegooijen** is the subject of the next paper (see also Van Ballegooijen, 1986). Van Ballegooijen (1985) recently pointed out an error in a proof of Parker (1972) of the necessity of an ignorable coordinate magnetohydrostatic (MHS) fields and further presented an algorithm for actually calculating fully three dimensional MHS fields subject to arbitrary boundary conditions. Consequently Van Ballegooijen takes the point of view that the formation of current sheets is not an intrinsic property of the coronal magnetic field, but that instead the field evolves through series of smooth equilibria in response to footpoint motions. In his contribution to this chapter Van Ballegooijen assumes that the

photospheric footpoint motions are random in nature and that as a result of this the separation between any two neighbouring fluid particles increases exponentially with time and consequently steeper and steeper gradients will develop in the magnetic field. As the field gradients grow larger, finally dissipation will grow to a large enough rate to balance energy input and a stationary state will develop. An interesting result of this analysis is that the timescale for establishing the stationary state is remarkably short, of the order of the "braiding time".

The heating rate predicted by the theory of Van Ballegooijen is a factor 40 short of the required heating rate for the solar corona and this result is mainly based on the observed value of the effective diffusion constant for photospheric motions. However, there may be small scale photospheric motions that so far have escaped detection and these could result in a much larger value for the effective diffusion constant and alleviate the discrepancy between theory and observations. Clearly then, high resolution observations are needed to determine the photospheric power spectrum.

It has been pointed out above that if most of the power in the photospheric spectrum is concentrated in motions with periods between 100 and 1000 seconds, large coronal magnetic structures are probably heated by the dissipation of MHD waves, while the small scale structures are heated by field aligned currents. Wave heating therefore must play a role in the solar corona, and, since most of the coronal X-ray emission comes from large loops, it may well be the dominant source of coronal heating.

Davila in his contribution calculates the heating rate that results from the mechanism of resonance absorption of Alfvén waves, that was proposed by Ionson (1978, 1982) as the heating mechanism for coronal loops. The physical basis of this mechanism is that Alfvén- or fast MHD waves get trapped in a coronal loop after entering it from the photosphere. Once in the corona, they keep on reflecting back and forth between the two footpoints of the loop, where there is a very sudden density increase by two orders of magnitude. Those waves that have a period equal to the Alfvén crossing time of the loop (or an integer fraction of it) are in phase with the incoming waves of the same period as they bounce off the loop footpoints and therefore they become reinforced. Thus the amplitude of the resonant waves in these loops builds up until dissipation limits further growth. In this situation the dissipation of energy equals the energy input at the footpoints and consequently the heating rate is independent of the damping coefficients. What does depend on these coefficients is the amplitude that the resonant waves attain in the stationary situation: the lower the damping rate, the higher the stationary amplitude. Observations of non-thermal line broadening in UV restrict this amplitude to 10-20 km/sec, but other observations in X-ray lines (Acton *et al.*, 1981) indicate amplitudes around 100 km/sec.

Davila assumes in his paper that a coronal loop is excited by an Alfvén wave with a given frequency. The Alfvén speed varies slowly over the loop and in a narrow layer the frequency of the incoming wave exactly matches the local resonance frequency. The incoming waves over the whole loop are resonantly absorbed in this layer and dissipate there. Essential in this process is the coupling between waves on neighbouring field lines because of the compressibility of the plasma. Davila calculates that the wave amplitude needed to supply the required coronal heating is 2-6 km/sec, well below the

limit set by the observations.

This wave heating theory is in many ways an attractive alternative to the current heating theories discussed above. It explains why a coronal loop, once it is formed, is preferentially heated. The increased density in the loop, compared to the surrounding corona, makes the Alfvén velocity in it smaller than that of the surrounding corona, and therefore its Alfvén crossing time larger. This means that the loop responds to a different part of the photospheric power spectrum than its surroundings and that part of the spectrum may contain more power. The theory, being concerned with the stationary heating of loops, does not explain why a loop should form. However, the current heating theories explain neither the formation nor the persistence of coronal structures at all, so in this aspect the wave heating theory is ahead. Clearly, any future comprehensive coronal heating theory should not only reproduce the required heating rate, but also its spatial distribution in loops, X-ray bright points, etc.

Two alternative forms of resonance wave heating of the stellar corona, with regard to the detailed dissipation process, have been proposed by Heyvaerts and Priest (1983) and by Hollweg (1984, 1986). There are no papers in these proceedings dealing with those theories, but I will discuss them briefly here for comparison. Heyvaerts and Priest consider a coronal loop with a slowly varying Alfvén velocity across it and assume the plasma is incompressible. The coronal waves that build up in it consequently have slightly different frequencies and will gradually grow out of phase across the field lines. Thus an increasingly large velocity shear develops in the loop until at a certain point dissipation limits further growth. This model has the advantage that the wave amplitude required to achieve the necessary coronal heating are not as large as that in Ionson's (1982) original work. Indeed they can remain within the constraints imposed by the observations. However, the time it takes to set up a stationary state in this model is very long compared with the lifetime of individual coronal structures.

A similar theory has been developed by Hollweg (1984, 1986). He describes a cascade of wave energy to smaller and smaller wavelengths until dissipation taps the wave energy at the smallest wavelength. The cascade is driven by the discontinuities in the wave velocities that are present along the boundary layers of the parts of the coronal field that are attached to different photospheric fibrils. Again the necessary heating is obtained by the development of strong shears in the velocity field.

The last contribution to this chapter on the subject of steady coronal heating is by Choudhuri. His basic result is that no net magnetic helicity is transferred into the corona by completely random footpoint motions, since these are as likely to introduce positive as negative helicity on a small scale. This result is relevant with regard to recent work of Heyvaerts and Priest (1984), in which it was pointed out that on a short time scale only as much energy can be dissipated in the corona as is consistent with helicity conservation. According to the paper by Choudhuri then, the conservation of magnetic helicity introduces no effective constraint on energy dissipation.

NON STATIONARY RELEASE OF MAGNETIC ENERGY

The emphasis of this introduction so far has been on the steady conversion of magnetic energy into thermal energy, that is responsible for the continuous X-ray emission from stellar coronae. This is justified because this process is responsible for the mere existence of stellar coronae and at the same time only poorly understood. Apart from this phenomenon, however, stellar coronae exhibit the splendid spectacle of stellar flares, a very sudden conversion of an enormous amount of energy (up to 10^{33} erg for solar flares) into radiation and mass ejections. It is generally assumed that the flare energy is built up and stored in the corona prior to the eruption, but the process is only partially understood.

The last five papers in this chapter are all related to the storage and sudden release of coronal magnetic energy. They form by no means a complete review of solar flare theory, as the papers on steady coronal heating do, and in this introduction I will neither make an attempt to review flare theory.

Hood and Velli, in their back to back contributions, investigate the stability of magnetic arcades in the corona to respectively ideal and resistive instabilities. Cylindrically symmetrical arcades of loops are widely used as a description of the field of a coronal filament prior to its eruption. The eruption of a filament is the origin of a two ribbon flare. A viable scenario for the physical cause of the filament eruption is that a threshold for the onset of an MHD instability is surpassed at the onset of the eruption. Checking the stability of coronal magnetic structures is a complicated procedure that involves the solution of series of ordinary differential equations, or the solution of partial differential equations, and generally it can only be done numerically. In his contribution Hood finds an approximate analytical criterion that is sufficient for the origin of localised instabilities. Nonlinear coupling of the unstable modes can lead to an explosive instability as those in filament eruptions. Hood's criterium is very convenient for a quick check of models for the magnetic field.

Velli in his paper includes the effect of resistivity in the same problem and finds that in some regions where the ideal MHD approximation predicts stability, slowly growing resistive instabilities may be present, which lead to energy release in 10 to 100 Alfvén crossing times. This result may be relevant with regard to preflare heating. One could imagine that as a coronal arcade evolves, it first becomes resistively unstable, and only later on surpasses the threshold for ideal instability. Consequently energy will be released in modest amounts before the whole structure erupts, just as is observed in two-ribbon flares.

Finally, it has been noted by Hood and Velli that the instabilities they describe automatically generate the sort of length scales needed for a steady heating mechanism. Indeed, as soon as the magnetic field departs from potential, resistive ballooning modes are excited and the saturation of these modes should lead to enhanced transport properties. The consequences for coronal heating have yet to be worked out.

In the contribution of **Einaudi** a similar problem regarding the stability of a model coronal field structure is addressed. He considers the influence a flow and viscosity have on the stability of a given magnetic field

configuration. It turns out that viscosity is in general more important than resistivity for the dissipation of energy, and since flows are regularly observed in the corona, especially in relation with filaments and prominences, this should be taken into account in any model for energy conversion.

The generation of an electric field during the decay phase of a two-ribbon flare is the subject of the paper by **Kopp and Poletto**. The electric field is generated along an X-type neutral line. A scenario for the eruption of filaments and the evolution of two-ribbon flares, including the generation of an electric field, is presented by Kuin and Martens elsewhere in these proceedings. Kopp and Poletto concentrate on the derivation of the electric field strength from the observed ribbon velocity during the flare and the observed normal component of the magnetic field. The electric field they find is strong enough to accelerate electrons to the very high energies that are needed to explain the hard X-ray emission of flares. From their model and that of Kuin and Martens it appears that the current sheet set up at the X-type neutral line is the dominant location for the flare energy release.

Finally **Steinolfson** describes a numerical experiment that has relevance for the problem of compact flares and that I further expect to be related with the formation of filaments. The experiment consists of a time dependent two dimensional MHD simulation of the response of a cylindrically symmetric flux tube to rotational motions of its photospheric footpoints. Thermal pressure gradients are neglected and the plasma is assumed to be incompressible. The dynamics then uncouple from the energetics and the problem becomes tractable.

Steinolfson finds that the loop initially evolves through a series of force free equilibria, as one would intuitively expect. However, when the field in an appreciable portion of the loop has undergone one rotation, a dynamical evolution sets in and the Lorentz force is now balanced by the flow dynamics. A rapid change in the field configuration then occurs, at the end of which some field lines make several rotations around the axis of the cylinder. Steinolfson notes that during the build-up stage enough energy is stored in the loop to account for the energy released in a compact flare. I further note that the rapid transition of the field in the loop from a situation with one rotation of the field around the axis to one with several rotations is a good model for the origin of filaments and prominences. In this case the field in and around the filament is the first approximation modelled by this cylindrically symmetric loop, with the axis of the loop identical to that of the filament.

CONCLUSIONS

A comprehensive quantitative theory of stellar coronal heating cannot be expected before we are able to fully understand solar coronal X-ray emission. The two major elements of the latter will be a theory of solar flares and one of steady coronal heating. There is a considerable number of theoretical possibilities for steady coronal heating, and most of them are outlined in this chapter. The main task for the near future is to tighten the observational constraints on coronal heating theories, so that at least a number of possibilities can be ruled out. The observations of Spacelab 2 and HRSO (the successor of SOT) can be used to get a better hold on the temporal and spatial dependence of the photospheric power spectrum, while high

sensitivity coronal instruments, like POF, may determine the magnitude of coronal wave motions.

On the theoretical side the problem of the spatial distribution of the heating in the solar corona - the preferential heating of loop structures and X-ray bright points - needs to be addressed. No coronal heating theory can claim any generality without solving this problem. Further the problem of the mere existence of force free coronal magnetic fields needs deeper analysis. Heating by topological dissipation of magnetic fields is difficult to rule out on observational grounds, even after a detailed photospheric power spectrum has become available, but then also, this theory can only be confirmed by ruling out all others.

Theoretical analysis, however, should be able to establish unambiguously the conditions for the existence of smooth force free magnetic fields, and hence the validity of the topological heating theory. Furthermore, the question regarding the conditions for topological dissipation transcends the problem of coronal heating. It is also of eminent importance for laboratory plasmas, especially in Tokamaks, and for many astrophysical magnetic fields, like the earth's magnetotail and galactic magnetic fields. Finally, in the view of the author, the problem has a great esthetical appeal: here we have a clear and well formulated theoretical question, and yet the final solution has eluded the astrophysical community for over 20 years.

Flare theory, the other building block for a theory of stellar X-ray emission, is even further from completion. A fairly general scenario for filament eruptions, leading to two ribbon flares (e.g. Kuin and Martens, these proceedings) has now become commonplace in the solar physics community, but we are far removed from **predicting** X-ray emission in flares from preflare observations of magnetic fields and velocity fields in the photosphere. The same spacecraft (HRSO and POF) that will determine photospheric and coronal motions in more detail for steady heating theory, as well as other satellites like MAX'91, will yield valuable information with regard to flare theory.

REFERENCES

- Acton, L.W., and 17 co-authors 1981: *Astrophys. J.* **244**, L137.
- Antiochos, S.K. 1986: "The Topology of Force-Free Magnetic Fields and its Implications for Coronal Activity", *Astrophys. J.*, in press.
- Berger, M.A. 1986a: *Geophys. Astrophys. Fluid Dyn.* **34**, 265.
- Berger, M.A. 1986b: "Braiding of Magnetic Flux by Two-Dimensional Random Boundary Motions", preprint.
- Heyvaerts, J., Priest, E.R. 1983: *Astron. Astrophys.* **117**, 220.
- Heyvaerts, J., Priest, E.R. 1984: *Astron. Astrophys.* **137**, 63.
- Hollweg, J.V. 1984: *Astrophys. J.* **227**, 392.
- Hollweg, J.V. 1986: *J. Geophys. Res.* **91**, 411.
- Ionson, J.A. 1978: *Astrophys. J.* **226**, 650.
- Ionson, J.A. 1982: *Astrophys. J.* **254**, 318.
- Ionson, J.A. 1985: *Astron. Astrophys.* **146**, 199.
- Ionson, J.A. 1986: *Solar Phys.* **100**, 289.
- Parker, E.N. 1972: *Astrophys. J.* **174**, 499.
- Parker, E.N. 1979: **"Cosmical Magnetic Fields"**, pp. 359-391, Oxford, Clarendon Press.
- Parker, E.N. 1983: *Astrophys. J.* **264**, 635.
- Parker, E.N. 1986: *Geophys. Astrophys. Fluid Dyn.* **35**, (in press).
- Spitzer, jr., L. 1962: **"Physics of Fully Ionised Gases"**, Chap. 5, Inter Science, New York.
- Van Ballegooijen, A.A. 1985: *Astrophys. J.* **298**, 421.
- Van Ballegooijen, A.A. 1986: "Cascade of Magnetic Energy as a Mechanism of Coronal Heating", *Astrophys. J.*, in press.
- Zeldovich, Ya. B., Ruzmaikin, A.A., Sokoloff, D.D. 1983: **"Magnetic Fields in Astrophysics"**, Gordon and Breach Science Publishers.
- Zweibel, E.G., Li, H-S, 1987: "The Formation of Current sheets in the Solar Atmosphere", *Astrophys. J.*, in press.

TOPOLOGICAL CONSTRAINTS AND THE EXISTENCE OF FORCE-FREE FIELDS

S. K. Antiochos

E. O. Hulburt Center for Space Research, Naval Research Lab

INTRODUCTION

A fundamental problem in plasma theory is the question of the existence of MHD equilibria. Given some initial configuration of the field and plasma, and given that the system can evolve only via ideal MHD, one asks whether the system can reach a static equilibrium state. This question obviously has great relevance to fusion devices; hence, it has received considerable attention for closed magnetic configurations (e.g. Moffatt 1985). There is reason to believe that the question of equilibria may also be very important to the study of the solar corona. Parker (1983a,b), in particular, has argued that the underlying cause for coronal heating is the lack of well-behaved magnetic equilibria. As a result of photospheric motions the coronal magnetic field must be distorted into a complex three-dimensional pattern. Parker argues that such a complex field topology can have no well-behaved equilibria in general. He further argues that the effect of this lack of well-behaved equilibria is to lead to the formation of current sheets. Since the corona is not perfectly ideal, the current sheets will dissipate rapidly, thereby heating the corona.

These arguments have some support from the recent work on equilibria in closed field geometries. Moffatt (1985) has shown that for topologically complex geometries, the magnetic field will evolve towards equilibrium configurations that, in general, have discontinuities, specifically current sheets. This occurs even for an evolution that is completely ideal, in which case the field for all finite times must be well-behaved. Moffatt's point is that the equilibrium state will be achieved only at infinite time so that discontinuities can, and usually will be created. Since this evolution is basically the one hypothesised by Parker in his coronal heating model, Moffatt's results are clearly strong support for the central points of this model. However, there is a critical difference between the types of topology considered by Moffatt and the corona. The coronal field lines are not closed; from the viewpoint of coronal equilibria the lines can be considered to terminate at the photospheric boundary. Therefore, one has to include the boundary conditions imposed by the photospheric motions on the possible evolution of the field. So far this has not been done, consequently Moffatt's results by themselves do not definitively settle the question of whether the solar coronal field has well-behaved equilibria in general.

Recently, Parker (1986) has presented a new proof for non-equilibrium based on topological arguments. This proof is limited to force-free

fields; however, this is not a significant restriction since force-free fields are believed to be a good approximation to the coronal field. They have been widely used in the past (e.g. Sturrock and Woodbury 1967; Barnes and Sturrock 1972; Sakurai 1979; Aly 1984; Yang, Sturrock and Antiochos 1986). Parker first argues that the coronal force-free field can generally be expressed in terms of two scalar functions. Although this is not true for arbitrarily complex field, it should be valid for the case where the field begins in some simple state and then evolves by ideal, finite motions. We make the same restriction in this work and consider only fields that can be described by two well-behaved Euler potentials (e.g. Stern 1966). Next, Parker points out that if the positions of the field-line footpoints at the photospheric boundary is fixed, then the pattern of wrappings and windings of the field lines in the corona imposes constraints on the possible evolution, and hence on the possible equilibria of the field. These constraints are due to the topology of the coronal field, which in turn is due to the history of the photospheric footpoint motions. In order for the field to be in equilibrium the two potentials must satisfy the two independent force-free equations as well as all the topological constraints. However, Parker argues that since the pattern of coronal wrappings and windings is arbitrary, one of the potentials is essentially fixed throughout by the topological constraints. This leaves only one free function to satisfy the two force equations; hence, the problem is overdetermined and no well-behaved solutions exist in the general case.

It is evident from these arguments and also from Moffatt's work that the issue of topological constraints is of crucial importance for the problem of the existence of equilibria. In this paper we will show that, contrary to Parker's claim, the topological constraints do not overdetermine the force-free problem. The source of the discrepancy between his results and ours is that we find that the topological constraints do not fix the value of one of the potentials in the corona. We show below that all the constraints are incorporated in the positions of the footpoints at the photospheric boundary, which fixes only the boundary values of the potentials. Since the force-free problem is naturally a Dirichlet-type boundary value problem, there is no reason to expect it to be overdetermined on the basis of these constraints.

Our result that the footpoint positions include all the topological constraints may appear counter-intuitive. If one considers the field as a collection of strings, then for a particular set of positions of the strings' footpoints, the strings should be able to wrap around each other in an infinite number of distinct patterns. Hence, the topology of the strings is clearly not determined solely by their footpoint positions. However, there is a key difference between the magnetic lines and a collection of strings. The field lines that we are considering must have a smooth and continuous distribution throughout the corona and on the boundary. Furthermore, all field lines must be connected to the photosphere. It is these requirements, that the field be smooth and well-connected throughout, that forces a one-to-one relationship between the footpoint positions and the coronal wrapping pattern.

CORONAL WRAPPING PATTERN

In this section we will show how the wrapping of any two field lines about each other can be determined from the footpoint positions, which is commonly referred to as the "connectivity". The discussion in this short contribution will necessarily be somewhat heuristic; a more rigorous and thorough demonstration of this result is given in Antiochos (1986).

First let us reemphasize that we are considering only those fields that can be written in terms of two well-behaved Euler potentials,

$$\vec{B} = \nabla \alpha \times \nabla \beta$$

This form is very convenient for expressing the connectivity. Note that α and β are constant along each field line and, hence, label each line. The footpoint positions is given simply by the value of α and β at the photospheric boundary.

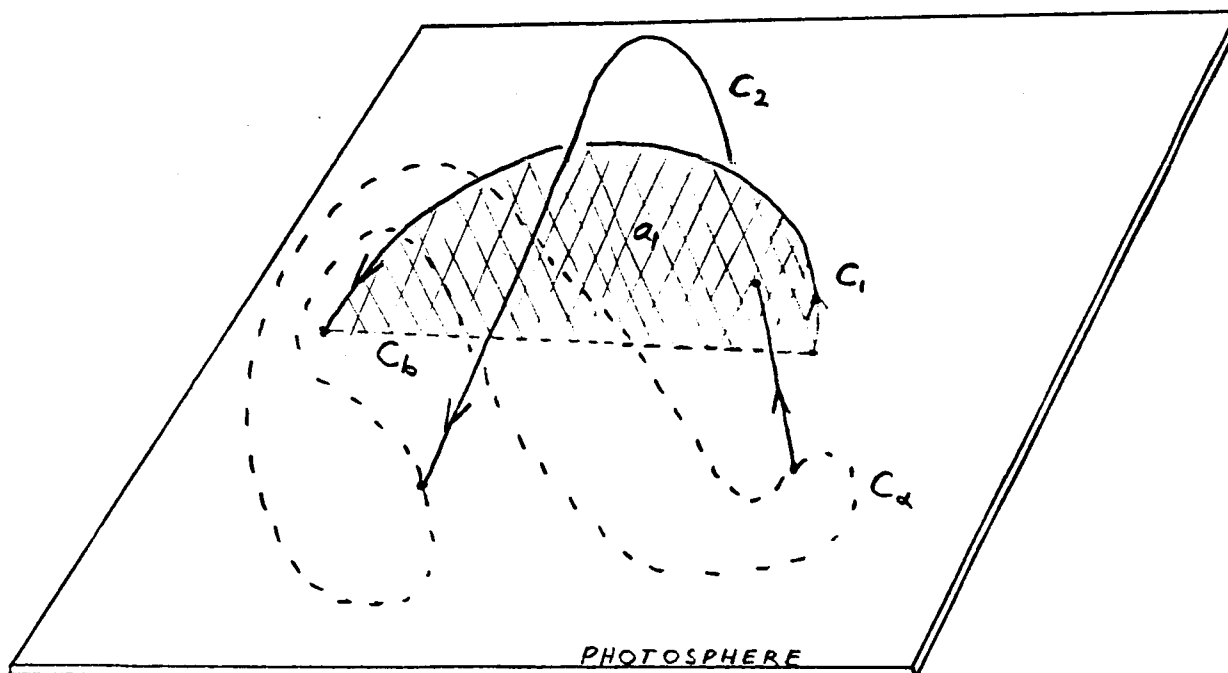


Figure 1. Illustration of curves used to determine the wrapping of field line C_2 about C_1 . Coronal field lines are indicated by solid lines, curves lying on the photospheric boundary (here shown as a plane) are indicated by broken lines. The area a_1 enclosed by field line C_1 and the boundary curve C_b is shaded.

Now consider any two field lines such as those illustrated in Figure 1. The coronal field lines are labelled as C_1 and C_2 . It seems intuitively obvious from the Figure that field line C_2 wraps once around C_1 . We can make this wrapping concept rigorous by connecting the two footpoints of C_1 on the photospheric boundary by a straight line, labelled C_b , and then considering the area \vec{a} , enclosed by the closed curve consisting of C_1 and C_b . We define the value of the wrapping of C_2 about C_1 to be given by sum of the number of times that C_2 intersects area \vec{a} , with each intersection assigned a value of +1 or -1 depending on the direction of the intersection. The wrapping of C_2 about C_1 has a value of -1 for the lines in the Figure 1.

Given the values of the potentials α and β throughout the corona, we can calculate the exact positions of the field lines and consequently the wrapping. However, the field line positions obviously contain a great deal more information than is required to determine the wrapping. We will now show that the values of α and β solely on the photospheric boundary are sufficient to fix the wrapping. The two different field lines C_2 and C_1 have a different value for at least one of the Euler potentials; assume that it is α so that $\alpha \neq \alpha_1$. Consider the surface $\alpha = \alpha_2$. If the connectivity is well-behaved everywhere in the corona and on the photosphere, we expect the Euler potentials to define a set of simple, well-behaved surfaces in this domain. The intersections of these surfaces with the photospheric boundary define the contours of constant α or constant β on the photosphere. In order to have a well-defined connectivity each contour of constant α must intersect each β contour at exactly two points on the photosphere; consequently, we expect that each contour consists of a single closed curve. For example, the boundary contour for $\alpha = \alpha_2$ is shown in Figure 1 as the closed curve C_α . Note that it can be considered to consist of two parts, each of which connects the two footpoints of field line C_2 . Now the key point is that field line C_2 lies completely on the surface $\alpha = \alpha_2$, while field line C_1 nowhere intersects this surface. This implies that with no change in the wrapping, we are free to deform C_2 down along the constant α surface until it just coincides with one of the parts of curve C_α . Since both C_b and C_α lie on the photospheric boundary the number of times that this deformed curve crosses area \vec{a} , must equal the number of times that either part of C_α crosses C_b . But this number depends only on the straight line C_b that connects the footpoints of C_1 and the contour of constant α on the boundary; therefore the wrapping can be determined solely by the values of α and β on the boundary.

We conclude that for a given set of footpoint positions the wrapping pattern in the corona is completely fixed. Contrary to the assumption implicit in Parker's arguments, one is not free to arbitrarily prescribe a wrapping pattern. Note that the wrapping pattern does not include all the possible topological features of the field (e.g. Berger 1986); however, by extending the arguments above it can be shown (Antiochos 1986) that all the topological features created by the footpoint motions

of well-behaved fields can be determined from the connectivity. Hence, the topological constraints are included in the boundary conditions on the Euler potentials and impose no additional restrictions on possible equilibria. Although this does not prove that equilibria always exist, it does show that the force-free problem is not overdetermined and that the existence of equilibria is still an open question.

ACKNOWLEDGEMENTS

This work was supported in part by a grant from the Office of Solar and Heliospheric Physics at NASA.

REFERENCES

- Aly, J. J. 1984, Ap. J., 283, 349.
Antiochos, S. K. 1986, Ap. J., (submitted).
Barnes, C. W. and Sturrock, P. A. 1972, Ap. J., 174, 659.
Berger, M. A. 1986, (these proceedings).
Moffatt, H. K. 1985, J. Fluid Mech., 159, 359.
Parker, E. N. 1986, Geophys. Ap. Fluid Dyn., 34, 243.
Parker, E. N. 1983a, Ap. J., 264, 635.
Parker, E. N. 1983b, Ap. J., 264, 642.
Sakurai, T. 1979, Pub. Ast. Soc. Japan, 31, 209.
Stern, D. P. 1966, Space Sci. Rev., 6, 147.
Sturrock, P. A. and Woodbury, E. T. 1967,
 "Plasma Astrophysics", (ed. P. A. Sturrock, New York: Academic
 Press), p. 155.
Yang, W. H., Sturrock, P. A. and Antiochos, S. K. 1986, Ap. J.,
 (in press)

THE TOPOLOGICAL DESCRIPTION OF CORONAL MAGNETIC FIELDS

Mitchell A. Berger
High Altitude Observatory
National Center for Atmospheric Research
Boulder, Colorado

INTRODUCTION

Determining the structure and behavior of solar coronal magnetic fields has been a central problem in solar physics. Unfortunately, even modelling the equilibrium states of the field has proven to be difficult in general, because the equations describing magnetic equilibria are nonlinear, and the boundary conditions can be of great complexity. One fruitful approach has involved studying idealized geometries which admit exact analytic solutions, or which can be conveniently modelled numerically (for a review, see Low 1986). Such geometries, because of their relative simplicity, work best when applied to large-scale or global structures. However, closed magnetic regions may contain significant structure on smaller scales, because convective motions in the photosphere can wrap the coronal field lines about each other in a complicated manner. Dissipation of this structure may provide the source of coronal heating in active regions (e.g., Parker 1972, 1983; Sturrock and Uchida 1981; van Ballegooijen 1986). Because of this possible role in coronal heating, it is important to understand the behavior of fields with complex wrapping patterns. Even though such fields may be too complicated to be described exactly, topological considerations provide useful information on the field behavior.

At the photosphere, the field is believed to be strongly localized into discrete flux tubes. As these flux tubes extend into the tenuous corona, they expand to fill available space. The chaotic photospheric motions braid the tubes about each other, and twist up field lines within the tubes. This induces coronal structure on a lengthscale corresponding to the typical distance d between the photospheric *footpoints* of the tubes (say $d \sim 10^3$ km for a plage region). Because of this, coronal fields can be conveniently modelled as a collection of simple tubes braided about each other. The rate at which photospheric motions braid coronal flux tubes has been investigated by Berger (1986b). Of course, field lines emanating from a positive footpoint do not generally form a single tube connecting to a single negative footpoint. First, even if initially the field consists of unbroken flux tubes, reconnection can break the tubes and redistribute their flux. Secondly, at the photosphere, some small amount of flux presumably exists between the localized tubes. (Frazier and Stenflo (1972) estimate $\sim 5\%$ of the flux in active regions may lie outside the tubes.) Third, photospheric tubes have a finite lifetime, and may occasionally disperse and reform.

We suggest, however, that on the intermediate scale d the physics may be qualitatively studied by considering a collection of simple coherent flux tubes. Whether or not coherent flux tubes exist, photospheric motions can still provide topological structure on the scale of 10^3 km, which may be crucial for heating. For example, in the top half of figure 1, large bundles of flux are twisted and braided. At the middle of the figure these bundles lose their identity and new bundles form. Nevertheless, the twisting and braiding in the top half cannot be removed by ideal (nonresistive) motions, because these motions preserve the field topology. At lengthscales of 10^3 km, the ordinary resistive timescale is large ($\sim 10^{12}$ s for $T = 10^6$ K), so rapid reconnection is needed to dissipate such structure (Parker 1972, 1983). After providing a rigorous definition of *field topology*, we discuss how the topology of a finite collection of flux tubes may be classified. Finally, we discuss the relevance of field topology to the question of the existence of smooth magnetostatic equilibria (defined to be equilibria without singular electric current sheets).

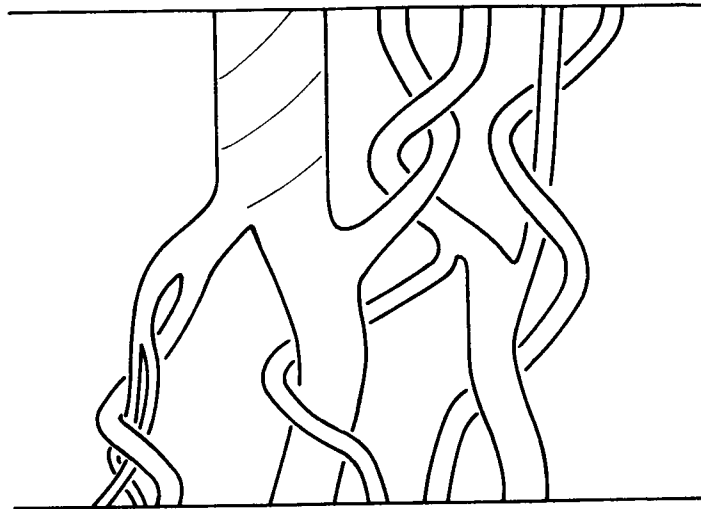


FIGURE 1

DEFINITION OF FIELD TOPOLOGY

Suppose we prepare the coronal field in some arbitrary initial state. Let the resistivity be zero, but include fluid viscosity. If the field is released from its initial state, it will thrash about until eventually relaxing to an equilibrium. Because the photosphere is relatively dense and slow, the footpoints should move little during this process ($\vec{B} \cdot \hat{n}|_{\text{photosphere}}$ is unchanged). This scenario has been employed recently to construct nonlinear force-free equilibria (Yang, Sturrock, and Antiochos 1986).

Because of the zero resistivity, field lines can not pass through each other during the motions. Thus, the initial wrapping pattern of the field lines severely restricts the possible wrapping patterns of the final equilibrium state. Of course, the initial and final wrapping patterns may look quite different, but in some deeper topological sense they must be equivalent. These considerations motivate the following definition: *two coronal field configurations are topologically equivalent if one can be deformed into the other by purely ideal motions vanishing at the photosphere* (Berger, 1986a). The *field topology* of a particular configuration refers to the *equivalence class* of topologically equivalent fields. Alternatively, the field topology may be considered as the set of all ideal MHD invariants of the field. With this definition, the field topology can only change if 1) the footpoints move, or 2) reconnection occurs. For example, the two braiding patterns in figure 2 are topologically equivalent.

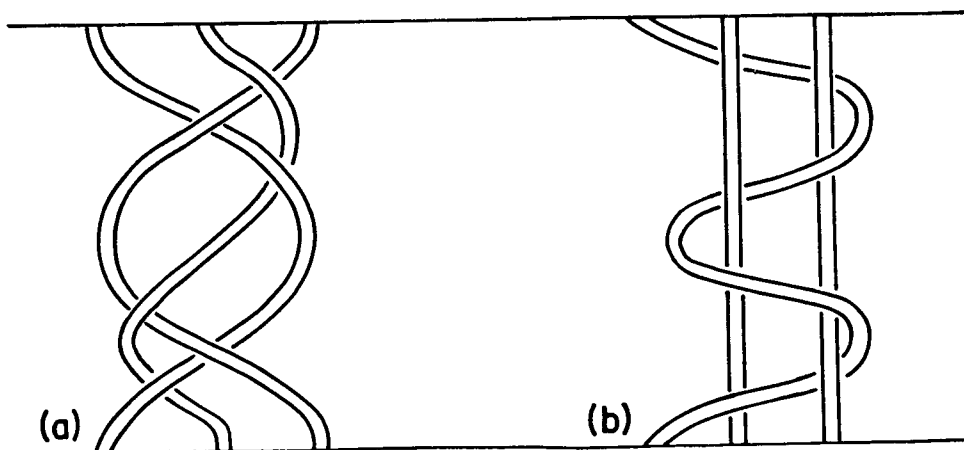


FIGURE 2

THE TOPOLOGY OF BRAIDED FLUX TUBES

First consider a single flux tube. We assume that the mapping of field lines from positive to negative endpoints is continuous. This mapping determines the topology, except for one source of ambiguity: the tube could be rotated by 2π without changing the mapping. Let \mathcal{T} be the net angle through which a field line rotates about the central axis of the tube (divided by 2π). The ambiguity can be removed by specifying \mathcal{T} for a field line on the outer boundary of the tube. The twist of other lines about the axis can be obtained by continuity. Alternatively, one could specify the *magnetic helicity* H (Moffatt 1969; Berger and Field 1984), which measures the tube's mean twist. For a uniformly twisted tube of twist \mathcal{T} and flux Φ , $H = \mathcal{T}\Phi^2$. In general, H/Φ^2 changes by ± 1 if the tube is rotated by 2π .

For two tubes, we suppose that the mapping of positive to negative footpoints is piecewise continuous, i.e. continuous within each tube, but not necessarily continuous across their boundary. Ambiguity arises because we can wrap one tube about the other through an angle $2n\pi$ without changing the mapping. Specifying the helicity of each tube individually, as well as the total helicity, will remove this difficulty. The total helicity is

$$H = \tau_1 \Phi_1^2 + \tau_2 \Phi_2^2 + 2L_{12}\Phi_1\Phi_2$$

(Berger 1986a). Here L_{12} measures the angle through which the tubes rotate about each other as they travel from positive to negative footpoints (averaged over the flux of the tubes). In general $L_{12} = r + n$, where $r \leq \frac{1}{2}$ is a function of the footpoint positions, and n changes by ± 1 if the tubes rotate about each other by an additional 2π . The quantity L_{12} is related to the Gauss linkage integral, in that it defines a linkage for curves with endpoints on a boundary surface. Two examples are shown in figure 3.

For three or more flux tubes, the order of braiding becomes important. For example, in figure 2 the linkage L between any two curves is zero, and yet the curves cannot be straightened out. We assume that the cross-section of each tube is simple enough to allow us to label a central field line the 'axis' of the tube. The braiding pattern of the axes can be described by finding a particularly simple configuration with the correct topology. Any braid can be placed in a unique form called a combed braid (Artin, 1950), where only one curve moves at a time (as in figure 2b). However, the configuration which minimizes the total length of the curves could be more relevant for modelling braided fields, because this configuration may approximate the pattern of the minimum magnetic energy state.

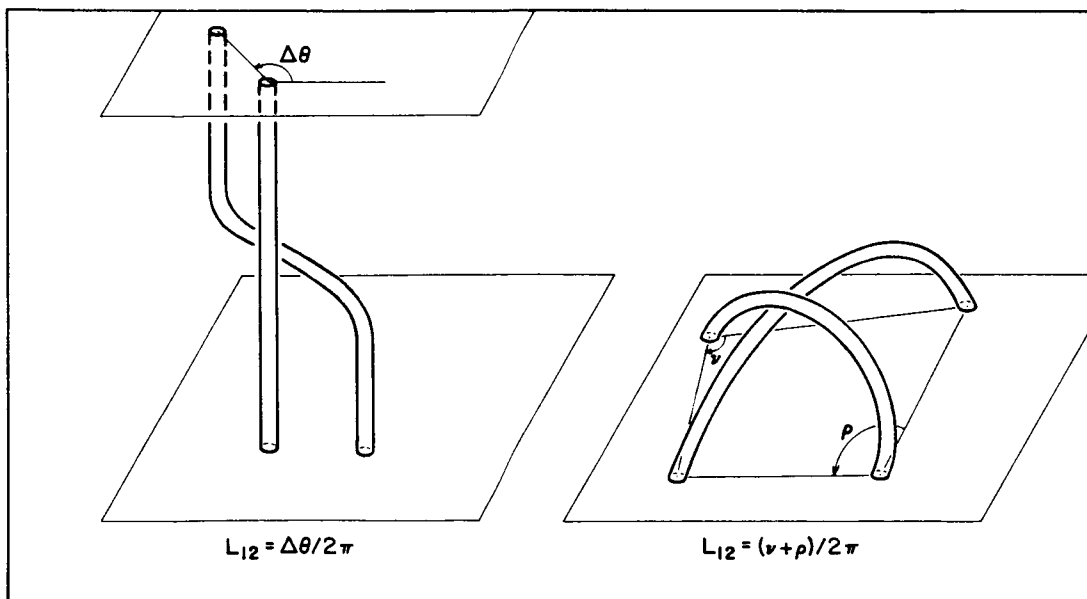


FIGURE 3

IMPLICATIONS FOR THE EXISTENCE OF SMOOTH EQUILIBRIA

Parker (1986) has shown that smooth equilibrium configurations (without current sheets) can only take very special forms. Because of this, he conjectures that very few field topologies allow smooth equilibrium solutions. Thus, as the coronal field topology evolves due to footpoint motions and reconnection, new smooth equilibria would generally be unavailable, leading to the formation of current sheets and reconnection. Examples of particular topologies which lack smooth solutions exist. For example, Low (1982) describes a two-dimensional quadrupole potential field with line tying on one boundary. If this field is distorted by continuous boundary motions, the only equilibrium solutions available consistent with the evolving footpoint distribution are potential fields with the wrong fieldline connectivity. The field contains a neutral point which is thought to collapse to a current sheet after the footpoint displacement (e.g. Sweet 1969).

Parker's assertion can be expressed in the following form: Of all possible field topologies, only a very small fraction possess smooth equilibrium configurations. This assertion has not been rigorously proven. One difficulty is that there exist infinitely many configurations corresponding to a given field topology (recall figure 2); if one configuration does not satisfy the conditions for smooth equilibrium, there conceivably might be another that does. However, topologically equivalent configurations share common features, such as the linkage numbers L between any two field lines. Such generic features might help determine the structure of possible equilibrium configurations. Here we will show that for the topology of figure 2, all possible configurations either have current sheets, or at least current layers which can be made arbitrarily thin.

Questions concerning the existence of equilibria are usually posed assuming that both the footpoint distribution and the boundary motions are continuous (van Ballegooijen 1985; Parker 1986; Zweibel and Li 1986); without continuity the formation of current sheets is trivial. Also, for simplicity the fields are assumed to stretch between two parallel planes. An initially uniform vertical field is subject to boundary motions which generate the topological structure. A result of van Ballegooijen (1985) should be mentioned in this context. Suppose we specify the transverse components of the field at one of the boundary planes. Van Ballegooijen found an ordering scheme which (within its domain of validity) can be used to obtain a smooth equilibrium configuration for the entire volume. What is not clear, however, is whether arbitrary field topologies possess equilibrium configurations that have smooth transverse fields at the boundaries. Thus the general existence of smooth equilibria for arbitrary field topologies remains unsettled.

Because of the strong localization of photospheric flux, let us model the coronal field by a collection of braided tubes, with a relatively small amount of 'intertube' flux providing continuity. In principle, the intertube flux can be made arbitrarily small. In practice, the intertube flux depends on the amount of background flux at the photosphere, the presence of sharp gradients in the photospheric velocity field, dissipative effects at the canopy level, etc. We will give an example where, in all possible configurations, the intertube flux carries substantial currents.

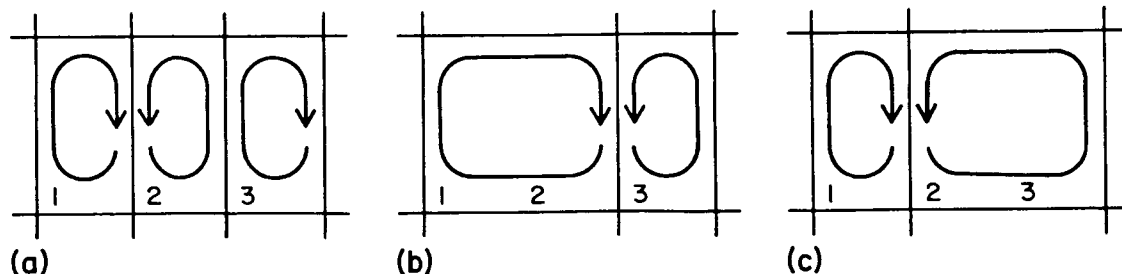


FIGURE 4

Consider an initially uniform vertical field. Subject the positive footpoints to flow patterns such as shown in figure 4. Neighboring field lines near a cell boundary diverge from each other exponentially in time, so the mapping of positive to negative footpoints will have steep but finite gradients at the cell boundaries. (I thank S. Antiochos for a discussion on this point). If the flow pattern does not change too rapidly, the

field forms approximately independent flux tubes above each cell. In figure 4a, three twisted flux tubes will be produced above the velocity cells shown, with alternating senses of twist (e.g. tube 1 will have positive helicity, 2 negative helicity, and 3 positive helicity). In figure 4b cells 1 and 2 have been combined. This flow pattern can be used to braid flux tubes 1 and 2 about each other. Figure 4c braids tubes 2 and 3. The topology of figure 2a can be produced by a sequence of six flow patterns alternating between 4b, and 4c.

Note that in figure 2 there are always pairs of tubes which, at different places in the figure, rotate both counterclockwise (+) and clockwise (−) about each other. As Parker (1986) points out, this situation creates grave difficulties for force-free fields ($\vec{J} = \alpha \vec{B}$). In particular, the condition $\vec{B} \cdot \nabla \alpha = 0$ implies that the sign of the current (which determines the sense of winding) does not change along a fieldline. We emphasize that *all possible configurations for this topology share this difficulty*: to obtain any other configuration, we must add additional braids of the tubes about each other. However, because the linking number L between any two tubes is a topological invariant, equal numbers of positive and negative twists must be added. In conclusion, the tubes themselves cannot carry the currents necessary to generate the correct field topology; these currents must instead be carried by the thin intertube flux. Unfortunately, we cannot say whether the intertube flux can itself satisfy the conditions for smooth (or stable!) equilibrium.

In conclusion, the fields in active regions to some approximation may resemble a collection of highly braided flux tubes, with only a small amount of flux in between. The topology of the braided tubes can be precisely described. If the example of figure 2 has any generality, then thin current layers, if not singular current sheets must inevitably form between the tubes. The braiding structure cannot be dissipated except by reconnection across these current layers. It is important to know for certain whether the layers have zero or finite thickness, because the width of the current layers can affect the dissipation timescale.

I thank B.C. Low, Aad van Ballegooijen, Spiro Antiochos, Gene Parker and Ellen Zweibel for clarifying discussions. The National Center for Atmospheric Research is supported by the National Science Foundation.

- Artin, E. 1950, "The Theory of Braids," *Am. Scientist* **38**, (112).
- Berger, M.A. 1986a, "Topological Invariants of Field Lines Rooted to Planes," *Geophys. Astrophys. Fluid Dyn.* **34**, (265).
- Berger, M.A. 1986b, "Braiding of Magnetic Flux by Two-Dimensional Random Boundary Motions," *preprint*.
- Berger, M.A. and G.B. Field 1984, "The Topological Properties of Magnetic Helicity," *J. Fluid Mech.* **147**, (133).
- Frazier, E.N. and Stenflo, J.O. 1972, "On the Small Scale Structure of Solar Magnetic Fields," *Solar Phys.* **27**, (330).
- Low, B.C. 1982, "Nonlinear Force-Free Magnetic Fields," *Rev. Geophys. Space Phys.* **20**, (145).
- Low, B.C. 1985, "Modelling Solar Magnetic Structures," in *Measurements of Solar Vector Magnetic Fields*, NASA Conf. Publ. 2374 (M.J. Hagyard, ed.), (49).
- Moffatt, H.K. 1969, "The Degree of Knottedness of Tangled Vortex Lines," *J. Fluid Mech.* **35**, (117).
- Parker, E.N. 1972, "Topological Dissipation and the Small-Scale Fields in Turbulent Gases," *Ap. J.* **174**, (499).
- Parker, E.N. 1983, "Magnetic Neutral Sheets in Evolving Fields, II. Formation of the Solar Corona," *Ap. J.* **264**, (642).
- Parker, E.N. 1986, "Equilibrium of Magnetic Fields with Arbitrary Interweaving of the Lines of Force I. Discontinuities in the Torsion," *Geophys. Astrophys. Fluid Dyn.* **34**, (243).
- Sturrock, P.A. and Y. Uchida 1981, "Coronal Heating by Stochastic Magnetic Pumping," *Ap. J.* **246**, (331).
- Sweet, P.A. 1969, "Mechanisms of Solar Flares," *Ann. Rev. Astron. Astrophys.* **7**, (149).
- van Ballegooijen, A.A. 1985, "Electric Currents in the Solar Corona and the Existence of Magnetostatic Equilibrium," *Ap. J.* **298**, (421).
- van Ballegooijen, A.A. 1986, "Cascade of Magnetic Energy as a Mechanism of Coronal Heating," *preprint*.
- Yang, W.H., P.A. Sturrock, and S.K. Antiochos 1986, "Force-free Magnetic Fields: the Magneto-Frictional Method," *preprint*.
- Zweibel, E.G. and H.S. Li 1986, "The Formation of Current Sheets in the Solar Atmosphere," *preprint*.

A COORDINATE FREE DESCRIPTION OF MAGNETOHYDROSTATIC EQUILIBRIA

P.C.H. Martens

NAS/NRC Research Associate
Laboratory for Astronomy and Solar Physics
NASA/Goddard Space Flight Center
Greenbelt, Maryland 20771

INTRODUCTION

This paper addresses the question what geometrical restrictions are imposed on static magnetic fields by the MagnetoHydro-Static (MHS) equations. This question is of obvious importance for the problem of coronal heating, since it has been argued by Parker (1972, 1979 and 1986; see references therein) that the MHS-equations in general overdetermine the magnetic field structure and that consequently the field needs to have some sort of symmetry to satisfy all the constraints imposed on it by the equations. The field in the solar corona is determined by the MHS equations and the boundary conditions at the corona/photosphere interface. The latter are the normal component of the magnetic field at the boundary (to ensure the continuity of the magnetic field) and the connectivity of the field lines, defined as the positions of all field line footpoints at the boundary (because the field lines are frozen in, Sturrock and Woodbury, 1967). These boundary conditions are completely arbitrary, because they are determined by the magnetic fields and the fluid motions in the photosphere and convection zone, that cannot be altered by the relatively weak forces from the coronal magnetic field. The general mathematical problem is therefore to determine the solutions of the MHS-equations in the corona subject to an arbitrary normal component of the magnetic field at the boundary and arbitrary connectivity.

It is very unlikely that these boundary conditions would conspire to satisfy any symmetry requirement that the MHS equations might impose. And even if they would at a given moment, only minor footpoint displacements - as a result of the photospheric velocity field - would destroy the symmetry. Hence the coronal magnetic field cannot be in static equilibrium at any time, and, according to Parker (1983), the force free condition will break down at some locations in the corona, where current sheets will form. In these sheets the dissipation of magnetic field is much larger than that calculated with classical resistivity and the resulting heating rate may be large enough to explain the observed non-thermal heating of the corona. This process is called **topological heating**.

Recently, however, Parker's hypothesis has been challenged by Van Ballegooijen (1985) and Antiochos (1986); see also their contributions in this chapter. Van Ballegooijen points out an error in Parker's (1972) original demonstration of the need for an ignorable coordinate and furthermore, by improving upon Parker's analysis, gives an algorithm for calculating solutions to the MHS equations, subject to arbitrary boundary conditions. Antiochos argues that the problem is generally well posed by showing that when the magnetic field is expressed in Euler potentials, the topology of the field in the corona is completely determined by the values of the potential at the boundary. Consequently there is no need for the formation of current sheets in

these analyses.

Clearly the question whether there is the requirement of some sort of symmetry in the solutions of the MHS equations deserves further attention. This symmetry has to be of a subtler form than that of an ignorable coordinate as once proposed (Parker, 1972), since recently explicit analytical examples have been given of fully 3-D magnetostatic equilibria (Low, 1985). The latter solutions still show some form of symmetry, however.

The problem is the more intriguing because it has recently been shown quite convincingly by Tsinganos *et al.* (1984) and Moffat (1985) - in very different ways - that magnetostatic equilibria in Tokamak type structures do lead to topological dissipation, when they do not exhibit symmetry. However, in Tokamaks the boundary conditions are quite different: here the requirement is that the normal component of the field vanishes everywhere at the surface of the containment vessel and hence the field is self contained (see Martens, 1985, for a comparison). The field lines in a Tokamak are either infinite in length, or close in themselves, quite the contrary of the structure of closed coronal fields, where the field lines are anchored at both ends. If there is a difference between closed coronal magnetic fields and Tokamak-type fields with regard to their intrinsic symmetry, this difference must be caused by the nature of the boundary conditions. The difference then is probably related to the fact that the corona/photosphere interface takes up the stresses from the coronal field, while the containment vessel of a Tokamak obviously doesn't.

In this paper I will take up the issue of the geometrical constraints on magnetostatic equilibria from a somewhat different point of view. I will write the MHS equations in a general coordinate system - not necessarily orthogonal - and then choose the coordinates in such a way that the pressure gradients and current density vector are along coordinate lines, which makes their expressions very simple. I will then try to determine what constraints the MHS equations impose on the geometry of the solutions, that is expressed in the metric tensor. The first results do indicate some restrictions to the possible geometries of the solutions, but these do not seem to represent some sort of symmetry. The analysis of this paper cannot be regarded as completed, and more definite results will be published in the literature.

THE MHS EQUATIONS IN ARBITRARY COORDINATE SYSTEMS

The basic equations governing magnetostatic equilibria are well known

$$(\nabla \times \vec{B}) \times \vec{B} - \nabla P = \vec{0} \quad (1),$$

$$\nabla \cdot \vec{B} = 0 \quad (2).$$

There are no general solutions known to this deceptively simple looking set of equations. The system is nonlinear because of the Lorentz-force term in Eq. (1): the sum of two solutions in general does not represent a third solution. All particular analytical solutions that are known to date have some sort of symmetry (Low, 1985).

An alternative notation of Eqs. (1) and (2) in an arbitrary orthogonal coordinate system is found after introduction of the metric tensor

$$g_{ij} = \begin{bmatrix} h_1^2 & 0 & 0 \\ 0 & h_2^2 & 0 \\ 0 & 0 & h_3^2 \end{bmatrix} \quad (3),$$

where the h_i represent the length of the unit vectors. The components of the magnetic field are identified with the three independent components of an antisymmetric 3-D tensor B^{ij} ,

$$B^{12} = \frac{B_3}{h_1 h_2}, \quad B^{23} = \frac{B_1}{h_2 h_3}, \quad B^{31} = \frac{B_2}{h_1 h_3} \quad (4).$$

The identification of the components of the magnetic field with those of an antisymmetric tensor, instead of with the components of a contravariant vector, will lead to a particularly simple formulation of the equations. Moreover, it accounts properly for the fact that the magnetic field is a pseudo-vector, instead of a real vector: by inspection of the expression for the Lorentz-force one finds that the magnetic field must remain the same under a mirror transformation of the the coordinates ($x \rightarrow -x$, etc.), since the Lorentz force and the current both will change sign.

The contravariant components of the current density vector are given by

$$j^i = \frac{(\vec{j} \cdot \hat{x}_i)}{h_i} \quad (5),$$

while the covariant components of the pressure gradient are given in the same way.

The basic equations in this notation are

$$P_{;k} = j^i B_{ki} \quad (6),$$

$$j^i = B^{ij} j_{;j} = \frac{1}{\sqrt{g}} (\sqrt{g} B^{ij})_{;j} \quad (7),$$

$$\{B_{ij;k}\} = 0 \quad (8).$$

Here $j_{;i}$ denotes covariant differentiation and j_i ordinary differentiation with respect to the variable denoted by the index. $\{...\}$ means a summation over all permutations of the indices of the tensor within the brackets. For the antisymmetric magnetic tensor it reduces to

$$B_{12;k} + B_{23;k} + B_{31;k} = 0 \quad (9).$$

FLUX SURFACE COORDINATES

Now I generalize the MHS equations (6) to (8) and suppose their validity in non-orthogonal coordinate systems. The expressions remain the same of course, only the metric tensor has off-diagonal elements. This allows one to

choose a coordinate system that makes the equations particularly simple. First I choose the pressure gradient parallel to the first unit vector and hence

$$P = P(x_1) \quad (10).$$

The isobaric surfaces are now by definition surfaces of constant x_1 . Further I choose x_2 and x_3 perpendicular to x_1 , but not necessarily perpendicular to each other. This means that the metric tensor has the form

$$g_{ij} = \begin{pmatrix} g_{11} & 0 & 0 \\ 0 & g_{22} & g_{23} \\ 0 & g_{23} & g_{33} \end{pmatrix} \quad (11),$$

and has therefore 4 independent components. From the force balance equations (7) and Eq. (11) it can now easily be shown that

$$\begin{aligned} j^1 &= 0 \\ B^{23} &= -B^{32} = 0 \\ B_{23} &= -B_{32} = 0 \end{aligned} \quad (12).$$

The equation expressing the divergencelessness of the magnetic field, Eq. (8), reduces to

$$B_{12}{}_{,3} + B_{31}{}_{,2} = 0 \quad (13),$$

with the solution,

$$\begin{aligned} B_{12} &= A_{,2} \\ B_{13} &= A_{,3} \end{aligned} \quad (14),$$

and $A(x_1, x_2, x_3)$ an arbitrary function. Now that the three components of the magnetic field have been reduced to one unknown function only one component of the force-balance equations remains to be satisfied,

$$P_{,1} = j^2 A_{,2} + j^3 A_{,3} \quad (15),$$

while the demand $j^1 = 0$ leads to a second constraint on the solutions (reminiscent of Low's (1980) compatibility relation).

So far the non-orthogonality of the coordinates has not been used. I make a small digression from my main argument now to explore somewhat further the compatibility constraint in orthogonal systems, $j^1 = 0$.

$$(\sqrt{g} B^{12})_{,2} + (\sqrt{g} B^{13})_{,3} = 0 \quad (16).$$

In an orthogonal coordinate system I can now reduce the force balance equation and the compatibility constraint to:

$$\left[\frac{A_{,2} h_3}{h_1 h_2} \right]_{,2} + \left[\frac{A_{,3} h_2}{h_1 h_3} \right]_{,3} = 0 \quad (17),$$

and,

$$h_1 h_2 h_3 P_{,1} = A_{,2} \left[\frac{A_{,2} h_3}{h_1 h_2} \right]_{,1} + A_{,3} \left[\frac{A_{,3} h_2}{h_1 h_3} \right]_{,1} \quad (18).$$

By trial and error one may find that it is extraordinarily difficult to obtain functions A that satisfy both constraints Eqs. (17) and (18). To give a short and very simple example I shall investigate the case where the isobaric surfaces are cylinders. We have $(x_1, x_2, x_3) = (r, \phi, z)$, $h_1 = h_3 = 1$, $h_2 = r$, and therefore Eqs. (17) and (18) reduce to

$$A_{,\phi\phi} + r^2 A_{,zz} = 0 \quad (19).$$

$$r P_{,r} = A_{,\phi} \left(\frac{A_{,\phi}}{r} \right)_{,r} + A_{,z} (A_{,z} r)_{,r} \quad (20).$$

The only solution of Eq.(19) that is consistent with $P = P(r)$ is

$$A(r, \phi, z) = f(r)z + g(r)\phi \quad (21),$$

and Eq. (20) takes the well known form

$$P_{,r} = \frac{1}{2} (B_{,\phi}^2 + B_{,z}^2)_{,r} + B_{,\phi}^2 / r \quad (22),$$

after the identification

$$g(r) = B_{,z} r, \quad f(r) = -B_{,\phi} \quad (23).$$

The solutions of Eq. (22) are well known (Lüst and Schlüter, 1954). I conclude that the requirement of cylindrical isobares introduces the necessity of cylindrical symmetry of the magnetic field. However, the general question one would like to answer remains: what are the restrictions imposed on the function A by Eqs. (17) and (18) in any coordinate system?

NON-ORTHOGONAL COORDINATES

I will proceed with the main line of my argument now and specify further the choice of the coordinate system. I choose the direction of the second unit vector along the current density vector, i.e.

$$j^1 = (0, j^2, 0) \quad (24).$$

It can be shown that with this choice of the second unit vector the coordinate system cannot be orthogonal anymore. In Fig. 1 a cylindrical surface is drawn that contains a set of field lines and a set of current density vectors. The first unit vector is by definition perpendicular to this surface, while the other two must lie within the surface. In the figure a current line is drawn which has the second unit vector everywhere parallel to it. In an orthogonal coordinate system the third unit vector must be everywhere perpendicular to the second one, but if one follows the third coordinate from point (x_1, x_2, x_3)

one finds that it intersects again the current line at the point $(x_1, x_2, x_3 + \Delta x_3)$. However, one may also follow the current line from the point (x_1, x_2, x_3) and then the second intersection is reached at $(x_1, x_2 + \Delta x_2, x_3)$. This point is physically the same as $(x_1, x_2, x_3 + \Delta x_3)$ and hence it must have the same coordinates; if not, the coordinate system becomes double (and multi-) valued. This requirement can be met by having x_2 and x_3 as cyclic coordinates: $x_2 + \Delta x_2 \equiv x_2$, and $x_3 + \Delta x_3 \equiv x_3$ (just as in spherical coordinates). However, now one runs into the contradiction that two physically different points (the first and the second intersection) have identical coordinates; a situation which is also undesirable. I conclude that it is impossible to choose a consistent isobaric orthogonal coordinate system if $\vec{j} // \vec{x}_2$.

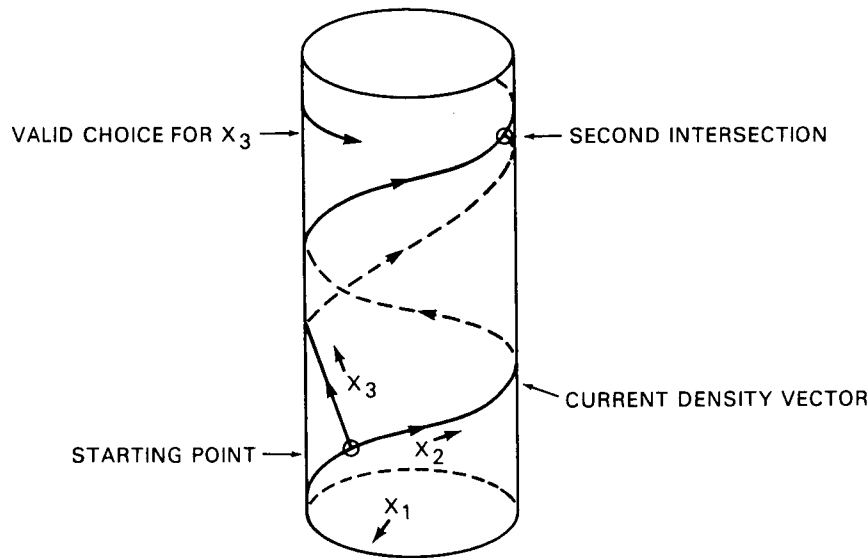


Figure 1. A demonstration of the inconsistency of an orthogonal coordinate system with one unit vector parallel to the pressure gradient and another with the current density vector.

A valid choice for the third coordinate is indicated in Fig. 1. It is clear that as one follows the third unit vector, the line will close in itself and there is no inconsistency. With this choice the third vector is not perpendicular anymore to the second and hence the term $g_{23}=g_{32}$ in the metric tensor must be nonzero.

Eqs. (14), (15) and (16) were derived for the metric Eq. (11). By the special choice for the second coordinate one finds in addition, because $j^3=0$,

$$(\sqrt{g}B^{31})_{,1} = 0 \quad (25).$$

Eqs. (16) and (25) are satisfied when

$$(\sqrt{g}B^{21}) = f(x_1, x_3) + m_{,3}(x_2, x_3) \quad (26),$$

and

$$(\sqrt{g}B^{31}) = -m_{\varphi 2}(x_2, x_3) \quad (27),$$

with f and m arbitrary functions. The force balance equation (15) now reduces to

$$\sqrt{g}P_{\varphi 1} = A_{\varphi 2}f_{\varphi 1} \quad (28).$$

The contravariant components of the field tensor may be eliminated with

$$A_{\varphi 2} = g_{11}g_{22}B^{12} + g_{11}g_{23}B^{13} \quad (29),$$

$$A_{\varphi 3} = g_{11}g_{32}B^{12} + g_{11}g_{33}B^{13} \quad (30),$$

and one is left with three equations, (26), (27) and (28), for the function A . For a given geometry g_{ij} , and arbitrary functions f , m and P , the function A is clearly overdetermined and consequently some restrictions must apply to the possible choices of the geometry. In this stage of the research it is not clear yet what these restrictions are, although it seems that the restrictions do not necessarily impose an ignorable coordinate.

More work along the lines of this paper is needed to shed light on the geometries that are consistent with MHS-equilibria. In particular the restrictions that the boundary conditions impose on the possible solutions will be investigated.

REFERENCES

- Antiochos, S.K. 1986: "The Topology of Force-Free Magnetic Field and its Implications for Coronal Activity", *Astrophys. J.*, in press.
- Low, B.C. 1980: *Solar Phys.* **67**, 57.
- Low, B.C. 1985: *Astrophys. J.* **293**, 31.
- Lüst, R., Schlüter, A. 1954: *Z. Astrophys.* **34**, 263.
- Martens, P.C.H. 1985: **"Magnetic Reconnection & Turbulence"**, M.A. Dubois, D. Gresillon, M.N. Bussac (eds.), p.79, Editions de Physique, Orsay.
- Moffat, H.K. 1985: *J. Fluid Mech.* **159**, 359.
- Parker, E.N. 1972: *Astrophys. J.* **174**, 499.
- Parker, E.N. 1979: **"Cosmical Magnetic Fields"**, pp. 359-391, Oxford, Clarendon Press.
- Parker, E.N. 1983: *Astrophys. J.* **264**, 642.
- Parker, E.N. 1986: *Geophys. Astrophys. Fluid Dyn.* **35**, in press.
- Solov'ev, L.S. 1972: **"Reviews of Plasma Physics"**, Vol. 6, p.239, M.A. Leontovich (ed.), Consultants Bureau, New York.
- Sturrock, P.A., Woodbury, E.T. 1967: **"Plasma Astrophysics"**, p.155, P.A. Sturrock (ed.), Academic Press, New York.
- Tsinganos, K.C., Distler, J., Rosner, R. 1984: *Astrophys. J.* **278**, 409.
- Van Ballegoijen, A.A. 1985: *Astrophys. J.* **298**, 421.

CASCADE MODEL OF CORONAL HEATING

A.A. van Ballegooijen
Center for Astrophysics
Cambridge, Massachusetts

INTRODUCTION

Coronal heating theories can be classified as either wave-heating or current-heating theories. According to the wave-heating model, convective motions below the solar surface generate MHD waves, which then propagate outward and dissipate their energy in the corona. Observations of line widths in the solar chromosphere seem to rule out the possibility that the corona is heated by acoustic- or slow mode MHD waves (Athay and White 1978), leaving Alfvén- and fast mode waves as possible candidates of energy transport. According to the current-heating model, the sub-surface convective motions cause random displacements of the photospheric magnetic footpoints, leading to twisting and braiding of the coronal magnetic field. The field-aligned electric currents associated with these twists are subject to resistive dissipation. The current-heating model applies only to "closed" magnetic structures such as coronal loops, whereas the wave model applies to both open structures (coronal holes) and closed structures (active regions). Another difference between the two models is the time scale τ of the photospheric motions: in wave-heating models, τ is smaller than or equal to the resonance time $2L/v_A$ of the loop, whereas in current-heating models $\tau \gg 2L/v_A$ (L is the loop length, v_A is the Alfvén speed).

The details of the mechanisms responsible for wave- and current dissipation are presently not well understood. The problem is that dissipative processes such as plasma resistivity and viscosity are unimportant on the large spatial scales of observable coronal structures: dissipation can occur only if there are strong gradients in the magnetic- and/or velocity field, with length scales of 1 km or less in the corona. A crucial problem in any theory of coronal heating is, therefore, to explain how such small-scale structures are generated. In the context of the wave-heating theory, phase-mixing of Alfvén waves, due to density inhomogeneities in the solar corona, provides a way to produce small-scale structures (Heyvaerts and Priest 1983, Sakurai and Granik 1984, Steinolfson 1985).

In the current-heating theory, which is the subject of the present paper, the magnetic energy associated with the braided magnetic field must be similarly transferred to smaller scales. The process by which this "cascade" of magnetic energy occurs is not well understood. Parker (1972, 1979, 1983, 1986) suggests that the process is due to an intrinsic nonequilibrium of magnetic fields: the equations of magnetostatic equilibrium seem to allow solutions only for certain restrictive cases, in which the vertical component of the vorticity in the photosphere is essentially a constant of motion (Parker 1986). Since the motions on the Sun do in general not have this nice property, the magnetic field cannot simply adjust to the slow, random motions applied at the photosphere, but is forced to evolve on the Alfvén time scale L/v_A . Parker assumes this dynamical relaxation leads to the formation of discontinuities (current sheets), where magnetic reconnection will occur until the topological constraints are satisfied. Hence, according to the nonequilibrium model the formation of small-scale structures is due to a relaxation process that takes place on the Alfvén time scale.

Recently, I proposed a somewhat different picture of the cascade process (van Ballegooijen 1985, 1986, hereafter papers I and II). According to this model there are no special restrictions on the velocity fields that may be applied at the photospheric boundary: the magnetic field in a coronal

loop can evolve slowly through a series of equilibrium states, without the necessity for magnetic reconnection. Hence, in our opinion the dynamical relaxation process proposed by Parker does not occur. The necessary condition for equilibrium found by Parker (1972) was shown to result from an incorrect ordering of terms in Parker's perturbation scheme (cf. appendix of paper I). Therefore, a firm mathematical basis for Parker's concept of nonequilibrium seems to be lacking.

In the absence of nonequilibrium, the magnetic field evolves through a series of equilibrium states. Hence the formation of small-scale structures such as current sheets cannot be due to the relaxation process by which magnetic equilibria are reached; if current sheet formation occurs in closed coronal structures, it must be a result of the quasi-static evolution process. We expect, therefore, that the time scale for current sheet formation is related to the time scale τ of the photospheric motions. To test this hypothesis, we need to understand the properties of braided magnetic fields as they evolve quasi-statically in response to random motions applied at the photospheric boundary. This is a rather difficult 3-dimensional problem, and a general procedure for computing statistical quantities such as the magnetic power spectrum are not known. However, one can gain some insight into the nature of the cascade process from a simplified 2-dimensional problem, in which only a single plane transverse to the mean magnetic field is considered (cf. paper II). In the following this model is briefly discussed.

STATISTICAL MODEL

Consider an initially uniform field $\mathbf{B}_0 = B_0 \hat{z}$, extending between two flat boundary plates located at $z = 0$ and $z = L$. We assume that the field is perturbed by a random, incompressible motion in the boundary plates, characterized by a correlation length ℓ and a correlation time τ (we assume $\ell \ll L$). Then the velocity field in the interior of the volume is given by:

$$\mathbf{v} = [v_x(x, y, z, t), v_y(x, y, z, t), 0], \quad (1)$$

and the magnetic field is approximately given by:

$$\mathbf{B} = B_0[b_x(x, y, z, t), b_y(x, y, z, t), 1], \quad (2)$$

where b_x and b_y denote the transverse field components ($b_x, b_y \ll 1$). Assuming ideal MHD, the induction equation can be written as:

$$\frac{db_x}{dt} = \frac{dv_x}{dz} \equiv a_x, \quad (3a)$$

$$\frac{db_y}{dt} = \frac{dv_y}{dz} \equiv a_y, \quad (3b)$$

where d/dz is the spatial derivative along fieldlines, and d/dt is the co-moving time derivative.

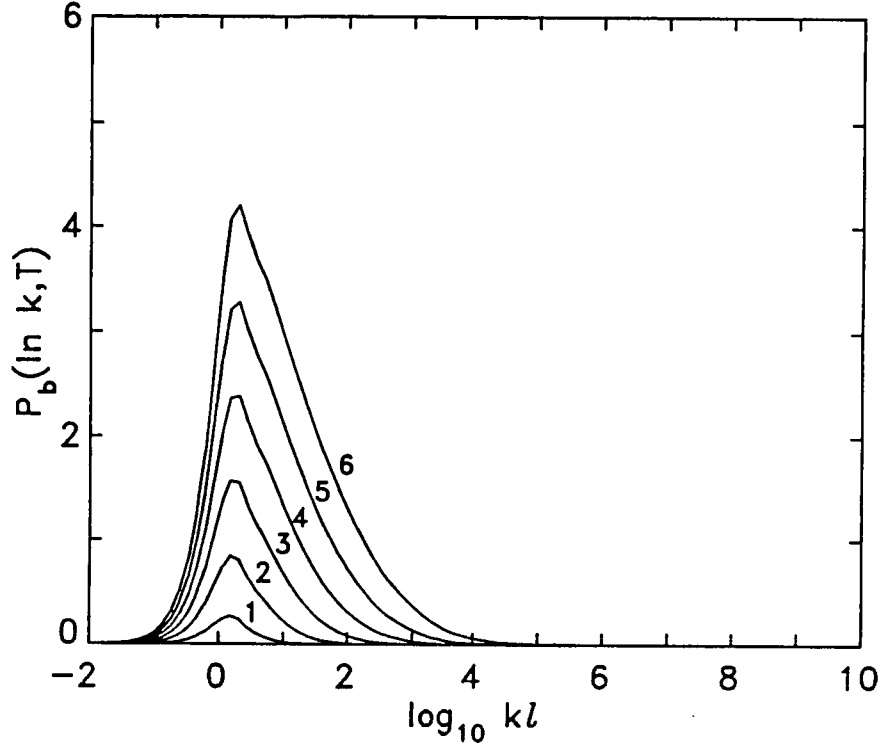
The basic idea of the model is to consider an arbitrary plane $z = z_0$ in the interior of the volume ($0 < z_0 < L$), and to consider the velocity $\mathbf{v}(x, y, z_0, t)$ and the velocity gradient $a_x(x, y, z_0, t)$ at this plane as the *independent* statistical variables. Integration of equation (3a) then yields the transverse field b_x :

$$b_x(\mathbf{R}, T) = \int_0^T a_x(\mathbf{r}(t), t) dt, \quad (4)$$

where $\mathbf{r}(t) = [x(t), y(t), z_0]$ is the path in the z_0 -plane that ends at position \mathbf{R} on time T . The correlation between the b_x -values at two different points \mathbf{R}_1 and \mathbf{R}_2 in the z_0 -plane is:

$$\begin{aligned} C_b(\Delta\mathbf{R}, T) &\equiv \langle b_x(\mathbf{R}_1, T) b_x(\mathbf{R}_2, T) \rangle \\ &= \int_0^T \int_0^T \langle a_x(\mathbf{r}_1(t'), t') a_x(\mathbf{r}_2(t''), t'') \rangle dt' dt''. \end{aligned} \quad (5)$$

By making suitable assumptions about the statistical properties of a_x , one can evaluate the right hand side of equation (5), which yields the magnetic correlation function $C_b(\Delta R, T)$. We omit here the details of the derivation, which is given in paper II. The magnetic power spectrum $P_b(k, T)$ as function of transverse wavenumber k is obtained by taking the Fourier transform of C_b with respect to ΔR .



The results of the calculation are displayed in the above figure, which shows the magnetic power spectrum (per unit $\log k$) as function of dimensionless wavenumber kl . The different curves correspond to times $T/t_b = 0.4, 0.8, 1.2, 1.6, 2.0$, and 2.4 , where t_b is the "braiding" time defined by:

$$t_b \equiv \frac{\ell^2}{u^2 \tau}, \quad (6)$$

and where ℓ , τ and u are the correlation length, correlation time and r.m.s. velocity of the photospheric motions, respectively. Note that magnetic energy, injected into the system at wavenumber $k \sim \ell^{-1}$, is rapidly transferred to larger k : the maximum wavenumber in the spectrum increases exponentially with time, implying a rapid cascade of magnetic energy towards smaller length scales. This cascade takes place on the time scale t_b , which is determined entirely by the statistical properties of the photospheric motions. Note, that t_b is somewhat larger than the correlation time τ , since the fluid displacements over one correlation time are generally smaller than the correlation length ($u\tau \leq \ell$).

The exponential increases of the maximum wavenumber derives from the fact that, in an incompressible random flow, the separation between closely neighboring fluid particles $\mathbf{r}_1(t)$ and $\mathbf{r}_2(t)$ increases exponentially with time; the e-folding time is of order t_b . Hence, the correlation function $\langle a_x(\mathbf{r}_1(t), t) a_x(\mathbf{r}_2(t), t) \rangle$ appearing on the right hand side of equation (5) vanishes for time differences $(T - t)$ larger than $t_b \ln(\ell/\Delta R)$, when the separation of the

particles becomes larger than the correlation length. As a result the correlation function $C_b(\Delta R, T)$ has a logarithmic dependence on ΔR , with a sharp peak at $\Delta R = 0$. The Fourier transform of C_b therefore has significant power at high wavenumbers.

The electric current density, $j_z = (c/4\pi)[\partial B_y/\partial x - \partial B_x/\partial y]$, involves the derivatives of the transverse field, and therefore the power spectrum of current-density fluctuations is given by $P_j(k, T) = k^2 P_b(k, T)$. It can be shown that the integral of $P_j(k, T)$ over wavenumber, which is equal to $\langle j_z^2(T) \rangle \equiv j_{rms}^2$, increases exponentially with time:

$$j_{rms}(T) \sim \frac{c}{4\pi} \frac{B_0}{L} \exp \left[2\sqrt{2\pi} \frac{T}{t_b} \right]. \quad (7)$$

This should be contrasted with the "free" magnetic energy, which increases only quadratically with time:

$$\frac{\langle B_{\perp}^2(T) \rangle}{8\pi} \approx \frac{B_0^2}{8\pi} \frac{2u^4 \tau^2 T^2}{\ell^2 L^2}. \quad (8)$$

Since the cascade of energy towards smaller scales proceeds exponentially in time, magnetic diffusion and reconnection will become important after a time t_1 which depends logarithmically on the magnetic Reynolds number:

$$t_1 \approx t_b \frac{\ln R_m}{6\sqrt{2\pi}}. \quad (9)$$

Here R_m is defined as:

$$R_m \equiv \frac{\ell^2}{\eta t_b}, \quad (10)$$

where η is the magnetic diffusivity based on the classical (Ohmic) resistivity. For the sun, $R_m \sim 10^{10}$, so that $t_1 \approx 1.5t_b$. This implies that only a small number of braids can be introduced into the system before reconnection becomes important.

I suggest that for $t \gg t_1$ a *statistically stationary state* develops, in which there is a continuous transfer of magnetic energy from the scale ℓ where the energy is put in, to the scale $\ell R_m^{-1/2}$ where the energy is dissipated. The dissipation rate E_H in this stationary regime can be estimated as the time derivative of expression (8), evaluated at the time t_1 when reconnection processes first become important; this yields:

$$E_H \sim \frac{B_0^2}{8\pi} \frac{2u^2 \tau \ln R_m}{3L^2 \sqrt{2\pi}}, \quad (11)$$

i.e., the heating rate depends logarithmically of the Reynolds number. Note that E_H is proportional to the product $u^2 \tau$, which is directly related to the effective diffusion constant of the photospheric motions:

$$D = \frac{1}{2} u^2 \tau \sqrt{2\pi}. \quad (12)$$

Observations of the spreading of active regions over time scales of months indicate that D is in the range of 150 - 425 km²/s (DeVore et al. 1985). With $B_0 = 100$ G and $L = 10^5$ km, parameters typical for large active regions, we find $E_H \sim 5 \times 10^{-5}$ erg/cm³/s, which corresponds to an energy flux of 2.5×10^5 erg/cm²/s at each footpoint. This energy flux is a factor 40 smaller than the observed radiative- and conductive losses in active regions (cf. Withbroe and Noyes 1977). There are a number of possible reasons for this discrepancy:

- 1) Our assumption that E_H equals the energy input rate at $t = t_1$ probably under-estimates the heating rate, since the input rate may continue to increase for some time after reconnection

first becomes important. To see whether this is the case, it is necessary to include magnetic diffusion in the above analysis.

- 2) There may be small-scale photospheric motions with $D > 1000 \text{ km}^2/\text{s}$ which have so far escaped detection.
- 3) It is possible that random photospheric motions are not the primary cause of coronal heating in active regions; periodic motion associated with Alfvén waves may be a more important source of energy.

In summary, we suggest that the quasi-static evolution of coronal magnetic structures is characterized by a cascade of magnetic energy to smaller length scales. This cascade process takes place on a time scale t_b determined entirely by the photospheric motions. The Ohmic heating rate E_H in the statistically stationary state was estimated using observational data on the diffusivity of photospheric motions; E_H turned out to be too small by a factor 40 when compared with observed coronal energy losses. However, given the fact that our theoretical estimate is based on a rather uncertain extrapolation to the diffusive regime, current heating cannot be ruled out as a viable mechanism of coronal heating.

REFERENCES

- Athay, R.G. and White, O.R. 1978, "Chromospheric and coronal heating by sound waves", *Ap. J.*, **226**, 1135
- DeVore, C.R., Sheeley, Jr., N.R., Boris, J.P., Young, Jr., T.R., and Harvey, K.L. 1985, "Simulations of magnetic-flux transport in solar active regions", *Solar Phys.*, in press
- Heyvaerts, J. and Priest, E.R. 1983, "Coronal heating by phase-mixed shear Alfvén waves", *Astr. Ap.*, **117**, 220
- Parker, E.N. 1972, "Topological dissipation and the small-scale fields in turbulent gases", *Ap. J.*, **174**, 499
- Parker, E.N. 1979, *Cosmical Magnetic Fields* (Oxford: Clarendon), Chap. 14
- Parker, E.N. 1983, "Magnetic neutral sheets in evolving fields. II. Formation of the solar corona", *Ap. J.*, **264**, 642
- Parker, E.N. 1986, "Dynamical nonequilibrium of magnetic fields with arbitrary interweaving of the lines of force. I. Discontinuities in the torsion", *Geophys. Ap. Fluid Dyn.*, **34**, 243
- Sakurai, T. and Granik, A. 1984, "generation of coronal electric currents due to convective motions on the photosphere. II. Resonance and phase mixing of Alfvén waves", *Ap. J.*, **277**, 404
- Steinolfson, R.S. 1985, *Ap. J.*, **295**, 213
- van Ballegooijen, A.A. 1985, "Electric currents in the solar corona and the existence of magnetostatic equilibrium", *Ap. J.*, **298**, 421 (paper I)
- van Ballegooijen, A.A. 1986, "Cascade of magnetic energy as a mechanism of coronal heating", *Ap. J.*, submitted (paper II)
- Withbroe, G.L., and Noyes, R.W. 1977, "Mass and energy flow in the solar chromosphere and corona", *Ann. Rev. Astr. Ap.*, **15**, 363

HEATING OF THE SOLAR CORONA BY THE RESONANT ABSORPTION OF ALFVEN WAVES

Joseph M. Davila

Laboratory for Astronomy and Solar Physics
NASA-Goddard Space Flight Center
Greenbelt, MD 20771

INTRODUCTION

It has been suggested that resonance absorption of low frequency magnetohydrodynamic waves could be responsible for heating the solar corona (Ionson, 1982; Hollweg, 1984). In this paper an improved method for calculating the resonance absorption heating rate is discussed and the results are compared with observations in the solar corona. To accomplish this, the wave equation for a mildly dissipative, compressible plasma is derived from the linearized magnetohydrodynamic equations for a plasma with transverse Alfven speed gradients. For parameters representative of the solar corona, it is found that a two scale description of the wave motion is appropriate. The large scale motion, which can be approximated as nearly ideal, has a scale which is on the order of the width of the loop. The small scale wave, however, has a transverse scale much smaller than the width of the loop, 0.3-250 km, and is highly dissipative. These two wave motions are coupled in a narrow resonance region in the loop where the global wave frequency equals the local Alfven wave frequency. Formally this coupling comes about from using the method of matched asymptotic expansions to match the inner and outer (small and large scale) solutions. The resultant heating rate can be calculated from either of these solutions. A formula derived using the outer (ideal) solution is presented, and shown to be consistent with observations of heating and line broadening in the solar corona.

DERIVATION OF THE BASIC EQUATIONS

The linearized momentum and induction equations can be written as

$$\frac{\partial \mathbf{v}}{\partial t} = - \frac{\nabla p}{\rho_0} + \frac{1}{4\pi\rho_0} \left[(\mathbf{B}_0 \cdot \nabla) \mathbf{B} + (\mathbf{B} \cdot \nabla) \mathbf{B}_0 \right] + \beta^2 \nabla^2 \mathbf{v} + \gamma^2 \nabla(\nabla \cdot \mathbf{v}) \quad (1)$$

$$\frac{\partial \mathbf{B}}{\partial t} = (\mathbf{B}_0 \cdot \nabla) \mathbf{v} - \mathbf{B}_0 (\nabla \cdot \mathbf{v}) - (\mathbf{v} \cdot \nabla) \mathbf{B}_0 + \alpha^2 \nabla^2 \mathbf{B} \quad (2)$$

where $\alpha^2 = c^2/4\pi\sigma$, $\beta^2 = \eta_{\perp}/\rho_0$ and $\gamma^2 = \eta_{\parallel}/\rho_0$. The functional forms for the viscosity coefficients, η , and the electrical conductivity, σ , are given in Braginskii (1965). By neglecting derivatives of the dissipation coefficients themselves, it is implicitly assumed in the equations above that dissipation processes are important only in a narrow layer, and that over this layer terms which are proportional to derivatives of the dissipation coefficients can be neglected. This is easily verified *a posteriori*. It is further assumed that all variations in \mathbf{B}_0 and ρ_0 are transverse to the field so that $v_A = v_A(x)$

only. The plasma is assumed to have $\beta \ll 1$ so that the transverse gradients of B_0 can be neglected and the total pressure p can be approximated as $p = B_0 B_z / 4\pi$. Take the time derivative of the momentum equation and use the induction equation to eliminate all derivatives of B . Since dissipation is assumed to be small, one can neglect terms which are proportional to products of the dissipation coefficients. Assume that the loop is driven at $z = 0$ and that at $z = L$ there is a perfectly reflecting boundary (see Hollweg, 1984 for more discussion on this point). Fourier transform the equation using

$$\mathbf{v}_\perp(x, y, z, t) = - \sum_{n=0}^{\infty} \cos(k_{zn} z) \int_{-\infty}^{\infty} \frac{d\omega}{2\pi} e^{-i\omega t} \mathbf{v}_{\perp n}(x, y, \omega) \quad (3)$$

This form automatically satisfies the boundary condition at $z = L$ as long as $k_{zn} = (2n + 1)\pi / (2L)$ with $n = 0, 1, 2, \dots$. Define the following dimensionless parameters $V_A^2(x) = v_A^2(x)/v_{A0}^2$, $R = v_{A0}/\omega\alpha^2$, $Pr_\parallel = \beta^2/\alpha^2$, and $Pr_\perp = \gamma^2/\alpha^2$, where v_{A0} is some typical value of the Alfvén speed within the loop, R is the magnetic Reynolds number and Pr_\perp and Pr_\parallel the magnetic Prandtl numbers associated with shear and compressional viscosity. With these definitions, all lengths measured in units of d the transverse scale of the loop, and $\kappa^2(x) = (\omega^2 d^2 / v_A^2(x) - k_z^2)$, the equation for the velocity can be written in the dimensionless form

$$\nabla_\perp(\nabla \cdot \mathbf{v}_\perp) + \kappa^2 \mathbf{v}_\perp = \frac{i}{R V_A^2(x)} \left\{ -\nabla^2 \rho_0 \mathbf{v}_{\perp n} + Pr_\perp \nabla^2 \mathbf{v}_{\perp n} + Pr_\parallel \nabla_\perp(\nabla \cdot \mathbf{v}) \right\} \quad (4)$$

The terms on the left hand side of this equation are the terms obtained from ideal MHD. Solutions of the ideal equation for various forms of the Alfvén speed profile have been discussed by several authors in the context of solar coronal heating (Ionson, 1982; Rae and Roberts 1982) and in the context of solar wind acceleration in coronal holes by Davila (1985). These investigations have demonstrated that this equation describes the propagation of MHD surface waves and guided wave modes in an inhomogeneous plasma.

The terms on the right are all due to dissipation and are therefore non-ideal MHD terms. In the solar corona these terms are "small" in most locations since they are all multiplied by the inverse of the magnetic Reynolds number R which is on the order of 10^{12} for typical solar parameters. The exception to this ordering is at the location $x = x_A$ where $\kappa^2(x_A) = 0$. At this location the first term on the left can only be balanced by the dissipative terms on the right even though they are small. Sufficiently far from x_A , in the outer region, the ideal MHD solution is a reasonable approximation to the actual solution. However, near x_A , in the inner region, the character of the solution changes (the equation changes from second to fourth order) and the assumption of ideal MHD is not valid. This is a classic example of a singular perturbation (Nayfeh, 1981). In the following paragraphs singular perturbation theory and the method of matched asymptotic expansions will be used to obtain a solution which is valid both outside and inside the resonance layer. To do this one must first reduce the coupled equations for the vector

components of the velocity to a single equation for one velocity component, say v_x .

To illustrate the basic idea of the resonance absorption layer and to demonstrate the matched asymptotic solution method, let us assume that the dominant dissipation mechanism is shear viscosity. This assumption cannot be completely justified at this point so it must be regarded simply as an *ansatz*. An investigation which incorporates ohmic, compressive viscous and shear viscous dissipation self consistently in a numerical solution is currently underway. The results of this investigation will be published when they become available. Under these assumptions the wave equation can be written

$$\nabla_{\perp}(\nabla \cdot \mathbf{v}_{\perp n}) + \kappa^2 \mathbf{v}_{\perp n} = i\epsilon \nabla^2 \mathbf{v}_{\perp n} \quad (5)$$

where $\epsilon = (1 + \text{Pr}) / (R V_A^2)$. An equation for v_{xn} correct to first order in ϵ can be obtained for the appropriate ordering $1 \gg k_y^2 \gg \kappa_z^2 \gg \epsilon k_y^2$

$$\frac{d}{dx} - \frac{\kappa^2}{k_y^2} \frac{dv_{xn}}{dx} - \kappa^2 v_{xn} = \frac{i\epsilon}{k_y^2} \frac{d^4 v_{xn}}{dx^4} \quad (6)$$

The outer solution is obtained by expanding the velocity, v_{xn} , as a power series in the small parameter ϵ . The lowest order term must then satisfy

$$\frac{d}{dx} - \frac{\kappa^2}{k_y^2} \frac{dv_{xn}^{(0)}}{dx} + \kappa^2 v_{xn}^{(0)} = 0 \quad (7)$$

Detailed solutions of this equation have been obtained before (Rae and Roberts, 1982; and Lee and Roberts, 1986). For our purposes it is only necessary to obtain the solution near the resonance layer, i.e. where $x \rightarrow x_A$ with x_A defined by the resonance condition $\kappa^2(x_A) = 0$. In this region, the first term dominates and the solution can be approximated as

$$v_{xn}^{(0)} \approx A \ln(x - x_A) \quad (8)$$

where A is the wave amplitude determined by matching boundary conditions at the driver.

The inner solution can be obtained by considering the scale stretching transformation given by $\zeta = (x - x_A)/a$, where a is the small scale parameter to be determined in the problem. For the case presented here $a^3 = \epsilon/\lambda$ where $\lambda = -k_z^2 d(\ln \rho)/dx$. Using the shear viscosity and resistivity coefficients given in Braginskii one can estimate $a \approx 0.3$ km. This is below the resolution of current instruments. Using the largest viscosity coefficient in Braginskii one can estimate $a_{\text{max}} \approx 250$ km. If this second estimate is more nearly correct, these sheets could be observed with instruments with resolution on the order of 0.1 arc second. Using the transformation described above, the inner equation can be written

$$\frac{d}{d\zeta} \left[\frac{d^2}{d\zeta^2} - i\zeta \right] \frac{dv_{xn}}{d\zeta} = -ik_y^2 a^2 \zeta v_{xn} \quad (9)$$

Assume a power law expansion of v_{xn} with a^2 as the expansion parameter, then the solution of the zeroth order equation is

$$v_{xn}^{(0)}(\zeta) = C_1 - C_2 \int_0^\infty dp \exp\left(-\frac{p^3}{3}\right) \left[\frac{1 - \exp(-ip\zeta)}{ip} \right] \quad (10)$$

In the limit as $\zeta \rightarrow \infty$ it can be shown that

$$v_{xn}(\zeta) \approx -iC_2 \ln(x - x_A) \quad (11)$$

This shows that by proper choice of the constants, namely $C_2 = iA$, the inner and outer solutions match as is physically required.

Although in the steady state the details of the velocity profile within the resonance layer do depend on the dissipation mechanism (eqn 10), the heating rate does not. The result presented below is obtained by considering the outer solution and integrating the Poynting flux over the entire surface of the resonance layer (Chen and Hasagawa, 1974). An equivalent result could be obtained from the inner solution by integrating the volumetric heating rate of Braginskii (1965) over the volume of the resonance layer. The result is

$$H = A_s \frac{B_0^2}{8\pi\omega d} \left[-\frac{1}{k_y^2} \frac{d(\kappa^2)}{dx} \right] |A|^2 \operatorname{Im} \left\{ \ln^*(x - x_A + i\phi) \right\} \Big|_{x_1}^{x_2} \quad (12)$$

where x_1 and x_2 denote the positions of the two surfaces of the resonance layer and A_s is the surface area of the resonance layer. If we consider the limit of this equation as $(x_1 - x_2) \rightarrow 0$ and use causality to choose the proper analytic continuation (McPherson and Pridmore-Brown, 1966; Kapraff and Tataronis, 1977; Mok and Einaudi, 1985; Einaudi and Mok, 1985; Bertin et al, 1986) the resulting heating rate is

$$H = A_s \frac{B_0^2}{8\pi\omega d} \frac{k_z^2}{k_y^2} \pi |A|^2 \quad (13)$$

To determine whether this heating rate is consistent with observational constraints, let us simply equate it to the observed radiation rate in soft x-rays to obtain an expression for the RMS velocity amplitude required to explain the observed emission. Using typical values of the parameters, $B_0=100$ G, $d=5 \times 10^8$ cm, $\Lambda(T)=10^{-22}$ (Rosner et al. 1978), $P=300$ sec, $k_y=2k_z$ and $\int n_e^2 dl = 10^{28-29}$ (Webb et al. 1986) one obtains an estimate of $V_{rms} = 2-6$ km/sec using the following expression.

$$V_{rms} = \left(\frac{\Lambda(T) \frac{2 \pi d}{P} \int n_e^2 dl}{\pi (B_0^2 / 8 \pi) (k_z^2 / k_y^2)} \right)^{1/2} \quad (14)$$

This is comparable to the observed value of 10-20 km/sec regularly seen from observations of non-thermal line broadening in the corona.

CONCLUSIONS

The primary conclusion to be drawn from these calculations is that to the level of the approximation adopted here, the observations of the heating rate and non-thermal line broadening in the solar corona are consistent with heating by the resonance absorption mechanism. This basic agreement is gratifying but several problems remain. The plane symmetry assumed here is highly idealized. It has been shown in the plasma physics literature that for the tokamak problem introducing cylindrical symmetry has presented no new physics. Nevertheless, when considering the heating rate to an accuracy of say factors of 2-5 the geometry factors must be properly accounted for. Second, observations of the turbulent power spectrum at the base of the corona are badly needed as input for the theory. These observations should be carried out in ions which are present at or above the transition region temperatures. It seems that EUV observations would be the most appropriate. Finally, other sources of dissipation must be considered. For although the heating rate is independent of the dissipation mechanism for any reasonable value of the coefficients, the amplitude of the velocity inside the resonance layer, and the width of the layer, both depend on the magnitude of the dissipation coefficient. High resolution instruments such as POF may be able to observe velocities within the narrow resonance regions in the reasonably near future. Therefore it is worthwhile to consider theoretically the observational consequences of various dissipation mechanisms now. In the work presented here, shear viscosity was assumed to be the dominant dissipation mechanism. This is not necessarily the case for solar conditions.

REFERENCES

- Bertin, G., Einaudi, G. and Pegoraro, F., 1986, *Comm. on Plas. Phy.*, in press.
 Braginskii, S.I., 1965, *Rev. Plasma Phys.*, **1**, 205.
 Chen, L. and Hasegawa, A., 1974, *Phys. Fluids*, **17**, 1399.
 Davila, J.M., 1985, *Ap. J.*, **291**, 328.
 Einaudi, G. and Mok, Y., 1985, *J. Plasma Phys.*, **34**, part 2, 259.
 Hollweg, J.V., 1984, *Ap. J.*, **277**, 392.
 Ionson, J.A., 1982, *Ap. J.*, **254**, 318.
 Kapraff, J.M., and Tataronis, J.A., 1977, *J. Plasma Phys.*, **18**, part 2, 209.
 Lee, M.A. and Roberts, B., 1986, *Ap. J.*, **301**, 430.
 McPherson, D.A. and Pridmore-Brown, D.C., 1966, *Phys. Fluids*, **9**, 2033.
 Mok, Y. and Einaudi, G., 1985, *J. Plasma Phys.*, **33**, part 2, 199.
 Nayfeh, A. H., 1981, *Introduction to Perturbation Techniques* (Wiley: New York)
 Rae, I.C. and Roberts, B., 1982, *Mon. Not. Roy. Astr. Soc.*, **201**, 1171.
 Rosner, R., Tucker, W. H., and Viana, G. S., 1978, *Ap. J.*, **220**, 643.
 Webb, D. F., Holman, G. D., Davis, J. M., Kundu, M. R., and Shevgaondar, R. K., 1986, *Ap. J.*, submitted.

MAGNETIC HELICITY AS A CONSTRAINT ON CORONAL DISSIPATION

Arnab Rai Choudhuri
High Altitude Observatory
*National Center for Atmospheric Research**
 Boulder, CO 80507

Introduction

An attractive scenario for the heating of coronal active regions has been developed in a series of papers by Parker (1983 and the references therein). The main idea is that the slow footpoint motions in the photosphere distort the overlying coronal field structures in a random fashion, and since there may not be equilibrium configurations without current sheets available for the coronal magnetic fields for arbitrary footpoint motions, we have a non-equilibrium situation giving rise to current sheet formations and energy dissipation. However, it seems virtually impossible to study the detailed dynamics of this non-equilibrium process with the present techniques of MHD. The only way of estimating the heating due to magnetic dissipation seems to be to invoke more global considerations which avoid the problem of describing the detailed dynamics. Parker (1983) suggested that one can calculate the heating by estimating the work done by the footpoints on the coronal magnetic fields. Sturrock and Uchida (1981) estimated the energy in the twists produced by the footpoint motions and assumed that the whole of that energy is available for dissipation. However, recently Heyvaerts and Priest (1984; see also Browning and Priest 1986) pointed out that because of the constraint imposed by the magnetic helicity conservation, all the energy that is fed into the corona by footpoint motions may not be available for dissipation. It has been rigorously demonstrated by Berger (1984) that the time-scale for magnetic helicity decay in coronal magnetic structures is indeed orders of magnitude larger than any relevant time-scale for coronal heating. Heyvaerts and Priest (1984) are certainly correct in pointing out that when footpoints put some energy in the corona, only that much of it can dissipate which is consistent with helicity conservation. However, we want to show that when one extends the Heyvaerts-Priest model to a statistics of completely random footpoint motions and takes sufficiently long time averages, the conservation of helicity *introduces no effective constraint* on energy dissipation, and all the energy in the twists is, in principle, available for dissipation, as proposed by Sturrock and Uchida (1981).

Taylor's Hypothesis and Magnetic Dissipation

The magnetic helicity for a magnetic configuration, which is the volume integral $K = \int \vec{A} \cdot \vec{B} \, dV$, is a measure of the linkage of flux lines and can be easily shown to be independent of gauge if the magnetic configuration is bounded by a closed surface on which $\vec{B} \cdot \hat{n} = 0$ everywhere. For a perfectly conducting plasma bounded by such a surface, Woltjer (1958) showed that the magnetic helicity is a constant of motion. But what happens if the plasma is not perfectly conducting and has a small but finite resistivity? Taylor (1974) advanced the provocative hypothesis that the total magnetic helicity of an isolated volume of plasma can still be considered to be approximately conserved over the time scale of energy decay. In other

* The National Center for Atmospheric Research is sponsored by the National Science Foundation.

words, when a plasma relaxes to the final static equilibrium state through non-equilibrium dynamical processes, we can think of those processes as a way of minimizing energy while keeping helicity (and any other conserved quantity) constant. For a plasma with negligible gas pressure compared to magnetic pressure, if one minimizes the energy with the helicity conservation as a constraint, then one obtains the force-free equation

$$\vec{\nabla} \times \vec{B} = \mu \vec{B}, \quad (1)$$

where μ is the Lagrange multiplier in the variational procedure. Taylor's hypothesis was remarkably successful in describing the final field configurations in the well-known "reversed pinch" experiments involving laboratory plasma relaxation (Taylor 1974).

Most astrophysical systems are not bounded by $\vec{B} \cdot \vec{n} = 0$ surfaces. So, in order to apply the above ideas to astrophysical plasmas, one has to generalize to bounding surfaces with field lines threading through them. For such open systems, Berger and Field (1984) showed that it is still possible to define a relative magnetic helicity with respect to a ground state potential configuration and make sure that all the physically relevant quantities turn out to be gauge-invariant. In such an open system, there can also be a helicity flow across the bounding surface. For a plane surface like the photosphere with footpoint motions lying in the plane, the rate of flow is given by

$$(\text{helicity flow}) = -2 \int (\vec{A}_P \cdot \vec{v}) (\vec{B} \cdot d\vec{s}), \quad (2)$$

where \vec{A}_P is the divergence-free vector potential for a potential field with the appropriate flux boundary conditions (for details see Berger 1984). One can generalize Woltjer's theorem (and probably Taylor's hypothesis) for such systems if one keeps track of the changes in the value of helicity within the volume as a result of flows across the boundary.

With this rather terse background, let us briefly summarize the main ideas presented by Heyvaerts and Priest (1984). Let us consider a magnetic region in the corona, which is initially in the Taylor state with helicity K_i and corresponding minimized energy W_i . The individual flux tubes in this region can conceivably interact with each other through neutral point reconnections at the boundaries, but, if the region is sufficiently separated from other magnetic regions, the whole region can be thought of as a candidate for the application of Taylor's hypothesis. As a result of footpoint motions, there will be a flow of both helicity and energy into that coronal magnetic region, with the energy flow across the boundary given by

$$(\text{energy flow}) = \frac{1}{4\pi} \int (\vec{B} \cdot \vec{v}) (\vec{B} \cdot d\vec{s}). \quad (3)$$

Let ΔK and ΔW be the additional amounts of helicity and energy put into the coronal region in some interval of time. Then the final magnetic configuration should have a helicity $K_i + \Delta K$, and suppose the energy of the corresponding Taylor-relaxed state is $W_i + \Delta W_f$. We do not expect *a priori* ΔW and ΔW_f to be equal, and the difference $\Delta W_{diss} = \Delta W - \Delta W_f$ is dissipated away. In other words, the whole of the energy ΔW put in the corona by the footpoint motions is not available for dissipation, but only a fraction ΔW_{diss} of it. One remarkable result of the detailed calculations was that when one considered the plasma to relax instantaneously to the Taylor state in response to footpoint motions, one found $\Delta W_{diss} = 0$. Only when the finite relaxation time (which should be small compared to deformation time scales for the model to work) is taken into account, ΔW_{diss} comes out to be non-zero.

Another interesting application of Taylor's hypothesis in astrophysics was made in the study of extragalactic jets, which provided an explanation of the non-axisymmetric oscillations observed in some jets and the associated magnetic structures inferred from synchrotron radiation (Königl

and Choudhuri 1985). In this problem also, it was found out that magnetic energy is available for dissipation only when the finite time for relaxation to Taylor state is taken into account (Turner 1986; Choudhuri and Königl 1986).

It has recently been pointed out that quite generally no magnetic energy can be available for dissipation, if a magnetic system always relaxes to the Taylor state instantaneously in response to changes at the boundary (Browning and Priest 1986; Berger 1985). This result helps us to understand the conclusions arrived at both by Heyvaerts and Priest (1984) and by Choudhuri and Königl (1986). A physical explanation of this result is also not difficult to give. Since the magnetic field in the Taylor state is well-behaved and without neutral points, we do not expect dissipation to take place if the system always remains in the Taylor state because of instantaneous relaxation. However, when the relaxation time is finite (but small compared to the deformation time), if we start deforming a magnetic system away from a Taylor state, initially it will tend to depart from the Taylor state until current sheets form, and afterwards dissipation may prevent further departures from Taylor state. Taylor's hypothesis is a particularly powerful tool in deriving the magnetic configuration of the final relaxed state in terms of conserved quantities and boundary conditions. However, when we apply this hypothesis to study the energy dissipation problem, we find that dissipation arises only due to departures from the Taylor state, and consequently any final expression for energy dissipation necessarily involves some arbitrary parameter describing the measure of departure from the Taylor state (or equivalently describing the relaxation time scale). It is found that the relaxation time has to be a few tens of Alfvén time in order to give the right sort of dissipation (Browning and Priest 1986; Choudhuri and Königl 1986).

It is interesting to note that Parker (1983) arrived at a similar conclusion from completely different considerations. He pointed out that the footpoints are able to do sufficient work on the coronal magnetic structures only if we allow stresses to build up for some time. In order to get the right value of the heating rate, the relaxation time for these stresses has to be of the order of a day (i.e. about 100 Alfvén transit times for a coronal loop, depending on the values chosen for different quantities). Parker (1983) also estimated that this relaxation time corresponds to a reconnection rate which is the geometric mean between the Sweet-Parker and the Petschek rates.

Extension of Heyvaerts-Priest Model for a Statistics of Completely Random Footpoint Motions

In a magnetic region in the corona, two processes go on side by side. One is the process of the growth of complexities in the field structures as a result of footpoint motions. The other process is dissipation, which attempts to burn away the increasing complexities. Except for a runaway situation where complexities build up more quickly than they can be dissipated away, we expect these two processes eventually to reach some sort of balance. In other words, we expect a "steady state" in the statistical sense such that the complexity of magnetic structures would statistically be maintained at the same level, provided the timescale of evolution of the coronal structure as a whole is much larger than all the time scales involved. In such a "steady state", whatever energy the footpoints are putting in the corona has to be dissipated away in order to preserve the balance. If helicity conservation prevents a part of this energy from being dissipated, then we have to figure out what eventually happens to this undissipated energy.

We can resolve this puzzle by extending the Heyvaerts-Priest model to a statistics of completely random footpoint motions. In order to understand the basic physics of the process, let us start with a magnetic region which is initially in the potential configuration, and then let the footpoint motions distort it. Following Berger and Field (1984), we measure the magnetic helicity relative to potential fields with the same flux boundary conditions. So, by definition, the initial helicity of our system is zero. Let us now consider a flux tube in the region that is being twisted. Neglecting curvature (which is not expected to change the basic physics), we imagine a cylindrically symmetric flux tube to be anchored between two parallel planes (initially without twist because its field is potential) and to be twisted by a rotationally symmetric velocity field at the bottom plane. Since the magnetic field can be upward or downward, and the velocity field can be

clockwise or anti-clockwise, we can have four cases as shown in Fig. 1. Initially $(\vec{B} \cdot \vec{v})$ for all four of them is zero so that we see from (3) that there is no energy flow at first. However, the twist due to footpoint motion gives rise to a ϕ -component of the magnetic field, and when that component is taken into account, it is easy to see that $(\vec{B} \cdot \vec{v}) (\vec{B} \cdot d\vec{s})$ is positive for all the four cases, i.e. energy is put into the corona in every case. Now let us look at the helicity flow. The divergence-free vector potential A_P for the initial field is in the ϕ -direction, one way for the upward field and the other way for the downward field. The footpoint motions we are considering do not change the flux boundary condition and hence do not change A_P . We thus find that $(A_P \cdot \vec{v}) (\vec{B} \cdot d\vec{s})$ is of one sign for the cases (a) and (c), and is of the opposite sign for the cases (b) and (d). In other words, when we sum over the four cases, there is no net helicity flow though there is net energy flow. If we use the gauge chosen by Heyvaerts and Priest (1984) and just use the fact that $A \rightarrow -A$ when $B \rightarrow -B$, then also we end up with the same conclusion.

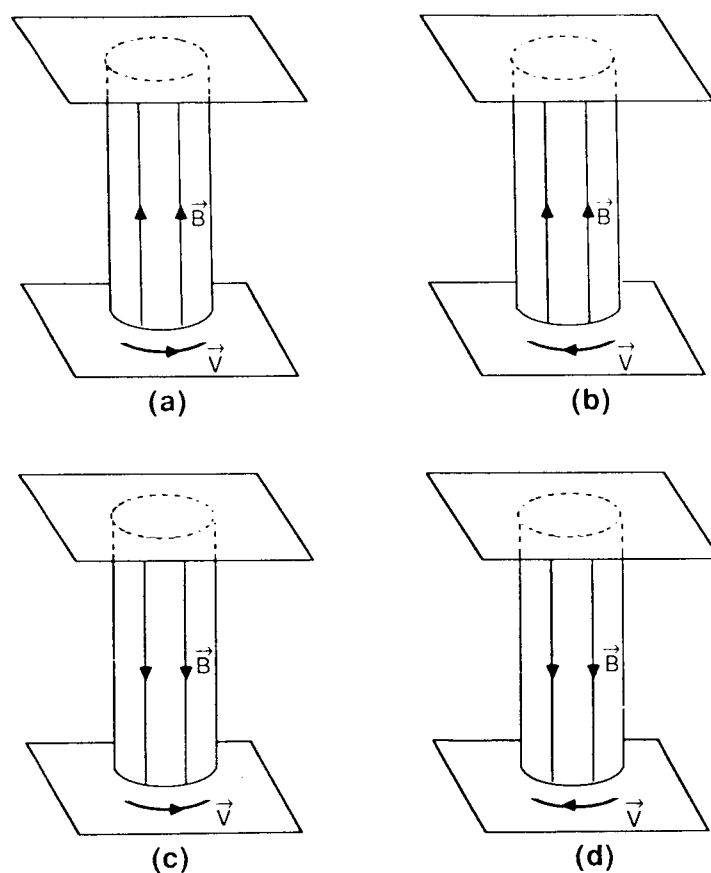


Figure 1

It is straightforward to generalize these conclusions for the case of flux tubes braiding around each other. So long as the footpoint motions are as likely to twist the tubes one way as the other way, the average statistical result will be the addition of energy to the coronal structures without addition of magnetic helicity. The footpoint motions will merely add positive helicity in some regions and negative helicity in others. There are bound to be statistical fluctuations

in the value of helicity. However, if one starts from a zero-helicity state and takes sufficiently long time averages, the average value of helicity would remain zero. A Taylor state with zero magnetic helicity is, by virtue of our definition of helicity, a potential field in which all the twist has been dissipated away. We thus conclude that Taylor's hypothesis imposes no constraint on energy dissipation for completely random footpoint motions. We have also seen that a magnetic system has to depart from the Taylor state to some extent if dissipation is to take place. Consequently, we expect that the footpoint motions and the dissipation together would maintain a coronal magnetic region at a steady level of complexity sufficiently removed from a potential configuration such that whatever energy goes into the work done by the footpoints ultimately comes out in the dissipation of the twists.

It is perhaps interesting to ask at this point if footpoint motions in the sun are really completely random so that coronal magnetic structures always have statistically zero helicity. One occasionally sees structures in the corona which seem to contain magnetic fields twisted in one way. However, this can arise only if these magnetic structures erupt through the photosphere with the twist already present, or else if there is a systematic component in footpoint motions. It is conceivable that solar rotation may have some subtle effect on the convection cells so that they preferably tend to put helicity of one sign in the corona, or there may be shearing motions in the photosphere due to dynamical reasons we are still ignorant of. Apart from such minor effects, we expect the footpoints to put mainly energy in the corona with very little net helicity.

Conclusion

Taylor's hypothesis has provided us a model for the relaxed magnetic configurations of not only laboratory plasmas, but also of astrophysical plasmas (Königl and Choudhuri 1985). However, energy dissipation is possible only for systems which depart from a strict Taylor state, and hence one has to introduce a parameter describing that departure, when one uses Taylor's hypothesis to estimate the dissipation (Heyvaerts and Priest 1984; Choudhuri and Königl 1986). An application of Taylor's hypothesis to the problem of coronal heating provides us with new insight into this difficult problem. When particular sorts of footpoint motions put energy and helicity in the corona, the conservation of helicity puts a constraint on how much of the energy can be dissipated. However, on considering a random distribution of footpoint motions, this constraint gets washed away, and Taylor's hypothesis is probably not going to play any significant role in the actual calculation of relevant physical quantities in the coronal heating problem.

I wish to thank Mitch Berger, Arieh Königl and B.C. Low for several enlightening conversations.

References

- Berger, M.A., 1984, "Rigorous New Limits on Magnetic Helicity Dissipation in the Solar Corona," *Geophys. Ap. Fluid Dyn.*, **30** (79).
- Berger, M.A., 1985, "Structure and Stability of Constant- α Force-Free Fields," *Ap. J. Suppl.*, **59** (433).
- Berger, M.A. and Field, G.B., 1984, "The Topological Properties of Magnetic Helicity," *J. Fluid Mech.*, **147** (133).
- Browning, P.K. and Priest, E.R., 1986, "Heating of Coronal Arcades by Magnetic Tearing Turbulence, Using the Taylor-Heyvaerts Hypothesis," (preprint).

- Choudhuri, A.R. and Königl, A., 1986, "Magnetic Energy Dissipation in Force-Free Jets," *Ap. J.*, November 1 (to appear).
- Heyvaerts, J. and Priest, E.R., 1984, "Coronal Heating by Reconnection in DC Current Systems. A Theory based on Taylor's Hypothesis," *Astron. Ap.*, **137** (63).
- Königl, A. and Choudhuri, A.R., 1985, " Force-Free Equilibria of Magnetized Jets," *Ap. J.*, **289** (173).
- Parker, E.N., 1983, "Magnetic Neutral Sheets in Evolving Fields. II. Formation of the Solar Corona," *Ap. J.*, **264** (642).
- Sturrock, P.A. and Uchida, Y., 1981, "Coronal Heating by Stochastic Magnetic Pumping," *Ap. J.*, **246** (331).
- Taylor, J.B., 1974, "Relaxation of Toroidal Plasma and Generation of Reverse Magnetic Fields," *Phys. Rev. Lett.*, **33** (1139).
- Turner, L., 1986, "Is Magnetic Energy the Source of Synchrotron Radiation in Jets?" *Ap. J.*, June 15 (to appear).
- Woltjer, L., 1958, "A Theorem on Force-Free Magnetic Fields," *Proc. Nat. Acad. Sci. USA*, **44** (489).

The Stability of Coronal and Prominence Magnetic Fields

by A W Hood, Applied Mathematics Department
St Andrews University, St Andrews, Scotland

INTRODUCTION

The magnetic fields in Prominences and Active Regions (Coronal Arcades) may be susceptible to a variety of instabilities. Ideal MHD instabilities are the fastest growing and criteria for checking stability are complicated by the line tying effect of the dense photosphere. In general, the line tying introduces a coupling of modes and obtaining stability criteria for a given prominence or arcade field involves either solving partial differential equations (Hood and Priest 1981, Hood 1983, Cargill *et al* 1986) or coupled O.D.E's (Einaudi & Van Hoven 1983) (from a truncated Fourier series). This can be a very time consuming exercise. What is needed is a simpler test applicable to any field.

LOCALISED MODES

Progress can be made by studying localised instabilities or Ballooning modes (Conner *et al* 1979; Dewar and Glasser 1983). By using a WKB approach, (Dewar and Glasser 1983), the idea is to study instabilities localised about a given magnetic flux, with a fast variation perpendicular to the equilibrium field and a slow variation along the field lines. This filters out the stable Alfvén and magnetoacoustic waves. Thus, all displacements to coronal arcades are of the form

$$\xi(r, \theta, z, t) = \xi(r, \theta) e^{i(S(r, \theta, z)/\epsilon + \omega t)} \quad (1)$$

where ϵ , the instability length scale, $\ll R_0$ the equilibrium length scale and $S(r, \theta, z)$, ω and the amplitudes $\xi(r, \theta)$ are all $O(1)$ quantities. (For coronal loops see Hood 1986a). The slow variation along the field occurs only when

$$\mathbf{k} \cdot \mathbf{B} = \nabla S \cdot \mathbf{B} = 0. \quad (2)$$

For cylindrically symmetric fields, with the photosphere situated at $\theta = \pm\pi/2$, a solution to Eq (2) is

$$S = S(r) + z - q\theta, \quad (3)$$

where $q = rB_z/B_\theta$. Substituting (1) and (3) into the linearised equations of motion (Hood 1986a) gives

$$B \frac{d}{ds} \left[\frac{k^2}{B} \frac{d\xi}{ds} \right] - 2K_s \left[\frac{\gamma \mu p B^2}{\gamma \mu p + B^2} \left[B \frac{d\eta}{ds} - 2K_s \xi \right] + \frac{\mu dp}{d\psi} \xi \right] + \frac{\rho \mu \omega^2 k^2}{B^2} \xi = 0 \quad (4)$$

$$B \frac{d}{ds} \left[\frac{\gamma \mu p B^2}{\gamma \mu p + B^2} \left[B \frac{d\eta}{ds} - 2K_g \xi \right] \right] + \mu \rho \omega^2 B^2 \eta = 0, \quad (5)$$

where, for cylindrical arcades, $Bd/ds = B_\theta d/dr$, $K_g = -B_\theta/rB^2$, $dp/d\psi = -(dp/dr)/B_\theta$, $k^2 = |VS|^2$. Strictly speaking the solutions to Eqs (4) and (5) with the line tying boundary conditions define a dispersion relation for $k^2 = k^2(r; \omega^2)$. The radial integration must satisfy a Bohr Sommerfeld condition (Dewar and Glasser 1983, Hood 1986a) and this defines the physical growth rate. However, if the least stable mode is of interest, the procedure is simpler. Now set $S'(r) \equiv 0$ and solve Eqns (4) and (5) to obtain $\omega^2(r)$. The *minimum* value of $\omega^2(r)$ defines the physical value of ω^2 for the least stable mode. If $\omega^2 < 0$, then there is an instability but, if $\omega^2 > 0$, the localised modes are stable.

For example, Hood (1986a) considered the field

$$B_\theta = B_0(r/b)/(1 + r^2/b^2) \quad B_z = B_0/(1 + r^2/b^2)$$

$$\mu p = B_0^2(1 - \lambda^2)/2(1 + r^2/b^2)$$

and solved equations (4) and (5) to obtain $\omega^2(r)$ as shown in Fig. 1.

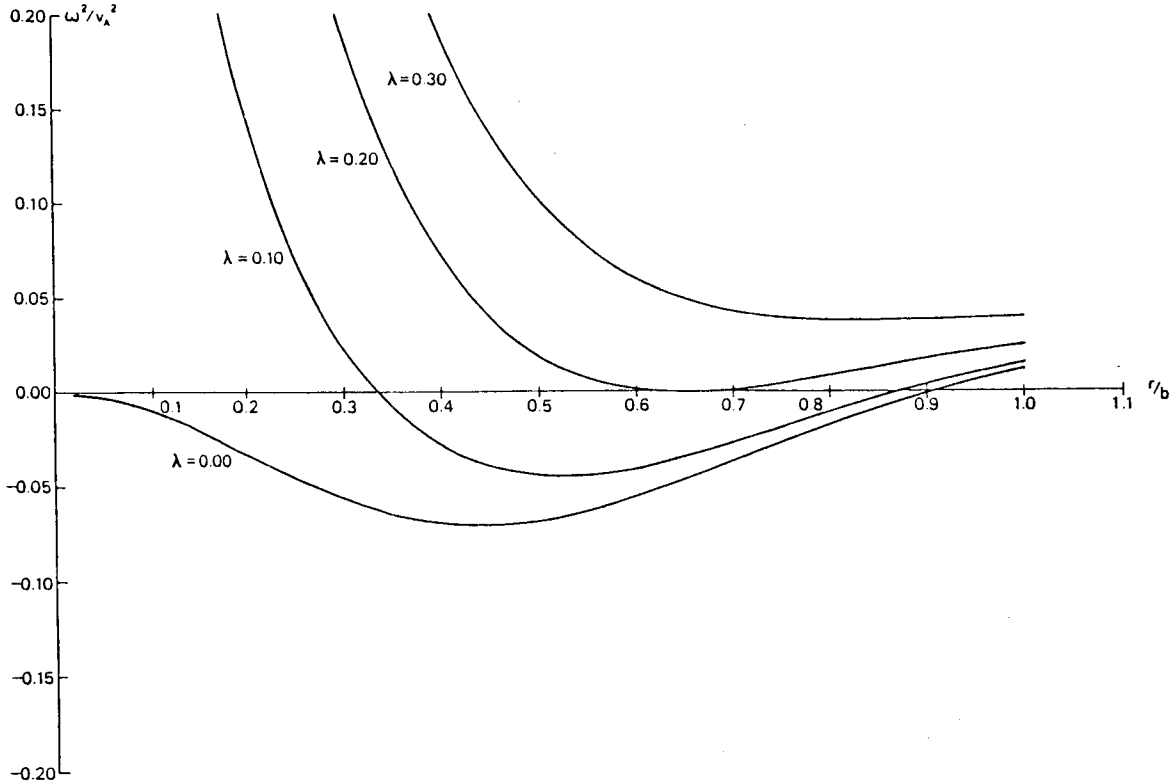


Fig. 1. The eigenvalue ω^2 of equations (4) and (5) is shown as a function of the radial coordinate for various values of λ . The physical value of ω^2 , for the least stable mode, is given by the minimum value. ω^2 is measured in units of $v_A^2 = B_0^2/\mu \rho b^2$ and $\gamma = 1$.

Equations (4) and (5) can be converted into quadratic form by multiplying by ξ and η , respectively and integrating. Then the sign of ω^2 can be determined by trial functions. Thus, it can be shown, (Hood 1986a), that the field is *definitely unstable* if

$$\frac{\pi^2}{4} B_z^2 \left[\frac{q'}{q} \right]^2 + \frac{2\mu p'}{r} + \frac{B^2}{r^2} + \frac{\gamma\mu p B_\theta^2}{r^2(\gamma\mu p + B^2)} < 0 \quad (6)$$

(see Spicer 1976 for a heuristic derivation with $\gamma = 0$). Equation (6) has been derived using the rigid boundary conditions, $\xi = 0$ on the photosphere but $\gamma = 0$ simulates the flow through boundary conditions of $\xi_\perp = 0$ and $\xi_\parallel \neq 0$ (Einaudi and Van Hoven 1983). The first term is the shear stabilisation, the second term is the driving term due to adverse pressure gradients. The last two terms provide line tying stabilisation due to Alfvén waves and compressional slow waves.

A CHECK ON LINE TYING CONDITIONS

Using the ballooning approximation, the photospheric line tying conditions can be investigated (Hood 1986b). Equations (4) and (5) were solved including a density variation along the field lines and, when the density difference between the photosphere and corona was increased to realistic values, the value of ω^2 rapidly approached the value predicted by the rigid boundary conditions. In addition, the values of ξ and η at the photosphere tend to zero. This suggests that the rigid boundary conditions are the correct boundary conditions (at least for localised modes).

THE EFFECT OF GRAVITY

The effect of gravity has been included by, for example, Zweibel 1981, Melville *et al* 1986a. Melville *et al* considered the linear equilibria of Zweibel and Hundhausen (1982) and showed that as soon as a magnetic island appeared the field became unstable. Interestingly enough, each field line (except the O point itself) was unstable *before* it formed an island. The analysis has been extended to other fields (Melville *et al* 1986b), and preliminary results suggest that, as the effect of gravity is increased, the fields become more susceptible to the Rayleigh-Taylor instability. However, a simple test, similar to Equation (6), has yet to be developed.

CONCLUSIONS

The significance of the localised instabilities is not yet fully understood. The nonlinear coupling of these modes may give rise to an explosive instability, with the modes coupling to longer wavelengths, (Mondt and Weiland, 1985). On the other hand, if the modes saturate early, then the main effect of the instability may be an enhancement of transport coefficients. Nonetheless, Equation (6) provides a simple test for the stability of cylindrical magnetic fields.

REFERENCES

- Cargill, P, Hood, A W and Migliuolo, S (1986) "Magnetohydrodynamic stability of line-tied coronal arcades III Necessary and sufficient conditions for

- stability", *Astrophys. J.*, in press.
- Conner, J, Hastie, J and Taylor, B (1979) "High mode number stability of an axisymmetric toroidal plasma", *Proc. Roy. Soc. London* **A365**, 1-17.
- Dewar, R and Glasser, A (1983) "Ballooning mode spectrum in general toroidal systems", *Phys. Fluids* **26**, 3039-3052.
- Einaudi, G and Van Hoven, G (1983) "The stability of coronal loops: Finite length and pressure profile limits", *Solar Phys.* **88**, 163-177.
- Hood, A W (1983) "Magnetic stability of coronal arcades relevant to two ribbon flares", *Solar Phys.* **87**, 279-299.
- Hood, A W and Priest, E R (1981) "Critical conditions for magnetic instabilities in force free coronal loops", *Geophys. Astrophys. Fluid Dynamics* **17**, 297-318.
- Hood, A W (1986a) "Ballooning instabilities in the solar corona: Condition for stability", *Solar Phys.*, in press.
- Hood, A W (1986b) "Photospheric line tying conditions for the MHD stability of coronal magnetic fields", *Solar Phys.*, submitted.
- Melville, J, Hood, A W and Priest, E R (1986a) "The ideal magnetohydrodynamic stability of tied magnetic field lines in a coronal magnetohydrostatic equilibrium", *Solar Phys.*, submitted.
- Melville, J, Hood, A W and Priest, E R (1986b) in preparation.
- Mondt, J P and Weiland, J (1985) "Nonlinear theory of large mode number ballooning modes in fully toroidal geometry", *J. Plasma Phys.* **34**, 143.
- Spicer, D S (1976) "An unstable arch model of a solar flare" NRL report 8036.
- Zweibel, E (1981) "MHD instabilities of atmospheres with magnetic fields", *Astrophys. J.* **249**, 731.
- Zweibel, E and Hundhausen, A (1982) "Magnetostatic atmospheres: A family of isothermal solutions", *Solar Phys.* **76**, 261.

Resistive Ballooning Modes in Line-Tied Coronal Arcades

by Marco Velli, Applied Mathematics Department
The University, St Andrews, Scotland

INTRODUCTION

Observations suggest that large scale instabilities in the solar corona, such as solar flares, act to release energy contained in complex magnetic structures, relaxing the fields to a simpler topology. This is possible only if resistive effects play an important role during the flaring process. When considering perturbations of a static equilibrium in a highly conducting magnetized plasma resistivity is usually negligible, as can be seen by examining the linearized induction equation

$$\partial \underline{B}_1 / \partial t = \nabla \times (\underline{v}_1 \times \underline{B}_0) + \eta \nabla^2 \underline{B}_1 \quad (1)$$

unless perturbations are constant along a field line ($\nabla \times (\underline{v}_1 \times \underline{B}_0) = 0$) or the length scale for diffusion becomes small. The presence of the sun's extremely dense photosphere, which anchors magnetic footpoints so that coronal disturbances must vanish there, would seem to exclude the first possibility (Hood 1984) except for very special equilibria (Mok and Van Hoven 1982). On the other hand modes which have a short wavelength perpendicular to the magnetic field and for which the second case occurs, called resistive ballooning modes, are known to be unstable in a wide range of conditions relevant to fusion plasmas (see, e.g. Drake and Antonsen 1985). We find that the same is true for arcades in the solar corona.

MODE EQUATIONS

The equations describing the linear evolution of resistive ballooning modes are obtained by using a modified WKB expansion in the short perpendicular wavelength ϵ , while variations of the perturbations along the field are described by a slowly varying amplitude, on which the line tying boundary conditions are imposed. In this way the resistive MHD equations are reduced (to lowest order in ϵ), to a fourth order system of ordinary differential equations for the amplitudes along the field lines:

$$\frac{d\tilde{\phi}}{d\theta} + r \left[1 + \frac{-K^2}{R\mu\gamma} \right] / K^2 \frac{B^2}{B_\theta^2} \tilde{A} = 0 \quad (2)$$

$$\frac{d\tilde{U}}{d\theta} + \frac{B}{B_\theta} \left[\frac{B^2 + \mu\gamma_s p}{\mu\gamma_s B^2} \right] \left[\tilde{p}r + \tilde{\phi} \frac{d \ln p}{d \ln r} \right] + 2\tilde{\phi} \frac{B_\theta}{B} + \frac{K^2}{R\mu\gamma} \frac{\mu p}{B B_\theta} r \tilde{p} = 0 \quad (3)$$

$$\frac{d\tilde{p}}{d\theta} + r\gamma^2 \mu p \frac{\tilde{U}}{p} \frac{B}{B_\theta} - \frac{\tilde{A}}{K^2} \frac{B^2}{B_\theta^2} \frac{d \ln p}{d \ln r} = 0 \quad (4)$$

*

$$\frac{d\tilde{A}}{d\theta} - 2\tilde{p} \frac{\mu p}{B^2} + \mu p \gamma^2 \tilde{\Phi} \frac{K^2}{B^2} = 0 \quad (5)$$

The arcade is symmetric around $\theta = 0$ and extends infinitely in the z -direction. The photosphere is located at $\theta = -\pi/2$ and $\theta = \pi/2$, where the line tying conditions are $\tilde{\Phi} = 0$, $\tilde{u} = 0$. $\tilde{\Phi}$, \tilde{p} , \tilde{A} , \tilde{u} are the perturbed scalar potential, pressure, parallel vector potential and flow velocity respectively. K^2 is the squared norm or the perpendicular wave number, and is a quadratic function of θ . R_m is the magnetic Reynolds number for the length scale ϵ . Equations (2)-(5) depend parametrically on r , and the resulting growth rate γ also is a function $\gamma = \gamma(r)$. The radial structure of the mode is therefore not established to lowest order. Details of this problem may be found in Hood, 1986. However, the maximum of the function $\gamma(r)$, when it is positive, is the actual physical growth rate of the mode (Connor, Hastie and Taylor 1978). The driving term for the instability is the radial pressure gradient, when it is negative, while magnetic shear and compressibility tend to have a stabilising effect. Our results will be illustrated for the equilibrium

$$\begin{aligned} B_\theta &= B_0 r e^{-r/2} \\ B_z &= \lambda B_0 (\sigma + (2 + 2r - r^2) e^{-r})^{1/2} \\ \mu p &= (1 - \lambda^2) B_0^2 / 2 (\sigma + (2 + 2r - r^2) e^{-r}) \end{aligned} \quad (6)$$

which depends on the parameters λ , σ . The same results hold in general because the local analysis depends on the values of fields and pressure on each surface independently.

RESULTS

In general, given an equilibrium, there are certain ranges of magnetic surfaces for which the system (2)-(15) predicts instability even without dissipation (Hood 1986). As expected we find that in this case resistivity has little influence on the growth rates that are found. On the other hand, in regions where the equilibrium is stable to ideal modes, we find that resistivity introduces a purely growing mode with eigenvalue γ depending linearly on the inverse magnetic Reynolds number R_m^{-1} . As ideal marginal stability is approached, or alternatively if the perpendicular wavelength is decreased, one finds that the power dependence decreases gradually to $\gamma \propto R_m^{-1/3}$, as shown in Fig. 1, where curves for different values of the equilibrium parameters are shown. The main conclusion is that within the resistive MHD approximation cylindrically symmetric arcades with pressure falling with radius are unstable to resistive localised modes; the growth rates, close to ideal marginal stability, are large, typically in the range $10^{-2} \omega_A < \gamma < 10^{-1} \omega_A$ so that it would appear that energy could be released during 10-100 Alfvén times. The wavelength of the modes is expected to be limited by the ion gyroradius, when stabilising drift effects must be taken into account. On the other hand the suggestion has been made (Weiland and Mondt 1985) that the nonlinear development of these localised modes could lead to an explosive instability. In any case the nonlinear evolution of resistive ballooning modes should be studied to assess their overall relevance to the violent and rapidly evolving phenomena observed on the sun.

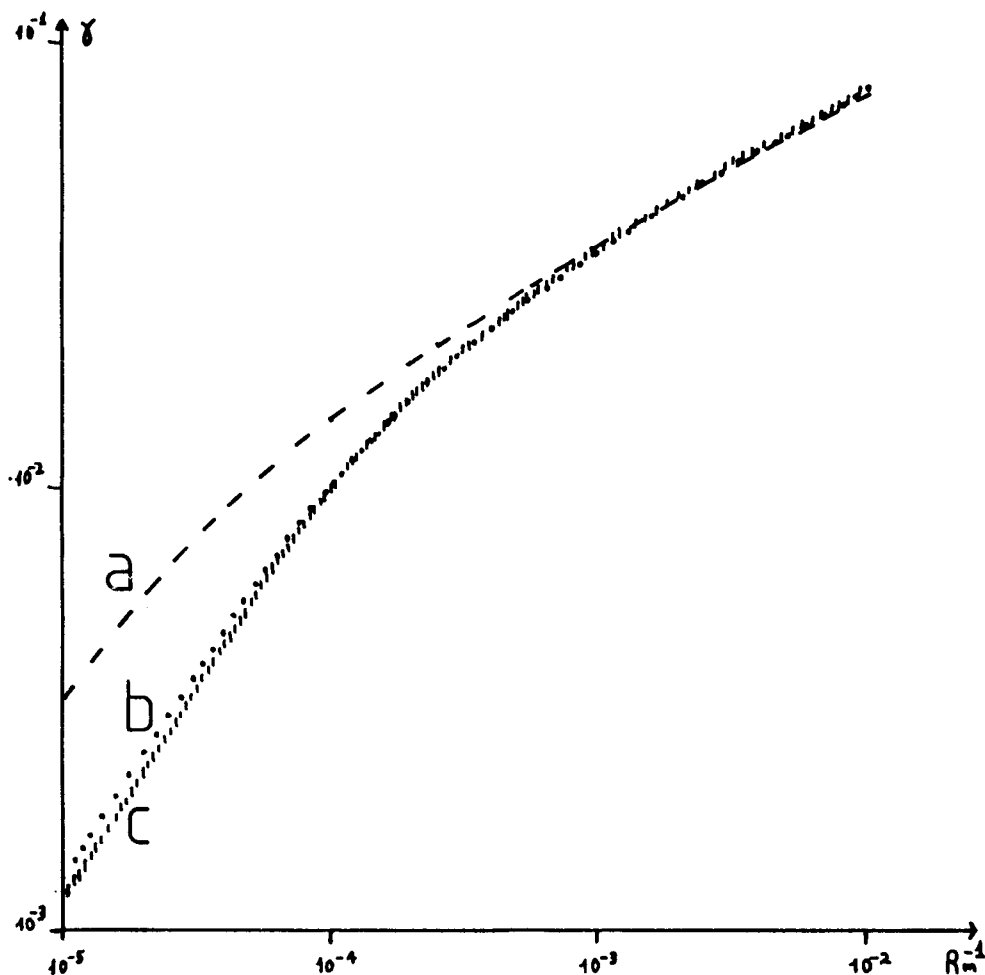


Fig. 1. Growth rate γ (normalised to the Alfvén frequency) as a function of R_m^{-1} for different values of equilibrium parameters: a- $\lambda = 0.14$, $\sigma = 0.25$, $r = 1.5$, b- $\lambda = 0.2$, $\sigma = 0.15$, $r = 1.76$, c- $\lambda = 0.21$, $\sigma = 0.20$, $r = 1.65$. In all cases, the equilibrium is ideally stable at every radius.

REFERENCES

- Connor, J.W., Hastie, R.J. and Taylor, J.B. (1979) "High mode number stability of an axisymmetric toroidal plasma", Proc. Roy. Soc. London A365, 1.
- Drake, J.F. and Antonsen, T.M. (1985) "Analytic theory of resistive ballooning modes", Phys. Fluids 28, 544.
- Hood, A.W. (1984) "An energy method for the stability of solar magnetohydrostatic atmospheres", Geophys. Astrophys. Fluid Dynamics 28, 223.
- Hood, A.W. (1986) "Ballooning instabilities in the solar corona: conditions for stability" Solar Phys., in press.
- Mok, Y. and Van Hoven, G. (1982) "Resistive magnetic tearing in a finite length pinch" Phys. Fluids 25, 636.
- Velli, M. and Hood, A.W. (1986) "Resistive ballooning modes in line tied coronal fields: I - arcades", submitted to Solar Phys.

EFFECTS OF FLOWS ON VISCOUS AND RESISTIVE MHD STABILITY

Giorgio Einaudi

Scuola Normale Superiore, 56100 Pisa (Italy)

In many solar applications the viscosity appears to be more important than resistivity and the observations show clearly that in some cases the fluid velocity is comparable to the local Alfvén velocity.

Equilibrium flows and viscosity can considerably change the properties of resistive instabilities.¹⁻⁵

In this paper it is shown that both the growth rate of the instability and the spatial profile of the mode strongly depend on few relevant parameters, namely the ratio r between the magnetic (a_B) and the velocity (a_V) scale lengths, the ratio V between the fluid (v_O) and the Alfvén (v_A) velocities and the ratio M between the Lundquist (S) and the Reynolds (R) numbers.

In order to discuss these instabilities in solar conditions, let us consider an idealized configuration in which the plasma is flowing in the z -direction along the magnetic field B_O with a velocity v_O . Both B_O and v_O vary in the x -direction. In order to take into account the shear of the magnetic field possibly induced by photospheric motions, we will consider $B_O \sim \tanh x/a_B$, so that resistivity can be important in a layer around $x = 0$.

As far as the velocity is concerned we will discuss two different velocity profiles, with different hydrodynamic stability properties.

Eq. a): $v_O \sim \tanh x/a_V + 1$ stable against Kelvin-Helmholtz instability

Eq. b): $v_O \sim \operatorname{sech} x/a_V$ unstable against Kelvin-Helmholtz instability.

Assuming the perturbations to behave as $\sim \exp [i(kz + \omega t)]$, the

linear stability analysis of the above configurations shows that the relevant parameters are ^{4,5}

$$r = \frac{a_B}{a_V}, \quad V = \frac{v_O}{V_A}, \quad S = \frac{\tau_R}{\tau_A}, \quad R = \frac{\tau_V}{\tau_A}, \quad \alpha = ka_B.$$

The resistive time τ_R and the viscous time τ_V are defined as:

$$\tau_R = \frac{4\pi a_B^2 \sigma}{c^2} \quad \tau_V = \frac{\rho a_B^2}{\eta_1}$$

c is the speed of light, σ the electrical conductivity.

$$\eta_1 = \frac{3}{10} \frac{n_i T_i}{\omega_{ci} \tau_i}$$

is the perpendicular viscous coefficient, using the same notations as Braginskii (1965). It can be shown that η_1 , which is the smallest of the coefficients appearing in the stress tensor, is the only one important in this calculation.⁶

The results can be summarized as follows:

- 1) The frequency $\omega = \omega_R + i\gamma$ of the mode is complex and $\omega_R \sim kv(0)$.
- 2) There exists a transition from a behaviour similar to the static tearing mode to a behaviour similar to a Kelvin-Helmholtz mode. This transition occurs when $\epsilon = r V \sim V^{1/3}$; here ϵ is a measure of the relative importance of the velocity gradients with respect to the magnetic gradients. When $\epsilon > V^{1/3}$, we find a stabilization for Equilibrium a and a rapid increase of the growth rate for Equilibrium b. This difference is due to the different stability properties against K.-H. modes of the two configurations.
- 3) It is well known that the viscosity stabilizes the static tearing mode. In presence of flows this is still true only when $\epsilon \ll 1$

or $S/R < 1$. Otherwise we have to distinguish between Equilibrium a) and b).

Equilibrium a) with $\varepsilon \sim V^{1/3}$ and $S/R > 1$:

The growth rate of the mode increases with the viscosity and presents a maximum value for $R \sim 20$ which is independent of the resistivity. For $R > 20$ the viscosity again stabilizes the mode.

Equilibrium b) with $\varepsilon > V^{1/3}$:

The viscosity is important and represents a stabilization factor only when $R \sim 1$.

- 4) In all cases there is a non-zero x-component of the magnetic field perturbation at $x = 0$ and therefore all these modes are reconnecting modes. The level of reconnection is a function of the growth rate of the mode, being bigger for slowly growing instabilities.
- 5) When $\varepsilon \gtrsim V^{1/3}$, in all cases the perturbations are not localized close to the resistive layer as in the static tearing mode, and therefore the typical scale length of the mode is a_B and not the width δ of the resistive layer as in the static case.

It is clear that the effects of the instability on the equilibrium configuration can be studied only through a non-linear analysis. Depending on the values of the relevant parameters the non-linear evolution of the instability can be very different.⁸ These exist situations (Eq.(b), $\varepsilon > V^{1/3}$, $\alpha \sim 1$) in which the instability can trigger a turbulent cascade with a consequent important dissipation of both the equilibrium magnetic and kinetic energies. In these cases the instability is similar to a Kelvin-Helmholtz instability with growth time few per cent of the Alfvén time and a small level of reconnection. There are other situations (Eq.(a), $\varepsilon \sim V^{1/3}$, $\alpha \lesssim 0.1$)

in which the instability does not produce a strong turbulence and a little amount of energy is involved, but it is easy to accelerate particles through the associated parallel (to B) electric field. In these cases the instability is similar to a resistive instability with growth time slower than in the previous case but with important effects due to the viscosity.

REFERENCES

- 1) I. Hofmann, Plasma Phys. 17, 143 (1975).
- 2) M. Dobrowolny, P. Veltri, and A. Mangeney, J. Plasma Phys. 29, 393 (1983).
- 3) R.B. Dahlburg, T.A. Zang, D. Montgomery, and H.Y. Hussaini, Proc. Natl. Acad.Sci. USA 80, 5798 (1983).
- 4) G. Einaudi, and F. Rubini, Phys. Fluids, Aug. 1986, in press.
- 5) G. Einaudi, and F. Rubini, Phys. Fluids, submitted.
- 6) S.I. Braginskii, Rev.Plasma Phys. 1, 205 (1965).
- 7) Y. Mok, Astron. Astrophys., submitted; U.C.I. Techn.Rept. 86-13.
- 8) V. Carbone, P. Veltri, and G. Einaudi, Proocedings II CESRA workshop on "Particle Acceleration and Trapping in Solar Flares", Aubigny, France, June 1986, in press.

LARGE-SCALE ELECTRIC FIELDS RESULTING FROM
MAGNETIC RECONNECTION IN THE CORONA

R.A. Kopp
Los Alamos National Laboratory

G. Poletto
Osservatorio Astrofisico di Arcetri

INTRODUCTION

Magnetic reconnection is an inevitable consequence of non-ideal MHD processes in the highly conducting coronal plasma. It occurs whenever the solar magnetic field has been stressed or topologically rearranged to the point where one or more imbedded sheet currents appear. Reconnection can take place on a wide variety of scales - ranging from small unresolved magnetic elements possibly related to the quasi-steady process of coronal heating (van Ballegooijen, 1985), to active region complexes that spawn major transient events, such as eruptive prominences, surges, and flares. Regardless of scale, however, or of the particular details of the reconnection process considered, the magnitude E_1 of the electric field in the vicinity of the neutral point (or "X"-line) is directly proportional to the merging rate, i.e. the rate at which plasma motions transport magnetic flux into the diffusion region where merging occurs:

$$E_1 = - \frac{1}{c} v_i B_i \quad (1)$$

(Petschek, 1963; Vasyliunas, 1975), where subscript i refers to quantities in the plasma inflow region near the neutral line.

At the present time the observational detection of strong d.c. E-fields at coronal heights has yet to be made but nevertheless holds promise (Foukal et al., 1983, 1984). This may ultimately provide the most direct means for probing the details of reconnection processes occurring there. In the following we have chosen to concentrate on a theoretical determination of the expected magnitude of E_1 , during the decay phase of two-ribbon flares. The major characteristics of these largest and most energetic of solar events are commonly interpreted in terms of reconnection occurring over an extended time interval above the chromospheric flare site, and we regard it as quite likely that coronal electric fields will first be detected here (e.g., in the associated post-flare loop system).

ELECTRIC FIELD CALCULATED BY THE METHOD OF FORBES AND PRIEST

According to the reconnection picture of two-ribbon flares (Hirayama, 1974, Kopp and Pneuman, 1976), the leading edges of the bright H α ribbons define at any instant the location in the chromosphere of the magnetic separatrices that meet at

the coronal neutral line. Forbes and Priest (1984) used this fact to derive the interesting result that, in a cartesian system with one ignorable coordinate (i.e., 2-D reconnection), the electric field at the neutral point can be expressed entirely in terms of chromospheric quantities, namely,

$$E_1 = \frac{1}{c} V_R B_n, \quad (2)$$

where V_R is the measured ribbon velocity and B_n is the normal component of the photospheric magnetic field at the ribbon leading edge. Note that the value of E_1 calculated from this expression is independent of the detailed shape of the merging coronal field lines; in particular, E_1 does not depend on the actual height of the neutral point itself.

We have applied the method of Forbes and Priest to the large two-ribbon flare of 29 July, 1973, for which both detailed H α observations and magnetic data are available. For this flare the ribbons were long, nearly straight, and parallel to each other, and a 2-D model for the coronal field geometry may be adequate. The lower curve in Figure 1 shows the temporal profile $E_1(t)$ calculated from Equation (2), using the ribbon leading-edge velocity as determined by Moore et al. (1980) and the photospheric magnetic data published by Michalitsanos and Kupferman (1974). One sees from this calculation that, as reconnection sets in at the beginning of the decay phase, the electric field grows rapidly to reach a maximum value of about 2 V/cm within just a few minutes. Thereafter E_1 declines monotonically with time, as one would expect for any relaxation process: as more and more of the magnetic flux disrupted by the flare reconnects, the merging rate itself decreases.

MAXIMUM RECONNECTION RATE

The upper curve in Figure 1 illustrates crudely the behavior which the electric field would have, were reconnection occurring at every instant at the maximum possible rate allowed by compressible reconnection theory (Soward and Priest, 1982), i.e., were the merging being highly forced by the inflow boundary conditions. This maximum merging rate corresponds to

$$E_1(\text{max}) = \frac{1}{c} B_i a_i M_A(\text{max}), \quad (3)$$

where $a_i \equiv B_i/(4\pi\rho)^{1/2}$ is the Alfvén speed in the inflow region and $M_A(\text{max})$ is an upper limit to the Alfvénic Mach number of the inflow provided by the theory. The reader is referred to Poletto and Kopp (1986) for specific details of this calculation. The important point to note is that, in addition to the general shape of the monotonic decline being similar for both curves, the maximum reconnection rate is more than an order of magnitude larger than the empirically determined rate. Thus, whereas in many physical situations (e.g. during the impulsive phase of geomagnetic storms or solar flares) reconnection is generally regarded as being strongly driven (Vasyliunas, 1975), such does not seem to be the case throughout the flare decay phase; here the merging proceeds at a much more leisurely pace dictated by dynamical relaxation of the external flow field.

RECONNECTION IN ACTUAL FLARE GEOMETRIES

Strictly speaking, the method of Forbes and Priest (1984) for calculating the electric field at the neutral line can be used only in certain 3-D geometries for which

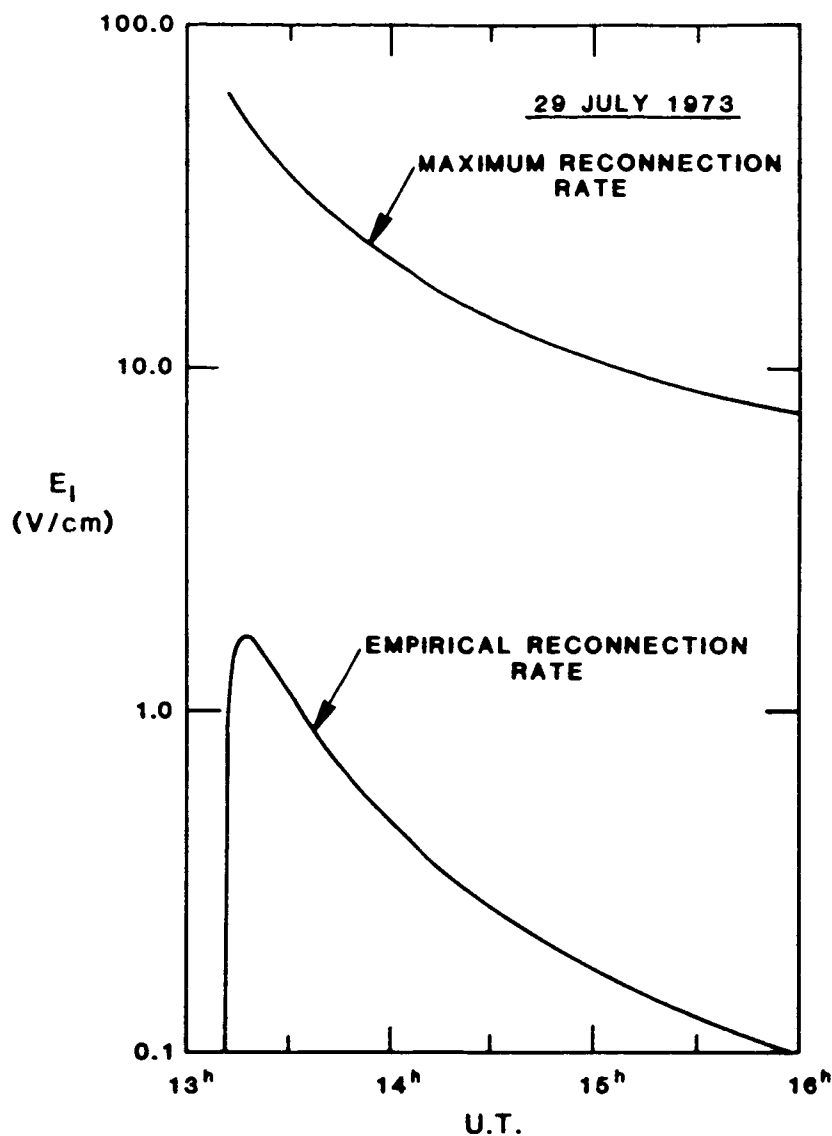


Figure 1. Time history of the electric field at the neutral line for the 29 July, 1973 flare, calculated by the method of Forbes and Priest (lower curve) and by the assumption of strongly driven reconnection (upper curve).

one coordinate is ignorable. Whereas the soft X-ray images from Skylab (Moore et al., 1980) suggest that this condition might have been approximately satisfied for the 29 July, 1973 flare, the vast majority of flares occur in regions of complex magnetic structure. We should inquire, then, as to what practical use can be made of the method in general.

Perhaps the most striking observational feature of the loop prominence systems associated with large flares, not taken into account in 2-D reconnection scenarios, is the tendency for individual loops to "lean away" from each other. Especially apparent when on occasion we view a loop system edgewise at the solar limb, this is generally attributed to an "edge effect" of the coronal magnetic field caused by the finite size of the active region (Forbes, 1985; Rust and Roy, 1971). A direct result of this "fanning out" of the loops is that the magnetic field

strength B_i in the inflow region will be smaller than it would be, were the loops situated in parallel planes.

A rough estimate of this effect on the reconnection rates presented above can be made as follows. Let L denote the length in the chromosphere threaded by field lines undergoing reconnection at higher levels (i.e. the length of the H α flare ribbons) and let L_x be the corresponding length of the X-line in the corona (i.e., the distance spanned by the tops of newly formed loops). Then, relative to the 2-D scenario described earlier, B_i will be smaller by the factor L/L_x . For a given inflow velocity v_i , E_1 (and thus the local rate of flux merging) will be smaller by the same amount. However, the maximum reconnection rate, as measured by $E_1(\text{max})$ in Equation (3), is proportional to B_i^2 and so decreases more rapidly than does E_1 as determined by the Forbes-Priest method. Given the uncertainties in the amount of spreading of the loops seen in the disk flare of 29 July, 1973, it is not possible to say precisely how much of the vertical displacement between the two curves of Figure 1 can be explained thusly. However, we do not consider it likely to bring them into perfect agreement in this way, as one would require $L/L_x < 0.1$ - a really large spreading factor for which there is no observational support.

In view of the paucity of empirical data on the 3-D loop geometry above any particular flare site, it is tempting to use the topological property on which the Forbes and Priest method was formulated in idealized 2-D geometries, to investigate the magnetic structure of more complex active regions. This may provide useful applications on at least two fronts. First, on the active region scale itself, we can replace Equation (2) by an integral relation for the total rate of flux merging, which gives the net potential difference Φ_1 along the coronal neutral line as a function of the instantaneous motion of either flare ribbon:

$$\Phi_1 = \int_0^{L_x} E_1(l_x) dl_x = \frac{1}{c} \int_0^L v_R(l) B_n(l) dl, \quad (4)$$

where the first path integral is taken along the coronal X-line and the second is along the ribbon. Φ_1 may be of practical importance for explaining the continuous acceleration of particles during the flare decay phase.

Second, even lacking detailed knowledge of the coronal field structure, on a fine spatial scale it should be possible to map fieldline connections between the two flare ribbons. This is because at any point l of a ribbon the quantity $1/c v_R(l) B_n(l)$ represents the local rate at which the magnetic separatrix is sweeping open flux into the growing arcade of closed loops. A newly formed closed field line should have the same value for this quantity at each of its footpoints. The fieldline connections thereby established might under ideal circumstances be compared with observed post-flare loop orientations, providing an additional test of the reconnection hypothesis. We are presently attempting to apply this method to the two-ribbon flare of 20 June, 1980.

REFERENCES

- Forbes, T.G.: 1985, private communication.
 Forbes, T.G., Priest, E.R.: 1984, in Solar Terrestrial Physics: Present and Future (NASA Reference Publ. 1120, ed. D.M. Butler and K. Papadopoulos, 1-35.
 Foukal, P., Miller, P., Gilliam, L.: 1983, Solar Phys. **83**, 83.

- Foukal, P., Landman, D.: 1984, Proc. IAU Coll. No. 86 (ed. G.A. Doschek), 25.
- Hirayama, T.: 1984, Solar Phys. 34, 323.
- Kopp, R.A. and Pneuman, G.W.: 1976, Solar Phys. 50, 85.
- Michalitsanos, A.G., Kupferman, P.: 1974, Solar Phys. 36, 304.
- Moore, R., McKenzie, D.L., Švestka, Z., Widing, K.G. and 12 co-authors: 1980, in Solar Flares (ed. P.A. Sturrock), (Colorado Associated University Press: Boulder), 341.
- Petschek, H.E.: 1963, in The Physics of Solar Flares (NASA SP-50), 425.
- Poletto, G., Kopp, R.A.: 1986, in The Lower Atmosphere in Solar Flares (ed. D.F. Neidig), in press.
- Rust, D.M., Roy, J.-R.: 1971, in Solar Magnetic Fields (ed. R. Howard), (Reidel Publ. Co.: Dordrecht-Holland), 569.
- Soward, A., Priest, E.R.: 1982, J. Plasma Phys. 28, 335.
- van Ballegooijen, A.A.: 1985, Astrophys. J. 298, 421.
- Vasyliunas, V.M.: 1975, Rev. Geophys. and Space Phys. 13, 303.

DYNAMIC EVOLUTION OF CORONAL MAGNETIC FIELDS

Richard S. Steinolfson
 Institute for Fusion Studies
 University of Texas at Austin
 Austin, Texas 78712

ABSTRACT

The response of coronal magnetic fields to photospheric motion is investigated using a time-dependent, two-dimensional MHD simulation. Starting with an initially uniform field, a circular section of the loop base is slowly rotated to represent the photospheric motion. The field lines at the base move with this flow in a manner consistent with the generated electric fields. The subsequent evolution of the field and flow can be characterized as passing through several distinct configurations. In the earliest phase the kinetic energy is negligible, and the current and field are parallel throughout most of the cylinder. This is followed by a period in which the field rotation increases, the axial field at and near the axis increases, and the axial field decreases in two cylindrical regions away from the axis. When the field in an appreciable portion of the cylinder has undergone one complete rotation, a rapid change in field configuration occurs with a large portion of the field making several rotations at large radii and a corresponding large reduction in the axial field.

INTRODUCTION

Based on the assumption that the energy source for some of the explosive behavior observed in the solar corona (e.g., flares, eruptive prominences) is the in-situ magnetic field, there has been considerable interest over the years to develop theories and, more recently, numerical models to describe the generation of this nonpotential magnetic energy. The present study will be concerned with the coronal loop, in which compact flares may occur, as opposed to coronal arcades, in which eruptive prominences and the more energetic two-ribbon flares may originate.

In the case of loops, one theory advocates their emergence from the convective zone as highly concentrated helically twisted flux ropes (Piddington, 1975). The problem here is to explain how the loop remains stable for relatively long time periods before suddenly going unstable. In this study, we adopt the opposing view that sheared, twisted fields in coronal loops form as a result of convective or photospheric motion at the base of initially potential coronal magnetic configurations.

Numerous studies of magnetic energy build-up in coronal fields have been based on the premise that the field evolution must satisfy the requirement of a vanishing Lorentz force (e.g., Sturrock and Woodbury, 1967; Zweibel and Boozer, 1985). The reasoning here being that unrealistically large thermal pressures would be required to balance the Lorentz force in the relatively low beta corona: a not unreasonable argument **providing** the dynamics are neglected. However, when the coronal motion is included in a low beta (ratio of thermal to magnetic pressures) plasma, a simple order-of-magnitude analysis estimates the following relation between the changes in velocity and magnetic field ($\delta v, \delta B$), the instantaneous values (v, B) and the local Alfvén velocity (v_a) when $\mathbf{J} \times \mathbf{B} \neq 0$:

$$\frac{v}{v_a^2} \delta v \approx \frac{\delta B}{B}.$$

Hence, as would be expected, the unbalanced Lorentz force can be balanced by the flow dynamics, although the question remains as to how large these flows must be. We now explore the interaction between the field and flow. For the simulation presented herein, the Lorentz force in the latter stages of evolution is far from vanishing, and the nonpotential magnetic energy is considerably larger than the kinetic energy.

MODEL AND COMPUTATIONAL PROCEDURE

A coronal loop is approximated by a cylinder with an initially uniform magnetic field. For this exploratory study gravity is neglected, the evolution is axisymmetric, and the corona is treated as

incompressible with a low enough beta that thermal pressure gradients are negligible. The dynamics now uncouple from the energetics, and the equations that must be solved are the following:

$$\frac{d\vec{v}}{dt} = \frac{1}{4\pi\rho}(\nabla \times \vec{B}) \times \vec{B},$$

$$\frac{\partial \vec{B}}{\partial t} = \nabla \times \left(\vec{v} \times \vec{B} - \frac{c^2\eta}{4\pi} \nabla \times \vec{B} \right).$$

These equations are solved numerically using the semi-implicit method of Harned and Kerner (1985). This differencing scheme offers the advantage of permitting time steps larger than those imposed by the fast modes (the explicit CFL condition). In addition, it is relatively simple to code, and the computing time for each time step is comparable to that for explicit methods. An extension of this method by Harned and Schnack (1986), which removes the shear Alfvén constraint and thereby remains stable for even larger time steps, is currently being investigated.

The boundary conditions at the loop center are trivial in this axisymmetric simulation. The maximum radius of the computational cylinder is large enough (twice the radius within which the base is rotated) that the physical variables at this boundary are not modified significantly: zero-order extrapolation is sufficient. At the loop mid-point a form of symmetry conditions, consistent with each end of the loop being rotated by the same amount in opposite directions, is used. The only velocity at the base is the rotation (azimuthal) velocity, which increases linearly out to three-fourths the maximum rotation radius and then decreases linearly to zero. The azimuthal magnetic field at the base is updated at each time step using the ideal induction equation, and zero-order extrapolation provides the radial field. The axial field is maintained constant at its initial uniform value at the base in order that the flux into the loop remain constant. One check on the numerical solution is to compute the flux through the loop mid-point. For the simulation in the following section, this flux remained within a few percent of the flux into the loop.

NUMERICAL RESULTS

The physical conditions for the simulation discussed here are: density = 10^9 cm^{-3} , initial magnetic field = 10.54g , temperature = $1.6 \times 10^6 \text{ K}$, Lundquist number = 10^4 , maximum rotation radius (a , the value used to normalize distance) = 10^9 cm , total loop length = $2 \times 10^9 \text{ cm}$. The initial beta and Alfvén velocity then become 0.1 and 727 km s^{-1} . The maximum rotation velocity is 10 km s^{-1} , which is 1.4% of the initial Alfvén velocity.

The evolution of the magnetic and kinetic energies is shown in Fig. 1. The plotted value is the nonpotential magnetic energy or that in excess of the initial value of $5.5 \times 10^{28} \text{ ergs}$. As illustrated in the figure, the current and field are approximately parallel in the early stages when the kinetic energy is negligible relative to the excess magnetic energy. This is true throughout the cylinder with the exception of thin layers at the cylinder base and center. Although the current and field are parallel (i.e., $\mathbf{J} = \alpha \mathbf{B}$), the quantity α varies considerably in space (for $t = 19.4 \text{ min.}$, $-6 < \alpha < 1.5$).

After approximately twenty minutes, the kinetic energy rises rapidly followed by a period of slower growth when both energies grow exponentially at about the same rate. After this latter stage both energies increase dramatically. The magnetic configuration differs in the above three phases (negligible kinetic energy, uniform growth, rapid rise), and each of these is discussed below.

The approximate exponential growth of the magnetic energy (up to the last phase) occurs at a rate of 0.036 in terms of the initial Alfvén time. (For comparison, this is about equal to the maximum growth of the tearing mode at a Lundquist number of 10^3 .) The present growth rate is independent of the Lundquist number.

Some of the field lines, typical of the field evolution in the first phase (negligible kinetic energy), are shown in Fig. 2. Distances in this and subsequent figures are normalized to the maximum rotation radius at the base, and the circle indicates the location of the maximum rotation. The azimuthal component has been zeroed out for this presentation to illustrate how these results compare with the analytic solution of Zweibel and Boozer (1985; Fig. 1). Both solutions indicate a bending of the field line

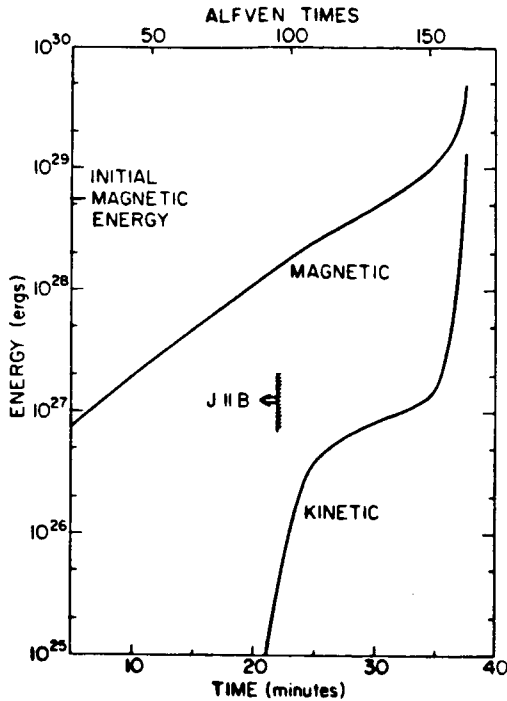


Figure 1. Temporal increase in excess magnetic and kinetic energies integrated over one half the cylinder length.

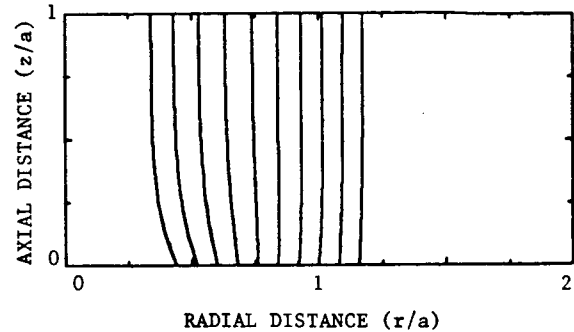


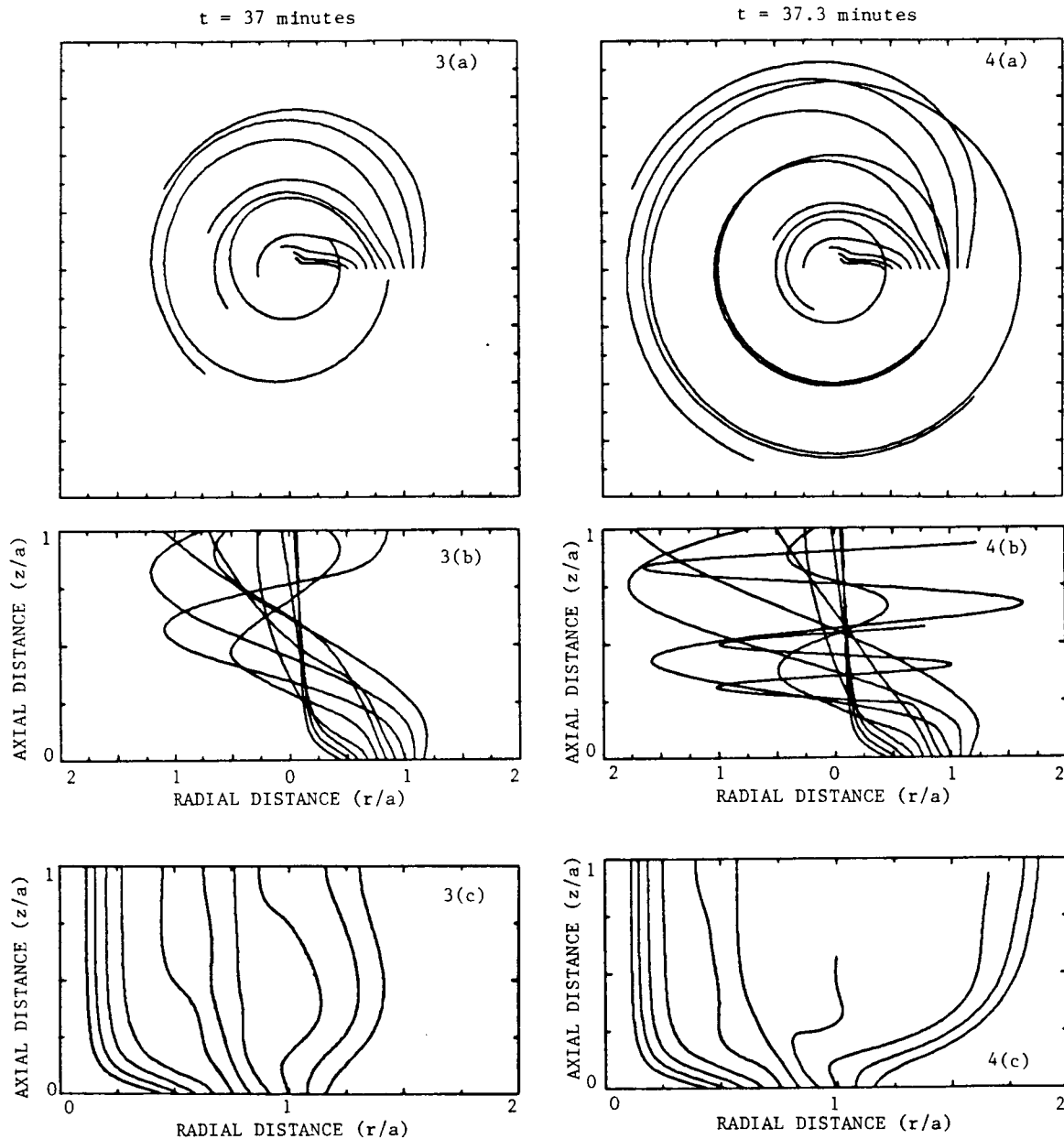
Figure 2. Field lines projected into the r - z plane for $t = 19.4$ minutes.

toward the axis (which is largest near the base) inside the maximum twist location, and a slight outward bending beyond the twisted region. Between the base and the loop mid-point, the field lines are rotated by a maximum of about 70° for the solution in Fig. 2. The increase in the axial field strength near the cylinder axis (and the consequent inward bending of the field lines) coincides with an azimuthal current in the positive azimuthal direction that peaks at a radius of about 0.2.

The primary current system established in the first phase prevails during the subsequent evolution. This system consists of (a) an axial current concentrated near the axis flowing toward the base, (b) a radial current inside the maximum rotation radius near the base and directed away from the axis, and (c) the azimuthal current referred to above. In the later stage additional currents develop near the radius of maximum twist and beyond.

During the second phase when the magnetic and kinetic energies grow at similar rates, the field twist and shear continually increase. The field lines near the transition between the second and third phase are shown in several views in Fig. 3. Notice that two field lines now undergo approximately one complete rotation between the base and loop mid-point. One starts at the base at the location of maximum rotation and the other is at the edge of the rotated region. It is interesting that the lines between these two only rotate about half as much. This behavior is mainly due to the fact that the lines with the large twist pass through regions where the axial field strength has been reduced to about 10% of its initial value, while between these regions the axial field increases by about 10%. Azimuthal currents in the negative (positive) azimuthal direction just inside (outside) the maximum rotation and the primary currents near the axis are consistent with the modified axial field. An axial current centered at maximum rotation flowing away from the base contributes to the large rotation at large radii.

A dramatic change in the field configuration occurs in the short interval (~ 18 sec) between the times in Fig. 3 and Fig. 4. Notice that this reconfiguration only occurs for the field lines originating at the location of maximum twist and beyond. The inner four field lines remain virtually unaffected. The axial field strength is now reduced substantially (down to 1% of the initial value) in a large region ($0.75 < r < 1.5$ and $0.2 < z \leq 1$). This axial field reduction permits some field lines to rotate several times before reaching the loop mid-point, as seen in Fig. 4 (a), (b). (Numerical problems are responsible for not



Figures 3,4. Field lines near the end of the uniform growth (37 minutes) and in the rapid growth (37.2 minutes) phase. The same field lines are shown in all views at both times. The field lines as they would appear when seen from the cylinder base are drawn in the top figures (a), and the view from the side is shown in the center figures (b). The bottom figures (c) correspond to the projection in Figure 2. The field line with the circle at the base is at the location of maximum rotation.

extending the two field lines to the mid-point in Fig. 4(b), (c)).

The axial field does not appear to have reversed direction in this simulation, although it does become very small. (Note that the fields may have temporarily reversed at times that were not selected for display.) In other simulations where the rotation velocity is a larger fraction of the initial Alfvén velocity (a higher density was used with the same rotation velocity), the axial field does reverse, and magnetic islands are formed for relatively short time periods. The qualitative evolution of this latter computation, however, is the same as for the solution discussed here.

Another reconfiguration occurs 0.2 minutes after the time used for the results in Fig. 4. In this case all of the field lines shown in Figs. 2-4 collapse toward the axis with comparatively small rotation (less than 270 degrees) and with the same general shape as the inner four lines in Fig. 3(c) and Fig. 4(c). This stage is not discussed further since it is questionable whether such behavior would ever be obtained if the solution had the extra degree of freedom available in a three-dimensional simulation.

CONCLUSION

This study has shown that photospheric motion can produce enough free magnetic energy in an initially potential magnetic loop to explain the energy source of the compact flare. However, in contrast to assumptions that are frequently made, the energy build-up does not evolve through a series of equilibrium states, the current and field do not remain parallel during the process, and when the current and field are parallel the proportionality between them (α) varies in space.

ACKNOWLEDGMENTS

The author has benefited considerably from conversations with Drs. D. Barnes, Z. Mikic, D. Schnack, T. Tajima, and E. Zweibel. This work was initiated with support from AFGL contract F19628-85-K-0006 and currently receives support from NASA under grant NAGW-846 and from the Atmospheric Science Section of NSF under grant ATM 85-06646. Acknowledgment is also made to NSF for providing computer time at the San Diego Supercomputer Center.

REFERENCES

- Harned, D.S., and Kerner, W. 1985, *J. Comp. Phys.*, **60**, 62.
- Harned, D.S., and Schnack, D.D. 1986, *J. Comp. Phys.* (in press)
- Piddington, J.H., 1975, *Astrophys. Space Sci.*, **34**, 347.
- Sturrock, P.A., and Woodbury, E.T. 1967, *Plasma Astrophysics*, ed. P.A. Sturrock (New York: Academic), p. 155.
- Zweibel, E.G., and Boozer, A.H. 1985, *Ap. J.*, **295**, 642.

BIBLIOGRAPHIC DATA SHEET

1. Report No. NASA CP-2442	2. Government Accession No.	3. Recipient's Catalog No.	
4. Title and Subtitle CORONAL AND PROMINENCE PLASMAS		5. Report Date December 1986	
		6. Performing Organization Code 602.6	
7. Author(s) A. I. Poland, Editor		8. Performing Organization Report No. 86BO536	
9. Performing Organization Name and Address Solar Physics Branch Laboratory for Astronomy and Solar Physics Goddard Space Flight Center Greenbelt, Maryland 20771		10. Work Unit No.	
		11. Contract or Grant No.	
		13. Type of Report and Period Covered Conference Publication	
12. Sponsoring Agency Name and Address National Aeronautics and Space Administration Washington, D. C. 20546		14. Sponsoring Agency Code	
15. Supplementary Notes			
16. Abstract <p>This report describes the results of a series of workshops conducted at Goddard Space Flight Center (GSFC) to better understand the physical processes occurring on the sun. The workshops were attended by approximately 80 people from government and academia who were selected for their expertise in solar research. There were several attendees from eastern and western Europe, Japan, and China as well as the U.S. The focus of the meeting was new insights into solar plasma physics provided by Solar Maximum Mission Satellite (SMM) data and new advances in theory. One of the more compelling results of the workshops was the necessity of including dynamics in understanding solar phenomena.</p>			
17. Key Words (Selected by Author(s)) Solar Physics, Plasma Physics, Solar Maximum Mission, Corona, Prominences		18. Distribution Statement Unlimited—Unclassified Subject Category 92	
19. Security Classif. (of this report) Unclassified	20. Security Classif. (of this page) Unclassified	21. No. of Pages 479	22. Price* A21